
THE UNIVERSITY *of* EDINBURGH

# Synaptome Mapping of the Postsynaptic Density 95 Protein in the Human Brain

*Olimpia E. Curran*

Doctor of Philosophy

University of Edinburgh

2017

# Declaration

I declare that this thesis was composed by myself and that the work contained therein is my own, except where explicitly stated otherwise in the text. I confirm that the work has not been submitted for any other degree or professional qualification.

(*Olimpia E. Curran*)

# Abstract

The past three decades of synaptic research have provided new insights into synapse biology. While synapses are still considered the fundamental connectors between the nerve cells in the central nervous system, they are no longer seen as simple neuron-to-neuron contacts. In fact, the estimated 100 trillion of human synapses are extremely complex, diverse and capable of performing sophisticated computational operations giving rise to advanced repertoires of cognitive and organic behaviours.

These intricate synaptic properties mean that existing methodologies for quantifying and characterising synapses are inadequate. Yet, understanding of synapse biology is crucial to deciphering human pathology as disruptions in synapse numbers, architecture and function have already been linked to many human brain disorders.

The purpose of this PhD was to evaluate a novel, high-throughput synaptic protein quantification method at a single synapse resolution in human post-mortem brain tissue. The method has already been successfully tested in our laboratory in genetically engineered mice, whereby synapses have been systematically quantified across a large number of areas to generate the first molecular maps of synapses, the synaptome maps.

In this project, methods have been developed to label human brain tissue with postsynaptic density protein 95 (PSD-95), the most common postsynaptic protein. We describe the use of PSD-95 combined with confocal microscopy and computational image analysis to quantify synaptic puncta immunofluorescence (IF) parameters in the human brain. In the first part of this study, the new method was used to quantify PSD-95 IF across selected 20 human brain regions to generate first PSD-95 human synaptome map. In the second part, PSD-95 IF was systematically assessed

across 16 hippocampal subregions. Finally, we confirmed that our novel synaptic quantification method was sensitive to hippocampal synaptic losses in patients with Alzheimer's Disease (AD). Such a high degree of systematic synapse quantification has not previously been reported in human brain tissue.

Our method is a promising approach for synaptic protein quantification in tissue with several potential applications in diagnosis and development of therapeutics for neurological and psychiatric disorders.

# Lay Summary

Synapses are the communication points between nerve cells in the brain. There are billions of synapses in the human brain and their powerful network-like connectivity determines how we think and behave. The canonical synapse has a simple architecture: each synapse has four basic components. Yet, each component is complex and made up of thousands of proteins. These proteins determine synaptic identity and provide clues to their diversity. One of the limitations of modern neuroscience is a lack of adequate tools to study the distribution, morphology and molecular characteristics of synapses at a large scale given their vast numbers and diversity. Modern technologies, however, are emerging to allow for study of synapses in great detail.

This thesis describes an application of one such modern technological tool to examine millions of synapses in the human brain tissue. Synapses were identified by adding a fluorescent tag to a synaptic protein. The fluorescent tag was counted, and the fluorescent signal it produced was analysed to provide information about the synapse diversity. The distribution of this synaptic protein tag across many human brain areas was presented as a synaptic map, or a synaptome. This process of synaptome mapping was applied to brain tissue obtained from normal individuals with no evidence of a neurological disease. Synaptome mapping was subsequently applied to a brain tissue in which there had been a diagnosis of a neurological disease. This work demonstrates that synaptome maps are very useful to examine possible synaptic changes in human brain disorders and to discover new aspects of the synaptic organisation.

The novelty of this work lies in the application of modern technology, including automated computational methods and powerful microscopy, to study synapses in human tissue. This technology could potentially be used to assess any neurological

or psychiatric condition with underlying changes in synaptic proteins, and reveal novel insights into the biology of these disorders.

*To Dan*

# Acknowledgments

I would like to express my deepest gratitude to my thesis supervisors, Professor Seth G. N. Grant and Professor Colin Smith for the continuous support of my PhD study, for patience, motivation, and immense knowledge.

Thank you to my committee members, Professor James Ironside and Professor Tara Spires-Jones for their insightful comments and encouragement.

I would like to offer my special thanks to the past and current members of the Grant, Smith and Spires-Jones' laboratories for their invaluable help with this project. Without their valued support it would not be possible to conduct this research.

I have been very fortunate to have incredible friends who kept encouraging me to work on this thesis and help me with the final touches. Thank you Richard Meehan, Sari Pennings, Melissa O'Neill, Hadil Abuarqoub, Diane Ritchie, Daria Locci and Alberto Sandri.

Words do not do justice to the expression of my debt to and appreciation of my husband, Dan. Thank you for always being there for me unconditionally.

My gratitude and recognition goes to the patients who donated their bodies to the Medical Research Council (MRC) Sudden Death Brain and Tissue Bank in Edinburgh to make this project possible.

Finally, I would like to thank my sponsor, the MRC Clinical Research Training Fellowship Scottish Clinical Pharmacology and Pathology Programme (SCP3).

This PhD thesis would not be possible without invaluable input and help from several members of the Grant, Smith and Spires-Jones' laboratories.

The entire image analysis was performed by Dr Zhen (Ricky) Qiu, who pioneered the G2CSynMaP methodology described in Chapter 2.9.1 and who was blind to the identity of raw images. Dr Fei Zhu is the creator of the PSD-95 knock-in mouse (Chapter 2.3.3), and she kindly provided images of the mouse presented in Figure 3.5 on page 118. She also performed the surgical procedures on mice used in this study as described in Chapter 2.3.5. All mice were routinely genotyped in the Grant laboratory by David Kerrigan and/or David Fricker according to an optimised protocol provided in Chapter 2.3.4. Melissa Cizeron provided mice quantification data used in Chapter 3.2.2. Dr Marcia Roy provided description of HUSPIR analysis of the LSCM cohort cases in Chapter 2.2.1 and Western blot analysis used in Chapter 3.3.1.

Rosemary Jackson from Prof Tara Spires-Jones' laboratory provided several of the HUSPIR and APOE results for the SDM cohort patients. Rosemary also performed with me the HUSPIR (Chapter 2.2.2) and APOE (Chapter 2.2.3) analyses on the SDM cohort cases with missing results according to protocols optimised in Prof Spires-Jones' laboratory.

Finally, human tissue was entirely processed and tissue sections were cut by the MRC Edinburgh Brain Bank staff managed by Chris-Anne McKenzie. Their input also included preparation of all H&E slides, Nissl slides and any other immunohistochemistry staining needed for staging of AD cases, but not the PSD-95 immunofluorescence staining.

Thank you all.

# Abbreviations

| | |
|---|---|
| A$\beta$ | Beta-amyloid |
| AD | Alzheimer's Disease |
| AER | Autofluorescence Eliminator Reagent |
| AMPA | $\alpha$-amino-3-hydroxy-5-methyl-4-isoxazolepropionic acid |
| ApoE | Apolipoprotein E |
| ASD | Autism Spectrum Disorders |
| AT | Array Tomography |
| BA | Brodmann's Area |
| CA | Cornu Ammonis |
| CA1-SML | CA1-Stratum Moleculare Lacunosum |
| CA1-SO | CA1-Stratum Oriens |
| CA1-SP | CA1-Stratum Pyramidale |
| CA1-SR | CA1-Stratum Radiatum |
| CA2-SML | CA2-Stratum Moleculare Lacunosum |
| CA2-SO | CA2-Stratum Oriens |
| CA2-SP | CA2-Stratum Pyramidale |
| CA2-SR | CA2-Stratum Radiatum |
| CA3-SL | CA3-Stratum Lucidum |
| CA3-SML | CA3-Stratum Moleculare Lacunosum |
| CA3-SO | CA3-Stratum Oriens |
| CA3-SP | CA3-Stratum Pyramidale |
| CA4 | Cornu Ammonis 4 |
| CB | Cerebellum |
| CERAD | Consortium to Establish a Registry for Alzheimer's Disease |
| CN | Caudate Nucleus |
| CNS | Central Nervous System |
| CNXII | Hypoglossal Cranial Nerve |
| CSF | Cerebrospinal fluid |
| CSU | Confocal Spinning Disc Unit |
| DABCO | 1, 4-DiAzaBiCyclo[2.2.2]Octane |
| DAPI | 4', 6'-DiAmidino-2-PhenylIndole |
| DG | Dentate Gyrus |
| DG-PL | DG-Polymorphic Layer |
| DG-SG | DG-Stratum Granulosum |

| | |
|---|---|
| DG-SM | DG-Stratum Moleculare |
| DLG | Disc Large homolog |
| EGFP | Enhanced Green Fluorescent Protein |
| EM | Electron Microscope/Microscopy |
| EMCCD | Electron Multyplying Charge-Coupled Device |
| ENABLED | Endogenouos Labelling via Exon Duplication |
| FMRP | Fragile X Mental Retardation Protein |
| FP | Fluorescent Protein |
| FTLD | Fronto-Temporal Lobar Degeneration |
| G2CSynMaP | Genes to Cognition Synaptome Mapping Pipeline |
| GFP | Green Fluorescent Protein |
| GK | Guanylate Kinase-like domain |
| HC | Hippocampus |
| HD | Huntington's Disease |
| HUSPIR | Human Synaptic Protein Integrity Ratio |
| IF | Immunofluorescence |
| ION | Inferior Olivary Nucleus |
| KI | Knock-in |
| KO | Knock-out |
| LC | Locus Coeruleus |
| LSCM | Laser Scanning Confocal Microscope |
| LTP | Long Term Potentiation |
| MAGUK | Membrane Associated Guanylate Kinases |
| MASC | MAGUK-associated Signalling Complex |
| MB | Midbrain |
| MD | Medulla |
| MSNs | Medium-sized Spiny Neurons |
| NFTs | Neurofibrillary Tangles |
| NMDA | N-methyl-D-aspartate |
| NMDAR | N-methyl-D-aspartate receptor |
| NO | Nitric Oxide |
| NP-C | Niemann-Pick Disease Type C |
| OCT | Optimal Cutting Temperature |
| PALM | Photoactivation Localisation Microscopy |
| PBS | Phosphate Buffered Saline |
| PCR | Polymerase Chain Reaction |
| PD | Parkinson's Disease |
| PDZ | Postsynaptic density-95/Discs large homolog/Zona occludens-1 |
| PET | Positron Emission Tomography |
| PFA | Paraformaldehyde |
| PMD | Post-mortem Delay/Integrity |
| PME | Post-mortem Examination |
| PN | Pontine Nuclei |
| PO | Pons |

| | |
|---|---|
| PSD | Postsynaptic Density |
| PSD-93 | Postsynaptic Density Protein - 93 |
| PSD-95 | Postsynaptic Density Protein - 95 |
| PSF | Point Spread Function |
| PSP | Progressive Supranuclear Palsy |
| PSP | Postsynaptic Proteome |
| RFLP | Restriction Fragment Length Polymorphism |
| RIN | RNA Integrity Number |
| SAP102 | Synapse Associated Protein 102 |
| SAP97 | Synapse Associated Protein 97 |
| SB | Sudan Black |
| SDBTB | Sudden Death Brain and Tissue Bank |
| SDM | Spinning Disk Microscope |
| SDS-PAGE | Sodium Dodecyl Sulfate Polyacrylamide Gel Electrophoresis |
| SEM | Scanning Electron Microscopy |
| SH3 | Src Homology 3 |
| SIM | Structured Illumination Microscopy |
| SN | Substantia Nigra |
| STED | STimulated Emission Depletion |
| STORM | Stochastic Optical Reconstruction Microscopy |
| SVA2 | Synaptic Vesicle Glycoprotein 2A |
| TEM | Transmission Electron Microscope/Microscopy |
| TH | Thalamus |
| VGluT | Vesicular Glutamate Transporter |
| VGluT1 | Vesicular Glutamate Transporter 1 |
| VGluT2 | Vesicular Glutamate Transporter 2 |

# Contents

# List of Figures

# List of Tables

# 1 Introduction

## 1.1 THE SYNAPSE

The synapse is the fundamental communication point between neurons in the central nervous system (CNS). Although highly specialised, the canonical synaptic structure comprises the following elements at the ultrastructural level: densities on the cytoplasmic faces in the pre- and postsynaptic membranes; named synaptic membrane densities; synaptic vesicles in the presynaptic axon terminal adjacent to the presynaptic density; and a synaptic cleft (Figure 1.1.A). At the light microscope level, the term synapse refers to the contact established by a presynaptic element (mostly an axon terminal or synaptic bouton) and a postsynaptic element (mostly a dendrite or a cell body). More recently, astroglia, a third partner in close contact with pre- and postsynaptic elements, have been shown to be involved in synaptic signal transmission giving rise to the concept of the "tripartite synapse" (Haydon, 2001). The extracellular matrix (Dityatev and Rusakov, 2011) and microglia (Schafer et al., 2013) are the most recent elements of synaptic machinery shown to be involved in synaptic information transfer, extending the synaptic terminology to "tetrapartite synapse" and "quad-partite" synapse, respectively. Importantly, as the concept of a synapse evolves, so is the growing evidence from physiological and genetic studies revealing an astonishing molecular complexity of synaptic compartments, with each structure containing a large number of distinct proteins. The presynaptic terminal, for instance, contains an estimated 485 different proteins (Weingarten et al., 2014) whereas the postsynaptic density (PSD), found at the postsynaptic terminal, harbours over a thousand different proteins (Husi and Grant, 2001*a*). However, despite the evidence for the molecular complexity of synapses and their compartments, little is known about the diversity of synapse types and their distribution.

Early studies led to the traditional classification of synapses into electrical and chemical types, depending on the differences between their apposition structures and functional properties (Pereda, 2014). Chemical synapses are sites of discontinuity where signal propagation is highly regulated and mediated by chemical substances called neurotransmitters (Figure 1.1.A). Electrical synapses are continuously connected gap-junction channels allowing bidirectional propagation of the electrical signals (Figure 1.1.B). Further studies subdivided synapses into

excitatory, inhibitory or modulatory depending on the actions of the chemical signals known as neurotransmitters. This physiological synaptic diversity was mirrored in early morphological studies demonstrating a corresponding morphological dichotomy. Using transmission electron microscopy (TEM) techniques, synapses were subdivided into two major morphological groups, type 1 and type 2, based on the ultrastructural features of presynaptic and postsynaptic structures (Gray, 1959) (Figure 1.1.C).

Type 1 synapses, typically located on dendritic shafts and spines, posses a long and very prominent postsynaptic thickening, known as the postsynaptic density. In contrast, type 2 synapses, mostly found on neuronal cell bodies, and known as axo-somatic synapses, have thin postsynaptic membranes (Figure 1.1.D). Type 1 synapses, also referred to as asymmetrical synapses, were later attributed to excitatory synapses, whereas type 2, or symmetrical synapses, were found to be inhibitory.

However, the above classification, established over 60 years ago, does not allow for adequate synapse categorisation (Klemann and Roubos, 2011). Synaptic diversity goes beyond the early descriptions and this is not surprising given the knowledge of complexity of neuronal systems. Modern high-throughput analysis of over 20,000 different genes at single neurons revealed that 70% of genes are expressed in less than 20% of cells. Thus, a high degree of molecular diversity between cell types is expected. This also implies that many synaptic types and subtypes have not yet been characterised (Hawrylycz et al., 2012; Lein et al., 2007).

Studies conducted in the last decade demonstrated the necessity for refinement of the existing synapse classification with molecular data highlighting the potential vast diversity of synapses (O'Rourke et al., 2012). A systematic knowledge of synapse diversity will be important for further understanding of synapse circuitry, development, plasticity, and ultimately, synapse-based susceptibility to human brain disorders. The knowledge of protein composition of synapses and synaptic subtypes will become clinically relevant as over 130 neurological and psychiatric conditions are caused by mutations in synaptic genes and the diseases of synapses ('Synaptopathies') are emerging as an unexplored cause of human brain diseases (Bayés et al., 2011). In fact, abnormal proteins of the PSD are responsible for the greatest disease burden in the CNS (Grant, 2012).

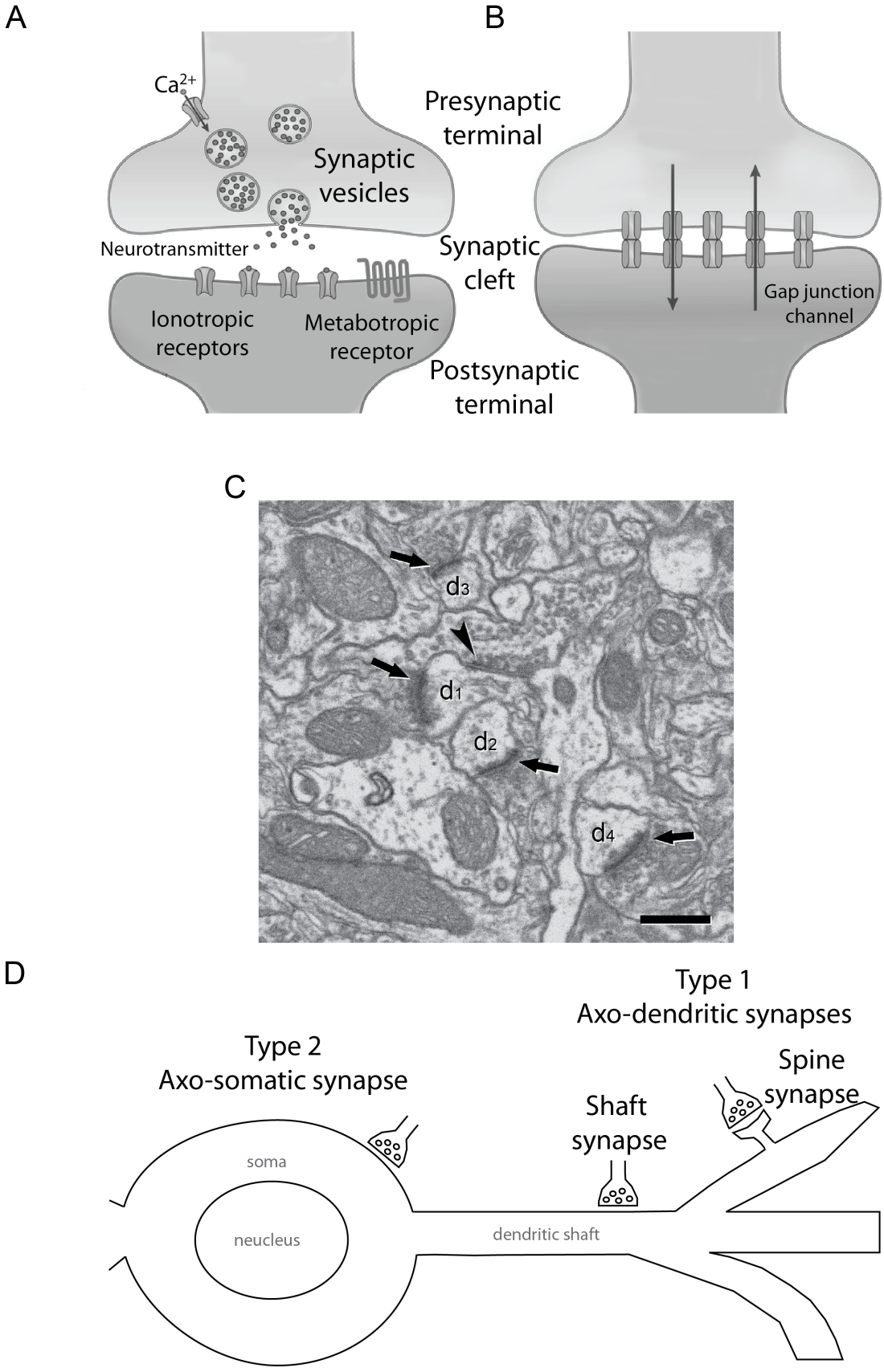


**Figure 1.1 Traditional view of types of synapses in the central nervous system.**

**A.** Schematic of a chemical synapse with its basic structure consisting of four compartments: presynaptic terminal, synaptic cleft, vesicles filled with neurotransmitters and postsynaptic terminal. Chemical synapses require ionotropic and metabotropic receptors for chemical transmission utilising neurotransmitters. **B.** Schematic of an electrical synapse with numerous intracellular gap junctions allowing for electrical transmission. Images in A and B adapted by permission from Macmillan Publishers Ltd: Nature Reviews Neuroscience (Pereda, 2014), copyright 2014. **C.** Ultrastructural features of asymmetric and symmetric synapses. Arrows point to four asymmetric (Type 1) synapses and an arrowhead points to a symmetric (Type 2) synapse on four dendritic spines (d1 to d4). Type 1 synapses have a thick postsynaptic density. Type 2 synapse has a thin postsynaptic density. Scale bar, 500 nm. Image reproduced from an open access article (Merchán-Pérez et al., 2009). **D.** Schematic of the typical neuronal location of synapses. Type 1 synapses (axo-dendritic) are found on dendritic spines and shafts. Type 2 synapses (axo-somatic) are typically found on the cell bodies.

---

## 1.2 GLUTAMATERGIC SYNAPTIC TRANSMISSION AND PLASTICITY

Synaptic transmission is the biological process by which a neuron communicates with a target cell across a synapse. It is regarded as the fundamental process underlying all complex behaviours including advanced cognitive abilities. The two main types of synaptic transmission in the mammalian CNS (excitatory and inhibitory) are carried out mainly via the chemical synapse. The predominant excitatory transmitter system uses glutamate as the major neurotransmitter that binds to the glutamate receptors. Glutamate receptors come in two forms: ionotropic, which are ligand-gated ion channels, and metabotropic, which mediate their effects by activation of a secondary messenger cascade. The ionotropic glutamate receptors are broadly classified into three subtypes based on pharmacological and electrophysiological properties: N-methyl-D-aspartate (NMDA), $\alpha$-amino-3-hydroxy-5-methyl-4-isoxazolepropionic acid (AMPA), and kainate receptors. AMPA and kainate receptors, also known as non-NMDA receptors, mediate rapid excitatory synaptic transmission. In contrast, NMDA receptor (NMDAR) activation generates slow synaptic potentials, which are involved in various forms of activity-dependent synaptic plasticity.

Synaptic plasticity is yet another property of synapses that plays a fundamental role in the formation, storage and removal of memory. This process allows synapses to modify the strength of transmission in accordance with electrochemical signals received: increased activity can strengthen synapses, but equally, reduced or lack of activity can weaken synapses or even result in their loss (Trachtenberg et al., 2002). Unlike non-NMDA receptors that mediate the fast excitatory postsynaptic potential (EPSPs) via monovalent ions, such as $Na^+$ or $K^+$, NMDA receptors have additional properties: they posses a high $Ca^{2+}$ permeability, are highly glutamate sensitive and display a voltage dependence that is blocked by external $Mg^{2+}$ (Nowak et al., 1984). NMDA receptors also require two agonists for activation: glutamate and glycine (Johnson and Ascher, 1987). While non-NMDA receptors are generators of electrical signals, NMDA receptors have additionally specialised as molecular 'coincidence detectors' (Blitzer, 2005), a functional property important for participation in learning. When glutamate is released at a synapse, unless the resting membrane is depolarised by high stimulus frequencies, generated by AMPARs, sufficient to relieve the resting $Mg^{2+}$ block, the NMDA receptors will not conduct. Once the $Mg^{2+}$ block is removed, there is $Ca^{2+}$ influx into the postsynaptic neuron allowing changes to be initiated at the synapse (Lynch et al., 1983; Malenka et al., 1988). NMDARs thus detect the coincidence of postsynaptic depolarisation and glutamate release at the synapse, initiate $Ca^{2+}$ influx and trigger one of the most important changes in synapses, known as long-term potentiation (LTP). Induction of LTP in the CA1 region of the hippocampus suggested its importance for encoding and storage of associate long-term memories (Bliss and Gardner-Medwin, 1973). Persistent modification of synaptic strength, such as LTP and its counterpart LTD (long-term depression), has subsequently been considered a cellular mechanism underlying learning and memory (Collingridge et al., 2004); direct evidence for this, nevertheless, is still lacking. Critically, recent studies have started to challenge these long-standing views and LTP may not be required for encoding associative memories (Bannerman et al., 2014).

Apart from the pivotal role NMDA receptors play in the synaptic transmission and plasticity that underlie learning and memory, dysfunction of NMDARs has been increasingly implicated in the pathophysiology of human neurological disorders that affect cognitive abilities (Lau and Zukin, 2007; Mota et al., 2014; Zhang et al., 2016).

NMDARs consist of seven subunits: one GluN1, four GluN2 (A, B, C, D) and two GluN3 (A and B), and typically contain the obligatory glycine-binding subunit GluN1 plus either glutamate-binding GluN2B or GluN2A or a mixture of the two (Moriyoshi et al., 1991). GluN1, GluN2 and GluN3 were previously called NR1, NR2 and NR3, respectively. *GRIN1*, *GRIN2* and *GRIN3* genes encode the respective NMDA receptor subunits. Recent genetic studies identified several single-nucleotide polymorphism (SNP) variants in some of the NMDAR subunit genes in conditions, such as schizophrenia, bipolar disorder, neurodevelopmental disorders and AD. For instance, a missense GRIN3A p.R480G variant encoding the GluN3A subunit showed a strong association with schizophrenia (Takata et al., 2013). A genetic variation of the GluN3B subunit, insCGTT, inserts four bases within the coding region of this NMDA subunit gene predisposes to schizoid type personality trait (Matsuno et al., 2015). A p.N615K substitution mutation in the GluN2A subunit gene causes early-onset epileptic encephalopathy (Endele et al., 2010). Lastly, in AD patients, a missense p.K1293R mutation of the GRIN2B gene was detected suggesting a close association between this mutation of the postsynaptic GluN2B-subunit and alteration of synaptic structures (Andreoli et al., 2014).

Dysfunction of NMDARs has already been therapeutically exploited as a potential treatment for AD, the commonest form of dementia, as will be discussed in later chapters. Memantine, a NMDA receptor antagonist, is one of only a few established medications approved worldwide for treatment of AD patients (Winblad et al., 2016). Memantine protects neurons by attenuating tau protein phosphorylation (Song et al., 2008). In clinical trials, memantine improved patients' cognitive functions, including memory, language, functional communication as well as activities of daily living (Wilkinson, 2012). It is worth pointing out that the only other group of drugs used to treat AD include acetylcholinesterase inhibitors (donepezil, galantamine and rivastigmine), and that despite all the scientific efforts, there are still very few approved effective drugs that can be used for AD treatment (Ruthirakuhan et al., 2016). Other drugs targeting NMDARs and showing promising therapeutic applications in treating AD include neramexane and ifenprodil. Neramexane is a non-competitive NMDAR antagonist that enhances long-term memory in adult rats (Rammes, 2009). Ifenprodil is a specific GluN2B receptor antagonist that prevents

A$\beta$-induced inhibition of LTP, impairment of synaptic transmission and retraction of synaptic contacts (Rönicke et al., 2011). Development of these NMDARs-targeting drugs further solidifies evidence for the role of NMDARs as a possible convergence point for A$\beta$ and tau toxicity in AD (discussed later).

In summary, the growing body of evidence demonstrates the relevance of synaptic receptors and their proteins to human brain diseases and how these could further be studied to progress development of new therapeutic strategies.

## 1.3 SCAFFOLD PROTEINS AT THE POSTSYNAPTIC DENSITY

In excitatory synapses, NMDARs are found in the postsynaptic density (PSD). PSD is a dense thickening of postsynaptic sub-membranous cytoskeleton within the neuronal dendritic (spine) compartment, as demonstrated by EM studies (Kennedy, 1993, 2000). Biochemical analyses of purified PSDs from different types of neurons have shown that PSDs consist of densely packed proteins that form disc-shaped multi-protein assemblies a few hundred nanometers in width and ≈30-50 nm in thickness (Chen et al., 2008; Harris and Weinberg, 2012). Since PSDs have a characteristic structure and are contiguous to the presynaptic active zone, where neurotransmitter release takes place, the PSD is able to receive, integrate and propagate various incoming signals. This, in turn, allows PSDs to have several functions, including the stabilisation of synaptic junctions, the concentration and regulation of neurotransmitter receptors, and the induction of the transcriptions in response to synaptic transmission. In addition, PSDs are the smallest unit of neuronal plasticity as they modify their shape and molecular machinery in response to local signals.

Recent proteomic approaches have significantly contributed to defining a quantitative molecular inventory of proteins making up PSDs. At the molecular level, PSDs are tremendously complex and contain thousands of proteins with variable regional abundances; these proteins include scaffold proteins, synaptic membrane receptors, neurotransmitter receptors, cell adhesion molecules, signalling enzymes, membrane trafficking proteins, cytoskeletal proteins kinases and phosphatases (Zhu et al., 2016). Central to the organisation of all these proteins in excitatory synapses are

scaffold proteins, in particular, those of the Membrane Associated Guanylate Kinases (MAGUK) family protein (Figure 1.2), of which the DLG1-4 subfamily of proteins is crucial for the PSD proteome integrity.

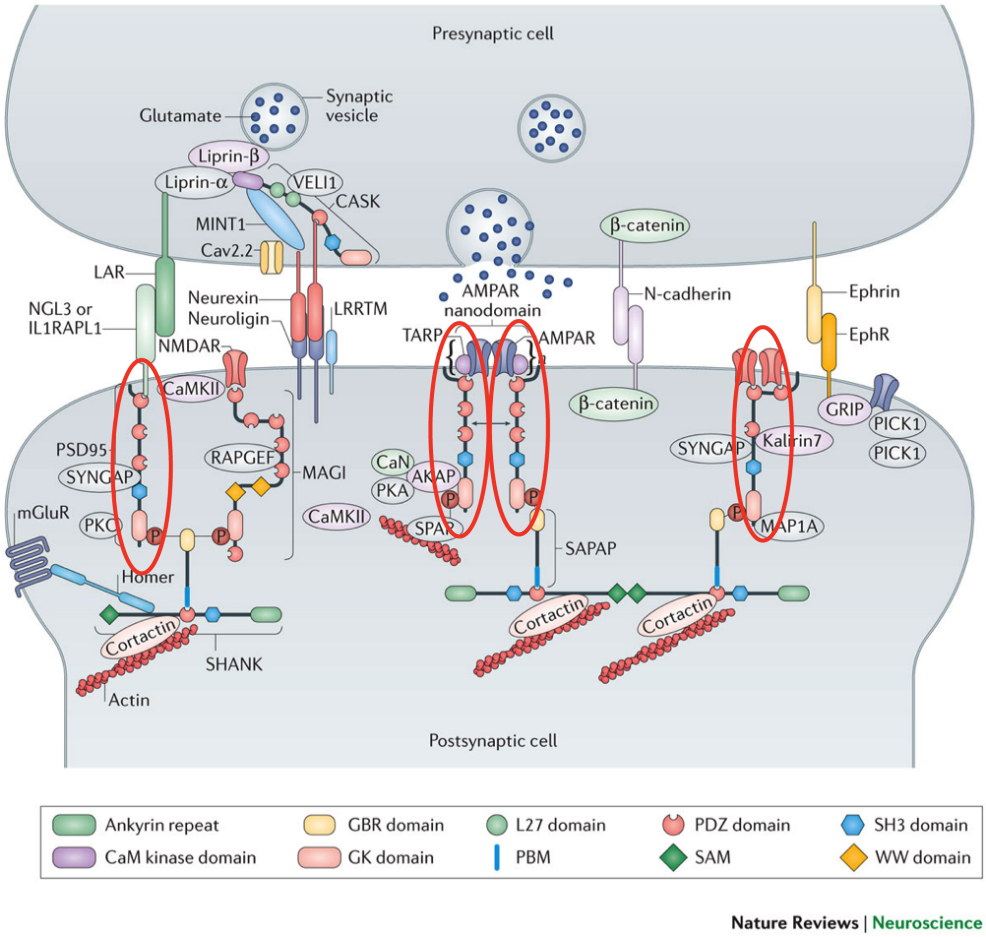


**Figure 1.2 Proteome organisation of PSDs mediated by scaffold proteins in excitatory synapses.**

The hundreds of proteins found at the excitatory synapses are organised by scaffold proteins, of which MAGUKs play central roles in interfacing synaptic membrane receptors or channels with signalling enzymes and cytoskeletal proteins in the PSD. The DLG1-4 subfamily of MAGUKs is believed to be one of the most critical proteins that determine the overall structure of PSDs. PSD-95, also known as DLG4 (highlighted in red ovals), is one of the best characterised members of the DLG1-4 subfamily central to PSD integrity. MAGUKs have modular structure allowing different members of interacting proteins to form multi-protein complexes. For simplicity, the figure shows the DLG-SAPAP-SHANK complex that can bind to glutamate receptors to form co-clustered nanodomains (the AMPA-type glutamate receptors complex (AMPA-RC)). The wide variety of proteins found at the PSD allow for numerous functions. For instance, multimerisation of DLG1-4 MAGUKs facilitates clustering of AMPARs. Synaptic adhesion molecules (e.g., IL1RAPL1) bind to MAGUKs by their cytoplasmic tails. Small GTPase regulatory proteins (SYNGAP, RAPGEF, SPAR, Kalirin 7) assemble synaptic protein complexes. Abbreviations: AKAP, A-kinase anchor protein; CaMKII, calcium/calmodulin-dependent protein

kinase II; CaN, calcineurin; Cav2.2, voltage-gated calcium channel subunit-$\alpha$ Cav2.2; EphR, ephrin receptor; GBR, GK-binding region; GK, guanylate kinase-like; GRIP, glutamate receptor-interacting protein; L27, LIN2-LIN7; LAR, leukocyte common antigen related; LRRTM, leucine-rich repeat transmembrane protein; MAGI, membrane-associated guanylate kinase inverted; MAP1A, microtubule-associated protein 1A; mGluR, metabotropic glutamate receptor; NGL-3, netrin-G3 ligand; NMDAR, NMDA-type glutamate receptor; PBM, PDZ-binding motif; PDZ, PSD95-DLG1-Zonula occludens 1; PKA, protein kinase A; PKC, protein kinase C; PICK1, protein interacting with C kinase 1; SAM, sterile $\alpha$-motif; TARP, transmembrane AMPAR regulatory protein; VELI1, vertebrate lin-7 homologue 1. Image adapted by permission from Macmillan Publishers Ltd: Nature Reviews Neuroscience (Zhu et al., 2016), copyright 2016.

---

### 1.3.1 MAGUK protein family

Studies have shown that within the PSD proteins are not uniformly distributed, but instead are assembled into multi-protein complexes (Husi et al., 2000; Schwenk et al., 2012). The prototype multi-protein complex within the PSD is formed by the MAGUK family of scaffold proteins. MAGUKs have a characteristic modular structure that allows for receptors and enzymes to bind in close proximity, but MAGUKs per se do not possess any intrinsic enzymatic properties (Funke et al., 2005). These modular protein-binding domains form large protein networks and MAGUKs represent just one superfamily of multi-domain proteins. MAGUKs tend to have three types of domains forming a common structure: a guanylate kinase-like (GK), a PDZ (Postsynaptic density-95/ Discs large homolog/Zona occludens-1) (PDZ) and a src homology 3 (SH3) domains.

MAGUK family of proteins have been classified phylogenetically into 10 subfamilies based on the PDZ-SH3-GK domains and they comprise the following subfamilies: calcium/calmodulin-dependent serine protein kinase (CASK), membrane protein palmitoylated (MPP), zona occludens (ZO), caspase recruitment domain containing MAGUK protein (CARMA), discs large 5 (DLG5), calcium channel $\beta$ subunit (CACNB), MAGUK with an inverted repeat (MAGI), and discs large 1-4 (DLG1-4) (Oliva et al., 2012)(Figure 1.3.A).

The DLG1-4 subfamily is one of the most studied MAGUKs due to its role in synapse formation and function. The first MAGUK to be discovered was Disc large 1 gene (Dlg1) in *Drosophila*, which was initially identified as a recessive oncogenic mutation (Stewart, Murphy, & Fristrom, 1972). Its protein, DLG, is the sole *Drosophila* representative of DLG subfamily of MAGUKs, also known as the Postsynaptic Density-95 (PSD-95) subfamily of MAGUKs, after its most abundant and best characterised member - the postsynaptic density 95 (PSD-95) protein. The mammalian homologue of DLG subfamily, however, consists of additional three members, namely Synapse Associated Protein 97 (SAP97), Postsynaptic Density Protein 93 (PSD-93) and Synapse Associated Protein 102 (SAP102). It is thought that the mammalian DLG1-4 subfamily members have evolved following two rounds of genome duplication events that took place approximately 500 - 600 million years ago (Emes and Grant, 2012) and which resulted in four paralogs of the ancestral gene Dlg1, present today in *Drosophila melanogaster* (Ryan and Grant, 2009). Furthermore, studies demonstrate that these proteins are also highly conserved between different species, including mice (Distler et al., 2014; Bayés et al., 2012; Collins et al., 2006), rats (Peng et al., 2004; Han et al., 2015), humans (Bayés et al., 2011, 2012) and most recently zebrafish (Bayés et al., 2017). The four members of the DLG1-4 subfamily proteins with their typical three tandem PDZ domains each are shown in Figure 1.3.B.

The "supertertiary" structure of PSD-95 includes three PDZ domains (Postsynaptic density-95/ Discs large homolog/Zona occludens-1), a src homology 3 (SH3) domain, and a guanylate kinase-like (GK) domain (Zhang et al., 2013) (Figure 1.3.C and D). PDZ domains are about 100 amino acid repeat sequences that mediate protein-protein interactions (Hung and Sheng, 2002). The SH3 domain is implicated in scaffold oligomerisation (McGee et al., 2001). The guanylate kinase-like (GK) domain is an enzymatically inactive region of approximately 300 amino acids at the C-terminus (Zhang et al., 2013).

MAGUKs are part of the signalling complexes present within the synapses. These are higher order structures which play a key role in detecting and processing the information that arrives at the postsynaptic terminal (Emes and Grant, 2012). The prototype postsynaptic signalling complex is known as MASC (MAGUK-associated

signalling complex). MASC contains the principal postsynaptic machinery involved in synaptic transmission and synaptic plasticity: ionotropic and metabotropic glutamate receptors, ion channels, adhesion proteins as well as MAGUKs and other scaffold proteins with their associated signalling enzymes and structural proteins (Figure 1.3.E).

The first MASC was identified to cluster with NMDA receptors and was subsequently called NMDA-R signalling complex (NMDA-RC)(Husi et al., 2000). The isolated NMDA-RC contained some 70 different postsynaptic proteins in addition to the PSD-95 (DLG4) member of the DLG1-4 subfamily of MAGUKs. The NMDA-RC is a subtype of PSD-95-dependent MASCs, and purification of PSD-95 itself results in an extensive list of more than 100 different proteins (Fernandez et al., 2009). Apart from MASCs, other receptor-coupled multi-complexes are found in the synapse, such as AMPA receptor complexes (AMPA-RC), or Shank-Homer-mGluR complexes (mGlu-RC). However, MASCs contain the majority proportion of the protein population of the PSD (Chen et al., 2015)(Figure 1.3.F).

The most recent analyses of organisation of postsynaptic proteins using *in vivo* models have provided further insights into the molecular hierarchy of the postsynaptic proteome (Frank and Grant, 2017). Specific subunits of postsynaptic proteins have been found to assemble into complexes that further associate with other proteins, in some cases as many as 50, to form supercomplexes (Figure 1.4). For instance, a recent study showed that NMDA receptors form NMDAR complexes and NMDAR supercomplexes (Frank et al., 2016). The most abundant components of the NMDAR complexes were the NMDAR channel subunits (GluN1, GluN2A and GluN2B) whereas the NMDAR supercomplexes additionally contained PSD-95 and PSD-93, two members of the DLG1-4 subfamily of MAGUKs. In the mouse forebrain, all PSD-95 was assembled into NMDAR supercomplexes, but only 3% of these contained NMDARs implying that NMDAR supercomplexes constitute a small subset of a much larger family to PSD-95 supercomplexes, most of which do not posses NMDARs. This astounding complexity of the postsynaptic proteome supports an emerging concept of the vast array of synaptic diversity. It is possible that the differential distribution of postsynaptic supercomplexes in the different brain areas could be one factor contributing to the synaptic heterogeneity (Frank and Grant, 2017).

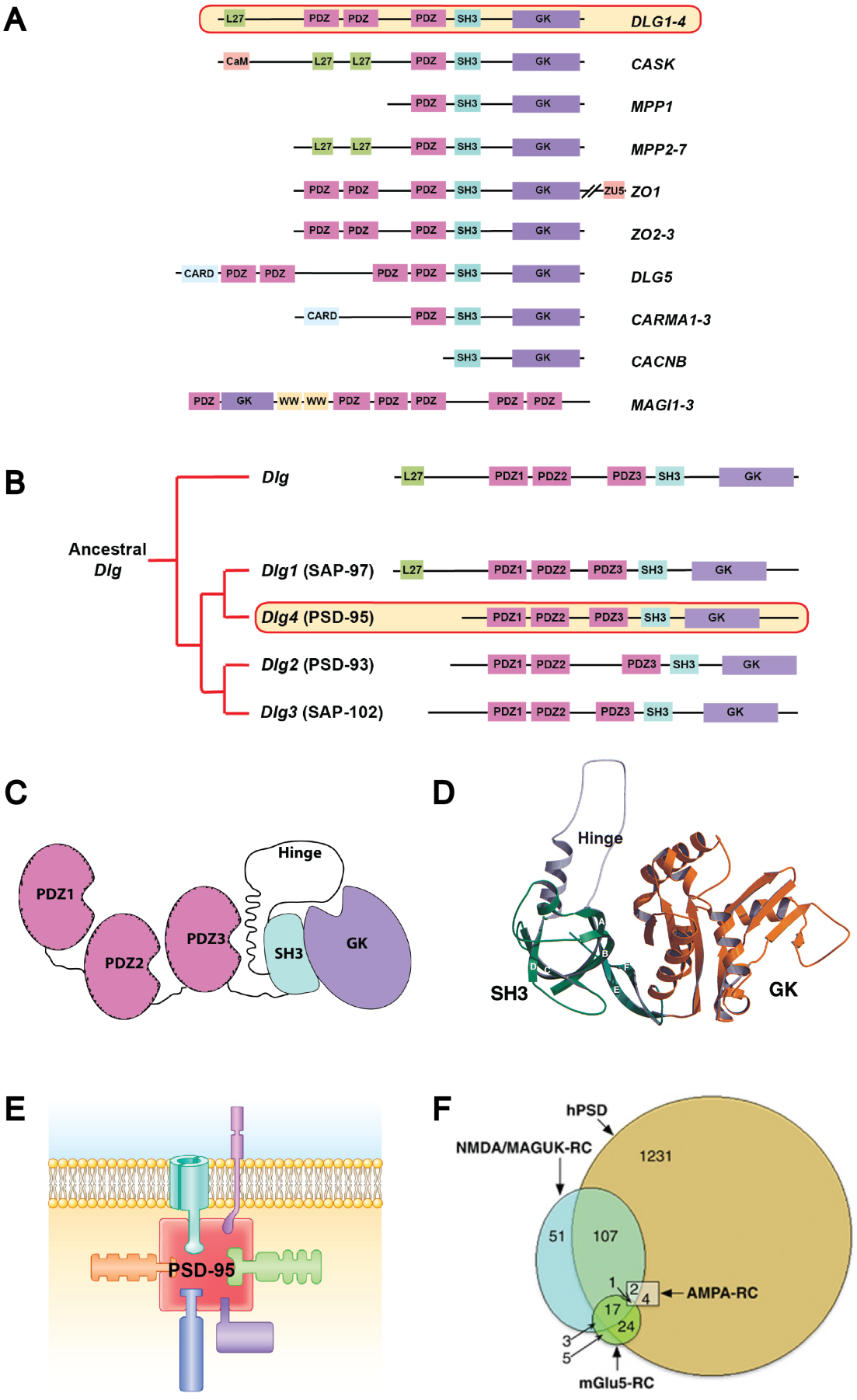


**Figure 1.3 PSD-95 as the key scaffolding protein of MAGUKs.**

**A.** Conserved domain organisation of the ten MAGUK subfamilies. As a key member of the DLG1-4 subfamily, PSD-95 shares a common modular structure with the rest of the MAGUK members. All members posses a GK domain with several PDZ domains N and/or C-terminal to the GK domain. All members except for MAGI have an SH3 domain immediately N-terminal to the GK domain. The smallest CACNB subfamily contains only the SH3 and GK domain. MAGUKs structure has been conserved throughout evolution with all, except MAGI and CACNB, subfamilies containing a $PDZ - SH3 - GK$ tandem. Image adapted from (Oliva et al., 2012; Zhu et al., 2012, 2016) **B.** Conserved domain organisation of individual members of the DLG1-4 subfamily. PSD-95 has arisen from genome duplication of an ancestral dlg gene about 500 million years ago. There are four paralogs of the vertebrate dlg gene giving rise to four proteins, of which PSD-95 (DLG4) is so far best characterised and studied. Image adapted from (Nithianantharajah et al., 2013) **C.** Schematic of the PSD-95 "supertertiary" structure showing five main modular components. PSD-95 has three PDZ modules. Each PDZ domain has a six $\beta$ strand and two $\alpha$ helix structure that binds specific peptide motifs at the C-terminal of targeted proteins to allow interactions with various proteins (Nourry et al., 2003). For instance, the first and second PDZ domains of PSD-95 protein interact with the C-terminal peptide sequence of NMDA receptor NR2A/B subunits (Kornau et al., 1995) and the C-terminal sequence of Shaker-type potassium channel (Kim et al., 1995). The third PDZ domain of PSD-95 binds to the C-terminal sequence of Neuroligin protein (Irie et al., 1997). PSD-95 also has one SH3 domain and one GK domain. Image republished from (Zhang et al., 2013), with permission from Elsevier; permission conveyed through Copyright Clearance Center, Inc. **D.** Ribbon structure of the PSD-95 SH3-GK module. The SH3 domain of PSD-95 contains an incomplete set of four $\beta$ strands forming the core domain (subdomain $\beta$A-D). The missing two strands (subdomain $\beta$E-F) are contributed from the GK domain, which is separated from the core SH3 domain by the hinge region. The unexpected insertion of the hinge region allows the GK domain to fold back and tether together with the SH3 domain to form a complete set of six $\beta$ strands. Image republished from (McGee et al., 2001), with permission from Elsevier; permission conveyed through Copyright Clearance Center, Inc. **E.** Organisation of signalling complexes. PSD-95 can assemble into multiprotein signalling complexes with a wide variety of proteins, including ion channels, structural proteins, cell-adhesion proteins, enzymes, or even other MAGUKs, forming MAGUK-associated signalling complexes, known as MASCs. MASCs comprise as much as 10% of all vertebrate PSP proteins. Image republished with permission of Annual Review from (Emes and Grant, 2012); permission conveyed through Copyright Clearance Center, Inc. **F.** Venn diagram illustrating the overlap of three gene complexes coding for glutamate multiprotein receptor complexes (NMDA-RC, mGlu5-RC and AMPA-RC) and their relative overlap within the proteins of the human PSD (hPSD). MASCs of NMDA-RC type form a substantial proportion of the total hPSD in comparison to mGlu5-RC and AMPA-RC. Numbers show genes in each gene set and their overlap for each glutamate type. Image reproduced from an open access article under the CC BY licence (Hill et al., 2014).

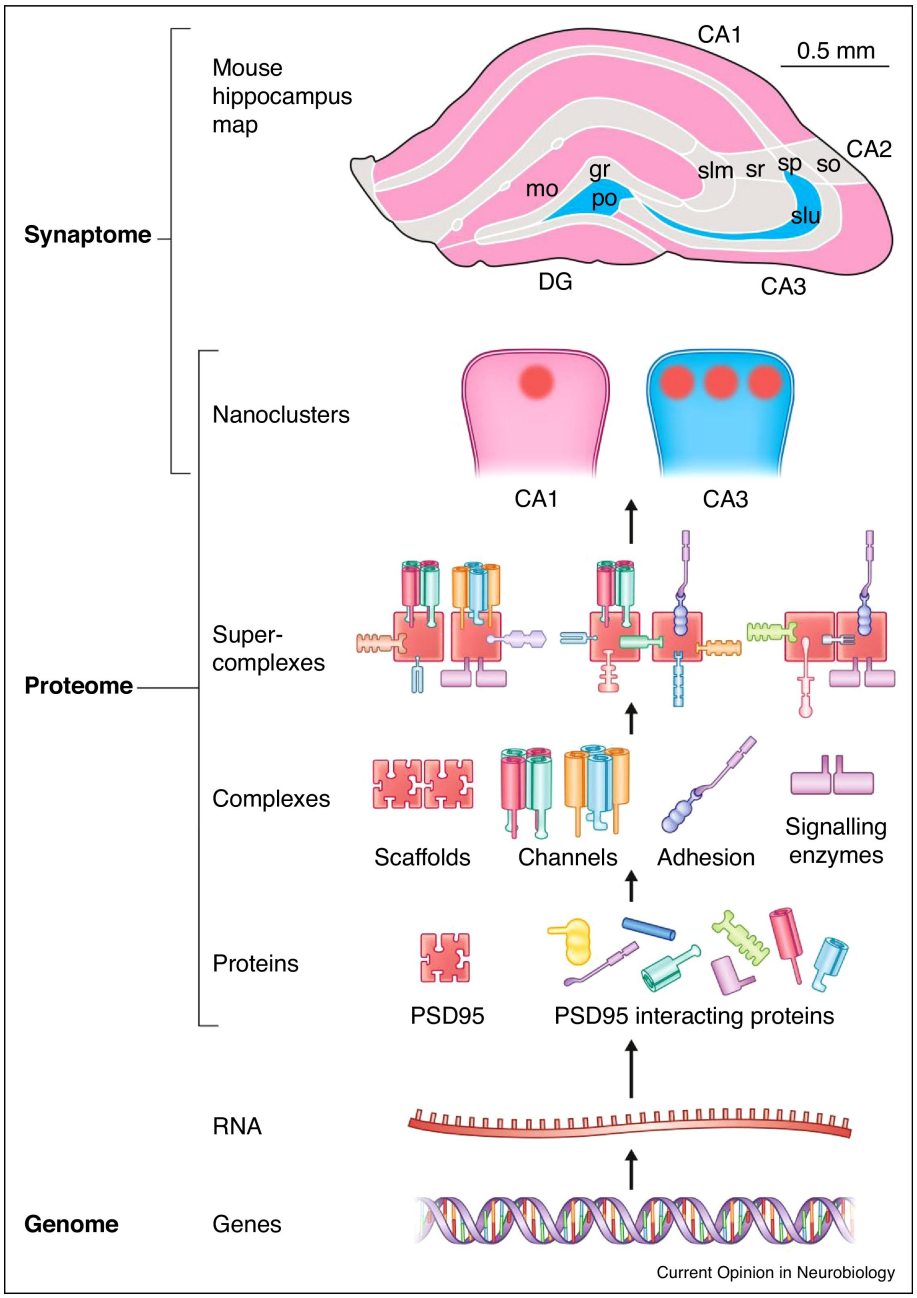


**Figure 1.4 Supramolecular organisation in the postsynaptic proteome.** Current and most up-to-date understanding of the postsynaptic density proteome organisation based on animal *in vivo* studies (Frank and Grant, 2017). Individual proteins, such as PSD-95, are encoded by the genome and transcriptome and then organised in a hierarchical way into complexes, supercomplexes and nanoclusters. Different synapses posses different combinations of nanoclusters and these synapses are then found in different brain areas. Image reproduced from an open access article under the CC BY licence (Frank and Grant, 2017).

### 1.3.2 Expression pattern of DLG1-4 subfamily of MAGUKs

The DLG1-4 subfamily of MAGUK proteins is highly expressed in the CNS, but there are distinct spatiotemporal and cellular differences between its members.

#### *1.3.2.1 General expression of DLG1-4*

The four protein members show distinct temporal and spatial distribution during different stages of development (Oliva et al., 2012). In rats, PSD-95 expression is low during embryonic and early postnatal development in most brain tissues, gradually increasing during postnatal development reaching maximum expression in adulthood (Al-Hallaq et al., 2001). The rat hippocampal PSD-93 expression profile is similar to PSD-95 with low expression in early development that increases in later stages of life (Sans et al., 2000). In contrast, rat hippocampal SAP102 expression is at its highest levels during early postnatal and juvenile stages of development. The SAP102 expression is at its lowest during embryogenesis, and it also decreases as it reaches the adulthood (Müller et al., 1996). Murine studies revealed that SAP97 shows an expression pattern that is opposite to PSD-95/PSD-93 in the hippocampus. In addition, in many brain areas, SAP97 levels decrease from the embryo to adult stages suggesting that the protein may participate in developmental processes of the CNS (Cai et al., 2008).

Human studies defining DLG1-4 proteins expression in development are scarce, and early studies described changes in relation to asymmetric synapses rather than DLG proteins themselves. However, human cortical expression (in areas BA46 and BA9) of PSD-95 has been studied in 42 subjects aged from 18 weeks gestation to 25 years old (Glantz et al., 2007). Using Western blot analysis, PSD-95 was shown to increase after birth, peak in early adulthood and slightly decrease in late adulthood. These changes are in agreement with those seen in the mouse and rodent cortices with Western blotting (Sans et al., 2000) and electron microscopy (Liu et al., 2004). Developmental expression patterns of the remaining three members of DLG subfamily have not been undertaken in humans.

In adulthood, the four members of the DLG1-4 subfamily proteins display a distinct heterogeneity pattern in their spatial distribution (Fukaya et al., 1999; Fukaya and Watanabe, 2000). In mice, using *in situ* hybridisation Fukaya et al. demonstrated that PSD-95, PSD-93 and SAP102 mRNAs were highly expressed in the telencephalon, with the highest concentrations found in cell bodies of the hippocampal pyramidal and granular cell layers. High signal levels were also detected in the olfactory bulb, laminae II-VI of the cerebral cortex, caudate-putamen and cerebellar cortex, with low to moderate levels detected in the thalamus, hypothalamus and the brainstem. On the other hand, PSD-93 mRNA was moderately expressed in the cerebellar Purkinje cell layer and sparingly expressed in the hypothalamus and brainstem. Only a few PSD-93 signals were reported in the thalamus (Fukaya et al., 1999). Light and electron microscopy revealed that cerebellum, rather than telencephalic structures, expressed SAP97 when stained with an anti-SAP97 antibody in rats (Müller et al., 1995). Immunoperoxidase staining of murine tissue with affinity-purified polyclonal antibodies against PSD-95, SAP102 and PSD-93 (to prevent cross-reactivity) yielded very similar distribution patterns of the three proteins to that previously described with mRNAs (Fukaya and Watanabe, 2000). Specifically, all three antibodies showed strong staining in the telencephalon, including the cerebral cortex, hippocampus, olfactory bulb and caudate-putamen. In the hippocampus, all three DLG proteins displayed high immunoreactivity in the dendritic areas of *stratum radiatum* and *stratum oriens* of the CA1 region. PSD-95 expression was also high in the *stratum lucidum* of the CA3 region. However, there were some differences between these areas. For instance, SAP102 was strongly labelled in the thalamus, whereas only weak staining was detected for PSD-95 and almost no labelling was detected for PSD-93. In the hindbrain, PSD-93 was restricted to cerebellar Purkinje cell bodies and dendrites, but was not detected in the brainstem structures (Brenman et al., 1996). This was in contrast to PSD-95, which was detected in the presynaptic axon terminals of basket cells, known as pinceau formation, and synaptic glomeruli. PSD-95 was also detected, albeit at low levels, in the brainstem.

At the synaptic level, it is generally agreed that PSD-95, SAP102 and PSD-93 are predominantly postsynaptic, while SAP97 occurs both pre- and postsynaptically (Aoki et al., 2001; Funke et al., 2005). Studies using TEM demonstrated that PSD-95,

PSD-93 and SAP102 are localised on PSDs associated with asymmetric axo-spinous junctions, the primary sites of glutamatergic receptors (Aoki et al., 2001). In addition, these proteins can also be expressed outside the synapses.

Non-neuronal tissues have also been found to express some members of DLG1-4. For instance, in rodents SAP97 is expressed in tissues, such as small intestine and choroid plexus (Müller et al., 1995). Rodent SAP102 mRNA or protein have not been detected in the liver, heart or muscle (Müller et al., 1996). In humans, Northern blot analysis detected SAP102 transcripts in the brain, pancreas, thyroid, trachea and prostate. Further immunohistochemical analysis using an anti-SAP102 polyclonal antibody localised protein expression mainly to non-proliferating cells of the trachea, prostate, stomach, spinal cord, heart, pancreas and oesophagus (Makino et al., 1997). Interestingly, in adult rat, *in situ* hybridisation demonstrated PSD-93 expression restricted to the brain, which is in contrast to PSD-93 mRNA detected in neurons of spinal cord, dorsal root ganglia, intestine, the thymus and submandibular gland in E15 rat embryo (Brenman et al., 1996).

#### *1.3.2.2 Subcellular localisation of DLG1-4*

Assessment of the subcellular localisation of the MAGUK family members has historically generated some discrepancies. Biochemical fractionation studies demonstrated a concentration of SAP102, PSD-95 and PSD-93 in the postsynaptic density (Brenman et al., 1998; Cho et al., 1992; Müller et al., 1996). These data were supported by TEM studies that showed that PSD-95, PSD-93 and SAP102 clustered directly over the thick PSD at asymmetric synaptic junctions, while SAP97 was also found at presynaptic membranes (Aoki et al., 2001; Roche et al., 1999; Sans et al., 2000). However, early immunocytochemical studies combined with light or electron microscopy (Cho et al., 1992; Kistner et al., 1993; Laube et al., 1996) described the distribution of DLGs in contrast with the mRNA expression patterns shown by *in situ* hybridisation (Fukaya et al., 1999). It was not until 1996 that Hunt et al. employed immunogold electron microscopy of forebrain synaptosomes to clarify that PSD-95 labelled the PSD (Hunt et al., 1996). The final breakthrough came with the introduction of protease antigen retrieval prior to immunohistochemistry to unmask

antibody epitopes (Fukaya and Watanabe, 2000). The modified immunostaining highlighted sharp, punctate synaptic staining patterns within the neuropil with empty dendritic shafts, in accordance with EM and mRNA results (Fukaya and Watanabe, 2000). Recently, the punctate staining was reported in a conditional knock-in (KI) mouse of PSD-95 with the fluorescent protein mVenus (Fortin et al., 2014).

Further studies have provided more detailed distributions of the DLG1-4 members (Oliva et al., 2012). As mentioned previously, PSD-95, PSD-93 and SAP102 are commonly found on asymmetric axo-spinous junctions. Rarely, PSD-95 can be located on axo-dendritic and axo-somatic synapses. PSD-95 can also be found at the non-synaptic portions of axons and dendritic shafts (Aoki et al., 2001). PSD-93 is typically found in the PSDs in dendrites, but it can also localise in non-synaptic portions of the axon and at presynaptic sites (Aoki et al., 2001). In rodents, SAP102 has been found outside the postsynaptic sites, in dendrites and axons. Similarly, human SAP102 has been found along axons and dendrites, but not in the cytoplasm of cerebral cortex neurons (Makino et al., 1997). SAP97 can be found pre- and postsynaptically. However, SAP97 immunostaining has also been found along the neck of spines, leaving the PSD unlabelled (Aoki et al., 2001). SAP97 has been found at the nodes of Ranvier and unmyelinated axons (Müller et al., 1995).

## 1.4 PROPERTIES OF PSD-95

This dissertation focuses on the distribution and quantification of PSD-95 protein throughout several areas of the human brain, as the distribution of this protein in humans remains poorly characterised. The following section describes in detail current knowledge of PSD-95 distribution and function.

PSD-95 was first cloned from rat brain preparations of the postsynaptic density. The isolated protein was identified as a 95 kDa homolog of the *Drosophila dlgA* gene product and was named disks large homolog 4 (DLG4), or postsynaptic density protein 95 (Cho et al., 1992). Subsequently, another group of researchers identified the same protein as a 90 kDa synapse-associated protein in rat cerebellum and named it synapse-associated protein 90 (SAP90) (Kistner et al., 1993).

### 1.4.1 Structure of PSD-95

#### *1.4.1.1 Primary sequence of PSD-95 gene*

The original description of human postsynaptic density protein gene *DLG4* reported it to be located on chromosome 17p13.1 and containing 22 exons (Stathakis et al., 1997, 2002). It was predicted that it would encode a 770-amino-acid structure that was 98.8% identical to rat PSD-95 and 98.5% identical to its mouse counterpart. Apart from the first 8 residues, human PSD-95 protein contained only three conservative amino acid changes from either rodent PSD-95/SAP90 protein. One of these differences occurred in the PDZ2 domain of the mouse protein, and the second difference was in the SH3 domain, where both the rat (Gly466) and the mouse (His455) sequences showed a single residue change relative to the other two homologs. Since the residues they affected were not conserved in other mammalian Dlg-related proteins, it was believed that these changes may not be functionally significant (Stathakis et al., 1997).

The *DLG4* gene is expressed in adults and fetuses. It is reported to be expressed in many human tissues in adulthood, including the brain, as demonstrated in Figure 1.5 on page 21. In addition, the Allen Brain Atlas Brain Explorer supports widespread cortical expression of the gene in adult human brain (Hawrylycz et al., 2012). According to the BrainSpan Atlas (Miller et al., 2014), in the developing human brain, there is a relatively robust expression of the *DLG4* gene from early gestation with a decrease at around 21 gestational weeks followed by increasing levels from 37 gestational weeks (Krishnan et al., 2017). Another resource, the BrainCloud (Colantuoni et al., 2011), reports fetal brain development from 14+ gestational weeks throughout life with expression increasing particularly during the first year (Krishnan et al., 2017).

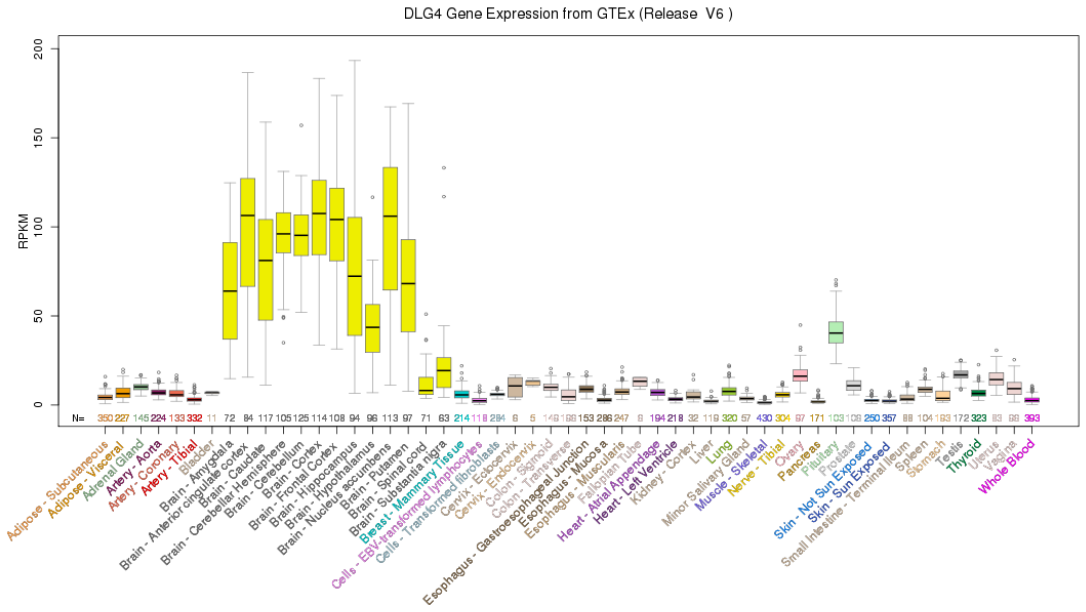


**Figure 1.5 DLG4 gene expression across tissues in humans.**
Open-access data on tissue expression of *DLG4* (PSD-95 gene) showing particularly high expression in various brain regions (yellow boxes). The highest median expression (107.49 RPKM) was found in the brain-Cortex. Expression values are reported in RPKM (Reads per Kilobase of Transcript per Million mapped reads), calculated from a gene model with isoforms collapsed to a single gene. The image has been downloaded from http://www.genome.ucsc.edu website and has been created using the data from the NIH Genome-Tissue Expression (GTEx) project also available at the GTEx Portal at http://www.gtexportal.org. The data is based on gene expression analysis in 53 tissues from GTEx RNA-seq of 8555 samples (570 donors).

#### *1.4.1.2 RNA expression of PSD-95 gene*

Based on Northern blot analysis of different human tissue types, there are six human PSD-95 transcripts (Stathakis et al., 1997). They are found in a wide variety of neural and non-neural tissues and they are 4.2, 5.4, 6.2, 8.3, 9.5 and 12.3-kb. The most abundant of these PSD-95 transcripts, the 4.2-kb, shows the highest expression in the brain, but is also strongly expressed in the heart, testis, ovary, and skeletal muscle. Moderate expression is seen in the lung, placenta, kidney, pancreas, spleen, thymus, prostate, small intestine and breast tissue, while weaker signals are detected in the liver and colon. The second most abundant transcript, the 6.2-kb, is detected at moderate levels in the pancreas and ovary and at low levels in the heart, placenta, lung, skeletal muscle, kidney, spleen, thymus, prostate, testis, small intestine, colon and mammary

gland, but not in the brain. The 8.3-kb and 9.5-kb messages are detected only at low levels in various non-neural tissues, but not the brain. Finally, two tissue-restricted transcripts (5.4 and 12.3-kb) are present only in the testis. The above expression pattern observed for human PSD-95 contrasts with that of rat PSD-95/SAP90 for which only two brain-specific mRNA transcripts of 3.8-kb and 6.2-kb have been found (Cho et al., 1992; Kistner et al., 1993). The major 3.5-kb mRNA is present in the forebrain and cerebellum, and the minor 6.0-kb mRNA is enriched in the cerebellum (Cho et al., 1992). The rat transcripts might correlate with the 4.2- and 6.2-kb transcripts detected in human studies. Kistner et al. (1993), however, reported that 6.2-kb rat is expressed only during embryonic development, implying that the 6.2-kb human PSD-95 might not be expressed in adults (Kistner et al., 1993). So, except for the brief interval during development *in utero*, in rat, only a single transcript is expressed by the gene-encoding rodent PSD-95/SAP90 and the transcript is only found in the brain.

While there may be several reasons as to why additional transcripts are detected in human tissue, including technical reasons, such as increased test sensitivity, it is entirely plausible that they may reflect true differences between human and rodent expression patterns. Interestingly, a complex pattern of neural and non-neural tissue transcripts has also been reported for Dlg, the Drosophila orthologue of PSD-95. This implies that *DLG4* may have maintained several ancestral functions in humans that appears to have been lost or have acquired new functions in rodents (Stathakis et al., 2002).

Finally, more recently, the human PSD-95 transcriptome expression was quantified in several major tissues in the human body as part of the Human Protein Atlas (Fagerberg et al., 2014). A quantitative transcriptomics analysis (RNA-Seq) was used to measure the normalised mRNA expression levels in 27 different human organs and tissues. The analysis based on 3 human samples revealed the highest expression of PSD-95 mRNA in the brain among all tested sites, as illustrated in Figure 1.6 on page 23.

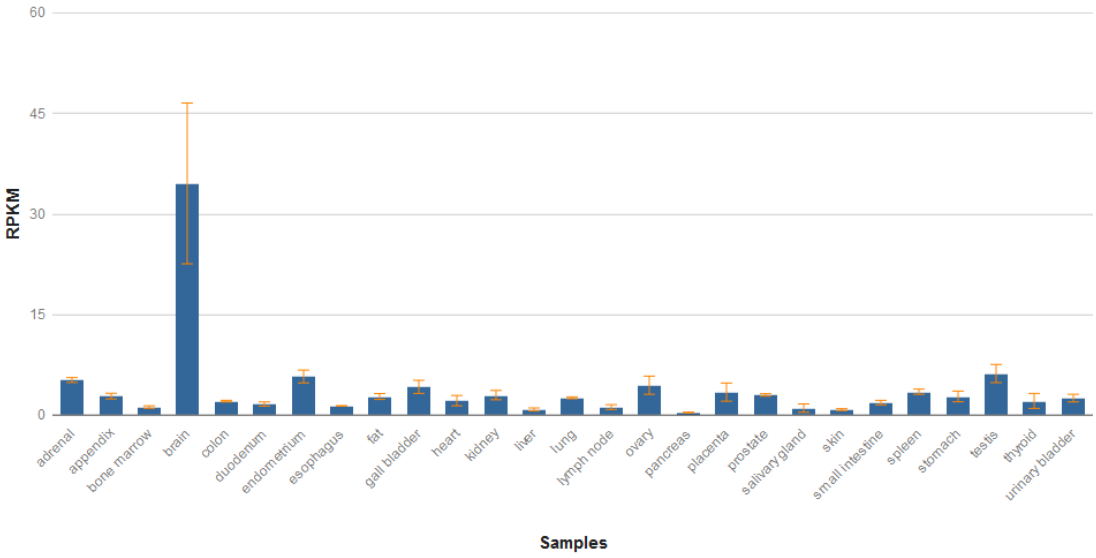


**Figure 1.6 The Human Protein Atlas PSD-95 mRNA expression.**
Barplots demonstrating expression of human PSD-95 mRNA in 27 different tissues from 3 individuals using RNA-seq as part of the Human Protein Atlas (Fagerberg et al., 2014). The normalised mRNA abundance is presented as FPKM (fragments per kilobase of exon model of mapped reads) values on y-axis. A FPKM of 1 roughly represents one mRNA molecule per average cell in the sample. The highest PSD-95 mRNA expression was reported in the brain (Mean FPKM 34.569 $\pm$ 11.992). The image has been downloaded from `http://www.ncbi.nlm.nih.gov/gene/1742/?report=expression&bioproject=PRJEB4337`.

#### *1.4.1.3 Alternative splicing of PSD-95 gene*

In humans, the first published analysis of splicing variants of *DLG4* determined that three different exons are alternatively spliced out of the 22 exons (Stathakis et al., 2002). Exon 3 was alternatively spliced in transcripts expressed in the brain; exon 20 was alternatively spliced out in transcripts expressed in breast and testis, and finally, an alternatively spliced exon 4 was found in the testis. However, even then it was noted that alternative splicing could not completely account for the number and size of the six DLG4 transcripts detected in the previous study (Stathakis et al., 1997) and a possibility of existence of additional alternatively spliced variants was considered.

Further interrogation of online resources, such as the Ensembl project (Yates et al., 2016) from `www.ensembl.org` website, and genome visualisation tools, such as the Biodalliance (Down et al., 2011) from `www.biodalliance.org` website, revealed that the human DLG4 gene has currently 10 transcripts (splice variants) that

code for 9 proteins, as demonstrated in Figure 1.7 and Table 1.1.

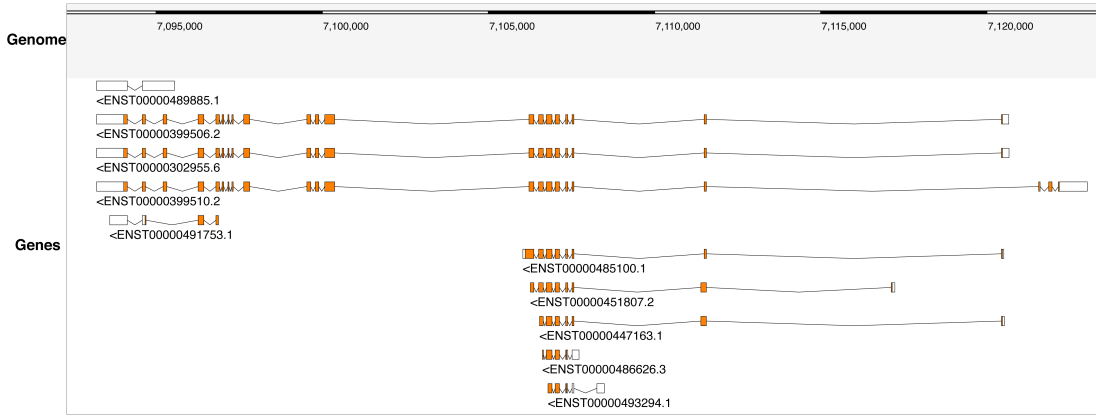


**Figure 1.7 Human DLG4 gene splice variants.**
Schematics demonstrating all known-to-date DLG4 gene splice variants in the human, as reported by the Biodalliance.org website (Down et al., 2011). Overall, 10 splice variants have been established for this gene. Graphics from Dalliance 0.13.0-dev at http://www.biodalliance.org.

**Table 1.1** Human DLG4 transcripts

| Name | Transcript ID | bp | Protein | Biotype | Exons |
|---|---|---|---|---|---|
| DLG4-001 | ENST00000399510.2 | 3975 | 767aa | Protein coding | 22 |
| DLG4-003 | ENST00000302955.6 | 3184 | 721aa | Protein coding | 20 |
| DLG4-002 | ENST00000399506.2 | 3185 | 724aa | Protein coding | 20 |
| DLG4-004 | ENST00000485100.1 | 1004 | 296aa | Protein coding | 8 |
| DLG4-006 | ENST00000451807.2 | 926 | 281aa | Protein coding | 8 |
| DLG4-007 | ENST00000447163.1 | 763 | 234aa | Protein coding | 7 |
| DLG4-009 | ENST00000486626.3 | 586 | 115aa | Protein coding | 5 |
| DLG4-008 | ENST00000493294.1 | 573 | 91aa | Protein coding | 5 |
| DLG4-011 | ENST00000491753.1 | 869 | 85aa | Nonsense mediated decay | 4 |
| DLG4-005 | ENST00000489885.1 | 1894 | No protein | Retained intron | 2 |

Table demonstrating a summary of all known DLG4 transcripts (splice variants) with transcript IDs, lengths in base pairs, proteins coded and exons, as freely available from the Ensembl project (Yates et al., 2016). Table downloaded from http://mar2017.archive.ensembl.org/Homo_sapiens/Gene/Summary?db=core;g=ENSG00000132535;r=17:7189890-7219702;t=ENST00000399510.

#### *1.4.1.4 Isoforms of PSD-95 protein*

In humans, three PSD-95 protein isoforms have been described, as reported on http://www.uniprot.org (The UniProt Consortium, 2017). Isoform 1, known as PSD-95-$\alpha$, has been chosen as the "canonical" sequence. It contains 724 amino acids and weighs 80,495 Da. Isoform 2, is known as PSD-95-$\beta$, has the longer sequence of 767 amino acids and a weight of 85,430 Da (Stathakis et al., 1997). Isoform 3, has the shortest amino acid sequence of 721 and a weight of 80,125 Da.

Existence of these alternative isoforms of PSD-95 protein provides yet more evidence of molecular diversity of this synaptic protein, this time at the sequence level. Combined, these data suggest that the production of the PSD-95 protein is regulated at multiple levels.

### 1.4.2 Expression of PSD-95

The overall expression patterns and localisation of PSD-95 protein has been described earlier in Chapter 1.3.2.1. Here additional information is provided.

#### *1.4.2.1 General expression of PSD-95*

The non-neural expression pattern of human PSD-95 has been conserved between rat and human proteins (Kornau et al., 1995). In non-neural tissue, the monoclonal antibody detected a prominent 85 kDa band in five tissue types, including the heart, kidney, lung, skeletal muscle and liver. Additionally two protein bands were recognised: an ≈80-kDa protein in the heart, lung, and skeletal muscle, and an ≈90-kDA protein in the liver.

The neural expression pattern of human PSD-95 is more complex. There are five bands of approximately 85-, 89-, 90-, 97-, and 109- kDa proteins, with the 97/109-kDa doublet showing the highest expression. Similar observations were made in the rat brain (Cho et al., 1992).

In mouse, PSD-95 mRNA distribution was consistent with previous results in adult rat brain using *in situ* hybridisation and immunohistochemistry. In particular, using *in situ* hybridisation, Fukaya and colleagues detected high levels of PSD-95 mRNAs in the telencephalon, although the pyramidal cell layer of the hippocampus displayed the highest expression. High levels were also detected in the cerebellar cortex, with low to moderate signals in various thalamic and brainstem regions (Fukaya et al., 1999).

#### *1.4.2.2 Heterogeneity of PSD-95 expression*

Apart from spatiotemporal and cellular DLGs heterogeneity in protein distribution described earlier, variation in DLG1-4 members localisation amongst adjacent PSDs was detected. For instance, some PSDs were devoid of PSD-95, PSD-93, or SAP102 in TEM preparations, suggesting that those PSDs without one DLG protein may utilise one of the others. In addition, in the same study, a weak but positive correlation between the PSD-95-immunolabelled particle numbers and the PSD length was found (Aoki et al., 2001). Even though the correlation was low, this finding provided evidence for heterogeneity in PSD-95 expression within individual synapses, since some PSDs expressed high levels of PSD-95, whereas others expressed lower levels. Furthermore, a proportion of synapses showed absence of PSD-95 labelling.

A recent study has provided an additional level of evidence for PSD-95 heterogeneity and demonstrated that PSD-95 may not be uniformly distributed within the PSD depending on the regional locatisation within the brain. Using a knock-in mouse and super-resolution microscopy, Broadhead et al. (2016) studied PSD-95 nanoclusters within the PSD. While size of the nanoclusters per synapse appeared conserved, the number of nanoclusters varied across different hippocampal subregions.

Overall, these observations add to the evidence for the concept of heterogeneity among DLG synapses at a protein level. Evidence shows that some PSDs might lack one or several members of DLG1-4 subfamily of proteins. In addition, as super-resolution studies reveal, protein distribution within the PSD may depend on location within the brain.

### 1.4.3 Binding partners of PSD-95

PSD-95 has no detectable enzymatic activity, but rather acts as an adaptor molecule through protein-protein interactions mediated by the discrete domains. The number of PSD-95 interacting protein partners is enormous and it would be difficult to provide an exhaustive list of all the proteins that are known to bind to PSD-95 (Figure 1.8 on page 28). The most important interactions are listed in Table 1.2 on page 32. This list contains a vast diversity of proteins belonging to different types of protein families, including ion channels, transmembrane proteins, neurotransmitter receptors, intracellular enzymes, adhesion molecules, cytoskeletal proteins and other scaffold proteins. As can be seen from the table, most of these PSD-95 interactors were defined using *in vitro* methods, including yeast-2-hybrid interaction and pull-down assays. These methods are thought to be useful in defining potential binary interactions between proteins, but do not accurately reflect the organisation of proteins *in vivo*, particularly when interactions are multivalent with more than two components involved (Frank and Grant, 2017). This fact has been highlighted by a recent study which demonstrated that some of *in vitro* defined interactions are not always found in *in vivo* testing. For instance, the canonical PDZ ligands of GluN2A and GluN2B have been found entirely dispensable *in vivo* for the assembly between NMDAR and DLG proteins, of which PSD-95 is a member (Frank et al., 2016).

#### *1.4.3.1 Transmembrane receptor binding partners of PSD-95*

PSD-95 interacts with several postsynaptic transmembrane receptors. For instance, in *in vitro* binding assays, rat PSD-95 interacts directly with the cytoplasmic tails of both Shaker-type voltage-gated $K^+$ channels (Kim et al., 1995) and the NR2 modulatory subunit of NMDA-type glutamate receptors (Kornau et al., 1995; Niethammer et al., 1996). In addition, co-transfection of heterologous cells with constructs encoding PSD-95 and with constructs encoding either type of transmembrane receptor gives rise to co-clustering of these proteins (Kim et al., 1995), suggesting that PSD-95 is an essential component in regulating the macrostructure of ion channels. Consistent with these *in vitro* studies, analysis of transgenic mice carrying a targeted mutation in

the gene encoding PSD-95 suggests that PSD-95 is essential in signal transduction by coupling the NMDA receptor to pathways that control bidirectional synaptic plasticity and learning (Migaud et al., 1998).

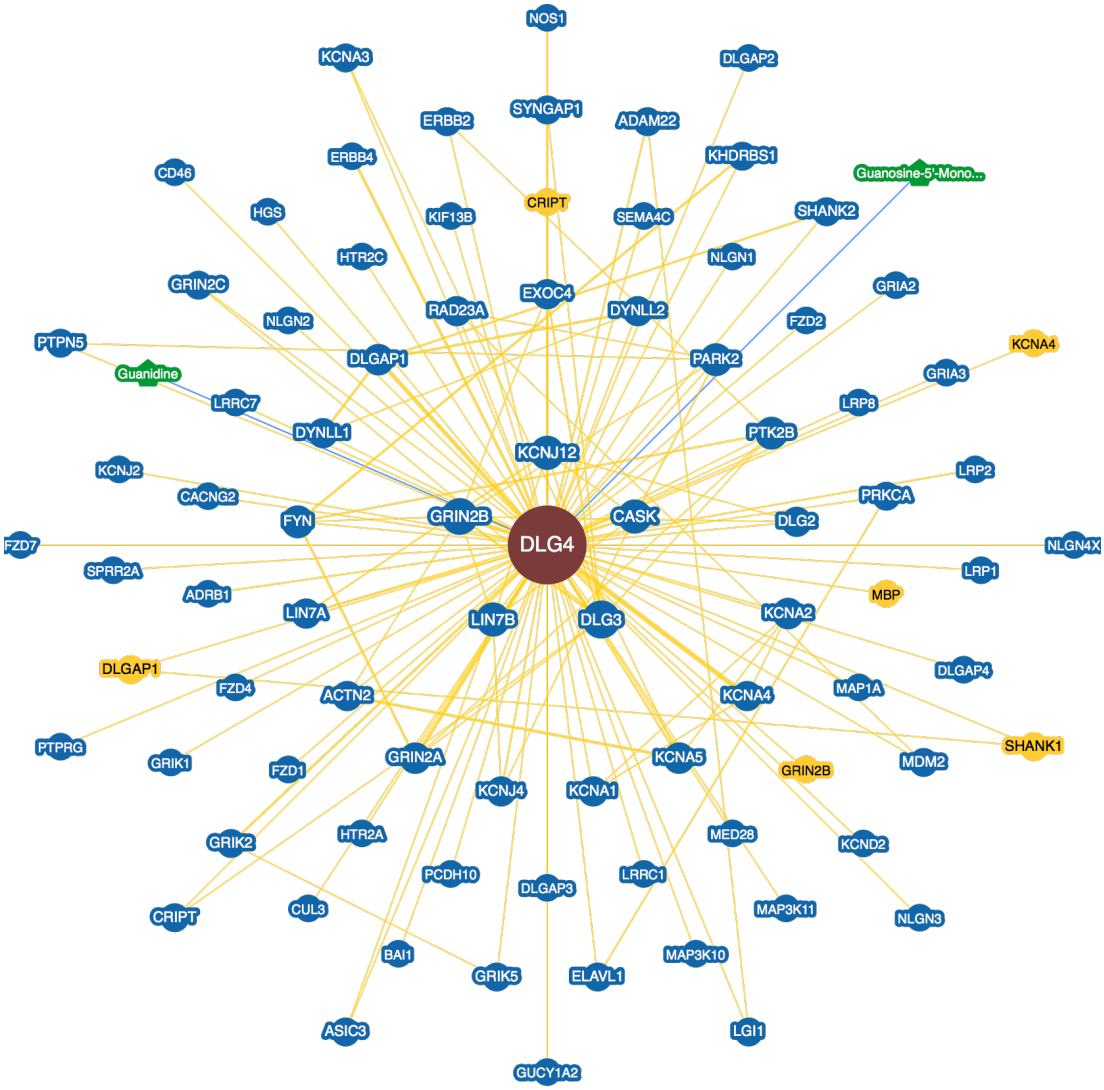


**Figure 1.8 Human PSD-95 (DLG4) network interactors.**
Schematics demonstrating the summary of all known PSD-95 (DLG4) interactors in the human from BioGRID (Stark et al., 2006). Overall, 197 physical interactions have been established for this protein. Overall network statistics revealed 88 total interactors (Nodes) and 133 total interactions (Edges). The interactor (Node) distribution showed 6 different organism nodes, as represented in yellow, and 2 chemical nodes (Guanidine and Guanosine-5'-Monophosphate), as shown in green. The image has been downloaded from (https://thebiogrid.org/108086/summary/homo-sapiens/dlg4.html).

#### 1.4.3.2 Signalling proteins of PSD-95

PSD-95 also binds to several intracellular signal transduction proteins. For instance, the first two PDZ domains of PSD-95 bind to the neuronal nitric oxide (NO) synthase (Brenman et al., 1996). Neuronal nitric oxide synthase is an enzyme activated by NMDA receptor-mediated $Ca^{2+}$ influx that catalyses the synthesis of nitric oxide, an important secondary messenger molecule. Importantly, the binding of NOS to PSD-95 has been clinically exploited, as will be described below.

Moreover, both *in vitro* and *in vivo* studies showed that PSD-95 binds SynGap, a Ras-GTPase-activating protein (Kim et al., 1998) that with several other proteins is associated with the neuronal cytoskeleton, including GKAP, myosin and dynein or SAPAPs (Kim et al., 1997; Naisbitt et al., 2000; Takeuchi et al., 1997).

#### 1.4.3.3 Clustering of PSD-95

Numerous studies suggest that PSD-95 is involved in the regulation of protein trafficking and clustering at the synapse. PSD-95 multimerisation, in particular, allows for association with postsynaptic membranes, other protein multimerisation, and clustering of cells surface receptors and ion channels. For instance, the SH3 and guanylate kinase domains of PSD-95 have been shown to associate in an intra-molecular fashion that has been reported to be necessary for clustering of membrane proteins (Shin et al., 2000). These domains may also contribute to multimerisation of PSD-95 in a head-to-tail fashion (Tavares et al., 2001; Tomita et al., 2001). Additionally, PSD-95 is able to dimerise via sequences in N-terminal residues (Tomita et al., 2001).

Overexpression of PSD-95 in hippocampal neurons leads to enhanced synaptic clustering of AMPA receptors but not NMDA receptors, as well as an increase in AMPA receptor mediated currents. This initially surprising finding, since PSD-95 binds to NMDA receptors and not to AMPA receptors, was subsequently explained by discovering that PSD-95 interacts with the AMPA receptor-associated protein stargazin, an important regulator of AMPA receptor trafficking (Schnell et al., 2002).

By regulating a dynamic pool of AMPA receptors, PSD-95 has therefore an additional direct role in regulating synaptic strength and thus synaptic plasticity.

These findings were replicated in *in vitro* studies using KO mutant mice. Knock-down PSD-95 brain slices and studies of PSD-95 KO mice have indicated that lack of PSD-95 leads to altered synaptic strength, so that LTP is enhanced while LTD is eliminated (Migaud et al., 1998). Furthermore PSD-95 KO mice showed significant deficiencies in a large repertoire of examined behaviours, including reduced spatial learning, simple operant conditioning, extinction or reversal of learned behaviours or attention experiments (Migaud et al., 1998; Komiyama et al., 2002; Nithianantharajah et al., 2013). A study by Nithianantharajah et al. (2013) demonstrated the central role of PSD-95 in all tested behaviours using KO mice for each of the four DLG paralogs. Mice lacking PSD-95 were not able to be tested in most cognitive tests. In contrast, SAP102 and PSD-93 KO mice showed only subtle behavioural deficits in complex tasks, albeit with opposing effects. In the same study, the researcher undertook comparative cognitive tests in human patients carrying mutations in the DLG2 gene coding for the PSD-93 protein. The human subjects displayed visual discrimination, learning impairments and lower flexibility when using touchscreens that were comparable with the defects observed in the PSD-93 KO mice. These data imply that the role of PSD-93 in cognition might be conserved between the humans and mice. This may also be true for PSD-95, but to this date, similar comparative studies using PSD-95 in human patients have not been possible since PSD-95 mutations in humans have not been clinically described (Nithianantharajah et al., 2013).

#### *1.4.3.4 Binding partners of PSD-95 and their relevance to human disease*

The interaction of PSD-95 and its partners have become important potential treatment targets in human disorders, such as stroke.

Since NMDAs are functionally coupled to neurotoxic signalling pathways, an obvious therapeutic approach is to block the receptors activated by glutamate. Antagonists at both NMDA and AMPA type glutamate receptors have demonstrated robust neuroprotection in rodent models of ischaemia (Dirnagl et al., 1999). Clinical

trials for stroke and traumatic brain injuries in humans have nevertheless failed (Lipton, 2006). The main reason is that inhibition of glutamate signalling impairs normal neuronal function resulting in unacceptable side effects. However, rather than targeting the NMDA receptor, it is possible to target its interacting protein in order to achieve neuroprotection.

Aarts et al. (2002) explored targeting the interaction between NMDA receptors and PSD-95 instead of the NMDA receptor (Aarts et al., 2002). The interaction between the PSD-95 and the GluN2B subunit of NMDA-receptors was first demonstrated by Kornau et al. (1995) who also showed that a nine-residue peptide mimicking the carboxyl-terminal of GluN2B was able to competitively inhibit this interaction (Kornau et al., 1995). Subsequently, Aarts and colleagues, using the same peptide, made it cell-permeable by fusing it to the membrane transduction domain of the human immunodeficiency virus-type 1 (HIV-1) transactivator of transcription (Tat) protein (Aarts et al., 2002). By transducing neurons with this peptide, called Tat-NR2B9c, the authors were able to dissociate PSD-95 from NMDA receptors by co-immunoprecipitation. This dissociation did not change NMDA receptor currents or $Ca^{2+}$ influx, but still had a neuroprotective effect against NMDA-induced excitotoxicity on cultured neurons, as well as after transient middle cerebral artery occlusion in rats (Aarts et al., 2002). Since the study was published, uncoupling of NMDA receptors from PSD-95 with consequent removal of nNOS from the proximity of the receptor became a potential therapeutic strategy for stroke. The Tat-NR2B9c peptide has subsequently been shown to be neuroprotective in nonhuman primate stroke models (Cook et al., 2012*a*,*b*) and has been found to be safe and cause a reduction, albeit not significant, in ischaemic stroke in patients undergoing surgery for aneurysms (Hill et al., 2012).

**Table 1.2** Selected PSD-95 interactors

| Protein | Description | Domain | Function | How* | References |
|---|---|---|---|---|---|
| Adam22 | A disintegrin and a metalloproteinase protein 22 | PDZ3 | Synapse maturation | 2 | (Fukata et al., 2006, 2017; Lovero et al., 2015) |
| AKAP79 | Scaffold for PKA, PKC and calcineurin | GK | Anchor for kinases and phosphatases | 3, 4b | (Colledge et al., 2000) |
| Arc/ Arg3.1 | Activity-regulated cytoskeleton associated protein | N/A | AMPA receptor trafficking and regulation | 2 | (Husi et al., 2000; Husi and Grant, 2001*b*; Fernández et al., 2017) |
| BEGAIN | Brain-enriched guanylate kinase-associated protein | GK | Organisation of synaptic junction components | 1 | (Deguchi et al., 1998) |
| Cript | Cysteine–rich interactor of PDZ three | PDZ3 | Recruitment of PSD-95 to microtubules, cytoskeletal anchoring | 1,2 | (Niethammer et al., 1998) |
| Cypin | Guanine deaminase enzyme | PDZ1-2 | Cytoskeleton assembly, regulation of dendritic branching, MAGUK trafficking | 4b | (Firestein et al., 1999) |
| Densin - 180 | Leucine-rich repeats brain-specific protein | PDZ1 | Protein organisation at postsynaptic membrane | 2 | (Ohtakara et al., 2002) |
| ErbB4 | Neuregulin (NRG) receptor tyrosine kinase | PDZ | Growth factor receptor, regulator of expression of voltage- and ligand-gated channels in neurons | 3 | (Garcia et al., 2000; Huang et al., 2001) |
| GKAP | Postsynaptic adaptor protein | GK | Assembly of multiprotein complexes, anchoring to cytoskeleton | 1 | (Kim et al., 1997; Takeuchi et al., 1997) |
| GPR85 | G protein coupled receptor 85 | PDZ1 | Regulation of neural and synaptic plasticity | 4b | (Fujita-Jimbo et al., 2015) |
| IRSp53 | Insulin receptor substrate p53 | PDZ2 | Scaffolding and adaptor protein | 3 | (Soltau et al., 2004) |
| KIF13b (GAKIN) | Kinesin Family Member 13b | GK | Trafficking of PSD-95 to the PSD | 4b | (Hanada et al., 2000) |
| Kv1 | Voltage-gated potassium channels | PDZ1-2 | Neuronal signalling | 3 | (Kim et al., 1995) |
| Maguin-1 | Membrane-associated guanulate kinase-interacting protein-1 | PDZ | Assembly of synaptic junctions components | 2 | (Yao et al., 1999) |

Continued on next page

**Table 1.2 – continued from previous page**

| Protein | Description | Domain | Function | How* | References |
|---|---|---|---|---|---|
| MAP1a | Microtubule-associated protein 1a | GK | Regulation of microtubule dynamics, neuronal morphogenesis | 4b | (Brenman et al., 1998) |
| Neuro -ligins | Neuronal cell surface adhesion proteins | PDZ3 | Formation and maintenance of synapses | 1, 4a | (Irie et al., 1997) |
| nNOS | neuronal Nitric Oxide Synthase | PDZ2 | Neurogenesis, regulation of glutamate receptor function | 3 | (Brenman, 1996; Gottschalk et al., 2009) |
| NR2A | Ionotropic glutamate receptor subunit | PDZ1-2 | Excitatory synaptic transmission, synaptic plasticity | 1, 3, 4a, 4b | (Cousins and Stephenson, 2012; Al-Hallaq et al., 2007) |
| NR2B | Ionotropic glutamate receptor subunit | PDZ1-2 | Excitatory synaptic transmission, synaptic plasticity | 3, 4a, 4b | (Kornau et al., 1995; Niethammer et al., 1996) (Cousins and Stephenson, 2012; Al Rahim and Hossain, 2013) |
| Preso | Membrane cytoskeletal linkers | C-T | Dendritic spine morphogenesis | 3, 4b | (Lee et al., 2008) |
| PSD-93 | Postsynaptic scaffold protein | N-T | Postsynaptic scaffold protein | 3, 2 | (Kim et al., 1996) |
| S-SCAM | Synaptic scaffolding molecule | GK | Assembly of multiprotein complexes, anchoring to cytoskeleton | 4b, 2 | (Hirao et al., 2000) |
| SALM2 | Cell adhesion-like molecules | PDZ | Differentiation of excitatory synapses | 3 | (Ko et al., 2006) |
| SAP102 | Postsynaptic scaffold protein | SH3, GK | Postsynaptic organisation | 1, 4b | (Masuko et al., 1999) |
| SAPAP | Postsynaptic adaptor protein | GK | PSD components assembly, anchoring to cytoskeleton | 4b, 2 | (Hirao et al., 2000) |
| SNX26 | Sorting nexin 26 - GTPase-activating protein for Cdc42 | PDZ | Dendritic spine formation, neuronal development | 3, 2 | (Kim et al., 2013) |
| SPAR | Spine-associated RapGAP | GK | Regulation of dendritic spine growth | 3 | (Pak et al., 2001) |
| Stargazin | Relative of $\gamma$-1 calcium channel | PDZ | AMPAR trafficking and localisation | 3 | (Chen et al., 2000) |
| SynGAP | Synaptic Ras-GTPase activating protein | PDZ1-3 | MAP kinase signalling, synaptic plasticity | 1, 2 | (Kim et al., 1998; Komiyama et al., 2002) |

* How are categories of evidence for interaction with PSD-95: 1 - yeast-2-hybrid, 2 - co-immunoprecipitation of endogenous proteins from brain extracts, 3 - co-immunoprecipitation from double-transfected heterologous cells, 4 - in vitro binding assay (4a - affinity chromatography with mass spectrometry or amino acid sequencing, 4b - GST pulldown). Abreviations: C-T, C-terminal; N-T, N-terminal.

## 1.5 IMAGING METHODS FOR VISUALISATION OF SINGLE SYNAPSES

Given our expanding knowledge about the extensive molecular diversity of synapses (O'Rourke et al., 2012), utilisation of high-throughput imaging systems, may be the best way to study synapses at a single synapse resolution. Currently, however, synapse imaging is limited to studying one part of the brain without the ability to appreciate any inter-regional differences or functional heterogeneity that has been revealed by the recent connectome studies (Oh et al., 2014). Nevertheless, various imaging methods have been utilised to investigate single synapses. While these techniques continue to contribute to better understanding of synapses, none are currently ideal.

### 1.5.1 Electron microscopy

Until recently, single synapses could only be visualised and characterised by EM, which remains the gold standard for investigating the interactions between individual molecules or molecular complexes (Hoenger, 2014; Kühlbrandt, 2014). However, EM is traditionally a time-consuming, labour intensive and volume-limited technique, despite advances that have greatly improved throughput (Harris et al., 2006; Knott et al., 2008). The method offers very limited proteomic discrimination and does not allow exploration of synapse diversity *in situ* as the integrity of tissue has to be broken into minute fragments, prohibiting acquisition of information about circuit context and cellular morphology.

### 1.5.2 Light microscopy

Postsynaptic densities are small (close to the resolution of the light microscopy at 250 nm) and their visualisation in the living state remains a challenge. However, they are big enough to be visualised by light microscopy (LM). The two most common light microscopes used to study synaptic components, such as PSD-95 IF labelled postsynaptic elements, are laser scanning confocal microscope (LSCM) and spinning disk microscope (SDM).

#### 1.5.2.1 *Laser scanning confocal microscopy*

Laser scanning confocal microscope with a typical xy-resolution of 180 - 250 nm and a z-resolution of 500 - 700 nm, has been the gold standard tool in examining synapses. LSCM utilises a single pinhole that restricts imaging to a thin optical fragment of tissue as it removes the out-of-focus light originating from other depths of tissue. LSCMs have been used to visualise single synapses in a range of assays from cell cultures to brain tissue slices. However, as the laser beam has to travel across the sample in order to acquire the complete image in a pixel-by-pixel manner, LSCM is relatively slow and less efficient than other microscopy systems, such as a spinning disk microscope (Wang et al., 2005).

#### 1.5.2.2 *Spinning disk confocal microscopy*

Spinning disk microscopy is a fast acquisition example of a confocal system that has been widely used for live imaging of rapid processes (Gräf et al., 2005). SDM is equipped with dual rotating disks (confocal spinning disk unit, CSU). The first disk contains micro-lenses that focus the light into the multiple pinholes of the second disk. The second disk, or Nipkow disk, allows illumination of multiple points of the same sample simultaneously allowing for high-speed confocal imaging. SDM has an equivalent horizontal resolution as LSCM, although its axial resolution is slightly compromised by the cross-talk between different pinholes (Wang et al., 2005). An advantage of using SDM is that they commonly use an electron multiplying charge-coupled device (EMCCD) that has better signal-to-noise performance and higher sensitivity in comparison to LSCM.

### 1.5.3 Array tomography

One of the recent methods for studying human synapses is array tomography (AT), a high-resolution imaging method that combines light and EM approaches to resolve fine synapse details (Micheva et al., 2010; Micheva and Smith, 2007). AT allows the immunofluorescence resolution of a single synapse and meticulous cataloguing

of synapses and thus exploration of the molecular diversity of synapses. In AT, a matrix of serial brain sections are arranged on coated glass slides, on which antibody labelling could be multiplexed to allow characterisation of synapses by fluorescence light microscopy. It is possible to acquire multidimensional immunofluorescence information about single synapses (up to 24, as compared with to the standard immunofluorescence limit of four). Another advantage is that AT can be automated and delivers very high experimental throughput with an estimated rate of one million synaptic puncta per hour. Importantly, AT has been extended to SEM imaging and correlative approaches. However, the method is also time-consuming and complicated.

### 1.5.4 Super-resolution microscopy

In addition, there are several technologies available to examine synapses collectively known as super-resolution microscopy or nanoscopy, and they include STimulated Emission Depletion (STED) microscopy; single-molecule localisation techniques, such as Photoactivation Localisation Microscopy/Stochastic Optical Reconstruction Microscopy (PALM/STORM); or Structured Illumination Microscopy (SIM) (Schermelleh et al., 2010). All these techniques exploit properties of fluorescent molecules and use various strategies to overpass the light diffraction limit. For instance, in STED microscopy, the focal plane is scanned with two overlapping laser beams. While the first laser excites the fluorophores, the second longer wavelength laser drives the fluorophores back to the ground state by the process of stimulated emission. Alignment of both laser beams reduces the volume of molecules fluorescing within the field of illumination leaving only a small central portion of STED-induced illumination to be able to fluoresce therefore reducing the point spread function (PSF) below the diffraction limit. Single-molecule localisation microscopy assures that only a small number of fluorophores are in the active emitting state. The fluorescence signal from each molecule can be fitted to a Gaussian distribution and its centre point can be detected with nanoscale position. Subsequently, single molecule positions from several thousand raw images are used to generate a density map with several hundred thousand single molecule positions within the plane of focus. Finally, in SIM microscopy, the sample plane is excited by a non-uniform wide-field illumination.

One of the great contributions of super-resolution microscopy to our understanding of synapses was the discovery that synaptic proteins are heterogeneously distributed within the PSD (Fukata et al., 2013). Unlike EM, which visualised synapses as uniform structures of different types, the super-resolution methods revealed a sub-synaptic architecture of proteins arranged into clusters (MacGillavry et al., 2013; Nair et al., 2013). In fact, studies demonstrated that PSD-95 protein in particular is composed of nanoclusters (MacGillavry et al., 2013; Broadhead et al., 2016). What is even more intriguing is that there is heterogeneity in cluster distribution in murine brain, providing yet another level of evidence of synaptic diversity. For instance, it has been demonstrated that in the circuitry of the hippocampus, there is an architecture to the organisation of synapses, where different hippocampal subregions express different numbers of nanoclusters (Broadhead et al., 2016).

### 1.5.5 Complimentary techniques

Complementing the above light microscopy techniques are a range of fluorescence protein-based synapse-detectors, widely used in animal studies, but not available for use in human tissue (Lee et al., 2016). Imaging synapses with LM by using engineered fluorescent protein (FP) tagged to synaptic proteins or targeted to synaptic structures enables fine-resolution visualisation of synaptic anatomy in neural areas and within large circuits. For instance, single component synaptic detection has been possible since the discovery of green fluorescent protein (GFP), which can be used to tag synaptic proteins while minimally interfering with their normal function. Unsurprisingly, PSD-95 has already been tagged with GFP (Broadhead et al., 2016; Nelson et al., 2013). The advantage of using fluorescence protein-based synapse-detectors is that these proteins are in close proximity to the targeted protein, which is a limitation when using antibodies, which can cause distance displacement issues.

However, in order for the FPs to be detected and used for brain-wide synaptic mapping, a partnership with technologies, such as gene delivery, was required to expand the single-synapse level analysis to systems level neuroscience. Gene delivery

technologies can broadly use germ line manipulation and viral injections. Genetic manipulation-based gene delivery led to the development of gene knock-in (KI) technology that substitutes wild-type genes with FP-tagged copies. Subsequently, proteins, such as PSD-95 can be expressed throughout the brain mimicking patterns of endogenous PSD-95. A PSD-95eGFP mouse produced using the gene delivery technology has been created in the Grant laboratory (Dr Zhu, manuscript in preparation, (Broadhead et al., 2016).

More recent development of this technique allows for a conditional KI strategy called endogenous labelling via exon duplication (ENABLED) (Fortin et al., 2014). When a PSD-95-ENABLED mouse is crossed with a dopaminergic cell-type specific DAT-Cre line, such as PSD-95mVenus, PSD-95 can be expressed specifically in dopaminergic neurons, allowing assessment of detailed PSD-95 distribution in dopaminergic systems. Therefore, once FP-based synaptic detectors are introduced into the brain using gene technology, appropriate brain-wide digital image analysis can be used to map synaptic anatomy and connectivity throughout the brain.

To summarise, visualisation and characterisation of synapses in brain tissue are typically performed on biopsy or post-mortem tissue using electron microscopy or immunohistochemistry combined with various light imaging platforms, such as brightfield, confocal or super-resolution microscopy. Supporting these techniques are fluorescent protein-based molecular detectors and gene delivery technologies, which allow for precise imaging of individual synapses. These tools combined whole-brain imaging (for instance, using SDM) and computational analysis allow for deciphering of synaptic anatomy across the whole brain. However, the major limitation of these techniques is that these tools are only available for animal studies.

### 1.5.6 Brain imaging

Finally, recent imaging techniques have been used to quantify synapses in the living human brain. Using positron emission tomography (PET) and a synapse-specific radioligand, for the first time, (Finnema et al., 2016) demonstrated that it is feasible to quantify synapses in nonhuman primates as well as healthy human

controls and patients with epilepsy. The radioligand, called [11C]UCB-J [(R)-1-((3(11C-methyl-11C)pyridine-4yl)methyl)-4-(3,4,5-trifluorophenyl) pyrrolidin-2-one] or [11C]UCB-J has been developed to bind to the presynaptic synaptic vesicle glycoprotein 2A (SVA2), which has been used as an *in vivo* proxy of synaptic density. The authors investigated 12 areas in the human brain and showed that [11C]UCB-J PET, not only can detect regional densities of SV2A across human brain, but also can reveal changes in synaptic density in patients with compared to healthy individuals. The SV2A-PET imaging is a promising, minimally invasive marker of synaptic density, particularly in diseases associated with synaptic loss, such as Alzheimer's disease. This imaging method could provide a valuable link between studies of synaptic diversity in human disease using both post-mortem tissue and *in vivo* imaging in living patients.

## 1.6 SYNAPTIC DISEASES OF THE HUMAN BRAIN

The human brain is estimated to contain approximately 100 trillion synapses arranged in intricate networks to generate complex human behaviours, including thinking, learning, memory, emotions and dreaming. Given the enormous synapse abundance together with a high synapse proteome complexity, it is not surprising that structural disruption and/or loss of synapses can result in network dysfunction with abnormal neuronal signalling, which clinically manifest as brain diseases.

Synaptic pathology has indeed been linked to a number of neurological conditions in humans (Lepeta et al., 2016). One study estimated that over 100 brain disorders are linked to mutations in genes encoding human postsynaptome (Bayés et al., 2011). In fact, a growing body of evidence reveals that disruption to synaptic proteins gives rise to synaptic diseases, or synaptopathies (Grant, 2012; Henstridge et al., 2016; Lepeta et al., 2016). As synaptopathies cross the traditional boundaries of neurology and psychiatry, they encompass a wide range of brain diseases spanning from common neurodegenerative disorders, such as Alzheimer's disease, Parkinson's disease or Huntington's disease, to neuropsychiatric disorders, such as schizophrenia, autism, intellectual disability, or rare neurodevelopmental disorders, such as Fragile X Syndrome. Currently, none of these disorders are curable. Therefore establishing

the impact of abnormal synaptic systems on health is crucial for increasing our understanding of, not only basic brain functions, such as learning and memory, but also the rational treatment for these progressive diseases. Understanding of synapses and their pathology is therefore an important part of scientific endeavour.

Finding a synaptic quantification method that is compatible with the structural complexity and volume of synapses in human tissue would be an important development. Whilst many of the synaptopathies are not subject to traditional neuropathological disease classifications, proteomic, genetic and phenotypic data could provide new insights into the pathophysiology of these diseases. Potential therapeutic modalities developed as a result of these new scientific data analyses could lead to the future restoration of optimal synaptic functions in synaptopathies.

Many MAGUK proteins have been linked to human brain disorders, including PSD-95. Below is a brief description of selected diseases, in which PSD-95 protein aberrations have been directly or indirectly implicated, and therefore would potentially benefit from our novel quantification method. Although this is not an exhaustive list, it provides an insight into the potential clinical impact of our new quantification technique.

### 1.6.1 Neuropsychiatric disorders

Neuropsychiatric disorders are an important group of conditions characterised by life-long cognitive dysfunction associated with different underlying causative genetic mechanisms and postsynaptic targets.

#### *1.6.1.1 Schizophrenia*

PSD-95 has been implicated in the pathogenesis of schizophrenia. For example, Felice Iasevoli et al demonstrated changes in protein and mRNA expression of several PSD members, including PSD-95, in post-mortem tissues from schizophrenic patients (Iasevoli et al., 2013). Furthermore, PSD-95 expression was reduced in prefrontal cortex of schizophrenic patients (Ohnuma et al., 2000). Increased levels

of PSD-95 and NMDA receptor subunits were significantly higher in post-mortem dorsolateral prefrontal cortex and occipital cortex of schizophrenics as compared to controls (Dracheva et al., 2001). Schizophrenics also had increased levels of PSD-95 transcripts. Moreover, multiple *de novo* mutations in genes coding for members of the DLG family members are associated with schizophrenia and polymorphic markers in DLG gene encoding for PSD-95 are associated with susceptibility to schizophrenia (Cheng et al., 2010). Another study further identified multiple mutations in synapse proteome with enrichment of mutations in the PSD and MASC complexes, including the MAGUK scaffold protein PSD-93 (Banerjee et al., 2014). In addition, patients with schizophrenia have been shown to possess enhanced PSD-95 - ErbB4 coupling (Hahn et al., 2006). Overall, the evidence suggests that schizophrenia is a complex glutamatergic synapse problem, in which PSD-95 is one of the affected proteins (Morrison and Pilowsky, 2007).

#### *1.6.1.2 Autism*

PSD-95 may be indirectly linked to autism. This is a complex neurodevelopmental disorder with a strong genetic link. Clinically autistic patients show impairments in social interaction with social and emotional deficits, impairments in relationships and stereotyped behaviours. Since the disorder encompasses a spectrum of clinical phenotypes, it is better defined as Autism Spectrum Disorders (ASD) (Brian et al., 2015; Lord and Bishop, 2015; de Schipper et al., 2015). It is believed that ASD is linked to abnormal expression of a diverse set of genes encoding synaptic proteins with related functions in synaptic development and activity (Zoghbi and Bear, 2012). Supportive evidence comes from genetic studies showing that mutations in the scaffolding protein Shank (Durand et al., 2007) and neurexin (Feng et al., 2006) are associated with autism. Both of these proteins interact with PSD-95, although a specific PSD-95 mutation in autism has not been yet demonstrated. More recently, two mutations in yet another protein interacting with PSD-95 via neuroligin receptor complex, GPR85, have been found in autism patients (Fujita-Jimbo et al., 2015). Moreover, a single nucleotide polymorphism (SNP), called rs13331, of exon 22 of PSD-95 has recently been shown to confer an association with an increased risk of

ASD (Wang et al., 2016). Increasingly, evidence supports the idea that there is an error in the general function for synaptic proteins working within common molecular pathways giving rise to ASD (Jiang and Ehlers, 2013).

#### *1.6.1.3 Fragile X syndrome*

Changes in PSD-95 have also been detected in Fragile X Syndrome (Tsiouris and Brown, 2004). This is an inherited form of mental retardation caused by silencing of a single gene (FMR1) that codes for the Fragile X mental retardation protein (FMRP). The FMRP protein is involved in mRNA translation and its expression is induced by mGluR activation. FMRP is involved in mGluR-mediated synaptic plasticity and activation of mGluR increases translation of PSD-95 via an FMRP-mediated mechanism. More recently, Zalfa and colleagues reported a new role for the FMRP in regulation of PSD-95 mRNA stability (Zalfa et al., 2007). Nevertheless, mutations in the human DLG3 gene, rather than DLG4, have been shown to be associated with X-linked mental retardation (Tarpey et al., 2004). It is believed that the truncating mutations of DLG3 impair the ability of SAP102 to interact with the NMDA receptor and/or with other proteins involved in signalling pathways downstream of the NMDA receptor.

#### *1.6.1.4 Drug addiction*

PSD-95 has been implicated in diminished behavioural and synaptic plasticity associated with psychostimulant drug addition. Reduced levels of PSD-95 have been found in animal models of chronic psychostimulant abuse (Yao et al., 2004). In addition, a study examining a direct interaction between the N-terminal region of PSD-95 and the dopamine D1 receptor revealed that PSD-95 reduces D1 receptor surface expression, reducing dopamine-mediated excitation of medium spiny neurons and cortical pyramidal neurons (Zhang et al., 2007). Moreover, PSD-95 knockout animals show enhanced D1-mediated responses. It therefore has been hypothesised that interactions between D1 receptors, PSD-95 and NMDA receptors provide a mechanism for simultaneous regulation of surface expression and prevent

excessive positive feedback generated between the two receptors, altering the balance between dopaminergic and glutamatergic signalling at individual spines by changing receptor/scaffold complexes.

### 1.6.2 Neurodegenerative disorders

Neurodegenerative disorders represent another group of conditions characterised by alterations in synaptic machinery and disrupted synaptic plasticity. Perturbed synaptic functions are thought to be secondary to synapses being exposed to pathologically-modified protein aggregates. For instance, accumulation of different abnormal protein aggregates, including A$\beta$ and hyperphosphorylated tau, $\alpha$-synuclein, and Huntingtin are the hallmarks of Alzheimer's disease, Parkinson's disease and Huntington's disease, respectively. Despite the different proteins underlying neurodegeneration, all these diseases share synaptic pathology as a common feature. The abnormal protein aggregates may induce synaptic loss in vulnerable brain areas. They may also alter synaptic proteins, impair synaptic vesicle transport and alter synaptic and dendritic morphology. The nature of the synaptic alteration, however, may not necessarily be the same within each disorder.

#### *1.6.2.1 Alzheimer's disease*

Alzheimer's disease (AD) is the most prevalent form of dementia in the elderly population (Scheltens et al., 2016). Patients suffering from AD characteristically develop progressive memory impairment, cognitive decline, personality changes, and ultimately, complete dependence on others (Sheng et al., 2012). The Apolipoprotein E (ApoE) gene is the most important genetic susceptibility factor for the disease, with the ApoE4 allele increasing the risk for AD threefold to fourfold in heterozygous cases (Kim et al., 2009; Yu et al., 2014). The neuropathological hallmarks of the disease are deposition of insoluble extracellular beta-amyloid (A$\beta$) plaques and intraneuronal hyperphosphorylated tau-positive neurofibrillary tangles (NFTs) (Selkoe et al., 2012). A very small fraction of AD patients (1-5%) have genetic form of the disease with the majority of AD cases being idiopathic (Gatz et al., 2006).

The best correlation between cognitive decline and neuropathological changes is observed with neurofibrillary tangles (Braak and Braak, 1990) and synaptic loss (Terry et al., 1991), whereas the relationship between the density of A$\beta$ plaques and loss of cognition is weaker. This suggests that the loss of synapses is sufficient to drive AD-related cognitive changes prior to loss of neurons (Selkoe, 2002; DeKosky and Scheff, 1990).

Although the mechanism for synapse loss is not fully understood, abnormal tau and amyloid proteins have both been implicated. The role of these proteins in triggering synaptic loss is still being elucidated. Soluble A$\beta$, rather than deposited plaques, has been considered the trigger for synaptic damage and subsequent cognitive decline in AD, with tau protein acting downstream of A$\beta$ in AD pathology (Ferreira et al., 2015; Bilousova et al., 2016). This idea is supported by identification of the pathogenic soluble A$\beta$ species at damaged synapses in AD (Takahashi et al., 2004) and their association with PSD *in vivo* (Koffie et al., 2009). The mechanisms of A$\beta$ toxicity are, however, not fully understood, but it has been shown that oligomers can interact with synaptic proteins, including PSD-95 (Pham et al., 2010). Contrary to this, there is evidence that the loss of neocortical synaptic inputs in AD could be independent from amyloid deposits (Masliah et al., 1993). Moreover, neurodegeneration in AD is not a direct result of extracellular A$\beta$ neurotoxicity (Carter and Lippa, 2001). In addition, synaptic deficits are observed in many neurodegenerative conditions, which are independent of any A$\beta$ pathology, such as Fronto-Temporal Lobar Degeneration (FTLD), Progressive Supranuclear Palsy (PSP), or Niemann-Pick Disease Type C (NP-C) (Jadhav, Cubinkova, Zimova, Brezovakova, Madari, Cigankova and Zilka, 2015). Thus, A$\beta$ pathology on its own may not be sufficient to act as a direct causal agent for synapse loss (Musiek and Holtzman, 2015). There are only a limited number of studies reporting tau protein as the direct candidate mediating synaptic protein loss. Instead, several lines of indirect evidence point to tau pathology being an important factor in mediating synaptic damage. For instance, as mentioned previously, tau pathology correlates well with the cognitive decline in patients affected by AD, it shows stronger correlation with synapse density and synapse loss parallels tangle formation. Moreover, synapse loss occurs in the same regions as tangle formation in AD brains (Davies et al., 1987), and higher tangle counts are associated with lower

levels of presynaptic proteins in AD (Honer, 2003). Finally, neurons with NFTs have selective synaptic deficits and show a 35-57% reduction in synaptophysin mRNA in the AD brain (Callahan et al., 2002). Although not definitive at this stage, the evidence for a well-established relationship between synaptic pathology and tau pathology appears stronger than for A$\beta$ pathology. Importantly, the modern understanding of AD incorporates these opposing views into a general scenario proposing synapse failure as underlying cause of cognitive decline (Lepeta et al., 2016).

In addition to the controversies regarding the causative factors in AD, there are further debates regarding the exact synaptic component targeted in AD. Early studies suggested that AD is predominantly a result of presynaptic dysfunction. For instance, conditional genetic inactivation of presenilins, proteins involved in generation of A$\beta$ forms, in the mouse forebrain led to impaired NMDA receptor function, defective LTP, defective learning and memory, and age-related neurodegeneration (Saura et al., 2004; Zhang et al., 2009). By genetically disrupting presenilins in hippocampal presynaptic (CA3) or postsynaptic (CA1) neurons, Zhang et al. (2009) showed that presynaptic, but not postsynaptic presenilin is required to support normal LTP as well as short-term plasticity and synaptic facilitation. The preferential presynaptic loss in AD has originally been documented in studies using electron microscopy (Masliah et al., 1991). More recently, the presynaptic changes are usually measured by detecting changes in synaptophysin immunoreactivity, synaptophysin being a synaptic vesicle protein (Selkoe, 2002). However, preferential reduction in postsynaptic compared with presynaptic elements has been documented based on decreased levels of drebrin, a postsynaptic actin-binding protein (Harigaya et al., 1996; Shim and Lubec, 2002). The pathological changes in PSDs due to dynamic rearrangements caused by proteins, such as drebrin, could alter the assembling and elimination of PSD components and subsequently might lead to a fast alteration of synaptic structures underlying normal function or pathological changes of synapses. Evidence to support this idea comes from studies demonstrating altered PSDs in pathological states. For instance, PSDs from frontal cortical regions of patients with AD, isolated and analysed using proteomic approaches, showed significant alterations in a range of postsynaptic proteins, including PSD-95 (Gong et al., 2009). The pathological changes in these PSD proteins could directly or indirectly affect the dendritic spine, synapse function

and homeostasis (Gong and Lippa, 2010). Further evidence that supports the idea that the postsynaptic component may also be involved in AD comes from studies examining tau protein. Historically, tau protein was believed to be mainly confined to axons, but recent studies indicate that it can also be found in both the nucleus and dendrites (Zempel et al., 2010; Ittner et al., 2010; Hoover et al., 2010). Importantly, tau has also been reported to accumulate in the somatodendritic compartment in AD (Ballatore et al., 2007; Li et al., 2011). Tau protein has been found in the PSD with one study ientifying tau in total synaptosomes isolated from a rat brain (Mondragón-Rodríguez et al., 2012). However, other studies have failed to reproduce this finding (Jadhav, Katina, Kovac, Kazmerova, Novak and Zilka, 2015). Even though evidence points to preferentially presynaptic axonal tau localisation, tau protein has been shown to migrate to dendrites following synaptic activation (Frandemiche et al., 2014). Mislocalisation of hyperphosphorylated tau in dendritic spines is thought to disrupt glutamate receptor trafficking and thus synaptic function (Hoover et al., 2010). Significantly, in synapses, tau protein has been found to interact with various proteins, including NMDAR and PSD-95 (Mondragón-Rodríguez et al., 2012). Finally, a recent meta-analysis of synaptic pathology in AD has clearly demonstrated that both pre- and postsynaptic components are affected in this neurodegenerative disease (de Wilde et al., 2016). Analysis of 57 synaptic markers revealed that the hippocampus and the frontal cortex showed similar reduction of synaptic markers, although more presynaptic markers were affected than postsynaptic markers. Interestingly, the difference between pre- and postsynaptic markers was the greatest in the hippocampus, as demonstrated in Figure 1.9 on page 47.

Lastly, several human studies have demonstrated alterations of PSD-95 in AD indicating the importance of this postsynaptic protein in AD pathogenesis (Love et al., 2006; Leuba, Savioz, Vernay, Carnal, Kraftsik, Tardif, Riederer and Riederer, 2008; Leuba, Walzer, Vernay, Carnal, Kraftsik, Piotton, Marin, Bouras and Savioz, 2008; Proctor et al., 2010). Even though human studies show inconsistent results, they could be explained by assessment of different anatomical areas and different techniques used. Animal studies are thought to be limited as they do not show the full spectrum of pathological changes observed in AD.

In summary, although there is increasing evidence that synaptic dysfunction is potentially one of the major determinants of AD, a direct link to disruptions in synaptic structure and function as the prime cause of AD is missing, and at present, AD could not be resolved as a simple synaptic dysfunction disorder. However, despite these limitations in our understanding of AD pathophysiology, there is a need to further investigate the role of abnormal synapses in AD to reveal their impact on the balance between the cause and effect in this disease.

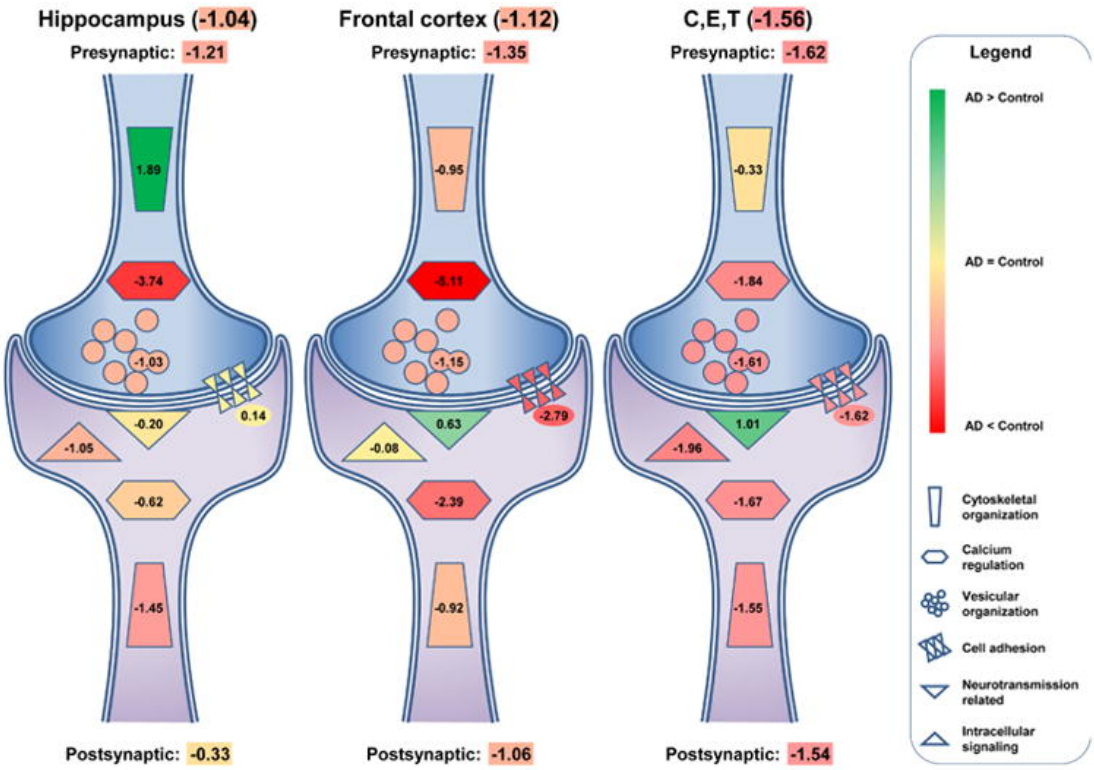


**Figure 1.9 Presynaptic and postsynaptic marker changes in AD.**
Schematic representation of presynaptic and postsynaptic marker changes in the hippocampus, the frontal cortex, C, E, T (cingulate gyrus, entorhinal cortex, and temporal cortex) in AD. In these areas, presynaptic markers are more affected than postsynaptic markers and the greatest difference between the synaptic terminals is seen in the hippocampus. The changes are measured in the standard mean differences (SDM) between the markers. Image reproduced from an open access article under the CC BY NC ND licence (de Wilde et al., 2016).

#### *1.6.2.2 Huntington's disease*

Huntington's disease (HD) results from a trinucleotide (CAG) repeat expansion in the huntingtin gene, giving rise to a polyglutamine expansion in the huntingtin protein. This causes selective degeneration of striatal GABAergic medium-sized spiny neurons (MSNs) that clinically manifests as movement disturbances (chorea and bradykinesia), cognitive deficits (dementia), and psychiatric problems (depression). Notably, wild-type huntingtin protein exists in the PSD and binds to PSD-95. Specifically, Sun et al. (2001) demonstrated that polyglutamine expansion impairs the ability of huntingtin protein to bind PSD-95 and promotes neuronal sensitivity to glutamate-mediated excitotoxicity, which may be important in the pathogenesis of Huntington's disease (Sun et al., 2001). Moreover, mutant protein has been found to alter normal trafficking of postsynaptic receptors in a transgenic model of HD, a finding that could be exploited clinically. More recently, Fan et al. (2009) demonstrated using a YAC transgenic mouse model of Huntington disease that uncoupling NR2B-containing NMDARs from PSD-95 eliminated excess NMDAR neurotoxicity in this system revealing a possible therapeutic modality for HD (Fan et al., 2009).

#### *1.6.2.3 Parkinson's disease*

Parkinson's disease (PD) is a movement disorder which can, in some cases, have associated dementia (Parkinson's disease dementia). It is caused by progressive loss of dopaminergic neurons projecting to the striatum. In Parkinson's disease dementia the clinical features include fluctuating cognitive impairment with loss of attention and executive function, visual hallucinations and pathognomonic motor disturbances of rigidity, pill-rolling tremor, bradykinesia and postural instability. PD is treated with exogenous L-DOPA to enhance dopamine signalling. Classically, neuropathology reveals accumulation of the presynaptic $\alpha$-synuclein protein forming neuronal intracytoplasmic aggregates called Lewy bodies, and extracellular Lewy neurites. PD is considered a presynaptic dysfunction, but postsynaptic compartment is also affected. For instance, L-DOPA diskinetic rats showed abnormal redistribution of NMDA receptor subunits in the striatum, including an increase in NR2A and a decrease

in NR2B subunits. The abnormal NR2B redistribution, in particular, was correlated to abnormal motor behaviour after chronic L-DOPA treatment (Gardoni et al., 2006). More recently, Chen et al. (2015) demonstrated decreased NMDA-dependent currents in cultured hippocampal neurones after $\alpha$-synuclein internalised NMDA receptors affecting $Ca^{2+}$ signalling (Chen et al., 2015).

### 1.6.3 Neurological disorders

Glutamate is the major excitatory amino acid neurotransmitter within the CNS and glutamate receptors are pivotal in mediating excitotoxic brain damage. Understanding how PSD scaffolding protein-protein interactions may contribute to NMDA receptor-mediated excitotoxic insults and how alteration of these interactions can reduce excitotoxic brain damage against glutamate-mediated excitotoxicity is an important area of research (Aarts et al., 2002). Stroke (Iasevoli et al., 2013) and epilepsy (Ying et al., 2004) are conditions where NMDA receptor-mediated excitotoxicity has been implicated in their pathogenesis. However, altered interactions between PSD-95, in particular, and NMDA receptors have been found in other neurological disorders, including transient global ischaemia, trauma or pain (Arundine and Tymianski, 2003; Sattler and Tymianski, 2000). Better understanding of how to disrupt the underlying synaptic interactions may offer better insight into future treatment of these conditions.

### 1.6.4 Conclusion remarks

Human brain disorders have a significant impact on affected individuals, families and society and greater understanding of the role of synaptic proteins in these diseases is necessary for the development of effective treatment modalities. The underlying molecular complexity of synapses, however, may be one of the reasons for the lack of progress in treating many of these disorders (Dieterich and Kreutz, 2016; Reig-Viader et al., 2017).

The enormous molecular synaptic complexity requires that our understanding of synapses may need to be adjusted from a belief that synapses are simple connectors

between neurons to understanding that they are complex dynamic structures capable of complex computations giving rise to complex behaviours and phenotypes. Perhaps then, rather than exploring 'single protein default' science, we should direct our thinking at changes affecting systems and a constellation of proteins. Alternatively, we could explore the 'single protein default', but at a much larger scale - at the whole brain scale. However, for that we need to take advantage of modern technology and computational powers available to researchers at present. Fortunately, diverse techniques of contemporary neuroscience combined with powerful computational capabilities have started to allow for the new technologies to be implemented.

One such powerful method of synapse quantification will be presented in this dissertation.

## 1.7 FINAL AIMS

There are two aims of this dissertation.

Firstly, to adapt the existing Genes to Cognition Synaptome Mapping Pipeline (G2CSynMaP), which comprises a standardised synapse imaging platform, quantification methodology and a bespoke image analysis, developed at the Grant laboratory to quantify synapses in a genetically modified mouse, to human tissue. This would lead to development of an automated, high-throughput, single-synapse resolution quantification method in the human material.

Secondly, to apply the G2CSynMaP pipeline to one of the most common neurodegenerative brain disorders, Alzheimer's disease. The hypothesis tested in the second part of this thesis will be that this novel synapse quantification method will demonstrate and confirm in accordance with current evidence that a postsynaptic protein, as exemplified by PSD-95, is altered in pathological human brain disorders.

PSD-95 is one of the most important scaffold proteins in the postsynaptic proteome. My interest also lay in studying human synapse diversity and how a disease state affects populations of synapses and their individual characteristics. The methodology applied here will ultimately lead to the creation of human synaptome maps that describe and chart excitatory synapses across a number of selected areas in the human brain tissue. I further hypothesise that the synaptome maps will be altered in AD. The results can potentially provide better insights into neuropathology of many other synaptic human brain diseases, particularly those that currently show little morphological change histologically, such as schizophrenia.

Throughout this thesis any referral to a synapse is synonymous with postsynaptic density (PSD). The term "PSD-95 synapses" is synonymous with PSD-95 antibody labelled postsynaptic density detected using immunofluorescence.

## 1.8 THESIS OVERVIEW

This thesis contains additional five chapters.

Chapter 2 provides a description of the materials and methods used in this thesis. It characterises the human and mouse brain tissues used, and describes the immunofluorescence technique and its validation procedures. It also includes descriptions of proteomic analyses performed on the same human cohort in our laboratory, courtesy of Dr Marcia Roy.

Chapter 3 presents the validation of immunofluorescent labelling using PSD-95 antibody in human tissue. Human and mouse controls are presented as well as the results of validation with proteomic techniques.

Chapter 4 describes the generation of PSD-95 synaptome maps in 20 human brain areas using G2CSynMaP analysis. These data were acquired using LSCM in human control brain tissue. Detailed descriptions of PSD-95 IF distribution across the human brain are provided as well as their comparison with a genetically modified mouse developed in the Grant laboratory. Presented are comprehensive data to illustrate inter-regional and intra-regional PSD-95 synaptic puncta heterogeneity in the human brain.

Chapter 5 provides an example of a clinical application of the human G2CSynMaP analysis to a human disorder. I will demonstrate how the novel PSD-95 IF quantification method can be successfully used to observe the re-organisation of the PSD-95 synaptome in pathology. These data were acquired using SDM and are based on human brain tissue obtained from Alzheimer's disease patients through the MRC Edinburgh Brain Bank. Re-organisation of hippocampal PSD-95 synaptic puncta IF maps will be presented. These comprehensive data are set to show how hippocampal PSD-95 synapses are modified by disease at individual and subregional levels.

Chapter 6 concludes with an overall discussion on the importance of our novel synapse quantification method and its possible future applications.

# 2 Materials and Methods

## 2.1 BRAIN TISSUE - HUMAN

### 2.1.1 Ethical approval

Post-mortem human brain tissue was obtained from the Medical Research Council UK (MRC) funded University of Edinburgh Sudden Death Brain and Tissue Bank (SDBTB). All procedures were approved by East of Scotland Research Ethics Service (EoSREC) 1 under tissue bank generic ethical approval for peer-reviewed projects (REC reference 11/ES/0022).

### 2.1.2 Human subjects

#### *2.1.2.1 Control cases*

There were two groups of control subjects used in this study. The first control group comprised brain tissue obtained from 4 control subjects (3 males, 1 female; mean age in years $\pm$ SD : 51$\pm$6.9) that was used to perform the PSD-95 mapping study using LSCM. The second group of control subjects was included in order to examine the hippocampal PSD-95 distribution in disease (9 males, 5 females; mean age in years $\pm$ SD : 60.07$\pm$10.13). Details of all human subjects used in this PhD project are listed in Table 2.1 on page 60. None of the control subjects had a history of dementia, neurological or psychiatric disorders. Human brain tissue donated to the SDBTB was processed according to the departmental protocols. Briefly, formalin-fixed paraffin-embedded 4 $\mu$m tissue sections are stained with haematoxylin and eosin (H&E) for routine neuroanatomical and neuropathological surveys. Selected sections are stained with a panel of antibodies, which include phosphorylated tau for neuronal and glial inclusions, $\beta$-amyloid for vascular and parenchymal amyloid deposition, ubiquitin for ubiquitinated aggregates and/or $\alpha$-synuclein for Lewy body pathology. This panel however is not exhaustive and other relevant antibodies may be used depending on the clinical and neuropathological findings. Gross anatomical and microscopic examinations of the brain tissue revealed only low neuropathological changes in the control brains. As human tissue is a scarce resource, tissue samples

were chosen from the left and right sides depending on tissue availability (Table B.1 on page 314). Information about handedness of human subjects was not available.

In contrast to biopsy material, human post-mortem brain tissue is more accessible for research. Ethical factors and the logistics of obtaining biopsy material from healthy controls are the main difficulties in obtaining biopsy specimens (Kay et al., 2013; Jones et al., 2017). However, the use of post-mortem material is associated with several limitations, the major being the post-mortem time (PT), i.e. the time from person's death to tissue fixation. Animal tissue is typically fixed by perfusion with no PT delay (PMD). Similarly, the human biopsy material can be fixed in formalin immediately after removal from the brain at surgery with no PT delay. However, the post-mortem tissue is almost never fixed immediately after death. Instead it is fixed after autopsy, which can be delayed several hours or days after demise. Yet, studies have shown, that the longer the PT delay, the larger time-induced detrimental changes are seen at the genetic, molecular, biochemical and structural levels in the tissue (Gonzalez-Riano et al., 2017). Importantly, PT delay has recently been shown to affect immunohistochemical staining of common markers used to analyse post-mortem tissue from control and diseased brains (Gonzalez-Riano et al., 2017). The same study further demonstrated that the levels of some metabolites are also affected in the autopsy material. Therefore knowledge of which markers are affected by PMD is important. Consequently, it is vital that the post-mortem tissue is well characterised and any results obtained using such material should consider the impact of PT delay factors on final conclusions. This should be particularly relevant when extrapolations from animal *in vivo* or functional data, not affected by PMD artefacts, are made to the human data without considering the PMD factors. For these reasons, post-mortem tissue collected by brain banks is assessed by a range of tissue quality markers, including post-mortem delay (PMD), tissue pH and RNA preservation using RNA integrity number (RIN) value (Millar et al., 2007). However, certain ante-mortem events, such as fever, anoxia and hypovolaemia, may have more profound adverse effects on the quality of brain tissue than post-mortem quality markers, such as short PMD at less than 24 hours. It is worth noting that no significant changes in the pH of the CSF or brain samples are thought to occur within a 24 hour PMD. The PMD in this project was calculated from the time of death to the time of removal of the brain from the skull

at autopsy (Trabzuni et al., 2011). All these quality markers were available from the SDBTB, as illustrated in Table 2.1 on page 60.

A tissue quality marker routinely recorded in the SDBTB databases is RIN number. Since PMD is thought to have a limited effect on mRNA quality (Harrison et al., 1995; Tomita et al., 2004; Trabzuni et al., 2011), the RIN measurement has been used to assess integrity of mRNA more reliably. All extractions and purification of RNA are performed by the Brain Bank neuropathology staff according to the existing protocols (Trabzuni et al., 2011). The RIN values are obtained using the Agilent 2100 Bioanalyzer (Agilent Technologies, UK Ltd). RINs and total RNA electropherograms are calculated by the 2100 Expert Software (Agilent Technologies, UK Ltd). The software algorithm analyses electrophoretic profiles of mRNA producing a numerical scale from 1 to 10, with 1 reflecting the most degraded RNA and 10 the most intact RNA. For very short PMI, RIN values above 7 are best for molecular research methods.

Another quality marker recorded by the SDBTB is the brain pH. It is obtained at post-mortem using a portable Hanna HI8424 hand-held pH meter with a glass bodied electrode (Fisher Scientific, Loughborough, UK). A single pH measurement from the lateral ventricle is obtained as it has been previously demonstrated that the pH does not vary between different brain regions (Stan et al., 2006; Monoranu et al., 2009). Brain pH is considered the most important post-mortem factor influencing RIN-based RNA integrity (Durrenberger et al., 2010; Monoranu et al., 2009; Trabzuni et al., 2011). Generally, a pH above 6.0 is considered the optimum for RNA preservation (Trabzuni et al., 2011).

In addition, the tissue from the initial 4 control cases was concomitantly assessed in the Grant laboratory for synaptic protein degradation using HUSPIR value (Bayés et al., 2014). The 4 control cases were specifically selected for the mapping study, as HUSPIR values and thus synaptic proteome integrity was already known for all the areas surveyed. In a separate experiment, further cases, including additional controls and AD subjects used in this study, were tested in Prof Tara Spires-Jones' laboratory for synaptic protein integrity using HUSPIR. Two further subjects (one control (SD63/13) and one AD (SD64/13)) have been tested and used in a publication (Henstridge et al., 2015), and they both showed good synaptic protein preservation.

#### 2.1.2.2 Alzheimer's Disease cases

The second part of the project examines the pathological human brains and included patients with evidence of abnormal tau deposits at the neuropathological examination. The extent of these tau deposits further subclassified cases into two tau stages: a Braak neurofibrillary tau tangle stage II and a Braak neurofibrillary tau tangle stage VI. The AD cases in this thesis were primarily selected on the basis of a Braak tangle stage of II for mild cognitive impairment/early AD group and Braak tangle stage of VI with a clinical diagnosis of dementia for the late AD group. The demographic characteristics of the AD groups have been shown previously in Table 2.1 on page 60. These two Braak stages, II and VI, were chosen to represent the early and late stages of AD disease, respectively. However, there are important limitations to the use of this terminology for the AD patient cohorts. The neuropathological diagnosis of AD requires fulfilment of the Consortium to Establish a Registry for Alzheimer's disease (CERAD) of 'definite AD' criterion in addition to a Braak tangle stage (i.e., according to the NIA-Reagan criteria stipulating that a high likelihood of a dementia is caused by AD pathology) (McKhann et al., 2011). This means that AD diagnosis requires ante-mortem history of dementia that can be then correlated with the Braak stage at neuropathological examination. It is, however, recognised that even this current classification system is flawed. The neuropathology of AD may be found across a broad clinical spectrum, which encompasses people who are cognitively normal, those with mild cognitive impairment, and those with dementia. Furthermore, patients with early Braak stages, i.e. the entorhinal stage I and II, may not display any cognitive symptoms. Moreover, it also is known that a proportion of neurologically intact individuals have hippocampal tau deposits, but show no evidence of dementia, and this is a part of their normal ageing process. At current state of knowledge, it is difficult to distinguish age-related changes from effects of undetected disease.

Throughout this thesis, I use the term AD to encompass the neuropathological diagnosis of AD, which includes the Braak stages. This is an important shortcoming in the definition of "AD groups" in this study limited by the fact that relevant clinical information was also limited for the entire cohort. However, as far as could be ascertained, none of the individuals in controls and Braak stage II (also referred to

as early AD) had history of dementia and of the 8 cases in the Braak stage VI (referred to as late AD) in only one case there was no information available about the patient's dementia status (Table 2.2 on page 61).

Finally, the limited availability of human cases meant that the majority of AD cases, primarily selected to this study based on Braak stages, included individuals, who were also consented to participate in the Lothian INtraCerebral Haemorrhage, Pathology, Imaging and Neurological Outcome (LINCHPIN) study. This prospective community-based study examined the causes of intracerebral haemorrhage using research autopsy in case of death (Samarasekera et al., 2015). Although care was taken to include only patients with anatomically intact hippocampi, it is not possible to exclude a potentially confounding effect of having double pathology, such as vascular disease and tau pathology, on PSD-95 synaptic puncta quantifications. Synaptic proteins levels have been reported to be altered in vascular dementia (Sinclair et al., 2015). Moreover, many patients have concomitant Alzheimer's disease and cerebrovascular disease, but lack of distinguishing features of dementia for these two conditions, is a recognised limitation of current diagnostic criteria.

### 2.1.3 Post-mortem procedures

At post-mortem examination (PME), brains were macroscopically dissected into 1 cm-thick coronal slices and sampled according to the SDBTB protocol (Samarasekera et al., 2013). Small tissue blocks were immediately fixed in 10% formaldehyde between 24-72 hours prior to further tissue processing and embedding in paraffin wax. The blocks were sampled from 13 neocortical areas (frontal x6, temporal x3, parietal x1 and occipital x2), 1 allocortical area (hippocampus), 2 subcortical grey matter areas (thalamus and caudate nucleus) and 4 infratentorial regions (midbrain, pons, medulla and cerebellum). An overview of the anatomic regions and subregions are summarised in Table 2.3 on page 62 and their location within the human brain is shown in Figure 2.3 on page 92. The 13 neocortical areas are defined as Brodmann's regions and include sensory (visual (BA17 and BA19), auditory (BA41/42)), motor (BA4), premotor (BA6/8), associative frontal (dorso-lateral (BA9, BA46), ventro-lateral (BA44/45), orbital (BA11/12)), associative temporal (BA20/21, BA38), associative

parietal (BA39) and associative occipito-temporal (BA37) regions. A brief summary of the cortical areas is provided in Table B.2 on page 315.

The pathological changes in neurodegenerative diseases are present throughout the brain parenchyma; however, careful selection of representative areas can allow for diagnosis of many disease entities (King et al., 2013). The choice of the anatomic regions examined in this study was restricted by the availability of all 20 blocks for all four control cases. Tissue blocks were macroscopically dissected by experienced pathologists according to the standard protocol of the SDBTB (Samarasekera et al., 2013). The selection of blocks closely followed topographical brain anatomy using patterns of the sulci and gyri. Regions of interest were further identified using an atlas of human brain (Mai and Paxinos, 1997). Nissl-stained sections from blocks immediately adjacent (where possible) to those used for immunofluorescence were examined to assess and confirm the distinctive cytoarchitectural features of various areas. In addition, absence of neuropathological findings was confirmed by routine examination of immunohistochemical and special stains available from the department of academic neuropathology. Some of the stains and markers available include H&E, phosphorylated Tau (pTau), amyloid-$\beta$ (A$\beta$), p62, CD68, ubiquitin and others.

In the first part of this study, a total of eighty 4 $\mu$m-thick formalin-fixed paraffin-embedded sections were labelled using the immunofluorescence technique. The same staining methods were followed for all 4 subjects. However, the staining procedure was adjusted for the SDM control groups; nevertheless all of the subjects within this group were labelled in the same way, as will be described in later chapters.

**Table 2.1** Characteristics of human subjects

| No | ID | Group | Age (years) | Sex | PMD (hours) | Brain weight (g) | Brain pH | RIN value | Cause of death |
|---|---|---|---|---|---|---|---|---|---|
| 1 | SD25/13 | Control (CTL) | 47 | M | 31 | 1690 | 6.50 | 5.30 | CAA |
| 2 | SD36/13 | Control (CTL) | 51 | M | 141 | 1510 | 6.30 | 5.85 | HPC |
| 3 | SD23/13 | Control (CTL) | 53 | M | 103 | 1650 | 6.10 | 5.65 | CAT |
| 4 | SD29/13 | Control (CTL) | 58 | M | 90 | 1470 | 5.90 | 4.80 | PE |
| 5 | SD38/13 | Control (CTL) | 58 | M | 49 | 1260 | 5.90 | 4.90 | CAA |
| 6 | SD03/14 | Control (CTL) | 59 | M | 74 | 1500 | 6.10 | 6.10 | MI |
| 7 | SD32/13 | Control (CTL) | 61 | M | 99 | 1270 | 6.20 | 6.15 | HPC |
| 8 | SD05/14 | Control (CTL) | 63 | M | 42 | 1460 | 6.30 | 4.50 | HPT |
| 9 | SD24/15 | Control (CTL) | 78 | M | 39 | 1290 | 6.17 | 6.50 | LBC |
| 10 | SD42/13 | Control (CTL) | 46 | F | 27 | 1210 | 6.50 | 4.90 | MI |
| 11 | SD10/15 | Control (CTL) | 57 | F | 113 | 1300 | 5.92 | 6.95 | CAA |
| 12 | SD35/14 | Control (CTL) | 59 | F | 53 | 1280 | 6.30 | 5.00 | CAA |
| 13 | SD14/13 | Control (CTL) | 74 | F | 41 | 1520 | 6.30 | 5.80 | PE |
| 14 | SD63/13 | Control (CTL) | 77 | F | 72 | 1320 | 6.50 | 5.60 | LBC |
| | | | | | | | | | |
| 1 | SD43/13 | Braak II (Early AD) | 67 | M | 77 | 1360 | N/A | 6.05 | ICH |
| 2 | SD28/14 | Braak II (Early AD) | 72 | M | 22 | 1430 | 6.40 | 3.75 | ICH |
| 3 | SD09/14 | Braak II (Early AD) | 83 | M | 39 | 1460 | 6.50 | 3.60 | ICH |
| 4 | SD60/13 | Braak II (Early AD) | 84 | M | 115 | 1443 | 6.30 | 5.25 | ICH |
| 5 | SD31/12 | Braak II (Early AD) | 68 | F | 80 | 1250 | 6.20 | 4.80 | BIS |
| 6 | SD13/14 | Braak II (Early AD) | 74 | F | 32 | 1316 | 6.30 | 3.20 | ICH |
| 7 | SD11/14 | Braak II (Early AD) | 90 | F | 35 | 1040 | 6.20 | 4.95 | ICH |
| 8 | SD40/14 | Braak II (Early AD) | 90 | F | 90 | 1302 | 6.02 | 3.25 | ICH |
| 9 | SD01/14 | Braak II (Early AD) | 91 | F | 93 | 1260 | 6.30 | 3.70 | ICH |
| 10 | SD18/14 | Braak II (Early AD) | 91 | F | 25 | 1060 | 5.90 | 3.70 | ICH |
| | | | | | | | | | |
| 1 | SD34/13 | Braak VI (Late AD) | 60 | M | 28 | 1389 | N/A | 4.20 | AD |
| 2 | SD39/13 | Braak VI (Late AD) | 86 | M | 21 | 1527 | 6.00 | 3.50 | ICH |
| 3 | SD62/13 | Braak VI (Late AD) | 87 | M | 58 | 1420 | 6.50 | 5.30 | ICH |
| 4 | SD64/13 | Braak VI (Late AD) | 57 | M | 58 | 1200 | 5.90 | N/A | AD |
| 5 | SD11/13 | Braak VI (Late AD) | 75 | F | 102 | 833 | N/A | N/A | AD |
| 6 | SD18/13 | Braak VI (Late AD) | 73 | F | 96 | 1090 | 6.20 | 5.50 | AD |
| 7 | SD02/14 | Braak VI (Late AD) | 87 | F | 89 | 1270 | 5.90 | 5.20 | VD |
| 8 | SD32/14 | Braak VI (Late AD) | 81 | F | 60 | 1289 | 6.50 | 3.70 | ICH |

Abbreviations: AD - Alzheimer's Disease, CAA - Coronary artery atherosclerosis, HPC - Haemopericardium, CAT - Coronary artery thrombosis, PE - Pulmonary thromboembolism, HPT - Haemoptysis, MI - Myocardial infarction, ICH - Intracerebral haemorrhage, BIS - Bowel ischaemia, VD - Vascular disease, LBC - Lothian Birth Cohort. F - female, M - male, N/A - not available. PMD - post-mortem delay. RIN - RNA integrity number. Throughout this thesis Braak II group is referred to as "Early AD or AD2" and Braak VI group is referred to as "Late AD or AD6". For the control group an alternative name of "CTL" is used.

**Table 2.2** Neuropathological staging of human tissue

| No | ID | Hx of Dementia | Thal A$\beta$ | Braak NFT | CERAD | CAA | APOE $\epsilon/\epsilon$ | HUSPIR |
|---|---|---|---|---|---|---|---|---|
| 1 | SD25/13 | No | 0 | 0 | 0 | 0 | 3/3 | 2.52 |
| 2 | SD36/13 | No | 0 | 0 | 0 | 0 | 3/3 | 0.92 |
| 3 | SD23/13 | No | 0 | 0 | 0 | 0 | 3/4 | 3.75 |
| 4 | SD29/13 | No | 0 | 0 | 0 | 0 | 3/4 | 2.19 |
| 5 | SD38/13 | No | 0 | 0 | 0 | 0 | 3/3 | 0.87 |
| 6 | SD03/14 | No | 0 | 0 | 0 | 0 | 3/3 | 3.59 |
| 7 | SD32/13 | No | 2 | I | 1 | 0 | 3/4 | 3.94 |
| 8 | SD05/14 | No | 0 | 0 | 0 | 0 | 3/4 | 1.75 |
| 9 | SD24/15 | No | 2 | I | 1 | 0 | 3/3 | 1.26 |
| 10 | SD42/13 | No | 0 | 0 | 0 | 0 | 3/3 | 1.83 |
| 11 | SD10/15 | No | 0 | 0 | 0 | 0 | 3/3 | 1.56 |
| 12 | SD35/14 | No | 0 | 0 | 0 | 0 | 3/4 | 2.19 |
| 13 | SD14/13 | No | 0 | 0 | 0 | 0 | 3/3 | 4.88 |
| 14 | SD63/13 | No | 2 | I | 1 | 2 | 3/2 | 0.72 |
| | | | | | | | | |
| 1 | SD43/13 | No | 1 | II | 1 | 0 | 3/3 | 0.69 |
| 2 | SD28/14 | No | 1 | II | 1 | 1 | 3/4 | 0.76 |
| 3 | SD09/14 | No | 4 | II | 3 | 2 | 3/3 | 0.29 |
| 4 | SD60/13 | No | 0 | II | 0 | 0 | 3/3 | 0.57 |
| 5 | SD31/12 | No | 2 | II | 2 | 1 | 3/4 | 0.83 |
| 6 | SD13/14 | No | 4 | II | 3 | 3 | 2/4 | 1.89 |
| 7 | SD11/14 | No | 1 | II | 1 | 0 | 2/3 | 1.49 |
| 8 | SD40/14 | No | 2 | II | 2 | 3 | 3/3 | 0.41 |
| 9 | SD01/14 | No | 2 | II | 2 | 1 | 3/3 | 0.96 |
| 10 | SD18/14 | No | 4 | II | 3 | 0 | 3/4 | 0.54 |
| | | | | | | | | |
| 1 | SD34/13 | Yes | 3 | VI | 2 | 3 | 4/4 | 0.80 |
| 2 | SD39/13 | Yes | 4 | VI | 3 | 1 | 3/4 | 0.61 |
| 3 | SD62/13 | Yes | 5 | VI | 3 | 3 | 3/3 | 2.47 |
| 4 | SD64/13 | Yes | 5 | VI | 3 | 1 | 3/4 | 0.96 |
| 5 | SD11/13 | Yes | 4 | VI | 3 | 3 | N/A | N/A |
| 6 | SD18/13 | Yes | 5 | VI | 3 | 0 | 4/4 | 1.87 |
| 7 | SD02/14 | Yes | 3 | VI | 3 | 3 | 3/3 | 3.38 |
| 8 | SD32/14 | N/A | 2 | VI | 3 | 3 | N/A | 0.86 |

Abbreviations: Hx of Dementia - History of Dementia; CERAD - Consortium to Establish a Registry for Alzheimer's disease; APOE, apolipoprotein E; HUSPIR, HUman Synaptic Protein Integrity Ratio; N/A - Not available. The APOE genotypes and HUSPIRs were performed on area BA41/42, except in two cases (SD36/13 and SD31/12) where it was performed on frontal and temporal samples, respectively (Brodmann's areas were not specified).

**Table 2.3** Human brain areas analysed in this study

| | | | |
|---|---|---|---|
| Neocortex | 1. | Motor cortex (BA4) | |
| | 2. | Premotor cortex (BA6) | |
| | 3. | Dorsolateral prefrontal (BA9) | |
| | 4. | Orbitofrontal (BA11/12) | |
| | 5. | Occipital (BA17) | |
| | 6. | Occipital (BA19) | |
| | 7. | Inferior temporal (BA20/21) | |
| | 8. | Occipitotemporal (BA37) | |
| | 9. | Temporal polar (BA38) | |
| | 10. | Inferior parietal (BA39) | |
| | 11. | Superior temporal (BA41/42) | |
| | 12. | Ventrolateral prefrontal (BA44/45) | |
| | 13. | Dorsolateral prefrontal (BA46) | |
| Allocortex | 14. | Hippocampus (HC) | - Cornu ammonis 1 (CA1) |
| | | | - Cornu ammonis 2 (CA2) |
| | | | - Cornu ammonis 3 (CA3) |
| | | | - Cornu ammonis 4 (CA4) |
| | | | - Dentate Gyrus (DG) |
| Subcortical areas | 15. | Thalamus (TH) | |
| | 16. | Caudate nucleus (CN) | |
| Cerebellum | 17. | Cerebellum (CB) | - Granular cell layer (GL) |
| | | | - Molecular cell layer (ML) |
| Brainstem areas | 18. | Midbrain (MB) | - Periaqueductal grey (PAG) |
| | | | - Substantia nigra (SN) |
| | 19. | Pons (PO) | - Locus coeruleus (LC) |
| | | | - Pontine nuclei (PN) |
| | 20. | Medulla (MD) | - Inferior olivary nucleus (ION) |
| | | | - Hypoglossal nerve (CNXII) |

BA, Brodmann's area; TH, thalamus; CN, caudate nucleus; HC, hippocampus; CA, cornu ammonis; DG, dentate gyrus; CB, cerebellum; GL, granular cell layer; ML, molecular cell layer; MB, midbrain; PAG, periaqeductal grey; SN, substantia nigra; PO, pons; LC, locus coeruleus; PN, pontine nuclei; MD, medulla; ION, inferior olivary nucleus; CNXII, nucleus of cranial nerve XII (the hypoglossal cranial nerve).

## 2.2 OVERVIEW OF HUMAN TISSUE ANALYSES

This thesis describes the distribution of the PSD-95 in two broad human cohorts using immunofluorescence.

The first cohort, referred to as LSCM-acquired samples, comprises 4 control cases that were concomitantly studied by Dr Marcia Roy in the Grant laboratory. Using proteomics approaches, Dr Roy supervised two additional types of proteomic analyses performed on this cohort: HUSPIR value analysis and Western blotting. In particular, these 4 human controls had all 20 human areas examined for protein degradation using HUSPIR value, as published in (Bayés et al., 2014). In addition, there was Western blot analysis performed on 12 cortical areas (manuscript in preparation by Dr Marcia Roy).

The second cohort, referred to as SDM-acquired samples, comprises 32 human subjects from whom only hippocampus has been examined. In addition to immunohistochemistry, most tissue was analysed for synaptic protein degradation using HUSPIR value. In addition, cases were ApoE genotyped.

### 2.2.1 HUSPIR analysis of LSCM-acquired samples

Due to the limited availability of brain biopsies from living patients, most human studies use post-mortem tissue. However, one of the limitations of the use of post-mortem samples is the variable proteolytic tissue degradation, which precludes detailed molecular analysis. While standard brain quality indicators, such as PMI, pH or RIN values are widely used to monitor the quality of post mortem tissue, they are thought to poorly predict the integrity of the postsynaptic proteome from tissue obtained from brain banks. A new quantitative biochemical quality marker, Human Synapse Proteome Integrity Ratio (HUSPIR), recently described by the Grant laboratory, has been developed to assess synapse proteomes. HUSPIR value is obtained by analysing GluN2B subunit of the N-methyl-D-aspartate receptor (NMDAR) immunoblots which show a normal intact 180 kDa band (referred to as Band1) along with two additional lower bands (Band2 and Band3) when there are

degradation products in the PM samples. To estimate the extent of degradation of PM samples, as assessed by HUSPIR, the ratio of Band1/Band2 intensity is calculated. HUSPIR value equal or above 1 is thought to reflect a high quality synapse proteome tissue.

The HUSPIR values for the 20 brain areas from the 4 control subjects used in this thesis have previously been published in (Bayés et al., 2014), and the method of obtaining HUSPIR values for the LSCM cohort is reproduced below. The values for each case and area were kindly provided by Dr Marcia Roy.

#### *2.2.1.1 Sample preparation*

In order to prepare the samples for the HUSPIR analysis, the synaptic proteins are isolated from post-mortem tissue. Human tissue was homogenised using a glass-teflon dounce at a tissue weight: buffer volume ratio of 100 mg: 1 ml. The homogenising buffer contained 0.32 M sucrose, 10 mM HEPES pH 7.4, 2 mM EDTA, 5 mM sodium o-vanadate, 30 mM NaF and a protease inhibitors cocktail (Roche). The homogenised tissue was centrifuged at 800 x g for 15 min at 4°C; supernatant removed and centrifuged at 10,000 x g for 15 min. The pellet was resuspended in Triton buffer (50 mM HEPES pH 7.4, 2 mM EDTA, 5 mM EGTA, 5 mM sodium-O-vanadate, 30 mM NaF, 1% Triton X-100 and protease inhibitors cocktail (Roche)) with half the volume used for homogenisation. The sample was then centrifuged at 30,000 x g for 30 min at 4°C and the final pellet was re-suspended in 200 $\mu$l of SDS buffer (50 mM Tris pH 7.4, 1% SDS) and used for immunoblotting.

#### *2.2.1.2 NR2B immunoblot and protein degradation quantification*

Following the extraction of the PSD proteins from all the regions of the four human control brains, they were subsequently separated by SDS-PAGE. On each SDS-PAGE, a triplicate has been performed for each brain sample. Similarly, the four brains for the same cortical region have been separated on the same gel allowing us to compare these results. Immunoblotting for NR2B was then performed to assess the Band1/Band2 ratio. In addition, a separate immunoblot for PSD-95 protein was performed to

determine the amount present in each sample.

The protein concentration was determined using the Bradford assay (1X Bradford Quickstart Reagent, Biorad). For immunoblotting, 10 $\mu$g of total protein was resolved on 4-12% NuPage precast SDS-PAGE gels. In particular, protein samples were mixed with 4X NuPage LDS sample buffer (Novex, Invitrogen) plus 0.1 M of dithiothreitol (DTT). Samples were boiled and separated using 4-12% NuPage Bis-Tris gels (Novex, Invitrogen). Proteins were electrophoretically transferred to PVDF membrane (Millipore) at 10V for 2 hours in order to ensure efficient transfer of high molecular weight proteins using a semi-dry transfer system (Bio-Rad).

The membrane was blocked for one hour at room temperature in 5% milk (diluted in 1X PBS - 0.1% Tween 20) then washed three times for 5 minutes in 1X PBS - 0.1% Tween 20. These washing conditions were used after incubation with primary and secondary steps. The membrane was incubated overnight at 4°C with the primary antibody (diluted in 1% milk, 1X PBS - 0.1% Tween 20). The secondary antibody, conjugated to horseradish peroxidase (diluted in 1% milk, 1X PBS - 0.1% Tween 20), was added for one hour at room temperature. In order to display the bands, the membrane was incubated for 60 seconds with Super Signal West Femto Maximum Sensitivity Substrate (Thermo Scientific) and the image was acquired using the Odyssey Fc (LI-COR).

Mouse anti-NR2B (1:1000, BD Biosciences) was used as the primary antibody. Sheep anti-mouse IgG-horseradish peroxidase (1:40000, GEHealthcare) was used as the secondary antibody. Protein expression levels were quantified using ImageStudioLite software.

#### *2.2.1.3 PSD-95 immunoblot quantification*

In a separate experiment, PSD-95 quantification in each of the above sample was determined by Western blot analysis. Tissue sample preparation and protein separation was identical to the methods used for determining the HUSPIR values described above. The primary antibody used was rabbit anti-PSD-95 (1:6000, LifeSpan Biosciences). The secondary antibody used goat anti-rabbit IgG-horseradish peroxidase (1:40000,

GEHealthcare). Protein expression levels were quantified using ImageStudioLite software. The analysis description as well as the results of this analysis were kindly provided by Dr Marcia Roy.

### 2.2.2 HUSPIR analysis of SDM-acquired samples

Measurement of post-mortem synaptic protein stability was also performed for the SDM cohort. Similarly to the LSCM samples, in order to establish synaptic protein degradation using the HUSPIR value (Bayés et al., 2014), synaptic proteins were extracted from frozen human brains and processed for Western blots. Fresh frozen samples from cortical area BA41/42 were collected from all cases where available. In two cases, SD36/13 and SD31/12, frontal and temporal cortical areas, respectively, were used instead, as BA41/42 areas were not available in the brain bank. Frozen tissue was not available in one case - SD11/13. The HUSPIR value for case SD32/14 was performed on an earlier occasion, and additional tissue was not available for further analysis. The HUSPIR analysis of the SDM-acquired samples was carried out in Prof Tara Spires-Jones' laboratory.

#### *2.2.2.1 Sample preparation*

Frozen tissue was removed from -80°C and individually homogenised using a pre-cooled dounce homogeniser filled with 500 $\mu$L ice-cold buffer A (a few short strokes were applied to disrupt the tissue, followed by fifteen 6-12 o'clock strokes to homogenise the tissue). Buffer A was made by mixing 25 mmol/L HEPES [pH 7.4], 1 tablet of complete EDTA-free protease inhibitor (Roche, UK, Product no 04 693 159 001), and phosphatase inhibitor cocktail set V (Calbiochem, USA, Product no 524629). A 500 $\mu$L aliquot was saved from each case sample. Each aliquot was mixed with 200 $\mu$L water and 75 $\mu$L 10% SDS and boiled to prepare the total extract. The protein concentration in each extract was quantified using a bicinchoninic acid assay (Pierce R BCA Protein Assay, USA, Product no 23224), according to the manufacturers instructions and using a spectrophotometer (Dynex Technologies). Equal amounts of proteins were then analysed by SDS-PAGE.

#### 2.2.2.2 NR2B immunoblot and protein degradation quantification

An equal volume of 35 $\mu$m of 2x Laemmlin buffer (Sigma, Product no S3401-1VL) was added to each protein sample to normalise protein concentration. The total volume of each sample was 70 $\mu$L. The samples were boiled at 100°C for 5 minutes, and then cooled to room temperature (and centrifuged at 13,000 for 10 s to collect condensation). Samples were then analysed by SDS-PAGE. NuPAGE® 4-12% Bis-Tris gels 1.0 mm x15 well (Invitrogen, Product no NP0323BOX) were used to perform separation of all proteins with a molecular weight less than ≈130 kDa. 20x NuPAGE® MES SDS running buffer (Novex, USA, Product no NP0002) was used for running Bis-Tris gels following diluting it 1:20 with dH2O. The SDS-PAGE gels were run in Invitrogen Novex® Mini-Cell (Invitrogen) with wells facing into the central chamber. The seals were closed and the central chamber filled with the running buffer. The running buffer was added to the outside chamber until it was higher than the foot of the gel. Fourteen microliter of each (1.5 mg/mL) protein sample was loaded into each of lane 2-15 of the gel one and lane 2-8 of the gel two. Protein loading was undertaken using Hamilton syringe with distilled water washes between each load. 14 $\mu$L was added to each well to avoid spillage. Five $\mu$L of molecular weight markers (Li-COR) were loaded into lane 1 of each gel at the end. The Novex® Mini-Cell tank was then connected to a power supply (Bio-Rad, Germany) and run at 95 V for 3 hours.

Upon the completion of the SDS-PAGE electrophoresis, transfer and blotting of protein were undertaken. The chilled transfer buffer was made by mixing 28.8 g of glycine, 6 g of Tris Base, 400 mL of methanol, all made up to 2 L with dH2O. A Nitrocellulose membrane (Bio-Rad, Germany, Product no 162-0112) was placed in the cold transfer buffer. Transfer sponges (Bio-Rad, Germany) and 3 mm blotting paper (Whatman) were soaked in the cold transfer buffer. The bonded sides of gel cassettes were separated with the end of a metal spatula and the gels were carefully removed from cassettes. The western transfer stack was assembled in a Mini-Transblot Electrophoretic Tranfer Cell (Bio-Rad, Germany) making sure air bubbles between the Nitrocellulose membrane and gel were eliminated. The transfer cell assembly was as follows: (2 sandwiches per tank)

- Black side of cassette
- 2 pads
- 1 blotting paper
- 1 SDS-PAGE gel
- 1 Nitrocellulose membrane
- 1 blotting paper
- 1 pad
- 1 blotting paper
- 1 SDS-PAGE gel
- 1 Nitrocellulose membrane
- 1 blotting paper
- 2 pads
- Clear side of cassette

The blot modules were placed into a chamber and filled with the transfer buffer, which was subsequently connected to a power source (Bio-Rad) and transferred at 30V for 120 min.

The Nitrocellulose membranes were removed from the western transfer assembly, cut into four pieces and each placed directly into four small containers filled with a 10 mL blocking solution comprising 5 mL of Odyssey® blocking buffer (Product no 927-400000) diluted in 5 mL of PBS to prevent desiccation. The blocking lasted for an hour at room temperature. The primary antibody was subsequently diluted in Odyssey® blocking buffer with 0.1% tween-20 mixed with 5 mL PBS. The membranes were incubated overnight at room temperature on the shaker. The total volume of antibody diluent was 10 mL per membrane/container. Twenty-four hours later, the membranes were washed 6 times, 5 min each at room temperature in PBS with 0.1% Tween. The secondary antibody (Donkey anti Mouse, Li-COR, Product no 926-32212) was diluted 1:5000 in saved Odyssey® blocking buffer for 60 min at room temperature on the shaker. The primary antibody used was mouse anti-NMDAR2B (BD Biosciences, 1:500, Product no 610416). Protein expression levels were quantified using ImageStudioLite software. The results of quantification are presented in the Appendix in Figure A.1 on page 310.

### 2.2.3 ApoE genotyping of SDM-acquired samples

The ApoE genotyping of the SDM subjects was carried out in Dr Tara Spires-Jones' laboratory. The process was divided into two phases: extraction of DNA from frozen tissue and polymerase chain reaction (PCR) analysis.

#### *2.2.3.1 DNA extraction for PCR*

In order to perform ApoE genotyping, DNA was extracted from frozen human tissue stored at -80°C until the time of DNA extraction. Isolation of DNA was performed using a standard DNA extraction kit - QIAamp® DNA Mini Kit (Qiagen, Germany, Product no 51304) according to the manufacturer's protocol, as described previously (Koffie et al., 2012). The extracted DNA was used as the template for polymerase chain reaction.

#### *2.2.3.2 PCR analysis*

The ApoE genotyping technique used in this study was based on restriction fragment length polymorphism (RFLP) and was performed on 22 cases. Briefly, to perform RFLP, PCR amplification of the single nucleotide polymorphism (SNP)-containing DNA region is undertaken first. This step is then followed by specific restriction enzyme cleavage of the PCR product to generate allele-discriminating DNA fragments (Ingelsson et al., 2003). Oligonucleotide sequences are listed in Table 2.4 on page 71.

DNA samples were amplified through PCR using forward primer 5'-taagcttggcacggctgtccaagg-3' and reverse primer 5'-ggcagtgtaccaggccggggcgaattctgt-3'. The PCR mixture consisted of 10 $\mu$l of Master Mix containing 0.5 $\mu$l of each primer, 1x DNA Taq amplification buffer (NE BioLabs, UK, Product no M0273), 200 $\mu$M each deoxyribonucleotide triphosphate (dNTP) (NE BioLabs, UK, Product no N0447L), 2 $\mu$l dimethyl sulfoxide (DMSO) (NE BioLabs, UK, Product no 12611) and 5.5 $\mu$l of dH2O to which 1.5 $\mu$l of genomic DNA and 1.25 units of Taq DNA polymerase (NE BioLabs, UK, Product no M0480)

were added separately to make up a total volume of 20 $\mu$l per sample.

After an initial denaturing step of 94°C for 10 min, the PCR was performed (Thermal Cycler, AB Applied Biosystems) for 32 cycles for denaturation at 94°C for 30 sec. The annealing temperature was set to 56°C for 30 seconds and the extension temperature was 72°C for 60 seconds. A final extension step of 72°C for 4 minutes was also included.

The PCR products were analysed by restriction pattern of ApoE alleles. In order to achieve this, the PCR products i.e. the amplified DNA, were digested with Hha I restriction fragment endonuclease (NE BioLabs, UK, Product no R0139S) for 3 hours at 37°C. The digested DNA fragments were separated by electrophoresis on a 20% TBE acrylamide gel (Invitrogen, Product no EC63155BOX) at 130 volt for 2 hours along a 100 bp DNA ladder (NE BioLabs, UK, Product no B7025S). Finally, the polymorphic patterns were visualised by ethidium bromide staining using UV transillumination. Raw ApoE genotyping gels are presented in the Appendix in Figure A.2 on page 311.

**Table 2.4** ApoE primers used to genotype human tissue

| ApoE Isoforms | DNA Products | Primers (5' -> 3') **Forward primer** -> *Reverse primer* -> Hha I site |
|---|---|---|
| $\epsilon$2 | 38bp | **taagcttGGCACGGCTGTCCAAGG**AGCTGCAGGCGGCGCAGGCC |
| | 16bp | CGGCTGGGCGCGGACATGGAGGACGTGTGCGGCCGCCTGGTGC |
| | 91bp | AGTACCGCGGCGAGGTGCAGGCCATGCTCGGCCAGAGCACCG |
| | 18bp | AGGAGCTGCGGGTGCGCCTCGCCTCCCACCTGCGCAAGCTGC |
| | 81bp | GTAAGCGGCTCCTCCGCGATGCCGATGACCTGCAGAAGTGCCT |
| | | *GGCAGTGTACCAGGCCGGGGCgaattctgt* |
| $\epsilon$3 | 38bp | **taagcttGGCACGGCTGTCCAAGG**AGCTGCAGGCGGCGCAGGCCC |
| | 16bp | GGCTGGGCGCGGACATGGAGGACGTGTGCGGCCGCCTGGTGC |
| | 91bp | AGTACCGCGGCGAGGTGCAGGCCATGCTCGGCCAGAGCACCG |
| | 18bp | AGGAGCTGCGGGTGCGCCTCGCCTCCCACCTGCGCAAGCTGC |
| | 48bp | GTAAGCGGCTCCTCCGCGATGCCGATGACCTGCAGAAGCGCCT |
| | 33bp | *GGCAGTGTACCAGGCCGGGGCgaattctgt* |
| $\epsilon$4 | 38bp | **taagcttGGCACGGCTGTCCAAGG**AGCTGCAGGCGGCGCAGGCCC |
| | 16bp | GGCTGGGCGCGGACATGGAGGACGTGCGCGGCCGCCTGGTGC |
| | 91bp | AGTACCGCGGCGAGGTGCAGGCCATGCTCGGCCAGAGCACCG |
| | 72bp | AGGAGCTGCGGGTGCGCCTCGCCTCCCACCTGCGCAAGCTGC |
| | 18bp | GTAAGCGGCTCCTCCGCGATGCCGATGACCTGCAGAAGCGCCT |
| | 48bp | *GGCAGTGTACCAGGCCGGGGCgaattctgt* |
| | 33bp | |

ApoE genotyping was performed using PCR. Forward primers are in **bold text**. Reverse primers are in *italic text* and Hha I sites are underlined.

## 2.3 BRAIN TISSUE - MICE

### 2.3.1 Ethical approval

The handling and treatment of all mice was in accordance with the UK Animals' Act (Scientific Procedures) 1986 and all procedures were approved by the British Home Office.

### 2.3.2 Animal cases

Three animals were sacrificed in this study, as follows:

1. One adult PSD-95 wild-type (WT) male mouse
   (PSD-95-GK strain (GBJ/479))

2. One adult PSD-95 knock-out (KO) male mouse
   (PSD-95-GK strain (GBJ4/478))

3. One adult PSD-95 genetically engineered knock-in (KI) female mouse
   (PSD-95eGFPxCMV-Cre(B6) strain 386)

### 2.3.3 Generation of PSD-95eGFP KI and KO mouse lines

The fluorescent PSD-95eGFP knock-in mouse line was created by Dr Fei Zhu under supervision of Professor Seth Grant. The detailed description of the mouse construction method is provided in Dr Zhu's PhD thesis and a brief description is given by Broadhead at al (Broadhead et al., 2016) and reproduced below. The gene targeting strategy used to construct the mouse line was previously described by Fernandez et al (Fernandez et al., 2009). The eGFP coding sequence was inserted into the open reading frame of PSD-95/Dlg4 gene at the 3'end immediately before its stop codon using recombineering in *Escherichia coli* as described in previously published methods (Zhou et al., 2004). Targeting plasmid DNAs were excised using XbaI and BclI endonuclease restriction sites and incorporated into mouse embryonic stem cells (ES).

Positive targeted ES cell clones were identified by PCR, cloned, expanded and frozen down before their injection into blastocysts from C57BL/6J mice. Homozygous mice were produced by backcrossing of adult chimeric males with wild-type females to generate heterozygous mice that were subsequently intercrossed. The function and localisation of the endogenous PSD-95 protein was then characterised in the eGFP mice to ensure that the insertion of the eGFP construct had not disturbed the protein. The tests revealed that the mouse line displayed normal physiological, behavioural and electrophysiological characteristics (Zhu et al., in preparation).

The fluorescent PSD-95eGFP knock-out mouse was constructed by a deletion of necessary exons of the DLG4 gene, which encodes the PSD-95 protein, giving rise to a loss-of-function mutation (Migaud et al., 1998). The mice were generated by gene targeting of 129 ES cells and backcrossing onto both the 129S5/SvEvBrd (129S5) background and C57BL/6J background in the heterozygous state. Intercrossing generated knock-out mice for control studies.

### 2.3.4 Genotyping of mice

All mice were routinely genotyped in the Grant laboratory by Mr David Kerrigan and/or Mr David Fricker according to an optimised protocol. Ear and tail tissue (approximately 5 $mm^2$) were collected following anaesthesia prior to perfusion. The tail sample was sent for genotyping and the ear sample was kept at -20°C as a back-up. Tail DNA was extracted and analysed by PCR. Briefly, DNA was extracted using MyTaq Extract-PCR kit (Bioline). DNA samples were amplified through PCR using forward and reverse primers. For PSD-95-GK strains, a forward primer GKoptFor2 and a reverse primer GKoptRev2 were used. For the PSD-95eGFP mouse, an f' PSD-95 primer $95GFPExF - N1$ and two $3'$ $95GFPUTRR - N1$ and $95GFPF - N2$ primers to distinguish the PSD-95 wild-type alleles $(+/+)$ from either the heterozygous (+/eGFP) or homozygous alleles (eGFP/eGFP) were used.

The PCR mixture consisted of 2.5 $\mu$l of 10X PCR Buffer, 0.15 $\mu$l of Taq enzyme, 0.5 $\mu$l of deoxyribonucleotide triphosphate (dNTPs, 10 mM), 0.5 $\mu$l of appropriate primers at various concentrations and 2 $\mu$l of DNA all mixed up with

double dH2O to a final total volume of 25 $\mu$l per sample.

PCR primers and mixtures were placed in the PCR machine and run at specific temperature cycles. PCR products were separated on 2% agarose gel in Tris-Acetate-EDTA (TAE) buffer contacting 0.5 $\mu$g/ml ethidium bromide and visualised by UV transillumination. Genotyping results revealed that the KO and KI were homozygotes (eGFP/eGFP) and the WT was a PSD-95 heterozygote (+/eGFP).

### 2.3.5 Surgical procedures

All mice underwent the same procedures. They were sedated with 670 mg/kg pentobarbital sodium (Euthatal, Merial Animal Health Ltd) by intraperitoneal injection and then intracardially perfused with 10 ml of phosphate buffered saline (PBS, Fisher Scientific) followed by 10 ml of 4% v/v paraformaldehyde (16% PFA, Alfa Aesar 16%, diluted 1:4 and dissolved PBS). The brain was dissected in its entirety and fixed 3-4 h at 4°C in 4% PFA. The brain was later placed in 30% sucrose (VWR Chemicals, w/v in PBS) at 4°C for 72 hours until it sank. The brain was then embedded in optimal cutting temperature (OCT) medium (VWR Chemicals) and frozen in liquid nitrogen with tissue cooled down in isopentane (2-Methylbutane, Sigma-Aldrich). Coronal sections (18$\mu$m thick) were cut with a cryostat (NX70 Thermo Fisher) through the whole brain. Sections were directly mounted on Superfrost®Plus (Thermo Scientific) slides, left to dry overnight and stored at - 80°C. Brain sections from the fluorescent PSD-95eGFP mouse were kept in darkness to preserve the fluorescence of the fusion protein.

## 2.4 ANTIBODY SPECIFICITY AND CONTROLS

The anti-PSD-95 mouse monoclonal antibody (IgG2a mAb K28/43, 1:250, UC Davis/NIH NeuroMab) was the main antibody used throughout this project. Specificity of this PSD-95 antibody has been validated using immunofluorescent staining in PSD-95 KO mouse and compared with that of the genetically engineered PSD-95eGFP/eGFP mouse and the wild-type mouse. A list of all anti-PSD-95 antibodies tested for specificity is shown in Table 2.5 on page 75. The results of

these tests are shown in a Supplementary Figure A.3 on page 312. A lack of PSD-95 immunoreactivity was found in the PSD-95 KO mouse using the NeuroMab antibody.

Further controls included in the immunocytochemical procedures were obtained either by omitting the primary antibody, omitting the secondary antibody, or replacing the secondary antibody with an inappropriate secondary antibody (i.e. an antibody directed against different species), as detailed in Chapter 3. No significant immunolabelling was detected under any of these conditions with the anti-PSD-95 NeuroMab antibody.

A comprehensive list of all the primary antibodies used in this project for fluorescent immunohistochemistry is shown in Table 2.6 on page 76.

Finally, a Western blot was carried out to confirm the anti-PSD-95 antibody specificity on human tissue, as shown in Chapter 3.1.1 in Figure 3.1 Panel 1.

**Table 2.5** PSD-95 antibodies tested for specificity

| No. | Source | Cat No. | Host (Isotype) | Conc. | Immunogen |
|---|---|---|---|---|---|
| 1 | NeuroMab | K28/43 | Mouse (Mono) | 1 in 250 | Fusion protein aa77-299 of human PSD95. |
| 2 | Abcam | Ab18258 | Rabbit (Poly) | 1 in 200 | Mouse PSD95, 50-150aa. |
| 3 | Frontier Institute | Af628 | Rabbit (Poly) | 1 in 200 | Mouse PSD95, 1-64aa. |
| 4 | GeneTex | GTX61948 | Rabbit (Mono) | 1 in 200 | Synthetic peptide corresponding to residues in the N-terminus of human PSD95. |
| 5 | Millipore | 04-1066 | Rabbit (Mono) | 1 in 200 | Synthetic peptide corresponding to residues in the N-terminus of human PSD95. |
| 6 | Synaptic Systems | 108E10 | Mouse (Mono) | 1 in 200 | Recombinant protein, PDZ domain, Mouse PSD95, 64-247aa. |
| 7 | Synaptic Systems | 360C5 | Mouse (Mono) | 1 in 250 | Information not provided. |
| 8 | Thermo | MA1-045 | Mouse (Mono) | 1 in 200 | Purified recombinant rat PSD95. |

Cat no., catalogue number; conc., concentration.

**Table 2.6** Primary antibodies used for immunohistochemistry

| Antibody | Species | Isotype | Company | Clone | Cat No. | Conc. |
|---|---|---|---|---|---|---|
| PSD-95 | Mouse | Mono (IgG2a) | NeuroMab | K28/43 | 75-028 | 1 in 250 |
| Synapsin1 | Rabbit | Mono (IgG) | Cell Signaling | N/A | 13197S | 1 in 200 |
| Synaptophysin | Rabbit | Mono (IgG) | Thermo | SP11 | RM-9111 | 1 in 200 |
| vGluT1 | Guinea Pig | Poly (IgG) | Millipore | N/A | AB5905 | 1 in 150 |
| Calbindin D-28K | Rabbit | Poly (IgG) | Swant | N/A | CB38 | 1 in 50 |

PSD-95, Postsynaptic density protein 95; vGluT1, vesicular Glutamate transporter 1; Cat no., catalogue number; conc, concentration; non-comm; non-commercial.

## 2.5 FLUORESCENT IMMUNOHISTOCHEMISTRY

Formalin-fixed paraffin-embedded human brain sections placed on microscope slides (Superfrost®Plus, Thermo Scientific) were first dewaxed and dehydrated as per the SDBTB neuropathology laboratory protocol. Briefly, sections were dewaxed in two 3-minute xylene washes followed by further four 3-minute graded alcohol washes, including two 74°OP (IMS99%) alcohol washes and two 70% alcohol washes. This was followed by a 15-minute wash in saturated alcoholic picric acid to remove any formalin sedimentation and a final wash in running tap water for 15 minutes. Antigen and heat retrieval techniques were used to enhance cell surface staining, antigen detection from antigen masked formalin-fixed paraffin-embedded sections and reduction of non-specific background staining. The slides were placed in 250ml of freshly made antigen retrieval solution of 0.1 M sodium citrate buffer (Fisher Scientific) at pH 6.0 and pressure cooked (A. Menarini Diagnostics) with a setting of maximum temperature of 125°C for 30 seconds. After cooling in tap water, sections were washed once with PBS and blocked with 5% bovine serum albumin (BSA, Sigma) in 1x TBS (Fisher BioReagents) containing 0.2% Triton X-100 for solubilisation for 1 hour at room temperature. Sections were then incubated with the primary antibody diluted in TBS containing 3% BSA in 0.2% Triton X100 (Sigma)

overnight at 4°C in 4$\mu$g/ml mouse anti-PSD-95 monoclonal IgG2a (NeuroMab) at dilution 1 in 250.

After three 5-minute washes with TBS containing 0.2% Triton X-100, secondary antibodies AlexaFluor®546 goat anti-mouse IgG2a ($\gamma$2a) (Molecular probes) were added at dilution 1:500; and sections were incubated for 2 hours at room temperature in 4$\mu$g/ml antibody. The original concentration was 2mg/mL. In addition, at the same time as the secondary antibody was applied, each immunohistochemical staining round was accompanied by nuclear cell counterstaining with 4',6-diamidino-2-phenylindole (1 $\mu$g/mL DAPI, Sigma, diluted 1:1000 in PBS). Finally, the slides were washed three times with TBS containing 0.2% Triton X-100. For elimination or reduction of lipofuscin-like autofluorescence, sections were subsequently treated with Autofluoresence Eliminator Reagent (AER)(Millipore Chemicon International). Lipofuscin pigment accumulates in the cytoplasm of brain cells and can hamper the use of fluorescence microscopy because of its broad excitation and emission spectra. AER is a commercially available Sudan Black B (SB)-based reagent that has been successfully used in studies using human tissue (Blazquez-Llorca et al., 2010). SB has been reported to provide the best compromise between the reduction of lipofuscin-like fluorescence and maintenance of specific fluorescent labels (Schnell et al., 1999). Briefly, the sections were first immersed in 70% ethanol for 5 minutes, followed by the Autofluoresence Eliminator Reagent (Millipore), which was applied for 30 seconds. Slides were washed in 70% ethanol for a further 3 minutes before being mounted with mounting medium and covered with a glass coverslip (thickness no 1.5, Menzel-Glaser). The mounting medium (Mowiol with 1,4-Diazabicyclo[2.2.2]octane (DABCO), Sigma-Aldrich) was left to curate overnight. The mounting medium stock was prepared by Mr Jamie Ross at Grant laboratory. It was constituted by dissolving a mixture of 96 g of glycerol (Sigma-Aaldrich, BioXtra >99%) and 38.4 g Mowiol (Calbiochem) in 192 ml 0.2M Tris buffer (pH 8.5) and 96 ml milliQ water (18.2 M$\Omega$). The entire solution was subsequently heated at 50°C until clear and divided into 10 ml aliquots that were centrifuged at 8,500 rpm for 15 min at 4°C. The collected supernatant was mixed with 2.5% DABCO in order to prevent bleaching of fluorescent samples. The final aliquots were stored at -20°C.

Due to the long acquisition times on the SDM, the application of AER was modified to minimise the loss of immunofluorescence. Following antigen retrieval, the sections were briefly washed in PBS. Drops of AER (approximately 100 $\mu$l) were added to each slide for 5 minutes at room temperature. The slides were then washed in PBS, before adding the blocking solution. The rest of the protocol remained unchanged.

## 2.6 NISSL (CRESYL VIOLET) STAINING

Cresyl violet acetate solution is used to stain Nissl substance in tissue. Nissl substance is composed of rough endoplasmic reticulum present in neurons. Cresyl violet stains the Nissl substance dark blue to purple. Tissue sections adjacent to those used for immunofluorescence were stained with Nissl stain for histological examination, region delineation and neuronal counting. The staining was performed according to the standard SDBTB protocol. Briefly, the slides were stained in 0.1% cresyl violet (1g cresyl violet, 10 ml of 1% acetic acid and 990 ml of distilled water) for 20 min at room temperature, and then rinsed in distilled water for 3 minutes followed by a wash in 95% alcohol until most of the stain had been removed. Finally, the slides were dipped in Histoclear (National Diagnostic) before being cleared in xylene and coverslipped in DPX mounting medium.

## 2.7 QUANTIFICATION OF PSD-95 COLOCALISATION WITH SYNAPTIC MARKERS

In order to validate PSD-95 as a reliable postsynaptic marker, two types of immunofluorescence (IF) staining were undertaken with PSD-95: double IF staining performed with synaptophysin or synapsin 1 antibodies; and triple IF staining with synapsin 1 and VGlut1 antibodies. Double IF was performed for LSCM and SDM images. Triple staining was undertaken for SDM images only. The two types of IF staining were subsequently quantified in a semi-automated method divided into two steps.

### 2.7.1 Quantification of colocalisation

Quantification of colocalisation comprised two steps. The first step utilised a trackmate plugin from Fiji software to detect synaptic puncta from IF images. For each image acquisition method (LSCM vs SDM) detection was achieved by manually setting up 3 parameters: approximate punctum radius, a threshold, and an addition quality threshold. Having established the best parameters for each microscopy method, the parameters were then inputted into a code written in the Matlab software to generate a list of xy coordinates for each punctum from each channel representing a synaptic marker in a text file.

In the second step, a custom-made plugin (Object Based Colocalisator version 0.5), developed by Dr Zhen Qui, was used to quantify IF synaptic puncta colocalisation between two synaptic markers. This plugin uses the previously generated text files with synaptic puncta co-ordinates to calculate the percentages of synaptic puncta colocalisation. For every detected signal in one channel, the plugin detects the distance with its closest neighbour in the second channel. Once the overall threshold distance is established, the percentages of puncta that have a nearest neighbour within this distance are returned. Two objects are considered colocalised if the distance between their centre positions is less or equal to the established overall distance threshold.

It is worth noting that given the high stain density of pre- and postsynaptic puncta, colocalisation can occur by chance. In order to ameliorate this, random colocalisation was assessed by 90 degrees clockwise rotation of synaptophysin or synapsin 1 (or VGluT1 images for the triple labelled images) and then comparing colocalisation with the original PSD-95-stained images.

### 2.7.2 Image analysis

For the double-labelled SDM images, 10 images obtained from the stratum pyramidale of hippocampal CA1 subregion from 4 control subjects (SD23/13, SD25/13, SD29/13 and SD38/13) were analysed. In addition, 10 images from superficial layers of BA46 from 4 control subjects (SD23/13, SD25/13, SD32/13 and SD42/13) were analysed.

Equal numbers of images were acquired per channel, and two channels were analysed. Colocalisation between PSD-95 synaptic puncta and the synapsin1 or synaptophysin synaptic puncta was calculated.

For the triple-labelled SDM images, 10 images from superficial layers of BA37 cortical area from 4 control subjects (SD23/13, SD25/13, SD32/13 and SD42/13) were analysed for colocalisation with synaptophysin and VGluT1. The overall distance threshold was set for 600 nm, pixel size was 84 nm and image size 512x512 pixels.

For the LSCM dataset, similar to the SDM dataset, double immunofluorescence was performed for PSD-95 and synaptophysin or synapsin 1. Colocalisation was calculated based on 10 images from superficial cortical layers of area BA46 from 4 cases (SD23/13, SD25/13, SD32/13 and SD42/13). Results were presented as percentage of colocalised puncta between PSD-95 and two markers, synaptophysin and synapsin1, respectively. Triple-labelling for LSCM images was not repeated. The overall distance threshold was set for 600 nm, pixel size was 46 nm and image size 1024x1024 pixels.

## 2.8 IMAGE ACQUISITION

All fluorescent images were acquired using one of three imaging platforms. In order to describe the distribution of PSD-95 across 20 human brain areas, the images were acquired with a laser scanning confocal microscope (LSCM). Images of the hippocampal distribution of PSD-95 were acquired using a spinning disk microscope (SDM). Widefield fluorescence microscopy was used to obtain image overview of whole human slides to confirm tissue integrity, neuroanatomy and guide structural annotation.

### 2.8.1 Widefield fluorescence microscopy

The brain section scans were acquired using a Zeiss Axio Scan.Z1 Slide Scanner (Carl Zeiss) with a x20 plan-apochromat lens (numerical aperture (NA) of the objective = 0.8 NA). Fluorescent images were obtained using sections stained with secondary

antibodies to Alexa Fluor 488 nm, DAPI 405 nm and Alexa Fluor 633 nm excitation light with laser exposures set at 40 ms, 50 ms and 60 ms, respectively. Pixel resolution using the x20 objective was 0.325 $\mu$m and the depth of images was 16 bits.

The widefield fluorescence microscopy system uses a Colibri.2 light emitting diode, which allows for a narrow-band illumination at 365 nm for DAPI, 470 nm for Alexa Fluor 488 (AF488) and 625 nm for Alexa Fluor 633 (AF633). First, the excitation light is filtered at 365 nm for DAPI and with band pass (BP) filters for AF488 at 470/40 nm and for AF633 at 640/30. Then, the light passes a colour splitter ("farb teiler" (Ft)), which sends excitation light towards the sample (DAPI: Ft 395 nm; AF488: Ft 495 nm; AF633: Ft 660 nm). Emission light reflected from the tissue passes through the colour splitter again and is filtered with BP filters before reaching the detector (DAPI: BP 445/50 nm; AF488: BP 525/50 nm; AF633: BP 690/50 nm). Light is finally detected with a Hamamatsu Orca-flash 4.0 monochrome camera (Scientific CMOS Sensor).

The scanner employs ZEN lite 2012 software (Zeiss) for image acquisition and adjustments. The slide scanner allows for visualisation of the whole mounted tissue sections. Coronal IF brain section images were background and contrast adjusted to provide reasonable comparison of expression. All control images were directly comparable with their negative controls using the same settings. The images acquired with the slide scanner were used for qualitative rather than quantitative purposes. In addition, brightfield sections of Nissl stained tissue were acquired using this microscope and the software. Nissl staining allowed for direct assessment of the cytoarchitecture of every tissue section used in this study.

### 2.8.2 Laser Scanning Confocal Microscope (LSCM)

To resolve individual synaptic puncta, fluorescently-labelled brain sections were captured by a Zeiss laser scanning confocal microscope (LSCM510). The LSCM set is equipped with an inverted Axiovert microscope combining a UV laser (405 nm, 25 mW), an argon laser (458/488/514 nm, 25 mW), a green helium laser (543 nm, 1mW), a red helium laser (633 nm, 5 mW) and a mercury arc lamp. The confocal laser system

was warmed up and stabilised for 30 minutes in order to avoid severe photopower fluctuations prior to image acquisition. In addition, the microscope detector PMT was adjusted to maintain a working linear range required for optimal visualisation of emissions from different fluorophores. The DAPI and blue fluorophore (Alexa Fluor 405) were excited by the UV 405 nm laser, and its emission read using a 420-480 nm band pass filter. Antibodies conjugated with red fluorophores (Alexa Fluor 546) were excited using 543nm laser and its emission read using 560-610 nm band pass filter. EGFP and green fluorophore (Alexa Fluor 488) were excited by the 488 nm laser and its emission read using a 505-550 nm band pass filter.

Images were obtained using a Zeiss Plan-Apochromat 63x oil-immersion objective lens (numerical aperture (NA) of the objective = 1.4 NA) with a frame size of 1024x1024 pixels and 8 bit depth. Each pixel measured 46 nm x 46 nm. The pinhole size was set to 1.0 times the Airy disk to maximally reject out-of-focus haze and to improve spatial resolution. For improved signal-to noise ratio, up to eight scans were averaged at each optical section. All raw images used for the analysis were obtained with x3.1 zoom as stacks of 6 image planes with z-step of 130 nm pixels and a total length of axial plane 780 nm pixels in accordance with Nyquist sampling. Images were saved as CZI files. Scale bars were added to the representative images using ImageJ application. The total area used for synaptic density determination varied depending on region, but for cortical areas 18 images per area per subject were acquired. Overall, 1510 confocal images were acquired in this part of the study. However, due to technical problems 21 images (1.4%) were excluded. The exclusion criteria were images with too low signal-to-noise ratio precluding adequate image analysis, images not aligned in z-stacks and images with overexposed synaptic puncta. In this study, it is estimated that more than half a billion individual synaptic puncta were identified and counted. Images for figures were prepared in Adobe Photoshop® and Adobe Illustrator® softwares. Where necessary images were adjusted for brightness for correct display, but no other corrections were made.

### 2.8.3 Laser Spinning Disk Microscope (SDM)

For high throughput, high-resolution data acquisition, high magnification x100 confocal images of PSD-95 and DAPI from 16 hippocampal subregions were captured using an Andor™ Technology SDM set up with an Olympus IX81 inverted microscope with oil immersion objective (Olympus UPlanSAPO, x100 oil immersion lens, NA 1.49). Detection was achieved with an Andor iXon Ultra monochrome back-illuminated electron multiplying charge coupled device (EMCCD) camera. For improved illumination and to reduce tiling artefact of the acquired images, the SDM set up included Borealis Perfect Illumination Delivery™. The obtained images were 512 x 512 pixels and 16 bit depth. Each pixel had dimensions of 84 x 84 nm. All cases acquired with SDM were captured with the same parameter settings: x100 lens at 488 nm and at 405 nm laser excitation with exposure times 40 ms and 60 ms, respectively, and laser power of 35% and 20% respectively. The Andor SDM set up had a Nipkow disk (CSU-X1) with a pinhole of 50 $\mu$m pixel size. It was equipped with 4 lasers for excitation at the following wavelengths: 405 nm for DAPI, 488 nm for AF488, 561 nm for AF564, and 640 nm for AF633. The images used for PSD-95 quantification were acquired using Quad-488 and Quad-405. Later, for colocalisation data, Quad-564 and Quad-633 were also used. The quad filter allows light through at four different wavelengths: 440/40, 521/21, 607/34 and 700/45 nm. For two-channel acquisition, a single dichroic mirror (400-410/486-491/560-570/633-647 nm) and a single quad filter were used to direct and filter the light from each channel to the sample. The two quad filters used avoided having to switch filters between channels, which speeded up acquisition time.

The SDM employs iQ3.3 software (Zeiss) for image acquisition. Acquisition of the entire hippocampus was performed by mosaic tiling. A single rectangular grid covered the entire section. Images were acquired without overlap between adjacent tiles. Images were saved as Tiffs and Image J software was used for further image adjustments and analysis. Multiple images per case were first stitched using Matlab software using a custom-written code for human tissue analysis to create an overall 16x downsized montages. The montages were subsequently manually delineated along structures or cortical layers using a polygon selection drawing tool within ImageJ

region of interest (ROI) Manager tool. The data with image sizes and tile numbers are seen in Table B.1 on page 314.

## 2.9 IMAGE PROCESSING AND ANALYSIS

For LSCM data, digital confocal images were acquired as Zeiss LSCM files (czi format) and then converted to 8-bit Tiff format. For SDM data, digital confocal images were acquired as 16-bit Tiff format. Image analysis was performed using a novel approach, called Ensemble, described in the next section. In addition, supplementary data were analysed using the National Institiute of Health (NIH) ImageJ software and the Corsen image plug-in, both freely available on the web. The Corsen image pre-processing has been written as a batch processing custom-modified code in the Grant laboratory, and it is widely used for processing and analysis of mouse data. This method of counting was validated on rodent data. Both methods are fully automated thus allowing efficient processing of a large number of images and ensuring an improved consistency of the results. Images were not altered in any way, e.g., by removing or adding image details. However, linear enhancement (brightness/contrast) with background subtraction and median filtering were used for later image figure preparation using Adobe Photoshop ® and Adobe Illustrator ®.

### 2.9.1 Ensemble image analysis

Ensemble is a novel, automated, high-throughput image analysis method. This synaptic puncta detection technique was developed and performed by Dr Zhen Qiu (manuscript in preparation). It was written in Python computing language and executed in Matlab software. Apart from the supplementary data, all data presented in this thesis have been analysed using the Ensemble method. This method has already been successfully applied to evaluate synaptic puncta parameters in genetically modified rodents in the Grant laboratory.

The first step in Ensemble image analysis requires generation of a training set of random images selected from the LSCM and the SDM datasets. These image sets were generated by Dr Qiu and subsequently manually, and independently, counted by

two individuals trained to recognise IF synaptic puncta. The manual counting was performed in the ImageJ plugin called "Cell Counter" which generated xy coordinates for each punctum in an image. These coordinates then were then "fed" into a machine learning algorithm and served as "ground truth" based on which the algorithm self-trained on how to localise the synaptic puncta. Two sets of training images were generated for the LSCM and the SDM datasets each.

The second step in the Ensemble image analysis involves detection of synaptic puncta, which is based on a multi-resolution image feature detection and supervised machine learning technique. A multi-resolution and multi-orientation version of 2nd-order nonlocal derivative (NLD) to calculate intensity differences, or image features, was developed by Dr Zhen Qiu for each of all individual puncta. For instance, for images with PSD-95 IF as many as 33 image features were calculated per punctum. These intensity differences were subsequently assembled as feature vectors of each individual punctum. In order to filter out extremely dim puncta and to avoid missing true synaptic puncta, an initial intensity detection threshold was set at a very low value. The candidate puncta were then classified as true puncta or background noise using the corresponding feature vectors and a classifier that was pre-trained with the training image set and a machine learning algorithm. The machine learning algorithm chosen for puncta detection is called an Ensemble learning method. It was selected partly because it is suitable to classify puncta with diverse intensities, as present in our images. Once trained, the Ensemble algorithm can automatically identify IF puncta. The Ensemble learning method is considered to be superior to existing detection methods when tested on simulated images and it reliably and efficiently recognises puncta when signal-to-noise ratio is low, which is a known limitation of human tissue stained with antibodies (Dr Zhen Qiu, personal communication and manuscript). Moreover existing punctum detection algorithms in fluorescence microscopy can only process images with similar punctum intensities and background noise and can only be applied to fluorescence microscopic images collected within very small areas of tissue rather than at the whole stained section scale (Chenouard et al., 2014). The Ensemble image analysis, is named after the Ensemble algorithm.

Finally, the Ensemble image analysis provides measurements of each detected

punctum. All synaptic puncta are identified as bright immunofluorescent dots and each punctum is described in terms of 2 parameters: mean punctum intensity and an area of punctum. Once a punctum is detected, it is identified as an object by the Ensemble algorithm. The object is then segmented by extracting a region of interest (ROI) around it. Nine pixels with highest intensities in the ROI are averaged and the maximum punctum intensity is calculated. To calculate mean punctum intensity, the boundaries around each object are defined as a percentage of the maximum intensity.

The mean punctum intensity is a measurement of the relative amount of PSD-95 protein within the PSD, since the absolute number of PSD-95 molecules cannot be resolved using a confocal imaging. Nevertheless, the mean punctum intensity provides a good insight into the differences in average packing of PSD-95 between areas or individuals. The area of the punctum is a measurement of the relative size of PSD-95 positive synapses. It is referred to as PSD-95 synaptic punctum size and it is given in $\mu m^2$. It is defined as the number of pixels within the object area. The final measurement provided by Ensemble image analysis is number of IF puncta per image. The measurements are calculated per 100 $\mu m^2$ and they are an approximation of puncta density per area.

### 2.9.2 Corsen image analysis

Corsen image analysis was undertaken for acquisition of supplementary data. Corsen is a free ImageJ plugin originally developed to calculate mRNA-mitochondria distances (Jourdren et al., 2010). The analysis is divided into two steps. The first step involves Corsen image pre-processing. Initially, a threshold is applied to the original image to create a cell mask, which identifies background (Image>Adjust>Threshold: Mean then Apply). The image is then processed using Corsen image processing macro with parameters (1,1,No) to form an "intermediate mask". In order to extract bright synaptic puncta from the "intermediate mask" image a second "particle mask" image is created with a threshold (Image>Adjust>Threshold: Default then Apply) and then ImageJ filter median (Process>Filter>median: r = 1) is applied to remove background. Finally, Corsen apply mask macro is used to create a "final image". The second step of the image analysis involves using the ImageJ "Analyze particles" plugin. The

"final image" is analysed using the plugin, which incorporates image detection i.e., segmentation algorithm that provides characterisation of the synaptic puncta in terms of density, size and intensity. The final step of the image processing involves generation of measurements, which are exported to excel spreadsheets for statistical analysis.

## 2.10 VALIDATION OF RESULTS WITH PSD-95EGFP MOUSE

### 2.10.1 Qualitative comparison with PSD-95eGFP mouse

In order to assess the validity of the staining procedures used in this study, a selection of PSD-95eGFP mouse IF images were qualitatively compared with those kindly provided by Dr Fei Zhu, the creator of the mouse model. The representative images of coronal sections from several mouse brain areas were acquired with the same microscope (LSCM) and with the same parameter set-up, as described above. The images were originally published in Dr Zhu's PhD thesis (Chapter 4 page 135 & 138).

### 2.10.2 Quantitative comparison with PSD-95eGFP mouse

To further assess the validity of the staining, a quantitative comparison between human and mouse data was performed. Images acquired with SDM from three PSD-95eGFP mice were quantitatively analysed using Corsen by Melissa Cizeron, a PhD student in the Grant laboratory. A direct comparison of KI mouse vs. human results was made for 3 male mice (aged 18 months) and 3 human male control subjects from 10 brain regions. The KI mouse data was acquired with SDM and analysed using Corsen analysis. Pearson correlation values were calculated to establish a degree of correlation between the two datasets. $P$ value of less than 0.05 was considered statistically significant.

## 2.11 HUMAN G2CSYNMAP

All acquired images were exclusively analysed by Dr Zhen Qiu who developed and undertook the raw image analysis. Dr Qiu was blinded to the clinical information of

all human cases. He was the principal scientist who pioneered a novel, high-throughput and automated image analysis pipeline.

The human version of the Genes to Cognition Synaptome Mapping pipeline (G2CSynMaP) has been developed from the mouse synaptome mapping pipeline. The rodent pipeline was originally developed for data based on the genetically modified knock-in mouse created by Dr Fei Zhu. The present study was undertaken in order to adapt the technique to human tissue. The rodent G2CSynMaP consists of four main components: 1. genetic tagging of synaptic proteins in knock-in mice, 2. tissue imaging, 3. image and data analysis, and 4. data storage and dissemination. The pipeline incorporates several advanced microscopic and data handling techniques that can characterise and map diversities of individual synaptic puncta at high near-diffraction-limit resolution (approximately 290 nm in xy). The human G2CSynMaP has a different first component whereby visualisation of proteins is achieved with labelling of proteins with antibodies using immunofluorescence techniques. The overview of the human G2CSynMaP pipelines are illustrated in Figures 2.1 and 2.2 on pages 90 and 91, respectively. Although the main principles of the image analysis were the same for all human data acquired, there were two main pathways of image analysis depending on which microscope was used to acquire the data.

The G2CSynMaP pathway for images acquired with a conventional laser scanning confocal microscope (LSCM) is shown in Figure 2.1 panel 1. The raw images were acquired with a 63x oil objective, as described previously. The generated data consisted of 6 z-staked 16-bit images measuring 1024 x 1024 pixels each, with each pixel measuring 46 x 46 nm. The raw data was analysed using the novel Ensemble method; depicted in Figure 2.1 panel 2. The Ensemble method is specifically designed to detect immunofluorescent synaptic puncta under a low signal-to-noise ratio and in a cluttered environment. The method combines results of multiple detectors to generate visual features of a single synaptic punctum. The synaptic features for human tissue include synaptic density, as a marker of synapse population, as well as synaptic intensity and size as measures of individual synaptic puncta. Additional features, such as circularity, aspect ratio, solidity or roundness of synaptic puncta were determined

for the rodent images. The results obtained following data analysis were colour-coded into synaptome maps, examples of which are as depicted in Figure 2.1 panel 3. An example of a cortical LSCM image flow acquisition is presented in Figure 2.1 panel 4. Brodmann's areas were defined using the freely available Allen Institute Human Brain Atlas (http://human.brain-map.org). Axio scan was used to visualise the cytoarchitecture of brain areas acquired with LSCM. For cortical areas, there were 18 images acquired with 3 images per layer, but this varied for the remaining human brain regions. The twenty human brain regions analysed are schematically presented in Figure 2.3 on page 92.

The G2CSynMaP pathway for images acquired with a laser spinning disc confocal microscope (SDM) is shown in Figure 2.2. This time the raw images were acquired with a 100x oil objective (Figure 2.2 panel 1). An additional step was added to this pipeline, namely stitching of thousands of images per one case using a custom written Matlab code, into a downsized 16x montage image. The montage image was then used to perform manual structural delineation of hippocampal subregions using ImageJ (Figure 2.2 panel 2). The raw data together with the delineations were subjected to Ensemble analysis in the same way as the LSCM data, as illustrated in Figure 2.2 panel 3.

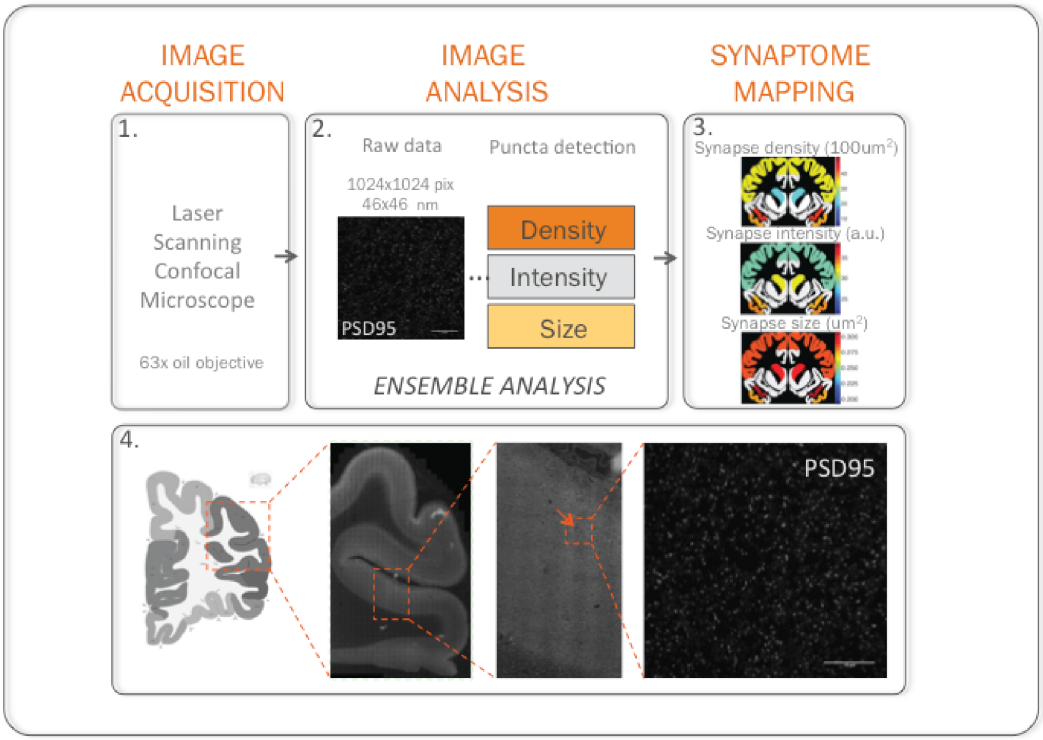


**Figure 2.1 Overview of human G2CSynMaP for LSCM data.**
Schematics explaining the human Genes to Cognition Synaptome Mapping Pipeline (G2CSynMaP) for images acquired with a conventional laser scanning confocal microscope (LSCM). **1.** Immunofluorescent anti-PSD-95 labelled raw images were acquired with a 63x oil objective lens. **2.** The raw data were analysed using a novel Ensemble quantification method, whereby each IF punctum within raw data image was analysed with various detectors to generate punctum features, including punctum density, intensity and size. **3.** Quantification results from the Ensemble analysis were converted into colour-coded scales generating synaptome maps of each synaptic feature. **4.** Example of a LSCM image acquisition flow.

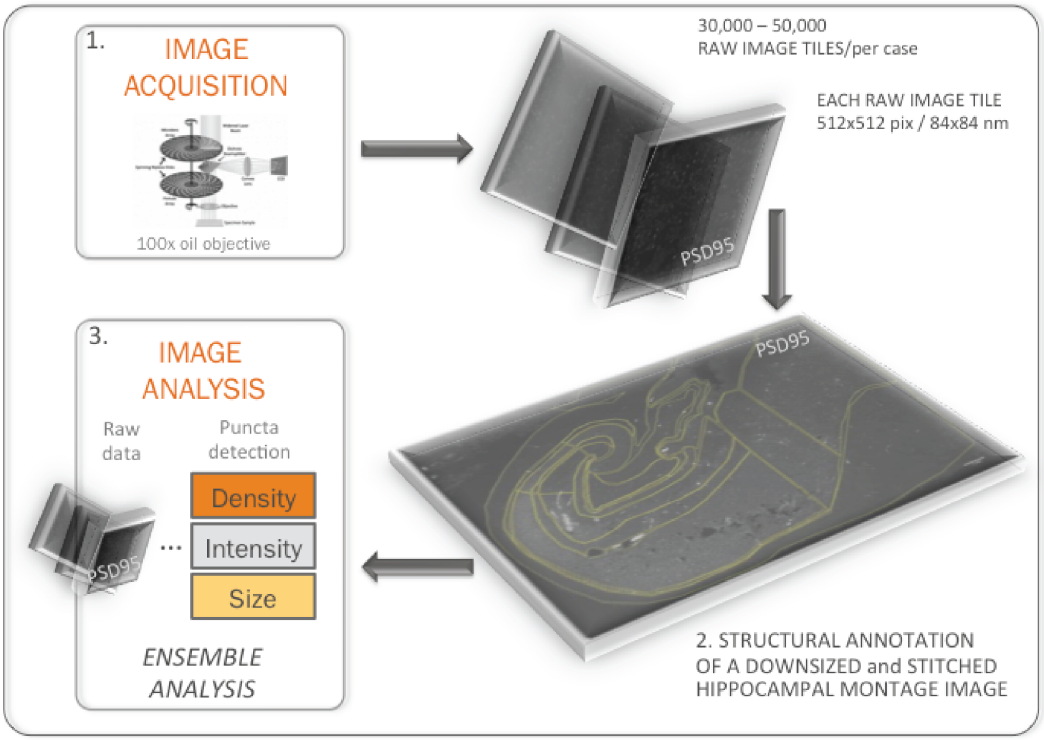


**Figure 2.2 Overview of human G2CSynMaP for SDM data.**
Schematics explaining the G2CSynMaP analysis for images acquired with a spinning disc microscope (SDM). **1.** Raw data were acquired with 100x oil objective lens. **2.** The additional step used in this analysis pipeline. The thousands of images obtained with SDM for each case were used to generate a downsized montage of all raw images for manual delineation of hippocampal subregions. **3.** Subsequent image analysis and synaptome mapping (not shown here) were the same as for the LSCM data.

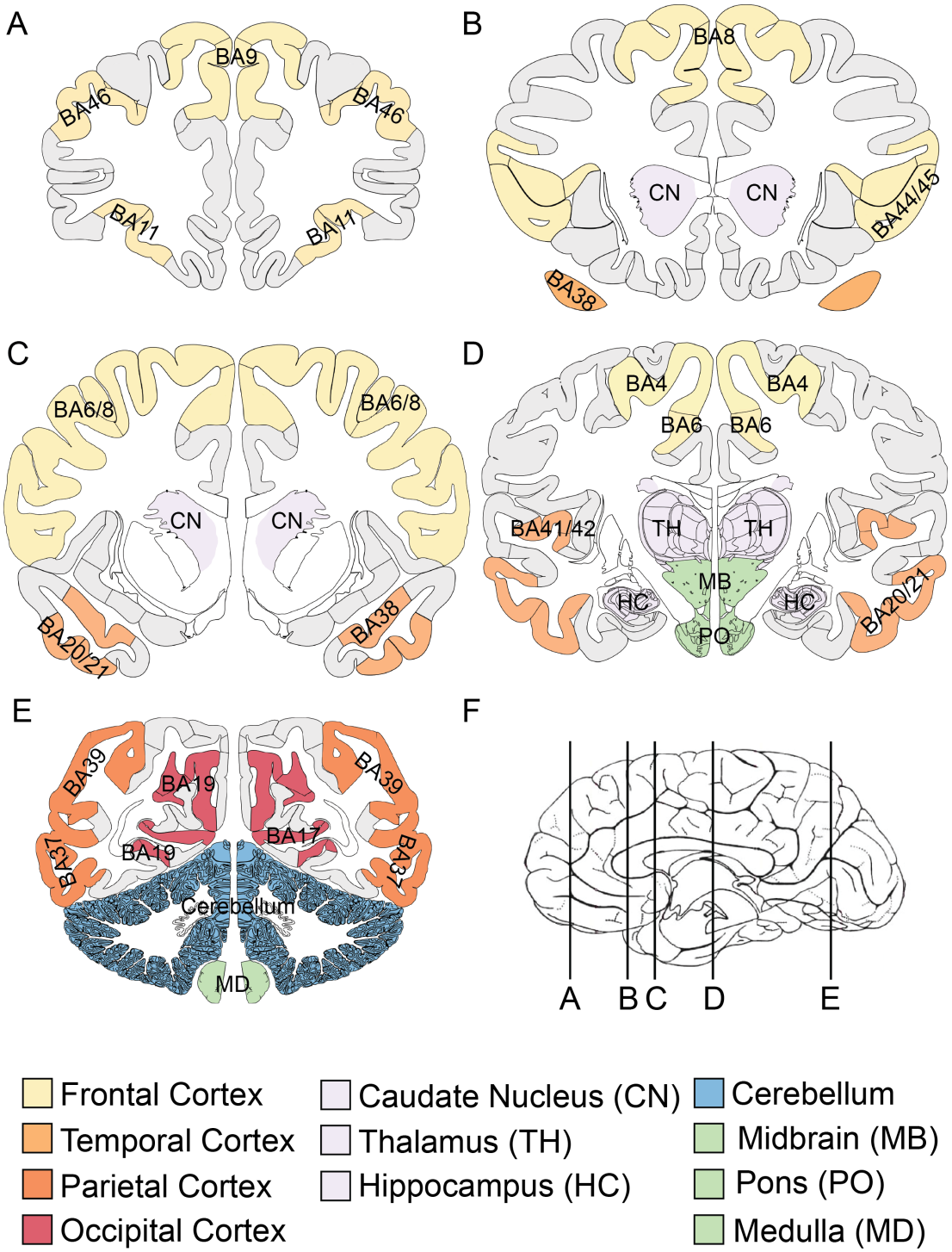


**Figure 2.3 Location of anatomical areas examined using LSCM.**
Schematics showing location of the 20 human brain areas examined using LSCM. **A-E** show coronal slices through the cerebral hemispheres. **F** shows the approximate levels at which the coronal sections have been collected at post-mortem examination. Images are not drawn to scale.

## 2.12 ESTIMATION OF NEURONAL DENSITY USING STEREOLOGY

In order to determine neuronal loss in the control and the two AD groups, a stereological optical dissector protocol was used to estimate neuronal density (Henstridge et al., 2015; West et al., 1991). Stereology methodology allows for reliable quantification of a 3-dimensional (3D) object based on 2-dimensional (2D) measurements. Typically, this is achieved by creating a z-stack of 2D images in order to create a 3D tissue model. Stereology utilises random, systematic sampling to provide unbiased and quantitative data. Normally, neuronal numbers are estimated using the combination of the optical dissector with the fractionator sampling scheme. The optical dissector uses a reference volume generated by two parallel sections separated by a known distance to count cells in a 3D space under the microscope. The fractionation process involves counting of neuronal nuclei with an optical dissector in a strictly random and systematic sampling scheme that covers a known fraction of the region being analysed. Since the fractionator's calculations do not require the exact thickness to the exact area of the section being analysed, the fractionator provides unbiased neuronal counts; independent of shrinkage, dimensional changes and expansion of tissue.

Optical dissectors were applied to the Nissl-stained sections (10 $\mu$m thick) adjacent to those used to count the synapses using SDM. Since most neurons are located in the pyramidal cell layer, neuronal density was estimated over the entire pyramidal cell layer in three subregions: CA1, CA2 and CA3. Only a selection of age- and gender-matched cases was analysed by this method, and the analysed group contained six individuals within each subgroup (Controls, n=6; AD Braak stage 2, n=6 and AD Braak stage 6, n=6). Counting was performed on a computer screen using a Zeiss Axio Imager. Z2 controlled by the stereology software (Stereo Investigator, version 11.02; MicroBrightField Bioscience Inc., Williston, VT, USA). Delineation of each subregion (one slide per case) was acquired with a 1.25x objective on the Zeiss microscope. A dissector grid of 100 $\mu$m x 100 $\mu$m was applied to each subregion and neurons were counted with a 20x objective using the optical dissector with uniform random field sampling. For 10 $\mu$m thick sections dissector height was set at 5 $\mu$m and top guard zone height was set at 1 $\mu$m, rendering a study volume of 5000 $\mu m^3$

per optical dissector. Neurons were identified based on the presence of large nucleoli, and were counted within each dissector grid in the height of the optical plane along the z-axis. The neuronal density was determined by using the optical fractionator workflow within the software. Total cell counts within all grids were divided by total images volume to generate densities of neurons per $mm^3$.

## 2.13 NEUROPATHOLOGICAL ASSESSMENT OF HUMAN TISSUE

All brains included in this thesis were examined according to the standard "ABC" neuropathological classification for Alzheimer's disease pathology (Table 2.7 on page 95). The three "ABC" score components include: Score A - assessment of the topographical progression of A$\beta$ pathology in the brain using the Thal scheme (Thal et al., 2002), Score B - assessment of the topographic progression of Tau neurofibrillary tangle pathology using the Braak scheme (Braak et al., 2006), and Score C - evaluation of the density of cored A$\beta$ neuritic plaques in the neocortex using the CERAD criteria (Mirra et al., 1991). Sections from the brains of all cases were stained using immunohistochemistry for A$\beta$ (6F/3D antibody, Dako, UK, Cat no M 0872) and phospho-tau (AT8 antibody, Thermo Scientific, UK, Cat no MN1020B) as per departmental protocols. Brief details of the scores are provided below.

Score A: Thal A$\beta$ progression phases (0 - 5): phase 0 - no cortical A$\beta$ deposits, phase 1 - neocortical regions affected with A$\beta$ diffuse and non-diffuse plaques, but not including CAA deposits present, phase 2 - additional allocortical areas affected by A$\beta$ plaques, phase 3 - diencephalic nuclei and the striatum affected, phase 4 - midbrain and medulla involved, and phase 5 - pons and cerebellum affected, as described in (Thal et al., 2002). The 6-point Thal phases derived from the anatomical location of A$\beta$-immunopositivity, can then be converted to 4-point A sores as follows: A0 (Thal phase 0), A1 (Thal phase 1 or 2), A2 (Thal phase 3) and A3 (Thal phases 4 or 5).

Score B: Braak & Braak neurofibrillary tangle pathology (0 - VI), modified for use with tau immunohistochemistry : stage 0 - no tau pathology, stage I - transentorhinal region affected, stage II - entorhinal region involved, stage III - occipito-temporal gyrus involved, stage IV - middle temporal gyrus involved, stage V

- peristriate cortex involved , and stage VI - striate cortex affected (Braak et al., 2006). The focus of this staging is on the distribution of neurofibrillary tangles (NFTs) as visualised with the phospho-tau antibody. These NFTs stages are converted to 4-point B scores as follows: B0 (stage 0), B1 (stage I and II), B2 (stage III and IV) and B3 (stage V and VI).

Score C: CERAD score (0 to 4) for density of neuritic plaques in the neocortex (superior and middle temporal gyri, middle frontal gyrus and the inferior parietal lobule), examined at 100x magnification, to obtain a semi-quantitative assessment of the single highest number of neuritic plaques per microscopic field. The scores are as follows: C0 - no neuritic plaques, C1 - sparse (between 1-5 neuritic plaques per 1 $mm^2$), C2 - moderate (between 6-19 neuritic plaques per 1 $mm^2$) and C3 - frequent (more than 20 neuritic plaques per 1 $mm^2$). Neuritic plaques are defined as argyrophilic dystrophic neurites, with or without dense amyloid cores. This scoring was performed using A$\beta$ staining rather than Bielschowsky silver stained sections of the grey matter of the neocortex, as originally described by (Mirra et al., 1991).

**Table 2.7** ABC neuropathological scoring for Alzheimer's disease

| Score A | Thal phase for A$\beta$ plaques | Score B | Braak and Braak NFT stage | Score C | CERAD neuritic plaque score |
|---|---|---|---|---|---|
| A0 | 0 | B0 | None | C0 | None |
| A1 | 1 or 2 | B1 | I or II | C1 | Sparse |
| A2 | 3 | B2 | III or IV | C2 | Moderate |
| A3 | 4 or 5 | B3 | V or VI | C3 | Frequent |

Overview of the three components of the "ABC" neuropathological scoring in Alzheimer's disease. To obtain the ABC score the numerical value for A, B and C components are added together. Abbreviations: A$\beta$ - amyloid beta; NFT - neurofibrillary tangles; CERAD - Consortium to Establish a Registry for Alzheimer's disease. In this thesis, numerical values for each component rather than ABC scores were used to make the results comparable with published studies. Modified from (Hyman et al., 2012).

In addition, cerebral amyloid angiopathy (CAA) was graded using a 4-tier grading system (0-3) to detect CAA in vessels in the leptomeninges, the brain parenchyma and brain capillaries, where grade 0 - was given if no amyloid was identified, 1 - scattered deposition on a few leptomeningeal or cortical blood vessels was present, 2 - more widespread deposits in vessels were seen, and 3 - severe and widespread deposition of amyloid was observed, as previously described in (Barker et al., 2013; Olichney et al., 1996).

Finally, the APOE genotypes and HUSPIRs were performed on area BA41/42, except in two cases (SD36/13 and SD31/12) where it was performed on a frontal and temporal samples, respectively (Brodmann's areas were not specified).

The combination of the results of these neuropathological assessments for all human subjects is shown in Table 2.2 on page 61.

## 2.14 STATISTICAL ANALYSIS

### 2.14.1 General considerations

Statistical analysis was carried out using R software (version 3.2.2) and/or GraphPad Prism version 6, both for Mac. Since SDM human data required huge storage capabilities ($\approx$ 22 terabytes were acquired in this project) only a limited number of cases could be acquired for practical reasons and no statistical methods were used to predetermine sample size. All data generated in this thesis was saved on the University of Edinburgh server provided by the Edinburgh Compute and Data Facility.

Three PSD-95 immunofluorescence punctum measurements were performed: counts (also referred to as density), intensity and size. For synaptic puncta density, the results are presented as the number of synaptic puncta per 100 $\mu m^2$ area; for intensity, as arbitrary units (a.u.) representing grey scale values; and for size as synaptic puncta area in $\mu m^2$. The punctum size is only an approximation when square root of the results was taken, as majority of puncta are not perfectly spherical. Only excitatory postsynaptic PSD-95 puncta were counted.

Where data are presented as box and whisker plots, the Tukey method was used. Within each boxplot, horizontal lines show the medians; box limits indicate the interquartile range (IQR) (inferior or 1st quartile range = 25th percentile, and superior or 3rd quartile range = 75th percentiles). Whiskers extend to data points that are less than 1.5x IQR away from the 1st/3rd quartile; outliers (data points above or below the whiskers) are usually represented by black circles, unless stated otherwise. Statistical analyses were performed where the outliers were included in the analysed data.

To visualise the inter-subject variability (in Chapter 4.5.4) as well as intra-experimental variation of PSD-95 staining (in Chapter 3.1.3), smoothing interpolation by loess method was performed using R function geom_smooth from the package ggplot2. Loess is a non-parametric graphical tool for fitting smooth curves to data. It does not require an a priori specification of the relationship between variables and can be used on data sets with a small data point numbers. Specific parameters used to generate scatterplots with loess curves will be presented separately in graphs' captions.

Normality of LSCM and SDM data distribution was analysed using D'Agostino & Pearson omnibus normality test (GraphPad Prism).

### 2.14.2 Comparison between two groups

In order to compare differences between two groups, an unpaired Student t-test was performed (e.g. comparisons of gender differences in Chapter 5.5 or left/right asymmetry in Chapter 5.6). For non-parametric data, a Mann-Whitney U test comparing ranks was performed (e.g. testing of PSD-95 antibody as a postsynaptic marker in Chapter 3.1.2). These analyses were performed using GraphPad Prism. The data are presented as the mean (or median) $\pm$ SD, unless stated otherwise. A significant level was set to $p < 0.05$.

### 2.14.3 Comparison between multiple groups

In order to compare differences between the control subjects and the disease groups (> 2) the non-parametric Kruskal-Wallis one-way ANOVA on ranks with Bonferroni-type p-value adjustment and post-hoc Dunn's multiple comparison tests were used to establish any statistical differences between subgroups (e.g. Chapter 5.7). Differences between multiple groups and multiple factors were compared using a two-way ANOVA. Sidak's post-hoc test was then used to find statistical differences between the different subgroups and interactions (e.g. Chapter 5.8). These analyses were performed using GraphPad Prism. The data are presented as the mean (or median) $\pm$ SD, unless stated otherwise. A significant level was set to $p < 0.05$.

### 2.14.4 Similarity matrices

In order to assess if there are any similarities between pairs of regions, similarity matrices were generated. Similarity was explained using spatial distance as a measure, in particular the Euclidean distance. The Euclidean difference of zero denotes perfect similarity. As the Euclidean distance value increases, the regions are less similar. The Euclidean distance between two pairs of regions is equal to the square root of the sum of the squared differences between them as shown below:

$$d = \sqrt{(a_2 - a_1)^2 + (b_2 - b_1)^2 + ... + (n_2 - n_1)^2}$$

where, $(a_2, b_2, ..., n_2)$ and $(a_1, b_1, ..., n_1)$ are pairs of coordinates and the Euclidean distance *d* represents a distance between the two points of coordinates.

Once the Euclidean distance was calculated for each pair of subregions assessed, it was plotted as a colour-coded matrix visually represented as a heatmap. A heatmap performs two actions on a matrix (Key, 2012). First, it reorders the rows and columns so that similar profiles are closer to one another and thus more visible to the eye. Second, each data entry in the data matrix is displayed as a colour, making it possible to view similar patterns graphically. There are two important steps in

generation of a heatmap and they include: data reordering using an agglomerative hierarchical clustering algorithm, as will be described in the section below, and data standardisation.

Standardisation of data is undertaken as a measure of handling the variability across synaptic parameters. To calculate the similarity matrices for our data, the three synaptic puncta parameters tested were first standardised by using the z-score normalisation formula as shown below:

$$z = \frac{x - \mu}{\delta}$$

where, $x$ is the value to be normalised, $\mu$ is the mean for the given parameter, and $\delta$ is the standard deviation of the population for the given parameter. It means that each parameter column (or row depending on matrix) in the heat map has a mean of 0 and a standard deviation of 1. This process removes systematic differences between different parameters, so that areas with the same profile have a small Euclidean distance.

### 2.14.5 Hierarchical clustering

In order to assess inter-subject and inter-regional similarities another data analysis tool was used, namely hierarchical clustering. Hierarchical clustering is an unsupervised statistical method for classifying a set of items into hierarchy of clusters (groups) according to the similarities among the items. The inter-subject similarity can be measured in several ways by estimating a distance (proximity or similarity) between data items or clusters. In hierarchical clustering, a matrix of distances is generated that gives rise to a binary tree of data built as the analysis successively merges similar groups of data. A graphical representation of the tree is a dendrogram which provides an interpretable representation of the data output. On the dendrogram the items are joined in a hierarchical fashion from the closest (most similar) to the furthest apart (most different) and the "Y" axis displays the proximity between the merging clusters. A set of instructions that creates the dendrogram is called a linking algorithm. The

linking algorithm defines how the clusters are agglomerated into larger clusters by measuring the distance between the objects. The agglomeration algorithm chosen to measure distances between data items in our data sets is known as the Ward method (Ward, 1963). The distance between the groups is defined as the amount of information lost (or error created) by summarising the objects into *n* clusters. At each step, the agglomeration is chosen which minimises this information loss, which is defined by the Error Sum of Squares (ESS) calculated as

$$minESS, ESS = \sum_{j=1}^{n}(\sum_{i=1}^{n_j} x_i^2 - \frac{1}{n_j}(\sum_{i=1}^{n_j} x)^2)$$

where, *j* is an index for each cluster, $n_j$ is the number of objects in cluster *j*, and *i* is an index for each object in cluster *j*. In general, the Ward method tends to produce tight concentric clusters. The Ward method is also referred to as a minimal increase of sum-of-squares (MISSQ) since the proximity between two clusters is the magnitude by which the summed squares in their joint cluster will be greater than the combined summed square in these two clusters.

The aim for generating the inter-subject dendrograms was to reveal if, based on the PSD-95 protein quantification results, the brain areas analysed clustered in any subgroups/categories that would demonstrate the similarity between the 4 subjects used in the LSCM cohort. The analyses were performed based on the 13 cortical areas as well as all 20 brain areas tested for each PSD-95 parameter.

The aim for generating the inter-regional dendrograms was to establish if PSD-95 proteome clustered into larger areas. These dendrograms were generated as part of heatmaps, and the analysis was performed based on averaging all three parameters for all 4 control subjects.

### 2.14.6 Cohen's *d*

In order to measure how practically significant an effect between the control and the diseased groups is, an effect size was calculated using Cohen's *d*. Cohen's *d* is a

measure of distance between two means, measured in standard deviations. The formula used to calculate the Cohen's *d* is shown below:

$$d = \frac{(M_1 - M_2)}{SDpooled}$$

where, $M_1$ and $M_2$ are the means for the first and second samples, and $SD_{pooled}$ is the standard deviation for the samples. $SD_{pooled}$ was further calculated using the formula shown below:

$$SD_{pooled} = \sqrt{\frac{\sum(X_1 - \overline{X_1})^2 + \sum(X_2 - \overline{X_2})^2}{n_1 + n_2 - 2}}$$

where, $X_1$ represents a sample point from the first sample, and $\overline{X_1}$ represents the sample mean for the first sample. Similarly, $X_2$ and $\overline{X_2}$ represent the sample point and the sample mean for the second sample, respectively. Finally, $n_1$ represents the sample size for the first sample and $n_2$ represents the sample size for the second sample.

Cohen's *d* of effect size informs how big the effect is compared to the standard deviation of the groups and in which direction (negative or positive) the effect changes, but does not inform about the statistical significance of the effect. In order to assess the statistical significance, effect sizes of the groups were compared by their confidence intervals. To calculate the confidence interval, the variance of the Cohen's *d* statistics was found using the formula below:

$$v = (\frac{n_1 + n_2}{n_1 * n_2} + \frac{d^2}{2(n_1 + n_2 - 2)})(\frac{n_1 + n_2}{n_1 + n_2 - 2})$$

where, $n_1$ represents the sample size for the first sample and $n_2$ represents the sample size for the second sample, and *d* represents calculated previously Cohen's *d* value. If the confidence intervals overlapped, the difference between the groups was statistically insignificant.

All the Cohen's *d* related calculations were performed using excel spreadsheets

freely available from the website (http://www.TrendingSideways.com).

## 2.15 BIOINFORMATICS AND VISUALISATION

All quantifications were compiled in the Microsoft Office Excel (2013 for MAC version). Graphs were generated using either R software (version 3.2.2) and/or GraphPad Prism version 6, both for Mac. The majority of analyses were performed in the open-source statistical programming language R. Dendrograms were generated with the use of *dendextend* package (Galili, 2015). Heatmaps were generated with the use of heatmap.2 function from the gplot R library. Where appropriate, figures and drawings were made with Adobe ® Photoshop (version CC 2015). Figures were compiled in Adobe ® Illustrator CS5 (version 15.1.0). This thesis was written in online LaTeX Editor ShareLaTeX (http://sharelatex.com) using a template prepared by Thomas Koeppe, 2006-7, which was then customised for this thesis.

# 3 Validation of PSD-95 antibody staining

## 3.1 TECHNICAL VALIDATION OF PSD-95 ANTIBODY STAINING

Labelling of tissue with an antibody using immunohistochemistry is a common method to identify protein expression used by the researchers working with human tissue sections. However, there are several well-known limitations in using antibodies and their validation is essential (Uhlen et al., 2016).

Firstly, antibody access to the studied protein epitopes, such as PSD-95, might be challenging due to the huge number of proteins present within the PSD that may mask the intended antigen. Secondly, fixation of human tissue with formalin creates multiple additional cross-links between the proteins. As a consequence, PSD-95 labelling with an antibody might have a low affinity and can give rise to off target staining if the antibody non-specifically labels proteins, which are more accessible than the PSD-95. One way of eliminating this problem is to use an antigen retrieval method, such as a heat-induced epitope retrieval, or a chemical-based epitope retrieval. Pepsin antigen retrieval has been successfully used in immunostaining of DLG1-4 family members (Fukaya and Watanabe, 2000). However, since antigen retrieval can still cause tissue distortion, tissue loss during the retrieval process or artifactual staining if not adequately titrated, adequate controls must be performed to ensure specificity of staining. Nevertheless, even with appropriate controls, such as omission of primary antibody or omission of secondary antibody, the staining may not be specific if there is a high level for sequence homology between various antigens as observed with the DLG1-4 proteins. In this scenario, the best control to perform is to stain a genetic knock-out animal tissue, which lacks the protein under test.

Finally, a PSD-95 synapse could also be reliably identified with electron microscopy, but this method is labour-intense and time-consuming. An alternative method involves double labelling the same tissue with another antibody already known to localise at synapses and measure colocalisation (Weiler et al., 2014).

In this section, a description of all controls used for antibody specificity is presented, including methods of validation of PSD-95 staining, such as antibody colocalisation and comparison with PSD-95 KO and KI mouse staining.

### 3.1.1 PSD-95 antibody specificity

To evaluate expression of PSD-95 protein in the human brain, a commercially available anti-PSD-95 mouse monoclonal antibody (IgG2a mAb K28/43, 1:250, UC Davis/NIH NeuroMab) against a human peptide corresponding to amino acids 77-299 (PDZ domains 1 and 2) was used. This region shows two amino acid changes (221/223 amino acids identical) between mouse and human proteins (I148 & I149), although these changes are not located at the PDZ domains. The antibody is predicted to recognise a molecular weight band between 95-110 kDa (varies with cell background due to phosphorylation) (Manning et al., 2012).

To confirm specificity of the anti-PSD-95 antibody, a Western blot analysis on human brain tissue was carried out. A protein band with an approximate molecular mass of 80 kDa, corresponding to the predicted size of naive PSD-95 protein, was selectively detected on an immunoblot of human cortical extract (area BA41), as shown in Figure 3.1 Panel 1. In addition, small peptide bands of molecular weights ranging from approximately 75 kDa to 30 kDa were also observed. Similar truncated peptides have been reported for human (Stathakis et al., 1997) and for rat (Cho et al., 1992; Kistner et al., 1993). These small peptide bands are believed to be attributable to alternatively spliced isoforms of the PSD-95 gene rather than degradation products (Hunt et al., 1996). It is based on the observation that when extract was probed with anti-tubulin, only one prominent protein band is observed, indicating that tubulin was not degraded and therefore the smaller PSD-95 bands are not a result of general proteolytic degradation (Stathakis et al., 1997).

The specificity of staining was also determined on frozen sections from mouse and human brains with and without anti-PSD-95 antibody. The punctate PSD-95 immunostaining was abolished when the primary antibody was omitted in either murine or human tissue, as illustrated in Figure 3.1 Panel 2&3. Similarly, in human tissue no punctate staining was detected when the secondary antibody was omitted or substituted with a secondary antibody from another species as shown in Figure 3.1 Panel 3. In addition, a knockout (KO) control to assess specificity of reactivity in mouse tissue was performed. No specific punctate staining was detected in the

PSD-95 KO mouse, as demonstrated in Figure 3.1 Panel 2. This is in keeping with previous negative KO staining with this antibody reported in mouse (Broadhead et al., 2016). Furthermore, specific co-localisation pattern of PSD-95 staining with other antibodies, including synaptophysin and synapsin 1, was evaluated, as previously described (Koffie et al., 2009) and will be demonstrated below in the next section 3.1.2.

Finally, in addition to testing the anti-PSD-95 antibody specificity for this project, the NeuroMab antibody has been validated by its originator, the UC Davis/NIH NeuroMab Facility, as being a reliable and specific to the antigen of interest (Rasband et al., 2002; Manning et al., 2012). See also http://neuromab.ucdavis.edu/catalog.cfm.

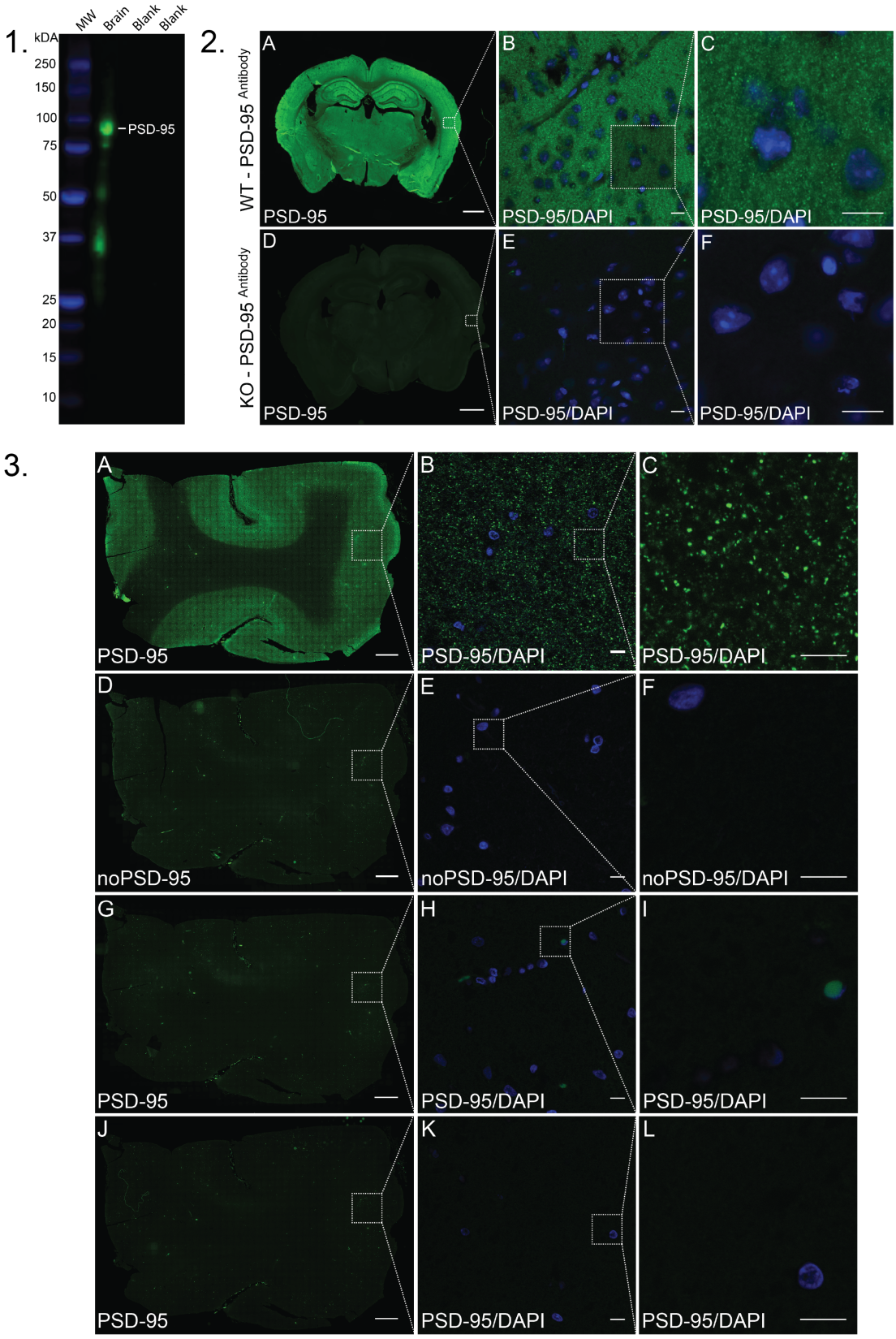


**Figure 3.1 Mouse and human controls of PSD-95 IF staining.**

**Panel 1** Validation of anti-PSD-95 NeuroMab antibody using Western blot analysis. Immunoblot against human PSD-95 protein from human cortical area BA41 demonstrated a strong band at approximately 80 kDa. Additional small peptide bands, ranging in size from approximately 75 kDa to 30 kDa, are believed to be alternatively

spliced isoforms of the PSD-95 gene rather than degradation products. Molecular weight (MW) in kDa indicated. **Panel 2** Mouse controls. The PSD-95 staining seen in a wild type mouse tissue **A** was abolished in the PSD-95 KO mouse **D**, low magnification (20x). Similarly, the punctate PSD-95 staining in the wild type mouse **B&C** was abolished at a high magnification (63x) in the KO mouse **E&F**. **Panel 3** Human controls. Images **A, D, G J** were obtained using a slide scanner and, apart from **A** which is a positive control, show overview of whole cortical sections lacking PSD-95 staining. Primary antibody was omitted from tissue in row starting with image **D**. The secondary antibody was omitted in the next row starting with **G**. Secondary antibody from a wrong species (anti-rabbit) was used in the last row of images starting from **J**. Occasional immunofluorescence staining in lipofuscin deposits and/or larger blood vessels was observed. The rest of images were obtained using the confocal microscope. Images **E,H&K** demonstrate absence of punctate staining at magnification 63x. Lack of PSD-95 punctate staining was further confirmed with a zoom 3.1, as seen in images **F,I &L**.

---

### 3.1.2 PSD-95 as a postsynaptic marker

To determine whether the PSD-95 antibody is a reliable excitatory post-synaptic marker, dual immunofluorescence labelling was performed with two general markers of thepre-synaptic terminal, namely synapsin 1 and synaptophysin, as shown in Figure 3.2 on page 112. Since PSD-95 is located close to the post-synaptic plasma membrane, the PSD-95 antibody is often used to define the post-synaptic compartment of the synapse adjacent to a synapsin 1-stained or synaptophysin-stained pre-synaptic compartment (Glantz et al., 2007; Koffie et al., 2009).

Synapsin 1 is a vesicle-associated actin-binding protein (De Camilli et al., 1983) and it is reportedly found in all cortical glutamatergic and GABAergic synapses (Micheva et al., 2010). Synapsin 1 immunoreactivity is a useful proxy for the identification of synapses, and antibodies against synapsin 1 have been used to estimate synapse counts (Busse and Smith, 2013).

Synaptophysin is a presynaptic vesicle membrane protein and is found in all nervous tissue (Wiedenmann and Franke, 1985). Synaptophysin immunoreactivity has been used as a marker of synaptic density (Masliah et al., 1990). The protein itself has been associated with many functions, including calcium binding, channel formation,

exocytosis, and synaptic vesicle recycling (Glantz et al., 2007), and importantly, changes in synaptophysin expression have been linked to human psychiatric diseases, such as schizophrenia. For example, studies reported reduced levels of synaptophysin in the prefrontal cortex of schizophrenic patients (Honer et al., 1999; Karson et al., 1999) giving rise to the hypothesis that schizophrenia might be a disorder of synaptic connectivity (Lewis and Lieberman, 2000).

In the first set of experiments, LSCM data was tested. Brain sections from the cortical area BA46 were double-labelled with PSD-95 and either synapsin 1 or synaptophysin. It was observed that a majority of the PSD-95 synaptic puncta were juxtaposed with the presynaptic markers and this was further confirmed with quantification of colocalisation analysis. As a control to account for random colocalisation, images from each corresponding datasets were rotated clockwise by 90° to stimulate random puncta. It was found that PSD-95 was statistically associated with synapsin 1. Median latencies in groups PSD-95 and synapsin 1 were 91.54 and 78.13; the distributions in the two groups differed significantly (Mann–Whitney $U$ = 13.41, n1 = n2 = 4, $p < 0.03$ two-tailed). In addition, PSD-95 was statistically associated with synaptophysin (median latencies in groups PSD-95 and synaptophysin were 87.83 and 75.67; the distributions in the two groups differed significantly (Mann–Whitney $U$ = 12.16, n1 = n2 = 4, $p < 0.03$ two-tailed).

Later, SDM images of triple-labelled synaptic puncta with a VGluT1 marker, in addition to synaptophysin and PSD-95, were obtained for another cortical area BA37. VGluT1 is an example of a presynaptic marker. It is the main vesicular glutamate transporter that accounts for up to 80% of glutamate uptake in the brain (Fremeau et al, 2004). It was observed that there was a significantly high colocalisation of PSD-95 with synaptophysin. Median latencies in groups PSD-95 and synaptophysin were 81.71 and 52.31; the distributions in the two groups differed significantly (Mann–Whitney $U$ = 29.41, n1 = n2 = 4, $p < 0.03$ two-tailed). A lower, but still significant association was also detected for PSD-95 and VGluT1 colocalisation (median latencies in groups PSD-95 and VGluT1 were 59.99 and 35.28; the distributions in the two groups differed significantly (Mann–Whitney $U$ = 24.72, n1 = n2 = 4, $p < 0.03$ two-tailed).

In addition, IF double-labelled images from the same cortical area BA46 were obtained using SDM. Similar to the LSCM data, it was observed that majority of PSD-95 synaptic puncta were significantly colocalised with synapsin 1. Median latencies in groups PSD-95 and synapsin 1 were 82.7 and 53.6; the distributions in the two groups differed significantly (Mann–Whitney $U$ = 29.11, n1 = n2 = 4, $p < 0.03$ two-tailed) as well as with synaptophysin. Median latencies in groups PSD-95 and synapsin 1 were 82.03 and 53.83; the distributions in the two groups differed significantly (Mann–Whitney $U$ = 28.2, n1 = n2 = 4, $p < 0.03$ two-tailed).

Finally, the CA1 hippocampal area was double labelled with PSD-95 and synapsin 1, and imaged using SDM. As before, it was observed that there was a significant colocalisation between the two synaptic markers, although not as high as for the BA46 cortical area. Median latencies in groups PSD-95 and synapsin 1 were 68.71 and 54.84; the distributions in the two groups differed significantly (Mann–Whitney $U$ = 13.87, n1 = n2 = 4, $p < 0.03$ two-tailed).

Overall, these colocalisation results indicate that the majority of the PSD-95 puncta are juxtaposed to presynaptic sites. There may be several reasons as to why not all synapses colocalise with PSD-95. For instance, it is possible that not all synapses are labelled with any of the three presynaptic markers given the vast synaptic molecular diversity. Furthermore, it is feasible that any discrepancies (under- as well as overestimations) are due to technical errors, such as false antibody labelling, imprecise detection analysis or inaccurate colocalisation measurements. These factors could have contributed to the surprising findings for analyses in the BA46 area, in particular. Even though the differences between the markers were significant, the automated colocalisation method generated a relatively high percent colocalisation in rotated images. There are several factors contributing to a lesser accuracy. For instance, other sources of fluorescent signal from autofluorescent tissue, such as lipofuscin or red blood cells, could have created additional false labelling. In addition, even though the parameters used for the colocalisation analyses were kept constant for the tested and rotated images, they were determined subjectively by visual inspection. Further rigorous testing against manual quantifications would allow for the numbers to be more precise. Alternatively, using other methods, such as electron microscopy, which

unambiguously identifies synapses, could have been used to validate my results.

Finally, there are potential limitations to the assumption that PSD-95 IF labelling adequately labels PSD-95 synapses. EM studies examining subcellular distribution of PSD-95 indicated that PSD-95 is not restricted to PSDs, but it is more prevalent at non-synaptic sites. For instance, only 10% of PSD-95 immunoreactivity was detected using DAB labelling for EM within layer 1 of the adult human cortex on dendritic spines (Aoki et al., 2001). The same authors reported 44% of axonal and 26% of dendritic shaft PSD-95 labelling present at non-synaptic sites. Moreover, 11% of PSD-95 labelling was found at non-synaptic glial component. In addition, not all synapses express PSD-95. When PSDs were probed for PSD-95 using the PEG labelling procedure, Aoki et al. (2001) demonstrated that approximately 60% of the morphologically identifiable asymmetric synapses showed PSD-95 expression. Although the number of examined synapses was very low at just over 250 synaptic profiles, this study additionally highlights possible limitations of using light microscopy rather than EM with its high resolution capabilities for PSD-95 IF labelling. Therefore, as outlined above, these data should not be taken as absolute PSD-95 values, but rather as relative tendencies until validated with additional techniques. Nevertheless, the associations tested were all significant suggesting that antibody labelled PSD-95 positive synaptic puncta can be assumed to represent a majority of postsynaptic PSD-95 terminals.

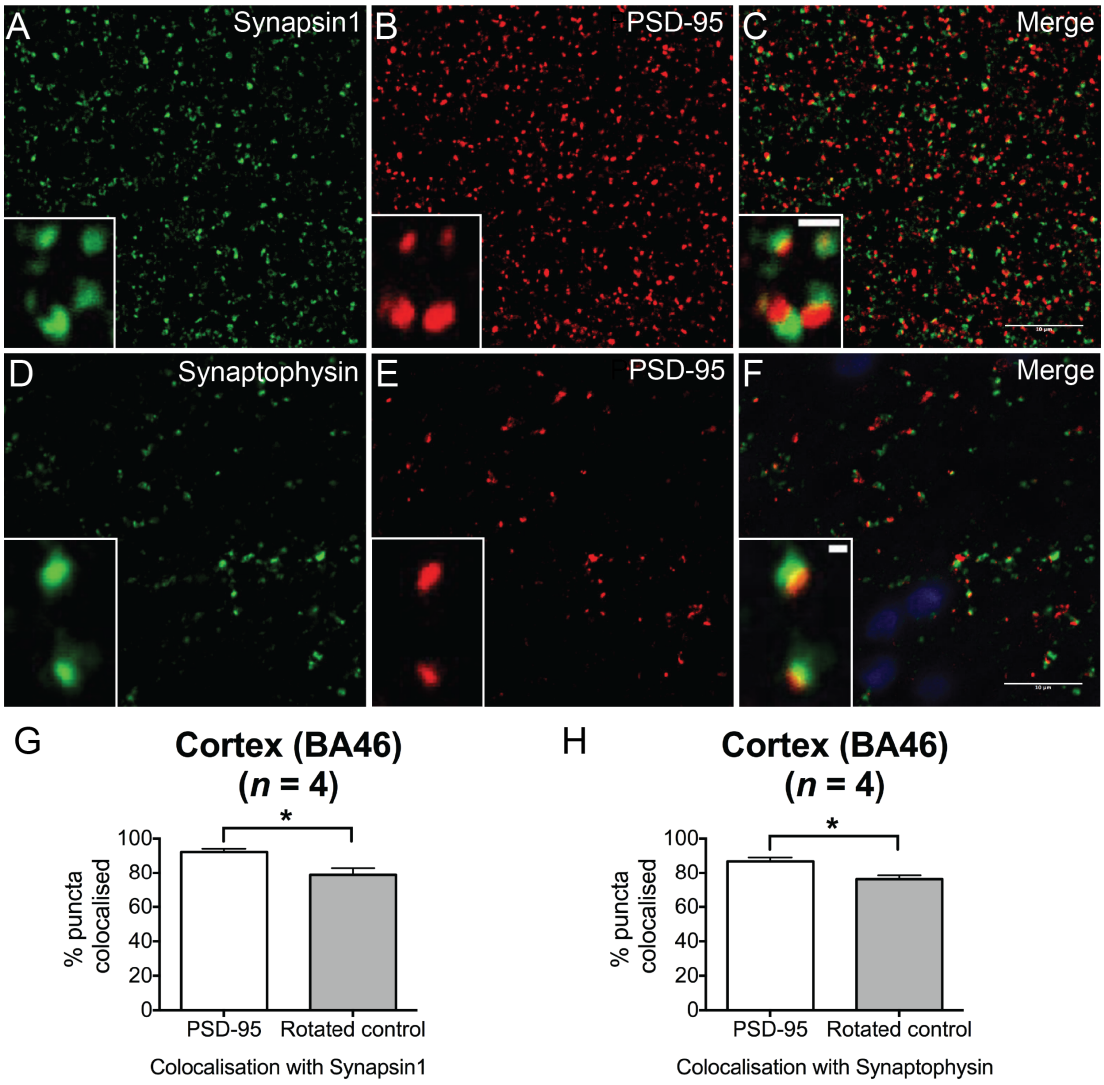


**Figure 3.2 PSD-95 as a reliable postsynaptic marker (LSCM data).**

**A-C** PSD-95 was co-stained with synapsin 1 antibody and **D-F** synaptophysin antibody. Both, synapsin 1 and synaptophysin, are examples of presynaptic markers and these images demonstrate that postsynaptic PSDs are opposed by a presynaptic terminal. Inlets in **C** and **F** demonstrate typical IF 'snowman' appearances of colocalised pre- and postsynaptic markers. Overall, the majority of PSD-95 puncta are juxtaposed to presynaptic terminals. Scale bars: C and F 10 $\mu$m, inlets in C and F 1 $\mu$m. **G-H** Quantification of percentage of PSD-95 positive puncta colocalisation with synapsin1 **G** and synaptophysin **H**. The rotated control shows the degree of random colocalisation obtained by clockwise rotation of the synapsin1 **G** or synaptophysin **H** images. The observed colocalisation with either presynaptic marker is significantly higher than expected by chance. Together, these data strongly suggest that the PSD-95 antibody is a reliable marker of PSDs. Images and quantifications are based on the LSCM data. Data are mean $\pm SD$. Significance levels were obtained using Mann-Whitney U test: *p $\leq 0.05$.

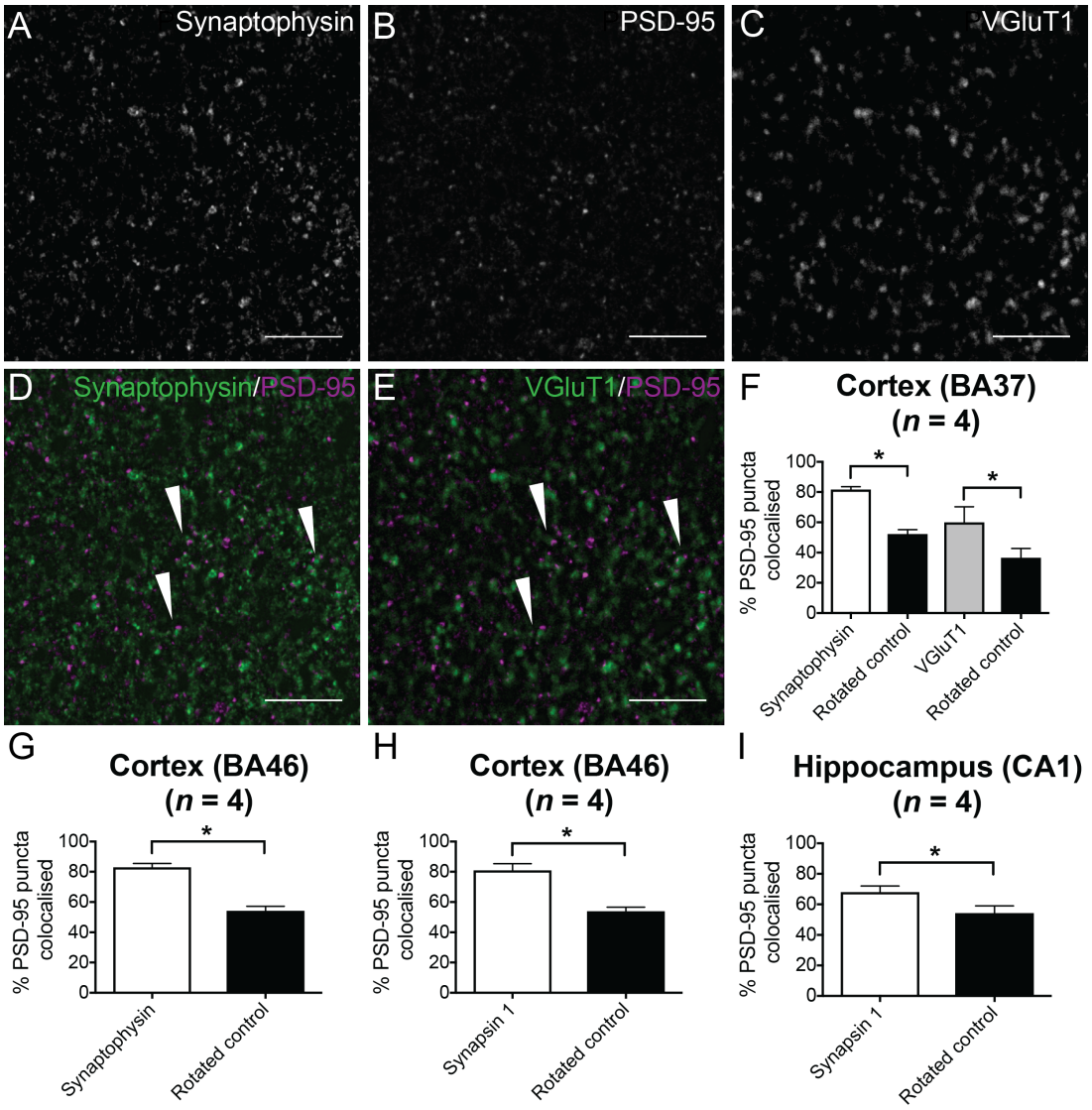


**Figure 3.3 PSD-95 as a reliable postsynaptic marker (SDM data).**

**A-F** PSD-95 was triple co-stained with synaptophysin antibody **A** and VGlut1 antibody **C** in the BA37 cortical area. Both, synaptophysin and VGluT1, are examples of presynaptic markers and these images demonstrate that postsynaptic PSDs are opposed by a presynaptic terminal as demonstrated in merged **D** and **E** images. Arrows in **D** and **E** demonstrate typical IF apposition appearances of colocalised pre- and postsynaptic markers. **F** Quantification revealed that overall, the majority of PSD-95 puncta are juxtaposed to presynaptic terminals. Scale bars: 10 $\mu$m. **G-H** Quantification of percentage of PSD-95 positive puncta colocalisation with synaptophysin **G** and synapsin 1 **H** in the BA46 cortical area. The rotated control shows the degree of random colocalisation obtained by clockwise rotation of the synaptophysin **G** or synapsin 1 **H** images. The observed colocalisation with either presynaptic marker is significantly higher than expected by chance. **I** Quantification of percentage of PSD-95 positive puncta in the CA1 subregion of the human hippocampus. Lower numbers of juxtaposed synapses were detected in comparison to the cortical areas, but there was still a significant difference between the tested and rotated controls. Together, these data strongly suggest that the PSD-95 antibody is a reliable marker of PSDs. Images and quantifications are based on the SDM data. Data are mean $\pm SD$. Significance levels were obtained using Mann-Whitney U test: *p $\leq 0.05$.

### 3.1.3 PSD-95 antibody staining consistency

Variability of immunohistochemical techniques using antibodies has been well documented (Fritschy, 2008; Rhodes & Trimmer, 2006). There are many sources of variation in antibody staining, including intrinsic tissue factors (e.g. post-mortem delays, mode of death, cause of death), laboratory protocols (e.g. change of chemicals), acquisition protocols (e.g. change of acquisition parameters) or tissue samples stained on different days following the same staining protocols.

To assess the potential variability of the PSD-95 antibody staining procedure, the experimental protocol was repeated three times for one case (SD23/13), as illustrated in Figure 3.4 on page 116. The PSD-95 staining procedure generated consistent staining with no significant differences between the experiments in quantification of PSD-95 IR in the 10 areas tested for the three parameters. Overall, there was good PSD-95 antibody staining consistency between the experiments. Among the three synaptic parameters tested, the PSD-95 puncta intensity was least consistent, with PSD-95 puncta density and size showing similar trends. The density of fluorescent PSD-95 puncta was relatively consistent for the cortical areas and the brainstem regions, with most staining variation being seen in the subcortical regions (TH and HC) and the cerebellum. This pattern of staining variability was repeated for the size of PSD-95 puncta, but with greater variation discrepancies, especially in the brainstem.

There could be several explanations for these staining discrepancies. For example, larger areas were imaged for the subcortical areas in comparison to the rest of the regions. Since the subcortical areas are naturally more heterogeneous with regard to cellular populations, the precise neuroanatomical region, and therefore the sampling of images, might not have been exactly identical which would have affected the results if areas of different PSD-95 density were sampled. Similarly, the brainstem areas do not have as homogenenous a cytoarchitecture as the cortical areas. In addition, very recent data assessing suitability of PM tissue in proteomics using HUSPIR ratio revealed that the cortical areas are least degraded and thus most preserved for PSD proteins in the cortical areas. On the other hand, the subcortical (TH and HC) and

infratentorial (CB, MB, PO and MD) regions were less reliable in terms of protein preservation. Therefore, while the staining consistency appears particularly good for well preserved areas, such as cortical regions, the deep grey nuclei and the brainstem regions are less reliable for at least two reasons: they are more heterogeneous and therefore sampling may not have been identical at each attempt, but also they are potentially more degraded so protein preservation may not be identical. However, the second argument may not necessarily apply as all repeated sections were obtained from the same tissue block.

Finally, it is interesting that of the four cortical areas tested, BA46 and BA17 both appeared less reproducible than BA20 and BA39 for all three synaptic parameters. It is known that the large dorsolateral prefrontal cortex that contains BA46 area is one of the more functionally heterogenous cortical region of the human neocortex. It may well be possible that this functional heterogeneity is reflected in underlying local spatial synaptic diversity. In a similar way, the primary visual cortex, known as area BA17, is instantly recognisable both macroscopically and microscopically, in unstained brain slices due to the heavily myelinated stria of Gennari in an additional cortical layer 4B. This cytoarchitectural peculiarity is a clear example of neuroanatomical diversity among the cortical areas. In this example, one could therefore foresee how the local neuronal diversity might give rise to local spatial synaptic diversity. Since large cortical sections were sampled for all four cortical areas, the discussed functional and anatomical diversities might have become apparent on repetitive testing; although as it was mentioned before they were not statistically significant.

In summary, there was overall good PSD-95 IF staining consistency between experiments. The consistency of PSD-95 staining was the best for the puncta size, followed by density and intensity. Cortical areas showed the least staining variability while the subcortical regions showed the most staining variation. The differences in staining might be related to the underlying subregional heterogeneity of the tested areas.

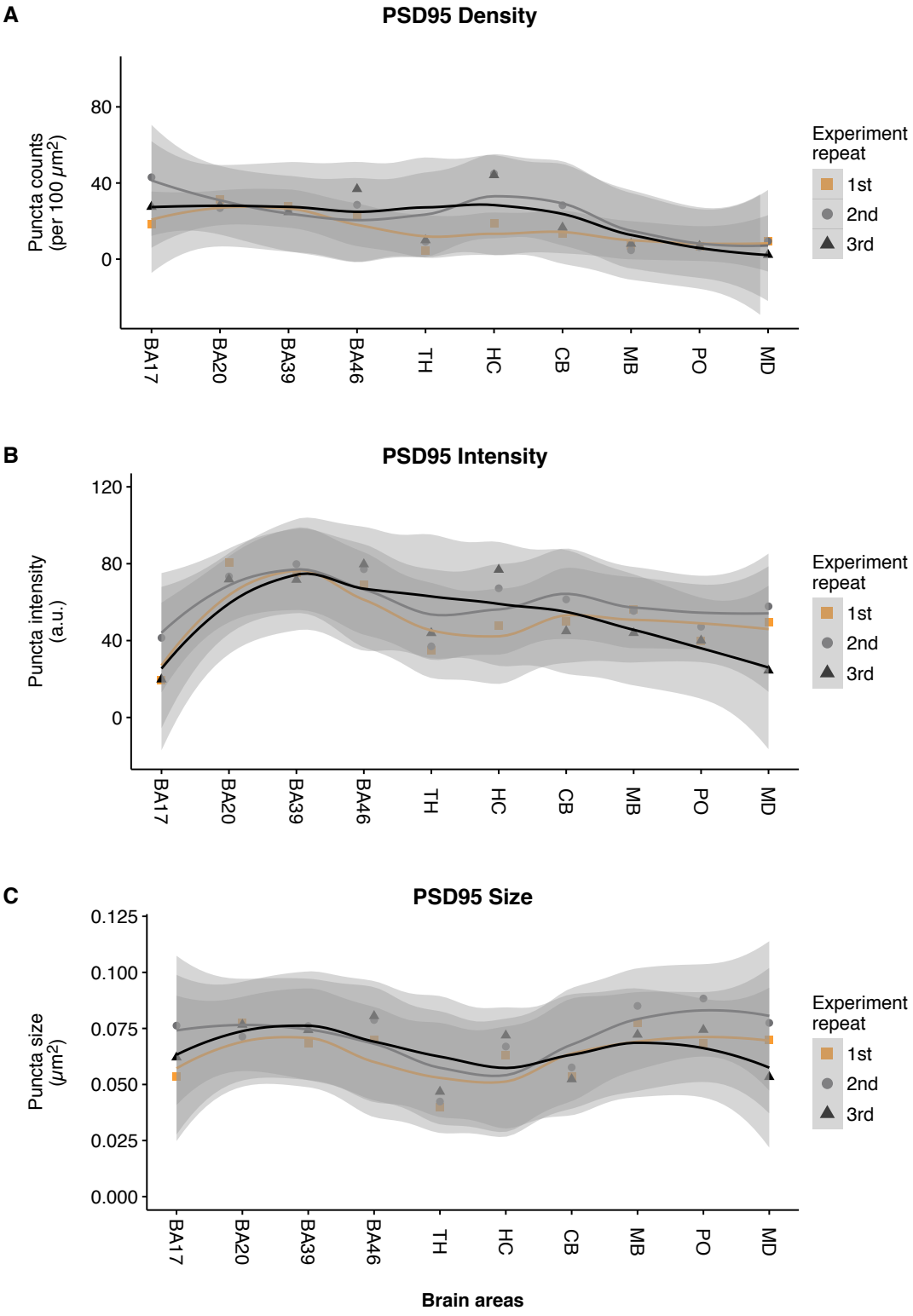


**Figure 3.4 PSD-95 antibody IF staining consistency.**

Scatterplots used to assess the consistency of PSD-95 staining among 10 regions for the three PSD-95 puncta parameters (density, intensity and size). **A.** PSD-95 puncta density results were most consistent for the cortical areas, and least consistent for the subcortical regions. **B.** PSD-95 puncta intensity measurements were most variable among the three puncta parameters. The greatest variations were observed in the subcortical areas (TH and HC) and the brainstem. **C.** PSD-95 puncta size results

showed most variation in the brainstem areas. The consistency was assessed by fitting a loess smoothing curve superimposed among the data points. Each colour-coded curve represents a repeated experiment. Data points (squares, circles and triangles) represent a mean value obtained for each tested area. Grey shadow areas represent 95% confidence intervals (CI). Smoothing interpolation by loess method was performed using R function geom _ smooth from the ggplot2 package: parameter settings were method = "loess", se = "95% CI" and span = "0.75" for the curve fitting.

---

## 3.2 COMPARISON OF PSD-95 IF STAINING IN HUMAN *vs.* MOUSE

The patterns of PSD-95 distribution obtained using antibody staining of human tissue were compared to those observed in the genetically modified mouse generated by gene targeting in the Grant laboratory. The knock-in mouse expresses a fluorescent protein (the Enhanced Green Fluorescent Protein (EGFP)) fused to an endogenous PSD-95 protein.

### 3.2.1 Qualitative comparison of PSD-95 distribution between human and mouse brains

Comparison between selected anatomical regions including cortex, thalamus, hippocampus and cerebellum revealed similarities of in the PSD-95 staining patterns between species, as shown in Figure 3.5 on page 118. A similar pattern of staining was observed in both species in the cortex and the thalamus. In both species, two distinct patterns of staining were observed in the cerebellar granular cell layer and in the molecular layer. In contrast, a similar pattern of staining noted in the hippocampal CA3 region of the mouse was observed in the human tissue, but in a different subregion. In mouse the pattern was seen in *the stratum lucidum*, but in human in *the stratum pyramidale*. Overall, these results suggest that the PSD-95 KI mouse is a good reference animal model to study the distribution of PSD-95 in the human brain. The distribution differences might be a reflection of functional and connectivity discrepancies between the species.

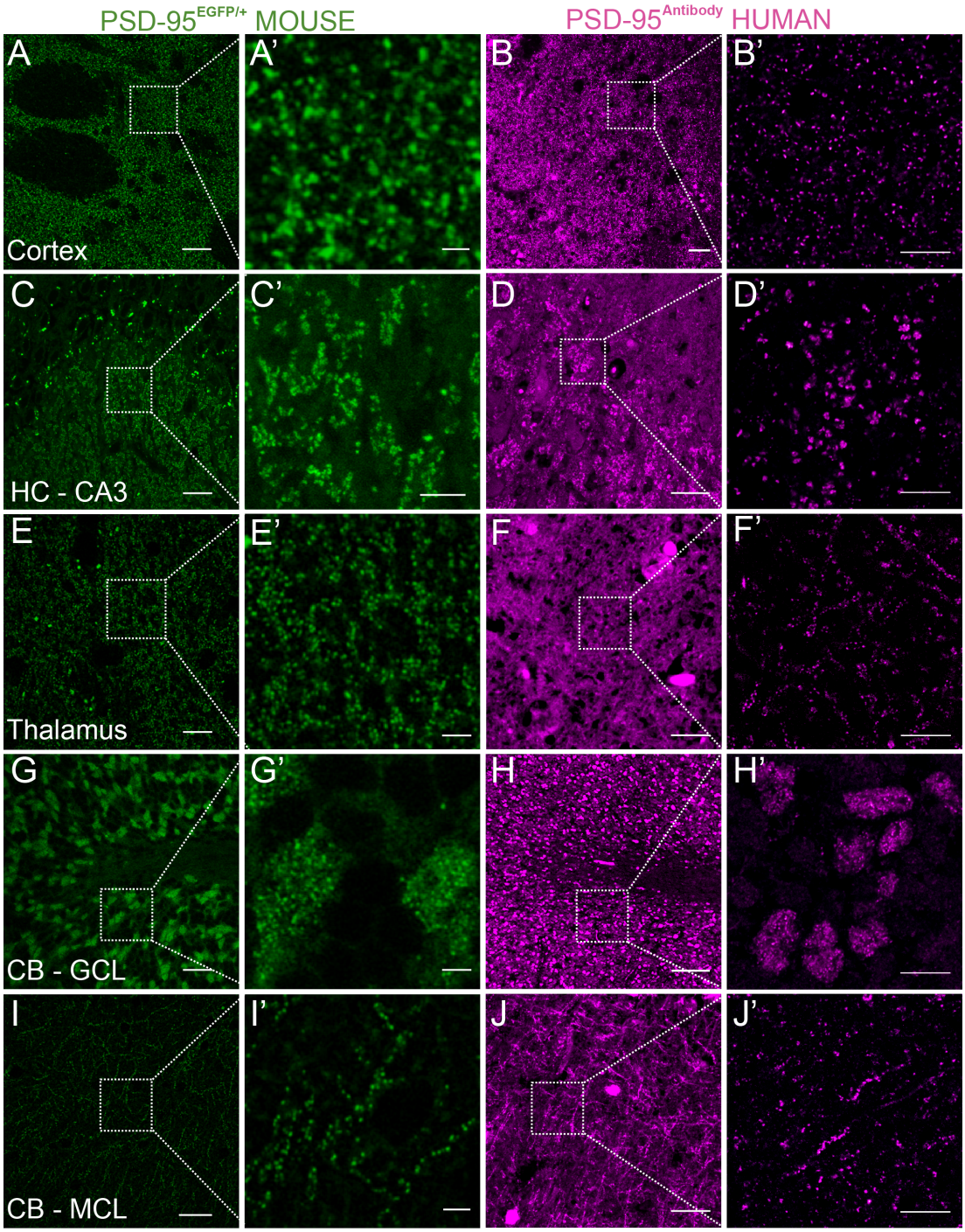


**Figure 3.5 Comparison of PSD-95 expression patterns between human and mouse in various brain regions.**

Tissue from mutant knock-in mouse was examined using direct fluorescence microscopy of PSD-EGFP fusion protein in the adult PSD-95 EGFP/+ heterozygote (in green). Human tissue was stained with PSD-95 antibody using indirect immunofluorescence (in magenta). There was a striking similarity in PSD-95 punctate staining observed in selected areas between the knock-in mouse and the human tissue. Similar patterns of staining were observed in cortex **A-B'** and thalamus **E-F'**. Two distinct patterns of staining were observed in both species in the cerebellum (in granular cell layer: **G-H'**; and in molecular cell layer: **I-J'**. In contrast, a similar pattern of staining was noted in hippocampal CA3 region. However, the pattern

occurred in two different subregions: in mouse in stratum lucidum **C-C'**, but in human in stratum pyramidale **D-D'**. Mice images were kindly provided by Dr Fei Zhu. Abbreviations: HC, hippocampus; CA3, cornu ammonis; CB, cerebellum; GCL, granular cell layer; MCL, molecular cell layer. Scale bars: A, C, E, G, I -20$\mu$m; A', E', G', I' -2$\mu$m; C' -5$\mu$m; B, D, J -30$\mu$m; F, H -100$\mu$m, B', D', F', H', J' -10$\mu$m.

---

### 3.2.2 Quantitative comparison of PSD-95 distribution between human and mouse brains

To further evaluate PSD-95 antibody staining in human tissue, a qualitative comparison of PSD-95 puncta measurements (puncta density, intensity and size) between the species was undertaken. The human data was acquired with LSCM and analysed using the Ensemble quantification method. The KI mouse data was acquired with SDM and analysed using the Corsen quantification method. Despite the different acquisition and quantification methods, overall, there were good, positive and linear correlations between the two species for the three synaptic puncta parameters tested (Figure 3.6 on page 124).

The high and significant Pearson's correlation value for PSD-95 puncta density suggests that despite different microscopy platforms both acquisition systems are comparable at detection of individual synaptic puncta. The slightly higher synaptic puncta numbers for the KI mouse might be due to a clearer immunofluorescent signal emitted by the KI mouse tissue. Images obtained from the antibody stained human tissue are notorious for low signal-to-noise ratio. The numerical differences are probably less likely to have resulted from using different imaging platforms, as SDM images were sampled at a lower rate and larger pixel size of 84 nm, rather than 46 nm by the LSCM obtained using the digital zooming.

In contrast, the different microscopy platforms might have contributed to differences in puncta intensity. Compared to SDM, synaptic puncta obtained with LSCM were dimmer. Since both platforms have different intensity detection systems, and thus different sensitivity and/or depth of detection, and use different acquisition

settings, such as gains or laser powers, the intensities they generate cannot be taken as absolute values and should not be directly compared. Nevertheless, well correlated intensities for different regions might be due to existing regional synaptic similarities between the species.

Finally, there was a good correlation between the species for the synaptic puncta size, although the human PSD-95 synaptic puncta were larger than rodent. The main explanation for this discrepancy might be due to the use of antibodies in the human tissue. Antibodies have intrinsic dimensions that can increase the size of the IF signal as they attach to the protein surface. One of the ways of improving the accuracy of this comparison, not undertaken in this study, would be to compare human tissue with a wild type mouse tissue labelled with the same PSD-95 antibody. Another explanation might be technical and be due to the use of different quantification methods, and therefore associated with setting up of different counting parameters. Nevertheless, despite different absolute size numbers, the size of PSD-95 puncta appears well correlated for both species.

## 3.3 CORRELATION BETWEEN IF AND WB FOR PSD-95 QUANTIFICATION

In the next set of experiments, comparisons were made between PSD-95 protein quantification obtained using IF and PSD-95 protein quantification using Western blots for the same 12 cortical regions from the same 4 human control cases.

In order to quantify differences between the different human cortical areas, PSD-95 protein levels were measured by calculating fluorescent intensity of PSD-95 antibody binding and comparing the measurements against fluorescent intensity of beta-tubulin. The ratio of the PSD-95 immunofluorescence measurements divided by the beta-tubulin immunofluorescence measurements resulted in normalised values of PSD-95 protein (fluorescence ratio) for each tested cortical area using Western blots. The only one cortical area not tested by WB, but examined using IF, was the occipital region BA19, which was shown to be most degraded among the cortical areas in the four control cases when assessed by HUSPIR.

### 3.3.1 Correlation between IF and WB by case

There were positive correlations found between the density of PSD-95 calculated using IF and PSD-95 measurements using WB for all four cases (Figure 3.7 on page 125). However, only one case (SD42/13) out of four showed a strong and a significant correlation between the two methods.

The discrepancy between the two methods in quantification of PSD-95 may be due to several factors. Firstly, different primary anti-PSD-95 antibodies were used. In the WB quantification method a polyclonal anti-rabbit PSD-95 antibody (LifeSpan Biosciences) was used, which have not been tested for specificity with the immunohistochemistry and thus may not have been as specific as the monoclonal anti-mouse PSD-95 NeuroMab antibody tested for the IF method. Polyclonal antibodies tend to recognise more than one epitope, therefore making them less specific.

In addition, unlike in IHC where the protein epitope is better preserved in its native conformation, in Western blotting protocol denaturation of proteins takes place, and therefore their native conformation is no longer preserved, disabling the efficacy of the antibody to recognise its epitope. This in turn may have affected the access of the antibody to the studied protein.

On the other hand, fresh tissue was used for WB, but it was formalin fixed for IF. It is known that any fixation of tissue can mask epitopes, making them less accessible and thus the antibody less reliable.

All these factors might have contributed to the lack of stronger correlations between the methods, albeit both were positive.

### 3.3.2 Correlation between IF and WB by parameter

Similar to the above data, positive correlations found between the three PSD-95 synaptic parameters calculated (density, intensity and size) calculated using IF and PSD-95 measurements using WB (Figure 3.8 on page 126). However, only one

parameter (PSD-95 synaptic punctum size) out of three showed a strong and a significant correlation. While it is difficult to speculate why the correlations observed were not as strong, the technical discrepancies between the methods, such as the use of a different primary antibody, different fluorescent detection methods and different quantification methods, may have all contributed to the observed differences.

Neither of the methods quantified absolute values of proteins, but only relative abundances. WB measured PSD-95 abundance in relation to beta-tubulin concentration assumed to be the same for each subject, whereas IF measured the protein quantity in a 2D area rather than a 3D space. Furthermore, both methods use different detection systems for assessing the intensity of immunofluorescence. In addition, in IF, the automated Ensemble IR quantification method was used, but in WB a more subjective use of box detection was used. Finally, it is possible that size of the punctum is a true reflection of protein differences between the areas.

## 3.4 CHAPTER DISCUSSION AND CONCLUSION

Taken together, the approaches and methodologies described in this chapter focused on validation of the monoclonal antibody PSD-95 IF. I aimed to maximise IHC staining efficiency and ensure uniformity of staining and IF acquisition as this technique is known for its pitfalls and artefacts. In general, the conditions used in my experiments were typical of those used in most laboratories for IHC staining. I used a monoclonal antibody to reduce cross-reactivity problems. Moreover, all sections were of uniform thickness and correct calibration of the microscopic and camera conditions was performed. All images were captured in a temperature- and light-controlled environment to optimise image acquisition conditions. Furthermore, the fixation time in formalin was relatively shorter for brain tissue blocks (maximum 3 days) than time undertaken in many other brain bank tissues (up to 3 weeks for whole brains) and should have yielded greater staining. Finally, in addition to ensuring the best staining and acquisition conditions, I thoroughly assessed the neuropathology and biochemistry of the post-mortem tissue to control for any variability in tissue quality that potentially could contribute to differential staining between subjects.

Initially, using various controls, I demonstrated that a specific post-synaptic PSD-95 antibody was used. I then showed that the human PSD-95 expression correlated, to a degree, with the PSD-95 KI mouse model. However, this analysis could have been improved by including additional comparisons with a PSD-95 antibody labelled wild type mouse. A direct comparison of antibody stained tissues from mouse and human would not only have eliminated technical differences, such as size and strength of IF arising from an antibody vs. IF arising from a fluorescent protein, but also prevented unknown confounds arising from introducing potential artefacts in genetically manipulated animals. On the other hand, species differences between human and rodent synapses have already been described (Jones et al., 2017). For instance, Jones et al. demonstrated that human neuromuscular junctions, a major subclass of peripheral nervous system synapse, are smaller and more fragmented in human than mouse and have a distinct, species specific molecular composition. Therefore, at least in some instances, synapses can be morphologically very distinct and species differences would be expected to exist for other subclasses of synapses. Finally, there were also positive, albeit less stronger, correlations with human tissue examined using a different method, WB. Further human correlative studies using proteomic analyses, such as mass spectometry, would additionally validate our findings.

Overall, I conclude that these results indicate that the PSD-95 antibody IF protocol I developed is a reliable method for studying distribution of PSD-95 protein in human post-mortem tissue.

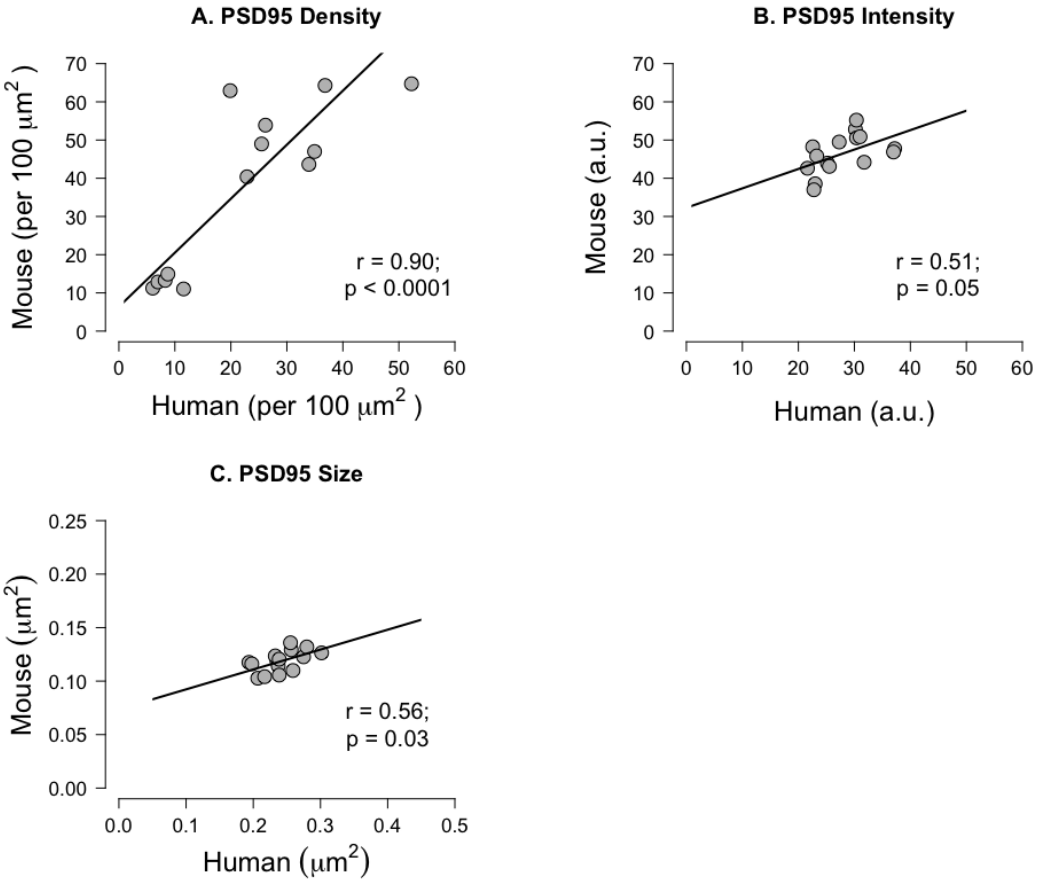


**Figure 3.6 Correlation of PSD-95 puncta parameters quantification between human and mouse.**

Scatterplots showing correlations of PSD-95 puncta parameters (density, intensity and size) quantified from 15 brain areas of KI mouse and human tissue stained using antibodies. **A.** There was a high, positive linear and significant correlation between the human and mouse PSD-95 puncta counts. **B.** A moderate, positive linear, and significant, correlation was found for PSD-95 puncta intensity. **C.** PSD-95 puncta sizes were moderately and significantly correlated between the species. Pearson's product-moment correlation (r) and p values are provided. Values are based on 3 male mice aged 12 months and 3 human males.

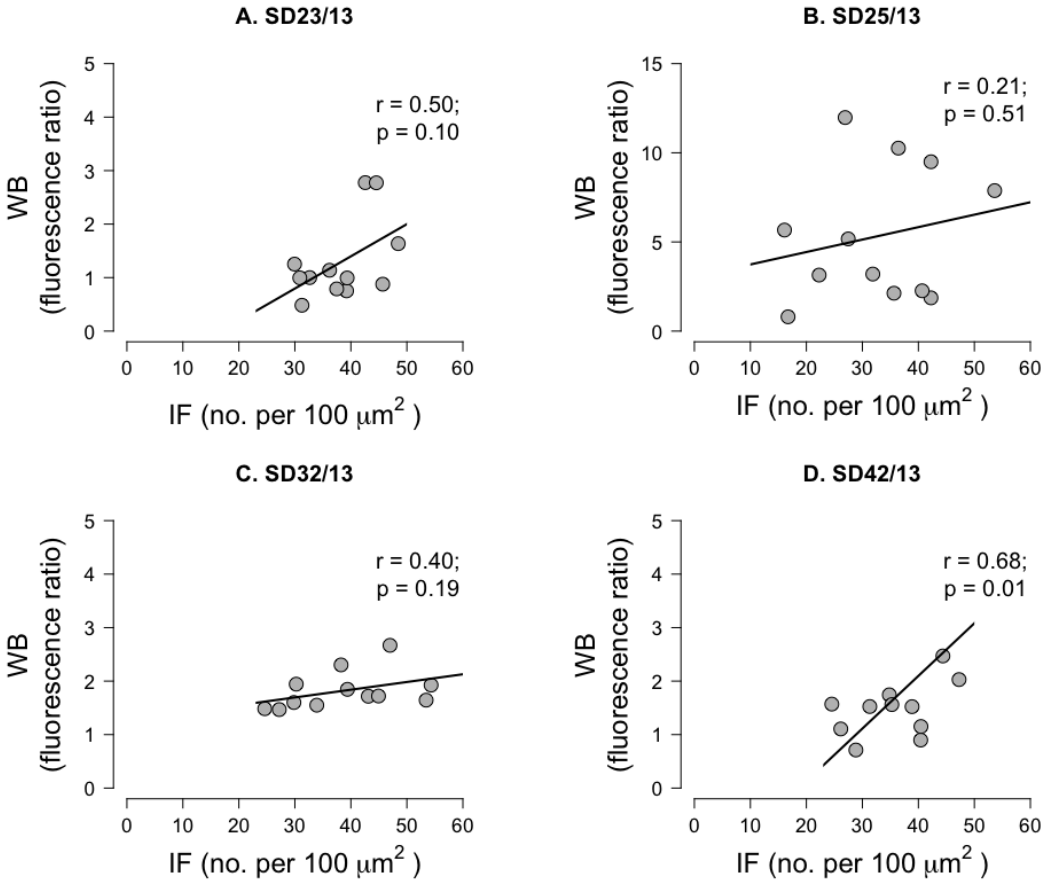


**Figure 3.7 Comparison between IF and WB for PSD-95 quantification by case.** Scatterplots showing positive correlations for 12 human brain areas between PSD-95 puncta density quantified using IF and normalised immunofluorescent PSD-95 ratios obtained using WB for four human control brain cases. **A.** There was a moderate, positive linear, but non-significant correlation between IF and WB for case SD23/13. **B.** There was a low, positive linear, and non-significant, correlation for case SD25/13. **C.** Low and non-significant correlation was found for the case 32/13. **D.** The only case with a high, positive linear, and significant correlation between the two methods. Pearson's product-moment correlation (r) and p values are provided.

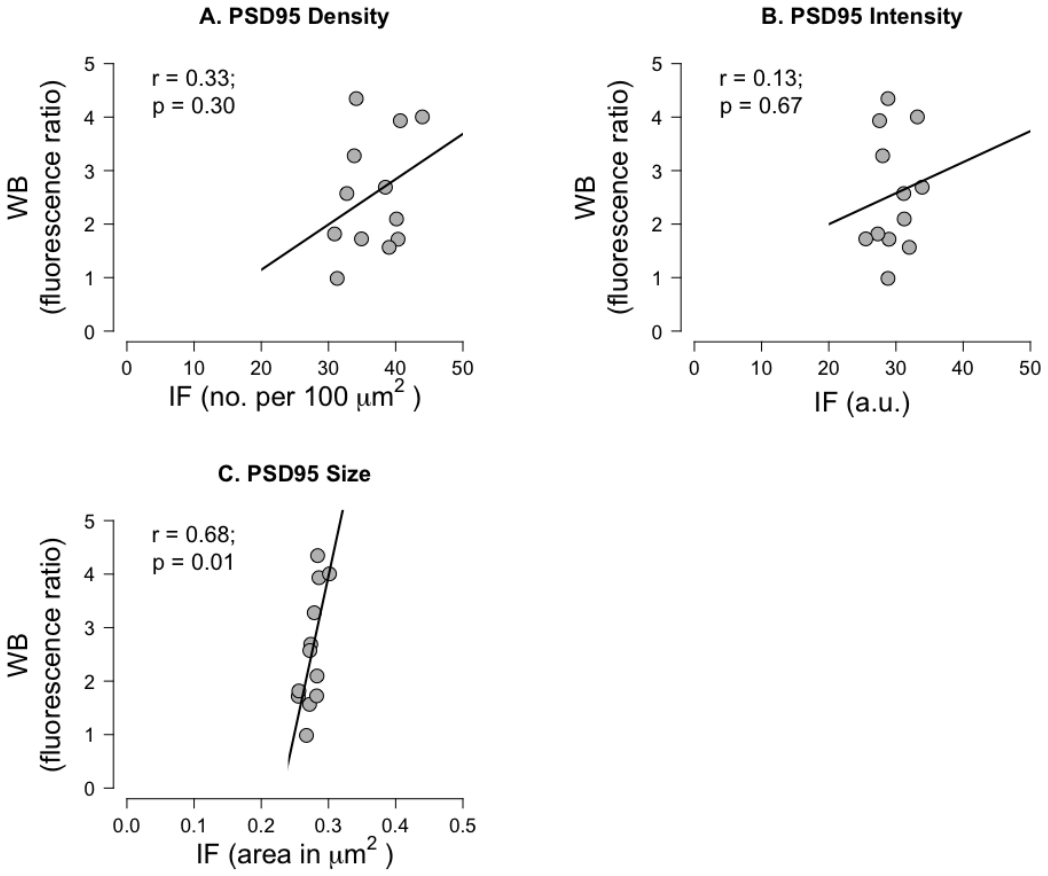


**Figure 3.8 Comparison between IF and WB for PSD-95 quantification by synaptic puncta parameters.**

Scatterplots showing correlations between PSD-95 puncta parameters (density, intensity and size) quantified from 12 human cortical brain areas using IF and WB quantification. **A.** There was a positive linear, but low and not significant correlation between the methods for PSD-95 counts. **B.** Positive linear, but even lower and still not significant, correlation was found for PSD-95 puncta intensity. **C.** The PSD-95 puncta size parameter was, however, moderately and significantly correlated between the methods for the 12 areas tested. Pearson's product-moment correlation (r) and p values are provided. Values are based on 12 areas from 4 control human cases.

# 4 PSD-95 synaptome mapping of the human brain

## 4.1 INTRODUCTION TO HUMAN PSD-95 SYNAPTOME MAPPING

The human brain comprises many anatomical regions with distinct cell types and patterns of functional connectivity that allow for development of human brain connectomes. An integral part of connectome studies is synaptome mapping, the description of the distribution of synapses based on their molecular diversity. While synaptome mapping has been achieved in rodents, maps of synaptic diversity across the human brain are lacking. In addition, the spatial distribution of human synaptic diversity remains unknown. One of the key elements limiting the rate of human synaptome mapping is the lack of robust methodologies to allow the detailed study of such abundant heterologous structures as synapses. To overcome these limitations a methodology is needed for reproducible and robust identification of synapse types at a molecular level, their resolution at individual synapse-level with a high-throughput analysis to accommodate the vast numbers.

The existing methods for studying synapses all have limitations, as has been described in Chapter 1.5. However, the G2CSynMaP methodology, described in Chapter 2.11, developed to study rodent synaptic diversity, has shown promising results (Zhu et al., submitted). The synaptic molecular identity of proteins was secured by the creation of a knock-in animal model carrying an in-frame fusion of a sequence encoding a fluorescent PSD-95 synaptic protein into the endogenous locus. Secondly, high-resolution, high-throughput imaging of the fluorescent PSD-95 using a confocal SDM was performed. Thirdly, an automated detection and analysis of PSD-95 fluorescent synaptic puncta was used that allowed for rapid analysis of millions of synapses. The rodent G2CSynMaP analysis therefore fulfilled the three criteria needed to create a map of synaptic diversity, or a synaptome, based on analysis of PSD-95 protein IR.

However, there are several limitations when trying to apply the G2CSynMaP method to human tissue. For example, while the data demonstrating synaptic diversity in mouse brain were obtained using a genetically modified animal, such genetic manipulation of human brain tissue is not possible. It is also not possible to study human brain regions in their entirety as has been done in rodents. Nevertheless,

alternatives are available. An antibody labelling approach to identify PSD-95 synapses could be used instead of genetic manipulations, and imaging of smaller areas of tissue could be performed.

My aim in this chapter was to quantify PSD-95 excitatory synapses in selected human brain regions using novel quantitative immunofluorescence (IF). Methods were developed for antibody labelling and quantification of synapses expressing PSD-95/Dlg4 in a range of human brain regions. I hypothesised that modifications of G2CSynMaP methodology to suit human tissue would allow for a description of human PSD-95 synaptic diversity using distinct PSD-95 puncta parameters, similarly to rodent data. In addressing this hypothesis, I have generated the PSD-95 maps based on analysis of three parameters of PSD-95 IF for selected human brain areas. The findings reveal an organisation of PSD-95 synaptic puncta diversity similar to rodent, and show structured organisation of PSD-95 in the human brain, both between and within anatomical areas.

## 4.2 SUMMARY OF METHODS USED

In order to analyse the diversity of PSD-95 synapses based on their distribution selected formalin-fixed paraffin-embedded human brain sections were labelled with PSD-95 antibody using IF. In total, imaging was performed on 80 brain sections (20 sections per case). The 20 areas chosen covered as many anatomical regions of interest as possible that were available for all 4 control cases. IF imaging was achieved using the laser scanning confocal microscope (Figure 2.1 Panels 1 & 4).

Indirect fluorescence from the secondary antibody was imaged using the same sets of acquisition parameters with an oil immersion lens (63X, NA 1.4). The Ensemble method (described in Chapter 2.9.1) was used to detect individual PSD-95 synaptic puncta, which were quantified per unit area to give a density value. In addition, individual PSD-95 punctum features were obtained: mean punctum intensity in grey values as arbitrary units and punctum size as area were obtained (Figure 2.1 Panel 2). Mean punctum values for each area in each of the 4 cases were then calculated and represented as a heatmap (Figure 2.1 Panel 3). The mean values

represented as colours were manually coloured using Adobe Photoshop®. The five representative coronal section drawings displaying the anatomical human brain regions imaged were delineated based on templates from the reference atlas of the Allen Human Brain Atlas (http://human.brain-map.org) (Figure 2.3 on page 92).

## 4.3 OVERALL DISTRIBUTION OF PSD-95 IN SELECTED HUMAN BRAIN AREAS

The PSD-95 IF stained and imaged brain sections displayed green fluorescent signals from the secondary antibody that were detected as tiny puncta. In general, as shown in Figure 4.1 on page 132, the puncta appeared intense and densely packed in the cortex and the hippocampus. However, even within the neocortex, different areas displayed different combinations of bright, dim, large and small puncta. In the remaining subcortical structures, including thalamus and caudate nucleus, the puncta tended to show moderate numbers and intensities. Intense and high counts of PSD-95 IR were also found in some parts of the cerebellum, such as the granular cell layer, but not others, such as white matter. Interestingly, both hippocampus and cerebellum showed distinct subregional distribution patterns of PSD-95 IR, as will be described in more detail in the next section. Although present within the brainstem, the synaptic puncta numbers were low in the midbrain, pons and medulla. In these structures the PSD-95 puncta also showed low levels of fluorescent intensity. In contrast, synaptic puncta were almost absent from the cortical and the cerebellar white matter.

Overall, there are clear differences in PSD-95 synaptic puncta densities, intensities and sizes between the regions and subregions. Importantly, this heterogeneous nature of PSD-95 distribution across the human brain is consistent with the previous *in situ* hybridisation and immunohistochemistry studies of PSD-95 distribution in mice (Fukaya et al., 1999; Fukaya and Watanabe, 2000) and with the knock-in mice generated in our laboratory (Zhu et al., submitted). Our data, similarly to the rodent data, highlights the importance of quantification of the existing distribution differences in order to understand the principles behind the patterns of synapse diversity.

Rodent investigations also demonstrated further differences in the distribution

patterns in several selected brain areas, so a more detailed description of the corresponding human regions was undertaken to assess if the PSD-95 distributions share interspecies similarities.

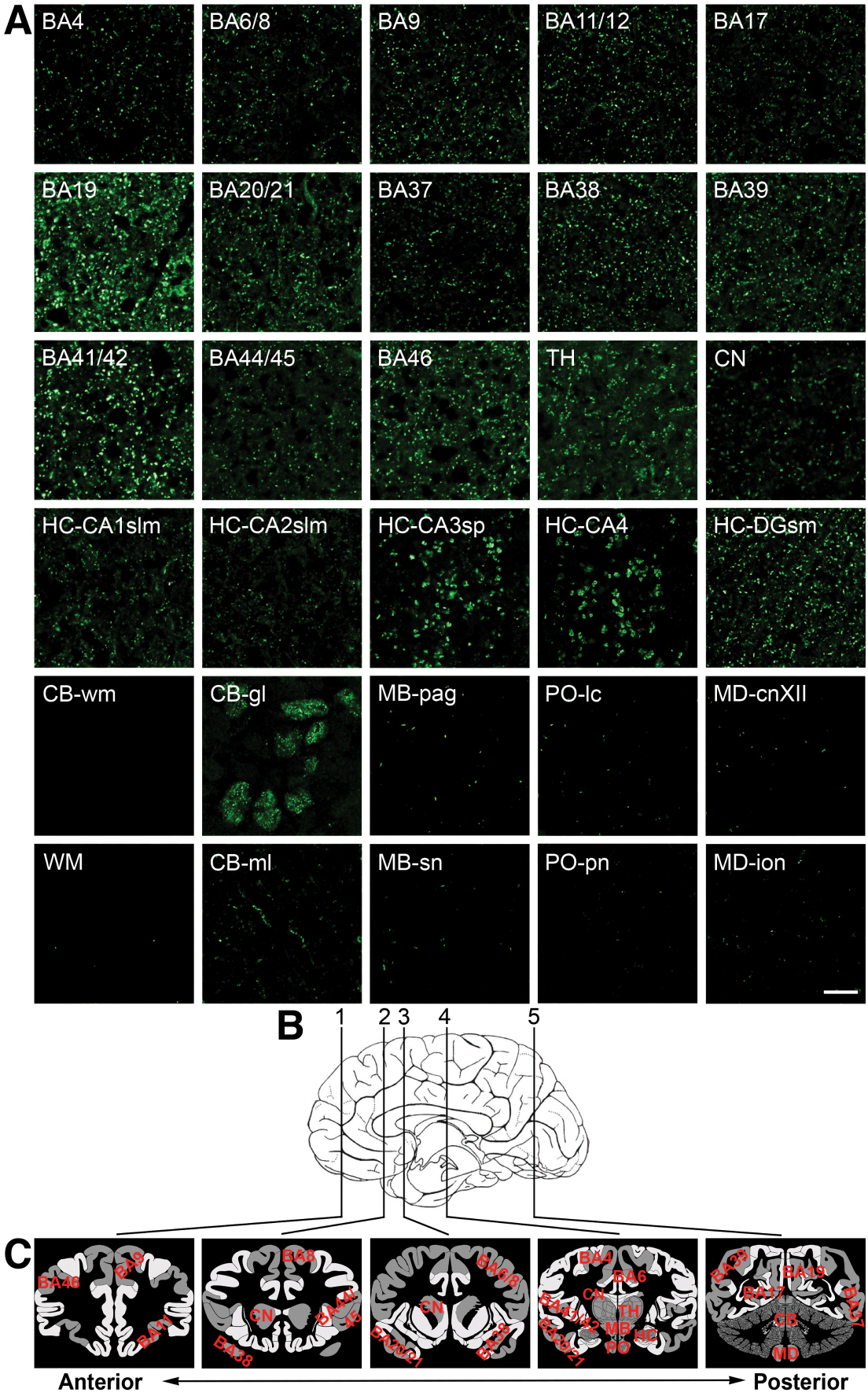


**Figure 4.1 Overall PSD-95 synaptic puncta diversity in the human brain.**

**Panel A.** Representative images from 30 different human brain subregions showing differences in patterns of distribution of PSD-95 IR. In general, cortical areas show similar, quite uniform, distribution of PSD-95 but with variations in puncta intensity and size, and to a lesser degree puncta counts, which do not show as much variations as for other brain subregions. This is in contrast to subcortical areas, which show clear differences in pattern of distribution related to underling anatomical heterogeneity of subregions (e.g. hippocampus or cerebellum). The brainstem structures, as represented by midbrain, pons and medulla, show sparse numbers of PSD-95 synaptic puncta. Almost no PSD-95 puncta are detected in the subcortical or cerebellar white matter. **Panel B.** All human tissue was sampled from coronal sections at levels approximated by vertical lines: 1 - at the level of gyrus rectus, 2 - at the level of genu of corpus callosum, 3 - at the level of temporal pole, 4 - at the level of posterior hippocampus and the lateral geniculate body, 5 - at the level of primary visual cortex. **Panel C.** Cartoons of human brain coronal sections corresponding to the levels defined in panel B. Each cartoon is labelled with areas imaged using LSCM, starting from anterior to posterior distribution. Areas are visualised according to the Allen Brain Atlas. Templates of these cartoons of coronal sections were modified from the Allen Brain Atlas (Human Brain) and include plate numbers: 10/106, 16/106, 19/106, 48/106 and 86/106. Abbreviations: BA, Brodmann area; TH, thalamus; CN, caudate nucleus; HC, hippocampus; CA, cornu ammonis; slm, stratum lacunosum – moleculare; sp, stratum pyramidale; DG sm, dentate gyrus stratum moleculare; CB, cerebellum; WM, white matter; gl, granular cell layer; ml, molecular cell layer; pag, periaquedactal grey; MB, midbrain; PO, pons; MD, medulla; lc, locus coeruleus; cnXII, central nucleus XII; sn, substantia nigra; pn, pontine nuclei; ion, inferior olivary nucleus. Scale bar in panel A: 10 $\mu$m.

---

## 4.4 DETAILED DISTRIBUTION OF PSD-95 IN SELECTED BRAIN AREAS

Detailed assessment of the PSD-95 IR distribution revealed several patterns of PSD-95 staining in selected human brain areas.

### 4.4.1 Hippocampus

The human hippocampus is broadly divided into two parts, the dentate gyrus (DG, area dentata or fascia dentata) and the hippocampus proper (CA, cornu ammonis). The hippocampus proper is further subdivided into four fields, CA1-4. CA4 comprises pyramidal-like cells that are located inside the hilus of the dentate gyrus. The dentate gyrus has three layers: the *granular* layer, the *molecular* layer and the *polymorphic*

layer. The *polymorphic* layer located in the hilus of the dentate gyrus merges with the CA4 field. The *granular* layer consists of cell bodies of the granule cells, the *molecular* layer consists of interwining apical dendrites of the granule cells, and the *polymorphic* layer contains the initial segments of the granule-cell axons as they join together to form the mossy fibre bundle. The hippocampus proper is a multilayered structure composed of: several layers including: the *alveus*, the *stratum oriens*, *stratum pyramidale*, the *stratum radiatum* and the *stratum lacunosum-moleculare*. Briefly, the *alveus* contains the axons of the pyramidal cells, the *stratum oriens* contains the basal dendrites of the pyramidal neurons, the *stratum pyramidale* consists of the cell bodies of the pyramidal cells, the *stratum radiatum* and the *stratum lacunosum-moleculare* contain the proximal and distal segments of the apical dendritic tree, respectively. In the CA3 field, the *stratum radiatum* is called *stratum lucidum* as it receives input from the mossy fibres originating from the axons of the dentate granule cells. CA1 is also referred to as Sommers sector. This area is susceptible to ischaemia showing selective vulnerability.

In the human hippocampus, there was intense punctate PSD-95 IR staining observed within CA1, CA3, CA4 as well as the dentate gyrus (DG), as seen in Figure 4.2 on page 139. The highest intensity of staining was seen in the CA1, followed by CA3, with the CA2 subregion showing the dimmest puncta. Bright PSD-95 IR was mostly observed within the dendritic layers of the hippocampus, including *stratum radiatum* and *stratum lacunosum-moleculare* as well as the *molecular layer* of the DG. The puncta observed in the neuropil of the pyramidal cell layer of the CA3 and CA4 subregions appeared very similar in size, intensity and pattern of staining: they were large, moderately bright, and formed a loose, rosette-like pattern of packing. This was in contrast to much denser, but smaller and brighter PSD-95 puncta in the CA1 subregion. Finally, while no staining was seen in the granule cells of the dentate gyrus, cell bodies of the pyramidal cell layer of CA1-4 subregions did demonstrate diffuse and moderate staining, which was abolished in the negative controls. A detailed description of PSD-95 IR labelling will be provided in Chapter 5.3.

In general, the PSD-95 IR in human hippocampus is consistent with the distributions in the dendritic layers of hippocampus of the knock-in PSD-95-eGFP

mouse created in our lab as well as the previous findings using antibodies against endogenous PSD-95 in mice (Fukaya and Watanabe, 2000). The most striking difference being the PSD-95 cell body staining of the pyramidal cell layers.

### 4.4.2 Cerebellum

The PSD-95 staining pattern was different in the human cerebellum (Figure 4.3 on page 141). The adult cerebellar cortex is a three-layer structure composed of an internal granular layer (IGL), Purkinje cell layer (PCL) organised into a single row of Purkinje cells (PC) and a molecular cell layer (MCL), as demonstrated with Nissl staining (Figure 4.3 A). PSD-95 IR puncta were detected in all three cortical layers, although the pattern of PSD-95 distribution varied between the subregions. Overall, the PSD-95 IR was higher in the GCL than in the MCL (Figure 4.3 B-I) and there was a noticeable absence of staining in the PCs. Higher magnification views (Figure 4.3 H-I) showed numerous and dense clusters of PSD-95 IR dispersed throughout the glomerular region of the GCL between the granule cells, corresponding to mossy and climbing fibers in the GCL, but the granular cells themselves showed only weak, non-specific staining. Closer examination of the PCL revealed that PSD-95 IR puncta were only detected in the terminal pinceau (also known as the presynaptic plexus) of cerebellar basket cells, surrounding the axon hillock regions of PCs, but the postsynaptic PCs neurons did not express the protein. Lastly, a much lower density of PSD-95 IR was detected within the neuropil of the MCL where the PSD-95 IF puncta tended to form a fine linear pattern. In addition, staining within the larger nuclei of stellate and basket cells, was observed as demonstrated in Figure 4.3 H. Finally, a high-resolution confocal imaging revealed that the dense PSD-95 clusters of GCL consisted of numerous distinct PSD-95 IR puncta presumably located on mossy and climbing fibres (Figure 4.3 J). Of note, the mossy fibres characteristically exhibit their rosette expansions (Castejón and Sims, 1999) and PSD-95 IR showed some clusters with rosette-like punctate formations (Figure 4.3 J arrowheads). In contrast, within the MCL neuropil, PSD-95 IR was most strongly localised to many small puncta situated along the dendrites of presumably paraller fibers since the parallel fibres have been shown to contain glutamatergic synapses (Landsend et al., 1997)(Figure 4.3 K). No punctate staining was observed

in the white matter (Figure 4.3 L).

These cerebellar observations of PSD-95 IR are consistent with previous work in adult animal cerebellum from a range of animals (Castejón et al., 2004). In rodents, PSD-95 was initially detected in the terminal pinceau of basket cells, surrounding the axon hillock of PCs. An antigen retrieval and mild protease treatment during IHC procedure allowed Fukaya and Watanabe (Fukaya and Watanabe, 2000) to further demonstrate strong punctate staining of PSD-95 associated with post-synaptic structures at glomeruli in the GCL and along dendrites on the MCL. Their IHC data were consistent with an earlier study that showed PSD-95 mRNA expression in the PCL, granular layer and in basket/stellate cells of the adult mouse (Fukaya et al., 1999). The numerous PSD-95 puncta in the MCL are thought to correlate with the PC dendritic PSDs making synaptic junctions with parallel and climbing fibres. These findings are in keeping with previous studies of mature cerebellar synaptic architecture using confocal laser microscopy (Castejón and Sims, 1999; Castejon and Sims, 2000).

### 4.4.3 Caudate nucleus

In human brain, the caudate nucleus is part of the basal ganglia, which are a group of subcortical grey nuclei primarily involved in the control of movement. However, studies have revealed that the basal ganglia are also involved in cognition, memory and learning (Calabresi et al., 1997; Graybiel, 1997) as well as addictive behaviours via their associations with reward systems (Schultz, 1998). The human basal ganglia is comprised of the globus pallidus, the substantia nigra, and the striatum. The striatum is further divided into the dorsal striatum, composed of caudate nucleus (CN) and putamen, and the ventral striatum comprising nucleus accumbens and olfactory tubercule. In rodents, the caudate and putamen are indistinguishable and referred to as the striatum. This study describes the PSD-95 distribution in the caudate nucleus only. The caudate nucleus is important in forming new associations to acquire explicit memories and in motor learning (Knowlton et al., 1996).

Overall, strong PSD-95 labelling was detected in the caudate nucleus, as demonstrated in Figure 4.4 on page 143. Low-powered magnification revealed that

the distribution of PSD-95 labelling was non-homogenous with small compartments of weaker staining, as demonstrated in Figure 4.4 B, G, H. No PSD-95 labelling was identified in serial control section processed using the immunostaining protocol without the anti-PSD-95 antibody (Figure 4.4 C). PSD-95 IR appeared slightly weaker in the smaller striosomal compartments in comparison to the matrix (Figure 4.4 D, E and F). The compartmental distribution of PSD-95 was, however, better visualised by performing double immunofluorescence staining of PSD-95 with Calbindin-D28K, a protein enriched in the matrix of the human striatum (Ito et al., 1992), as seen in Figure 4.4 G-K. Compared with the striosomes, the matrix compartment appeared strongly stained for PSD-95. PSD-95 exhibited not only a dendritic pattern of staining, but also showed somatic staining, presumably in medium spiny neurons (MSNs) as seen previously (Ouimet et al., 1998). In summary, the PSD-95 staining pattern in the caudate nucleus is entirely in agreement with that recently described in human tissue using a much higher sensitivity immunohistochemistry technique to demonstrate the striosome and matrix compartments of the human neostriatum (Morigaki and Goto, 2015). Our results in the CN, therefore, additionally confirm specificity of our PSD-95 staining technique.

### 4.4.4 Thalamus

In the human thalamus, the PSD-95 IR signals were diffuse and the intensities were overall moderate (Figure 4.5 on page 145). Some lightly PSD-95-labelled cell bodies of neurons were also identified in all four subjects, although their precise cytoarchicetual identity was not determined. Similar data from mice showed that these stained neurons predominantly localised to the ventro-posterior and dorsal thalamic nuclei. Double immunofluorescent labelling demonstrated that they also tended to be restricted to non-GABAergic neurons as no co-localisation with GABA-immunoreactive cells was seen (Liu et al., 2004). Analysis of human PSD-95 transcripts revealed that they were found in large glutamatergic relay neurons as well as in small GABAergic interneurons in the dorsomedial and anterior thalamic nuclei (Clinton et al., 2003).

Interestingly, subsequent quantification of human PSD-95 IR signals in terms

of density, intensity and size, revealed that the thalamic PSD-95 IR staining showed most variability among the areas examined. Although this variability of staining could be explained by inter-subject variability, it could also partly be explained by the fact that an overall PSD-95 thalamic expression was determined rather than a nucleus-by-nucleus distribution. This is because it was not possible to identify discrete thalamic nuclei in the original tissue sections. Our overall findings are, nevertheless, in agreement with previous studies in mice (Fukaya and Watanabe, 2000) and in human (Clinton et al., 2003, 2006). In particular, Clinton et al., demonstrated that the PSD-95 transcript not only varies among the control subjects, but also within six different thalamic nuclei examined: the highest levels were found in the anterior and reticular nuclei and the lowest in the central nuclei. As mentioned above, our study did not assess PSD-95 distribution in any specific thalamic nucleus, but rather demonstrated PSD-95 in the thalamus as a whole. However, the underlying thalamic nuclei PSD-95 distribution heterogeneity may account for the thalamic variability results found in our study if different nuclei were imaged for each case.

### 4.4.5 Brainstem structures

Three brainstem structures, the midbrain (Figure 4.6 on page 146), pons (Figure 4.7 on page 147) and medulla (Figure 4.8 on page 148), were probed for PSD-95 IR and overall showed sparse and weak fluorescent signals in these areas. These findings are in agreement with the published *in situ* hybridisation and immunohistochemistry results showing low PSD-95 expression in the hindbrain areas (Fukaya and Watanabe, 2000). They are also in agreement with the rodent PSD-95 knock-in results (Zhu et al., submitted).

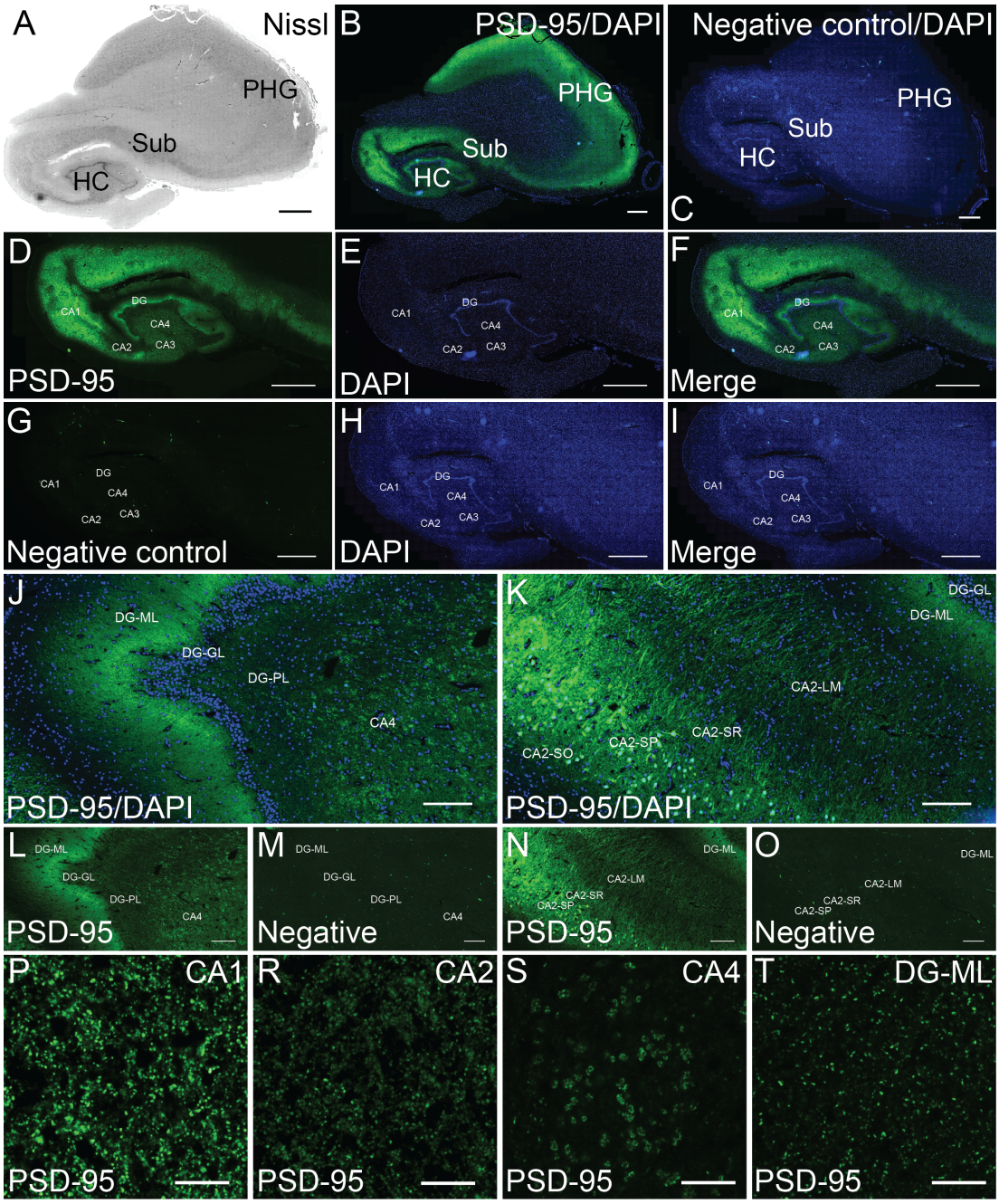


**Figure 4.2 PSD-95 shows a distinct pattern of staining in the human hippocampus.**

**A.** Low magnification image of a Nissl-stained section of human hippocampus assessing the basic neuroanatomy. **B.** Low magnification fluorescent images showing PSD-95 IR. The most intense labelling is observed in the hippocampus as well as adjacent cortex of the parahippocampal gyrus. **C.** The same section stained without the primary antibody showing absence of PSD-95 IR. **D.** Close up on hippocampus with PSD-95 IR. **E.** Dapi, and a merged image in **F** are shown for comparison with images of negative control in **G-I**. **J.** Zoomed in detail of the same tissue section showing intense staining of PSD-95 IR in the molecular layer of DG. **L.**The same section as in **J.** showing PSD-95 IR only and a negative control in **M. K.** In human tissue, strong PSD-95 IF is observed in cell bodies of the pyramidal cells. An example from CA2 subregion. PSD-95 IR **N** and a negative control in **O** demonstrating a lack of staining

in the cell bodies. **P-T** Examples of higher magnification PSD-95 staining in various subregions of the hippocampus. The highest intensity of staining was observed in CA1 and DG-ML, followed by CA3 and CA4, and finally by CA2. Scale bars: A-I 2000 $\mu$m, J-O 200 $\mu$m, and P-T 10 $\mu$m. HC, Hippocampus; Sub, Subiculum and PHG, Parahippocampal gyrus. DG, Dentate gyrus; DG-ML, DG molecular layer, DG-PL, DG pleomorphic layer; DG-GL, DG granule cell layer; SR, Stratum radiatum; SO, stratum oriens; LM, lacunosum-moleculare.

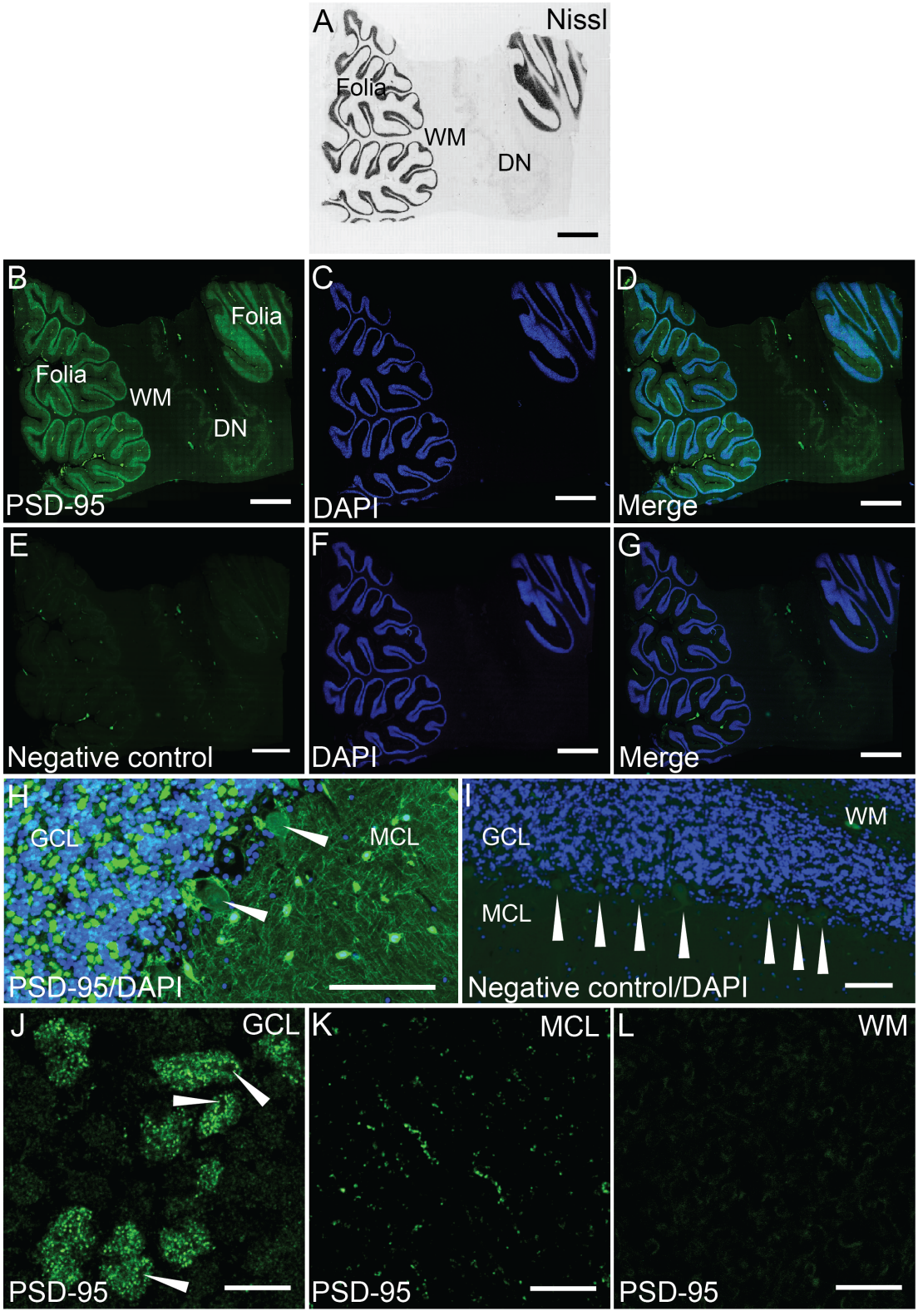


**Figure 4.3 PSD-95 shows a distinct pattern of staining in the human cerebellum.**

**A.** Low magnification image of a section of human cerebellum stained with Nissl in order to assess the basic neuroanatomy: cerebellar cortex (folia), white matter and the dentate nucleus. **B-D.** Low magnification fluorescent images showing PSD-95 IR **B**, Dapi **C** and a merged image **D** in the same section as **A.** The most intense labelling is observed in the cerebellar folia. **E.** The same section stained without the primary antibody showing absence of PSD-95 IR. Dapi **F** and a merged image in **G** are shown

for comparison with images in **B-D. H.** Zoomed in detail of the same tissue section showing large clusters of PSD-95 IR in GCL. In MCL, PSD-95 is observed as fine linear pattern with strong labelling of larger nuclei. The cell bodies of Purkinje cells do not stain with PSD-95 (arrowheads), but PSD-95 IR is present in the terminal pinceau of basket cells, surrounding the axon hillock region of PCs. **I.** The PSD-95 staining is not observed in the negative control section. Arrowheads point to lack of staining around and within PCs. **J.** Higher magnification PSD-95 staining in the GCL showing numerous intense puncta within the clusters. Arrowheads point to areas of rosette-like punctate formations. In contrast, PSD-95 IR within MCL was mostly localised along the dendrites **K.** No punctate PSD-95 labelling was present in the cerebellar white matter **L.** GCL - granular cell layer. MCL - molecular cell layer. Scale bars: A-G 2000 $\mu$m, H-I 100 $\mu$m, and J-L 10 $\mu$m.

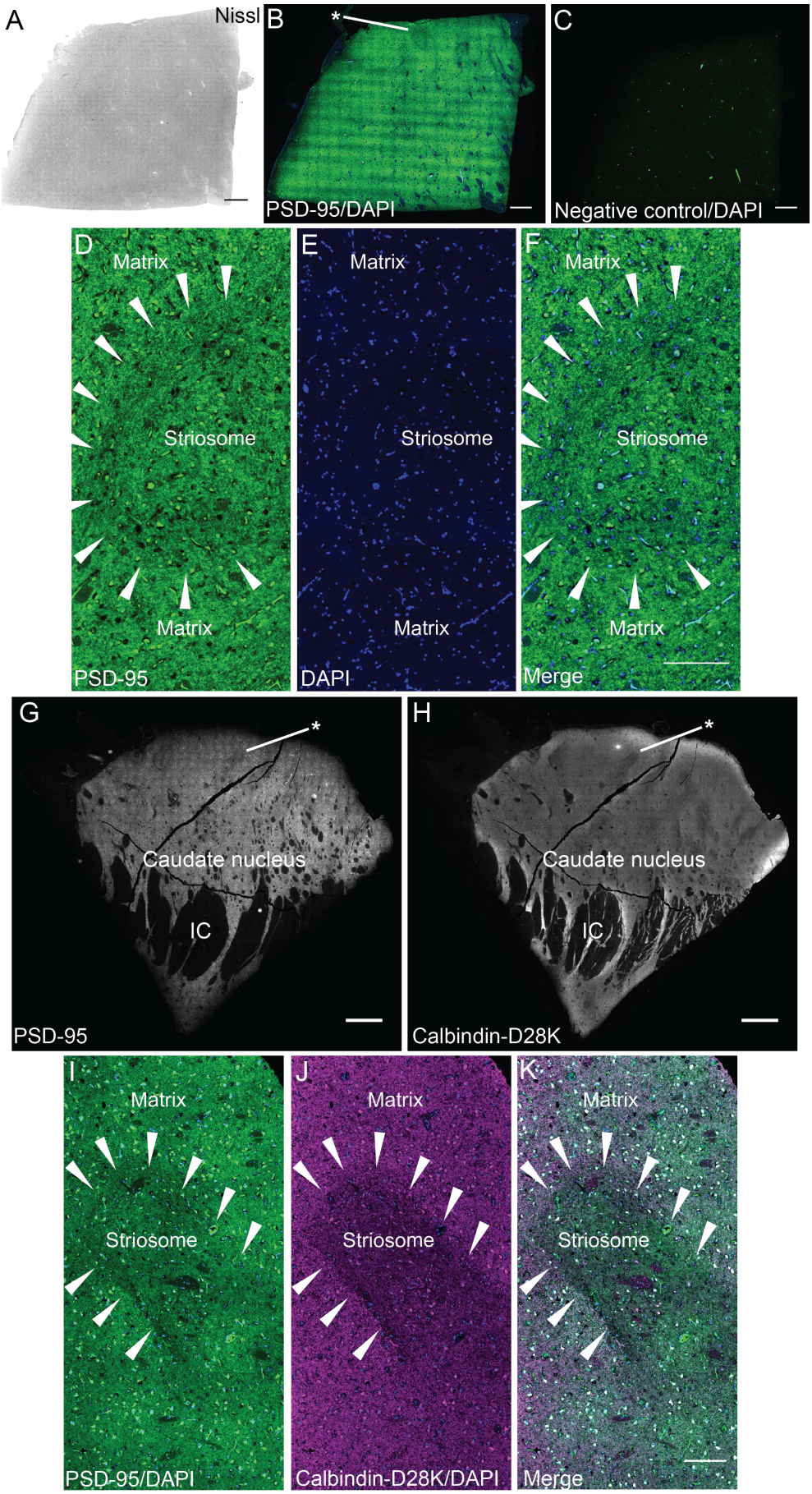


**Figure 4.4 Compartmental staining of PSD-95 in the human caudate nucleus.**

**A.** Low magnification image of a section of human caudate nucleus stained with Nissl to assess basic neuroanatomy (case SD23/13). **B.** At low magnification, PSD-95 IF was not homogenous and small darker patches were identified scattered within the region. A star (*) denotes one such darker patch, a striosome. **C.** Omission of PSD-95 primary antibody showed lack of PSD-95 IF. **D-F** Zoomed in detail of the same patch as in **B** showing slightly darker PSD-95 IF at the edge of the striosome as pointed by the arrowheads. Somatic staining of PSD-95 was seen, presumably in MSNs, in addition to dendritic PSD-95 IR puncta. **G.** Low magnification image from another case (SD42/13) also showing scattered darker patches identified with PSD-95 IF within caudate nucleus. A star (*) points to a striosome. **H.** The same patch was much better visualised with Calbindin-D28K antibody. IC – internal capsule. **I-K** Zoomed in detail of the same patch as in **G and H** outlined by the arrowheads. **I.** Darker striosomal staining was seen with PSD-95 IF. **J.** A much darker Calbindin-D28K staining within a striosome in **J**. **K.** Merged image. Scale bars: A-C and G-H 2000 $\mu$m, D-F and I-K 100 $\mu$m.

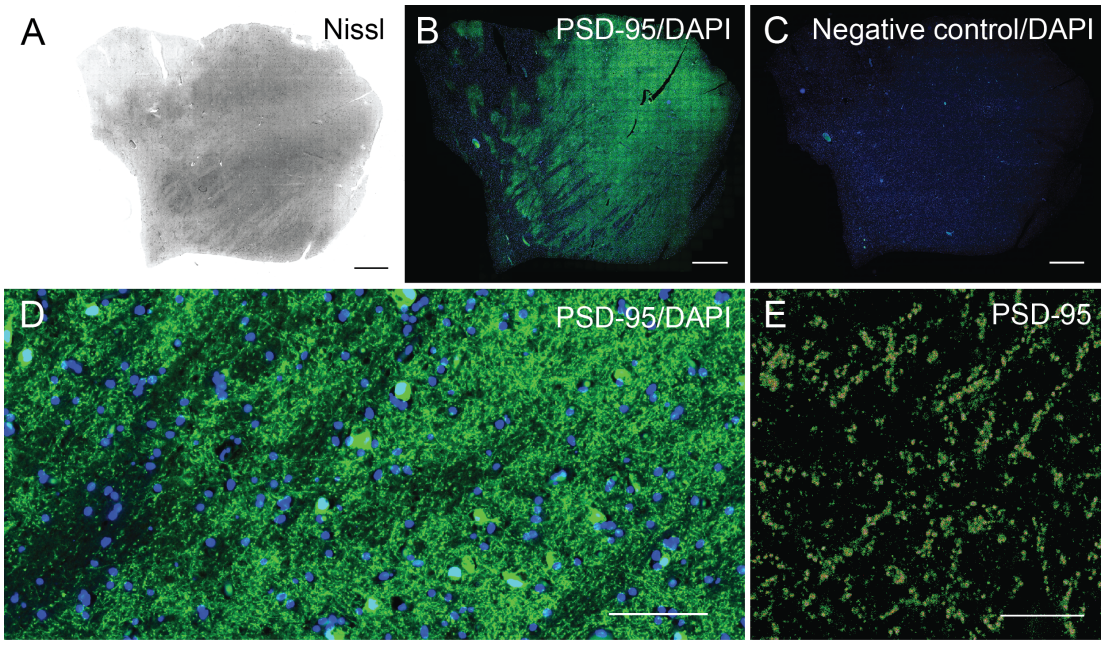


**Figure 4.5 PSD-95 pattern of staining in the human thalamus.**

**A.** Low magnification image of a section of human thalamus stained with Nissl to assess basic neuroanatomy (case SD23/13). **B.** At low magnification, PSD-95 IF was variable but prominent throughout the section **C.** Omission of PSD-95 primary antibody showed lack of PSD-95 IF. **D** Zoomed in detail of the same case as in **A** showing detailed punctate PSD-95 IF staining. **E.** High magnification image obtained with LSCM showing PSD-95 IF within the thalamus. Scale bars: A-C 2000 $\mu$m, D 100 $\mu$m and E 10 $\mu$m.

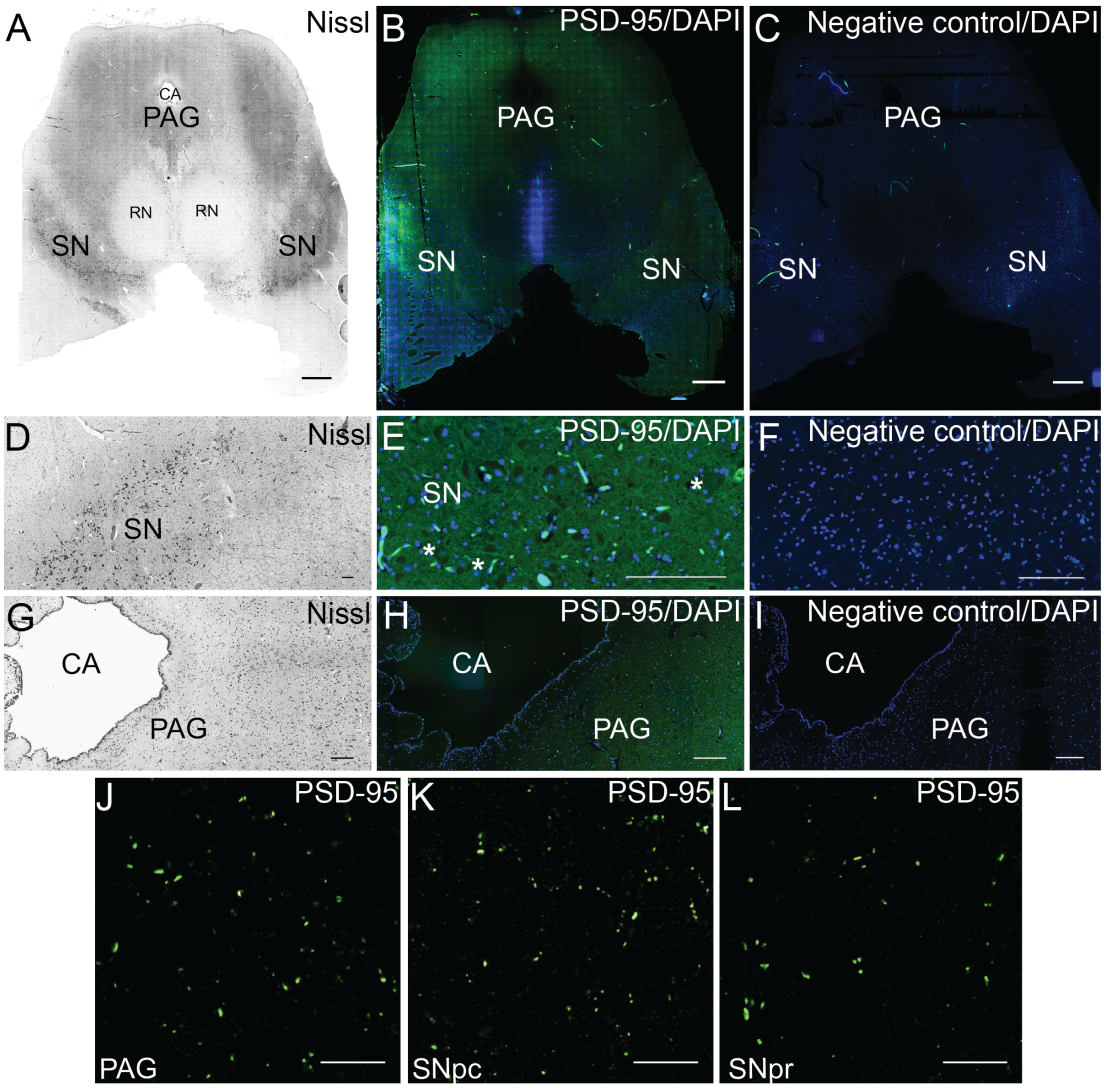


**Figure 4.6 PSD-95 pattern of staining in the human midbrain.**

**A, D, G.** Low magnification images of sections of human midbrain stained with Nissl to assess basic neuroanatomy (case SD23/13). **B, E, H.** At low magnification, PSD-95 IF was not very prominent throughout the region **C, F, I.** Large pigmented neurons of the substantia nigra are pointed by (*).Omission of PSD-95 primary antibody showed lack of PSD-95 IF. **D-F** Zoomed in details of three subregions: **J** periaqueductal grey (PAG), **K** substantia nigra pars compacta (SNpc), and **L** substantia nigra pars reticularis (SNpr), confirm the overall sparse PSD-95 IF within the midbrain. Scale bars: A-C 2000 $\mu$m, and D-I 100 $\mu$m, and J-L 10 $\mu$m.

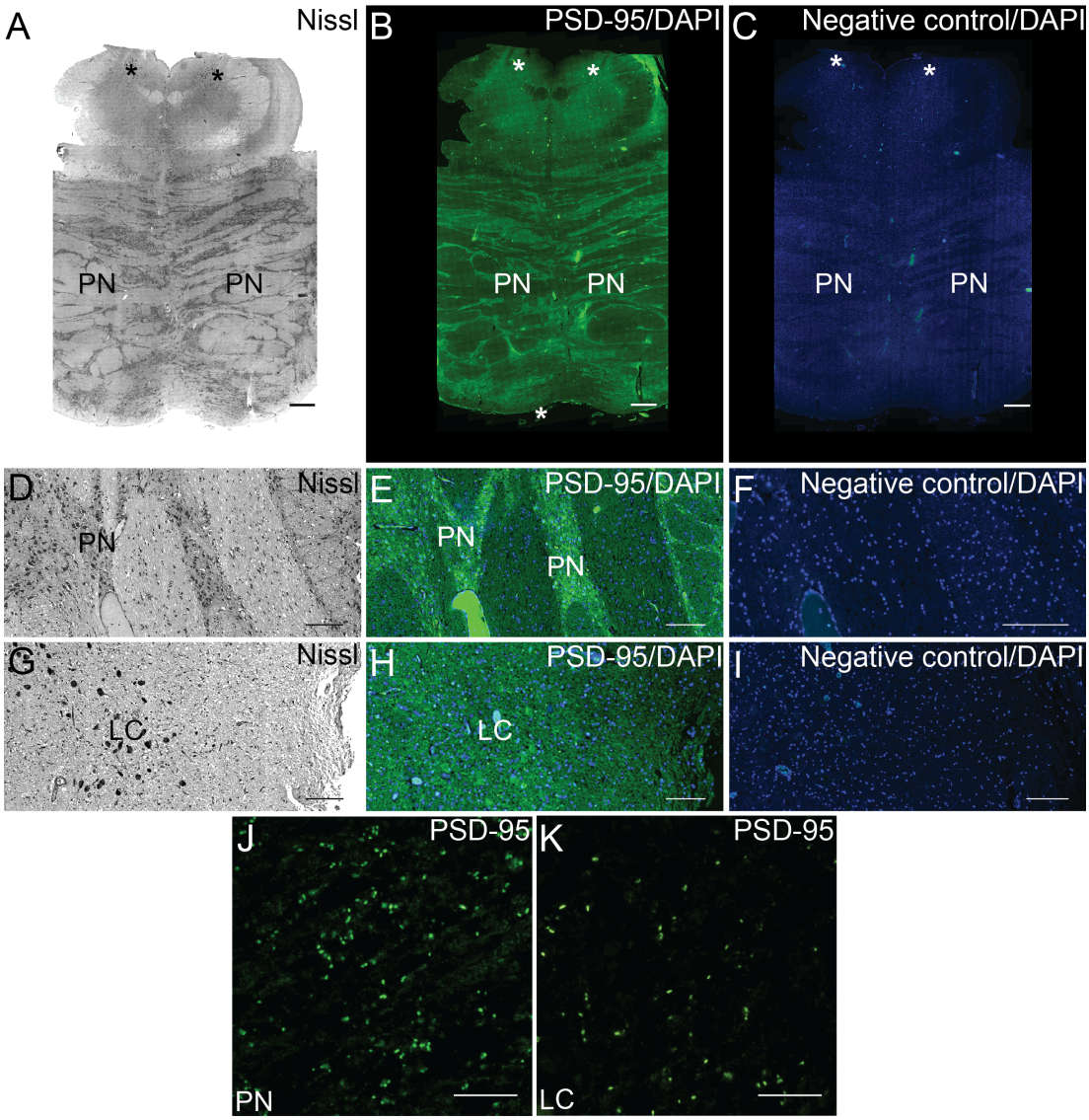


**Figure 4.7 PSD-95 pattern of staining in the human pons.**

**A, D, G.** Low magnification images of sections of human midbrain stained with Nissl to assess basic neuroanatomy (case SD23/13). Subregions studied included the pontine nuclei (PN) and the small loci coerulei (LC) pointed by (*). **B.** At low magnification, PSD-95 IF was bright in the pontine nuclei. **C, F, I** Omission of PSD-95 primary antibody showed lack of PSD-95 IF. **D-I** Zoomed in detail of the two subregions showed bright staining within PN **E** and sparser staining within LC **H.** High magnification images obtained with LSCM confirmed bright PSD-95 synaptic puncta in PN **J** and bright, but sparser IR within the LC **K**. Scale bars: A-C 2000 $\mu$m, D-I 100 $\mu$m, and J-K 10 $\mu$m.

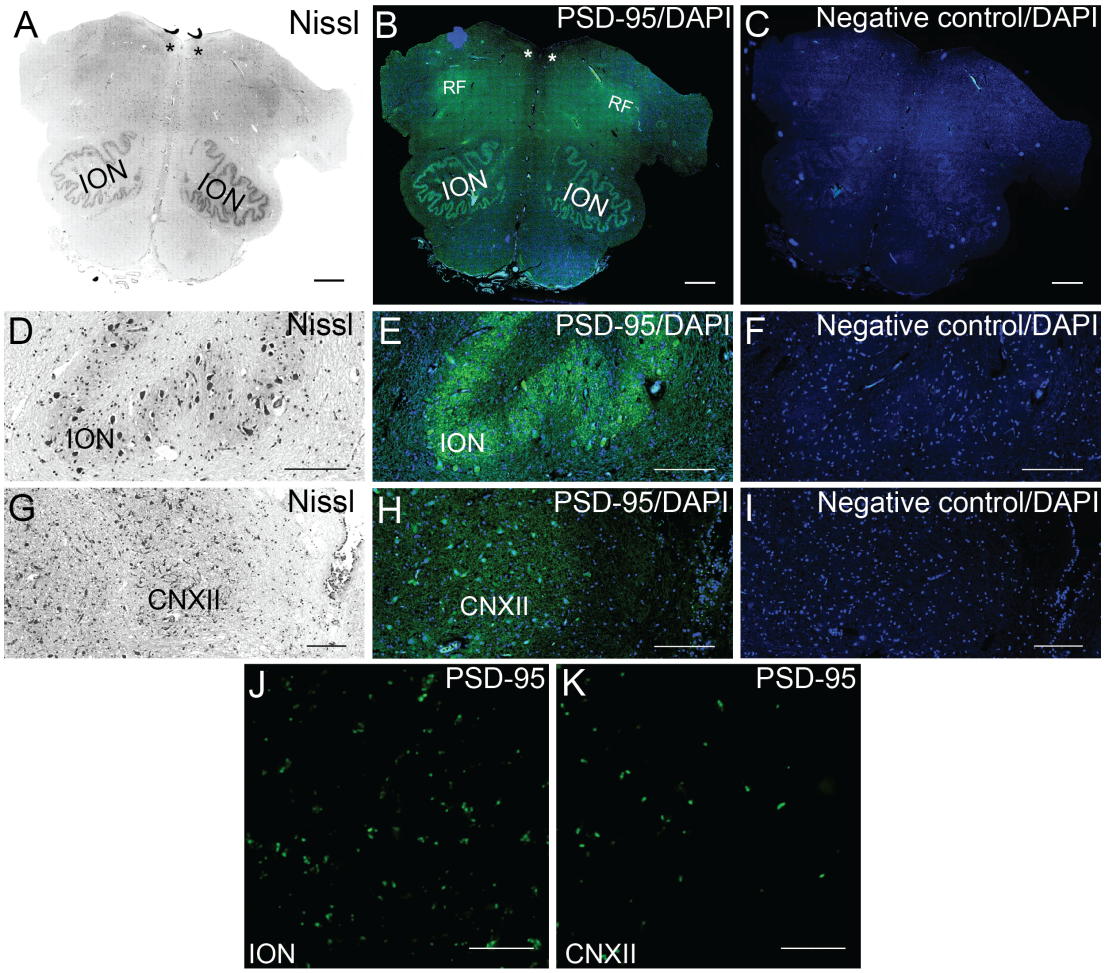


**Figure 4.8 PSD-95 pattern of staining in the human medulla.**

**A, D, G.** Low magnification images of sections of human medulla stained with Nissl to assess basic neuroanatomy (case SD23/13). **B.** Subregions examined included the inferior olivary nuclei (ION) and the small nuclei of the cranial nerve XII (CNXII) denoted by (*). **E.** At low magnification, PSD-95 IF was particularly bright in the ION. **H.** Sparser IR was seen in the CNXII. **C, F, I.** Omission of PSD-95 primary antibody showed lack of PSD-95 IF. **D-I.** Zoomed in details of the two subregions showed bright staining within ION **E** and sparser staining within CNXII. **H.** High magnification images obtained with LSCM confirmed bright PSD-95 synaptic puncta in ION **J** and bright, but sparser IR within the CNXII **K**. Scale bars: A-C and G-H 2000 $\mu$m, D-F and I-K 100 $\mu$m.

## 4.5 PSD-95 QUANTIFICATION ACROSS SELECTED HUMAN BRAIN AREAS

A key output of this research has been the implementation in human tissue of a novel, high throughput PSD-95 synaptic puncta quantification method, called Ensemble. Each detected PSD-95 immunoreactive (IR) punctum was quantified in terms of its intensity, measured in arbitary units (a.u.), and size, measured in $\mu m^2$. In addition, density of synaptic puncta per 100 $\mu m^2$ was calculated as an approximate measure of synapse population within each region studied.

### 4.5.1 PSD-95 synaptic puncta density

The density of PSD-95 IR puncta was quantified in 20 human brain areas (Figure 4.9 A on page 151). In general, the highest density of PSD-95 puncta was detected in the cortical areas. The subcortical regions and the hippocampus also had high numbers of PSD-95 puncta. The lowest density of PSD-95 IR puncta was observed in the brainstem structures.

Amongst the cortical areas, BA19 (secondary visual cortex) (mean $\pm$ SD: 51.74 $\pm$ 11.68) showed the highest number of PSD-95 puncta, while BA4 (motor cortex) (29.91 $\pm$ 7.18) had the lowest numbers. Within the subcortical and allocortical regions, the hippocampus showed the highest numbers of PSD-95 puncta (44.21 $\pm$ 16.22), which was only second low to one cortical area (BA19), followed by thalamus (36.10 $\pm$ 22.42), cerebellum (30.68 $\pm$ 10.76) and caudate nucleus (23.38 $\pm$ 14.22). The brainstem structures: midbrain (8.02 $\pm$ 4.14), pons (6.26 $\pm$ 2.39) and medulla (7.41 $\pm$ 4.30) all showed similar values, but recorded the lowest densities of PSD-95 puncta amongst the regions examined.

### 4.5.2 PSD-95 synaptic puncta intensity

The intensity of PSD-95 IR puncta was quantified in 20 human brain areas (Figure 4.9 B on page 151). In general, the brightest PSD-95 puncta were detected in the cortical, allocortical and subcortical areas. The dimmest PSD-95 puncta were observed in the

brainstem structures.

Amongst the cortical areas, BA19 (secondary visual cortex) (mean ± SD: 40.6 ± 9.91) showed the brightest PSD-95 puncta, while BA4 (motor cortex) (25.51 ± 3.52) had the dimmest. Within the subcortical regions, the thalamus showed the brightest PSD-95 puncta (38.15 ± 15.40), which was second only to the cortical area (BA19), followed by cerebellum (32.8 ± 5.72) and caudate nucleus (31.77 ± 8.82). Then followed the hippocampus (30.59 ± 5.80). The brainstem structures: midbrain (21.8 ± 2.29), pons (22.23 ± 3.05) and medulla (21.54 ± 2.65) all showed similar intensity, but were the least intense PSD-95 puncta amongst all the examined regions.

### 4.5.3 PSD-95 synaptic puncta size

The size of PSD-95 IR puncta was quantified in 20 human brain areas (Figure 4.9 C on page 151). In general, the biggest PSD-95 puncta were detected in the cortical areas. In contrast, the subcortical, allocortical and brainstem regions showed smaller PSD-95 puncta with the exception of the caudate nucleus, which showed relatively large PSD-95 puncta.

Amongst the cortical areas, BA19 (secondary visual cortex) (mean ± SD: 0.28 ± 0.03) had the biggest PSD-95 puncta, while BA11 (frontal cortex) (0.26 ± 0.03) had the smallest puncta. The caudate nucleus showed PSD-95 puncta as large as the cortical areas (0.294 ± 0.05), whereas the hippocampus (0.245 ± 0.04), thalamus (0.221 ± 0.06) and cerebellum (0.216 ± 0.03) had puncta comparable in size to the brainstem structures. Amongst the brainstem structures: the pons (0.246 ± 0.08), had the biggest puncta, followed by the medulla (0.222 ± 0.06) and the midbrain (0.188 ± 0.07), the midbrain showing the smallest PSD-95 puncta amongst all the regions examined.

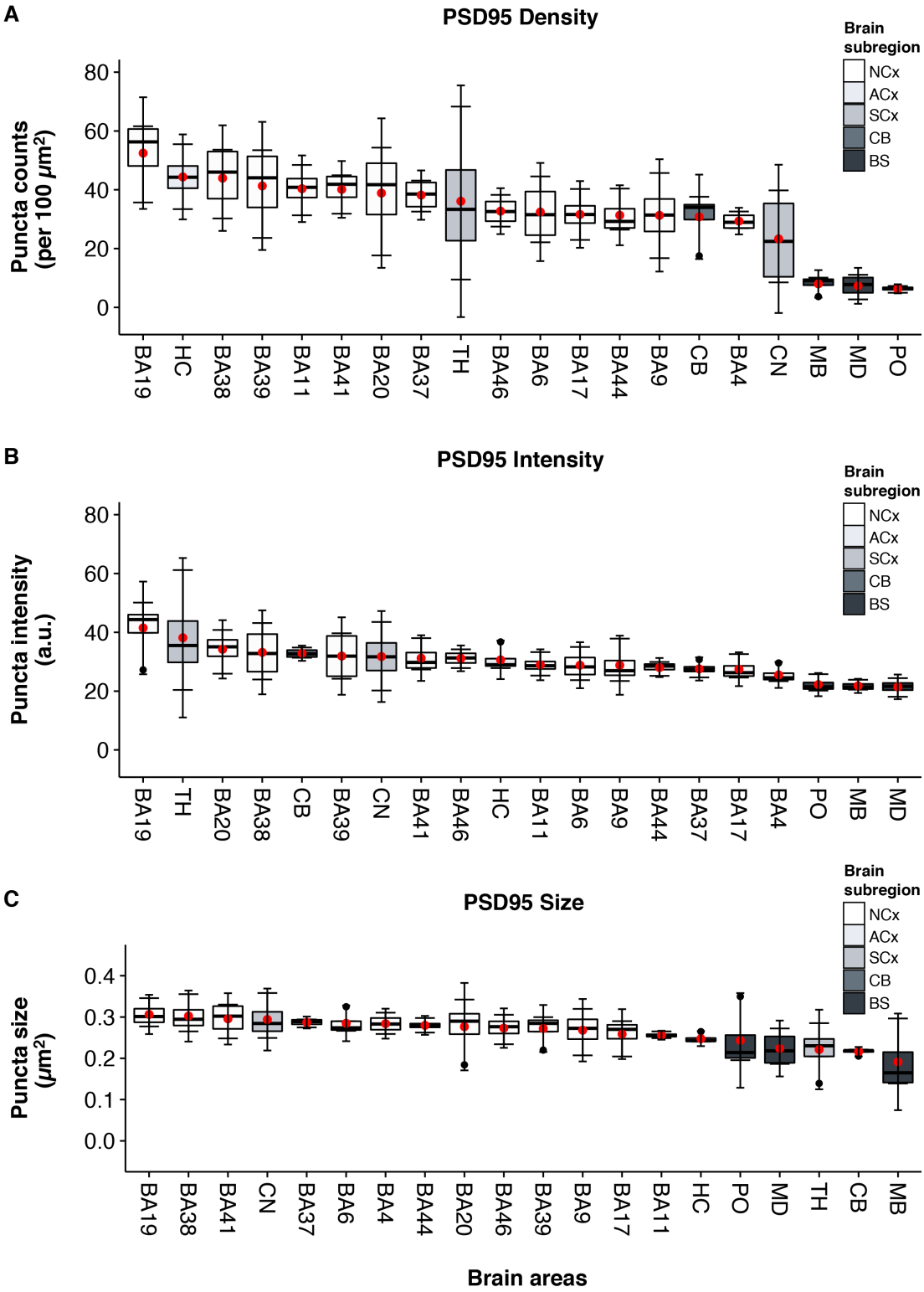


**Figure 4.9 PSD-95 quantification in the control human brain.**

Boxplots showing quantification of PSD-95 synaptic puncta in 20 human brain areas from 4 control cases ordered by means. Data are subdivided by colour into 4 subregions and presented by punctum density (A), punctum intensity (B) and punctum size (C). Within each boxplot, horizontal lines show the medians; box limits indicate the interquartile range (IQR) (inferior or 1st quartile range = 25th percentile, and superior or 3rd quartile range = 75th percentiles) as determined by R software using

*ggplot2* package; whiskers are defined by Tukey and extend to data points that are less than 1.5x IQR away from the 1st/3rd quartile; outliers are represented by black circles. Red circles represent mean ± SD which are shown with smaller error bars calculated using $mean\_cl\_normal$ function from ***Hmisc*** package. Brain subregions: NCx, neocortical areas; ACx, allocortex; SCx, subcortical areas; CB, cerebellum; and BS, brainstem. Brain areas: BA, Brodmann area; HC, hippocampus; TH, thalamus; CN, caudate nucleus; CB, cerebellum; MB, midbrain, PO, pons; MD, medulla.

---

### 4.5.4 PSD-95 inter-subject variability across human brain

Having quantified the PSD-95 synaptic parameters, I examined inter-subject variability for PSD-95 synapses using two approaches. These approaches would also inform with regard to the reproducibility of PSD-95 parameter distributions since less variation between the individuals would increase the reproducibility of our results.

Initially, I examined the inter-subject differences using the loess method. Analysis of PSD-95 density per individual revealed that one case (SD23/13) appeared to differ from the remaining three (Figure 4.10 A on page 154). Unlike the other three cases, this case showed much higher numbers of PSD-95 synaptic puncta in 3 cortical areas; BA4 (mean ± SD: 44.54 ± 5.44), BA6 (45.69 ± 4.47), BA9 (48.46 ± 4.76), and much lower numbers in all remaining areas. However, given the small number of this cohort, this apparent discrepancy might still be a true reflection of subject variability. All means, medians and SD values are presented in a supplementary Table B.3 on page 316.

Analysis of PSD-95 intensity per individual revealed that, similarly to the density parameter, one case (SD23/13) appeared to differ from the remaining three cases (Figure 4.10 B on page 154). Unlike the other three cases, this case showed much brighter PSD-95 synaptic puncta in 3 cortical areas; BA4 (mean ± SD: 24.95 ± 1.41), BA6 (35.02 ± 4.87), BA9 (37.88 ± 4.74), and much dimmer puncta in all remaining areas. However, given the small number of this cohort, this apparent discrepancy may still be a true reflection of subject variability. All means, medians and SD values are presented in a supplementary Table B.4 on page 317.

Analysis of PSD-95 puncta size per individual revealed that two cases showed very similar patterns of PSD-95 size distribution (case SD32/13 and SD42/13). Two cases appeared to have partially different patterns of PSD-95 sizes. One case (SD23/13) had particularly large PSD-95 synapses in the hippocampus, the caudate nucleus and the brainstem regions. In contrast, the second case (SD25/13) showed a tendency for the cortical synapses to be much smaller than the other 3 cases (Figure 4.10 C on page 154). Overall, a general pattern of PSD-95 synaptic puncta size distribution that emerged showed that the cortical areas tended to have larger synapses than the subcortical and the brainstem areas. Moreover, of all synaptic parameters, the PSD-95 synaptic size exhibited the most inter-subject variations in comparison to the density and the intensity of synapses. All means, medians and SDs values are presented in a supplementary Table B.5 on page 318. Overall, the analyses identified reproducible PSD-95 distribution patterns across the four independent human brains for each PSD-95 parameter (Figure 4.10 on page 154). However, the analyses also demonstrated that one individual (SD23/13) showed greater variation when compared to the remaining 3 control cases. An additional comparison of PSD-95 IF synaptic puncta distribution from different brain areas within the same individual are shown in (Figure 4.11 on page 156).

As a second approach, I examined the inter-subject differences based on the brain regions of all 4 individuals by performing hierarchical clustering on PSD-95 synaptic parameters. This analysis demonstrated that there are general similarities between the cases based on each PSD-95 synaptic parameter i.e. density (Figure 4.12 on page 157), intensity (Figure 4.13 on page 158) and size (Figure 4.14 on page 159). There is a tendency for areas to cluster into two main branches. However, each case showed specific clustering of areas for each parameter, which is most likely a reflection of individual differences. In fact, further detailed data analysis by each area separately confirmed significant differences between the individuals, as will be shown in the next paragraph.

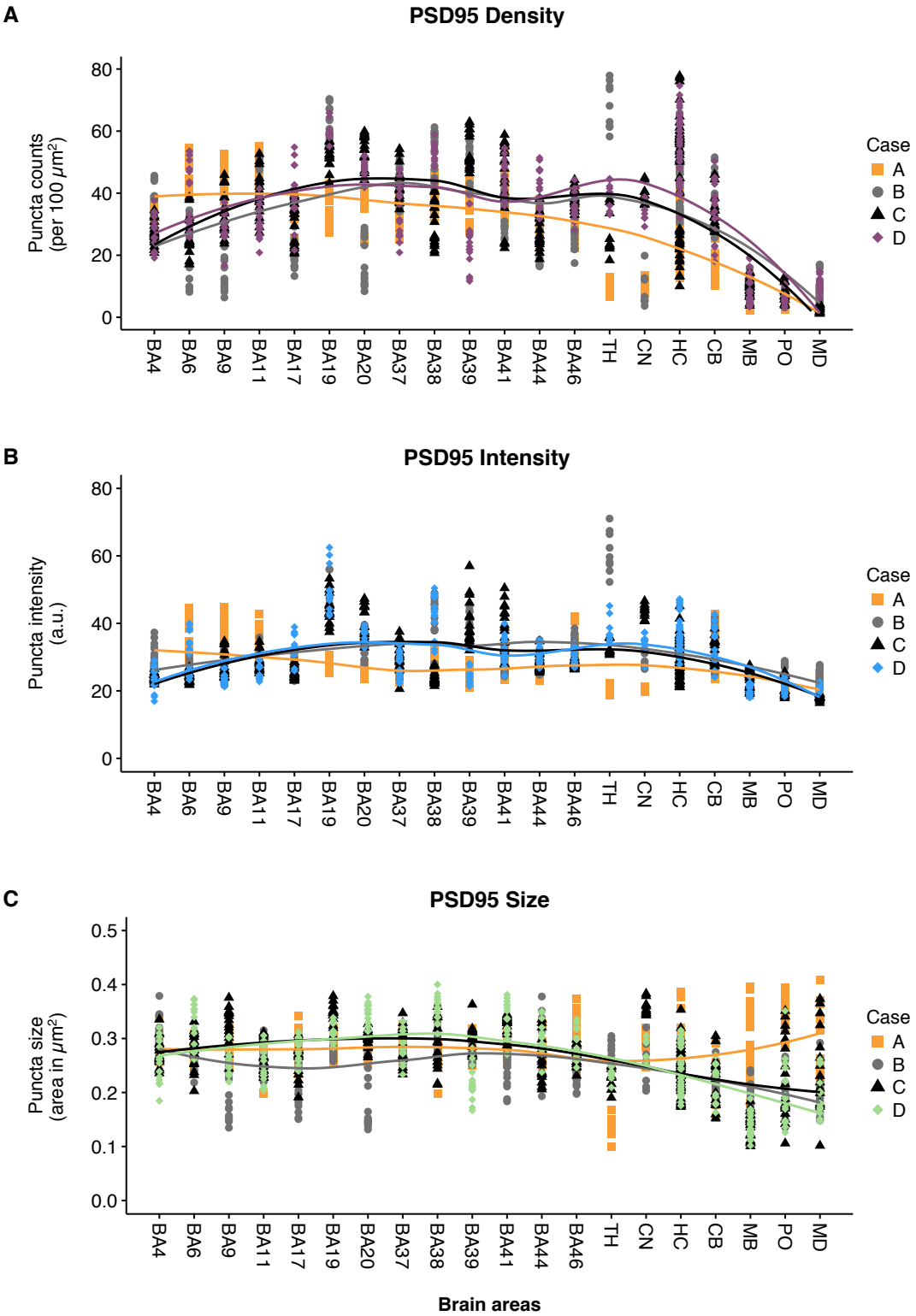


**Figure 4.10 Inter-subject PSD-95 distribution patterns variability.**

Scatterplots used to assess the inter-subject variability between the four control cases for the three PSD-95 puncta parameters: density (A), intensity (B) and size (C). Cases B, C and D appear fairly similar for all parameters in contrast to the case A. The inter-subject variability was assessed by fitting a loess smoothing curve superimposed among the data points for each subject. Smoothing interpolation by loess method was performed using R function from the ggplot2 package: parameter settings were

method = "loess" and span = "0.75" for curve fitting. Each colour-coded curve represents a subject. For clarity, colour of subject D was changed to reflect different parameter examined. Each data point represents a result of quantification from an image obtained with LSCM. The data points are coded by shapes (squares, circles, triangles and diamonds) and are kept constant for each subject. Cases: A - SD23/13, B - 25/13, C - 32/13 and D - 42/13. Brain areas: BA, Brodmann area; HC, hippocampus; TH, thalamus; CN, caudate nucleus; CB, cerebellum; MB, midbrain, PO, pons; MD, medulla.

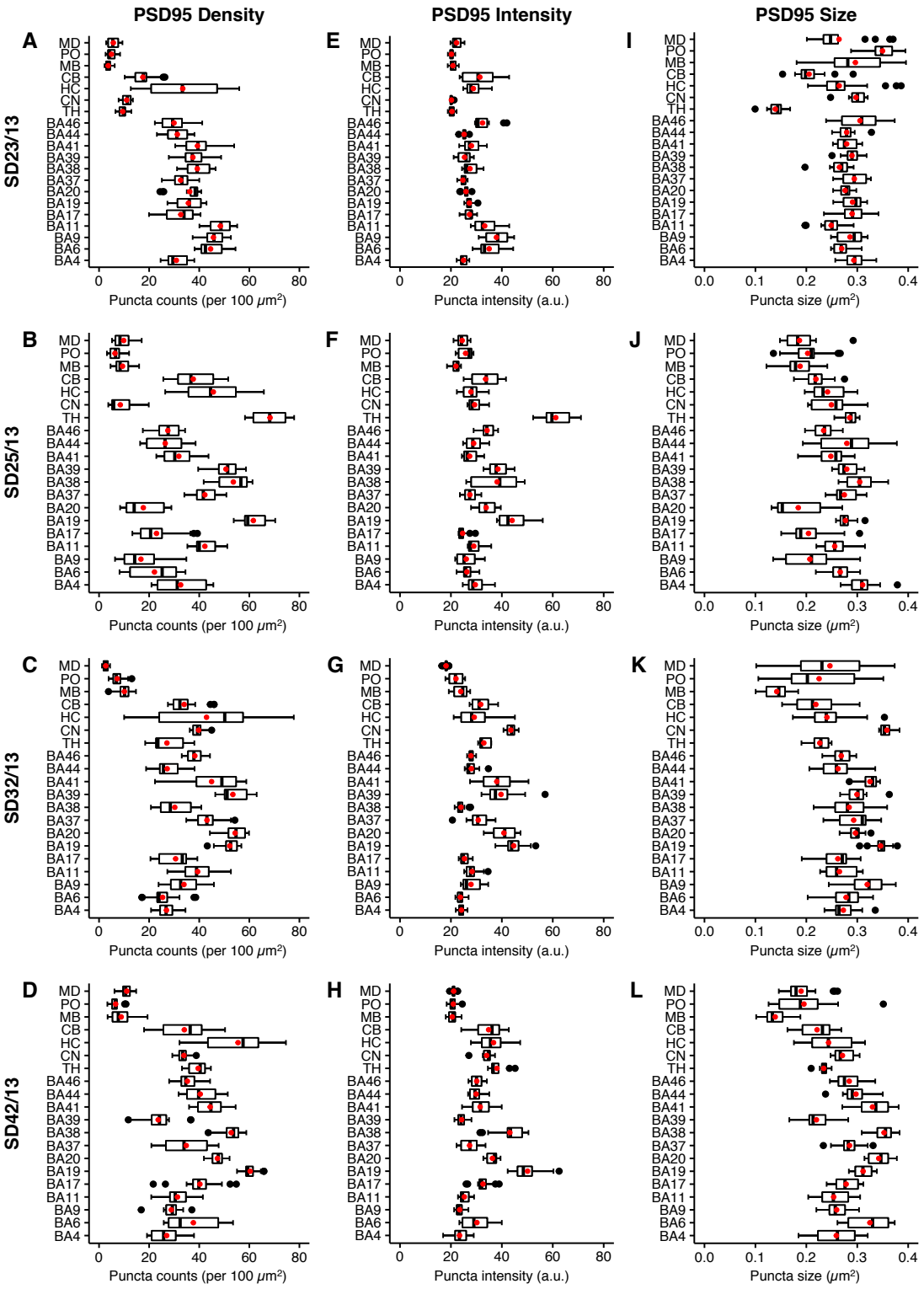


**Figure 4.11 Comparison of PSD-95 synaptic puncta parameters distribution from different brain areas within the same individual brains.**

Boxplots demonstrating PSD-95 IF labelling in four individual brains for the three PSD-95 puncta parameters: density (A, B, C, D), intensity (E, F, G, H) and size (I, J, K, L). Cases B, C and D appear fairly similar for all parameters in contrast to the case A. Cases: A, E, I - SD23/13, B, F, J - SD25/13, C, G, K - SD32/13 and D, H, L - SD42/13. Brain areas: as before.

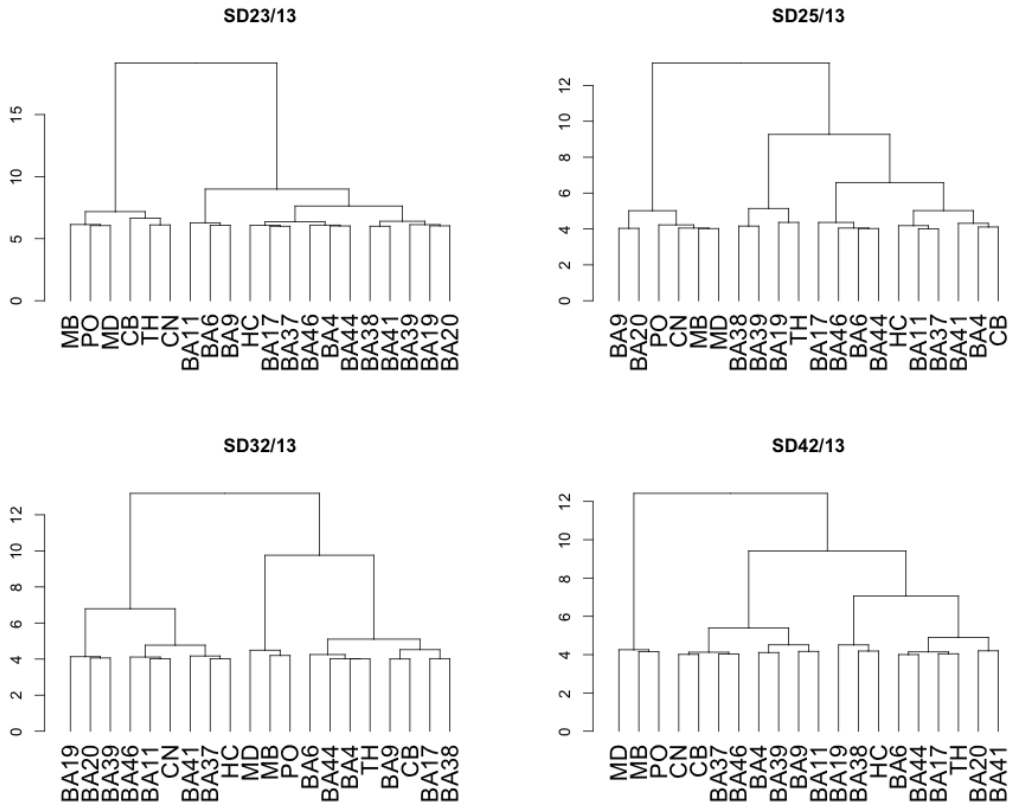


**Figure 4.12 PSD-95 inter-subject similarity based on puncta density.**
Similarity of the PSD-95 synaptic puncta densities between individuals. Individual clustering dendrograms showing the similarities between 20 areas based on PSD-95 synaptic puncta mean densities. The dendrograms are based on the Euclidean differences between the mean value for each region. The clustering method used was Ward.D. The analysis was performed using R software. Cases: A - SD23/13, B - SD25/13, C - SD32/13 and D - SD42/13. Brain areas: BA, Brodmann area; HC, hippocampus; TH, thalamus; CN, caudate nucleus; CB, cerebellum; MB, midbrain, PO, pons; MD, medulla.

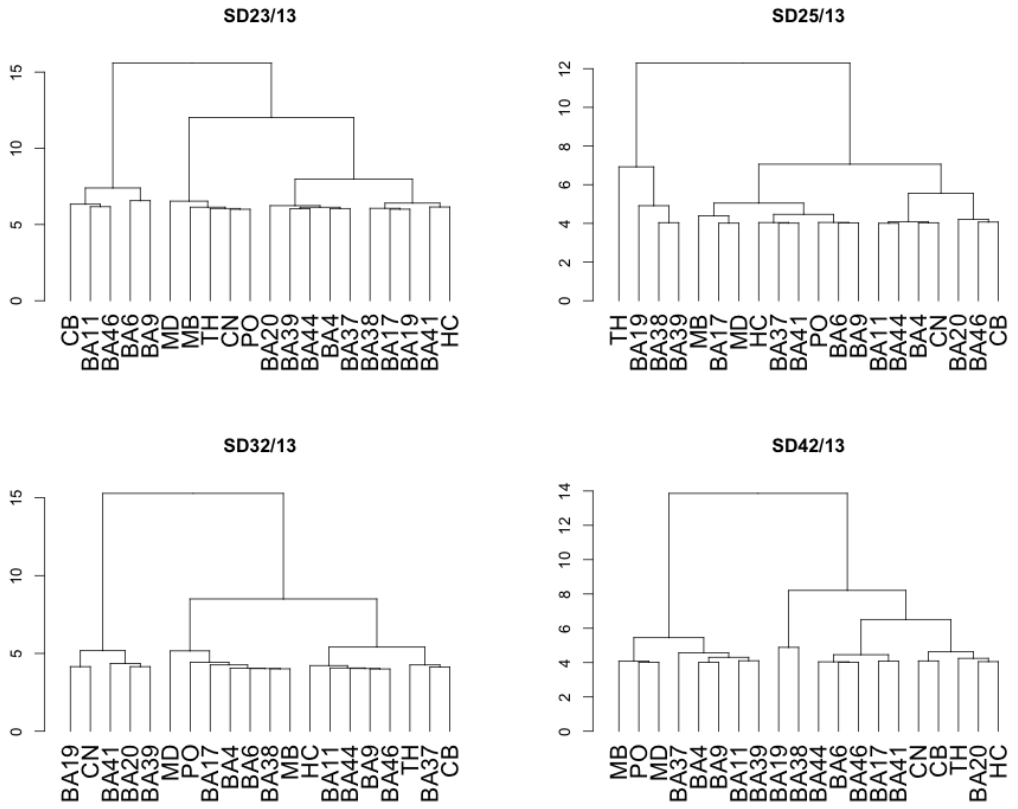


**Figure 4.13 PSD-95 inter-subject similarity based on puncta intensity.**
Similarity of the PSD-95 synaptic puncta intensities between individuals. Individual clustering dendrograms showing the similarities between 20 areas based on PSD-95 synaptic puncta mean intensities. The dendrograms are created as described previously. Cases: A - SD23/13, B - SD25/13, C - SD32/13 and D - SD42/13. Brain areas: BA, Brodmann area; HC, hippocampus; TH, thalamus; CN, caudate nucleus; CB, cerebellum; MB, midbrain, PO, pons; MD, medulla.

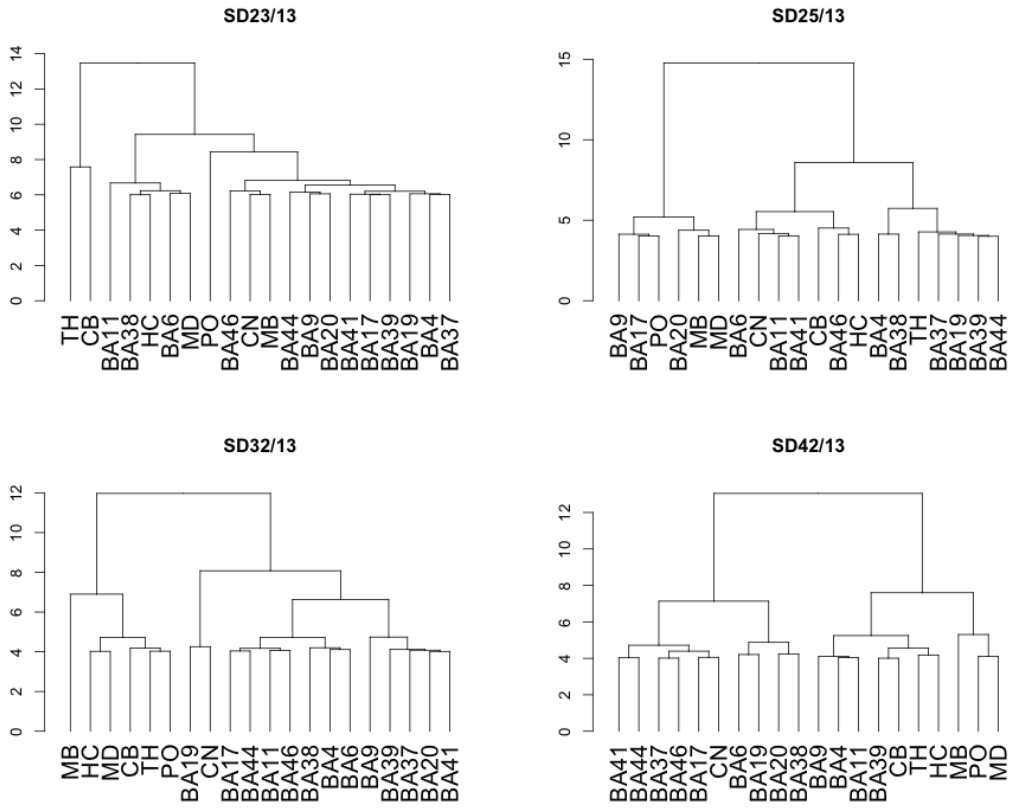


**Figure 4.14 PSD-95 inter-subject similarity based on puncta size.**
Similarity of the PSD-95 synaptic puncta sizes between individuals. Individual clustering dendrograms showing the similarities between 20 areas based on PSD-95 synaptic puncta mean sizes. The dendrograms are created as described previously. Cases: A - SD23/13, B - SD25/13, C - SD32/13 and D - SD42/13. Brain areas: BA, Brodmann area; HC, hippocampus; TH, thalamus; CN, caudate nucleus; CB, cerebellum; MB, midbrain, PO, pons; MD, medulla.

### 4.5.5 PSD-95 synaptic puncta inter-subject inter-regional variation

In the previous section I established that there appear to be a general pattern of inter-regional PSD-95 variation for each synaptic parameter, which can be identified despite individual differences. I next asked if this pattern is still preserved when each area is examined separately for each synaptic parameter for each individual. Inter-subject variation has been well documented in human studies (Uylings et al., 2005; Caspers et al., 2006). Such variation would also be expected in the present study.

The analyses for PSD-95 synaptic puncta density (Figure 4.15 on page 162), intensity (Figure 4.16 on page 163) and size (Figure 4.17 on page 164) demonstrate consistently that within each anatomical area examined, there are many significant differences between the subjects with no discernable pattern of differences for each parameter. Moreover, significant differences between individuals observed for one synaptic parameter do not inform about differences in any of the remaining two parameters. For instance, an absence of significant PSD-95 density differences between individuals for the cortical area BA4, does not follow for the PSD-95 intensity and size, where significant differences between the cases are seen. In the cerebellum, there are no significant individual differences for PSD-95 intensity and size, but the PSD-95 densities significantly differ between the cases. Overall, the two examples are the exceptions rather than the rule, as a majority of the analysed areas do show significant differences between the individuals for every PSD-95 synaptic parameter at each anatomical level.

However, despite the inter-subject differences, the general trends have been preserved: the synaptic puncta were generally less numerous and slightly dimmer in the brainstem areas, but brighter and more numerous in the cortical and subcortical regions. These differences were particularly obvious for the PSD-95 density parameter, and less prominent, but still present for the intensity parameter. A general size distribution pattern has also been preserved for the synaptic sizes, which were low in the brainstem and subcortical areas, but much higher sizes were found in the cortical regions.

Taken collectively, these data inform that there are significant topographical inter-subject differences for each PSD-95 synaptic parameter. However, the overall individual inter-regional PSD-95 distribution patterns appear to follow a global organisation arrangement whereby inter-subject differences become less significant.

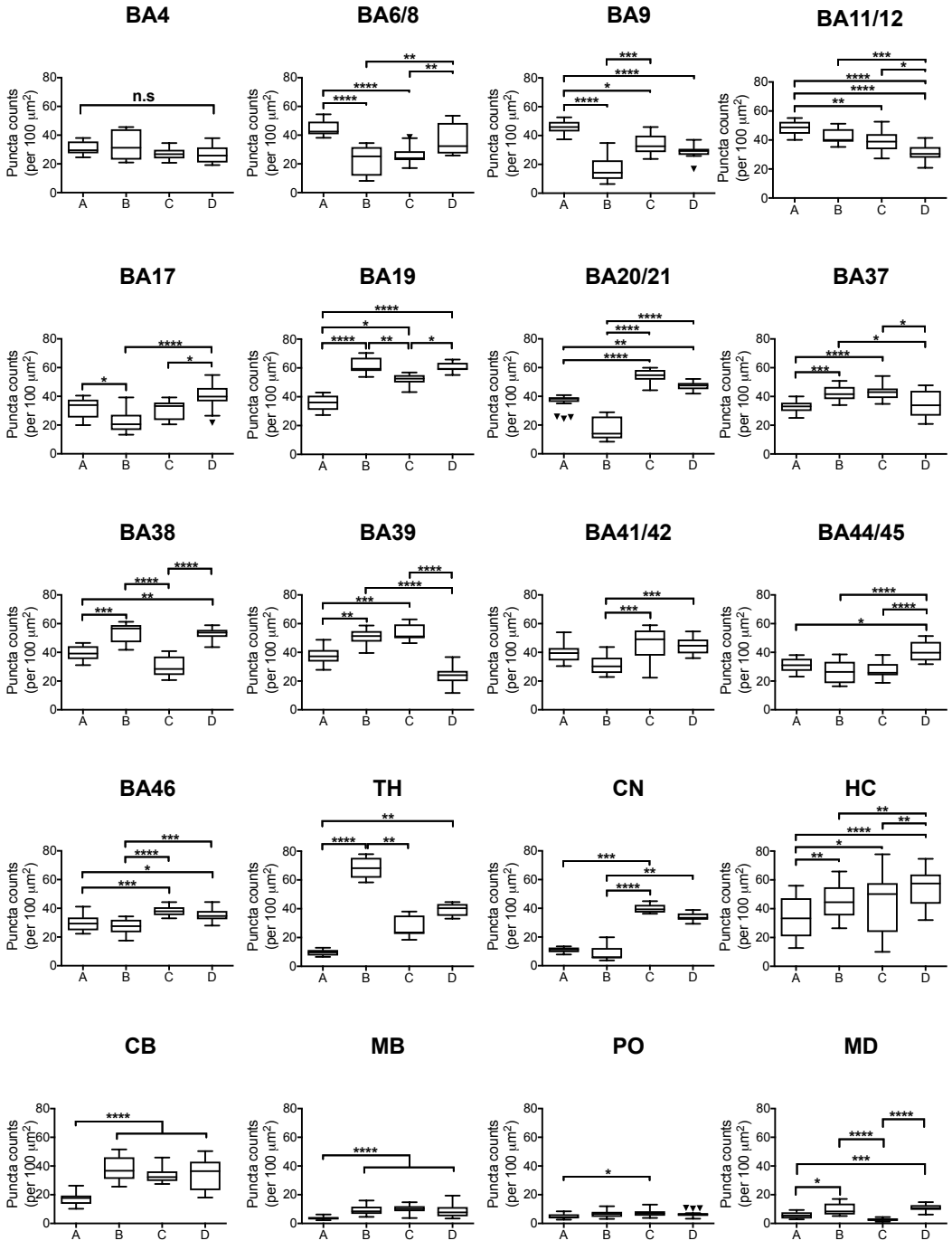


**Figure 4.15 PSD-95 density quantification by case and area.**
Inter-subject variability by brain area of PSD-95 puncta density in 20 control human brain areas (n=4). Data were analysed with Kruskal-Wallis ANOVA on ranks with Dunn's post-hoc test and are presented as boxplots with median and whiskers plotted by Tukey method (outliers are displayed as black triangles below and above the whiskers). Cases: A - SD32/13, B - SD25/13, C - SD32/13 and D - SD42/13. Significance levels: $*p < 0.05$, $**p < 0.01$, $***p < 0.001$, $****p < 0.0001$. Density is expressed as number of puncta per 100 $\mu m^2$. Brain areas: BA, Brodmann area; HC, hippocampus; TH, thalamus; CN, caudate nucleus; CB, cerebellum; MB, midbrain, PO, pons; MD, medulla.

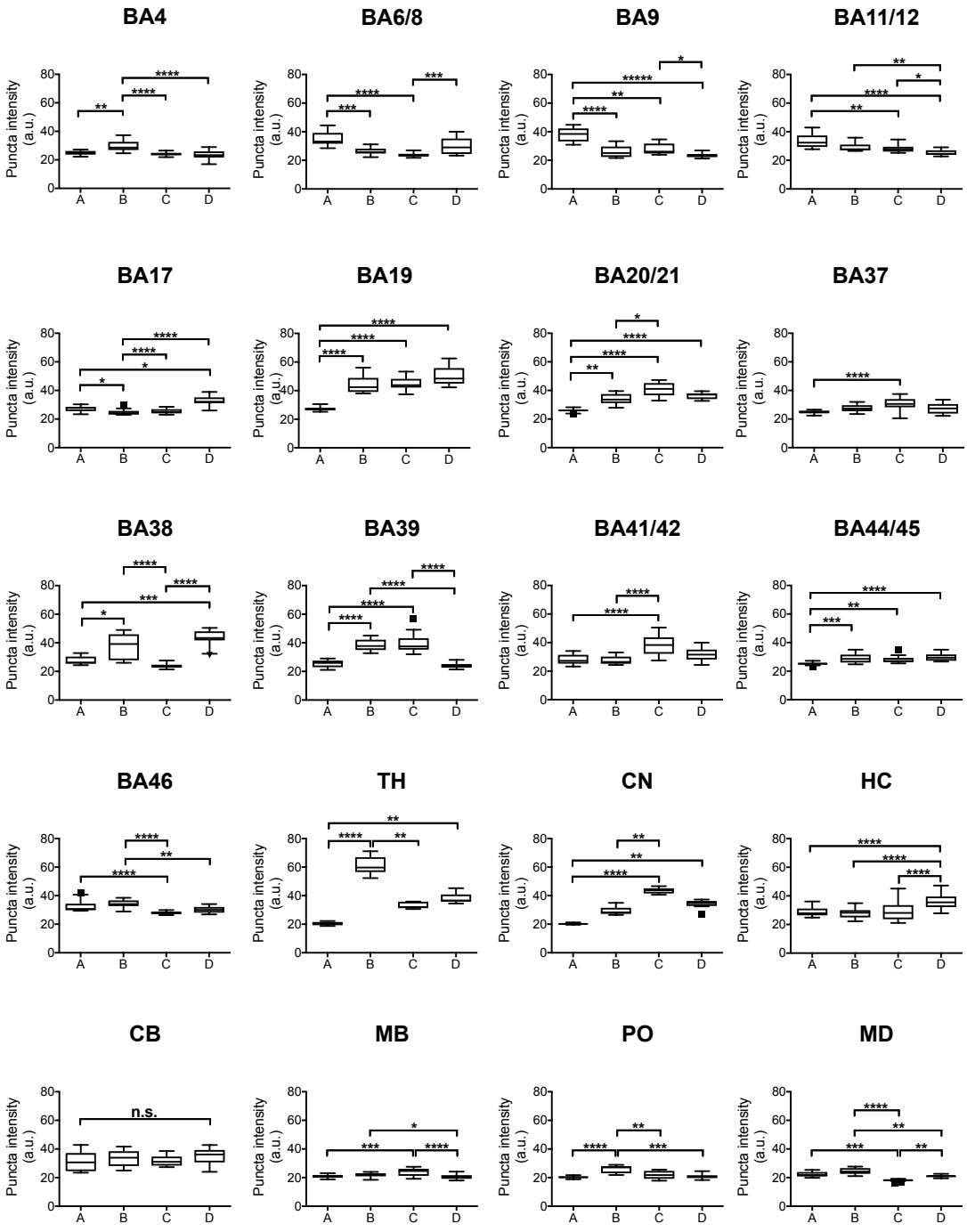


**Figure 4.16 PSD-95 intensity quantification by case and area.**
Inter-subject variability by brain area of PSD-95 puncta intensity in 20 control human brain areas (n=4). Data were analysed with Kruskal-Wallis ANOVA on ranks with Dunn's post-hoc test and are presented as boxplots with median and whiskers plotted by Tukey method (outliers are displayed as black squares below and above the whiskers). Cases: A - SD23/13, B - SD25/13, C - SD32/13 and D - SD42/13. Significance levels: $*p < 0.05$, $**p < 0.01$, $***p < 0.001$, $****p < 0.0001$. Intensity is expressed as arbitrary units (a.u.). Brain areas: BA, Brodmann area; HC, hippocampus; TH, thalamus; CN, caudate nucleus; CB, cerebellum; MB, midbrain, PO, pons; MD, medulla.

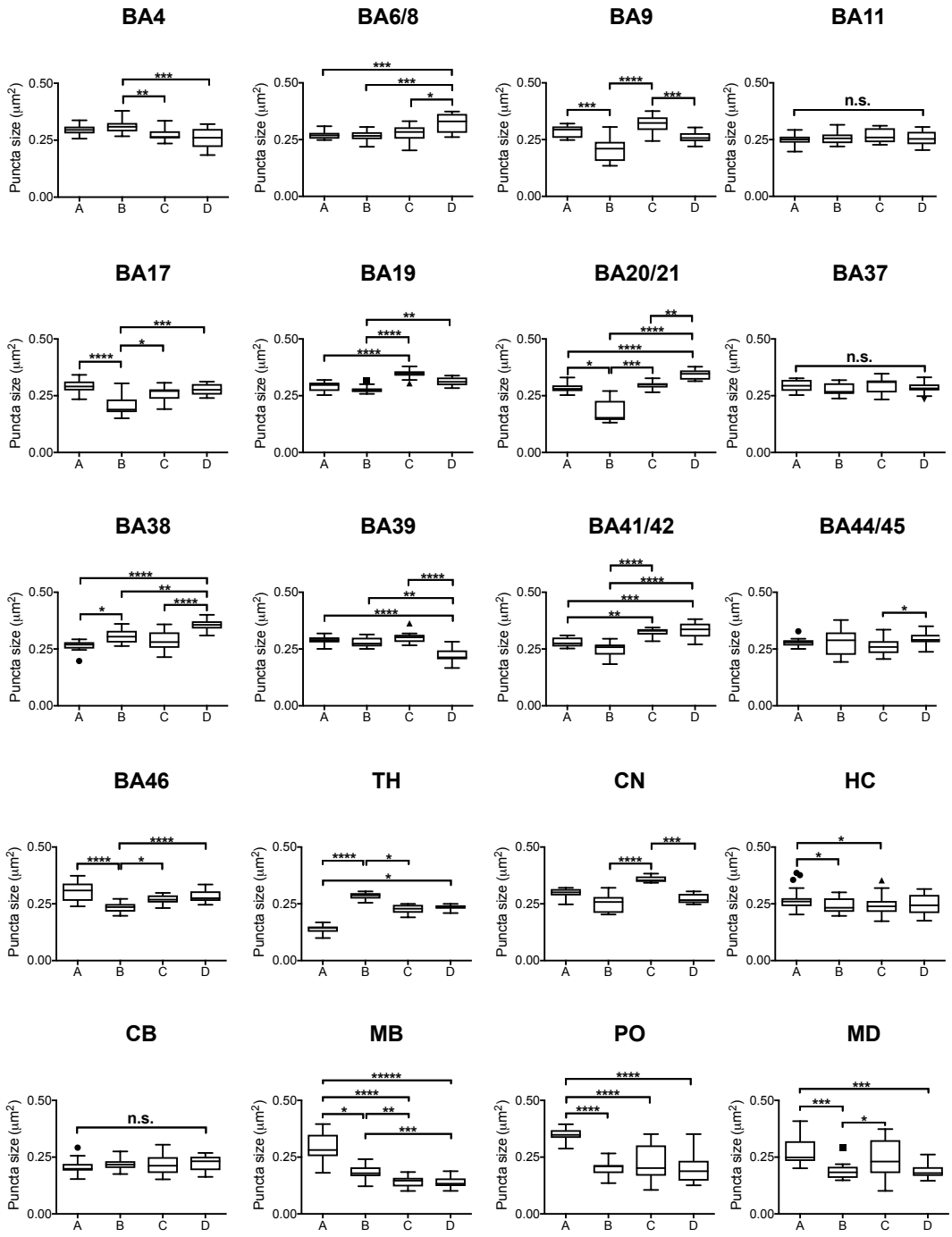


**Figure 4.17 PSD-95 size quantification by case and area.**

Inter-subject variability by brain area of PSD-95 puncta size in 20 control human brain areas (n=4). Data were analysed with Kruskal-Wallis ANOVA on ranks with Dunn's post-hoc test and are presented as boxplots with median and whiskers plotted by Tukey method (outliers are displayed as black shapes: triangles, circles or squares, below and above the whiskers). Cases: A - SD23/13, B - SD25/13, C - SD32/13 and D - SD42/13. Significance levels: $*p < 0.05$, $**p < 0.01$, $***p < 0.001$, $****p < 0.0001$. Size is expressed as area in $\mu m^2$. Brain areas: BA, Brodmann area; HC, hippocampus; TH, thalamus; CN, caudate nucleus; CB, cerebellum; MB, midbrain, PO, pons; MD, medulla.

## 4.6 SYNAPTOME MAPPING OF PSD-95 IN SELECTED HUMAN BRAIN AREAS

Analysis of PSD-95 puncta parameters using the G2CSynMaP methodology was undertaken to acquire the first comprehensive quantitative study of synapse diversity in 20 human brain areas. The distribution of PSD-95 puncta density, intensity and size is illustrated as heatmaps in Figure 4.18 on 166. Overall, these maps reveal that PSD-95 synapses display an organised pattern of expression. The heatmap colours indicate the mean levels of each parameter compared to other subregions with red spectrum indicating high and blue spectrum indicating low values.

The cortical areas and the hippocampus have high numbers of PSD-95 synapses. Among the cortical regions, the frontal areas tend to have less PSD-95 synapses than the temporal, parietal and occipital regions. The synapses of the frontal areas also tend to be less intense than the synapses in the remaining three lobes. Overall, the size of synapses appears homogeneous throughout the cortical areas with the most ventral frontal areas having the smallest PSD-95 puncta.

The subcortical areas, such as thalamus and the caudate nucleus, as well as the hippocampus generally show a variable pattern of synaptic puncta parameters based on mean values. For instance, the thalamus shows intermediate numbers of synapses, which are bright, but small. On the other hand, the caudate nucleus has a low number of moderately bright, but large synapses. The hippocampal synapses are numerous, but at most only moderately bright and have a size similar with other areas.

Finally, the infratentorial regions appear to have overall relatively homogeneous PSD-95 puncta parameters. However, the brainstem synapses are in general in low number, dim and small in comparison to the rest of brain areas. The cerebellum, however, has a relatively brighter synapses than the rest of the brainstem regions.

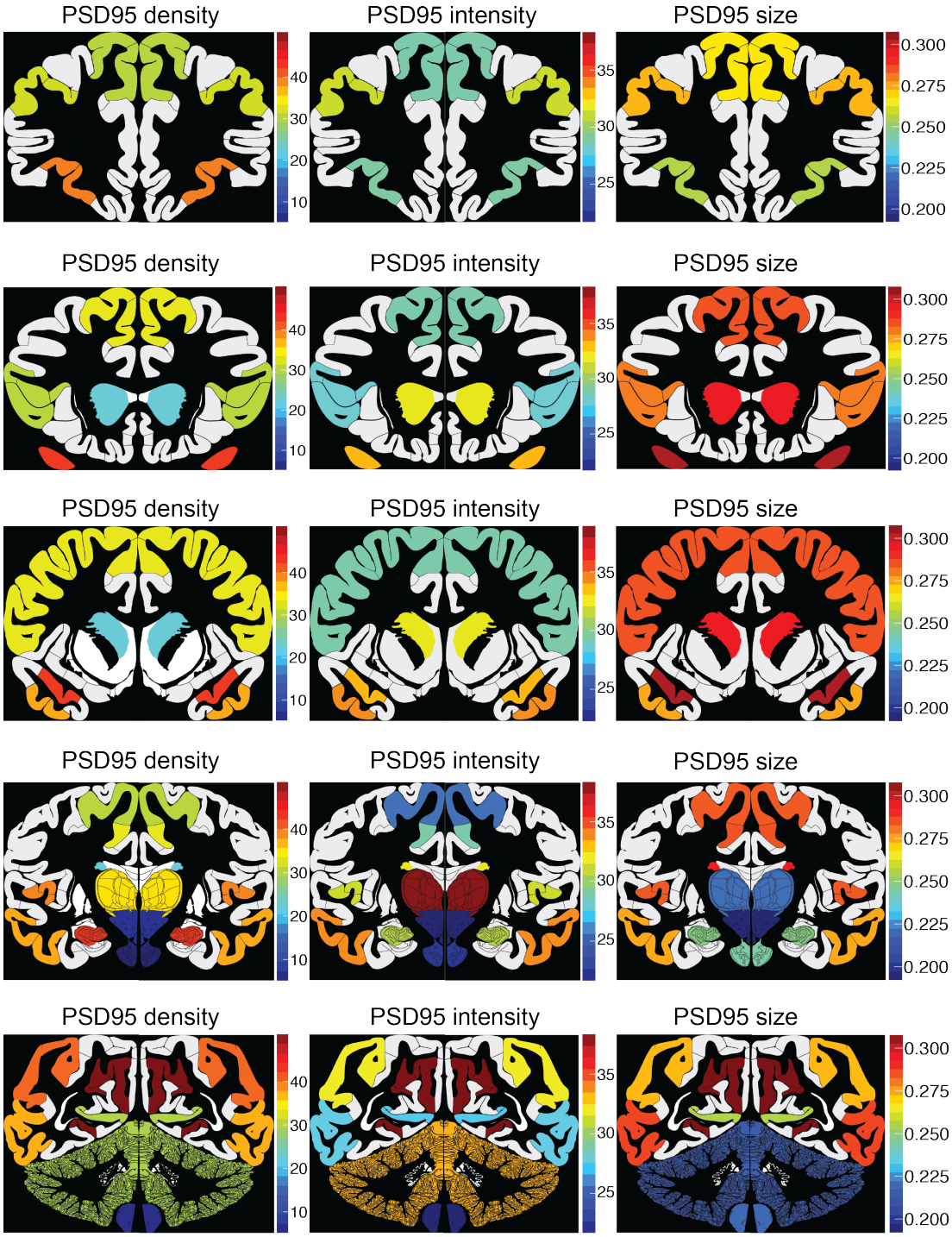


**Figure 4.18 PSD-95 synaptome in the human brain.**
Colour-coded PSD-95 synaptome map showing inter-regional synapse diversity in 20 human brain areas. The maps show representative five coronal sections through the human brain. Templates of these coronal sections were taken and amended from the Allen Brain Atlas (Human Brain) and include numbers: 10/106, 16/106, 19/106, 48/106 and 86/106. The 20 areas are as follows: 13 cortical (BA4, BA6/8, BA9, BA11/12, BA17, BA19, BA20/21, BA37, BA38, BA39, BA41/42, BA44/45, BA46); 3 subcortical areas (hippocampus, caudate nucleus and thalamus); cerebellum and the three brainstem structures (midbrain, pons and medulla). Grey-coloured areas were not included in the analysis. Data are expressed as mean of density, intensity and size for 4 control cases. Density is expressed in number of puncta per 100 $\mu m^2$, intensity in a.u units and size in $\mu m^2$ punctum area. Drawn not to scale.

### 4.6.1 PSD-95 inter-regional similarities

Once the PSD-95 quantification values were generated for the 20 human brain areas, it was possible to examine the inter-regional similarities based on the four control human brains. This process involved generation of a similarity matrix (Figure 4.19 A on page 170). Briefly, the mean values from the 4 control cases for each area for the three PSD-95 synaptic puncta parameters were normalised using the z-score formula as detailed in the methods section in Chapter 2.14. The normalised data were then used to generate the Euclidean distances based on pairwise comparisons between the areas. A Euclidean distance of zero indicates that two areas are identical, whereas large distance numbers indicate dissimilarities. The middle diagonal line shows the Euclidean distance of zero formed by each subarea with itself. Using the same data, a heatmap was generated to elucidate the contribution of each parameter to the inter-region similarity (Figure 4.19 B).

Several patterns of similarity between regions emerged (Figure 4.19 C). Firstly, the most striking observation is that there is a clear division between the supra- and the brainstem. The three brainstem regions (midbrain, pons and medulla) are very similar to each other, but markedly different to the rest of the brain regions. As the heatmap in Figure 4.19 B demonstrates, this dissimilarity from the rest of the brain areas reflects consistently low values of the three PSD-95 synaptic puncta parameters in these areas. On the basis of these data, it appears that this organisation of PSD-95 distribution and diversity is a reflection of the local functionalities and connections rather than between gross anatomical regions.

Secondly, the cortical areas show close similarity with each other. These cortical similarities might be the reflection of the underlying overall anatomical uniformity, although even in our data, it is evident that the cortical areas are not necessary homogeneous for PSD-95. One pattern that emerged is that the cortical areas can be further subdivided into two subgroups based on the synaptic parameters diversity. The first group consists of cortical areas with high synaptic numbers that are bright and big in size. This group includes predominantly temporal (BA38, BA20, BA41) areas, but also a frontal (BA46) and a parietal (BA39) areas. Interestingly, the

temporal BA38 area stands out in terms of the highest values for all three parameters when compared to other areas within this cortical subgroup. The second subgroup of cortical areas has synapses that are generally dim, but big in size. This group includes frontal areas (BA6, BA9 and BA44), a parietal area (BA37) as well as the primary visual cortex of the occipital lobe (BA17) and the primary motor cortex of the caudal frontal area (BA4). The visual association area within the occipital cortex (BA19) is unique in our analysis with the highest number of the brightest and the largest synaptic puncta among all regions. This striking dissimilarity to the other cortical areas and the brainstem, in particular, makes BA19 more similar to the subcortical regions, such as the thalamus and the cerebellum, although they have much smaller, but still good numbers of bright synapses.

The last pattern that emerged is a synaptically diverse group that displays various patterns of similarity between its members. For instance, the thalamus, the cerebellum and the hippocampus have many bright synapses that tend to be small. In contrast, the caudate nucleus has bright and large synapses, but not as many as the other subcortical subregions. Interestingly, with regards to PSD-95 synapses both the hippocampus and the caudate nucleus share more similarities with the cortices rather than the subcortical regions. The similarity between the synapses in the hippocampus and the orbitofrontal cortical area BA11/12 is particularly interesting since there are close functional and neuronal connections between these regions that are relevant in brain disorders, such as Alzheimer's disease. These differences between the subcortical areas are potentially the reflection of their underlying anatomical heterogeneity; the hippocampus proper contains at least 16 different subregions, the thalamus consists of numerous nuclei and the cerebellar cortex is divided into three layers. It seems inconceivable that this anatomical diversity is not mirrored in synaptic diversity. Although these data cannot address this issue entirely, this is certainly the case with the hippocampus. In contrast, the relatively uniform internal structure of the caudate nucleus represents yet a different pattern of between region similarities in the subcortical regions, whereby it may be a reflection its distinct function and connectivity rather than gross anatomical similarity seen with the cortical areas.

In summary, in this subsection, I have demonstrated that there are several very

specific patterns of the PSD-95 inter-regional similarities across the human brain. The lack of similarities between regions provide potential substrates for anatomical and functional differences between the specific regions. On the other hand, the similarities may predict anatomical and functional similarities. These general patterns of inter-regional similarities can be applied to many biological systems and, for example, have been described at the gene expression level in the mouse brain (Lein et al., 2007). However, more importantly, very similar patterns of the PSD-95 based regional similarities have now been described in the mouse brain (Grant lab, personal communication).

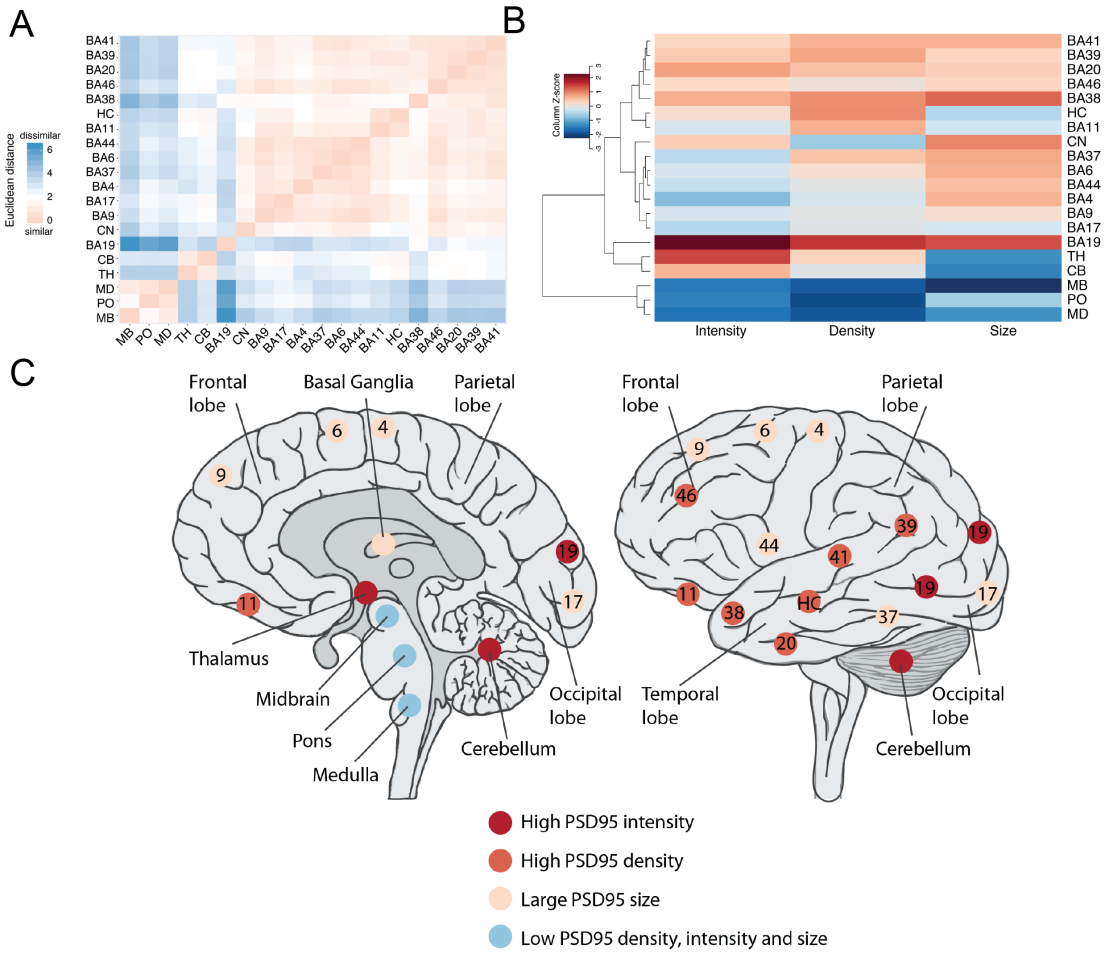


**Figure 4.19 PSD-95 inter-region similarity across the human brain.**
**A.** Similarity matrix based on the inter-region pairwise similarity values calculated using the Euclidean distance between 20 human brain areas. The matrix is based on standardised average values from 4 control cases (SD23/13, SD25/13, SD32/13 and SD42/13) for the three PSD-95 synaptic puncta parameters (density, intensity and size) from each brain area. The distance between two objects is 0 (red) when they are identical (perfectly similar). The greater the distance the stronger the dissimilarity between the regions (darker blues). **B.** Heatmap showing the differences and similarities between the regions based on the 3 synaptic puncta parameters. Rows correspond to areas and columns to synaptic parameters. The dendrogram represents area similarity on the basis of the Euclidean distances between the 20 regions. Brain areas: BA, Brodmann area; HC, hippocampus; TH, thalamus; CN, caudate nucleus; CB, cerebellum; MB, midbrain, PO, pons; MD, medulla. **C.** Graphical representation of a neuroanatomical map of PSD-95 synaptic parameters distribution based on hierarchical clustering of the 20 areas. The areas could be separated into 4 subgroups, as indicated by the colours, in accordance to the most persistent synaptic feature within the subgroup. Three subgroups appear well defined (with only occasional exceptions): a subgroup of areas with high PSD-95 numbers were predominantly distributed around the temporal lobe and some frontal areas. A second subgroup of large PSD-95 sizes was located mostly in the frontal lobe. The third subgroup contained areas with dim, small and infrequent PSD-95 synaptic puncta, which were distributed in the brainstem. There was also a fourth, most heterogeneous, group made of areas with bright PSD-95 synapses, but of different sizes and numbers and various locations. Numbers within the coloured circles indicate Brodmann areas.

### 4.6.2 PSD-95 inter-cortical similarities

Our findings have showed that, in general, the cortical areas tend to cluster into 3 subgroups, of which 2 have rather similar PSD-95 synapses apart from their size (Figure 4.20 on page 172). Both of these subgroups overall have low numbers of dim synaptic puncta. However, one subgroup shows areas with larger PSD-95 synapses (BA37, BA6, BA44, BA4) when compared to other areas (BA11, BA46, BA9 and BA17). With the exception of BA37, which is found in the temporal lobe, and BA17 found in the occipital lobe, both subgroups contain areas that are found in the frontal lobe. Moreover, both subgroups contain areas with primary brain functions, such as primary visual cortex (BA17), motor cortex (BA4) or Broca's speech production region (BA44/45). In addition, a functional connectivity between these 2 subgroups has been previously described (Graham and Whistler, 1975). The visual ventral pathway is a connectome between the primary visual area (BA17) and the BA37 area, which then connects to the tertiary areas within the prefrontal (BA46) and orbitofrontal (BA11) cortex. This pathway is thought to be involved in the visual object processing and recognition, the ability of which is lost in damage to this pathway resulting in an inability to name and identify everyday objects. The third subgroup of cortical areas appear to have numerous bright PSD-95 synapses in contrast to the previously described two subgroups. It contains cortices which predominantly are found in the temporal lobe apart from the secondary visual BA19 area found in the occipital lobe. In fact, BA19 shares least similarity with the rest of this subgroups members.

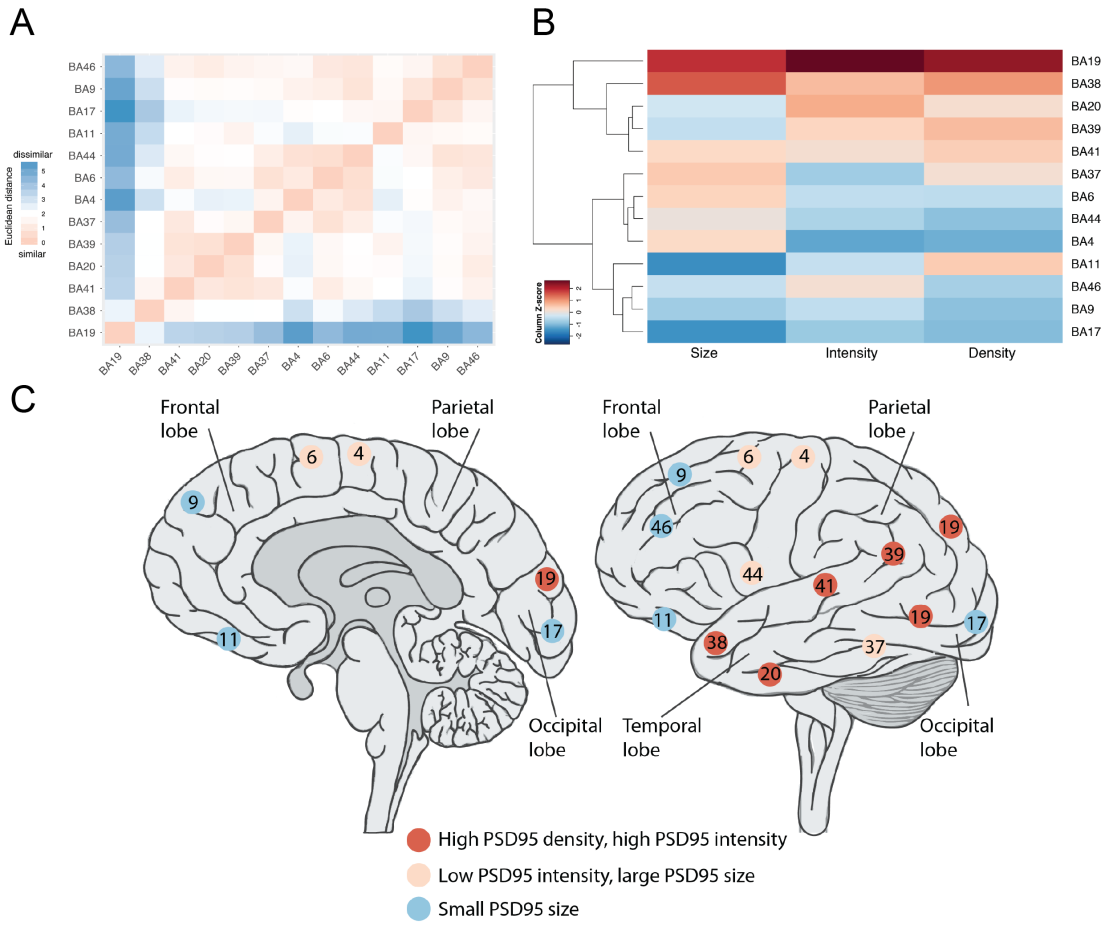


**Figure 4.20 PSD-95 inter-cortical similarity in the human brain.**
**A.** Similarity matrix based on the inter-cortical pairwise similarity values calculated using the Euclidean distance between 13 human cortical areas. The matrix is based on standardised average values from four control cases (SD23/13, SD25/13, SD32/13 and SD42/13) for the three PSD-95 synaptic puncta parameters (density, intensity and size) from each isocortex area. The distance between two objects is 0 (red) when they are identical (perfectly similar). The greater the distance the stronger the dissimilarity between the regions (darker blues). **B.** Heatmap showing the differences and similarities between the cortical regions based on the 3 synaptic puncta parameters. Rows correspond to areas and columns to synaptic parameters. The dendrogram represents area similarity on the basis of the Euclidean distances between the 13 cortical regions. Brain areas: BA, Brodmann area. **C.** Graphical representation of a neuroanatomical map of PSD-95 synaptic parameters distribution based on hierarchical clustering of the cortical areas. The 13 cortical areas could be separated into three subgroups, as indicated by the colours, in accordance to the most persistent feature for each cortical area within the subgroup. Therefore, a subgroup of cortical areas with high PSD-95 numbers of bright synaptic PSD-95 puncta were mostly distributed around the temporal lobe. A second subgroup of cortical areas with dim PSD-95 synapses of large size were located predominantly in the posterior part of the frontal lobe. Finally, the third subgroup contained areas with small PSD-95 synapse sizes and was distributed at the opposite ends of the brain, i.e. in the most anterior part of the frontal lobe and in the occipital lobe. Numbers within the coloured circles indicate Brodmann areas.

## 4.7 CHAPTER DISCUSSION AND CONCLUSIONS

In this chapter, I have mapped distribution of PSD-95 protein in 20 human brain areas into PSD-95 synaptome diversity maps. These PSD-95 synaptome maps are based on analysis of three PSD-95 IF puncta parameters. The PSD-95 synaptome mapping has been achieved in the rodent brain using the G2CSynMaP methodology (Zhu et al., submitted).

### 4.7.1 Patterning of PSD-95 expression at the whole-brain level

One of the most striking finding of this study is a highly patterned expression of PSD-95 between major anatomical brain regions. High expression of PSD-95 synapses was found in the cerebrum in the neocortical areas and the subcortical regions. In contrast, PSD-95 expression was sparse in the brainstem structures. Although no human studies have been identified that describe PSD-95 distribution differences between the cerebrum, the subcortical nuclei and the brainstem, these findings are in general agreement to those described in mouse using the G2CSynMaP methodology, which showed that the brainstem structures tended to have the fewest, dimmest and smallest PSD-95 synapses. This pattern therefore appears to be conserved between the human and mouse. There may be several reasons behind this specific PSD-95 synaptic distribution. It is possible that there are more connections present within the cerebrum, and therefore more synapses, than within the brainstem. Alternatively, it may be that there are similar populations of synapses within the different regions, but a smaller population of glutamatergic type synapses and more synapses utilising different neurotransmitters within the brainstem. Finally, the number of synapses may be similar, but they may not necessary contain PSD-95 molecules. More studies are required to understand this organisation of PSD-95 at the whole-brain level. For instance, ultrastructural studies could provide some answers by quantifying the density of symmetric and asymmetric synapses in cerebrum vs. brainstem.

Comparative human studies reporting density of synapses are infrequent and mostly based on ultrastructural methods that are limited to neocortical areas (DeFelipe

et al., 2002; O'Kusky and Colonnier, 1982; Beaulieu and Colonnier, 1989) and selected hippocampal subregions (Scheff et al., 1996; Scheff and Price, 1998). Nevertheless, interesting comparisons are still possible to make. For instance, our data demonstrate that the variability in density of PSD-95 synapses between the neocortical areas is narrower, on average 51 to 30 synaptic puncta per 100 $\mu m^2$, in BA19 and BA4, respectively, than the rest of the other regions, for example 44 to 6 per 100 $\mu m^2$ in the hippocampus to pons, respectively. Previous EM studies reported relatively constant numerical density of synapses between different cortical areas and different species. For instance, a lack of systematic differences between different cortical regions, for areas 6,8 and 17, were found in the mouse (Schüz and Palm, 1989) similar to our data showing PSD-95 synaptic numbers for areas BA6 and BA17. Furthermore, similar synaptic numbers were reported for diverse neocortical areas of the rhesus monkey, which included the motor cortex, somatosensory cortex, prefrontal cortex and visual cortex (Rakic et al., 1986; Zecevic and Rakic, 1991). Another early ultrastructural study showed relatively little variation in synaptic density between areas that were cytoarchitectonically and functionally different, such as the motor and visual cortex, in the mouse and monkey (Cragg, 1967). In agreement with these reports, our results also demonstrate that PSD-95 densities, and intensities, for BA4 and BA17 are very similar. Finally, densities of synapses in the human visual, auditory and prefrontal cortices were also found to be similar (Huttenlocher and Dabholkar, 1997). However, contrary to the reported quantifications, the numbers of human neocortical synapses are lower than quantified in this project. For instance, the variability quoted for the cortical areas in the rhesus monkey was between 13 to 20 synaptic profiles per 100 $\mu m^2$ (Rakic et al., 1986; Zecevic and Rakic, 1991). For instance, adult rhesus monkey had 13 asymmetric synapses per 100 $\mu m^2$ in the somatosensory cortex as demonstrated by electron microscopic examination (Zecevic and Rakic, 1991). A slightly higher range of 20 to 36 synaptic profiles per 100 $\mu m^2$ was reported in human temporal cortex based on EM examination of 2195 synaptic profiles (DeFelipe et al., 2002).

The reasons for the differences are likely to be methodological: our results are based on analyses of an estimated half a billion of synaptic puncta vs. less than approximately 10 000 synaptic profiles using EM. Most studies also report quantifications of asymmetric synapses rather than the PSD-95 synapses, although

postsynaptic proteins, like PSD-95, have generally been assumed to accurately represent the location of the PSD (Meyer et al., 2014). There are important limitations of using the PSD-95 antibody labelling as highlighted in Chapter 3.1.2. Finally, the use of a high throughput analysis is probably also more likely to overestimate the actual numbers given the complexity and scale of the whole dataset. Previous studies examining the synaptic subtypes and molecular diversity using antibodies, such as array tomography, have reported challenges with such complicated human synaptic data (Busse and Smith, 2013; Weiler et al., 2014). Last but not least, the reasons for the differences may reflect species differences, as previously described in Chapter 3.4. However, while caution in the interpretation of our results should be applied, the main scope of our analysis is in demonstrating synaptic changes across many areas. Reassuringly, despite the discrepancies in the actual numbers, the trends appear in accordance with the published data.

With regard to PSD-95 intensity, the pattern of PSD-95 staining is very similar to that observed with the density parameter. If it is assumed that the PSD-95 intensity reflects the density of the PSD-95 molecules packed within a synapse, then a similar conclusion to that outlined above can be drawn: the neocortical areas may be more connected than the brainstem structures, thus requiring more PSD-95 molecules within synapses to reflect greater connectivity. A very similar general pattern of PSD-95 intensity distribution was observed in mouse using the G2CSynMaP methodology. However, as expected, there were differences between specific areas. For instance, intensity within the thalamus was much higher among the 20 areas examined in humans than that observed in mouse, where 12 brain regions were compared. There may be methodological reasons behind these differences, such as different PSD-95 visualisation techniques (antibody staining vs. EGFP fluorescent protein expression), anatomical differences (the thalamus as a collection of separate nuclei vs. a specific thalamic nucleus being analysed) or varied image acquisition methods (LSCM vs SDM). The differences may also reflect species differences, but further studies would be necessary to confirm any of these theories.

Finally, our analyses revealed that the average PSD-95 synaptic puncta size, as assessed by calculating PSD-95 punctum area, ranged between $0.28 \pm 0.03$

$\mu m^2$ in BA19 to 0.188 $\pm$ 0.07 $\mu m^2$ in midbrain. If it is assumed that synaptic puncta sizes are circles, then these values would correspond to human PSD-95 synaptic diameter estimates between 546 to 489 nm. For comparison, using the same methodology, PSD-95 sizes reported in mouse varied between 0.157 $\pm$ 0.001 $\mu m^2$ in the hypothalamus to 0.127 $\pm$ 0.002 $\mu m^2$ in the cerebellum, which would correspond to approximately 447 to 402 nm. Of note, PSD-95 synaptic puncta size in the human cerebellum measured 0.216 $\pm$ 0.03 $\mu m^2$, which corresponded to 524 nm. Overall, these quantifications demonstrate that the human PSD-95 synapses were in general larger than the murine ones. Methodological differences might account for the discrepancies, but they may also reflect true species differences. Comparative EM studies tend to report on sizes of all synapses (symmetrical and asymmetrical grouped together) as represented by the length of the postsynaptic thickening, also known as synaptic apposition length. In the published EM literature, the rodent synaptic sizes tend to be smaller than in human. For instance, the mean synaptic apposition length in human temporal cortex was reported as 280 nm; in mouse barrel cortex 220 nm; and mouse visual cortex 210 nm (DeFelipe et al., 2002). Another study estimated the apposition synaptic length as 289 nm in the human hippocampal dentate gyrus inner molecular layer (Scheff and Price, 1998), which is much lower than the values we have identified (558 nm), even though our result represents a mean for the whole of hippocampus rather than one subregion. Despite the correct trends, in contrast to these numbers, the values obtained using the G2CSynMaP methodology are approximately twice as large as the EM generated data. However, the G2CSynMaP methodology relies on analysis of immunofluorescence and not true synaptic structures. Our reported size values will be overestimated as the IF signals measured are increased by a number of parameters, such as the physical size of the secondary antibodies used. This is why the methodology we are using reports on relative changes between numerous areas rather than definite absolute values based on physical measurements of synapses.

### 4.7.2 Conserved PSD-95 regional distribution

Our results have allowed us to describe several patterns of PSD-95 distribution in selected brain areas. Previous studies have demonstrated similarities in PSD-95

distribution in the mammalian brains from different species and it should be anticipated that the same general principles of synapse distribution would be conserved. Indeed, our data further confirm the validity of differential patterning of synapses within the mammalian brain by substantiating it with human data.

While PSD-95 antibody staining has allowed us to make comparisons in relation to the differential distributions of PSD-95 between the human and rodent, some of the data could have been predicted from known physiological, functional or cytoarchitectural regional heterogeneity. The caudate nucleus is perhaps the best example to illustrate this phenomenon. It has been known that the striatal complex comprises a mosaic of two chemoarchitecturally distinct compartments. This is evident in the caudate nucleus (and the putamen not described here) whereby striosome and matrix compartments exist. These compartments differ in their composition of not only most intrinsic neurochemical markers, but also in their connectivity with specific compartmental inputs and outputs (Crittenden and Graybiel, 2011). For example, the striosomes have low levels of acetylcholinesterase (AChE) activity, but matrices have high levels of AChE activity (Faull and Villiger, 1988). This acetylcholinesterase histochemistry dichotomy is mirrored in other aspects of striosome/matrix division. For instance, inputs from the thalamus tend to terminate on both dendritic spines and dendritic shafts of neurons in the striosomes, whereas within the matrix the inputs mostly terminate on shafts. This compartmental selectivity might be related to the fact that inputs from one of the intralaminar nuclei of the thalamus, the parafascicular nucleus, terminate on shafts of cholinergic interneurons located in abundance in the striatal matrix. Moreover, the main afferent connections of the striosomes are predominantly limbic-related, but the matrices are linked with associative and sensorimotor regions. Striosomal MSNs receive preferential inputs from deep cortical layer Vb, whereas in the matrix, MSNs receive inputs from cortical layers III-Va. Therefore our findings in relation to the PSD-95 distribution in the caudate nucleus have demonstrated that this underlying dichotomy is also preserved at the level of synapses, as exemplified by just one synaptic protein: low expression levels of PSD-95 were found in the striosomes wheereas high expression levels of PSD-95 are concentrated in the matrix. Importantly, any disruption or dysfunction to this striatal compartmental patterning may have profound clinical implications and could also lead

to new insights into human brain disease. For instance, it has been discovered that in HD, brains from patients who present early with mood deficits, such as depression, anxiety and compulsively repetitive behaviours, tend to show reduced cell densities in striosomes more frequently than patients who present with motor symptoms (Tippett et al., 2006). It was subsequently demonstrated that the striosome limbic loop is affected in HD patients with primarily emotional deficits as this group suffered from neuronal loss in the anterior cingulate cortex, which forms a part of the "limbic" anatomy (Thu et al., 2010). It would be interesting to determine if in HD there is a preferential loss or gain of PSD-95 synapses from the two striatal compartments.

The use of the genetically modified mouse and the SDM has allowed for greater insights into synaptic diversity. For instance, the overall moderate numbers of moderately intense PSD-95 puncta have been found in both rodent and human thalamus. However, the G2CSynMaP pipeline applied to eGFP mice allows for a more detailed assessment of synaptic diversity than is possible in human tissue. In particular, in mice, it has been demonstrated that the thalamic ventral posterior nucleus receives two sources of excitatory glutamatergic inputs, which can be distinguished by differential expression of the presynaptic VGluT proteins (Graziano et al., 2008). VGluT1 positive synapses receive inputs from the cerebral cortex, whereas VGluT2 positive synapses receive inputs from the spinal cord and the brainstem. Using the G2CSynMaP methodology, it was possible to further determine that VGluT1 synapses originating from the somatosensory cortex express PSD-95 and SAP102 proteins at their postsynaptic sites, whereas the VGluT2 synapses tend to express PSD-95 protein only (Grant lab, personal communication). This finding confirms that the diversity of DLG protein expression can be related to the identity of the presynaptic terminal. In future, it would be interesting to determine if such differential expression of DLG synapses is found in the human thalamus. For technical reasons, such an experiment would require sampling of two sections of thalamus from one case as the ventral nuclear group in the human thalamus spans a large distance. It would be necessary to sample the ventral anterior and ventral lateral nuclei receiving inputs from the brainstem in one section and the ventral posterior nucleus receiving inputs from the cortex in the second section.

### 4.7.3 PSD-95 inter-regional similarities

One of our main findings from this study is that inter-regional synapse diversity tends to follow general principles of large-scale anatomical organisation between certain brain areas, but also differs in some important global organisational properties. Examination of the PSD-95 synaptic puncta inter-regional similarities reveals that human brain regions tend to cluster based on the similarity of the synaptic diversity. In the greater context, this should not be a surprise as evidence based on healthy human brain imaging and computational studies demonstrate the existence of human structural and functional clusters, or networks, within the brain (Sporns and Betzel, 2016). Structural or anatomical networks typically use diffusion tension MRI to model the physical wiring of brain networks. Similar to our results, it has been described that there are short-range/local connections that constitute the local circuitry as well as long connections that may be associated with intrahemispheric association fibres or interhemispheric commissural fibres (He et al., 2007). In agreement with these findings, our data demonstrate that, based on PSD-95 synaptic diversity, the cortical areas tend to cluster together. For example, close association of areas within the temporal lobe, such as BA20, BA38 or BA41, or within the frontal lobe, such as BA6, BA4, BA44 and BA9, may reflect the existence of the local anatomical connections between these areas, such as arcuate or U-fibres. Although not reported within the brainstem, the existence of local circuits allowing for rapid and efficient exchange of information and processing between these regions would also apply here. The selected number of areas examined is a limitation of this study, in that it does not allow for examination of long-distance circuits. However, our results from the intercortical PSD-95 similarities may indirectly support this phenomenon. For instance, the BA17 and BA38 clustering might reflect the existence of white matter fibre tracts, such as the middle lateral fascicle, although more evidence need to be provided to support this finding. While studies examining the structural networks are often spatially compact, the functional networks can be more widely distributed and fluctuate in relation to cognitive states. The functional networks are devised from statistical analyses that do not show direct dependence on metabolic or material cost and can go beyond static descriptions of structural brain networks. In fact, functional networks in the

course of changes in an individual's cognitive state, such as learning, have been shown to undergo reorganisation (Bassett et al., 2013). In this particular study, the existence of a kind of core-periphery brain organisation with brain regions that were more and less flexible with learning was demonstrated. The authors showed that there was a relatively inflexible set of core regions, comprised mostly of visual and sensorimotor areas, which formed fixed over time and cohesive networks of brain areas. In contrast, higher-order association areas tended to be more flexible. Although highly speculative, it is interesting that our data have demonstrated that the areas with primary brain functions, such as primary visual cortex (BA17), primary motor cortex (BA4) or Broca's speech production area (BA44/45) tend to have innumerate small and dim PSD-95 synapses, which is in contrast to the associative cortical areas, such as secondary visual cortex (BA19), speech comprehension Wernicke's area (BA41/42) or the language comprehension BA38 area (Ardila et al., 2014; Pascual et al., 2015), all of which show numerous brighter and larger PSD-95 synapses.

There are some very important limitations of the human brain connectivity data and any modern human brain mapping based on MRI imaging that include: a lack of specificity, inter-subject variability and low anatomical resolution. Most *in vivo* neuroimaging studies rely on macroscopic landmarks and take gyral and sulcal patterns as criteria for parcellating the cortex. While the inference from macroscopical landmarks to cytoarchitecture may be useful, it lacks the precision of the histology. For example, comparison of high-resolution post-mortem and *in vivo* MRI images with microscopic histology led to the conclusion that the MRI signal mainly reflects the variation of the myelin density throughout the cortical areas rather than is explained by the laminar variation of the cytoarchitecture (Eickhoff et al., 2005).

Although, it is still possible to make inference from the current non-invasive imaging techniques using human data, as demonstrated above, the animal data has overcome these issues with the use of more invasive techniques. A mesoscale connectome of the mouse brain which describes a comprehensive neuronal connections using a combination of a genetic approach using adeno-associated viral vectors and two-photon tomography to image EGFP-labelled axons has been reported (Oh et al., 2014). In this study, similarity in connection patterns between cortico-cortical

connections, and also within the brainstem structures was reported. This is in agreement with the presented human PSD-95 synaptic diversity similarity patterns. The authors also demonstrated a highly interconnected pattern of the rodent cortico-thalamic network, which cannot not yet be demonstrated using our methods at the synaptic level. Nevertheless, it could be speculated that the human patterns would be of similar complexity given the high similarity in underlying anatomical heterogeneity of the thalamus. Interestingly, overall the thalamus demonstrated a mixed picture of PSD-95 synapses which were bright and numerous, but small, which is in contrast to cortical areas that tend to have either many bright and big synapses or less numerous large but dim ones. This heterogeneity of thalamic PSD-95 synapses might be the reflection of the complex underlying thalamic connectivity patterns. Another piece of evidence supporting our finding comes from previous gene expression studies in rodents (Lein et al., 2007) that similar to our data demonstrate that cortical areas share similarities between each other more closely than that seen with other brain regions. Moreover, recent analysis of rodent PSD-95 synaptome maps in our lab also demonstrated similar patterns of inter-regions similarities in line with that seen in human brain areas (Zhu et al., submitted).

Overall, our results confirm that a global organisation patterns apply at a synaptic level and, in particular, provide yet another level of evidence for a cortical subset of highly similar regions in healthy human whole-brain networks.

### 4.7.4 PSD-95 inter-cortical similarities

The inter-cortical region similarity analysis revealed that the cortices tend to cluster based on the synaptic diversity. In general, our data demonstrate that the temporoparietal regions show a higher synaptic diversity "blueprint" in comparison to the frontal regions. Also, the secondary associative areas appear more diverse than the cortices with primary brain functions, such as the motor cortex (BA4) of the frontal lobe or the visual cortex (BA17) of the occipital lobe. In contrast, the primary auditory cortex (BA41/42) of the temporal lobe appears more diverse. However, it is possible that its location within the temporal cortex, and therefore the connections with other brain areas, that is more significant than the primary cortical function, as will be

explained below.

Firstly, it may be of clinical significance that the cortical areas that have numerous, bright and large synapses are also mostly located in the temporal lobe. The temporal pole (BA38), superior temporal gyrus (BA41/42) and inferior temporal gyrus (BA20) are the Brodmann's areas that are commonly associated with human neurodegenerative disorders. Some of the neurodegenerative diseases that are known to affect these regions include corticobasal degeneration (Boxer et al., 2006), frontotemporal dementia (Rohrer et al., 2008) and Alzheimer's disease (Dickerson et al., 2009). AD commonly involves temporal areas, resulting in associated language problems, memory deficits and both visuospatial and attention disorders. On the other hand, brain diseases are beginning to be understood in the context of large-brain networks rather than single region pathologies (Seeley et al., 2009). Connections linking spatially distributed cortical areas may thus be clinically relevant and clinical symptoms can be traced to the brain connections with other areas. For instance, the visuospatial problems present in AD or indeed other brain disorders might arise from dysfunction of the middle lateral fascicle that connects the BA38 area with BA19 (Makris et al., 2013).

Secondly, a pattern of synaptic diversity might be a predictor of symptoms in disease. For instance, AD is generally considered to be a typically cortical disease with cortical signs and symptoms i.e., cognitive deterioration. Alzheimer pathology initially affects the temporal lobe with patients presenting with memory and language problems. However, in different diseases with different symptoms, different sets of areas are affected. For instance, in the behavioural variant of frontotemporal dementia, the underlying pathology also involves subcortical structures and circuits, such as cingulate gyrus, insula and frontal cortex. These areas are involved in cognitive processing, but even more in behavioural symptoms (Möller et al., 2016). Schizophrenia is yet another disorder characterised by behavioural disturbances among other symptoms, and schizophrenia has been mapped to brain structures including the dorsolateral prefrontal cortex and anterior cingulate cortex (Lewis et al., 2003; Tamminga and Holcomb, 2005).

Another interesting consequence related to the different patterns of cortical

synaptic diversity is their possible impact on at least two aspects of disease course. Specifically, the pattern of synaptic diversity, and its subsequent modification in a disease process, may be related to, firstly, the sequence of involvement of the cortical areas in the course of a disease, and secondly, the severity of symptoms of the disease. For instance, as human brain imaging has shown, the regional cortical thinning in AD correlate with severity of symptoms of the disease (Dickerson et al., 2009). It has been demonstrated that ventromedial temporal and inferior parietal cortex are affected very early in the disease course. On the other hand, regions, such as superior parietal and frontal cortex, do not show appreciable changes until symptoms are more prominent, suggesting that these areas are affected later in the course of the disease. These patterns of sequence of involvement might be related to the synaptic diversity "blueprint", whereby areas with many large and bright synapses (and therefore with a high content of different types of synaptic proteins) might also be affected early in the disease course, especially if these areas hold a great potential to lose proteins and thus to reduce their synaptic diversity potential. Similarly, it has been shown that symptom severity within the very mild AD patients correlated with medial temporal and inferior parietal thinning. However, symptom severity within a more advanced stage (Braak stage VI) correlates with thinning in frontal regions. This spacial (different areas) and temporal (different stages) dichotomy suggests temporoparietal involvement prior to frontal involvement in AD. Our data have shown that temporoparietal regions, such as BA20, BA38, BA41, BA39, are the most PSD-95 synapse diverse, and therefore it could be speculated that these areas are affected early in the disease, and are, again, the ones with most potential to reduce their synaptic diversity. On the other hand, it could be speculated that the changes in the synapse diverse areas are noticeable first as there are potentially many synaptic proteins that can be lost. In contrast, cortical areas that have fewer synapses with a more limited repertoire of proteins to start with, as implied by their small size and dim intensity, may not reveal the changes as quickly if their composition is not affected early in the disease stage or if their limited protein composition is more resilient to the disease process.

Finally, one can also speculate, that there may be disease processes that target primarily the cortical areas with the reduced synaptic diversity potential as evidenced by limited numbers of small and dim synapses. If these areas are affected early in the

disease process, the symptoms of the disorder might be the reflection of the cortical areas affected, but they would also develop early in the disease process, presumably as the synaptic proteins repertoire is modest to start with and any changes would have a great impact on the resulting phenotype.

In summary, similarity of cortical areas based on PSD-95 synaptic parameters, that are indicators of synaptic diversity, may be a reflection of potential susceptibility of groups of cortical areas to disruption in disease. The different patterns of disease susceptibility based on regional synaptic similarities can be observed in a range of human brain disorders. Cortical areas with high numbers of bright and large synapses might have a high synaptic diversity potential or "blueprint" that may be an indicator of potentially high susceptibility to disruption in pathology. On the other hand, areas with low synaptic diversity potential may occur earlier in the disease course. Lastly, the synaptic diversity "blueprint" is most probably specific to one synaptic protein, as demonstrated with the PSD-95 synaptic protein in this chapter. However, when more synaptic proteins are examined, there is a greater likehood of regional diversity reflecting the synaptic diversity of the proteins examined (Roy et al., 2018).

### 4.7.5 Inter-subject PSD-95 variability

One of the important observations of this chapter is considerable inter-individual variability for every PSD-95 synaptic parameter within the 20 human areas examined. There may be more than one explanation accounting for this finding, depending on the subregions examined.

Firstly, a consistent correspondence between Brodmann's cortical areas, as defined by macroanatomical landmarks at post-mortem tissue sampling, and each PSD-95 synaptic parameter was not identified. This variability was evident when each PSD-95 synaptic parameter was examined separately to elucidate if there is a pattern of regional distribution for all 20 areas, but even more so when each area was considered separately for each individual. The human tissue collected by the Edinburgh Brain Bank relies on identification of Brodmann's areas by macroanatomical landmarks. There are several flaws associated with this approach to tissue collection. Firstly,

there are limitations inherent in the original Brodmann maps. The original Brodmann description of cytoarchitectonic cortical areas was obtained in an observer-dependent method strongly influenced by the investigator's criteria for defining microstructural borders. Secondly, the original maps were published as schematic drawings without any additional integration of functional or structural data. Finally, the maps did not take into account the inter-individual variability of the cortical areas relative to macroscopical landmarks. In addition there are issues relating to the extrapolation from macroscopic landmarks into Brodmann's maps. This issue was previously mentioned in relation to the imaging studies (Uylings et al., 2005), but it also applies directly to tissue collection. Although brain tissue was collected by neuropathologists, the coronal sections were not sliced at identical distances and were not registered with MRI prior to dissection. This lack of precision together with the knowledge of variability of sulcal patterns in the human brain might, at least partially, have contributed to the considerable variability between the individuals. On the other hand, even studies describing modern techniques of cytoarchitectonic parcellation, which use an observer-independent delineation method of cytoarchitectonic borders and integrate imaging data to create 3 dimensional maps of human cortex based on more than one brain, have consistently reported a significant topographical subject-variability (Caspers et al., 2006). Interestingly, two classes of variability have been described in human mapping studies (Rademacher et al., 1993). The class 1 variability is not predictable from macroscopical landmarks and the class 2 variability is predictable from visible landmarks. The class 2 variability has been reported in primary neocortical areas and could play a role in the present study. Importantly, class 1 variability could also be relevant in the present study since PSD-95 distribution may not follow the known macroanatomical landmarks. In fact, mapping of the PSD-95 rodent synaptome using unsupervised computational methods has already revealed that there are many more synapse-defined areas in a mouse brain than traditionally described using macroanatomical landmarks (Zhu et al., submitted).

The underlying anatomical heterogeneity of the subcortical areas may have contributed to the inter-subject differences. For instance, the human brain tissue collection did not allow for consistent identification of thalamic nuclei. Therefore, different thalamic nuclei could have been collected for each tested control case. This

would be in agreement with the rodent data clearly illustrating that each thalamic nucleus has a different content of synapses (Zhu et al., submitted).

### 4.7.6 Limitations of the chapter

In this chapter I provided a description of a high resolution high throughput analysis of the PSD-95 IF labelled images. This allowed us to create a detailed and a comprehensive map of the PSD-95 synaptic puncta diversity of the brain regions examined based on three parameters of IF. However, several limitations of this part of my PhD thesis can be recognised.

First, although the data presented are extremely comprehensive, no other technique was used to validate the PSD-95 synaptic density measurements, such transmission electron microscopy or array tomography, and no additional data concerning molecular or functional aspects of the PSD-95 synapses being studied are provided. Therefore our human protein PSD-95 distribution maps will need to be further validated in order to fully represent PSD-95 synaptome diversity maps.

Second, the sample size is necessarily relatively small as it was chosen to match the proteomic analysis undertaken on the same cohort by other members of the Grant laboratory.

Third, as is the case for any study, I cannot exclude that the results are artefacts of an unmeasurable covariate. However, the cases are well characterised (although not matched) in terms of potential confounders, such as age, gender, cause of death, as well as tissue variables, such as PMI, HUSPIR, RNA quality and pH. Nevertheless, our cohort included 3 male brains and only one female brain. Since gender differences in synapse number has been described, additional cases of female brains would allow me to clarify if there are gender differences in the PSD-95 synaptomes.

Fourth, although as many as 20 areas were included in the analysis, it would be impossible to have complete coverage of all human brain areas and we may have missed important PSD-95 protein distribution in other brain regions.

Fifth, the data do not inform how the PSD-95 synapse distribution relates to glia and/or neurons. No attempt was made to correlate data with electron microscopy or supra resolution microscopy, which would further confirm our findings. One of the reasons behind this is a lack of such comprehensive human data on so many regions. While most studies report on one or two regions, they all differ in their techniques and methods precluding a comprehensive analysis of data. One of the important future developments would include prospective collection of tissue for further EM analysis, and standardisation of techniques. However, given the limitations of IHC and EM techniques, correlations between the datasets may not be necessary be found, as demonstrated by previous human studies (Scheff, 2003).

Finally, due to limited tissue availability, no attempts could be made to establish if the PSD-95 distribution is symmetrical in the human brain. Previous studies have demonstrated structural and functional asymmetries in several regions of human cortex, including frontal, temporal and occipital regions (Toga and Thompson, 2003) and synaptic asymmetries would therefore be expected. However, this is contrast to the recent finding of symmetrical DLG synaptome maps in mouse brain (Grant lab, personal communication). In future, it would thus be interesting to confirm or refute the asymmetric PSD-95 distribution in the human brain.

### 4.7.7 Conclusions

Taken together, this chapter demonstrates PSD-95 protein distribution heterogeneity in control human brains. Our PSD-95 distribution map adds to the knowledge of regional differences in the control human brain. Moreover, it serves as a comprehensive baseline dataset with which to compare PSD-95 distribution and diversity in other brain areas, and can be applied to other species and to human pathological changes associated with disease states.

# 5 PSD-95 synaptome map reorganisation in disease

## 5.1 INTRODUCTION TO HIPPOCAMPAL PSD-95 SYNAPTOME MAPPING

Human brain mapping has been a century-old goal of neuroscientists who are eager to reveal the intricacies of the workings of the human brain. However, the first ever human connectome map of cerebral cortex based on architecture, function, connectivity and topography has only recently been created using a high-quality neuroimaging and tissue staining approach (Glasser et al., 2016). Despite this, development of a high-resolution tissue-based cellular-scale map has been somewhat more challenging primarily due to the complexity and the enormous size of the human brain in comparison to any other living organism (DeFelipe, 2015). Unsurprisingly, several attempts at producing tissue-based human maps have been made including, Brodmann's description of cytoarchitecture developed by assessing Nissl stained sections in 1909. More than a century later, a second cellular-scale Nissl-based map of just one human brain was published that took 9 years to create using the most advanced bioinformatics available at that time (Amunts et al., 2013). Recently, a more detailed map of a female human brain was published based on neuroimaging, high-resolution Nissl histology (1um/pixel) and chemoarchitecture (Ding et al., 2016). Needless to say, a subcellular-scale synaptic map of human brain has never been attempted.

This chapter will describe a pilot study of creating a first ever subcellular-scale PSD-95 synaptic map of the human hippocampus based on the G2CSynMaP methodology described in Chapter 2.11. Apart from concentrating my efforts on only one human brain area, namely the hippocampus, the other main difference between the current and previous chapter lies in the use of a different imaging method. A high-throughput single-synapse resolution SDM is utilised in order to image hippocampal coronal sections in their entirety. This method will enable the creation of the most comprehensive ever human hippocampal synaptome maps based on millions of synapses.

Studies in human have revealed that the hippocampus is involved in the formation of new memories involving episodic and autobiographical events, time and place, in addition to acquisition and storage of semantic memories associated with ideas, meaning, and concepts (Hassabis et al., 2007; Ekstrom and Bookheimer, 2007;

Chadwick et al., 2010). Moreover, together with other medial temporal structures, the hippocampus is involved in the formation of long-term declarative memories. This cognitive processing occurs via various connections with multiple brain regions; hippocampal neuronal connections include an excitatory trisynaptic circuit, composed of the perforant pathway, mossy fibres, and Schaffer collaterals, running from dentate granule cells to CA3 and to CA1 pyramidal neurons, which further connect to extrahippocampal limbic and neocortical neuronal circuits (Frotscher et al., 2006; Witter, 2007; Lu et al., 2013). The major input to the hippocampus (CA1-3) and the dentate gyrus is from the entorhinal cortex (the perforant pathway) (Isokawa et al., 1993). The dentate gyrus projects to the CA3 field of the hippocampus via the mossy fibres (Lim et al., 1997), and CA3, in turn, projects to CA1 (via axonal processes called Schaffer collaterals) (Szirmai et al., 2012).

The aims of this chapter are two-fold. Firstly, I aim to describe human synapse diversity in 16 hippocampal subregions using the PSD-95 IF puncta parameters (density, intensity and size) described earlier. I will visualise this diversity by creating hippocampal synaptome maps. Secondly, using the same methodology, I aim to create synapse diversity synaptome maps in a diseased hippocampus. I hypothesise that a disease state will change the synaptome maps. I have generated the first synaptome maps of disease-free and disease-burdened human hippocampus. The findings reveal organisation of synaptic diversity within the hippocampal subregions, which are changed in pathological states, potentially providing a substrate for the observed clinical phenotype.

## 5.2 SUMMARY OF METHODS USED

In order to describe the diversity of PSD-95 synapses in the human hippocampus, post-mortem tissue was immunofluorescently stained as described previously in Chapter 2.5. Fourteen posterior hippocampi from control cases were processed for immunohistochemistry, imaged with the SDM and analysed using the Ensemble method. Indirect fluorescence from the secondary antibody attached to the PSD-95 primary antibody was acquired using the same sets of acquisition parameters with an oil immersion lens (100x, NA1.4). Images were acquired in two-dimensional

planes only as acquisition of three-dimensional datasets would have been prohibitively large in terms of data size. Several thousands of images were generated for each hippocampus and a dataset of a several hundred Gigabytes (GB) was stored for each image (Table B.1 on page 314). The individual puncta detection was achieved using the Ensemble method that generated results describing puncta population per unit area (density) as well as the individual puncta characteristics, such as punctum intensity and size. At the same time, the stitched montages of the hippocampal images were delineated for 16 hippocampal subfields according to the on-line reference Allen Human Brain Atlas (http://human.brain-map.org) and an atlas of the human hippocampus (Duvernoy, 1988) with the help of Nissl images for each individual hippocampus to account for individual differences between the cases (Figure 5.1 on page 193). Mean punctum parameters were then calculated for each anatomical subfield delineated and represented as an overview heatmap.

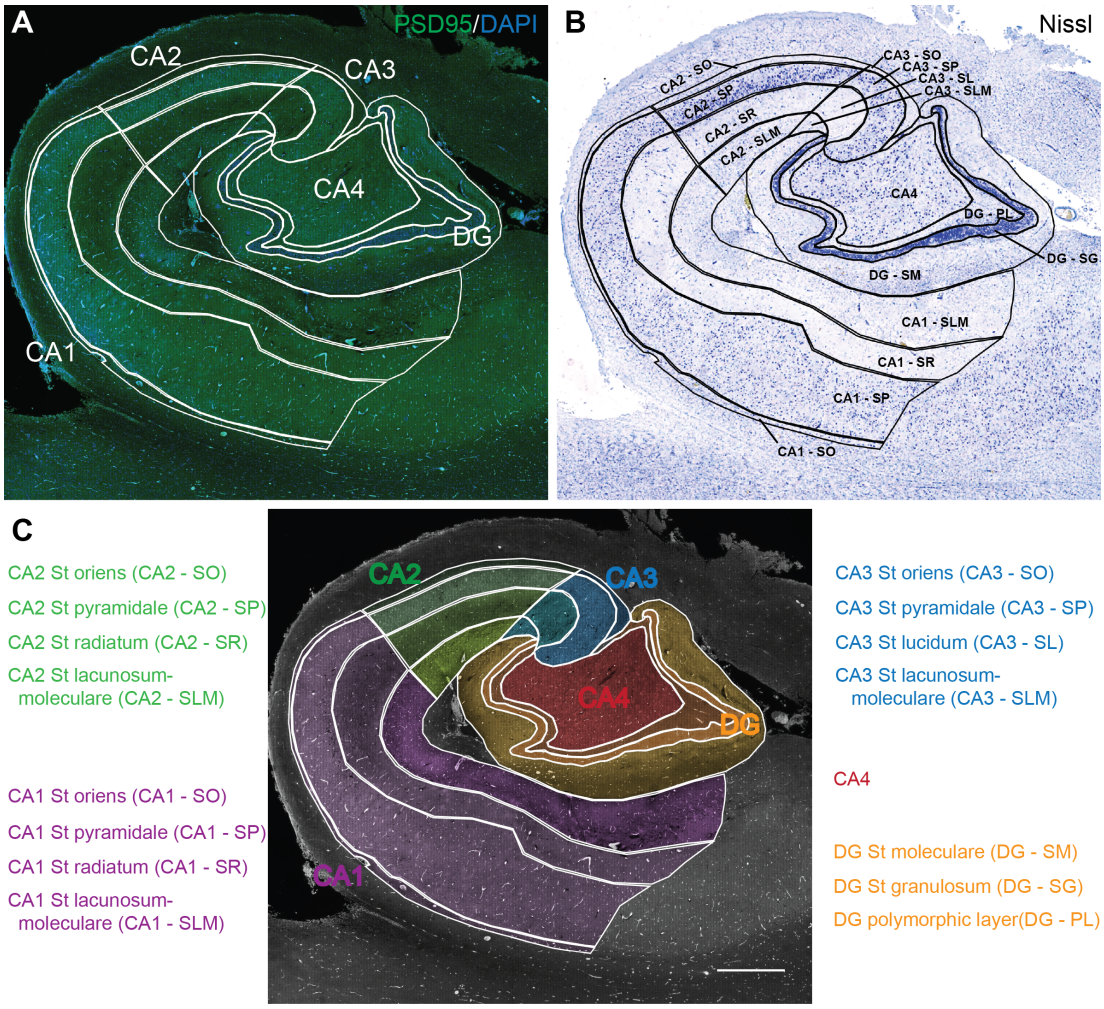


**Figure 5.1 Delineations of human hippocampal subregions.**
Low-power photomicrographs of a posterior human hippocampus demonstrating delineation of 16 subregions, to illustrate the main areas (CA1-4 and DG) and major cellular layers, using stitch images acquired by the SDM and created in the Matlab software (A and C), and a Nissl-stained section acquired with the Axio scan (B). All abbreviations used in panel B are displayed in panel C. Scale bar 1 mm. The hippocampal section comes from case SD40/14. Abbreviations: St, stratum; CA, Cornu Ammonis; CA1-SML, CA1 - Stratum Moleculare-Lacunosum; CA1-SR, CA1 - Stratum Radiatum; CA1-SP, CA1 - Stratum Pyramidale; CA1-SO, CA1 - Stratum Oriens; CA2-SML, CA2 - Stratum Moleculare-Lacunosum; CA2-SR, CA2 - Stratum Radiatum; CA2-SP, CA2 - Stratum Pyramidale; CA2-SO, CA2 - Stratum Oriens; CA3-SML, CA3 - Stratum Moleculare-Lacunosum; CA3-SL, CA3 - Stratum Lucidum; CA3-SP, CA3 - Stratum Pyramidale; CA3-SO, CA3 - Stratum Oriens; CA4, Cornu Ammonis 4; DG-SM, DG - Stratum Moleculare; DG-SG, DG - Stratum Granulosum; DG-PL, DG - Polymorphic Layer.

## 5.3 DISTRIBUTION OF PSD-95 ACROSS CONTROL HUMAN HIPPOCAMPUS

Detailed anatomy of the human hippocampus has been described previously in Chapter 4.4.1. In general, among human regions, the hippocampus is an area rich in glutamatergic PSD-95 synapses as described previously in Chapter 4.5.1.

Similar to previous findings described using LSCM, detailed imaging using SDM confirmed that the hippocampus contained many PSD-95 IR synaptic puncta. The highest intensity of staining was present in the CA1, followed by CA3, CA4 with CA2 subregion showing the dimmest puncta. Bright PSD-95 IR was generally observed within the dendritic layers of the hippocampus, including *stratum radiatum* and *stratum lacunosum-moleculare* as well as the *molecular layer* of the DG. The *stratum oriens* layer is thin in human hippocampus and difficult to assess on inspection given the brightness of the adjacent pyramidal cell layer in all 3 CA regions. The puncta observed in the neuropil of the pyramidal cell layer of CA3 and CA4 subregions appeared very similar in size, intensity and pattern of staining: they were large, moderately bright, and formed a loose, rosette-like pattern of packing typical of thorny excrescent synapses of these regions. This was in contrast to much denser, but smaller and brighter PSD-95 puncta in the CA1 subregion. Finally, while no staining was seen in the granule cells of the dentate gyrus, the cell bodies of the pyramidal cell layer of CA1, CA2 and CA3 subregions did demonstrate diffuse and moderate staining, as observed previously with LSCM and described in Chapter 4.4.1. Representative PSD-95 IR distribution in a control human hippocampus is presented in Figure 5.2 on page 195.

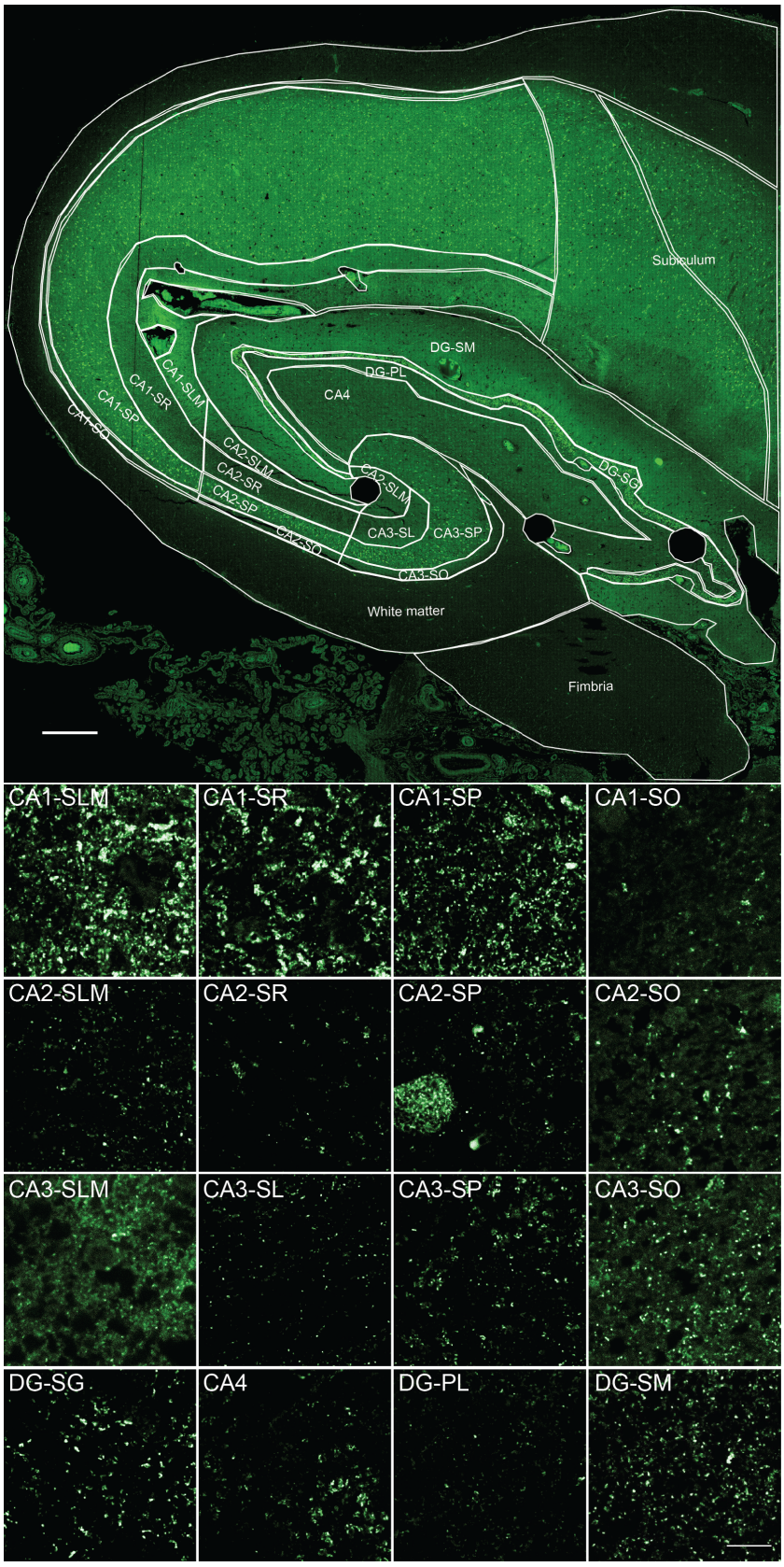


**Figure 5.2 Detailed PSD-95 distribution in the control hippocampus.** Representative SDM-acquired images showing PSD-95 IR pattern of labelling in 16 hippocampal subregions from a control case SD42/13. Scale bars: 1 mm and 10 $\mu$m. Abbreviations - see Figure 5.1 on page 193.

## 5.4 QUANTIFICATION OF PSD-95 ACROSS CONTROL HUMAN HIPPOCAMPUS

Quantification of PSD-95 synaptic puncta parameters based on images obtained with SDM further confirms the existence of subregional heterogeneity between the 16 hippocampal subregions analysed. The highest regions of PSD-95 IR density were observed in the CA4 (mean $\pm$ SD: 85.20 $\pm$ 7.55 puncta per 100 $\mu m^2$), followed by CA2 (79.9 $\pm$ 9.98), CA1 (78.9 $\pm$ 98.95), CA3 (76.9 $\pm$ 8.36) and the dentate gyrus (55.1 $\pm$ 8.15). Among cellular layers, the *stratum pyramidale* had the highest numbers of PSD-95 puncta for all subregions with very comparable numbers (CA1 - SP, 83.99 $\pm$ 10.02; CA2 - SP, 84.42 $\pm$ 12.06; CA3 - SP, 84.10 $\pm$ 9.32 and CA4, 85.20 $\pm$ 7.55). The existence of CA4 in humans remains controversial and the region is not described in animal hippocampi. Our data demonstrate that CA4 very closely resembles CA3 pyramidal layer, indicating that at a PSD-95 synaptic protein level, these two subregions appear very similar. Our findings are in contrast to the rodent data which indicate that CA1 is the highest PSD-95 density region and the cell body layers (CA3-SP, CA2-SP and CA1-SP and DG-GL) have the lowest density and intensity of PSD-95 expression. One important difference between the rodent and human data is the fact that the antibody used on human tissue also labels the pyramidal neuronal cell bodies, the location of which was not described in the genetically modified rodents. The pyramidal cell bodies' PSD-95 synaptic puncta detected and counted using the Ensemble method would have been counted, therefore overestimating the human numbers in comparison to rodents. Similar to the rodent data, however, the CA1 region contained more PSD-95 puncta in comparison to CA3 area. Detailed analysis of subregions further revealed that *stratum radiatum*, which contains proximal apical dendrites from pyramidal neurons consistently shows the second highest density of PSD-95 synapses in the CA1-3 areas (CA1 - SR, 81.68 $\pm$ 11.07; CA2 - SR, 79.81 $\pm$ 9.99; CA3 - SL, 80.59 $\pm$ 10.15). The other dendritic layers, *stratum oriens* and *lacunosum - moleculare* containing basal and distal apical dendrites, respectively, show similar numbers of PSD-95 synapses in the CA1-3 areas. Similar to the rodent data, subregions of the dentate gyrus did not show many PSD-95 synapses with the lowest numbers being quantified for DG-PL (41.54 $\pm$ 4.62) and DG-SG (55.67 $\pm$ 13.61). However, as expected the dendritic layer of the dentate gyrus, the DG-SM (68.10 $\pm$

16.41) had the highest number of PSD-95 puncta in the dentate gyrus, and they were of a similar number to PSD-95 puncta in the CA3-SML (67.51 $\pm$ 16.03).

With regards to PSD-95 puncta intensity, the trends observed are more difficult to explain, but the brightest PSD-95 synapses were observed in the CA1-SP (36423 $\pm$ 4585 a.u.) and the dimmest in the CA3-SML (24249 $\pm$ 6235). Interestingly, the PSD-95 puncta of *stratum oriens* showed a relatively consistent pattern of being dim in all three CA areas.

Finally, regarding the PSD-95 size, there was very little variation between the subregions with the largest PSD-95 synapses being quantified for CA1-SML (0.1310 $\pm$ 0.0064 per $\mu m^2$) and the smallest for CA3-SML (0.1109 $\pm$ 0.0180). Although large synapses were observed in the human pyramidal cell layers, this was not reflected in the quantification. This could be due to the fact that there were numerous small pyramidal cell body PSD-95 puncta resulting in the overall caculated PSD-95 synaptic puncta size being smaller than the actual observed puncta size from images of these subregions.

In summary, I have described the diversity of PSD-95 synaptic puncta expression in the hippocampal subfields. This complexity of PSD-95 expression most likely reflects differential expression patterns of individual synaptic puncta parameters, which highlights the importance of detecting synaptic proteins at the level of individual synapses. Quantification of PSD-95 synaptic puncta parameters is displayed in Figure 5.3 on page 198 and values are shown in Table 5.1 on page 223.

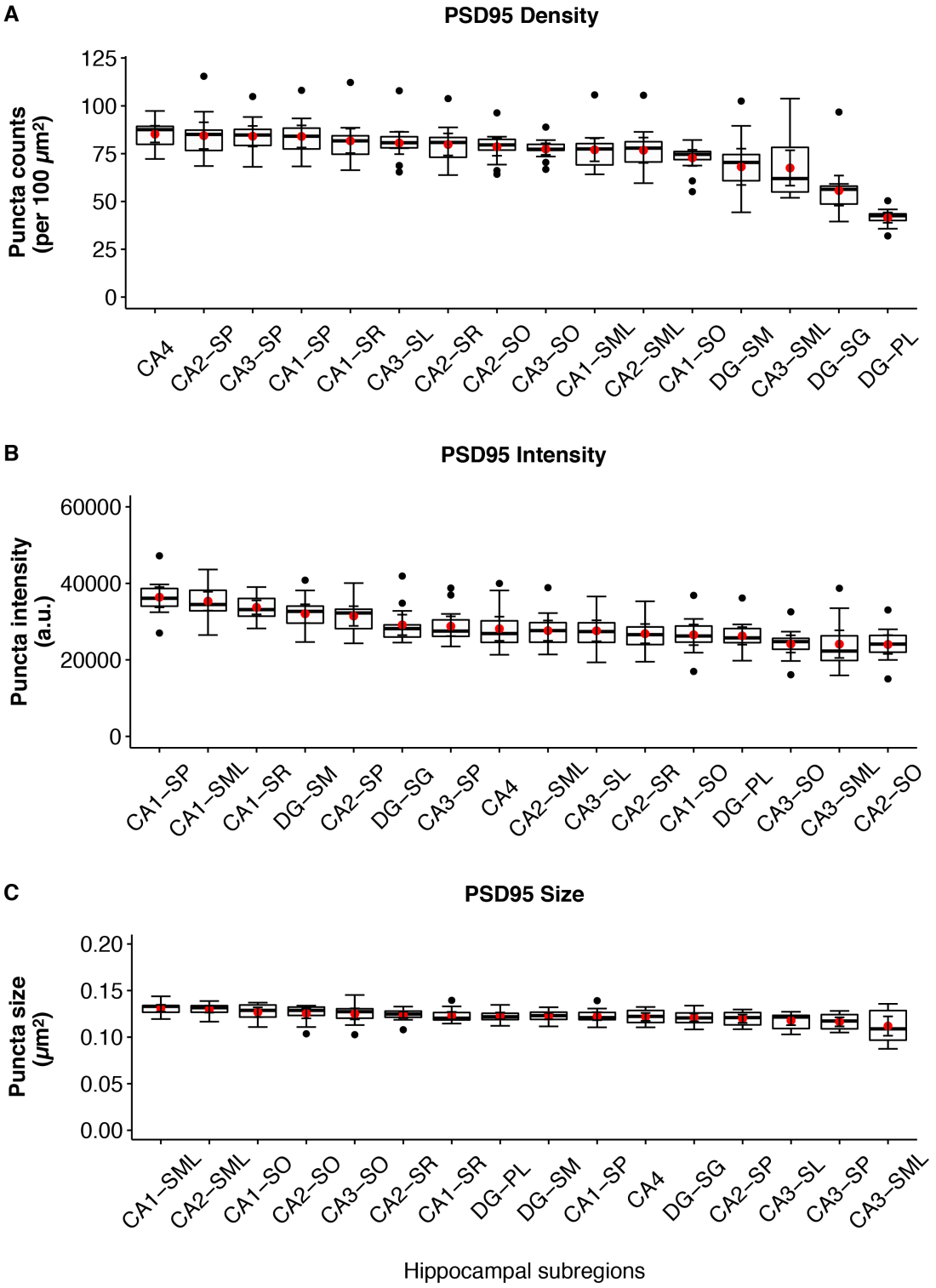


**Figure 5.3 Subregional distribution of hippocampal PSD-95 puncta parameters in the control SDM cohort.**

Boxplots showing quantification of PSD-95 synaptic puncta in 16 human hippocampal subregions from 14 control cases. Data are subdivided into 3 parameters as PSD-95 punctum density (A), punctum intensity (B) and punctum size (C). Within each boxplot, horizontal lines show the medians; box limits indicate the interquartile range (IQR) (inferior or 1st quartile range = 25th percentile, and superior or 3rd quartile range = 75th percentiles) as determined by R software; whiskers are defined by Tukey

and extend to data points that are less than 1.5x IQR away from the 1st/3rd quartile; outliers are represented by black circles. Red circles represent mean of 14 cases ± SD, which is represented as a smaller error bar. Boxplots for each parameter are ordered from the highest to the lowest mean values. Abbreviations - see Figure 5.1 on page 193.

---

## 5.5 PSD-95 GENDER DIFFERENCES IN HUMAN CONTROL HIPPOCAMPUS

The data allowed me to assess whether distribution of PSD-95 synaptic parameters differs between men and women. In general, no significant differences could be observed in the 16 hippocampal subregions from the control cases for PSD-95 synaptic puncta density, intensity and size (Table B.6 on 319 and Figure 5.4 on 200). The only exception being one significant difference for PSD-95 intensity in the CA2 stratum oriens, whereby women had significantly lower PSD-95 puncta intensities than men. In fact, a consistently lower density of PSD-95 puncta was observed in women in all but two subregions (CA1 stratum oriens and polymorphic layer of the dentate gyrus). This trend was also seen for intensity of PSD-95 synaptic puncta whereby our analysis showed that all subregions to have dimmer PSD-95 puncta in women. In contrast, women tended to have bigger PSD-95 synapses in comparison to men in some regions, but not all. Although these trends were observed, the actual differences were not statistically significant apart from the one comparison detailed above.

As gender differences have been reported in relation to neuronal density in other brain areas (Witelson et al., 1995; Rabinowicz et al., 1999), a subset of control cases matched for age had their neuronal densities counted using the stereology method described in Chapter 2.12. For the cases analysed, no significant differences were found between women and men regarding either PSD-95 synaptic or the neuronal densities (Table B.7 on page 320 and Figure 5.5 on page 201).

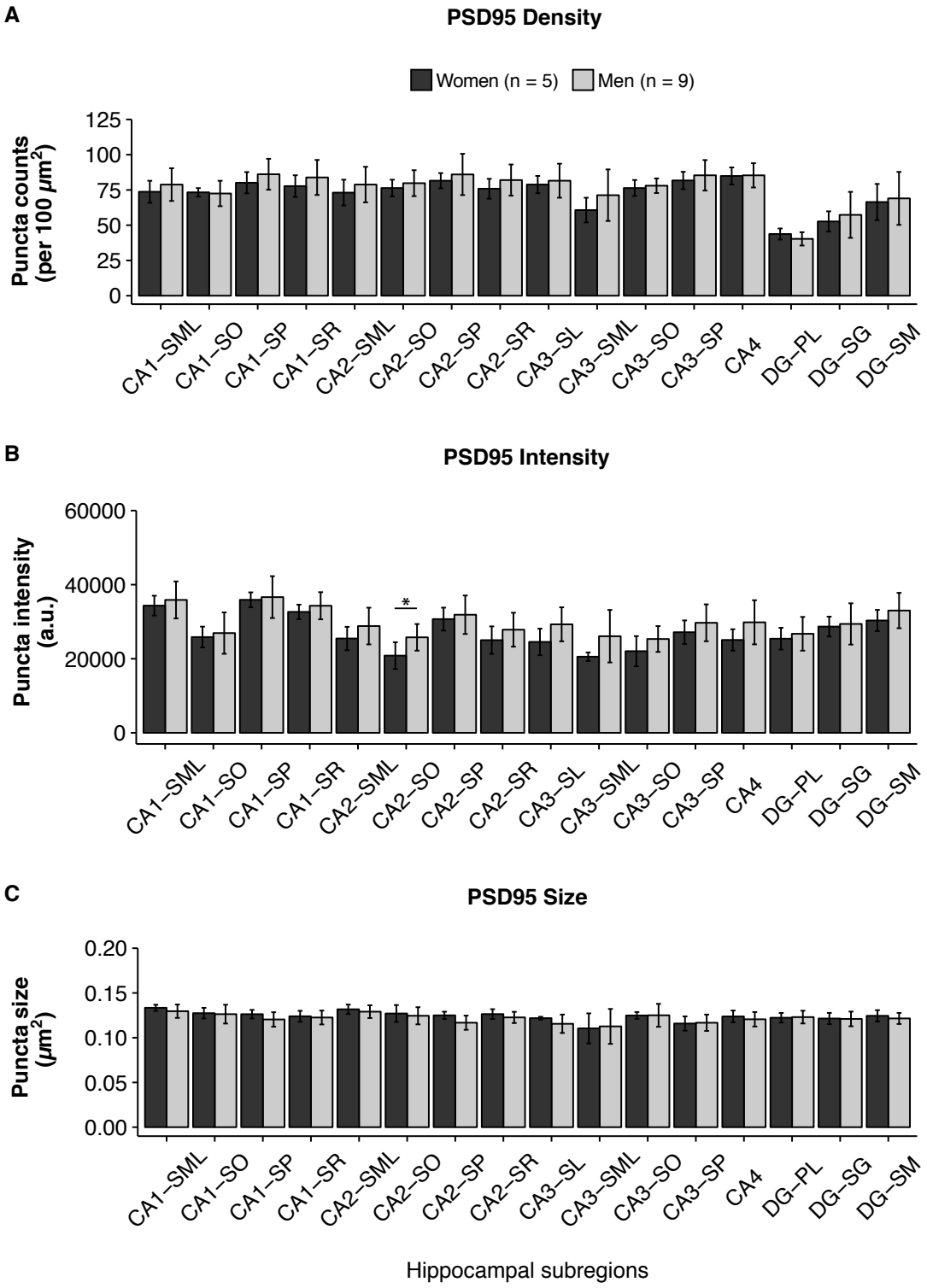


**Figure 5.4 Gender differences in human control hippocampal PSD-95.**
Bar graphs showing a general lack of significant gender differences in PSD-95 synaptic puncta parameters in 16 human hippocampal subregions from 14 control cases. A significant gender difference was obtained for only one subregion: the CA2 stratum oriens. Data are subdivided into 3 parameters: PSD-95 punctum density (A), punctum intensity (B) and punctum size (C). Data represent mean ± SD. Abbreviations - see Figure 5.1 on page 193.

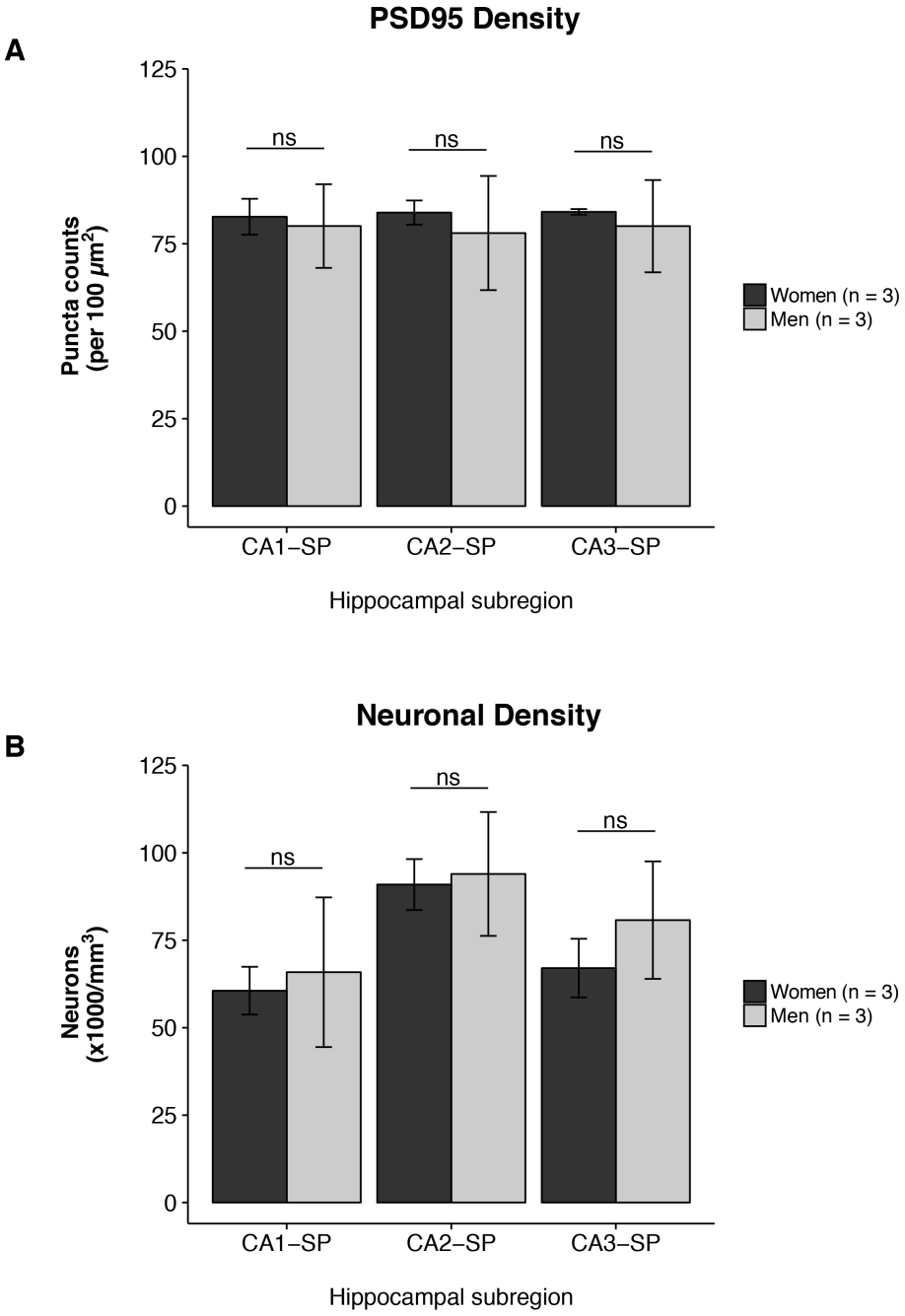


**Figure 5.5 Gender differences in PSD-95 synaptic and neuronal densities in human control hippocampus.**

Bar graphs of the PSD-95 density and neurons in men and women in three hippocampal strata pyramidalae from control cases. (A) Bar graphs showing the PSD-95 densities (mean ± SD) in three strata pyramidalae (CA1, CA2 and CA3) demonstrating that there are no significant differences between women and men. Data were obtained using the Ensemble method. (B) Bar graphs showing the neuronal densities (mean ± SD) in the same hippocampal subregions as for the PSD-95 synaptic densities showing that there are also no significant gender differences. Data were obtained using stereology technique described in Chapter 2.12. Statistical comparisons were performed by using the unpaired Student t test with the aid of the Prism statistical package. The control cases used were as follows: women (SD10/15, SD63/13 and SD35/14) and men (SD23/13, SD24/15 and SD32/13).

## 5.6 PSD-95 LATERALITY DIFFERENCES IN HUMAN CONTROL HIPPOCAMPUS

The data also allowed me to assess whether distribution of PSD-95 synaptic puncta parameters differs between left and right hippocampus. No significant differences were observed in the 16 hippocampal subregions from the control cases for PSD-95 synaptic puncta density, intensity and size (Table B.8 on 321 and Figure 5.6 on 203). However, in agreement with imaging studies, I observed rightward asymmetry in the hippocampal subregions. In particular, the numbers and intensity of PSD-95 puncta displayed a trend of being more numerable, brighter but slightly smaller on the right side. In contrast with previous research, none of the differences I report are statistically significant.

As an absence of left/right asymmetry for neuronal densities has previously been reported in control hippocampus (Zaidel et al., 1997), I used the previously introduced subset of control cases matched for age to estimate their neuronal densities estimated using the stereology method described in Chapter 2.12. For the six cases analysed using stereology, there were no significant differences found between left and right side with regards to the PSD-95 synaptic densities or the neuronal densities (Table B.9 on page 322 and Figure 5.7 on page 204). This is in agreement with previous studies reporting no differences between neuronal cell densities in the two sides of the brain (Mouritzen Dam, 1979; Zaidel et al., 1997).

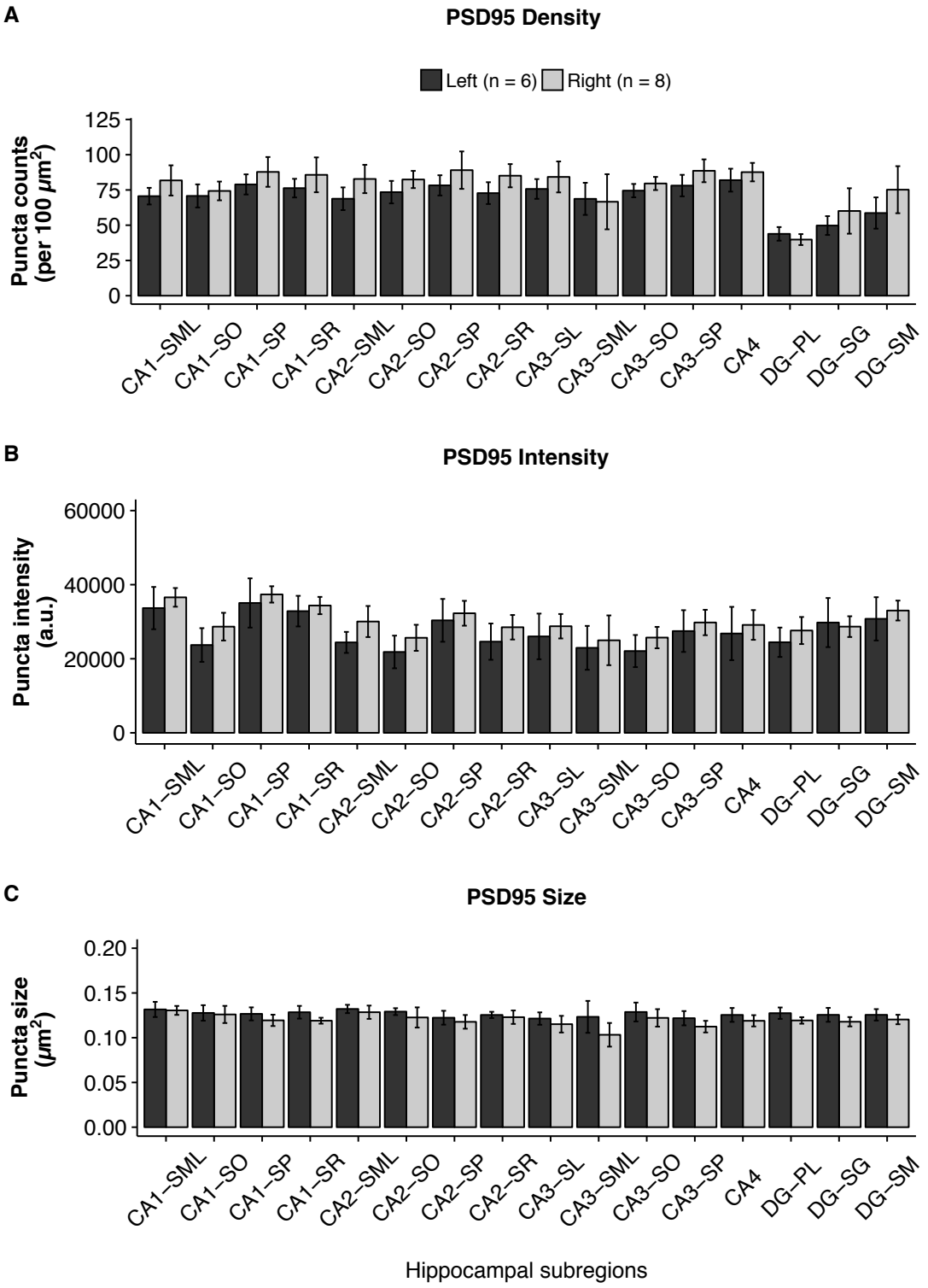


**Figure 5.6 Absence of left/right asymmetry in the human control hippocampal PSD-95 synaptome map.**

Bar graphs showing a lack of significant left/right differences in PSD-95 synaptic puncta parameters in 16 human hippocampal subregions from 14 control cases. Data are subdivided into 3 parameters: PSD-95 punctum density (A), punctum intensity (B) and punctum size (C). Data represent mean ± SD. Abbreviations - see Figure 5.1 on page 193.

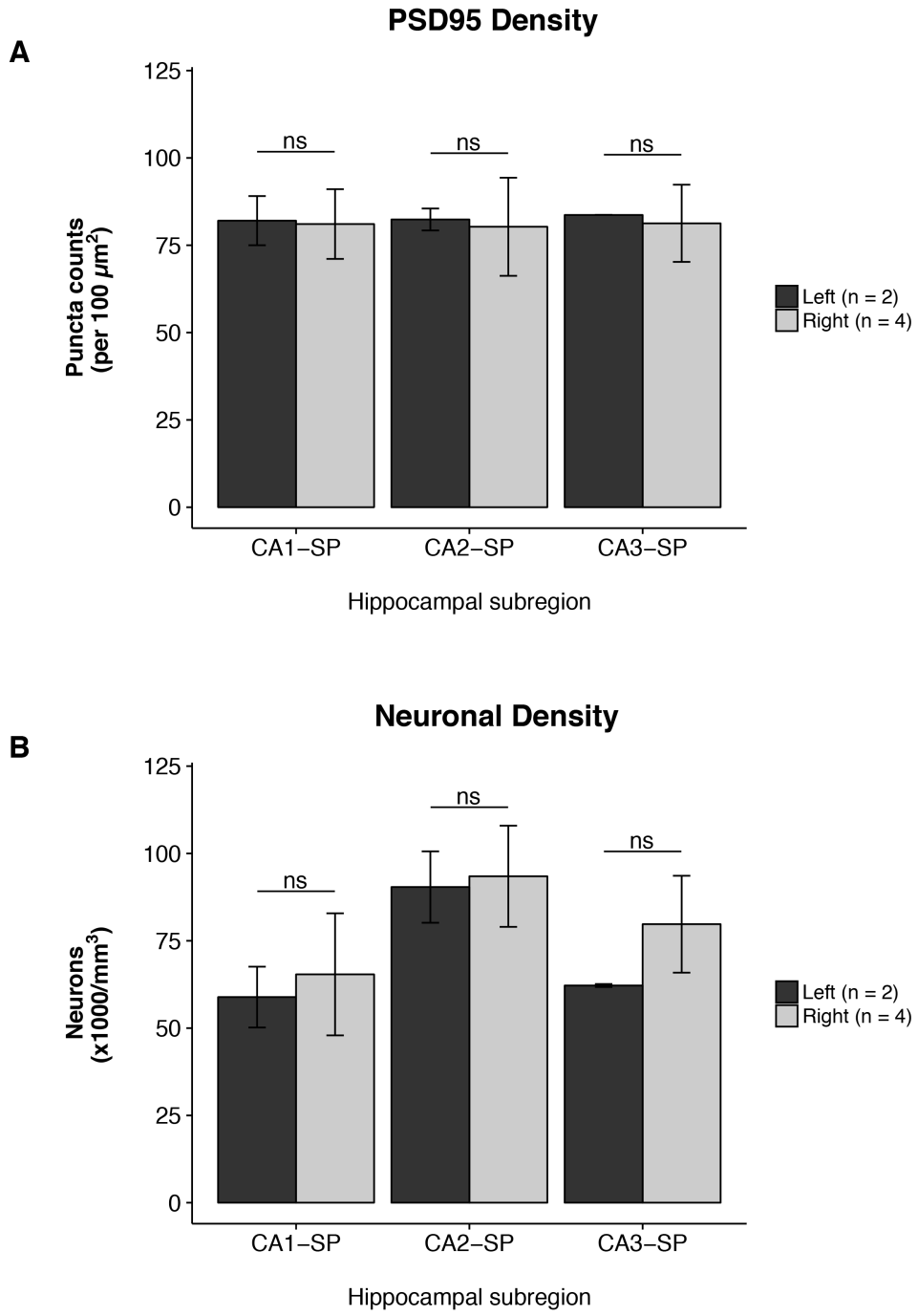


**Figure 5.7 Laterality differences in PSD-95 synaptic and neuronal densities in human control hippocampus.**

Bar graphs of the PSD-95 density and neurons in men and women in three hippocampal strata pyramidalae from control cases. (A) Bar graphs showing the PSD-95 densities (mean ± SD) in three strata pyramidalae (CA1, CA2 and CA3) demonstrating that there are no significant differences between left and right side. Data were obtained using the Ensemble method. (B) Bar graphs showing the neuronal densities (mean ± SD) in the same hippocampal subregions as for the PSD-95 synaptic densities showing that there are also no significant left/right differences. Data were obtained using stereology technique described in Chapter 2.12. Statistical comparisons were performed by using the unpaired Student t test with the aid of the Prism statistical package. The control cases used were as follows: left (SD63/13 and SD35/14) and right (SD23/13, SD10/15, SD24/15 and SD32/13).

## 5.7 OVERVIEW OF PSD-95 CHANGES IN DISEASED HUMAN HIPPOCAMPUS

Having quantified PSD-95 synapses in normal hippocampus, we next examined the effect of a pathological state on PSD-95 synapses in the human hippocampus. An overview of the frequency distributions between the controls and the two AD stages examined demonstrated that there are significant differences in PSD-95 synaptic puncta parameters in diseased human hippocampus compared with the controls (Figure 5.8 on page 207 and Tables B.10 and B.11 on page 323).

In general, and as expected, there is a loss of PSD-95 synaptic puncta in AD in comparison with the control group. The mean ($\pm$ SD) count of PSD-95 puncta decreased from 74.7 ($\pm$ 8.31) per 100 $\mu m^2$ in controls to 47.42 ($\pm$ 2.72) in early Alzheimer's type pathology and to 25.86 ($\pm$ 3.08) in late Alzheimer's type pathology. There appears to be no overlap between individuals within each examined group with a progressive loss of PSD-95 synapses as the two AD stages advance. The PSD-95 density parameter appears to be well segregated to the three experimental groups. Notably, the PSD-95 density data are not normally distributed within each group with the controls showing most variations in PSD-95 counts among the individuals. In AD, the individuals become less heterogeneous when PSD-95 synaptic counts are concerned.

Regarding PSD-95 intensity, the PSD-95 puncta tend to become dimmer as the disease progresses. The mean ($\pm$ SD) intensity of PSD-95 puncta decreased from 28887 ($\pm$ 3873) in arbitrary units in controls to 20608 ($\pm$ 1601) in early Alzheimer's type pathology and to 12726 ($\pm$ 3555) in late Alzheimer's type pathology. However, the distinction between the groups is not as clear as for the PSD-95 counts. The data are still not normally distributed, but there is a greater variation between the individuals within each group in comparison to the PSD-95 count parameter. While it is possible to separate the controls and the late Alzheimer's type pathology stage cases based on the PSD-95 intensity, the individuals within early Alzheimer's type pathology group fall in-between the control and the late Alzheimer's type pathology cases.

Finally, the PSD-95 puncta size parameter shows different characteristics from

the other two parameters. PSD-95 puncta are generally smaller in early Alzheimer's type pathology, but as the pathology progresses, the puncta become bigger. The mean ($\pm$ SD) size of PSD-95 puncta decreased from 0.1226 ($\pm$ 0.006) $\mu m^2$ in controls to 0.0895 ($\pm$ 0.003) in early Alzheimer's type pathology but then increased to 0.1007 ($\pm$ 0.007) in late Alzheimer's type pathology, although it remained smaller than in controls. The PSD-95 size parameter appears to differentiate the individuals in the early Alzheimer's type pathology stage from the controls. The late Alzheimer's type pathology cases include individuals with greater PSD-95 sizes variation than the remaining two groups. Last but not least, unlike the other two parameters, the size parameter tends to show a normal distribution for all three experimental groups.

Overall, these data demonstrate several interesting points. While it is apparent that hippocampal PSD-95 synapses are adversely affected in AD, our data further suggest that different populations of PSD-95 synapses, as represented by the three PSD-95 parameters, may be affected differently in this disease.

In keeping with the existing literature (Sultana et al., 2010), our data confirm that there is a loss of PSD-95 synapses in the human hippocampus. Moreover, in agreement with the published data, the losses in PSD-95 numbers increase with the disease progression as represented by the Braak stages. However, the PSD-95 synaptic parameters appear to posses different discriminatory qualities at different disease stages. The intensity parameter differentiated the late Alzheimer's type pathology stage individuals from the controls, while the size parameter separated the early Alzheimer's type pathology stage cases from the controls. These attributes may be a reflection of varying responses of different populations of PSD-95 synapses to insults occurring at different stages for a given pathological process. For instance, it could be speculated that in the early AD stage large PSD-95 synapses are preferentially lost and that at the later stages, a compensatory mechanism takes place resulting in larger-sized synapses. Similarly, the late Alzheimer's type pathology stage may be associated with a substantial loss of a population of bright synapses that are more resistant to the disease insults at early Alzheimer's type pathology stages.

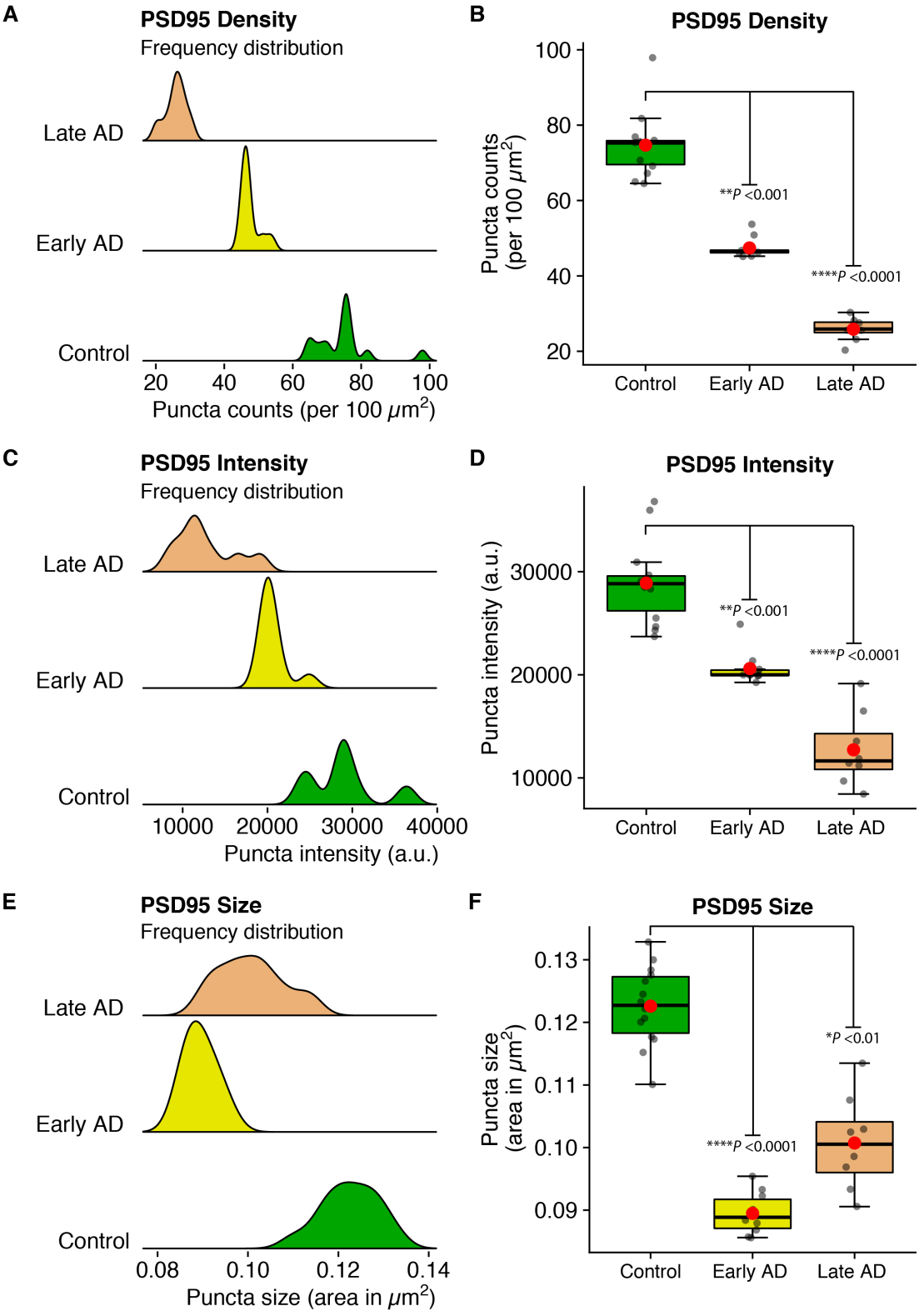


**Figure 5.8 Overview of hippocampal PSD-95 changes in AD disease.**

Frequency density plots and box plots demonstrating changes in PSD-95 synaptic puncta parameters in AD as compared to the controls. **(A)** There is a loss of PSD-95 synaptic puncta in AD in comparison with the control group. **(B)** This loss compared with the controls is statistically significant as assessed with Kruskal-Wallis rank sum test for non-parametric data with a Bonferroni-type p-value adjustment ($\chi^2$ = 27, df = 2, p-value = 1.371e-06) with post hoc Dunn's multiple comparisons tests denoted

with asterisks. **(C)** PSD-95 puncta become dimmer as the disease progresses. **(D)** These changes are also significant as demonstrated with Kruskal-Wallis test ($\chi^2$ = 26.204, df = 2, p-value = 2.041e-06) with post hoc Dunn's multiple comparisons tests denoted with asterisks. **(E)** PSD-95 puncta are generally smaller in early AD, but as the disease progresses, the puncta become bigger. **(F)** Similarly to the previous parameters, these changes were found significant according to Kruskal-Wallis test ($\chi^2$ = 25.964, df = 2, p-value = 2.302e-06) with post hoc Dunn's multiple comparisons tests denoted with asterisks. Plots are based on mean values for all regions per each individual (n = 32 cases in total, of which controls = 14, early AD = 10 and late AD = 8). For clarity, frequencies are calculated using $stat\_joy$ function in *ggjoy* package in R. The $stat\_joy$ estimates the data range and bandwidth for the density estimation from the entire data at once, rather than from each individual making the plots look more uniform. Within each boxplot, horizontal lines show the medians; box limits indicate the interquartile range (IQR) (inferior or 1st quartile range = 25th percentile, and superior or 3rd quartile range = 75th percentiles) as determined by R software; whiskers are defined by Tukey and extend to data points that are less than 1.5x IQR away from the 1st/3rd quartile. The individual data points are shown as grey dots. Red circles represent mean for each group.

---

Surprisingly, the direction of changes was not the same for the three parameters, with the size parameter displaying opposite effects to the remaining two. As suggested, this may be due to the existence of a compensatory mechanism for a subset of PSD-95 synapse populations, e.g., smaller synapses, but not for others.

My results stress the importance of thorough neuropathological staging for detection of changes in PSD-95 synaptic diversity. Certain changes may not be apparent if different stages of the pathological processes are not well defined.

Finally, although hippocampal data tend to be reported consistently in AD, discrepancies in other areas have been reported. This may be explained by the existence of synaptic diversity and thus different synapse populations being affected in different locations. However, if information on synaptic diversity is not available and only one aspect of synapses, such as count rather than diversity, is being examined, any conclusions drawn may not be a true reflection of synaptic changes.

## 5.8 DETAILS OF PSD-95 CHANGES IN DISEASED HUMAN HIPPOCAMPUS

Having detected changes in hippocampal PSD-95 synapses in cases with Alzheimer's type pathology of different stages, I next examined in detail the effect of this disease on PSD-95 synapses in the 16 hippocampal subregions. I present results for changes in PSD-95 synapses in 16 hippocampal subregions at two different stages of Alzheimer's type pathology, the early Braak stage II and the late Braak stage VI, for three synaptic parameters. Neurons and synapses are progressively lost in AD in tandem with the spread of tau pathology throughout the brain (Ingelsson et al., 2004). Moreover, synaptic loss in AD can occur regionally and it appears disproportionately large in the hippocampus (Honer et al., 1992). However, detailed synaptic changes across the hippocampal subregions have not been described. I anticipate that Alzheimer's type pathology will contribute to hippocampal changes in PSD-95 synaptic parameters, but that the effect might differ across hippocampal subregions. Figure 5.9 on page 210 demonstrates an overview of PSD-95 regional changes for all three parameters in the three experimental groups. As expected, the individual regional changes differ between the subfields tested, but the overall patterns of changes appear very similar except for a persistently consistent difference in one area, namely the CA3 stratum moleculare-lacunosum (CA3-SML). Remarkably, the patterns of changes in PSD-95 synaptic parameters for this one region clearly stand out from the remaining hippocampal subfields. In addition, a second subregion appears to differ from the others, but the different pattern is present only for the PSD-95 density parameter. This additional area is the pleomorphic layer of the dentate gyrus, in which the loss of PSD-95 synaptic puncta appears to occur at a late stage in the development of AD. The PSD-95 numbers are similar for the controls and the early stage of Alzheimer's type pathology.

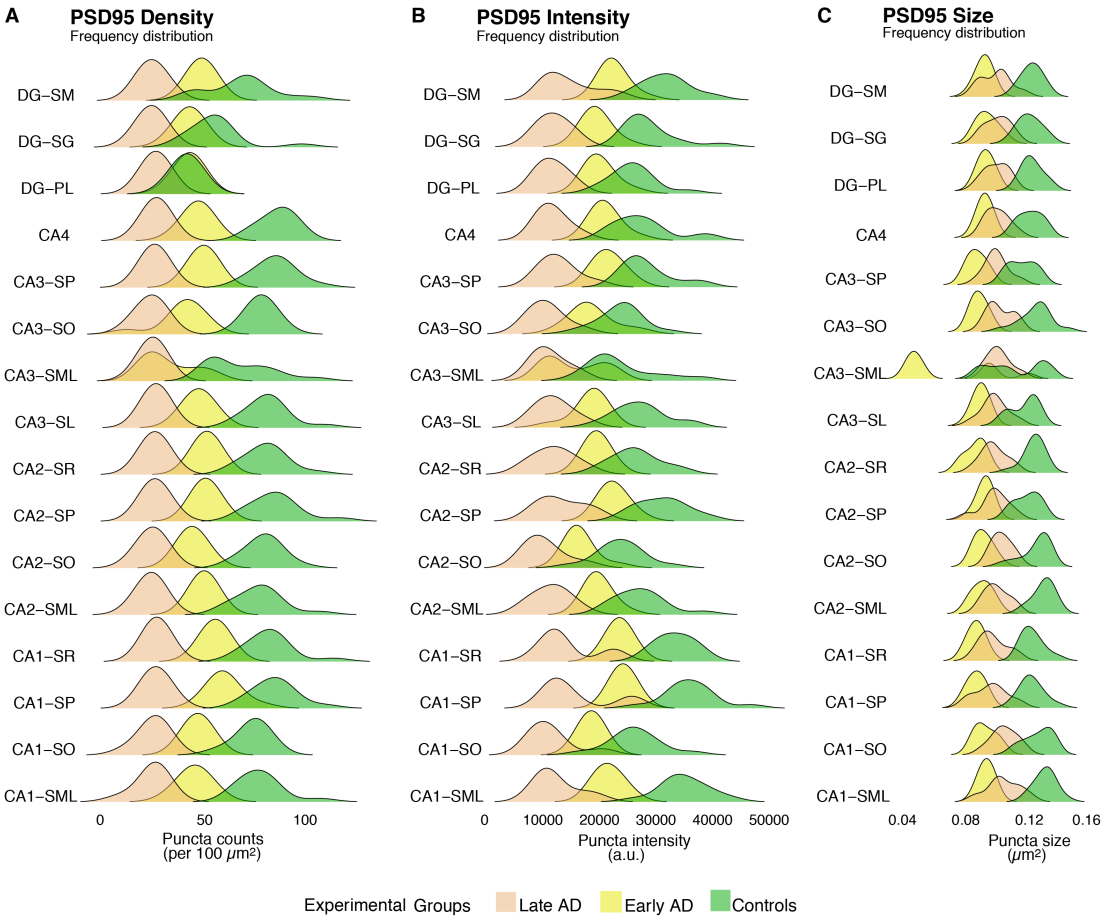


**Figure 5.9 Subregional hippocampal PSD-95 changes in AD disease.**
Frequency density plots showing changes in PSD-95 synaptic puncta parameters in AD as compared to the controls across 16 hippocampal subregions. **(A)** As described before, there is a loss of PSD-95 synaptic puncta in AD in comparison with the control group for all subregions. However, different patterns of synaptic loss are observed in two hippocampal subareas. It appears that the PSD-95 loss within the CA3 stratum moleculare-lacunosum in the early AD stage is as severe as during the late stage. On the other hand, in the pleomorphic layer of the dentate gyrus, synaptic losses occur mostly in the late stage. Here the number of PSD-95 synapses appear very similar for the controls and the early AD stage. **(B)** PSD-95 puncta become dimmer as the disease progresses across the subregions. However, similarly to the density, the pattern of intensity is different within the CA3 stratum moleculare-lacunosum. This subregion stands out from the rest with the intensity of PSD-95 synapses already decreasing severely in the early AD stage. **(C)** As seen previously, the PSD-95 puncta are generally smaller in early AD, but as the disease progresses, the puncta become bigger across the subregions. However, the same hippocampal subregion, the CA3 stratum moleculare-lacunosum, stands out due to its different pattern of change in synaptic size. The decrease in PSD-95 size appears particularly marked for the CA3-SML subfield in the early AD stage. Plots are based on mean values for all subregions per each individual (n = 32 cases in total, of which controls = 14, early AD = 10 and late AD = 8). Individual data points for each subgroup and PSD-95 parameter are shown in Figures 5.10, 5.11, 5.12 on pages 216, 217, 218, respectively. For clarity, frequencies are calculated using *stat_joy* function in *ggjoy* package in R. The binwidths were adjusted for each parameter to accentuate the patterns. Abbreviations - see Figure 5.1 on page 193.

Next, the three PSD-95 synaptic puncta parameters were quantified and a two-way analysis of variance (ANOVA) tested changes for each synaptic parameter. This assessed a 2 (controls vs. early Alzheimer's type pathology, controls vs. late Alzheimer's type pathology, or early Alzheimer's type pathology vs. late Alzheimer's type pathology) by 16 hippocampal subregions between cases ANOVA. Table 5.1 on page 223 shows the condition means, standard deviations and sample sizes for each examined group, each subregion and each synaptic parameter. The expectation is that these results will provide further insights into the effects of Alzheimer's type pathology on PSD-95 synaptic changes in the individual hippocampal subregions.

### 5.8.1 Control *vs.* early Alzheimer's type pathology stage

Regarding PSD-95 density, patients with Alzheimer's type pathology had lower numbers of PSD-95 synapses in comparison to controls. Disease state (controls vs. early Alzheimer's type pathology), hippocampal subregion (16 in total) and the interaction of the two variables (disease state x subregion) appeared to influence the PSD-95 estimates. As predicted form previous research, a main effect of having the disease was observed. Overall, the controls had more synapses than patients diagnosed with early Alzheimer's type pathology, $Mean_{controls} = 74.7$ per 100 $\mu$m$^2$ vs. $Mean_{earlyAD} = 47.4$, F(1, 351) = 871.27, $p < 0.0001$. Moreover, an effect of hippocampal subregion on the estimate of synaptic density was noted, F(15, 351) = 18.26, $p < 0.0001$. The mean greatest losses in PSD-95 synaptic numbers were found for CA4 subregion, $Mean_{CA4} = 38.33$ and the least (significant) mean losses were recorded for stratum granulosum of the dentate gyrus, $Mean_{DG-SG} = 12.79$. I also report the observation of a statistically significant interaction between the disease state and hippocampal subregion. The effect of disease state was not the same for each of the 16 hippocampal subregions, F(15, 351) = 7.38, $p < 0.0001$. A subsequent Sidak's post hoc analysis revealed that the expected effect of early Alzheimer's type pathology on PSD-95 density occurred for all but one (the polymorphic layer of the dentate gyrus) hippocampal subregions. Thus it appears that any conclusions about how early Alzheimer's type pathology affects PSD-95 synaptic density need to further take into account the hippocampal region that is affected.

PSD-95 synaptic puncta intensities were also lower for patients with early AD in comparison to controls. Similarly to PSD-95 density, a main effect of having the disease on PSD-95 synaptic punctum intensity was observed. Overall, the controls had brighter synapses than patients diagnosed with early AD, $Mean_{controls}$ = 28887 in arbitrary units versus $Mean_{earlyAD}$ = 20608, F(1, 352) = 433.27, p $<$ 0.0001. Moreover, an effect of hippocampal subregion on the estimate of synaptic intensity was noted, F(15, 352) = 14.81, p $<$ 0.0001. The mean greatest losses in PSD-95 synaptic brightness were for CA1 stratum moleculare-lacunosum subregion, $Mean_{CA1-SML}$ = 13345 and the least mean losses were recorded for CA3 stratum moleculare-lacunosum, $Mean_{CA3-SML}$ = 5155. Finally, I report the observation of a statistically significant interaction between the disease state and hippocampal subregion. The effect of disease state was not the same for each of the 16 hippocampal subregions, F(15, 352) = 1.79, p = 0.00346. A subsequent Sidak's post hoc analysis revealed that the expected effect of early AD on PSD-95 intensity occurred for all hippocampal subregions. Thus it appears that any conclusions about how early AD disease affects PSD-95 synaptic intensity need to further take into account the hippocampal region that is affected.

Finally, PSD-95 synaptic puncta sizes were recorded lower for patients with early AD in comparison to controls. Similarly to the previous two parameters, a main effect of having the disease on PSD-95 synaptic punctum size was observed. Overall, the controls had larger synapses than patients diagnosed with early AD, $Mean_{controls}$ = 0.1226 in $\mu$m$^2$ area vs. $Mean_{earlyAD}$ = 0.0893, F(1, 351) = 1526.66, p $<$ 0.0001. Moreover, an effect of hippocampal subregion on the estimate of synaptic size was noted, F(15, 351) = 9.84, p $<$ 0.0001. The mean greatest losses in PSD-95 synaptic size were for CA3 stratum lucidum, $Mean_{CA3-SL}$ = 0.048 and the least mean losses were recorded for DG stratum granulosum, $Mean_{DG-SG}$ = 0.026. I also report the observation of a statistically significant interaction between the disease state and hippocampal subregion when size is concerned. The effect of disease state was not the same for each of the 16 hippocampal subregions, F(15, 351) = 2.62, p = 0.0009. A subsequent Sidak's post hoc analysis revealed that the expected effect of early AD on PSD-95 size occurred for all hippocampal subregions. It appears that any conclusions about how early AD disease affects PSD-95 synaptic size need to further take into

account the hippocampal region that is affected.

### 5.8.2 Control *vs.* late Alzheimer's type pathology stage

The same analysis was performed for the late Alzheimer's type pathology group. With regards to PSD-95 density, Alzheimer's type pathology patients in the latest stage of the disease had lower numbers of PSD-95 synapses in comparison to controls. Disease state (controls vs. late AD), hippocampal subregion (16 in total) and the interaction of the two variables (disease state x subregion) appeared to influence the PSD-95 estimates. As predicted from previous research, a main effect of having the disease was observed. Overall, the controls had more synapses than patients diagnosed with late Alzheimer's type pathology, $Mean_{controls} = 74.7$ per 100 $\mu$m$^2$ vs. $Mean_{lateAD} = 25.81$, F(1, 319) = 2407, $p < 0.0001$. Moreover, an effect of hippocampal subregion on the estimate of synaptic density was noted, F(15, 319) = 9.21, $p < 0.0001$. The mean greatest losses in PSD-95 synaptic numbers were for CA4 subregion, $Mean_{CA4} = 58.12$ and the least significant mean loss was recorded for stratum granulosum of the dentate gyrus, $Mean_{DG-SG} = 14.7$. Finally, I report the observation of a statistically significant interaction between the disease state and hippocampal subregion. The effect of disease state was not the same for each of the 16 hippocampal subregions, F(15, 391) = 8.507, $p < 0.0001$. A subsequent Sidak's post hoc analysis revealed that the expected effect of late AD on PSD-95 density occurred for all hippocampal subregions. Thus it appears that any conclusions about how late Alzheimer's type pathology stage affects PSD-95 synaptic density need to further take into account the hippocampal region that is affected.

PSD-95 synaptic puncta intensities were also lower for patients with late Alzheimer's type pathology in comparison to controls. Similarly to PSD-95 density, a main effect of having the disease on PSD-95 synaptic punctum intensity was observed. Overall, the controls had brighter synapses than patients diagnosed with late AD, $Mean_{controls} = 24018$ in arbitrary units versus $Mean_{lateAD} = 12731$, F(1, 319) = 1133, $p < 0.0001$. Moreover, an effect of hippocampal subregion on the estimate of synaptic intensity was noted, F(15, 319) = 7.525, $p < 0.0001$. The mean greatest losses in PSD-95 synaptic brightness were for CA1 stratum moleculare-lacunosum

subregion, $Mean_{CA1-SML} = 22650$ and the least mean losses were recorded for CA3 stratum lucidum, $Mean_{CA3-SL} = 12503$. There was a statistically significant interaction between the disease state and hippocampal subregion. The effect of disease state was not the same for each of the 16 hippocampal subregions, F(15, 319) = 1.992, p = 0.0154. A subsequent Sidak's post hoc analysis revealed that the expected effect of late AD on PSD-95 intensity occurred for all hippocampal subregions. Thus it appears that any conclusions about how late Alzheimer's type pathology stage affects PSD-95 synaptic intensity need to further take into account the hippocampal region that is affected.

Finally, PSD-95 synaptic puncta sizes were recorded lower for patients with late Alzheimer's type pathology in comparison to controls. Similarly to the previous two parameters, a main effect of having the disease on PSD-95 synaptic punctum size was observed. Overall, the controls had larger synapses than patients diagnosed with late Alzheimer's type pathology, $Mean_{controls} = 0.1226$ in $\mu$m$^2$ area vs. $Mean_{lateAD} = 0.1007$, F(1, 319) = 522.5, $p < 0.0001$. Moreover, an effect of hippocampal subregion on the estimate of synaptic size was noted, F(15, 319) = 2.519, $p = 0.0015$. The mean greatest loss in PSD-95 synaptic size was recorded for CA2 stratum moleculare-lacunosum, $Mean_{CA2-SML} = 0.029$ and the least mean loss was recorded for CA3 stratum lucidum, $Mean_{CA3-SL} = 0.0104$, although it was not significant. The least significant loss was recorded for CA3 stratum oriens, $Mean_{CA3-SO} = 0.0161$. Unlike with all the previous estimations, the interaction between the disease state and hippocampal subregion when PSD-95 synaptic puncta size was considered was not statistically significant, F(15, 319) = 1.354, p = 0.1684.

### 5.8.3 Early *vs.* late Alzheimer's type pathology stage

For completeness, the same analysis was performed for both Alzheimer's type pathology groups. With regards to PSD-95 density, the early Alzheimer's type pathology patients had more synapses than patients diagnosed with late Alzheimer's type pathology, $Mean_{earlyAD} = 47.4$ per 100 $\mu$m$^2$ vs. $Mean_{lateAD} = 25.81$, F(1, 254) = 1415, $p < 0.0001$. An effect of hippocampal subregion on the estimate of synaptic density was noted, F(15, 254) = 8.378, $p < 0.0001$. The mean greatest losses in

PSD-95 synaptic numbers were for CA1 stratum pyramidale subregion, $Mean_{CA1-SP}$ = 32.91 and the least significant mean loss was recorded for CA3 stratum lucidum, $Mean_{CA3-SL}$ = 7.936. There was a statistically significant interaction between the disease state and hippocampal subregion, F(15, 254) = 5.84, $p < 0.0001$. A subsequent Sidak's post hoc analysis revealed that the expected effect of late Alzheimer's type pathology on PSD-95 density occurred for all hippocampal subregions. The early Alzheimer's type pathology cases had brighter synapses than patients diagnosed with late Alzheimer's type pathology, $Mean_{earlyAD}$ = 20608 in arbitrary units vs. $Mean_{lateAD}$ = 12731, F(1, 254) = 441.7, $p < 0.0001$. Moreover, an effect of hippocampal subregion on the estimate of synaptic intensity was noted, F(15, 254) = 6.495, $p < 0.0001$. The mean greatest losses in PSD-95 synaptic brightness were observed for CA4 subregion, $Mean_{CA4}$ = 9335, and the least mean significant losses were recorded for CA2 stratum oriens, $Mean_{CA2-SO}$ = 6277. However, for PSD-95 puncta intensity, statistically insignificant interaction between the disease stage and hippocampal subregion was seen for these groups, F(15, 254) = 0.822, p = 0.653.

Notably, the late Alzheimer's type pathology cases had larger synapses than patients diagnosed with early Alzheimer's type pathology, $Mean_{earlyAD}$ = 0.0893 in $\mu$m$^2$ area vs. $Mean_{lateAD}$ = 0.1007, F(1, 254) = 146.8, $p < 0.0001$. Moreover, an effect of hippocampal subregion on the estimate of synaptic size was observed, F(15, 254) = 4.249, $p < 0.0001$. The mean greatest loss in PSD-95 synaptic size was recorded for CA3 stratum lucidum, $Mean_{CA3-SL}$ = 0.0375, and the least mean significant loss was recorded for CA2 stratum radiatum, $Mean_{CA2-SR}$ = 0.0116. Finally, for PSD-95 puncta size, the interaction between the disease stage and hippocampal subregion was statistically significant, F(15, 254) = 3.644, $p < 0.0001$.

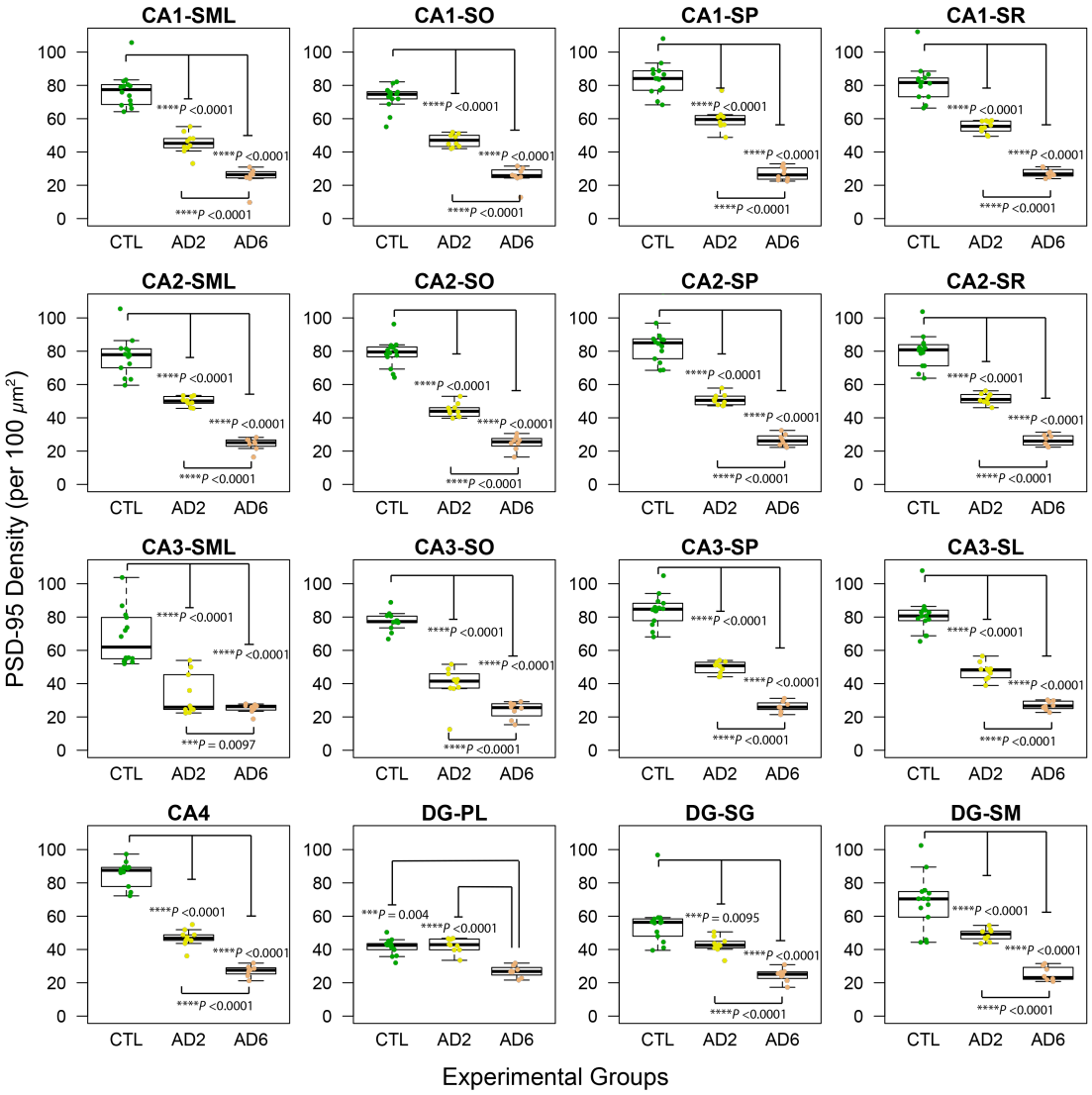


**Figure 5.10 Subregional distribution of hippocampal PSD-95 puncta density.** Boxplots of PSD-95 puncta densities in three experimental groups in 16 hippocampal subregions demonstrating loss of synapses in AD cases in comparison to the controls. Data are presented as boxplots with median and whiskers plotted by Tukey method. Individual data points are superimposed on the boxplots. CTL, Controls (n = 14); AD, Alzheimer's Disease; AD2, Early AD Braak stage II (n = 10); AD6, late AD Braak stage VI (n = 8). Statistical differences between groups are based on data presented in Table 5.1 on page 223. Significance levels: * $p < 0.05$; ** $p < 0.01$; *** $p < 0.001$; **** $p < 0.0001$. Abbreviations - see Figure 5.1 on page 193.

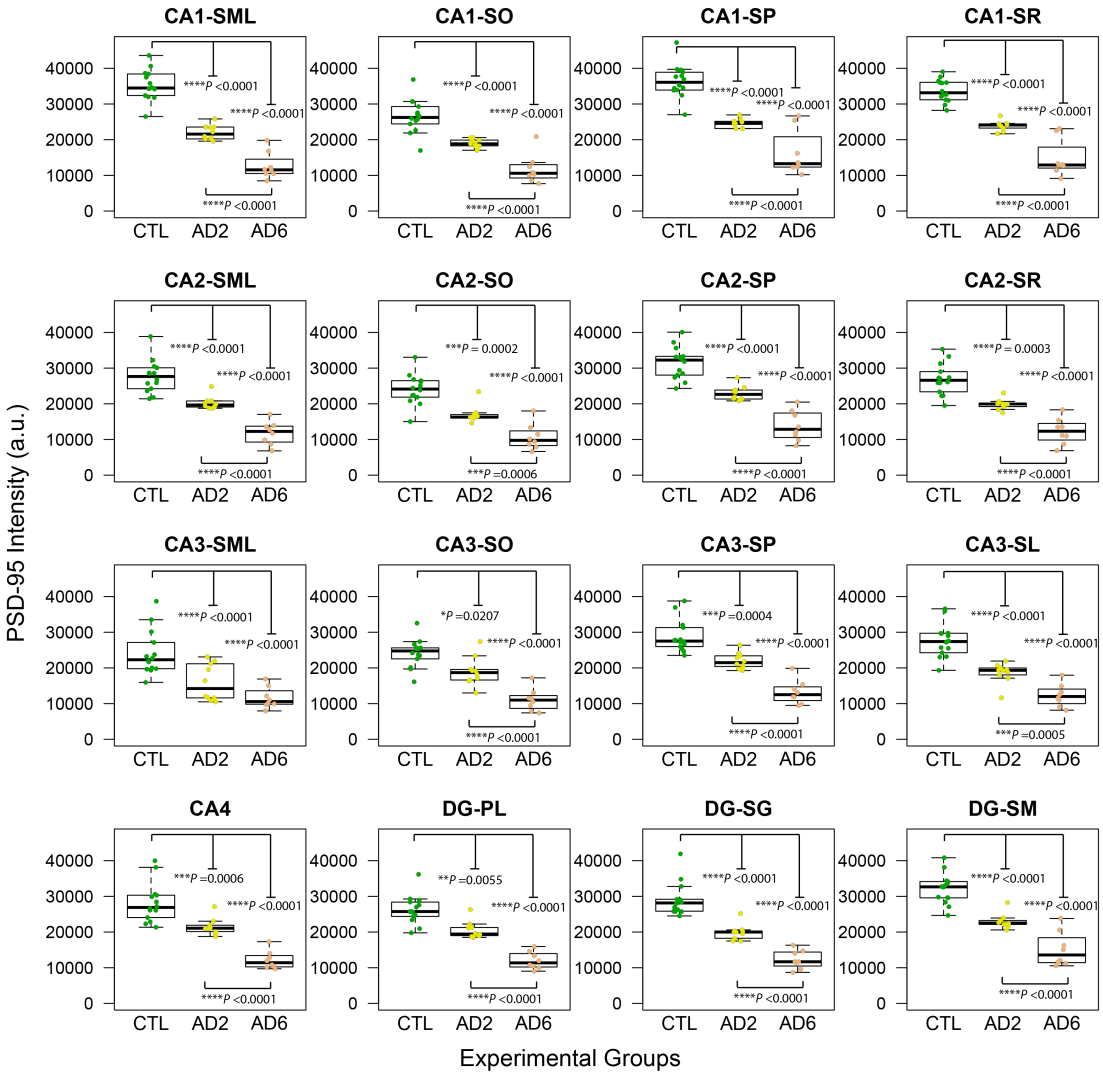


**Figure 5.11 Subregional distribution of hippocampal PSD-95 puncta intensity.** Boxplots of PSD-95 puncta intensities in three experimental groups in 16 hippocampal subregions demonstrating loss of synapse intensities in AD cases in comparison to the controls. Data are presented as boxplots with median and whiskers plotted by Tukey method. Individual data points are superimposed on the boxplots. CTL, Controls (n = 14); AD, Alzheimer's Disease; AD2, Early AD Braak stage II (n = 10); AD6, late AD Braak stage VI (n = 8). Statistical differences between groups are based on data presented in Table 5.1 on page 223. Significance levels: * $p < 0.05$; ** $p < 0.01$; *** $p < 0.001$; **** $p < 0.0001$. Abbreviations - see Figure 5.1 on page 193.

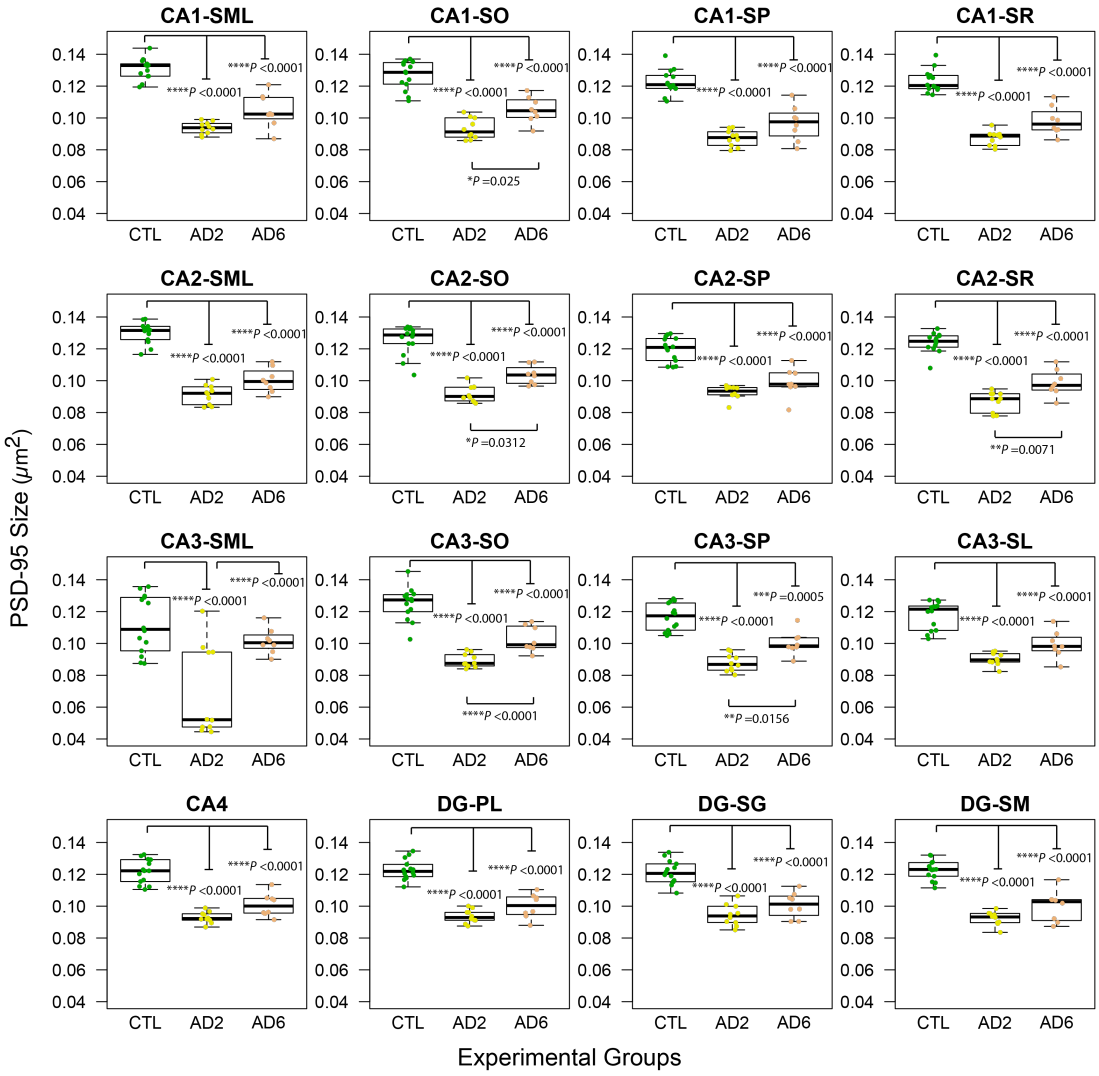


**Figure 5.12 Subregional distribution of hippocampal PSD-95 puncta size.** Boxplots of PSD-95 puncta sizes in three experimental groups in 16 hippocampal subregions demonstrating an overall reduction in synapse sizes in AD cases in comparison to the controls. Data are presented as boxplots with median and whiskers plotted by Tukey method. Individual data points are superimposed on the boxplots. CTL, Controls (n = 14); AD, Alzheimer's Disease; AD2, Early AD Braak stage II (n = 10); AD6, late AD Braak stage VI (n = 8). Statistical differences between groups are based on data presented in Table 5.1 on page 223. Significance levels: * $p < 0.05$; ** $p < 0.01$; *** $p < 0.001$; **** $p < 0.0001$. Abbreviations - see Figure 5.1 on page 193.

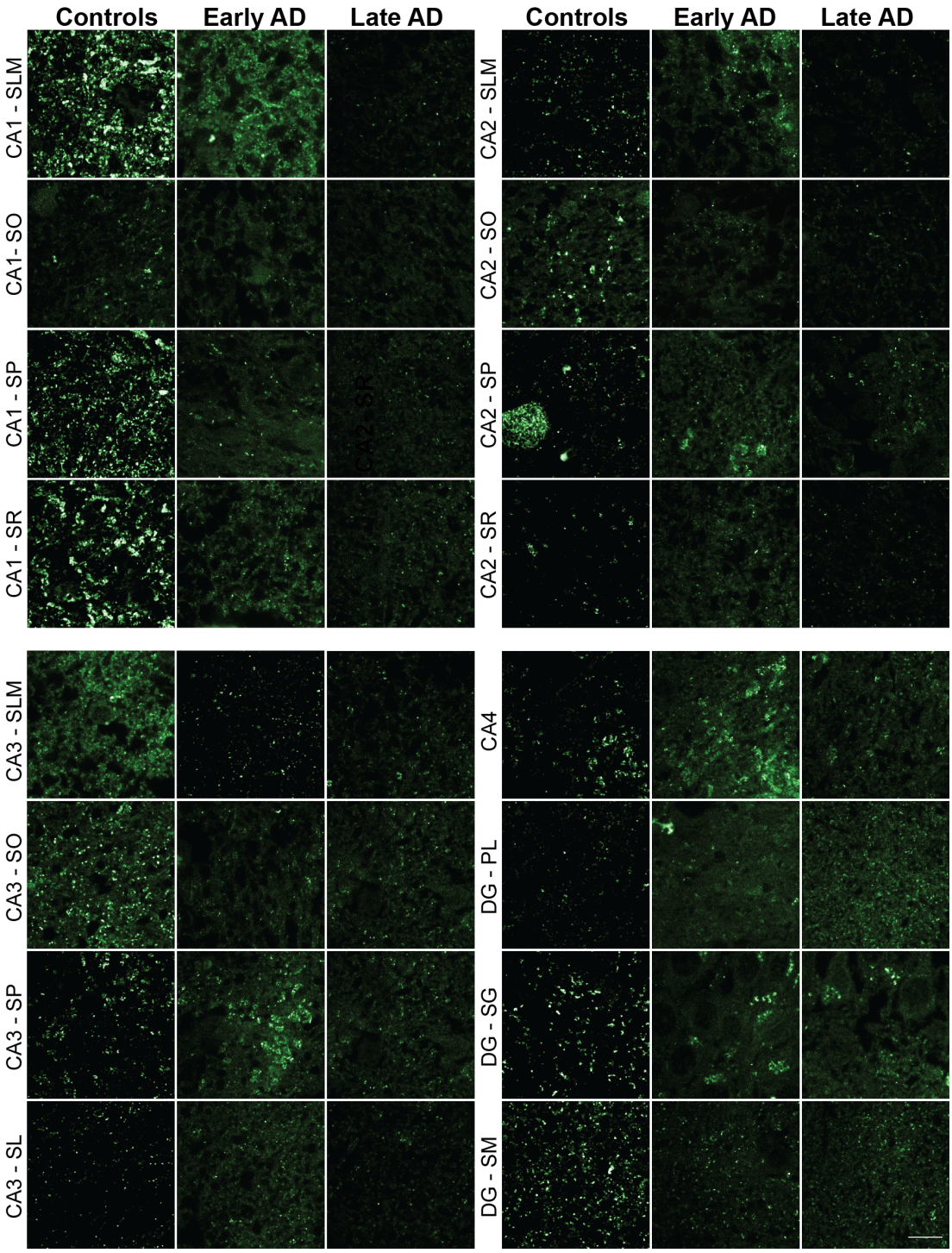


**Figure 5.13 Changes in distribution of hippocampal PSD-95 expression in AD.** High-resolution SDM images demonstrating changes in expression of PSD-95 in 16 different hippocampal subregions between controls, the early AD stage and the late AD stage. For most subregions, losses in PSD-95 synaptic puncta in AD in comparison with controls are evident in the images. However, any differences from the detailed quantification presented previously might represent individual differences. Images were obtained from the following cases: controls - SD42/13, early AD - SD40/14 and late AD - SD02/14. Scale bar 10 $\mu$m. Abbreviations as previously.

## 5.9 HIPPOCAMPAL PATTERNING OF PSD-95 SYNAPTOME CHANGES IN AD

Next, in order to determine the spatial distribution of differences between the control and the Alzheimer's type pathology groups, Cohen's d values were calculated (Table 5.2 on page 224) and represented as heatmaps.

Among 16 hippocampal subregions, the PSD-95 puncta density, intensity and size in patients with Alzheimer's type pathology were significantly lower when compared to controls for all but the polymorphic layer of the dentate gyrus (DG) and the stratum moleculare-lacunosum of the CA3 subregion. In general, effect sizes were largest for the densities, moderate for the sizes and smallest for the intensities (Figure 5.14 on page 225). The more advanced Alzheimer's type pathology stage, the greater the loss of PSD-95 puncta parameters for densities and intensities, but not for the puncta sizes where the milder Alzheimer's type pathology stage experienced far greater losses in size than the later stages of Alzheimer's type pathology. Specific changes for each parameter are illustrated in Figure 5.15 to show changes between the controls and the early Alzheimer's type pathology group and in Figure 5.16 to show changes between the controls and the late Alzheimer's type pathology group.

For PSD-95 densities, the most significant effect was seen in the CA3 stratum oriens for both Alzheimer's type pathology groups (d = -6.68, 95% confidence interval (CI) -8.97 to -4.39, p <0.0001 for control vs. early Alzheimer's type pathology group, and d = -10.35, 95% CI -13.84 to -6.87, p <0.0001 for control vs. late Alzheimer's type pathology group). The least significant effect was seen for DG stratum granulare for both Alzheimer's type pathology groups (d = -1.18, 95% CI -2.10 to -0.25, p <0.0001 for control vs. early Alzheimer's type pathology group, and d = -2.77, 95% CI -4.05 to -1.49, p <0.0001 for control vs. late Alzheimer's type pathology group). The only subregion which showed non-significant effect size was the DG polymorphic layer (d = 0.25, 95% CI -0.60 to 1.10, p >0.999 for control vs. early AD group). Moreover, this was the only region in which a positive effect was recorded for all three parameters for all group combinations.

For PSD-95 intensities, significant effect size was highest in the stratum

moleculare-lacunosum of the CA1 subregion for both Alzheimer's type pathology groups (d = -3.79, 95% CI -5.24 to -2.35, p <0.0001 for control vs. early AD group, and d = -5.54, 95% CI -7.56 to -3.52, p <0.0001 for control vs. late AD group). Significant effect size was lowest for stratum oriens of the CA3 (d = -1.31, 95% CI -2.25 to -0.37, p = 0.0207) for control vs. early AD group, and stratum moleculare-lacunosum of the CA3 (d = -2.35, 95% CI -3.54 to -1.16, p <0.0001) for control vs. late AD group.

For PSD-95 sizes, the most significant effect size was seen in the CA1 stratum moleculare-lacunosum for control vs. early Alzheimer's type pathology group (d = -6.76, 95% CI -9.02 to -4.51, p <0.0001), and the CA2 stratum moleculare-lacunosum for control vs. late Alzheimer's type pathology group (d = -4.22, 95% CI -5.92 to -2.52, p <0.0001). Significant effect size was lowest for the CA3 stratum moleculare-lacunosum (d = -2.35, 95% CI -3.50 to -1.20, p = 0.0207) for control vs. early Alzheimer's type pathology group, and the CA3 stratum pyramidale (d = -2.00, 95% CI -3.12 to -0.88, p = 0.00005) for control vs. late Alzheimer's type pathology group. However, similarly to the early Alzheimer's type pathology group, the overall lowest, but not significant effect size was found for the CA3 stratum moleculare-lacunosum (d = -0.68, 95% CI -1.62 to 0.25, p = 0.1038).

Several significant differences were also found between the Alzheimer's type pathology groups. However, they were not as consistent as the differences between the controls and the Alzheimer's type pathology groups described above. In general, effect sizes were greatest for the PSD-95 densities and moderate for intensities (Figure 5.14 on page 225). The effect of Alzheimer's type pathology on the PSD-95 synaptic puncta sizes all showed positive trends, but a majority of these results were also not significant. Within the Alzheimer's type pathology groups, for PSD-95 densities, significant effect size was highest in the CA1 stratum radiatum (d = -8.76, 95% CI -12.12 to -5.39, p <0.0001) and lowest in the CA1 stratum moleculare-lacunosum (d = -3.23, 95% CI -4.77 to -1.69, p <0.0001). In addition, Alzheimer's type pathology had a significant effect on synaptic puncta densities in the stratum moleculare-lacunosum of the CA3 (d = -0.84, 95% CI -1.88 to 0.19, p = 0.0097), but the confidence intervals included zero. For PSD-95 intensities, the greatest significance was seen in CA4 (d = -3.85, 95% CI

-5.58 to -2.13, p <0.0001) and least significance in the CA1 stratum pyramidale (d = -1.95, 95% CI -3.17 to -0.73, p <0.0001). The size of the effect found in the CA3 stratum moleculare-lacunosum (d = -0.99, 95% CI -2.05 to 0.06, p = 0.0693) was not significant, and the confidence intervals included zero. Finally, for PSD-95 sizes, the size of the effect size was highest in the stratum oriens of the CA3 subregion (d = 2.15, 95% CI 0.89 to 3.42, p = 0.0071) and lowest in the stratum radiatum of the CA2 (d = 1.62, 95% CI 0.47 to 2.77, p = 0.0354). These differences are illustrated as heatmaps in Figure 5.17 on page 228.

**Table 5.1** Mean differences in PSD-95 density, intensity and size between groups for 16 human hippocampal subregions in the SDM cohort

| Subregion | Control Group Mean | SD | Early AD Group Mean | SD | Late AD Group Mean | SD | p value Ctr vs Early AD | p value Ctr vs Late AD | p value Early AD vs Late AD |
|---|---|---|---|---|---|---|---|---|---|
| **Density** | | | | | | | | | |
| CA1-SML | 76.98 | 10.39 | 45.34 | 6.27 | 24.81 | 6.47 | <0.0001 | <0.0001 | <0.0001 |
| CA1-SO | 72.79 | 7.28 | 46.96 | 3.79 | 25.46 | 5.74 | <0.0001 | <0.0001 | <0.0001 |
| CA1-SP | 83.99 | 10.02 | 59.91 | 7.22 | 27.00 | 3.90 | <0.0001 | <0.0001 | <0.0001 |
| CA1-SR | 81.68 | 11.07 | 55.20 | 3.59 | 27.34 | 2.56 | <0.0001 | <0.0001 | <0.0001 |
| CA2-SML | 76.78 | 11.46 | 50.00 | 2.76 | 24.27 | 4.05 | <0.0001 | <0.0001 | <0.0001 |
| CA2-SO | 78.58 | 8.11 | 44.56 | 4.02 | 24.92 | 4.39 | <0.0001 | <0.0001 | <0.0001 |
| CA2-SP | 84.42 | 12.06 | 50.91 | 3.29 | 26.57 | 3.52 | <0.0001 | <0.0001 | <0.0001 |
| CA2-SR | 79.81 | 9.99 | 51.35 | 3.12 | 26.43 | 3.33 | <0.0001 | <0.0001 | <0.0001 |
| CA3-SML | 67.51 | 16.03 | 33.12 | 12.25 | 25.18 | 2.93 | <0.0001 | <0.0001 | 0.0097 |
| CA3-SO | 77.42 | 5.21 | 42.67 | 5.20 | 24.12 | 5.04 | <0.0001 | <0.0001 | <0.0001 |
| CA3-SP | 84.10 | 9.32 | 49.65 | 3.60 | 26.29 | 3.15 | <0.0001 | <0.0001 | <0.0001 |
| CA3-SL | 80.59 | 10.15 | 47.51 | 5.10 | 26.92 | 2.69 | <0.0001 | <0.0001 | <0.0001 |
| CA4 | 85.20 | 7.55 | 46.88 | 5.05 | 27.08 | 3.25 | <0.0001 | <0.0001 | <0.0001 |
| DG-PL | 41.54 | 4.62 | 42.67 | 4.18 | 26.84 | 3.45 | >0.9999 | 0.0041 | <0.0001 |
| DG-SG | 55.67 | 13.61 | 42.88 | 4.65 | 24.60 | 4.01 | 0.0095 | <0.0001 | <0.0001 |
| DG-SM | 68.10 | 16.41 | 48.80 | 3.49 | 25.17 | 4.21 | <0.0001 | <0.0001 | <0.0001 |
| **Intensity** | | | | | | | | | |
| CA1-SML | 35334 | 4262 | 21989 | 2015 | 12684 | 3740 | <0.0001 | <0.0001 | <0.0001 |
| CA1-SO | 26586 | 4686 | 18909 | 1255 | 11786 | 4139 | <0.0001 | <0.0001 | <0.0001 |
| CA1-SP | 36423 | 4585 | 24558 | 1249 | 16213 | 6305 | <0.0001 | <0.0001 | <0.0001 |
| CA1-SR | 33742 | 3179 | 23915 | 1370 | 14743 | 5155 | <0.0001 | <0.0001 | <0.0001 |
| CA2-SML | 27845 | 4579 | 20213 | 1792 | 11795 | 3513 | <0.0001 | <0.0001 | <0.0001 |
| CA2-SO | 24591 | 4243 | 16972 | 2364 | 10695 | 3610 | 0.0002 | <0.0001 | 0.0006 |
| CA2-SP | 31713 | 4458 | 22931 | 1987 | 13799 | 4259 | <0.0001 | <0.0001 | <0.0001 |
| CA2-SR | 27211 | 4371 | 19882 | 1456 | 12311 | 3672 | 0.0003 | <0.0001 | <0.0001 |
| CA3-SML | 24249 | 6235 | 15893 | 5115 | 11604 | 2984 | <0.0001 | <0.0001 | 0.0693 |
| CA3-SO | 24706 | 3904 | 19001 | 3980 | 11051 | 3124 | 0.0207 | <0.0001 | <0.0001 |
| CA3-SP | 29357 | 4469 | 21972 | 2205 | 13185 | 3351 | 0.0004 | <0.0001 | <0.0001 |
| CA3-SL | 28291 | 4740 | 18648 | 2803 | 12279 | 3160 | <0.0001 | <0.0001 | 0.0005 |
| CA4 | 28787 | 5476 | 21475 | 2315 | 12140 | 2555 | 0.0006 | <0.0001 | <0.0001 |
| DG-PL | 26647 | 3985 | 20512 | 2382 | 12005 | 2419 | 0.0055 | <0.0001 | <0.0001 |
| DG-SG | 29664 | 4632 | 19897 | 2190 | 12261 | 2598 | <0.0001 | <0.0001 | <0.0001 |
| DG-SM | 32551 | 4280 | 22962 | 2069 | 15148 | 4840 | <0.0001 | <0.0001 | <0.0001 |
| **Size** | | | | | | | | | |
| CA1-SML | 0.1310 | 0.0064 | 0.0938 | 0.0037 | 0.1047 | 0.0106 | <0.0001 | <0.0001 | 0.0644 |
| CA1-SO | 0.1278 | 0.0089 | 0.0932 | 0.0066 | 0.1052 | 0.0081 | <0.0001 | <0.0001 | 0.0250 |
| CA1-SP | 0.1231 | 0.0075 | 0.0873 | 0.0051 | 0.0967 | 0.0109 | <0.0001 | <0.0001 | 0.1840 |
| CA1-SR | 0.1233 | 0.0070 | 0.0873 | 0.0045 | 0.0981 | 0.0089 | <0.0001 | <0.0001 | 0.0683 |
| CA2-SML | 0.1316 | 0.0064 | 0.0913 | 0.0060 | 0.1003 | 0.0082 | <0.0001 | <0.0001 | 0.3009 |
| CA2-SO | 0.1265 | 0.0092 | 0.0919 | 0.0052 | 0.1036 | 0.0058 | <0.0001 | <0.0001 | 0.0312 |
| CA2-SP | 0.1207 | 0.0078 | 0.0927 | 0.0041 | 0.0991 | 0.0091 | <0.0001 | <0.0001 | 0.7774 |
| CA2-SR | 0.1256 | 0.0061 | 0.0870 | 0.0063 | 0.0986 | 0.0081 | <0.0001 | <0.0001 | 0.0354 |
| CA3-SML | 0.1109 | 0.0180 | 0.0640 | 0.0238 | 0.1014 | 0.0079 | <0.0001 | 0.1038 | <0.0001 |
| CA3-SO | 0.1266 | 0.0103 | 0.0893 | 0.0043 | 0.1026 | 0.0080 | <0.0001 | <0.0001 | 0.0071 |
| CA3-SP | 0.1173 | 0.0084 | 0.0878 | 0.0055 | 0.1003 | 0.0073 | <0.0001 | 0.0005 | 0.0156 |
| CA3-SL | 0.1188 | 0.0087 | 0.0902 | 0.0039 | 0.0992 | 0.0084 | <0.0001 | <0.0001 | 0.2354 |
| CA4 | 0.1228 | 0.0075 | 0.0929 | 0.0035 | 0.1008 | 0.0072 | <0.0001 | <0.0001 | 0.4546 |
| DG-PL | 0.1236 | 0.0063 | 0.0936 | 0.0042 | 0.1000 | 0.0076 | <0.0001 | <0.0001 | 0.7644 |
| DG-SG | 0.1223 | 0.0073 | 0.0943 | 0.0067 | 0.1008 | 0.0080 | <0.0001 | <0.0001 | 0.7567 |
| DG-SM | 0.1234 | 0.0062 | 0.0923 | 0.0043 | 0.1000 | 0.0097 | <0.0001 | <0.0001 | 0.4974 |

Statistically significant differences were found between the control group (n=14) and the AD groups (n=10 for early AD group and n=8 for late AD group). Differences between groups were calculated using an ordinary two-way ANOVA. Sidak's multiple comparisons tests were used to calculate p values between the subregions. Adjusted p values are reported with level of significance set at $p < 0.05$. Abbreviations: AD - Alzheimer's disease, Ctr - Control; SD - standard deviation.

**Table 5.2** Effect size of the difference of PSD-95 density, intensity and size for 16 human hippocampal subregions in the SDM cohort

| | Ctr vs AD2 | | | Ctr vs AD6 | | | AD2 vs AD6 | | |
|---|---|---|---|---|---|---|---|---|---|
| | Effect size | Lower CI | Upper CI | Effect size | Lower CI | Upper CI | Effect size | Lower CI | Upper CI |
| **Density** | | | | | | | | | |
| CA1-SML | -3.54 | -4.92 | -2.16 | -6.62 | -8.96 | -4.28 | -3.23 | -4.77 | -1.69 |
| CA1-SO | -4.24 | -5.79 | -2.68 | -6.98 | -9.43 | -4.54 | -4.53 | -6.47 | -2.60 |
| CA1-SP | -2.68 | -3.87 | -1.50 | -6.78 | -9.17 | -4.40 | -5.49 | -7.73 | -3.24 |
| CA1-SR | -2.22 | -3.80 | -0.64 | -6.00 | -8.16 | -3.85 | -8.76 | -12.12 | -5.39 |
| CA2-SML | -2.98 | -4.23 | -1.73 | -5.39 | -7.42 | -3.35 | -7.72 | -10.83 | -4.60 |
| CA2-SO | -5.05 | -6.82 | -3.27 | -7.63 | -10.27 | -4.99 | -4.69 | -6.68 | -2.71 |
| CA2-SP | -3.53 | -4.90 | -2.15 | -5.82 | -7.92 | -3.72 | -7.18 | -9.99 | -4.36 |
| CA2-SR | -3.59 | -4.98 | -2.19 | -6.44 | -8.72 | -4.15 | -7.76 | -10.77 | -4.74 |
| CA3-SML | -2.36 | -3.47 | -1.24 | -3.25 | -4.64 | -1.85 | -0.84 | -1.88 | 0.19 |
| CA3-SO | -6.68 | -8.97 | -4.39 | -10.35 | -13.84 | -6.87 | -3.62 | -5.33 | -1.91 |
| CA3-SP | -4.58 | -6.23 | -2.93 | -7.47 | -10.06 | -4.88 | -6.85 | -9.56 | -4.15 |
| CA3-SL | -3.91 | -5.39 | -2.44 | -6.44 | -8.72 | -4.16 | -4.88 | -6.93 | -2.83 |
| CA4 | -5.77 | -7.75 | -3.80 | -9.11 | -12.2 | -6.01 | -4.55 | -6.49 | -2.61 |
| DG-PL | 0.25 | -0.60 | 1.10 | -3.46 | -4.91 | -2.01 | -4.08 | -5.88 | -2.29 |
| DG-SG | -1.18 | -2.10 | -0.25 | -2.77 | -4.05 | -1.49 | -4.17 | -6.00 | -2.35 |
| DG-SM | -1.51 | -2.47 | -0.54 | -3.19 | -4.57 | -1.81 | -6.18 | -8.65 | -3.70 |
| **Intensity** | | | | | | | | | |
| CA1-SML | -3.79 | -5.24 | -2.35 | -5.54 | -7.56 | -3.52 | -3.21 | -4.75 | -1.67 |
| CA1-SO | -2.07 | -3.13 | -1.01 | -3.28 | -4.68 | -1.88 | -2.46 | -3.80 | -1.12 |
| CA1-SP | -3.27 | -4.59 | -1.95 | -3.84 | -5.39 | -2.29 | -1.95 | -3.17 | -0.73 |
| CA1-SR | -3.78 | -5.22 | -2.34 | -4.76 | -6.56 | -2.97 | -2.58 | -3.94 | -1.21 |
| CA2-SML | -2.00 | -3.05 | -0.96 | -3.71 | -5.27 | -2.14 | -3.21 | -4.81 | -1.61 |
| CA2-SO | -1.96 | -3.00 | -0.92 | -3.30 | -4.71 | -1.90 | -2.11 | -3.37 | -0.86 |
| CA2-SP | -2.33 | -3.45 | -1.22 | -4.02 | -5.62 | -2.43 | -2.87 | -4.31 | -1.42 |
| CA2-SR | -2.00 | -3.04 | -0.95 | -3.51 | -4.97 | -2.05 | -2.84 | -4.28 | -1.41 |
| CA3-SML | -1.42 | -2.37 | -0.46 | -2.35 | -3.54 | -1.16 | -0.99 | -2.05 | 0.06 |
| CA3-SO | -1.31 | -2.25 | -0.37 | -3.59 | -5.07 | -2.11 | -2.19 | -3.46 | -0.92 |
| CA3-SP | -1.84 | -2.86 | -0.82 | -3.80 | -5.33 | -2.26 | -3.18 | -4.71 | -1.65 |
| CA3-SL | -2.20 | -3.29 | -1.12 | -3.60 | -5.08 | -2.12 | -2.15 | -3.41 | -0.89 |
| CA4 | -1.49 | -2.46 | -0.53 | -3.43 | -4.87 | -1.99 | -3.85 | -5.58 | -2.13 |
| DG-PL | -1.68 | -2.68 | -0.69 | -4.05 | -5.66 | -2.45 | -3.55 | -5.18 | -1.91 |
| DG-SG | -2.42 | -3.55 | -1.29 | -4.18 | -5.82 | -2.54 | -3.21 | -4.75 | -1.67 |
| DG-SM | -2.56 | -3.72 | -1.40 | -3.77 | -5.30 | -2.24 | -2.20 | -3.47 | -0.92 |
| **Size** | | | | | | | | | |
| CA1-SML | -6.76 | -9.02 | -4.51 | -3.22 | -4.61 | -1.84 | 1.43 | 0.32 | 2.55 |
| CA1-SO | -4.17 | -5.72 | -2.63 | -2.50 | -3.72 | -1.28 | 1.65 | 0.49 | 2.81 |
| CA1-SP | -5.33 | -7.17 | -3.48 | -2.92 | -4.24 | -1.61 | 1.16 | 0.08 | 2.23 |
| CA1-SR | -5.85 | -7.84 | -3.85 | -3.23 | -4.62 | -1.84 | 1.58 | 0.44 | 2.73 |
| CA2-SML | -6.18 | -8.27 | -4.09 | -4.22 | -5.92 | -2.52 | 1.28 | 0.15 | 2.42 |
| CA2-SO | -4.27 | -5.84 | -2.70 | -2.66 | -3.91 | -1.40 | 2.13 | 0.87 | 3.39 |
| CA2-SP | -4.15 | -5.68 | -2.61 | -2.50 | -3.73 | -1.28 | 0.95 | -0.10 | 1.99 |
| CA2-SR | -6.01 | -8.05 | -3.97 | -3.71 | -5.22 | -2.20 | 1.62 | 0.47 | 2.77 |
| CA3-SML | -2.35 | -3.50 | -1.20 | -0.68 | -1.62 | 0.25 | 2.06 | 0.78 | 3.34 |
| CA3-SO | -4.27 | -5.84 | -2.70 | -2.34 | -3.53 | -1.15 | 2.15 | 0.89 | 3.42 |
| CA3-SP | -3.89 | -5.36 | -2.42 | -2.00 | -3.12 | -0.88 | 1.97 | 0.75 | 3.19 |
| CA3-SL | -3.86 | -5.33 | -2.40 | -2.16 | -3.31 | -1.01 | 1.44 | 0.32 | 2.55 |
| CA4 | -4.66 | -6.33 | -2.99 | -2.83 | -4.12 | -1.53 | 1.44 | 0.32 | 2.56 |
| DG-PL | -5.25 | -7.08 | -3.42 | -3.34 | -4.75 | -1.92 | 1.09 | 0.02 | 2.15 |
| DG-SG | -3.80 | -5.25 | -2.35 | -2.69 | -3.95 | -1.43 | 0.89 | -0.14 | 1.93 |
| DG-SM | -5.53 | -7.44 | -3.63 | -2.99 | -4.32 | -1.66 | 1.07 | 0.01 | 2.13 |

Abbreviations: AD - Alzheimer's disease, AD2 - Early AD stage II; AD6 - Late AD stage VI; Ctr - Control; CI - 95% confidence interval.

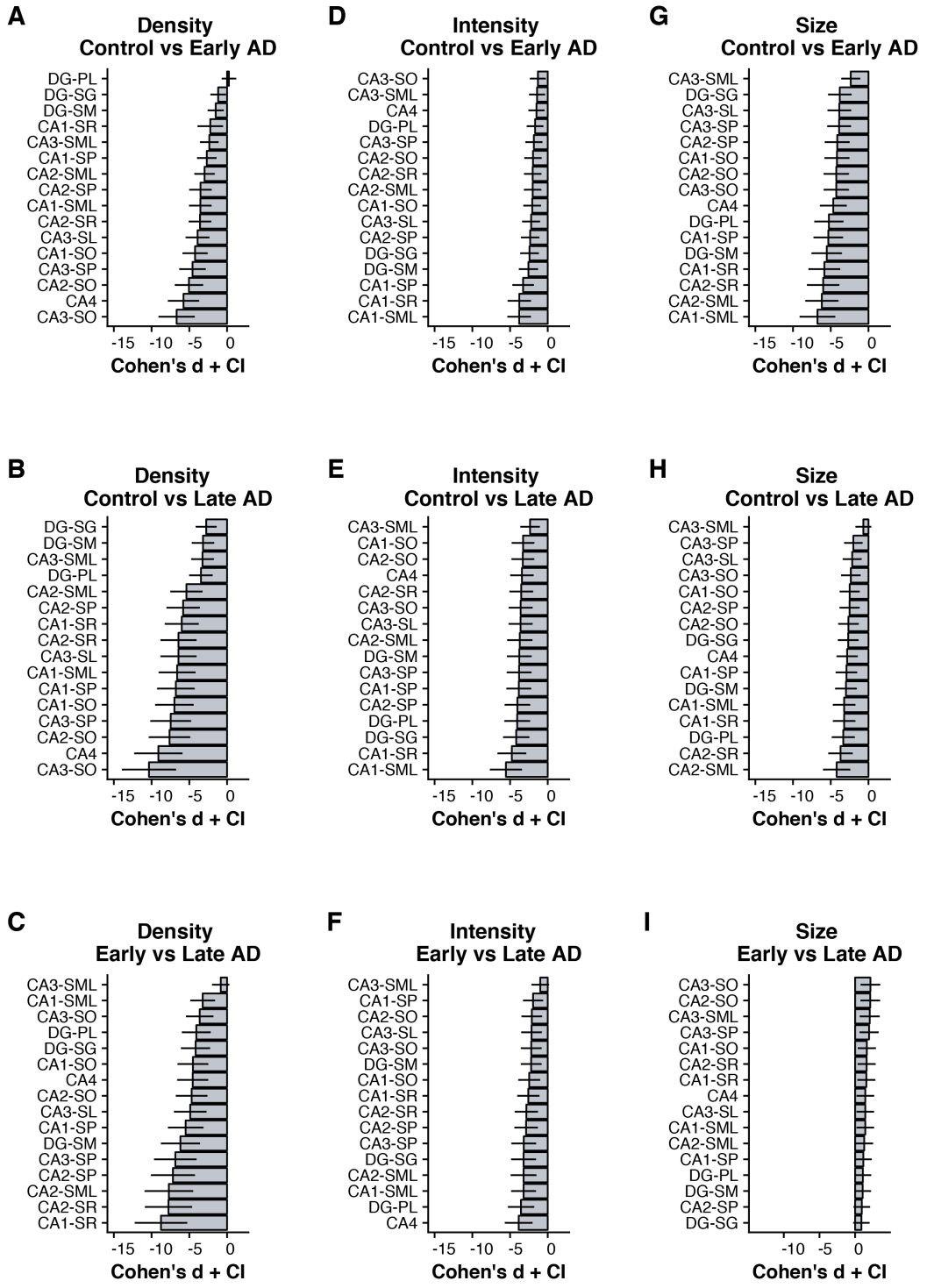


**Figure 5.14 Hippocampal PSD-95 effect size ranks in the SDM cohort.**
Cohen's d effect size ranks of PSD-95 density (A, B, C), PSD-95 puncta intensity (D, E, F), and PSD-95 puncta size (G, H, I) in the entire SDM cohort by one of three groups: controls vs. early AD (A, D, G), controls vs. late AD (B, E, H), and early AD vs. late AD (C, F, I). Among PSD-95 parameters, the greatest changes were observed for density. Among groups, the greatest changes were seen in late AD. However, for PSD-95 size, the losses were greatest in the early rather than the late AD group. AD, Alzheimer's Disease; CI, 95% confidence interval.

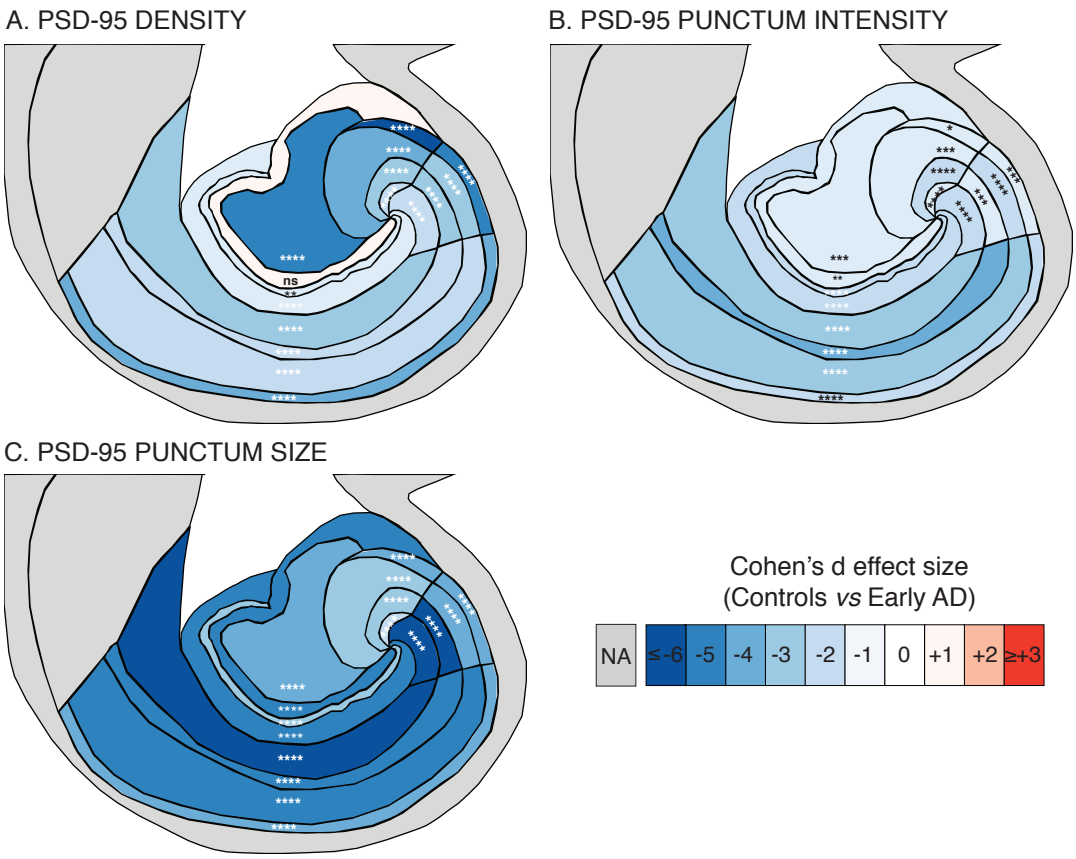


**Figure 5.15 Hippocampal subregional PSD-95 synaptome reorganisation in early AD compared to controls.**

Spatial distribution of differences between controls (n = 14) and the early AD group (n = 10) represented by heatmaps of the Cohen's d values in 16 hippocampal subregions for PSD-95 puncta density **(A)**, PSD-95 puncta intensity **(B)** and PSD-95 puncta size **(C)**. Blue, white and red colours indicate a decrease, no change or an increase, respectively, of the PSD-95 parameter measured in early AD group compared to controls. Significant differences, measured using two-way ANOVA, are indicated by asterisks with significance levels: * $p < 0.05$; ** $p < 0.01$; *** $p < 0.001$; **** $p < 0.0001$; ns, not significant. Abbreviations: AD, Alzheimer's Disease; NA, Not applicable.

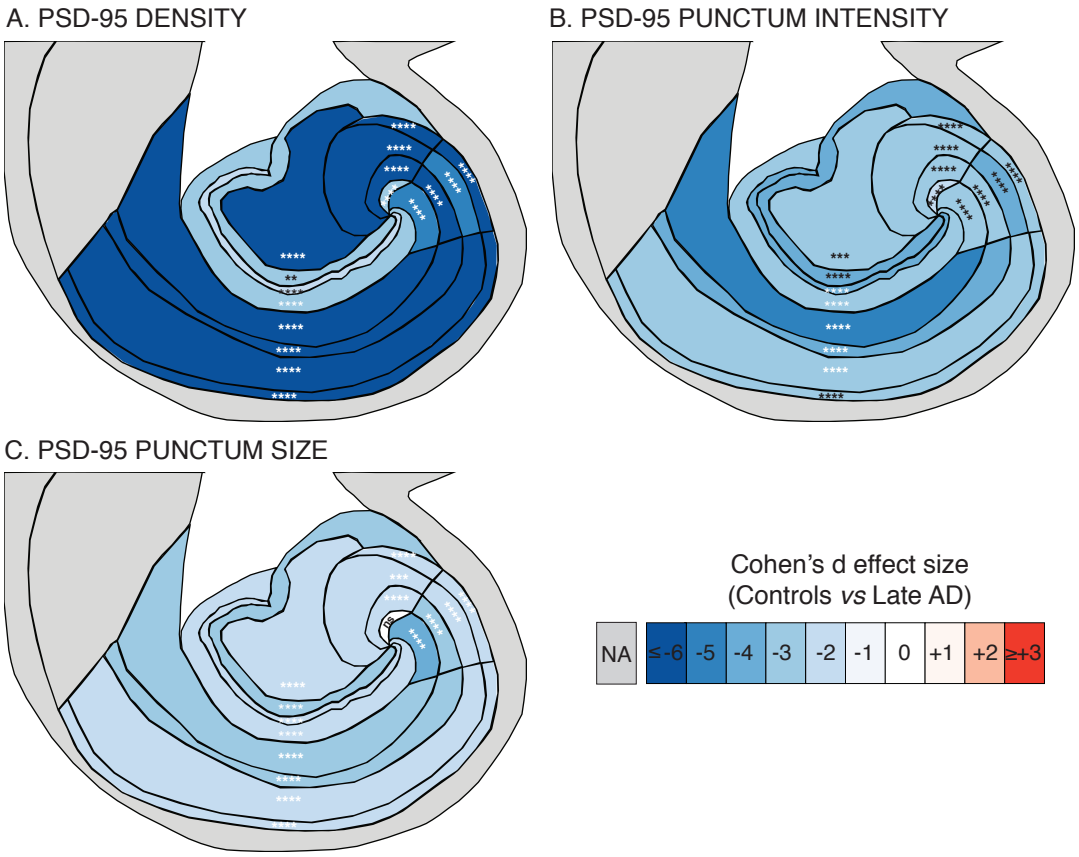


**Figure 5.16 Hippocampal subregional PSD-95 synaptome reorganisation in late AD compared to controls.**

Spatial distribution of differences between controls (n = 14) and the late AD group (n = 8) represented by heatmaps of the Cohen's d values in 16 hippocampal subregions for PSD-95 puncta density **(A)**, PSD-95 puncta intensity **(B)** and PSD-95 puncta size **(C)**. Blue, white and red colours indicate a decrease, no change or an increase, respectively, of the PSD-95 parameter measured in early AD group compared to controls. Significant differences, measured using two-way ANOVA, are indicated by asterisks with significance levels: * $p < 0.05$; ** $p < 0.01$; *** $p < 0.001$; **** $p < 0.0001$; ns, not significant. Abbreviations: AD, Alzheimer's Disease; NA, Not applicable.

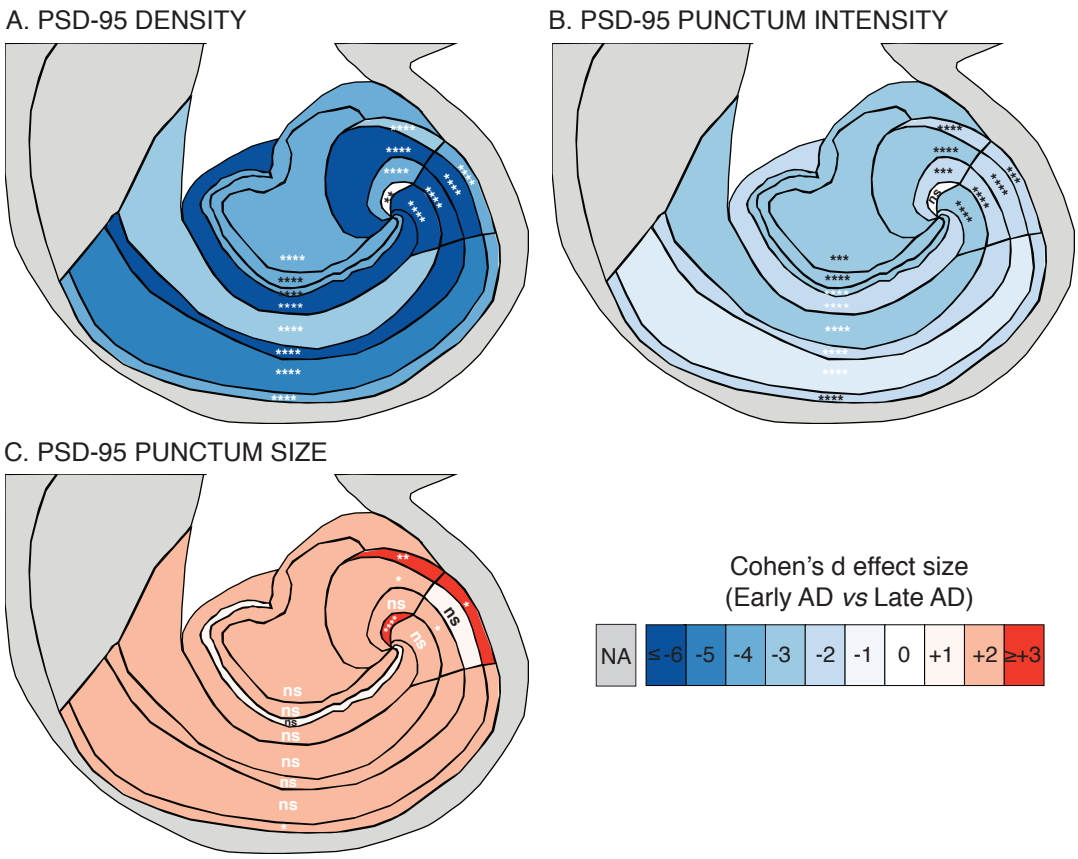


**Figure 5.17 Hippocampal subregional PSD-95 synaptome reorganisation in early *vs.* late AD.**

Spatial distribution of differences between early AD (n = 10) and the late AD group (n = 8) represented by heatmaps of the Cohen's d values in 16 hippocampal subregions for PSD-95 puncta density **(A)**, PSD-95 puncta intensity **(B)** and PSD-95 puncta size **(C)**. Blue, white and red colours indicate a decrease, no change or an increase, respectively, of the PSD-95 parameter measured in early AD group compared to controls. Significant differences, measured using two-way ANOVA, are indicated by asterisks with significance levels: * $p < 0.05$; ** $p < 0.01$; *** $p < 0.001$; **** $p < 0.0001$; ns, not significant. Abbreviations: AD, Alzheimer's Disease; NA, Not applicable.

## 5.10 PSD-95 AND CORRELATION WITH NEUROPATHOLOGY

The study of human post-mortem tissue is essential for investigation of neurodegenerative diseases, particularly as no animal or cellular model can fully recapitulate all aspects of the human pathology. However, the acquisition of human brain after death can affect the brain tissue quality and is prejudicial to the reliability of scientific data based on such material. Therefore, it is important that post-mortem artefacts are defined, standardised and either eliminated or factored into experiments. Since the research in this thesis is based on the examination of human post-mortem brain tissue, in this section, I determined the influence of several putative measures of post-mortem tissue quality on the experiments undertaken in this study.

All brains originated from the SDBTB where the tissue has detailed neuropathological characterisation. I specifically examined the relationships between the results of the PSD-95 synaptic parameter quantification (the PSD-95 density, intensity and size) and various markers for post-mortem brain tissue quality (pH, RIN, PMI, HUSPIR) as well as various established neuropathological parameters (A$\beta$ and CAA). The overview of all the markers and parameters examined and their values for each experimental group (Controls, Early Alzheimer's type pathology and Late Alzheimer's type pathology) are presented in Table 5.3 on page 231.

A summary of the case demographics for the SDM cohort are presented in Figure 5.18 A-C on page 232. Overall, the SDM cohort comprised 14 controls (mean age 60.1 $\pm$ 10.13), 10 cases with early Alzheimer's type pathology (mean age 81 $\pm$ 9.83) and 8 cases with late Alzheimer's type pathology (mean age 75.75 $\pm$ 11.91). The subjects differed significantly with respect to age between the groups ($F(2, 29) = 12.98$, $p < 0.0001$), with the control group cases being significantly younger than either of the AD groups, but there were no significant differences in age between the two AD groups; Figure 5.18 A. When all cases were stratified by gender, there were 17 males (mean age 66.12 $\pm$ SD 13.03) and 15 females (mean age 75.53 $\pm$ SD 13.67). The age difference between the genders was not significant; Figure 5.18 B. Finally, analysis of age by gender and by experimental group revealed that the control group had almost twice as many males (n = 9, mean age 58.67 $\pm$ 8.85) as females (n = 5, mean age 62.60

$\pm$ 12.82). The early Alzheimer's type pathology group had 4 males (mean age 76.50 $\pm$ 8.35) and 6 females (mean age 84.00 $\pm$ 10.26). The genders were equally split in the late Alzheimer's type pathology group (n = 4 each) and the ages were as follows: male mean age 72.50 $\pm$ 16.22 and female mean age 79.00 $\pm$ 6.33. A two-way ANOVA analysis revealed that there were differences between the experimental groups, but not within the genders ($F(2, 26) = 10.58$, $p < 0.0004$); Figure 5.18 C.

There were no significant differences between the experimental groups with respect to brain weight ($F(2, 29) = 2.626$, $p < 0.0895$).

When markers of tissue quality were examined, there were no significant differences between the groups with respect to brain pH ($F(2, 29) = 0.18$, $p < 0.8364$). There were, however, significant differences between the groups with respect to RIN values ($F(2, 29) = 8.273$, $p < 0.0016$). The control group had significantly higher RIN values (5.6 $\pm$ 0.71) vs. the early Alzheimer's type pathology group (4.2 $\pm$ 0.97) which had the lowest RIN values. The late Alzheimer's type pathology group had the intermediate values between the three groups (4.6 $\pm$ 0.88).

In the subsections that follow, I determined in greater details the effects of tissue and protein degradation on PSD-95. I then correlated the PSD-95 results with the two most common pathological changes after tau pathology related to AD beta amyloid pathology and the cerebrovascular pathology. Tau pathology was used to determine the experimental groups (the early Alzheimer's type pathology and the late Alzheimer's type pathology groups). Next, I examined the potential effects of APOE genotypes on our results, and finally, I determined the correlation with the neuronal loss.

**Table 5.3** Neuropathological assessment of the SDM cohort

| | | **Control Group Mean ±(SD)** | **Early AD Group Mean ±(SD)** | **Late AD Group Mean ±(SD)** | **p-value Control *vs* Early AD** | **p-value Control *vs* Late AD** | **p-value Early AD *vs* Late AD** |
|---|---|---|---|---|---|---|---|
| Gender | M | 9 | 4 | 4 | | | |
| | F | 5 | 6 | 4 | | | |
| Age (years) | | 60.1 (10.13) | 81.0 (9.83) | 75.8 (11.90) | 0.0001* | 0.0059* | 0.549 |
| BW (grams) | | 1409 (153) | 1292 (147) | 1252 (217) | 0.233 | 0.109 | 0.874 |
| Brain pH | | 6.2 (0.21) | 6.2 (0.18) | 6.2 (0.28) | 0.970 | 0.900 | 0.823 |
| RIN value | | 5.6 (0.71) | 4.2 (0.97) | 4.6 (0.88) | 0.0016* | 0.051 | 0.711 |
| PMD (hours) | | 69.57 (35.00) | 60.80 (33.69) | 64.00 (30.06) | 0.803 | 0.925 | 0.978 |
| HUSPIR value | | 2.3 (1.29) | 0.8 (0.50) | 1.6 (1.05) | 0.0067* | 0.312 | 0.353 |
| HUSPIR score (1 - 4)** | | 3.6 (0.63) | 2.5 (1.08) | 3.3 (0.76) | 0.0066* | 0.624 | 0.148 |
| A$\beta$ Thal score (0 - 5) | | 0.4 (0.85) | 2.2 (1.62) | 3.9 (1.13) | 0.0287* | < 0.0001* | 0.254 |
| Braak NFT stage (0 - VI) | | 0.2 (0.43) | 2.0 (0.00) | 6.0 (0.00) | 0.0037* | < 0.0001* | 0.103 |
| CERAD score (0 - 3) | | 0.2 (0.43) | 1.8 (1.03) | 2.9 (0.35) | 0.0070* | < 0.0001* | 0.308 |
| CAA score (0 - 3) | | 0.1 (0.53) | 1.1 (1.20) | 2.1 (1.25) | 0.078 | 0.0005* | 0.361 |

All parameters were tested for normality with D'Agostino & Pearson omnibus normality test. If passed, ordinary one-way ANOVA with Tukey's multiple comparison post-hoc test was undertaken (for Age, BW, PMD, HUSPIR value and score). If failed, non-parametric Kruskal-Wallis test with Dunn's post hoc analysis was performed. Adjusted p values are reported with level of significance set at $p < 0.05$. Significant differences are highlighted with an asterisk. Standard deviations are reported in parentheses. Abbreviations: PMD, post-mortem delay; BW, brain weight; RIN, RNA integrity number; CERAD, Consortium to Establish Registry for Alzheimer's Disease. NFT, neurofibrillary tangles; CAA, cerebral amyloid angiopathy; HUSPIR, human synaptic protein integrity ratio. M, males; F, females. **HUSPIR score was created to form categorical ranges, as follows: [<0.49] = 1; [0.5 – 0.69] = 2; [0.7 – 0.99] = 3; [>1] = 4.

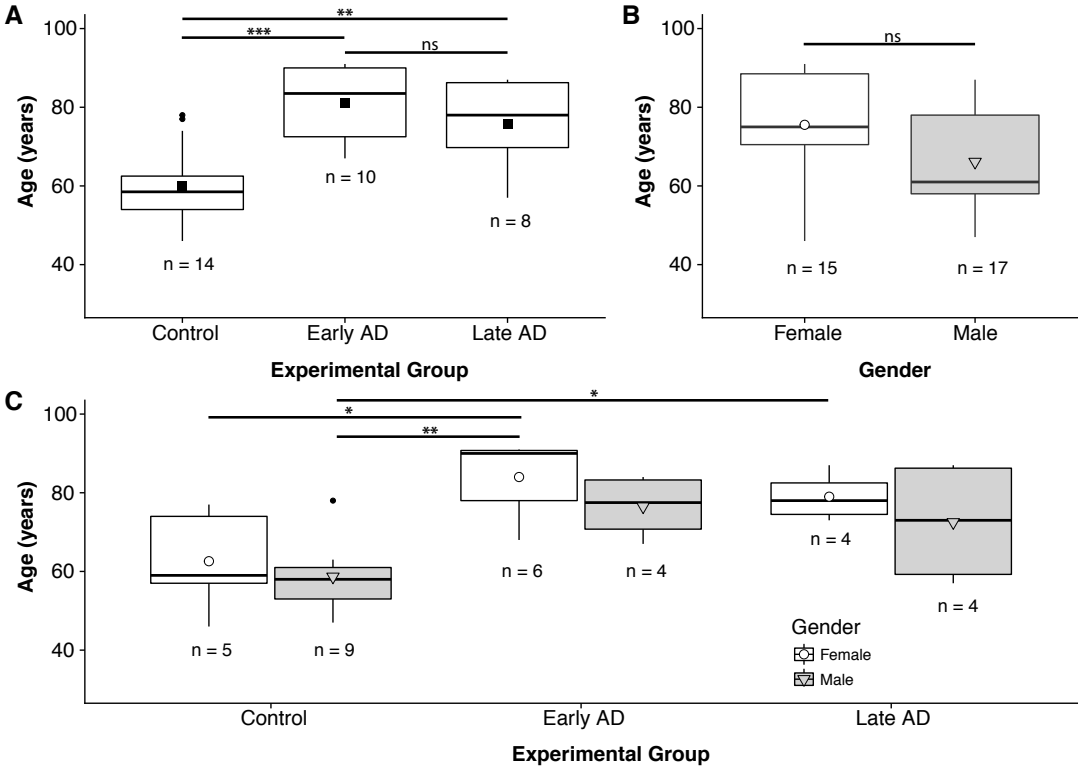


**Figure 5.18 Summary of age characteristics of the SDM cohort by gender and experimental group.**

**A.** Boxplots showing age differences by experimental group. The control group cases were significantly younger than either of the AD groups, but there were no significant differences between the two AD groups; one-way Anova, $F(2, 29) = 12.98$, $p < 0.0001$. **B.** Boxplots showing age differences by gender. No significant age differences were seen between the genders; unpaired two-tailed t-test, $t = 1.993$, $df = 30$, $p = 0.0554$. **C.** Boxplots showing differences in age by experimental group and gender. There were significant differences between the groups; two-way Anova, ($F(2, 26) = 10.58$, $p < 0.0004$). Tukey's multiple comparisons tests revealed three significant differences as highlighted in the figure. Within each boxplot, horizontal lines show the medians; box limits indicate the interquartile range (IQR) (inferior or 1st quartile range = 25th percentile, and superior or 3rd quartile range = 75th percentiles) as determined by R software; whiskers are defined by Tukey and extend to data points that are less than 1.5x IQR away from the 1st/3rd quartile; outliers are represented by black circles. Black squares, white circles and white triangles represent mean values. Significance levels: * $p < 0.05$; ** $p < 0.01$; *** $p < 0.001$; **** $p < 0.0001$; ns, not significant.

### 5.10.1 PSD-95 and protein degradation markers

Although specific measurements for PSD-95 protein post-mortem degradation were not performed in this study, associations between the PSD-95 protein levels and indicators of post-mortem tissue degradation, namely PMD and HUSPIR values, were explored.

#### *5.10.1.1 PSD-95 vs. PMD*

Overall, one-way analysis of variance revealed no statistical difference in post-mortem delay (PMD) between the cohort subgroups ($F(2,29) = 0.21$, $p = 0.81$). The mean ($\pm$ SD) PMD values were 69.57 ($\pm$ 35.00), 60.80 ($\pm$ 33.69) and 64.00 ($\pm$ 30.06) for control, early stage Alzheimer's type pathology and late stage Alzheimer's type pathology groups, respectively (Table 5.3 on page 231).

PSD-95 puncta density and intensity measurements also demonstrated a lack of significant correlation with PMD in the entire experimental SDM cohort (Pearson's product-moment correlation $r = 0.079$, $p = 0.6675$ and $r = 0.069$, $p = 0.707$, for density and intensity, respectively; Figure 5.19 A-C on page 234). There was a weak positive correlation of PMD with PSD-95 puncta size, but it was not significant ($r = 0.235$, $p = 0.195$).

Further analyses of the relationships between PMD and PSD-95 within each cohort subgroup confirmed a lack of significant interactions with all three PSD-95 parameters (Figure 5.19 D-F).

In summary, my data demonstrated that there was no dependence of PSD-95 parameters on PMD in our experimental cohort.

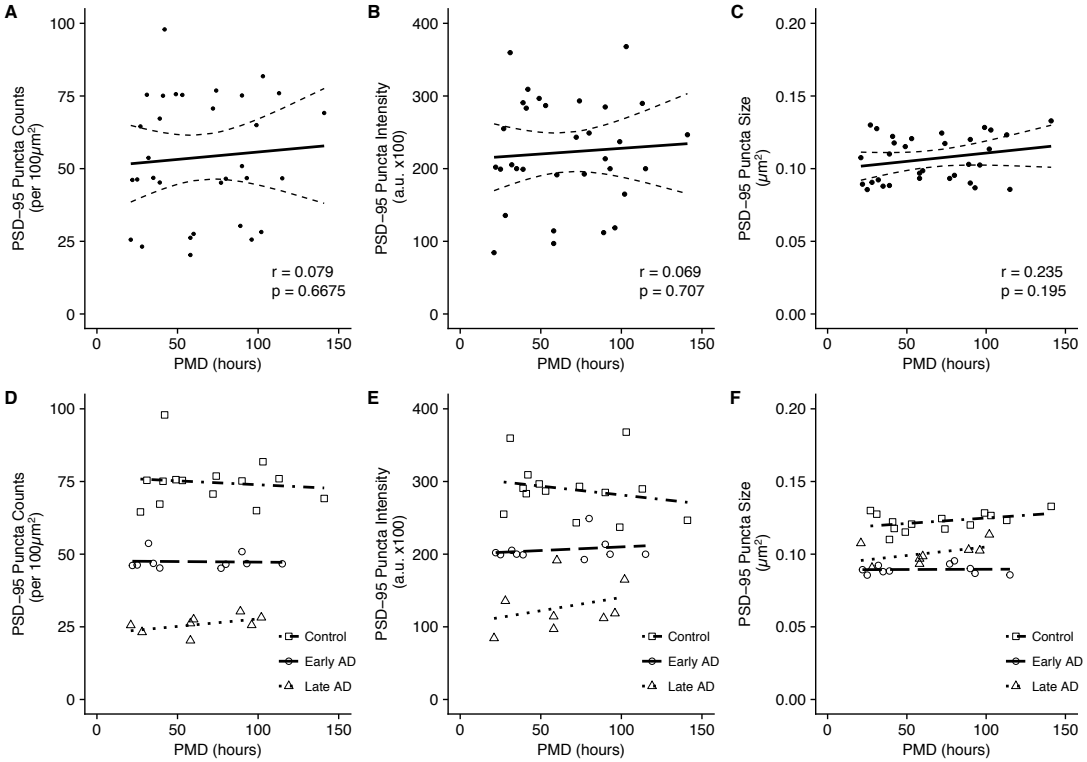


**Figure 5.19 PSD-95 synaptic puncta parameters *vs.* PMD in the SDM cohort.**

**A-C.** The relationship of (A) PSD-95 puncta density, (B) PSD-95 puncta intensity, and (C) PSD-95 puncta size in the entire SDM cohort to PMD showed absence of significant correlations for each parameter (Pearson's product-moment correlation r = 0.079, p = 0.6675; r = 0.069, p = 0.707; and r =0.235, p = 0.195, respectively). The solid lines represent the best-fit linear regression lines. The interrupted lines represent the 95% confidence intervals. **D-F.** Additional testing of (D) PSD-95 puncta density, (E) PSD-95 puncta intensity, and (F) PSD-95 puncta size against PMD within each experimental group (Control, Early AD and Late AD), demonstrated no interaction between PMD within each group and the tested PSD-95 protein parameter, indicating that PSD-95 protein is not modified by PMD despite significant differences between the groups in PSD-95 counts, intensity and size. The lines for each subgroups indicate best-fit linear regression. Each data point represents a separate brain. AD, Alzheimer's Disease; a.u., arbitrary unit.

#### *5.10.1.2 PSD-95 vs. HUSPIR*

In the first instance, one-way analysis of variance revealed that there was a difference in synaptic protein degradation, as assessed by the HUSPIR value, between the cohort subgroups ($F(2,28) = 5.58$, $p = 0.0091$). The mean ($\pm$ SD) HUSPIR values were 2.3 ($\pm$ 1.29), 0.8 ($\pm$ 0.50) and 1.6 ($\pm$ 1.05) for control, early stage Alzheimer's type pathology and late stage Alzheimer's type pathology groups, respectively (Table 5.3 on page 231). There was a significant difference between the control and the early stage Alzheimer's type pathology group (mean difference = 1.44, $p = 0.0067$).

Secondly, PSD-95 puncta density, intensity and size measurements demonstrated positive correlations with HUSPIR which were significant for the PSD-95 density and size (Pearson's product-moment correlation $r = 0.37$, $p = 0.043$; $r = 0.34$, $p = 0.060$; and $r = 0.540$, $p = 0.002$, for density, intensity and size, respectively; Figure 5.20 A-C on page 237 in the overall experimental cohort.

Finally, further analyses of the relationships between HUSPIR and PSD-95 within each cohort subgroup revealed an absence of any significant interactions between HUSPIR and all three PSD-95 parameters, although the differences between the subgroups remained significant (Figure 5.20 D-F). In summary, it appears that HUSPIR in our experimental cohort did not significantly affect the PSD-95 protein.

However, since it is the value above 1 that is important for the HUSPIR value and many cases had values just below 1, the data were grouped into 4 categorical scores to evaluate whether the lower HUSPIR values had similar effects as the values equal or above 1. The categorical data were converted from HUSPIR values into HUSPIR scores and the same analysis was performed to investigate further correlations.

To start with, one-way analysis of variance revealed significant difference in the protein degradation marker (HUSPIR score) between the cohort subgroups ($F(2,28) = 5.63$, $p = 0.0088$). The mean ($\pm$ SD) HUSPIR score were 3.6 ($\pm$ 0.63), 2.5 ($\pm$ 1.08) and 3.3 ($\pm$ 0.76) for control, early stage Alzheimer's type pathology and late stage Alzheimer's type pathology groups, respectively (Table 5.3 on page 231). There was a significant difference between the control and the early AD group (mean difference

= 1.14, p = 0.0067). These results show the same trends for both the HUSPIR value and the HUSPIR score in terms of groups with most degraded synaptic proteins for each parameter (the controls having the least degraded synaptic proteins followed by the late and then the early stage Alzheimer's type pathology groups). Moreover, the data demonstrate that the early stage Alzheimer's type pathology group had the most degraded synaptic proteins for both HUSPIR estimations, and that they were significantly lower when compared to the control group.

Secondly, I assessed whether there was any relationship between each of the PSD-95 synaptic puncta parameters and an increasing HUSPIR score in the hippocampus (Figure 5.21 A-C on page 238). A Kruskall-Wallis test showed there were no significant variations in the PSD-95 density, intensity and size between the HUSPIR scores ($\chi^2$ = 3.46, p = 0.326; $\chi^2$ = 3.15, p = 0.370 ;$\chi^2$ = 6.58, p = 0.087; for each parameter respectively).

Then, I established that all PSD-95 puncta parameters demonstrated positive correlations with the HUSPIR score (Spearman's rank correlation rho = 0.32, p = 0.07; rho = 0.32, p = 0.08; and rho = 0.46, p = 0.010 for density, intensity and size, respectively; (Figure 5.21 D-F) across the entire SDM cohort. However, only PSD-95 size parameter showed a significant correlation with HUSPIR score.

Finally, further analyses of the relationships between HUSPIR and PSD-95 within each experimental subgroup confirmed lack of significant interactions for all of the three PSD-95 parameters (Figure 5.21 G-I).

In summary, similar to the HUSPIR value, the HUSPIR score in my experimental cohort was dependent on the experimental group, but did not influence the extent of synaptic protein degradation.

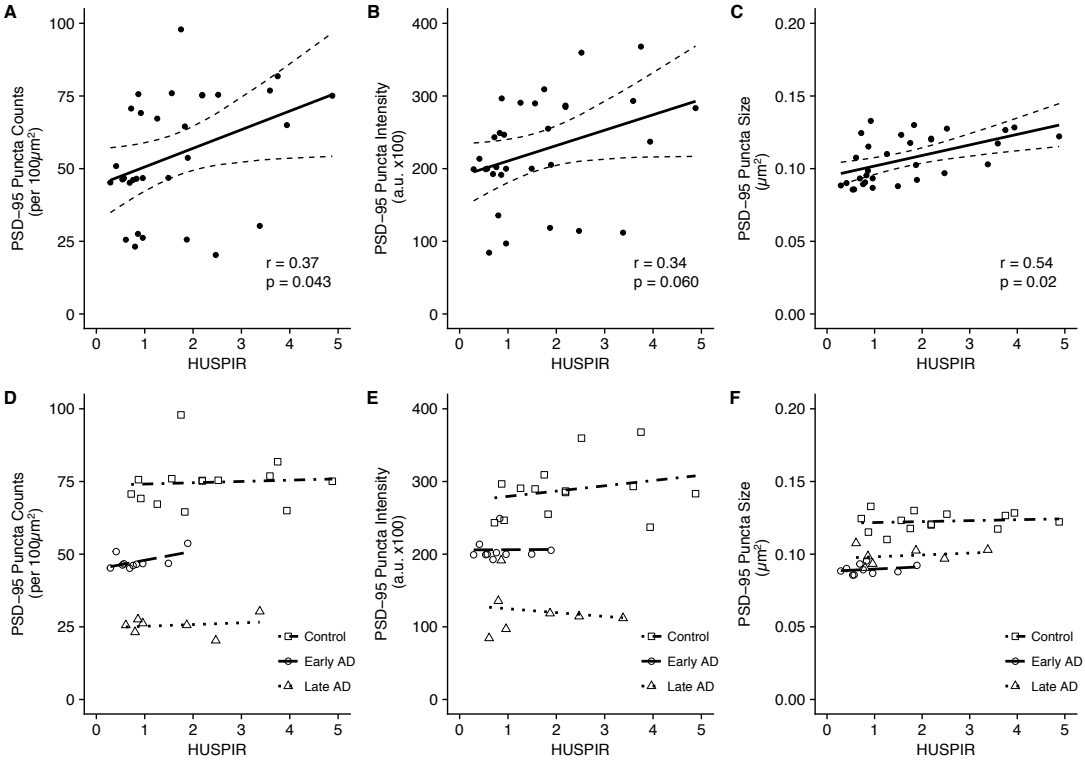


**Figure 5.20 PSD-95 synaptic puncta parameters *vs.* HUSPIR value in the SDM cohort.**

**A-C.** The relationship of (A) PSD-95 puncta density, (B) PSD-95 puncta intensity, and (C) PSD-95 puncta size in the entire SDM cohort to HUSPIR value showed significant positive correlations for the PSD-95 density and size, but not the intensity (Pearson's product-moment correlation r = 0.37, p = 0.043; r = 0.34, p = 0.060; and r = 0.540, p = 0.002, for density, intensity and size, respectively). The solid lines represent the best-fit linear regression lines. The interrupted lines represent the 95% confidence intervals. **D-F.** Additional testing of (D) PSD-95 puncta density, (E) PSD-95 puncta intensity, and (F) PSD-95 puncta size against HUSPIR within each experimental group (Control, Early AD and Late AD), demonstrated no interaction between HUSPIR value within each group and the tested PSD-95 protein parameter, indicating that PSD-95 protein is not modified by HUSPIR value despite significant differences between the groups in PSD-95 counts, intensity and size. The lines for each subgroups indicate best-fit linear regression. Each data point represents a separate brain. AD, Alzheimer's Disease; a. u., arbitrary unit.

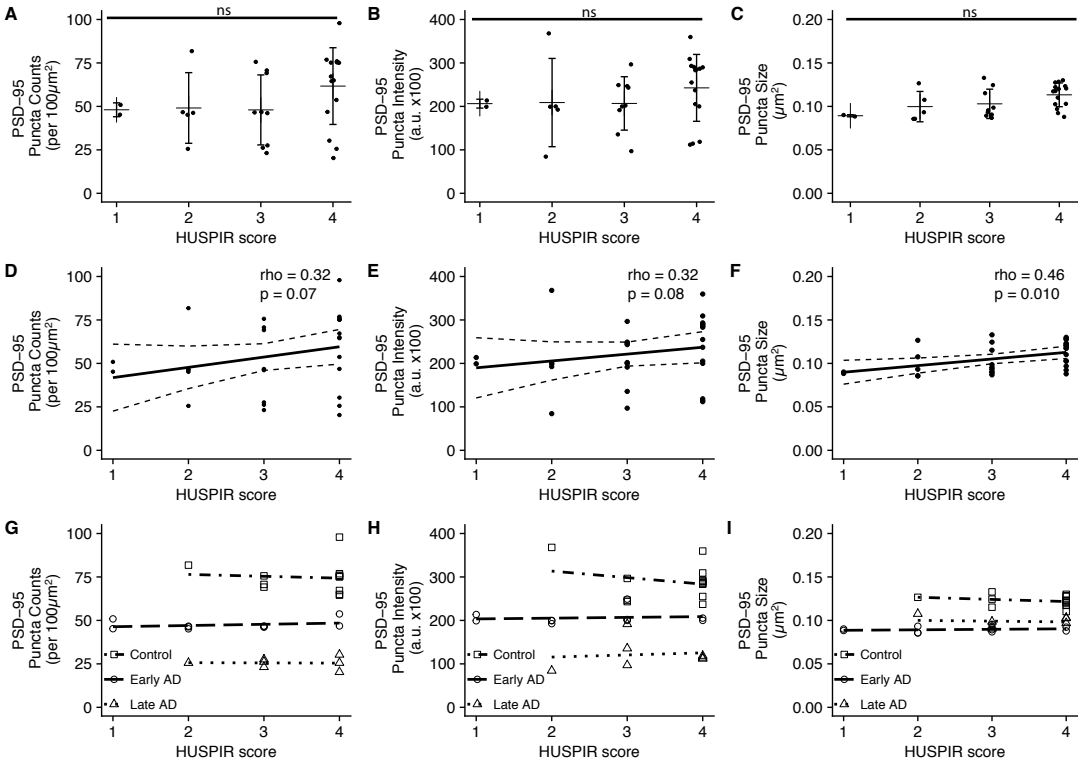


**Figure 5.21 PSD-95 synaptic puncta parameters *vs.* HUSPIR score in the SDM cohort.**

**A-C.** Levels of (A) PSD-95 puncta density, (B) PSD-95 puncta intensity, and (C) PSD-95 puncta size in the hippocampus from the experimental cohort to synaptic protein degradation, as defined by HUSPIR score. PSD-95 puncta counts were the highest (A), their intensity was the brightest (B), and their size was the biggest (C) when the synaptic proteins were most preserved (HUSPIR score 4). However, no significant differences were found between the scores for any of the PSD-95 parameters. Horizontal lines represent mean values for each HUSPIR score and errorbars represent ± SD. **D-F.** The relationship of (D) PSD-95 puncta density, (E) PSD-95 puncta intensity, and (F) PSD-95 puncta size in the whole cohort to HUSPIR score showed positive correlations for each parameter (Spearman's rank correlation rho = 0.32, p = 0.07; rho = 0.32, p = 0.08; and rho = 0.46, p = 0.010 for density, intensity and size, respectively), but only size was significant. The solid lines represent the best-fit linear regression lines. The interrupted lines represent the 95% confidence intervals. **G-H.** Additional testing of (G) PSD-95 puncta density, (H) PSD-95 puncta intensity, and (I) PSD-95 puncta size against HUSPIR score within each experimental group (Control, Early AD and Late AD), however, demonstrated no interaction between the HUSPIR score within each group and the tested PSD-95 protein markers, indicating that PSD-95 protein is not independently modified by synaptic protein degradation despite obvious differences between the groups in PSD-95 counts, intensity and size. There was a clear change in PSD-95 size, in particular, between the groups (I). The lines for each subgroups indicate best-fit linear regression. Each data point represents a separate brain. AD, Alzheimer's Disease; a.u., arbitrary unit. HUSPIR score was created to form categorical ranges as follows: [<0.49] = 1; [0.5 – 0.69] = 2; [0.7 – 0.99] = 3; [>1] = 4.

### 5.10.2 PSD-95 and A$\beta$ burden

All brains were characterised according to the ABC scoring classification (Hyman et al., 2012) as described in Chapter 2.13. The human cases belonging to the early and the late stages Alzheimer's type pathology groups were originally defined according to the topographic progression of Tau neurofibrillary tangle pathology (Braak staging) (Braak et al., 2006). However, amyloid plaques have long been considered a hallmark of AD, which is why they were incorporated in the CERAD criteria for AD (Mirra et al., 1991). Of note, early studies demonstrated that numerical density of amyloid plaques correlates with the severity of AD-related cognitive impairment (Roth et al., 1967; Perry et al., 1978; Wilcock and Esiri, 1982). Other studies have since questioned the role of amyloid plaques in AD (DeKosky and Scheff, 1990; Price et al., 1991; Scheff et al., 1993) and even demonstrated that there is no correlation between senile plaques and cognitive decline in AD (Arriagada et al., 1992).

In this section, I wanted to examine the relationship between the PSD-95 synaptic puncta parameters and amyloid plaques, as defined by two out of the three criteria of the ABC scoring classification for AD, namely the topographic progression of A$\beta$ pathology in the brain (Thal phases) (Thal et al., 2002) and the density of mature (senile) neuritic plaques Consortium to Establish a Registry for Alzheimer's Disease (CERAD) (Mirra et al., 1991).

#### *5.10.2.1 PSD-95 vs. Thal*

Firstly, I assessed whether there were any significant differences in topographical A$\beta$ distribution scores between the three experimental groups using the Kruskal-Wallis ANOVA (the non-parametric alternative to ANOVA) test. I identified a significant difference between the experimental groups ($\chi^2$ = 19.23, p $<$ 0.0001). On a six-point scale from 0 to 5, the control group had the lowest Thal scores of 0.4 $\pm$ 0.85 (mean $\pm$ SD), followed by the early stage Alzheimer's type pathology group (2.2 $\pm$ 1.62) and the late stage Alzheimer's type pathology group (3.9 $\pm$ 1.13) (Table 5.3 on page 231). Three Dunn's post hoc pairwise comparisons between the groups were

performed. The comparison of controls with the late stage Alzheimer's type pathology group individuals was significant and revealed that late group stage Alzheimer's type pathology patients had the most severe Thal scores (mean difference = -17.13, $p < 0.0001$). The Thal scores were less severe for the early stage Alzheimer's type pathology group (mean difference = -9.72, p = 0.029). No significant differences were found between the two stages of Alzheimer's type pathology groups (mean difference = -7.41, p = 0.25) although the latest stage Alzheimer's type pathology stage was associated with higher Thal scores (Table 5.3 on page 231). In summary, the extent of A$\beta$ distribution, as assessed by Thal score, was significantly greater in the patients when compared to controls, but did not differ significantly between the two Braak stages.

I then combined the three groups and asked whether there was any relationship between each of the PSD-95 synaptic puncta parameter and the extend of A$\beta$ distribution in the hippocampus (Figure 5.22 A-C). There was significant variation in the PSD-95 density between the Thal scores ($\chi^2$ = 22.88, p = 0.0004). The subsequent post-testing revealed a significant reduction in PSD-95 density in cases with Thal severity of 5 compared with those of 0 (mean difference = 20.58, $p < 0.01$). There was also significant variation in the PSD-95 intensity between the Thal scores ($\chi^2$ = 22.68, p = 0.0004), with post-testing showing a significant reduction in PSD-95 intensity in cases with Thal severity of 4 compared with those of 0 (mean difference = 16.46, $p < 0.05$) and in cases with Thal severity of 5 compared with those of 0 (mean difference = 19.96, $p < 0.01$). Finally, there was a significant variation in the PSD-95 size between the six scores ($\chi^2$ = 13.14, p = 0.022), but the post-testing revealed that the reduction in PSD-95 size was not significant for any of the Thal scores.

I next examined whether changes in PSD-95 synaptic parameters correlated with topographical A$\beta$ distribution when we combined the three experimental groups (Figure 5.22 D-F). The results of the Spearman's correlation analyses revealed that all three PSD-95 synaptic puncta parameters were significantly negatively correlated with Thal score (Spearman's rank correlation rho = -0.806, p = 2.667e-08; rho = -0.799, p = 4.005e-08; and rho = -0.516 , p = 0.002524, for PSD-95 puncta density, intensity and size, respectively).

Finally, I evaluated whether levels of PSD-95 parameters varied once the three experimental groups were separated (Figure 5.22 G-I). Although the initial exploration of data showed moderate negative correlations between the PSD-95 parameters and the severity of Thal, stratification of data by experimental groups revealed no dependence of PSD-95 parameters on Thal severity. However, the PSD-95 density and intensity levels were significantly lower in the AD groups and the reductions followed AD progression in relation to the extend of topographical A$\beta$ distribution. In contrast, although the PSD-95 size was lower in the AD groups, the PSD-95 size in the early stage Alzheimer's type pathology group were the smallest.

To summarise, the analysis of the SDM cohort demonstrated that topographical A$\beta$ distribution was associated with significantly reduced PSD-95 parameters' levels, and an increased extension of topographical A$\beta$ distribution led to a corresponding reduction in the PSD-95 synaptic diversity. However, topographical A$\beta$ distribution does not independently contribute to PSD-95 synaptic damage as within each experimental group there was no dependence of PSD-95 synaptic puncta parameters on Thal scores. Instead, the PSD-95 IF parameters are dependent on Braak stages, which are associated with reductions in PSD-95 synaptic parameters.

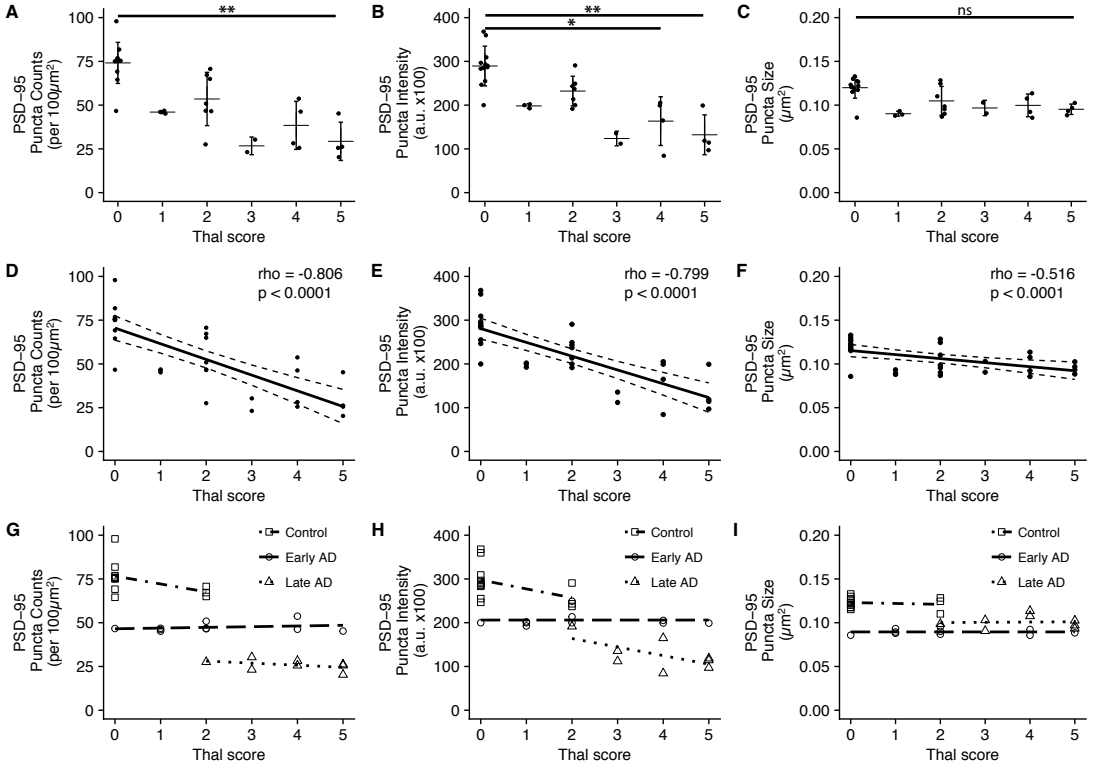


**Figure 5.22 PSD-95 parameters and topographical A$\beta$ distribution (Thal score) in the human posterior hippocampus from the SDM cohort.**

**A-C.** Levels of (A) PSD-95 puncta density, (B) PSD-95 puncta intensity, and (C) PSD-95 puncta size in the hippocampus from the experimental cohort to topographical distribution of A$\beta$ plaques as defined by Thal score. PSD-95 puncta counts were the highest (A), their intensity was the brightest (B), and their size was the biggest (C) in the absence of A$\beta$ pathology (Thal score 0). There was a general trend of PSD-95 puncta becoming dimmer and smaller, with decreasing numbers, as the A$\beta$ plaques became more spread throughout the brain. Horizontal lines represent mean values for each Thal score and errorbars represent $\pm$ SD. **D-F.** The relationship of (D) PSD-95 puncta density, (E) PSD-95 puncta intensity, and (F) PSD-95 puncta size in the whole cohort to A$\beta$ topographical distribution showed significant negative correlations for each parameter (Spearman's rank correlation rho = -0.806, $p < 0.0001$; rho = -0.799, $p < 0.0001$; and rho = -0.516, $p < 0.0001$, respectively). The solid lines represent the best-fit linear regression lines. The interrupted lines represent the 95% confidence intervals. **G-I.** Additional testing of (G) PSD-95 puncta density, (H) PSD-95 puncta intensity, and (I) PSD-95 puncta size against A$\beta$ spread within each experimental group (Control, Early AD and Late AD), however, demonstrated no interaction between A$\beta$ distribution by Thal score within each group and the tested PSD-95 protein markers, indicating that PSD-95 protein is not modified by A$\beta$ spread despite obvious differences between the groups in PSD-95 counts, intensity and size. There was a clear change in PSD-95 size, in particular, between the groups (I). The lines for each subgroups indicate best-fit linear regression. Each data point represents a separate brain. AD, Alzheimer's Disease; a. u., arbitrary unit.

#### *5.10.2.2 PSD-95 vs. CERAD*

Initially, I assessed whether there were any significant differences in severity of A$\beta$ distribution scores between the three experimental groups using the Kruskal-Wallis ANOVA (the non-parametric alternative to ANOVA) test. There was a significant difference between the experimental groups ($\chi^2$ = 22.93, p $<$ 0.0001). On a four-point scale from 0 to 3, the control group had the lowest CERAD scores of 0.2 $\pm$ 0.43 (mean $\pm$ SD), followed by the early stage Alzheimer's type pathology group (1.8 $\pm$ 1.03) and the late stage Alzheimer's type pathology group (2.9 $\pm$ 0.35) (Table 5.3 on page 231). Three Dunn's post hoc tests were performed. The comparison of controls with the late stage Alzheimer's type pathology group individuals was significant and revealed that late group stage Alzheimer's type pathology patients had the most severe CERAD scores (mean difference = -18.2, p < 0.0001). The CERAD scores were less severe for the early stage Alzheimer's type pathology group (mean difference = -11.27, p = 0.007). No significant differences were found between the two AD groups (mean difference = -6.92, p = 0.31) (Table 5.3 on page 231).

I subsequently asked whether there was any relationship between each of the PSD-95 synaptic puncta parameter and the severity of A$\beta$ distribution in the hippocampus (Figure 5.23 A-C). There was significant variation in the PSD-95 density related to the CERAD scores ($\chi^2$ = 21.69, p < 0.0001). The post-testing revealed a significant reduction in PSD-95 density in cases with CERAD severity of 3 compared with those of 0 (mean difference = 18.18, p < 0.0001). There was also significant variation in the PSD-95 intensity between the CERAD scores ($\chi^2$ = 21.53, p = 0.0001), with post-testing showing a significant reduction in PSD-95 intensity in cases with CERAD severity of 3 compared with those of 0 (mean difference = 18.51, p < 0.0001). Finally, there was a significant variation in the PSD-95 size related to the four CERAD groups ($\chi^2$ = 12.86, p = 0.005). The post-testing showed a significant reduction in PSD-95 size in cases with CERAD severity of 3 compared with those of 0 (mean difference = 11.58, p < 0.05) and in cases with CERAD severity of 2 compared with those of 0 (mean difference = 16.08, p < 0.05).

I next examined whether changes in PSD-95 synaptic parameters correlated

with severity of A$\beta$ plaques when we combined the three experimental groups (Figure 5.23 D-F). The results of the Spearman's correlation analyses revealed that all three PSD-95 synaptic puncta parameters were significantly negatively correlated with CERAD score (Spearman's rank correlation rho = -0.833, p = 3.185e-09; rho = -0.832, p = 3.594e-09; and rho = -0.571 , p = 0.0006439, for PSD-95 puncta density, intensity and size, respectively).

Finally, I evaluated whether levels of PSD-95 parameters varied once the three experimental groups were separated (Figure 5.23 G-I). Although the initial exploration of data showed good correlations between the PSD-95 parameters and the severity of CERAD score, stratification of data by disease groups revealed no dependence of PSD-95 parameters by CERAD severity. However, the PSD-95 density and intensity levels were significantly lower in the AD groups and the reductions followed AD progression in relation to the severity of A$\beta$ distribution. In contrast, although the PSD-95 size was lower in the AD groups, the PSD-95 sizes in the early AD group were the smallest.

Overall, the analysis of the SDM cohort, demonstrated that the severity of A$\beta$ distribution was associated with significantly reduced PSD-95 parameter levels, and an increased severity of A$\beta$ pathology led to correspondingly reduced the PSD-95 synaptic diversity. However, severity of A$\beta$ pathology does not independently contribute to PSD-95 synaptic damage as within each experimental group there was no dependence of PSD-95 parameters with regard to A$\beta$ severity. Instead, in agreement with existing literature, the stage of Alzheimer's type pathology was associated with a significant reduction of PSD-95 parameters.

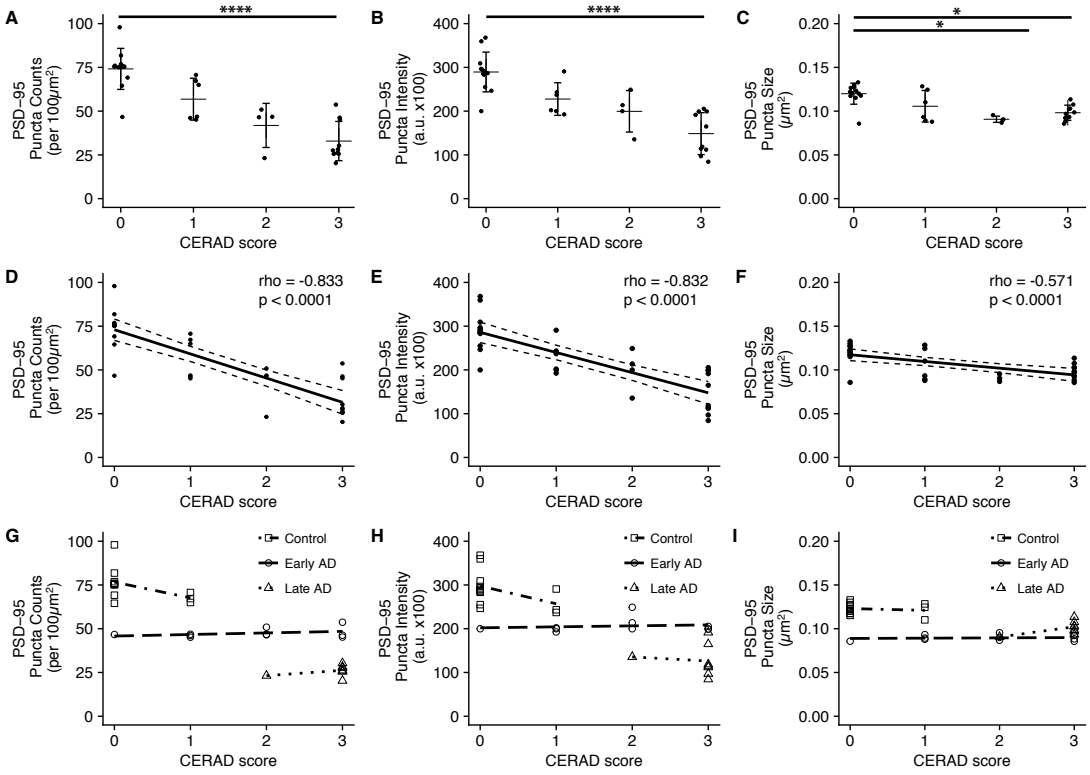


**Figure 5.23 PSD-95 parameters and severity of A$\beta$ pathology (CERAD score) in the human posterior hippocampus from the SDM cohort.**

**A-C.** Levels of (A) PSD-95 puncta density, (B) PSD-95 puncta intensity, and (C) PSD-95 puncta size in the hippocampus from the experimental cohort to severity of A$\beta$ plaques, as defined by CERAD score. PSD-95 puncta counts were the highest (A), their intensity was the brightest (B), and their size was the biggest (C) in the absence of A$\beta$ pathology (CERAD score 0). There was a clear negative trend of PSD-95 puncta becoming dimmer and fewer, as A$\beta$ plaque burden increased. Horizontal lines represent mean values for each CERAD score and errorbars represent $\pm$ SD. **D-F.** The relationship of (D) PSD-95 puncta density, (E) PSD-95 puncta intensity, and (F) PSD-95 puncta size in the whole cohort to A$\beta$ burden severity showed significant negative correlations for each parameter (Spearman's rank correlation rho = -0.833, p = 3.185e-09; rho = -0.832, p = 3.594e-09; and rho = -0.571 , p = 0.0006439, respectively). **G-H.** Additional testing of (G) PSD-95 puncta density, (H) PSD-95 puncta intensity, and (I) PSD-95 puncta size against A$\beta$ severity within each experimental group (Control, Early AD and Late AD), however, demonstrated no interaction between A$\beta$ burden severity by CERAD score within each group and the tested PSD-95 protein markers, indicating that PSD-95 protein is not independently modified by A$\beta$ pathology despite obvious differences between the groups in PSD-95 counts, intensity and size. There was a clear change in PSD-95 size, in particular, between the groups (I). The solid lines represent the best-fit general linear regression lines. The grey shadow areas represent the 95% confidence intervals. AD, Alzheimer's Disease; a.u., arbitrary unit.

### 5.10.3 PSD-95 and vascular pathology

The majority of AD cases show some degree of cerebrovascular pathology. Cerebral amyloid angiopathy (CAA) is common in AD, but its relationship to other aspects of AD pathology, including synaptic dysfunction, is unclear. There is a possible interdependence between the vascular pathology, such as CAA, and the beta amyloid pathology in AD. Increased A$\beta$ may cause vascular dysfunction through vasoconstriction, impairments of cerebral autoregulation and functional hyperaemia. Deposition of A$\beta$ in the wall of blood vessels causes CAA (Olichney et al., 1995; Ellis et al., 1996). Interestingly, risk factors for cerebrovascular disease and vascular dementia (VaD) are similar to risk factors for AD.

In AD, synaptic loss has been well documented for presynaptic proteins (Masliah et al., 1991). Postsynaptic proteins, such as PSD-95, have also been found to be reduced in AD and minimal cognitive impairment (Love et al., 2006; Scheff et al., 2011). Moreover, reduced cortical presynaptic protein levels have been reported in vascular dementia (Sinclair et al., 2015). However, the effects of cerebrovascular pathology specifically on synaptic diversity in AD are not known.

In this section, I examined the effects of cerebrovascular pathology, as exemplified by cerebral amyloid angiopathy, on PSD-95 synapses and their diversity in human hippocampal sections from the SDM cohort. The severity of CAA pathology has been assessed in the H&E sections. The scores were compared against the PSD-95 synaptic puncta parameters results obtained with the G2CSynMaP methodology. The relationships between the PSD-95 protein expression and CAA were subsequently examined. Confirmation of reduced PSD-95 levels with increasing CAA pathology severity would further validate our new quantification method. In addition, I hypothesised that the diversity of the PSD-95 would be reduced in the two stages of Alzheimer's type pathology in comparison to the controls with increasing severity of CAA.

#### *5.10.3.1 PSD-95 vs. CAA*

As the CAA data was not normally distributed, I used the Kruskal-Wallis ANOVA to assess whether there were any significant differences in CAA between the three experimental groups. There was a significant difference between the experimental groups ($\chi^2$ = 14.71, p = 0.0006). On a four-point scale from 0 to 3, the control group had the lowest CAA scores of 0.1 $\pm$ 0.53 (mean $\pm$ SD), followed by the early stage Alzheimer's type pathology group (1.1 $\pm$ 1.20) and the late stage Alzheimer's type pathology group (2.1 $\pm$ 1.25) (Table 5.3 on page 231). Three Dunn's post hoc tests were performed. The comparison of controls with the late AD group individuals was significant and revealed that late stage stage Alzheimer's type pathology patients had the most severe CAA scores (mean difference = -13.99, p < 0.0005). The CAA scores between the controls and the early stage Alzheimer's type pathology group (mean difference = -7.78, p = 0.078) and between the two AD groups (mean difference = -6.21, p = 0.36) were not significant (Table 5.3 on page 231).

I asked whether there was any relationship between each of the PSD-95 synaptic puncta parameter and the CAA severity in the hippocampus (Figure 5.24 A-C). There was significant variation in the PSD-95 density between the CAA scores ($\chi^2$ = 13.39, p = 0.0039). The subsequent post-testing revealed a significant reduction in PSD-95 density in cases with CAA score of 3 compared with those of 0 (mean difference = 13.18, p < 0.01). There was also significant variation in the PSD-95 intensity between the CAA scores ($\chi^2$ = 12.16, p = 0.001), with post-testing showing a significant reduction in PSD-95 intensity in cases with a CAA score of 3 compared with those of 0 (mean difference = 12.76, p < 0.05). Finally, there was no significant variation in the PSD-95 size between the four CAA groups ($\chi^2$ = 6.55, p = 0.0875).

I next examined whether changes in the PSD-95 synaptic parameters correlated with CAA when we combined the three experimental groups (Figure 5.24 D-F). The results of the Spearman's correlation analyses revealed that all three PSD-95 synaptic puncta parameters were significantly negatively correlated with CAA score (rho = -0.616, p = 0.00018; rho = -0.603, p = 0.00026; and rho = -0.398, p = 0.024, for PSD-95 puncta density, intensity and size, respectively).

Finally, I evaluated whether levels of PSD-95 parameters varied once the three experimental groups were separated (Figure 5.24 G-I). The initial exploration of data showed good correlations between the PSD-95 parameters and the severity of CAA, but stratification of data by disease groups revealed no dependence of PSD-95 parameters by CAA severity. However, similarly to SVD, the PSD-95 density and intensity levels were significantly lower in the Alzheimer's type pathology groups and the reductions followed Alzheimer's type pathology progression in relation to the severity of CAA. In contrast, although the PSD-95 size was lower in the AD groups in comparison to controls, the PSD-95 size parameter in the early stage Alzheimer's type pathology group was the smallest.

In summary, the analysis of the SDM cohort has demonstrated that CAA was associated with significantly reduced the PSD-95 parameters' levels, and an increased severity of CAA led to a corresponding reduction in the PSD-95 synaptic diversity. However, CAA does not independently contribute to PSD-95 synaptic damage as within each experimental group there was no dependence of PSD-95 parameters on SVD severity. Instead, the Alzheimer's type pathology stage was associated with a significant reduction of PSD-95 parameters with the exception of the PSD-95 size parameter that was most severely affected in the early stage Alzheimer's type pathology rather than the late stage Alzheimer's type pathology.

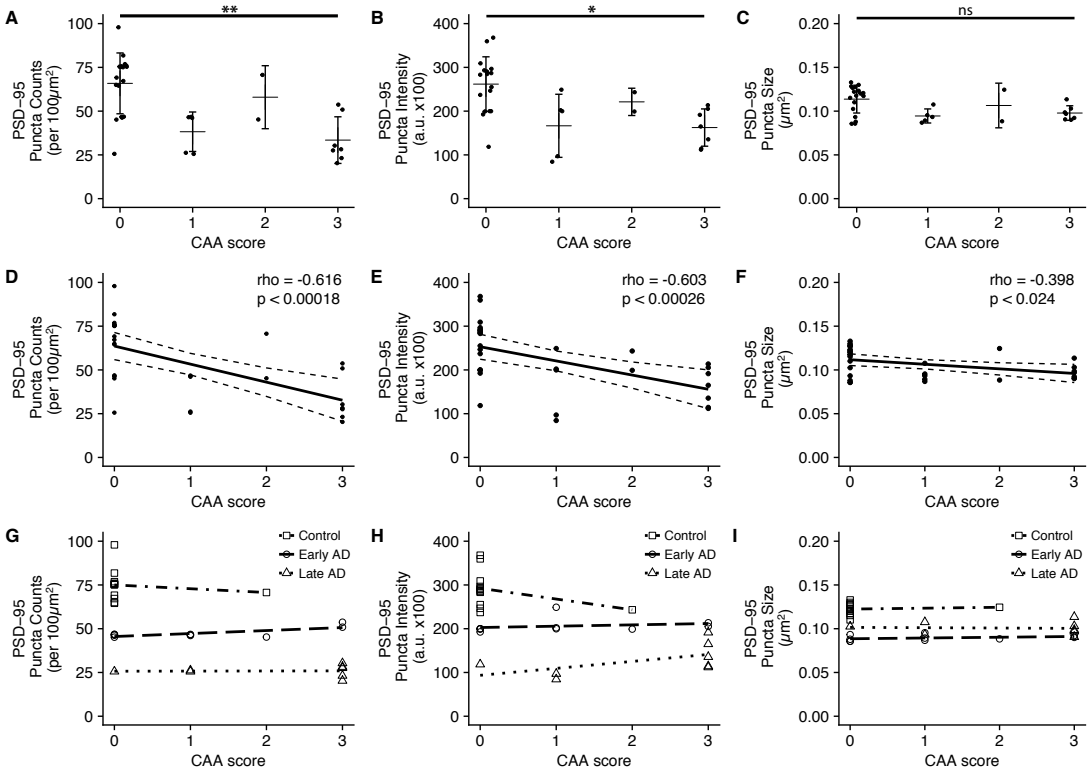


**Figure 5.24 PSD-95 protein and cerebral amyloid angiopathy (CAA) in the human posterior hippocampus from the SDM experimental cohort.**

**A-C.** Levels of (A) PSD-95 puncta density, (B) PSD-95 puncta intensity, and (C) PSD-95 puncta size in the posterior human hippocampus from the SDM experimental cohort to cerebral amyloid angiopathy (CAA) severity. Horizontal lines represent mean values for each CAA score and errorbars represent ± SD. **D-F.** The relationship of (D) PSD-95 puncta density, (E) PSD-95 puncta intensity, and (F) PSD-95 puncta size in the examined cohort to CAA severity showed significant negative correlations for each parameter (Spearman's rank correlation rho = -0.616, p = 0.00018; rho = -0.603, p = 0.00026; and rho = -0.398, p = 0.024, respectively). The solid lines represent the best-fit general linear regression lines. The interrupted lines in D-F represent the 95% confidence intervals. **G-I.** Further testing of (G) PSD-95 puncta density, (H) PSD-95 puncta intensity, and (I) PSD-95 puncta size against CAA severity within each experimental group (Control, Early AD and Late AD) showed no interaction between CAA severity within each group and the tested PSD-95 protein parameter, indicating that PSD-95 protein is not modified by CAA severity despite clear differences between the groups in PSD-95 levels for each parameter. The interrupted lines in G-I represent the best-fit general linear regression lines. AD, Alzheimer's Disease; a.u., arbitrary unit. Significance levels: * $p < 0.05$; ** $p < 0.01$; *** $p < 0.001$; **** $p < 0.0001$; ns, not significant.

### 5.10.4 PSD-95 and ApoE genotyping

Apolipoprotein E (ApoE) $\epsilon$4 is the single most potent and common genetic risk factor for sporadic AD (Corder et al., 1993). Compared with the ApoE $\epsilon$3/$\epsilon$3 genotype, having just one $\epsilon$4 allele increases risk more than 3-fold and having two $\epsilon$4 alelles increases the risk more than $\approx$12-fold (Roses, 1996). Conversely, the ApoE2 allele is a protective factor that reduces the risk of AD (Chartier-Harlin et al., 1994). Synapse loss is a strong correlate of cognitive dysfunction in AD (DeKosky and Scheff, 1990) and brain-imaging studies have implied the occurrence of synaptic dysfunction decades before AD onset in ApoE $\epsilon$4 patients (Reiman et al., 1996). More recently, using array tomography, Koffie et al, described a mechanistic link between apoE isoforms and oligomeric A$\beta$ that accumulates specifically at synaptic sites in human AD brains (Koffie et al., 2012). The study demonstrated that oligomeric A$\beta$ acts in concert with the ApoE4 isoform to accelerate synaptotoxic damage.

Since the ApoE4 isoform has been shown to exert synaptic toxicity in AD, I set to investigate whether the deleterious effects of this isoform on PSD-95 synapses could be detected in our SDM cohort. All cases have been ApoE genotyped as described in Chapter 2.2.3. In addition to demonstrating that the ApoE4 isoform is associated with PSD-95 synaptic changes, our data could potentially extend the knowledge of synapse damage in terms of (i) PSD-95 synaptic puncta parameters changes, and (ii) the early vs. late stage Alzheimer's type pathology disease effects.

First of all, I examined the distribution of ApoE genotypes and alleles within the SDM cohort (Table 5.4 on page 251). ApoE gneotypes were obtained for 16 AD and 14 control subjects. Of the 16 AD cases, 10 belonged to the early stage Alzheimer's type pathology group and 6 to the late stage Alzheimer's type pathology group. Of the 10 early stage Alzheimer's type pathology group: four were heterozygous for the $\epsilon$4 allele and none were homozygous. Of the 6 late stage Alzheimer's type pathology group: two were heterozygous and two were homozygous for the $\epsilon$4 allele. Just over one-third of control cases were heterozygous for the $\epsilon$4 allele and none were homozygous for the $\epsilon$4 allele. The most prevalent genotype in our cohort was E3/E3 and the E4/E4 genotype was only found in the late stage

Alzheimer's type pathology group. These findings are generally in agreement with the cited literature which quotes a worldwide frequency of 8.4%, 77.9% and 13.7% for the $\epsilon$2, $\epsilon$3 and $\epsilon$4 alleles, respectively (Farrer, 1997). In AD patients, the frequency of the $\epsilon$4 allele dramatically increases to ≈40%. In our AD cohort, the $\epsilon$4 allele increased to 29% in the AD group overall, but up to 50% in the late AD. However, since there were only 6 ApoE genotyped cases in the late stage Alzheimer's type pathology group, the interpretation of these findings might be limited.

**Table 5.4** Genotypes and alleles frequencies for ApoE in the SDM cohort

| Frequencies | | Control | Total AD | Early AD | Late AD |
|---|---|---|---|---|---|
| Genotypic | | | | | |
| | E2/E2 | 0(0.00) | 0(0.00) | 0(0.00) | 0(0.00) |
| | E2/E3 | 1(0.07) | 1(0.06) | 1(0.10) | 0(0.00) |
| | E2/E4 | 0(0.00) | 1(0.06) | 1(0.10) | 0(0.00) |
| | E3/E3 | 8(0.57) | 7(0.44) | 5(0.50) | 2(0.33) |
| | E3/E4 | 5(0.36) | 5(0.31) | 3(0.30) | 2(0.33) |
| | E4/E4 | 0(0.00) | 2(0.13) | 0(0.00) | 2(0.33) |
| | Total | 14(1.00) | 16(1.00) | 10(1.00) | 6(1.00) |
| Allelic | | | | | |
| | $\epsilon$2 | 1(0.03) | 2(0.06) | 2(0.10) | 0(0.00) |
| | $\epsilon$3 | 22(0.79) | 20(0.65) | 14(0.74) | 6(0.50) |
| | $\epsilon$4 | 5(0.18) | 9(0.29) | 3(0.16) | 6(0.50) |
| | Total | 28(1.00) | 31(1.00) | 19(1.00) | 12(1.00) |

Secondly, I examined the relationship between the PSD-95 synaptic density, intensity and size and the $\epsilon$4 allele frequency. Since the presence of this allele is associated with an increased risk of AD, I speculated that having both copies of the allele may result in lower PSD-95 synaptic parameters values. Indeed, it appeared that the presence of two $\epsilon$4 alleles is associated with a decrease in the PSD-95 synaptic numbers and intensity, but not the size. However, as there were only 2 subjects in the homozygous $\epsilon$4 allele group, further statistical analysis of the data were not possible as numbers were too low. In addition, no significant differences were found between the groups with none or only one $\epsilon$4 allele for all three parameters of the PSD-95 puncta. Overall, the $\epsilon$4 allele dose does not influence the PSD-95 synaptic parameters in my cohort of cases. However, it must be noted that this analysis is compromised by small

number of cases studied.

Thirdly, I investigated the effect of having the $\epsilon$4 isoform on the PSD-95 synapses. Data from array tomography on human data have demonstrated a genotype-specific differences of synaptic loss whereby having one or two copies of $\epsilon$4 allele (ApoE E3/E4 or ApoE E4/E4, combined referred to as ApoE Ex/E4) was associated with decreases in the synaptic density in the AD patients (Koffie et al., 2012). I therefore asked if these genotype-specific changes can be observed in our SDM cohort. The investigated cohort was divided into two groups depending on ApoE genotype: E3/E3 *versus* any patient with an $\epsilon$4 isoform (either one or two) as seen in Figure 5.26 on page 255. My data confirm that there are significant losses in the PSD-95 synaptic puncta density, intensity and size in patients compared with the neurologically intact controls. These changes in the PSD-95 synaptic puncta parameters are observed in both, the early and the late Braak stages. In addition, as expected, the late stage Alzheimer's type pathology group sees the greatest deleterious synaptic changes for density and intensity, but not size. However, I do not observe the genotype-specific differences between the E3/E3 and the Ex/E4 genotypes. While the results of my data are compromised by the small numbers, there are several differences between our study and the study by (Koffie et al., 2012). For instance, their data refer to the presynaptic elements with no evidence for the genotype-specific changes in the postsynaptic proteins. Notably, the PSD-95 protein has been examined, but no significant genotype-specific observations were reported. However, the ApoE effect on synapses in the array tomography study was correlated with accumulation of oligomeric A$\beta$, and oligomeric A$\beta$ has not been assessed in the present study. While further correlations between the Thal phases and CERAD scores could be undertaken to evaluate the relationship between my results of APOE status and the A$\beta$ burden, the number of cases would have to be increased to make the findings significant.

Lastly, I examined in detail the effect of the ApoE4 specific genotypes on the PSD-95 synapse parameters. For the three groups, comparisons were made between the control group with an E3/E3 genotype and a group with either one (E3/E4), two (E4/E4) or a combination (x/E4) of the $\epsilon$4 allele (Figure 5.27 on page 256). While the losses in PSD-95 synaptic parameters are significant between the control *versus*

the diseased E3/E3 groups, no significant differences are observed for the comparisons within the diseased groups containing at least one ApoE4 isoform. However, apart from the PSD-95 synaptic puncta size, which do not appear to be affected by the presence of the $\epsilon 4$ allele regardless of the disease stage, the PSD-95 puncta density and intensity show losses in accordance to the Alzheimer's type pathology stage progression. In other words, the later stages show greater losses in number and intensity of PSD-95 synaptic puncta. As previously, the results demonstrate no evidence for a genotype-specific PSD-95 synaptic losses.

To conclude, the main findings of this part of the thesis are that when ApoE genotypes are taken into account (i) the synaptic losses are particularly prominent, but not significant, for the numbers and intensities of PSD-95 synaptic puncta, and that (ii) for these PSD-95 synaptic parameters, the losses are greater with the AD disease progression. However, the frequency of each genotype across the study groups, and for E4/E4 in particular, is too limited to make any further meaningful conclusions and, in particular, I am unable to confirm the evidence for the ApoE genotype-specific synaptotoxicity as my data cannot show if $\epsilon 4$ allele on its own has a deleterious effect on synapses. Taken together, these data do not support the evidence of an impact of ApoE $\epsilon 4$ genotype on PSD-95 in the hippocampus in AD. Nevertheless, it appears that our novel quantification methodology shows a trend in accordance with the published data. A much larger cohort of patients is required to ully assess any potential interactions between ApoE4 genotype PSD-95 pathology.

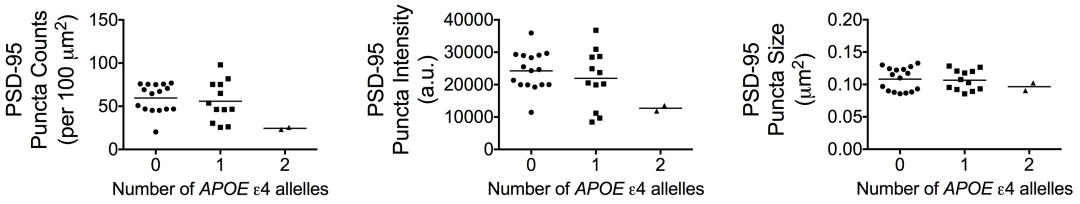


**Figure 5.25 The relationship between the number of the ApoE $\epsilon$4 allele and the PSD-95 synaptic parameters.**

Scatterplots of the three PSD-95 synaptic puncta parameters in relation to the number of the $\epsilon$4 allele. The horizontal lines represent the mean values for each parameter in cases possessing 0, 1 or 2 ApoE $\epsilon$4 alleles. It appears that for the density and the intensity parameters, the homozygous genotype is associated with lower values. Number of the $\epsilon$4 allele made no difference to the size of the PSD-95 synaptic puncta. However, none of these results were statistically significant. Normality of the data was assessed using the D'Agostino & Pearson omnibus normality test. Both, the density and the intensity data were normally distributed, but the numbers were too small for the PSD-95 size normality assessment. Subsequently, the Kruskal-Wallis tests revealed a lack of significant associations for the parameters tested. However, the trends showed that the increase in the number of the $\epsilon$4 allele led to fewer PSD-95 puncta, which were dimmer and slightly smaller.

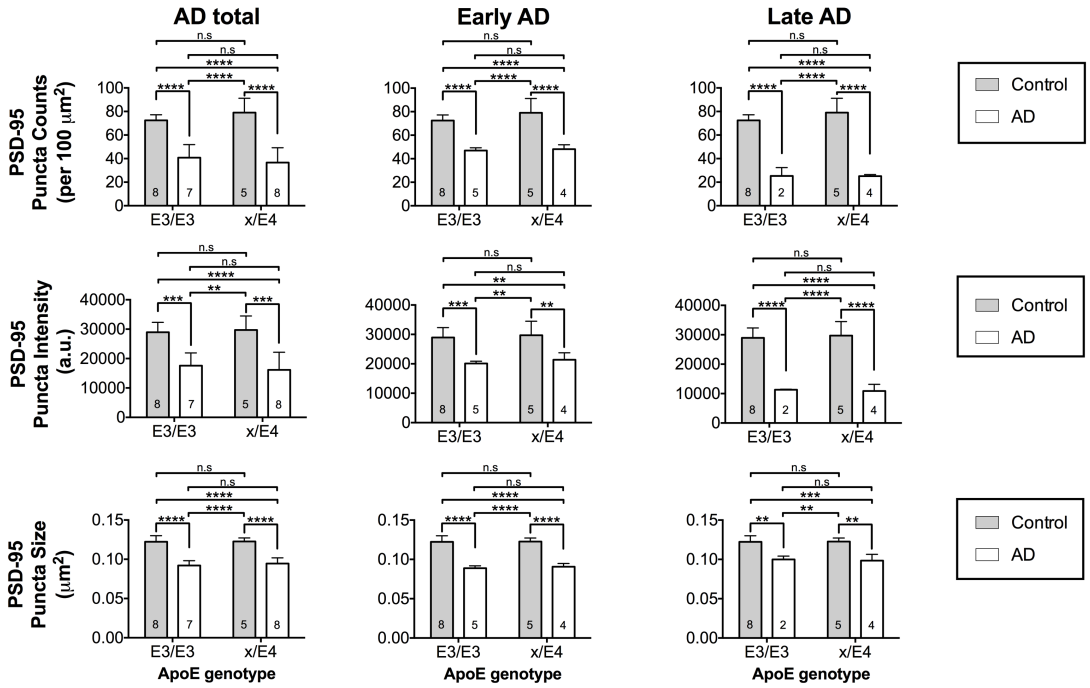


**Figure 5.26 The PSD-95 synaptic parameters are significantly altered in AD, but having an $\epsilon$4 allele does not contribute to additional synaptic deterioration.**

Barplots of the three PSD-95 synaptic puncta parameters demonstrating the relationship between the ApoE E3/E3 genotype and any ApoE genotype containing the $\epsilon$4 allele. In order to establish if the AD disease stage also contributes to synaptic changes, the data have been separated in three ways: by the total AD group (the first column), the early AD cases (the middle column) and the late AD cases (the third column). The number of cases in each group is indicated at the bottom of each bar. There were significant synaptic changes between the control cases and the groups affected by the AD. However, having the $\epsilon$4 allele did not further affect the synapses in our cohort. In addition, even though the synaptic changes were greater with the disease progression, the Kruskal-Wallis tests revealed that the genotypes containing the $\epsilon$4 allele had no additional deleterious effect on synapses. The bars represent the mean values of each PSD-95 synaptic puncta parameters: PSD-95 puncta density (top row), the intensity (middle row) and the size (bottom row). Error bars represent standard deviations. Significance levels: * $p < 0.05$; ** $p < 0.01$; *** $p < 0.001$; **** $p < 0.0001$; ns, not significant.

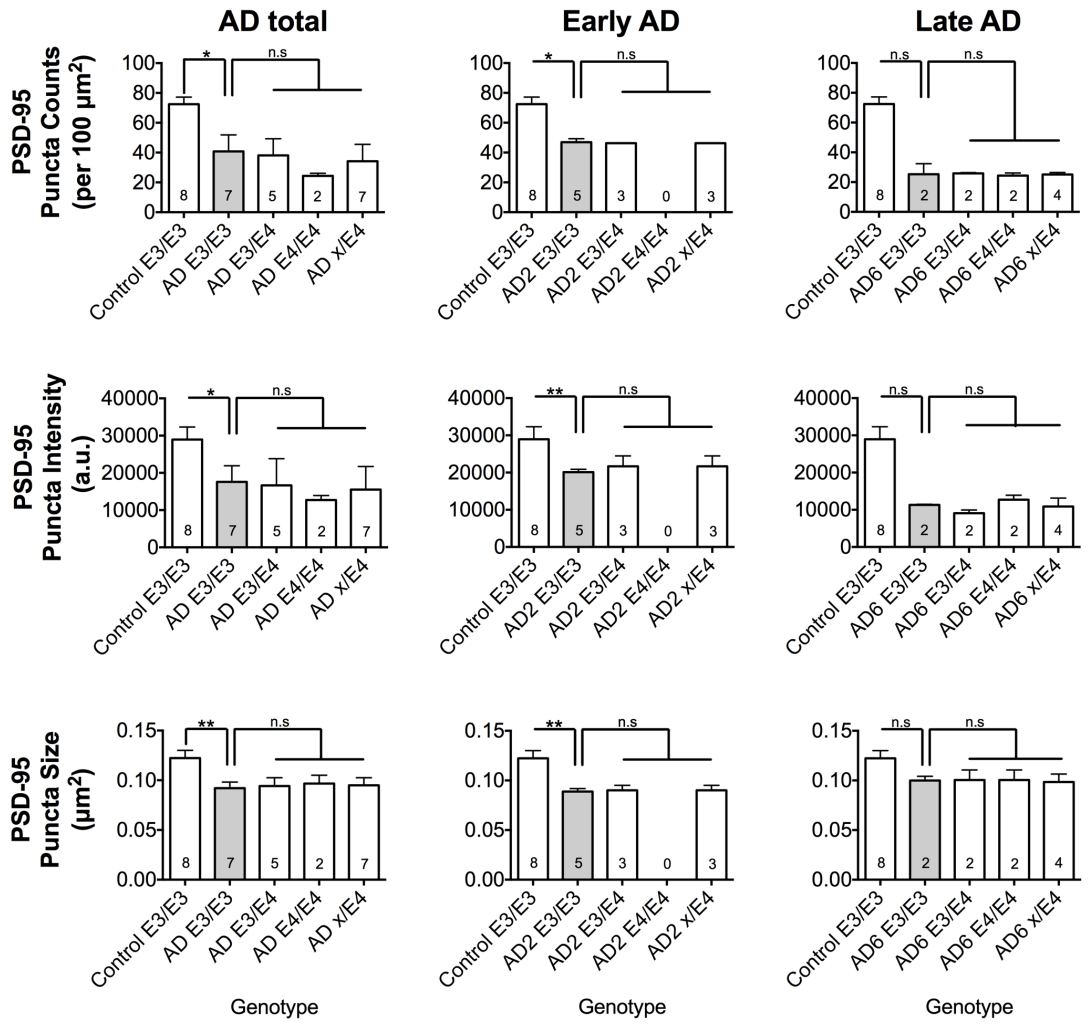


**Figure 5.27 The ApoE genotypes with the $\epsilon$4 allele do not additionally alter PSD-95 diversity in AD cases.**

Barplots of the three PSD-95 synaptic puncta parameters demonstrating the relationship between the ApoE E3/E3 genotype and combinations of all ApoE genotypes containing the $\epsilon$4 allele (except the E2/E4 genotype). Although, the changes were significant between the control vs. the AD groups, no significant changes between the genotypes within the AD groups were observed. Similarly to the previous figure, the disease stage affected the synaptic parameters, but did not cause additional deleterious synaptic changes. The bars represent the mean values of each PSD-95 synaptic puncta parameters: PSD-95 puncta density (top row), the intensity (middle row) and the size (bottom row). Error bars represent standard deviations. Differences between the genotypes were tested using the Kruskal-Wallis test. Shown are the significance results obtained by Dunn's multiple comparisons test. Significance levels: * $p < 0.05$; ** $p < 0.01$; ns, not significant. The number of cases in each group is indicated at the bottom of each bar. The results were limited due to small number of cases in each group.

### 5.10.5 PSD-95 and neuronal loss

In AD research, synapses have, to date, not been studied in detail due to the belief that since the synaptic losses closely follow the neuronal losses, the synaptic dysfunction is irreversible. However, there is mounting evidence that synaptic damage may precede cognitive decline in AD by several decades and could potentially be reversible (Holtzman et al., 2011), particularly as the synapse is a very obvious pharmacological target. This therefore offers a potential window of therapeutic opportunity in AD based around synapse-directed therapeutics.

In this part of my study, I thus wanted to ask two questions related to the neuronal loss in AD. Firstly, I asked if our data support the well established hypothesis that synaptic losses follow the neuronal losses, and secondly, if we can demonstrate synaptic losses in the early stages of disease progression. To answer these questions, we counted the neurons in the pyramidal cell layers (PCL) of the hippocampus using the stereology techniques described in Chapter 2.12, and compared the neuronal changes with synaptic alterations. I used the PCL as it contains easily identifiable and quantifiable neurons. The comparisons were made for a subset of cases from the SDM cohort that was age-matched with similar PMD and HUSPIR values.

The results of my finding are presented in Figure 5.28 on page 258. In agreement with the literature, I demonstrated that the CA2 region has the greatest density of neurons, followed by the CA3 and CA1 regions (Padurariu et al., 2012). As expected, there were no significant differences in neuronal loss in all CA regions tested between the control and the early stage Alzheimer's type pathology groups. There was a significant loss of neurons in the late stage Alzheimer's type pathology group in comparison to the early stage and the control groups. The PSD-95 synaptic puncta density for exactly the same cohort of cases revealed an absence of significant differences between the three CA regions within each tested group. However, as the pathology progressed, the synaptic density loses increased for all CA regions. In summary, the data are in agreement with the trends in neuronal loss in AD. Moreover, I demonstrated that the synaptic losses do take place prior to neuronal losses in cases with the early stages of Alzheimer's type pathology.

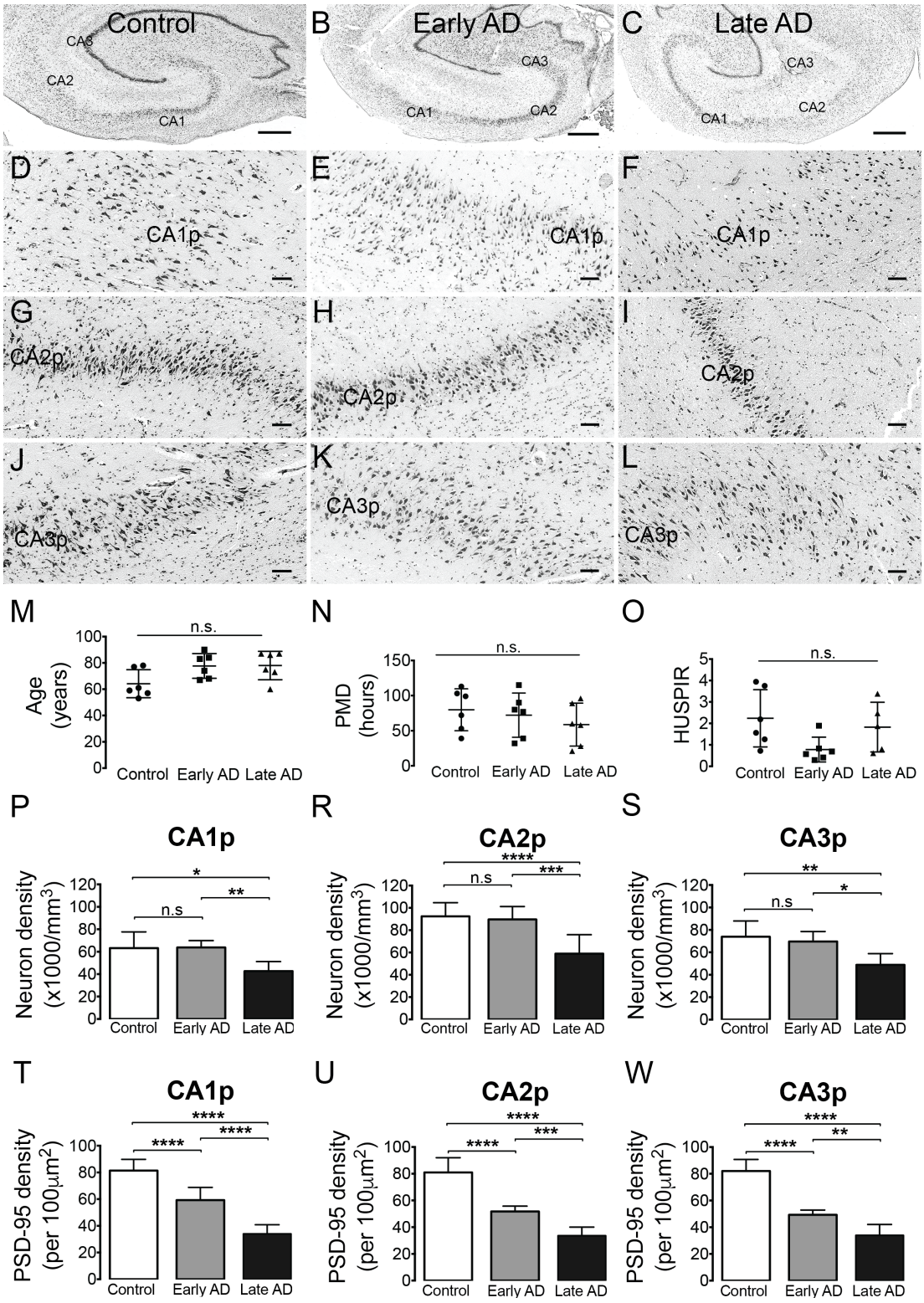


**Figure 5.28 Correlation between the neuronal loss and the PSD-95 synaptic puncta density in the human hippocampus.**

**A-L** Representative images of Nissl-stained hippocampal sections from the controls (the first column: A, D, G, J), the early AD cases (the middle column: B, E, H, K) and the late AD cases (the last column: C, F, I, L) illustrating the neuronal losses in the CA1 stratum pyramidale (D-F), the CA2 stratum pyramidale (G-I) and the CA3 stratum pyramidale (J-L). **M-N** In order to make the data comparable, 3 males

and 3 females were chosen from each group that were matched for age, PMD and HUSPIR. There were no statistical differences between the three groups for age (P), PMD (N) and HUSPIR (O). **P-S** The neuronal densities were counted for each group within each pyramidal layer of the CA hippocampal region. **T-W** To make comparable comparisons, the same cases had their PSD-95 synaptic puncta densities calculated. Overall, the data demonstrate that synaptic losses follow the neuronal losses as the disease stage progresses. However, for the early AD group, synaptic losses are evident before the neuronal losses take place. Normality of the data was assessed using the D'Agostino & Pearson omnibus normality test. Subsequently, the Kruskal-Wallis tests revealed a lack of significant associations for the parameters tested. Error bars represent standard deviations. Significance levels: * $p < 0.05$; ** $p < 0.01$; *** $p < 0.001$; **** $p < 0.0001$; ns, not significant. Scale bars: A-C 1 mm; D-L 100 um.

---

## 5.11 CHAPTER DISCUSSION AND CONCLUSION

In this chapter, I describe the distribution of one key postsynaptic protein, the PSD-95 protein, within the human hippocampus. I used an automated, high-throughput quantification method, which uses the fluorescent image detection machine learning algorithms to classify PSD-95 IF puncta into three parameters: puncta density, intensity and size. This new quantification method has allowed me to demonstrate in great detail the distribution of PSD-95 IR puncta in the control human hippocampus across 16 subregions. My findings further contribute towards the knowledge about the postsynaptic proteome. The postsynaptic proteome is tremendously complex and contains thousands of proteins ranging from scaffold proteins, synaptic membrane receptors, neurotransmitter receptors, cell adhesion molecules, signalling, metabolic and trafficking proteins (Bayés et al., 2012). According to our current understanding of the postsynaptic proteome, its complexity is a reflection of the hierarchical organisation of all these proteins into complexes, supercomplexes and nanoclusters (Frank et al., 2016; Frank and Grant, 2017). Studies in mice have already revealed that in hippocampus different synapses have different combinations of PSD-95 nanoclusters (Broadhead et al., 2016). Moreover, these PSD-95 nanoclusters are differentially distributed in the hippocampal subregions. Therefore, the regional diversity in human PSD-95 IR distribution may also reflect the differential allocation of this protein into postsynaptic complexes and supercomplexes based on subtypes of synapses and

populations of these subtypes that define each hippocampal region. However, further validation of the presented findings with other methods, such as array tomography, electron microscopy or super-resolution microscopy, are needed to confirm our hypothesis.

The new quantification method allowed me to obtain additional information about PSD-95 distribution in the human hippocampus. For example, I was able to demonstrate that there were no significant gender differences in the distribution of PSD-95 synaptic puncta parameters. Few studies have examined the effect of gender at the synaptic level and they have generated conflicting data. For instance, in monkeys no sex differences existed in the synaptic density in prefrontal cortex (Peters et al., 2008). In contrast, human superior temporal gyrus had less synapses in women when compared to men (Alonso-Nanclares et al., 2008). However, rodent apical dendritic spines of the CA1 pyramidal cells (stratum radiatum) were reported to have more synapses in female rats (Shors et al., 2004). It is possible that these discrepant results could be explained by the cytoarchitectonic differences of the regions and/or species differences.

The G2CSynMaP was also used to explore hippocampal gender differences in wild type mouse (Grant lab, personal communication). Similar to human data, there were no gender differences for hippocampal PSD-95 puncta density and intensity. However, contrary to the human data, the PSD-95 puncta sizes were found to be significantly smaller in female mice in several hippocampal subregions (CA1-SO, CA1-SR, CA2-SLM, CA3-SLM and CA3-SR). However, it was noticed that the significance levels were very close to the significance level threshold at $p = 0.0458$, and that three out of four female mice tested were litter mates housed in the same environment, the implication being that that was synchronisation of their oestrous cycles. Research has shown that spine density can vary depending on the phase in the oestrous cycle (Luine and Frankfurt, 2013), and thus these mice results might have represented a particular time of the cycle. With regard to the human data, it is worth noting that all, but one, of the human donors were postmenopausal and even the youngest woman was aged 46. Therefore, we can speculate that hormonal levels may have an effect on PSD-95 synapse size and low oestrogen levels may be associated

with some compensatory changes, or selective small synapse loss, leading to larger synapse sizes. This may explain the differences seen between the adult rodent and human data, with a trend to smaller PSD-95 synapse sizes being observed in adult mice. However, at this stage we do not have full clinical histories, which would include relevant information about hormone replacement therapy, to make any further meaningful conclusions. Further studies with appropriately chosen controls and higher numbers of cases are needed to confirm the effects of gender on synapses in the human hippocampus.

There were no significant differences in the distribution of PSD-95 synaptic puncta parameters between left and right hippocampus. Brain lateralisation and handedness are believed to be an integral part of human psychology and behaviour (Toga and Thompson, 2003). The left hemisphere is considered to support language and logical thinking, while the right hemisphere takes part in creativity and intuition (Corballis, 2014). Several imaging studies have additionally identified the lateralisation of brain structures. For instance, rightward asymmetry has been reported in the hippocampus (Wang et al., 2001; Pedraza et al., 2004; Qiu et al., 2009; Kallai et al., 2005; Okada et al., 2016) and amygdala (Pedraza et al., 2004; Qiu et al., 2009; Kallai et al., 2005; Okada et al., 2016). Interestingly, human brain lateralisation has also been explored with molecular genetics and genomics (Francks, 2015). A recent re-analysis of large gene expression datasets (Hawrylycz et al., 2012; Pletikos et al., 2014) detected left/right asymmetry of gene expression in post mortem adult brain (Karlebach and Francks, 2015). Robust evidence for lateralisation was found at the level of gene sets for synaptic transmission in data from the superior temporal and primary auditory cortex. Nevertheless, human studies examining the laterality in post mortem tissue are very limited and do not appear to show left/right asymmetry in the hippocampus from control cases (Mouritzen Dam, 1979; Zaidel et al., 1997). In particular, Zaidel et al. (1997) reported absence of left/right differences not only in neuronal densities, but also in synapses. To my knowledge, no human studies to date have conducted a detailed and comprehensive PSD-95 synaptic analysis on the postsynaptic lateralisation of hippocampal subregions using human post mortem tissue, and the dataset presented here represents the first detailed assessment of PSD-95 synaptic lateralisation in human hippocampus.

Similar to gender differences, the G2CSynMaP methodology was used to explore hippocampal left/right asymmetry differences in wild type mice in nine main areas, one of which included the hippocampus (Grant lab, personal communication). In line with the human data, there were no laterality differences for hippocampal PSD-95 puncta density, punctum intensity and size, and no differences were seen for the remaining eight areas assessed (cortical subplate, neocortex, fibre tracts, hypothalamus, thalamus, olfactory areas, pallidum and striatum). This is in contrast to other published animal data. For instance, Shinohara et al. (2008) demonstrated left-right asymmetry of postsynaptic CA1 pyramidal cell synapse sizes. CA1 synapses receiving neuronal input from the right CA3 pyramidal cells were larger than those innervated by the left CA3 (Shinohara et al., 2008).

Finally, one important limitation of the human analysis is a lack of clinical information regarding the patients' handedness. As handedness gives an indication of the dominant hemisphere in the brain, it would be useful to correlate my findings with this information. Further studies with clinically well characterised controls and higher numbers of cases are needed to confirm the effects of left/right asymmetry on PSD-95 synapses in the human hippocampus.

The PSD-95 synaptome based on IR is reorganised in disease. I have demonstrated that depending on the stage of Alzheimer's type pathology, the PSD-95 synaptic puncta parameters are differently affected. In agreement with published literature, losses in hippocampal synaptic numbers have been described previously (Scheff et al., 1996; Scheff and Price, 1998; Counts et al., 2014; Sultana et al., 2010). However, changes in PSD-95 synaptic puncta intensity and size, which may represent different synapse populations, are novel findings. In particular, the changes in PSD-95 puncta size are one of the more interesting findings in this project. A significant inverse correlation has been reported between synaptic density and size of surviving synapses as measured by the length of the postsynaptic density in AD (Scheff et al., 1990). These increases in synaptic size of the apposition length have been interpreted as a compensatory response, rather than a selective loss of small synapses (DeKosky and Scheff, 1990; Scheff et al., 1990, 1993). Changes in contact length have also been reported in the animal studies (Hillman and Chen, 1984) and transgenic mice (Cambon

et al., 2000). Similarly to the study by Scheff et al. (1990), I found increases in PSD-95 synaptic puncta in the late stage Alzheimer's type pathology stage in comparison to the early AD stage. In contrast to Scheff et al. (1990), I have found that the control cases still have larger synaptic puncta than the AD patients. Furthermore, examination of the frequency distributions of the synaptic puncta sizes between the experimental groups revealed that although the overall shape of the distributions between the areas tested were fairly similar, they were not exactly the same between the experimental groups, suggesting that different changes occurred throughout the entire distributions of synapses. This would imply that a possibility of a preferential loss of small synapses from the neuropil may take place as a different compensatory mechanism to the one mentioned above. As it was previously suggested, the changes in synapses may not be necessarily of one specific type, but may reflect the changes of many different kinds in line with the known changes in various neurotransmitters in AD (Scheff, 2003).

Regional PSD-95 synaptome reorganisation in AD identifies vulnerable regions and synapse populations. Analysis of hippocampal regional PSD-95 changes in AD demonstrated that all the 16 subregions are affected in AD. However, it appears that the insults at the synaptic levels are not uniform across the subregions. My data have identified that one area, the CA3 stratum moleculare-lacunosum, is particularly vulnerable to insults associated with AD. PSD-95 synapses in this subfield showed vulnerability in the early Alzheimer's type pathology stage whereby the synaptic losses in counts and intensity were almost as severe as in the advanced stage group. Interestingly, the decrease in PSd-95 synaptic size in the early stages for this area was more severe than for any of the concomitantly examined subfields.

My results demonstrate that AD leads to synaptic changes in the hippocampus. This is in keeping with numerous previous studies showing loss of synapses in AD both in the hippocampus and the neocortex (Terry et al., 1991; DeKosky and Scheff, 1990; Scheff and Price, 1998; Scheff et al., 2011, 2015, 2016). Moreover, evidence suggests that the strongest correlation with cognitive decline is with synaptic number and regional neuronal loss rather than neurofibrillary tangle and neuritic plaques pathology (DeKosky and Scheff, 1990; Scheff et al., 2006, 2007, 2011, 2015). However, the question of what causes the loss of synaptic connectivity in AD, ultimately resulting

in dementia, has not been fully answered. The correlative neuropathology findings aimed at answering this question. There is evidence to suggest that early cognitive problems in AD may be due to diffuse amyloid deposits that alter synaptic integrity. In particular, soluble oligomers are thought to disrupt hippocampal synaptic plasticity by changing the induction of long-term potentiation (LTP) via effects on the postsynaptic receptors (Li, 2010). Prior studies have shown that the presynaptic component is most likely unaffected by the oligomers (Cheng et al., 2009; Shankar et al., 2008; Townsend et al., 2006). As part of my analysis, I confirmed that the severity (CERAD score) and the extent (Thal phase) of amyloid pathology distribution differed between the controls and AD groups. However, I did not observe any significant correlations with PSD-95 density, intensity or size with Alzheimer's type pathology progression. Therefore my results, coupled with other findings, questions the role of amyloid deposits as the sole cause of synapse loss in AD (Scheff et al., 1990, 1993).

The genetic risk factor for AD, ApoE $\epsilon$4, has been suggested as a prominent factor in the development of pathology in AD (Roses, 1996). Cognitively normal $\epsilon$4 carriers have been found to have more significant AD-related pathology than non-carriers (Vos et al., 2013). Moreover, imaging studies demonstrated that ApoE $\epsilon$4 carriers showed significantly greater amyloid load, as determined by Pittsburgh compound-B (PiB) imaging, associated with lower cognitive tests (Ikonomovic et al., 2008; Kantarci et al., 2012), suggesting that ApoE $\epsilon$4 modifies the harmful effect of A$\beta$ on cognition (Mufson et al., 2016). I found that PSD-95 levels for all synaptic parameters tested were lower in AD, but were not associated with ApoE $\epsilon$4 status. Therefore, based on the SDM cohort, my study failed to demonstrate that the presence of ApoE $\epsilon$4 has significant deleterious effects on PSD-95 synaptic puncta parameters in the hippocampus in AD. The findings, nevertheless, are in keeping with previous studies demonstrating the lack of influence of ApoE $\epsilon$4 on synapses in AD. For instance, recently Scheff et al. (2016) reported no significant effects of hippocampal amyloid load or ApoE $\epsilon$4 status on Braak score despite losses in synaptic proteins, including PSD-95. However, our numbers in the late AD group were too small to extrapolate any further as to whether there is strong evidence for synaptic toxicity caused by the ApoE genotype.

The effects of ApoE $\epsilon$4 have also been extended to vascular pathology in AD. Cerebrovascular lesions are relatively common in autopsied cases of AD (Olichney et al., 2000). For instance, one of the most common vascular pathology that is found includes cerebral amyloid angiopathy (CAA). CAA is a disease in which amyloid deposits within the walls of meningeal and parenchymal blood vessels. Sporadic CAA is thought to affect between 80% to 90% of AD cases and approximately 30% of the neurologically-normal elderly (Love et al., 2014). CAA has also been shown to be strongly associated with cerebrovascular lesions, including infarctions (Olichney et al., 1995). In this thesis, I describe the effects of CAA on PSD-95 synapse diversity. Overall, similarly to the findings with amyloid, the results demonstrate that there is no evidence for a direct association between the CAA pathology and PSD-95 changes in hippocampal AD in my cohort.

In summary, the neuropathological correlative data support the view that it may well be a combination of factors rather than one pathology that contributes to the clinical presentations in AD. However, there are important limitations that should be taken into account when interpreting the above results. For instance, one potential confound in the study is that the controls were significantly younger than patients with the early stage Alzheimer's type pathology (Braak II) and the late stage Alzheimer's type pathology (Braak VI). However, only subtle age-related changes in synapses have been described in animal studies, which showed that ageing is not associated with synapse loss in hippocampus (Morrison and Baxter, 2012). For example, using stereological techniques, a lack of age-related synapse loss in CA1 area has been described in rats (Geinisman et al., 2004; Calhoun et al., 2008). Nevertheless, it is possible that the age discrepancy could lessen the main findings of PSD-95 loss in hippocampus in AD patients. One of the ways of assessing the impact of age differences would be to perform more complex regression analyses that take age into account. Another potential confounding factor is associated with the selection of patients from the LINCHPIN study. Although only cases with intact hippocampi were selected, we cannot exclude the influence of cerebrovascular disease on synaptic loss. In the future, a selection of cases without any cerebral haemorrhage would allow for better analysis.

Having demonstrated PSD-95 synaptic loss in my cohort, I then examined if the spatiotemporal and laminar pattern of synaptic loss matches that of neuronal loss. It has been shown that the cortical synaptic loss is not just related to neuronal loss as it can exceed the existing neuronal loss within a particular area (Serrano-Pozo et al., 2011). This indicates that synapse loss occurs prior to the neuronal loss and that the remaining neurons become less well connected to their synaptic partners than would be anticipated by assessment of the number of viable neurons surviving in a particular circuit only. This is thought to be why synaptic density is the best correlate of cognitive decline in AD. In agreement with this statement, my stereology data confirm that the synaptic changes occur early in the AD, prior to neuronal losses.

It is difficult to tease apart contributions of each individual brain area in a disease, such as AD. Studying the effects of a disease on specific anatomical subregions rather than extrapolating about the impact on the whole brain based on one selected subregion, may help to piece together the relevant circuitry affected by Alzheimer's type pathology pathology.

In conclusion, I have added human PSD-95 synaptome mapping to the range of approaches used to study hippocampal organisation and anticipate that this approach will make an important contribution to the understanding of the organisation of the hippocampus and the changes it undergoes in pathological states. These findings may also provide a new foundation for future studies of the human hippocampus in health and disease.

# 6 Discussion and Conclusion

## 6.1 SUMMARY OF FINDINGS

This thesis presents a novel methodology, the G2CSynMaP, for the quantification of PSD-95 synapses and generation of PSD-95 protein distribution maps in human post-mortem tissue. When further validated, this method is hoped to lead to description of PSD-95 synaptome maps. The methodology has previously been used to examine the brains of genetically modified rodents and has been specifically adapted for the use in human tissue.

## 6.2 LIMITATIONS

The implications of our findings are somewhat limited by practical, histological and methodological considerations specific to the present study.

### 6.2.1 Practical issues

One of the most difficult aspects in human brain research is the limited availability of suitable tissue. Although a thorough neuropathological examination of all tissues used in this project was undertaken, I cannot rule out the possibility that factors, such as prolonged agonal state and terminal periods of hypoxia, could have adversely affected the synaptic proteins examined. In addition, the early stage Alzheimer's type pathology group included subjects with known cerebrovascular disease as all cases had been received through the Lothian Intracerebral Haemorrhage, Pathology, Imaging and Neurological Outcome (LINCHPIN) study, a prospective community-based research study examining the causes of brain haemorrhages using research autopsy in case of death (Samarasekera et al., 2015). Although care was taken to exclude cases with significant pathologies, such as ischaemic strokes or haemorrhages, the possibility of double pathology affecting the synaptic proteins in this particular subgroup cannot be entirely excluded.

### 6.2.2 Histological issues

Any evaluation of synaptic numbers in human tissue should be viewed judiciously (Scheff, 2003). The size and the complexity of the organisation of the human brain makes a definite reconstruction of the human synaptome currently beyond the limits of existing technology. However, discrete sampling of small areas in an unbiased manner with integration of additional data from other sources, such as light microscopy and electron microscopy, makes it possible to determine the range of variability of synaptic assessment rather than provide absolute numbers (DeFelipe, 2015). However, firstly, it would be necessary to define the impact of histological artefacts that could lead to misrepresentations of results. For instance, atrophy of tissue could be regional and artificially increase the packing density of synapses. Changes in section thickness, as a result of histological procedures, can also dramatically alter determination of volume density. Therefore, without knowledge of the definable anatomical structural data for a given examined region, any synaptic estimations would be difficult to interpret. The main limitation of this project is the lack of correlative data on any tissue parameters, such as tissue thickness, the volume of fraction of tissue elements (neuropil, neurons, glia and blood vessels), or neuron and glia density per volume. The only exception is the stereological data on neuronal density in Chapter 2.12. However, the aim of this project was not as much as to estimate the absolute synaptic numbers, but to reveal trends between areas and how they change in a pathological process. To obtain more comprehensive data about the synaptic numbers estimated in this project, I would further require not only assimilation of data from another source, such as electron microscope or array tomography, but also I would need to account for numerous additional sources of variability, including the type of cells, age of cases, or species examined. Finally, although various correlative comparisons of synaptic changes using IHC and conventional EM techniques do tend to reveal a general agreement in the finding that synaptic numbers decline in AD, there is still a great deal of variation in actual synapse counts between the techniques. A study conducted to specifically address the issue of the various methodological and demographic variations possibly contributing to the reported numerical synaptic discrepancies, found no significant correlations between the two techniques for synapse numbers loss in the frontal cortex

(area BA9 laminas III and V), even when the same cases were examined (Scheff, 2003). The reasons for the failure to demonstrate strong correlation were thought to be related to both: i) specific conditions related to IHC staining efficiency and; ii) limitations of using EM. Therefore, no technique is perfect and even an integrative approach might be incomplete.

### 6.2.3 Methodological issues

Methodological limitations specific to the present study and to the use of human tissue include small sample size and the use of post-mortem tissue rather than biopsy material. There are also methodological considerations related directly to the design of the G2CSynMaP methodology and they include limited whole-brain sampling and limited dimensionality of image acquisition.

#### *6.2.3.1 Sample size*

There is significant biological variation between individuals in human studies and this can make identification of significant data points difficult unless there is a sufficiently large sample size. The results of the present study are all noteworthy because they emerged from a study with 32 subjects that had detailed neuropathological characterisation. I examined more subjects and/or synapses than other human tissue-based quantitative studies to date. However, it is still small sample size and subject to possible unintended sampling bias. I can only generalise based on this sample size, but I am confident that my results are a reliable indication of the synaptic diversity within the human brain. Nevertheless, given the difficulties and constrains of human histological research, the validity of conclusions can be challenged. The present data were collected with appropriate controls and analysed using methods validated in rodents. Thus, as far as valid conclusions can be drawn from human data, the current study does contribute to our understanding of human synaptic diversity.

#### 6.2.3.2 *The use of human post-mortem tissue*

The scarcity of human brain tissue that is suitable for the study of synapses is one of the most challenging issues to face human synaptic research (Acebes, 2017). Biopsy material is considered to be the gold standard due to better tissue quality when compared to post-mortem specimens. However, the main limitation with regard to using biopsy material is the availability of tissue and ethical restrictions. Autopsy therefore remains the main source of human tissue for research, but its use is complicated by several limitations.

Long post-mortem delays greater than 5 hours result in poor preservation of the ultrastructure of the autopsy brain tissue and is thought not to be adequate for detailed quantitative analysis (Alonso-Nanclares et al., 2008). This is one of the main reasons why synaptic mapping data and studies using human brain tissues are limited. A recent Focused Ion Beam milling and Scanning transmission Electron Microscopy (FIB/SEM) study reported promising quantitative results of human brain cortical areas from AD patients based on the ultrastructure of synapses (Blazquez-Llorca et al., 2013), but most studies employ indirect methods to count synapses in human brains, such as counting synaptophysin-positive puncta and using conventional light and/or confocal microscopy (Arendt, 2009), or as in this project, counting PSD-95-positive puncta and using confocal microscopy. Ideally, human brain tissue would be collected with a PMD less than 2 hours, and analysed using methodologies that are normally used to examine the brain of experimental animals (DeFelipe, 2015). While the latter has been achieved in this project, the former has not, with much longer PMD times. Previous studies have indeed demonstrated that in human tissue PSD-95 showed a significant decrease in protein levels with PMD greater than 24 hours (Siew et al., 2004). They reported a 36% decrease in PSD-95 levels between 24 and 48 hours in the frontal cortex was reported, although the PSD-95 levels in the temporal cortex remained unchanged. In rodents, Glantz et al. (2007) estimated that PSD-95 levels decreased by almost 65% after a 24 hours PMD (Glantz et al., 2007). Stability of PSD-95 protein levels in this project was not tested, but no significant differences in any of the three PSD-95 parameters tested were observed within each examined experimental group studied with increasing PMD. Nevertheless, in this project, apart

from PMD, the HUSPIR value has been used, with its principal function of assessing the integrity of the synaptic proteins to provide better assessment of synaptic "quality". No significant effect of HUSPIR was observed in the studied cohort.

By using a brain bank post-mortem cases, my cohort is not a sample that is population based, but rather one of convenience and therefore not totally representative of a general population. There are certain limitations of using the brain bank material, mostly related to the limited clinical information about the subjects. For example I may not know to what extent different medications may have had an effect on my data as this information may not be available for all cases.

#### *6.2.3.3 Limited whole-brain sampling*

While it is possible to study synaptome changes across the whole brain in small animals, such as mice, it is not possible, at present, to obtain this whole-brain scanning approach using human tissue. This is due to the significantly greater size of the human brain in comparison to other animals (DeFelipe, 2011). For instance, the first whole-brain animal PSD-95 synaptome mapping has been achieved using five coronal sections through one mouse brain. For comparison, a coronal section through the posterior human hippocampus on its own was larger than any of the whole-brain sections from the mice. As such, the PSD-95 synaptome maps that are created can only give a snapshot of synaptic changes rather than the global overview required to gain a better understanding of the brain synaptome connectivity. However, the maps that I present in this thesis, are the most detailed and comprehensive human PSD-95 synaptome maps that exist to date. The analysis used included areas that are "synapse-deprived", such as the brainstem regions, in addition to well characterised "synapse-rich" neocortical or hippocampal regions. The findings might provide better insights into future synaptic research. For example, characterisation of synaptic changes in human diseases in the "synapse-deprived" areas should not lead to the misleading conclusion that these areas are particularly affected in the pathological conditions. Nevertheless, unlike the rodent synaptome mapping, which allows for the unbiased assessment of synapses in numerous regions simultaneously, the human version of G2CSynMaP cannot, at this stage, overcome this technical limitation.

However, the rapid rate of developments in the computing and data analysis fields mean undoubtedly that it will be possible to create the whole-brain human synaptome maps in the near future.

#### *6.2.3.4 Limited dimensionality of data*

This project produced data based on examination of over half a billion synapses, but at the expense of generating over 22 terabytes (TB) of data. There are several challenges with big data generation, including subsequent dataset processing, comprising visualisation, interpretation or storage. One such pertinent issues, related to this project, encountered even before big data processing, was limited availability of data acquisition resulting in limited dimensionality of the SDM images. So, while it was possible to acquire rodent data at several z-planes, I failed to generate the equivalent data using human tissue. The main issue in trying to replicate the rodent analysis was persistent SDM software performance failure due to the enormous image data size acquired. As mentioned above, in all likelihood, these issues are temporary given the speed of developments in the computing and image analysis fields. However, not being able to present the data based on the 3 dimensional reconstruction, is the limitation of the current study.

## 6.3 FUTURE DIRECTIONS

### 6.3.1 Synaptome map correlation with human cognition

Understanding the architecture of human neural circuits remains one of the neurobiology's major challenges. Our current understanding of how populations of neurons interconnect to produce perception, memory and behaviour is limited. To decipher the intricacies of the workings of the human brain requires not only understanding of how individual neurons work, but also of their synaptic structure and connectivity. The focus of recent research has been on greater understanding of the brain connectome and how patterns of synaptic connectivity between the neurons may contribute to a better understanding of human brain disorders. Mapping of synapses

and their classifications into the "synaptome" (the complement of all synapses in the brain or part thereof) has been possible to even better appreciate the impact of synaptic brain circuitry on human cognition and its pathology. Unsurprisingly, this project has generated many additional questions. For instance, how do normal synaptomes correlate with cognitive abilities in neurologically intact humans? How do brain diseases reorganise these synaptic maps and correlate with cognitive abnormalities? It is anticipated that further descriptions between cognitively intact, clinically well characterised individuals and normal synaptic maps as well as neurologically affected patients and pathological synaptomes will address some of these questions.

### 6.3.2 Synaptome map correlation with imaging studies

Non-invasive imaging methods are commonly used in clinical practice to interpret morphological variations in brain diseases. Increasingly, comparisons between imaging studies and histological analyses in the same objects are possible. For instance, high correlations between quantitative parameters in *ex-vivo* MRI and their quantitative measurements in histological sections from temporal lobe structures, including hippocampus, have been reported (Delgado-González et al., 2015). However, and rather excitingly, the possibility to perform *in vivo* synaptic quantifications using non-invasive MRI methods opens new approaches to study synaptopathies in human patients. A recent study of a new synapse-specific position emission tomography (PET) tracer for detection and visualisation of synaptic loss in human brain disorders is of particular interest, especially as synaptic loss is closely related to cognitive dysfunction (Finnema et al., 2016). Future studies describing associations between the comprehensive synaptome descriptions based on the G2CSynMaP methodology presented in this project, synaptic density imaging and clinical cognitive testing could prove of great value in the assessment and staging of human brain disorders linked to neurodevelopmental and cognitive disorders beyond the common neurodegenerative diseases.

## 6.4 CONCLUSION

In conclusion, this thesis addressed the original aims. 1) It adapted an existing high-throughput synapse quantification methodology, the G2CSynMaP, previously developed to examine rodent brain, to human tissue. 2) It showed that the G2CSynMaP methodology can be successfully used to demonstrate human synaptic diversity and its reorganisation in pathological states.

This method is now poised to answer further questions related to human synapse biology in a comprehensive and quantitative manner and to examine other human brain disorders.

# Bibliography


Aarts, M., Liu, Y., Liu, L., Besshoh, S., Arundine, M., Gurd, J. W., Wang, Y.-T. T., Salter, M. W. and Tymianski, M. (2002), 'Treatment of ischemic brain damage by perturbing NMDA receptor- PSD-95 protein interactions', *Science* **298**(5594), 846–850.

Acebes, A. (2017), 'Brain Mapping and Synapse Quantification In vivo: It's Time to Imaging', *Frontiers in Neuroanatomy* **11**(March), 17.

Al-Hallaq, R. A., Conrads, T. P., Veenstra, T. D. and Wenthold, R. J. (2007), 'NMDA di-heteromeric receptor populations and associated proteins in rat hippocampus.', *The Journal of neuroscience : the official journal of the Society for Neuroscience* **27**(31), 8334–43.

Al-Hallaq, R. A., Yasuda, R. P. and Wolfe, B. B. (2001), 'Enrichment of N-methyl-D-aspartate NR1 splice variants and synaptic proteins in rat postsynaptic densities', *Journal of Neurochemistry* **77**(1), 110–119.

Al Rahim, M. and Hossain, M. A. (2013), 'Genetic deletion of NP1 prevents hypoxic-ischemic neuronal death via reducing AMPA receptor synaptic localization in hippocampal neurons.', *Journal of the American Heart Association* **2**(1), e006098.

Alonso-Nanclares, L., Gonzalez-Soriano, J., Rodriguez, J. R. and DeFelipe, J. (2008), 'Gender differences in human cortical synaptic density.', *Proceedings of the National Academy of Sciences of the United States of America* **105**(38), 14615–9.

Amunts, K., Lepage, C., Borgeat, L., Mohlberg, H., Dickscheid, T., Rousseau, M.-E., Bludau, S., Bazin, P.-L., Lewis, L. B., Oros-Peusquens, A.-M., Shah, N. J., Lippert, T., Zilles, K. and Evans, A. C. (2013), 'BigBrain: An Ultrahigh-Resolution 3D Human Brain Model', *Science* **340**(6139), 1472–1475.

Andreoli, V., De Marco, E. V., Trecroci, F., Cittadella, R., Di Palma, G. and Gambardella, A. (2014), 'Potential involvement of GRIN2B encoding the NMDA receptor subunit NR2B in the spectrum of Alzheimer's disease', *Journal of Neural Transmission* **121**(5), 533–542.

Aoki, C., Miko, I., Oviedo, H., Mikeladze-Dvali, T., Alexandre, L., Sweeney, N. and Bredt, D. S. (2001), 'Electron microscopic immunocytochemical detection of PSD-95, PSD-93, SAP-102, and SAP-97 at postsynaptic, presynaptic, and nonsynaptic sites of adult and neonatal rat visual cortex', *Synapse* **40**(4), 239–257.

Ardila, A., Bernal, B. and Rosselli, M. (2014), 'The Elusive Role of the Left Temporal Pole (BA38) in Language: A Preliminary Meta-Analytic Connectivity Study', *International Journal of Brain Science* **2014**, 1–7.

Arendt, T. (2009), 'Synaptic degeneration in Alzheimer's disease.', *Acta neuropathologica* **118**(1), 167–79.

Arriagada, P. V., Growdon, J. H., Hedley-Whyte, E. T. and Hyman, B. T. (1992), 'Neurofibrillary tangles but not senile plaques parallel duration and severity of Alzheimer's disease.', *Neurology* **42**(3 Pt 1), 631–9.

Arundine, M. and Tymianski, M. (2003), 'Molecular mechanisms of calcium-dependent neurodegeneration in excitotoxicity', *Cell Calcium* **34**(4-5), 325–337.

Ballatore, C., Lee, V. M.-Y. and Trojanowski, J. Q. (2007), 'Tau-mediated neurodegeneration in Alzheimer's disease and related disorders.', *Nature reviews. Neuroscience* **8**(9), 663–72.

Banerjee, A., Wang, H.-Y., Borgmann-Winter, K. E., MacDonald, M. L., Kaprielian, H., Stucky, A., Kvasic, J., Egbujo, C., Ray, R., Talbot, K., Hemby, S. E., Siegel, S. J., Arnold, S. E., Sleiman, P., Chang, X., Hakonarson, H., Gur, R. E. and Hahn, C.-G. (2014), 'Src kinase as a mediator of convergent molecular abnormalities leading to NMDAR hypoactivity in schizophrenia.', *Molecular psychiatry* **20**(August), 1–10.

Bannerman, D. M., Sprengel, R., Sanderson, D. J., McHugh, S. B., Rawlins, J. N. P., Monyer, H. and Seeburg, P. H. (2014), 'Hippocampal synaptic plasticity, spatial memory and anxiety.', *Nature reviews. Neuroscience* **15**(3), 181–92.

Barker, R., Wellington, D., Esiri, M. M. and Love, S. (2013), 'Assessing White Matter Ischemic Damage in Dementia Patients by Measurement of Myelin Proteins', *Journal of Cerebral Blood Flow & Metabolism* **33**(7), 1050–1057.

Bassett, D. S., Porter, M. A., Wymbs, N. F., Grafton, S. T., Carlson, J. M. and Mucha, P. J. (2013), 'Robust detection of dynamic community structure in networks.', *Chaos (Woodbury, N.Y.)* **23**(1), 013142.

Bayés, A., Collins, M. O., Croning, M. D. R., van de Lagemaat, L. N., Choudhary, J. S. and Grant, S. G. N. (2012), 'Comparative study of human and mouse postsynaptic proteomes finds high compositional conservation and abundance differences for key synaptic proteins.', *PloS one* **7**(10), e46683.

Bayés, A., van de Lagemaat, L. N., Collins, M. O., Croning, M. D. R., Whittle, I. R., Choudhary, J. S. and Grant, S. G. N. (2011), 'Characterization of the proteome, diseases and evolution of the human postsynaptic density.', *Nature neuroscience* **14**(1), 19–21.

Bayés, , Collins, M. O., Galtrey, C. M., Simonnet, C., Roy, M., Croning, M. D. R., Gou, G., van de Lagemaat, L. N., Milward, D., Whittle, I. R., Smith, C., Choudhary, J. S. and Grant, S. G. N. (2014), 'Human post-mortem synapse proteome integrity screening for proteomic studies of postsynaptic complexes.', *Molecular brain* **7**(1), 88.

Bayés, , Collins, M. O., Reig-Viader, R., Gou, G., Goulding, D., Izquierdo, A., Choudhary, J. S., Emes, R. D. and Grant, S. G. N. (2017), 'Evolution of complexity in the zebrafish synapse proteome.', *Nature communications* **8**, 14613.

Beaulieu, C. and Colonnier, M. (1989), 'Number and size of neurons and synapses in the motor cortex of cats raised in different environmental complexities.', *The Journal of comparative neurology* **289**(1), 178–81.

Bilousova, T., Miller, C. A., Poon, W. W., Vinters, H. V., Corrada, M., Kawas, C., Hayden, E. Y., Teplow, D. B., Glabe, C., Albay, R., Cole, G. M., Teng, E. and Gylys, K. H. (2016), 'Synaptic Amyloid-$\beta$ Oligomers Precede p-Tau and Differentiate High Pathology Control Cases.', *The American journal of pathology* **186**(1), 185–98.

Blazquez-Llorca, L., García-Marín, V. and DeFelipe, J. (2010), 'GABAergic complex basket formations in the human neocortex.', *The Journal of comparative neurology* **518**(24), 4917–37.

Blazquez-Llorca, L., Merchán-Pérez, , Rodríguez, J.-R., Gascón, J. and DeFelipe, J. (2013), 'FIB/SEM technology and Alzheimer's disease: three-dimensional analysis of human cortical synapses.', *Journal of Alzheimer's disease : JAD* **34**(4), 995–1013.

Bliss, T. V. and Gardner-Medwin, a. R. (1973), 'Long-lasting potentiation of synaptic transmission in the dentate area of the unanaestetized rabbit following stimulation of the perforant path.', *The Journal of physiology* **232**(2), 357–374.

Blitzer, R. D. (2005), 'Teaching resources. Long-term potentiation: mechanisms of induction and maintenance.', *Sci.STKE.* **2005**(309), tr26.

Boxer, A. L., Geschwind, M. D., Belfor, N., Gorno-Tempini, M. L., Schauer, G. F., Miller, B. L., Weiner, M. W. and Rosen, H. J. (2006), 'Patterns of Brain Atrophy That Differentiate Corticobasal Degeneration Syndrome From Progressive Supranuclear Palsy', *Archives of Neurology* **63**(1), 81.

Braak, H., Alafuzoff, I., Arzberger, T., Kretzschmar, H. and Del Tredici, K. (2006), 'Staging of Alzheimer disease-associated neurofibrillary pathology using paraffin sections and immunocytochemistry', *Acta Neuropathologica* **112**(4), 389–404.

Braak, H. and Braak, E. (1990), 'Alzheimer's disease: striatal amyloid deposits and neurofibrillary changes.', *Journal of neuropathology and experimental neurology* **49**(3), 215–24.

Brenman, J. E., Christopherson, K. S., Craven, S. E., McGee, A. W. and Bredt, D. S. (1996), 'Cloning and characterization of postsynaptic density 93, a nitric oxide synthase interacting protein.', *The Journal of neuroscience : the official journal of the Society for Neuroscience* **16**(23), 7407–15.

Brenman, J. E. e. (1996), 'Interaction of nitric oxide synthase with the postsynaptic density protein PSD-95 and alpha1-syntrophin mediated by PDZ domains.', *Cell* **84**(5), 757–67.

Brenman, J. E., Topinka, J. R., Cooper, E. C., McGee, a. W., Rosen, J., Milroy, T., Ralston, H. J. and Bredt, D. S. (1998), 'Localization of postsynaptic density-93 to dendritic microtubules and interaction with microtubule-associated protein 1A.', *The Journal of neuroscience : the official journal of the Society for Neuroscience* **18**(21), 8805–13.

Brian, J. A., Bryson, S. E. and Zwaigenbaum, L. (2015), 'Autism spectrum disorder in infancy', *Current Opinion in Neurology* **28**(2), 117–123.

Broadhead, M. J., Horrocks, M. H., Zhu, F., Muresan, L., Benavides-Piccione, R., DeFelipe, J., Fricker, D., Kopanitsa, M. V., Duncan, R. R., Klenerman, D., Komiyama, N. H., Lee, S. F. and Grant, S. G. N. (2016), 'PSD95 nanoclusters are postsynaptic building blocks in hippocampus circuits.', *Scientific reports* **6**, 24626.

Busse, B. and Smith, S. (2013), 'Automated Analysis of a Diverse Synapse Population', *PLoS Computational Biology* **9**.

Cai, C., Li, H., Kangasniemi, A., Pihlajamaa, T., Von Ossowski, L., Kerkelä, K., Schulz, S., Rivera, C. and Keinänen, K. (2008), 'Somatostatin receptor subtype 1 is a PDZ ligand for synapse-associated protein 97 and a potential regulator of growth cone dynamics', *Neuroscience* **157**(4), 833–843.

Calabresi, P., De Murtas, M. and Bernardi, G. (1997), 'Discussion', *Neuroscience* **78**(1), 39–60.

Calhoun, M. E., Fletcher, B. R., Yi, S., Zentko, D. C., Gallagher, M. and Rapp, P. R. (2008), 'Age-related spatial learning impairment is unrelated to spinophilin immunoreactive spine number and protein levels in rat hippocampus', *Neurobiology of Aging* **29**(8), 1256–1264.

Callahan, L. M., Vaules, W. A. and Coleman, P. D. (2002), 'Progressive reduction of synaptophysin message in single neurons in Alzheimer disease.', *Journal of neuropathology and experimental neurology* **61**(5), 384–95.

Cambon, K., Davies, H. A. and Stewart, M. G. (2000), 'Synaptic loss is accompanied by an increase in synaptic area in the dentate gyrus of aged human apolipoprotein E4 transgenic mice.', *Neuroscience* **97**(4), 685–92.

Carter, J. and Lippa, C. F. (2001), 'Beta-amyloid, neuronal death and Alzheimer's disease.', *Current molecular medicine* **1**(6), 733–7.

Caspers, S., Geyer, S., Schleicher, A., Mohlberg, H., Amunts, K. and Zilles, K. (2006), 'The human inferior parietal cortex: Cytoarchitectonic parcellation and interindividual variability', *NeuroImage* **33**(2), 430–448.

Castejón, O. J., Fuller, L. and Dailey, M. E. (2004), 'Localization of synapsin-I and PSD-95 in developing postnatal rat cerebellar cortex.', *Brain research. Developmental brain research* **151**(1-2), 25–32.

Castejon, O. J. and Sims, P. (2000), 'Three-dimensional morphology of cerebellar climbing fibers. A study by means of confocal laser scanning microscopy and scanning electron microscopy.', *Scanning* **22**(4), 211–7.

Castejón, O. and Sims, P. (1999), 'Confocal laser scanning microscopy of hamster cerebellum using FM4-64 as intracellular staining.', *Scanning* **21**(1), 15–21.

Chadwick, M. J., Hassabis, D., Weiskopf, N. and Maguire, E. A. (2010), 'Decoding individual episodic memory traces in the human hippocampus.', *Current biology : CB* **20**(6), 544–7.

Chartier-Harlin, M. C., Parfitt, M., Legrain, S., Pérez-Tur, J., Brousseau, T., Evans, A., Berr, C., Vidal, O., Roques, P. and Gourlet, V. (1994), 'Apolipoprotein E, epsilon 4 allele as a major risk factor for sporadic early and late-onset forms of Alzheimer's disease: analysis of the 19q13.2 chromosomal region.', *Human molecular genetics* **3**(4), 569–74.

Chen, L., Chetkovich, D. M., Petralia, R. S., Sweeney, N. T., Kawasaki, Y., Wenthold, R. J., Bredt, D. S. and Nicoll, R. A. (2000), 'Stargazin regulates synaptic targeting of AMPA receptors by two distinct mechanisms.', *Nature* **408**(6815), 936–43.

Chen, X., Levy, J. M., Hou, A., Winters, C., Azzam, R., Sousa, A. A., Leapman, R. D., Nicoll, R. A. and Reese, T. S. (2015), 'PSD-95 family MAGUKs are essential for anchoring AMPA and NMDA receptor complexes at the postsynaptic density.', *Proceedings of the National Academy of Sciences of the United States of America* **112**(50), 6983–92.

Chen, X., Winters, C., Azzam, R., Li, X., Galbraith, J. a., Leapman, R. D. and Reese, T. S. (2008), 'Organization of the core structure of the postsynaptic density.', *Proceedings of the National Academy of Sciences of the United States of America* **105**(11), 4453–4458.

Cheng, L., Yin, W.-J., Zhang, J.-F. and Qi, J.-S. (2009), 'Amyloid beta-protein fragments 25-35 and 31-35 potentiate long-term depression in hippocampal CA1 region of rats in vivo.', *Synapse (New York, N.Y.)* **63**(3), 206–14.

Cheng, M. C., Lu, C. L., Luu, S. U., Tsai, H. M., Hsu, S. H., Chen, T. T. and Chen, C. H. (2010), 'Genetic and functional analysis of the DlG4 gene encoding the post-synaptic density protein 95 in schizophrenia', *PLoS ONE* **5**(12), e15107.

Chenouard, N., Smal, I., de Chaumont, F., Maška, M., Sbalzarini, I. F., Gong, Y., Cardinale, J., Carthel, C., Coraluppi, S., Winter, M., Cohen, A. R., Godinez, W. J., Rohr, K., Kalaidzidis, Y., Liang, L., Duncan, J., Shen, H., Xu, Y., Magnusson, K. E. G., Jaldén, J., Blau, H. M., Paul-Gilloteaux, P., Roudot, P., Kervrann, C., Waharte, F., Tinevez, J.-Y., Shorte, S. L., Willemse, J., Celler, K., van Wezel, G. P., Dan, H.-W., Tsai, Y.-S., Ortiz de Solórzano, C., Olivo-Marin, J.-C. and Meijering, E. (2014), 'Objective comparison of particle tracking methods.', *Nature methods* **11**(3), 281–9.

Cho, K.-O., Hunt, C. A. and Kennedy, M. B. (1992), 'The rat brain postsynaptic density fraction contains a homolog of the drosophila discs-large tumor suppressor protein', *Neuron* **9**(5), 929–942.

Clinton, S. M., Haroutunian, V., Davis, K. L. and Meador-Woodruff, J. H. (2003), 'Altered transcript expression of NMDA receptor-associated postsynaptic proteins in the thalamus of subjects with schizophrenia.', *The American journal of psychiatry* **160**(6), 1100–9.

Clinton, S. M., Haroutunian, V. and Meador-Woodruff, J. H. (2006), 'Up-regulation of NMDA receptor subunit and post-synaptic density protein expression in the thalamus of elderly patients with schizophrenia.', *Journal of neurochemistry* **98**(4), 1114–25.

Colantuoni, C., Lipska, B. K., Ye, T., Hyde, T. M., Tao, R., Leek, J. T., Colantuoni, E. A., Elkahloun, A. G., Herman, M. M., Weinberger, D. R. and Kleinman, J. E. (2011), 'Temporal dynamics and genetic control of transcription in the human prefrontal cortex.', *Nature* **478**(7370), 519–23.

Colledge, M., Dean, R. a., Scott, G. K., Langeberg, L. K., Huganir, R. L. and Scott, J. D. (2000), 'Targeting of PKA to glutamate receptors through a MAGUK-AKAP complex.', *Neuron* **27**(1), 107–19.

Collingridge, G. L., Isaac, J. T. R. and Wang, Y. T. (2004), 'Receptor trafficking and synaptic plasticity', *Nat Rev Neurosci* **5**(12), 952–962.

Collins, M. O., Husi, H., Yu, L., Brandon, J. M., Anderson, C. N. G., Blackstock, W. P., Choudhary, J. S. and Grant, S. G. N. (2006), 'Molecular characterization and comparison of the components and multiprotein complexes in the postsynaptic proteome.', *Journal of neurochemistry* **97 Suppl 1**, 16–23.

Cook, D. J., Teves, L. and Tymianski, M. (2012*a*), 'A Translational Paradigm for the Preclinical Evaluation of the Stroke Neuroprotectant Tat-NR2B9c in Gyrencephalic Nonhuman Primates', *Science Translational Medicine* **4**(154), 133–154.

Cook, D. J., Teves, L. and Tymianski, M. (2012*b*), 'Treatment of stroke with a PSD-95 inhibitor in the gyrencephalic primate brain - with comments', *Nature* **483**(7388), 213–217.

Corballis, M. C. (2014), 'Left brain, right brain: facts and fantasies.', *PLoS biology* **12**(1), e1001767.

Corder, E. H., Saunders, a. M., Strittmatter, W. J., Schmechel, D. E., Gaskell, P. C., Small, G. W., Roses, a. D., Haines, J. L. and Pericak-Vance, M. a. (1993), 'Gene dose of apolipoprotein E type 4 allele and the risk of Alzheimer's disease in late onset families.', *Science (New York, N.Y.)* **261**(5123), 921–3.

Counts, S. E., Alldred, M. J., Che, S., Ginsberg, S. D. and Mufson, E. J. (2014), 'Synaptic gene dysregulation within hippocampal CA1 pyramidal neurons in mild cognitive impairment.', *Neuropharmacology* **79**, 172–9.

Cousins, S. L. and Stephenson, F. A. (2012), 'Identification of N-methyl-D-aspartic acid (NMDA) receptor subtype-specific binding sites that mediate direct interactions with scaffold protein PSD-95.', *The Journal of biological chemistry* **287**(16), 13465–76.

Cragg, B. G. (1967), 'The density of synapses and neurones in the motor and visual areas of the cerebral cortex.', *Journal of Anatomy* **101**(4), 639–654.

Crittenden, J. R. and Graybiel, A. M. (2011), 'Basal Ganglia disorders associated with imbalances in the striatal striosome and matrix compartments.', *Frontiers in neuroanatomy* **5**, 59.

Davies, C. A., Mann, D. M., Sumpter, P. Q. and Yates, P. O. (1987), 'A quantitative morphometric analysis of the neuronal and synaptic content of the frontal and temporal cortex in patients with Alzheimer's disease.', *Journal of the neurological sciences* **78**(2), 151–64.

De Camilli, P., Harris, S. M., Huttner, W. B. and Greengard, P. (1983), 'Synapsin I (Protein I), a nerve terminal-specific phosphoprotein. II. Its specific association with synaptic vesicles demonstrated by immunocytochemistry in agarose-embedded synaptosomes.', *The Journal of cell biology* **96**(5), 1355–73.

de Schipper, E., Lundequist, A., Coghill, D., de Vries, P. J., Granlund, M., Holtmann, M., Jonsson, U., Karande, S., Robison, J. E., Shulman, C., Singhal, N., Tonge, B., Wong, V. C., Zwaigenbaum, L. and Bölte, S. (2015), 'Ability and Disability in Autism Spectrum Disorder: A Systematic Literature Review Employing the International Classification of Functioning, Disability and Health-Children and Youth Version', *Autism Research* **8**(6), 782–794.

de Wilde, M. C., Overk, C. R., Sijben, J. W. and Masliah, E. (2016), 'Meta-analysis of synaptic pathology in Alzheimer's disease reveals selective molecular vesicular machinery vulnerability', *Alzheimer's & Dementia* **12**(6), 633–644.

DeFelipe, J. (2011), 'The Evolution of the Brain, the Human Nature of Cortical Circuits, and Intellectual Creativity', *Frontiers in Neuroanatomy* **5**, 29.

DeFelipe, J. (2015), 'The anatomical problem posed by brain complexity and size: a potential solution', *Frontiers in Neuroanatomy* **9**(August), 1–16.

DeFelipe, J., Alonso-Nanclares, L. and Arellano, J. I. (2002), 'Microstructure of the neocortex: comparative aspects.', *Journal of neurocytology* **31**(3-5), 299–316.

Deguchi, M., Hata, Y., Takeuchi, M., Ide, N., Hirao, K., Yao, I., Irie, M., Toyoda, A. and Takai, Y. (1998), 'BEGAIN (brain-enriched guanylate kinase-associated protein), a novel neuronal PSD-95/SAP90-binding protein.', *The Journal of biological chemistry* **273**(41), 26269–72.

DeKosky, S. T. and Scheff, S. W. (1990), 'Synapse loss in frontal cortex biopsies in Alzheimer's disease: correlation with cognitive severity.', *Annals of neurology* **27**(5), 457–64.

Delgado-González, J. C., Mansilla-Legorburo, F., Florensa-Vila, J., Insausti, A. M., Viñuela, A., Tuñón-Alvarez, T., Cruz, M., Mohedano-Moriano, A., Insausti, R. and Artacho-Pérula, E. (2015), 'Quantitative Measurements in the Human Hippocampus and Related Areas: Correspondence between Ex-Vivo MRI and Histological Preparations.', *PloS one* **10**(6), e0130314.

Dickerson, B. C., Bakkour, A., Salat, D. H., Feczko, E., Pacheco, J., Greve, D. N., Grodstein, F., Wright, C. I., Blacker, D., Rosas, H. D., Sperling, R. A., Atri, A., Growdon, J. H., Hyman, B. T., Morris, J. C., Fischl, B. and Buckner, R. L. (2009), 'The cortical signature of Alzheimer's disease: regionally specific cortical thinning relates to symptom severity in very mild to mild AD dementia and is detectable in asymptomatic amyloid-positive individuals.', *Cerebral cortex (New York, N.Y. : 1991)* **19**(3), 497–510.

Dieterich, D. C. and Kreutz, M. R. (2016), 'Proteomics of the Synapse–A Quantitative Approach to Neuronal Plasticity.', *Molecular & cellular proteomics : MCP* **15**(2), 368–81.

Ding, S.-L., Royall, J. J., Sunkin, S. M., Ng, L., Facer, B. A., Lesnar, P., Guillozet-Bongaarts, A., McMurray, B., Szafer, A., Dolbeare, T. A., Stevens, A., Tirrell, L., Benner, T., Caldejon, S., Dalley, R. A., Dee, N., Lau, C., Nyhus, J., Reding, M., Riley, Z. L., Sandman, D., Shen, E., van der Kouwe, A., Varjabedian, A., Write, M., Zollei, L., Dang, C., Knowles, J. A., Koch, C., Phillips, J. W., Sestan, N., Wohnoutka, P., Zielke, H. R., Hohmann, J. G., Jones, A. R., Bernard, A., Hawrylycz, M. J., Hof, P. R., Fischl, B. and Lein, E. S. (2016), 'Comprehensive cellular-resolution atlas of the adult human brain', *Journal of Comparative Neurology* **524**(16), 3127–3481.

Dirnagl, U., Iadecola, C. and Moskowitz, M. A. (1999), 'Pathobiology of ischaemic stroke: an integrated view', *Trends in Neurosciences* **22**(9), 391–397.

Distler, U., Schmeisser, M. J., Pelosi, A., Reim, D., Kuharev, J., Weiczner, R., Baumgart, J., Boeckers, T. M., Nitsch, R., Vogt, J. and Tenzer, S. (2014), 'In-depth protein profiling of the postsynaptic density from mouse hippocampus using data-independent acquisition proteomics.', *Proteomics* **14**(21-22), 2607–13.

Dityatev, A. and Rusakov, D. A. (2011), 'Molecular signals of plasticity at the tetrapartite synapse', *Current Opinion in Neurobiology* **21**(2), 353–359.

Down, T. A., Piipari, M. and Hubbard, T. J. P. (2011), 'Dalliance: interactive genome viewing on the web.', *Bioinformatics (Oxford, England)* **27**(6), 889–90.

Dracheva, S., Marras, S. A. E., Elhakem, S. L., Kramer, F. R., Davis, K. L. and Haroutunian, V. (2001), 'N-methyl-D-aspartic acid receptor expression in the dorsolateral prefrontal cortex of elderly patients with schizophrenia', *American Journal of Psychiatry* **158**(9), 1400–1410.

Durand, C. M., Betancur, C., Boeckers, T. M., Bockmann, J., Chaste, P., Fauchereau, F., Nygren, G., Rastam, M., Carina, I., Anckarsäter, H., Sponheim, E., Goubran-Botros, H., Delorme, R., Chabane, N., Mas, P. D., Bieth, E., Rogé, B., Héron, D., Burglen, L., Gillberg, C., Gillberg, I. C., Anckarsäter, H., Sponheim, E., Goubran-Botros, H., Delorme, R., Chabane, N., Mouren-Simeoni, M.-C., de Mas, P., Bieth, E., Rogé, B., Héron, D., Burglen, L., Gillberg, C., Leboyer, M. and Bourgeron, T. (2007), 'Mutations in the gene encoding the synaptic scaffolding protein SHANK3 are associated with autism spectrum disorders.', *Nature genetics* **39**(1), 25–27.

Durrenberger, P. F., Fernando, S., Kashefi, S. N., Ferrer, I., Hauw, J.-J., Seilhean, D., Smith, C., Walker, R., Al-Sarraj, S., Troakes, C., Palkovits, M., Kasztner, M., Huitinga, I., Arzberger, T., Dexter, D. T., Kretzschmar, H. and Reynolds, R. (2010), 'Effects of antemortem and postmortem variables on human brain mRNA quality: a BrainNet Europe study.', *Journal of neuropathology and experimental neurology* **69**(1), 70–81.

Duvernoy, H. M. (1988), *The Human Hippocampus*, 1 edn, J.F. Bergmann-Verlag, Munich.

Eickhoff, S., Walters, N. B., Schleicher, A., Kril, J., Egan, G. F., Zilles, K., Watson, J. D. G. and Amunts, K. (2005), 'High-resolution MRI reflects myeloarchitecture and cytoarchitecture of human cerebral cortex.', *Human brain mapping* **24**(3), 206–15.

Ekstrom, A. D. and Bookheimer, S. Y. (2007), 'Spatial and temporal episodic memory retrieval recruit dissociable functional networks in the human brain.', *Learning & memory (Cold Spring Harbor, N.Y.)* **14**(10), 645–54.

Ellis, R. J., Olichney, J. M., Thal, L. J., Mirra, S. S., Morris, J. C., Beekly, D. and Heyman, A. (1996), 'Cerebral amyloid angiopathy in the brains of patients with Alzheimer's disease: The CERAD experience, part XV', *Neurology* **46**(6), 1592–1596.

Emes, R. D. and Grant, S. G. (2012), 'Evolution of Synapse Complexity and Diversity', *Annual Review of Neuroscience* **35**(1), 111–131.

Endele, S., Rosenberger, G., Geider, K., Popp, B., Tamer, C., Stefanova, I., Milh, M., Kortum, F., Fritsch, A., Pientka, F. K., Hellenbroich, Y., Kalscheuer, V. M., Kohlhase, J., Moog, U., Rappold, G., Rauch, A., Ropers, H. H., von Spiczak, S., Tonnies, H., Villeneuve, N., Villard, L., Zabel, B., Zenker, M., Laube, B., Reis, A., Wieczorek, D., Van Maldergem, L. and Kutsche, K. (2010), 'Mutations in GRIN2A and GRIN2B encoding regulatory subunits of NMDA receptors cause variable neurodevelopmental phenotypes', *Nat Genet* **42**(11), 1021–1026.

Fagerberg, L., Hallström, B. M., Oksvold, P., Kampf, C., Djureinovic, D., Odeberg, J., Habuka, M., Tahmasebpoor, S., Danielsson, A., Edlund, K., Asplund, A., Sjöstedt, E., Lundberg, E., Szigyarto, C. A.-K., Skogs, M., Takanen, J. O., Berling, H., Tegel, H., Mulder, J., Nilsson, P., Schwenk, J. M., Lindskog, C., Danielsson, F., Mardinoglu, A., Sivertsson, A., von Feilitzen, K., Forsberg, M., Zwahlen, M., Olsson, I., Navani, S., Huss, M., Nielsen, J., Ponten, F. and Uhlén, M. (2014), 'Analysis of the human tissue-specific expression by genome-wide integration of transcriptomics and antibody-based proteomics.', *Molecular & cellular proteomics : MCP* **13**(2), 397–406.

Fan, J., Cowan, C. M., Zhang, L. Y. J., Hayden, M. R. and Raymond, L. A. (2009), 'Interaction of postsynaptic density protein-95 with NMDA receptors influences excitotoxicity in the yeast artificial chromosome mouse model of Huntington's disease.', *The Journal of neuroscience : the official journal of the Society for Neuroscience* **29**(35), 10928–38.

Farrer, L. A. (1997), 'Effects of Age, Sex, and Ethnicity on the Association Between Apolipoprotein E Genotype and Alzheimer Disease', *JAMA* **278**(16), 1349.

Faull, R. L. and Villiger, J. W. (1988), 'Multiple benzodiazepine receptors in the human basal ganglia: a detailed pharmacological and anatomical study.', *Neuroscience* **24**(2), 433–51.

Feng, J., Schroer, R., Yan, J., Song, W., Yang, C., Bockholt, A., Cook, E. H., Skinner, C., Schwartz, C. E. and Sommer, S. S. (2006), 'High frequency of neurexin $1\beta$ signal peptide structural variants in patients with autism', *Neuroscience Letters* **409**(1), 10–13.

Fernández, E., Collins, M. O., Frank, R. A. W., Zhu, F., Kopanitsa, M. V., Nithianantharajah, J., Lemprière, S. A., Fricker, D., Elsegood, K. A., McLaughlin, C. L., Croning, M. D. R., Mclean, C., Armstrong, J. D., Hill, W. D., Deary, I. J., Cencelli, G., Bagni, C., Fromer, M., Purcell, S. M., Pocklington, A. J., Choudhary, J. S., Komiyama, N. H. and Grant, S. G. N. (2017), 'Arc Requires PSD95 for Assembly into Postsynaptic Complexes Involved with Neural Dysfunction and Intelligence.', *Cell reports* **21**(3), 679–691.

Fernandez, E., Collins, M. O., Uren, R. T., Kopanitsa, M. V., Komiyama, N. H., Croning, M. D., Zografos, L., Armstrong, J. D., Choudhary, J. S. and Grant, S. G. (2009), 'Targeted tandem affinity purification of PSD-95 recovers core postsynaptic complexes and schizophrenia susceptibility proteins', *Molecular Systems Biology* **5**(269), 269.

Ferreira, S. T., Lourenco, M. V., Oliveira, M. M. and De Felice, F. G. (2015), 'Soluble amyloid-$\beta$ oligomers as synaptotoxins leading to cognitive impairment in Alzheimer's disease.', *Frontiers in cellular neuroscience* **9**(May), 191.

Finnema, S. J., Nabulsi, N. B., Eid, T., Detyniecki, K., Lin, S.-f., Chen, M.-K., Dhaher, R., Matuskey, D., Baum, E., Holden, D., Spencer, D. D., Mercier, J., Hannestad, J., Huang, Y. and Carson, R. E. (2016), 'Imaging synaptic density in the living human brain', *Science Translational Medicine* **8**(348), 96–348.

Firestein, B. L., Firestein, B. L., Brenman, J. E., Aoki, C., Sanchez-Perez, A. M., El-Husseini, A. E.-D. and Bredt, D. S. (1999), 'Cypin: a cytosolic regulator of PSD-95 postsynaptic targeting.', *Neuron* **24**(3), 659–72.

Fortin, D. A., Tillo, S. E., Yang, G., Rah, J.-C. J.-C., Melander, J. B., Bai, S., Soler-Cedeno, O., Qin, M., Zemelman, B. V., Guo, C., Mao, T., Zhong, H., Soler-Cedeño, O., Qin, M., Zemelman, B. V., Guo, C., Mao, T. and Zhong, H. (2014), 'Live Imaging of Endogenous PSD-95 Using ENABLED: A Conditional Strategy to Fluorescently Label Endogenous Proteins', *The Journal of neuroscience : the official journal of the Society for Neuroscience* **34**(50), 16698–712.

Francks, C. (2015), 'Exploring human brain lateralization with molecular genetics and genomics.', *Annals of the New York Academy of Sciences* **1359**(1), 1–13.

Frandemiche, M. L., De Seranno, S., Rush, T., Borel, E., Elie, A., Arnal, I., Lanté, F. and Buisson, A. (2014), 'Activity-dependent tau protein translocation to excitatory synapse is disrupted by exposure to amyloid-beta oligomers.', *The Journal of neuroscience : the official journal of the Society for Neuroscience* **34**(17), 6084–97.

Frank, R. A. and Grant, S. G. (2017), 'Supramolecular organization of NMDA receptors and the postsynaptic density', *Current Opinion in Neurobiology* **45**, 139–147.

Frank, R. A. W., Komiyama, N. H., Ryan, T. J., Zhu, F., O'Dell, T. J. and Grant, S. G. N. (2016), 'NMDA receptors are selectively partitioned into complexes and supercomplexes during synapse maturation', *Nature Communications* **7**, 11264.

Frotscher, M., Jonas, P. and Sloviter, R. S. (2006), 'Synapses formed by normal and abnormal hippocampal mossy fibers.', *Cell and tissue research* **326**(2), 361–7.

Fujita-Jimbo, E., Tanabe, Y., Yu, Z., Kojima, K., Mori, M., Li, H., Iwamoto, S., Yamagata, T., Momoi, M. Y. and Momoi, T. (2015), 'The association of GPR85 with PSD-95-neuroligin complex and autism spectrum disorder: a molecular analysis.', *Molecular autism* **6**(1), 17.

Fukata, Y., Adesnik, H., Iwanaga, T., Bredt, D. S., Nicoll, R. A. and Fukata, M. (2006), 'Epilepsy-related ligand/receptor complex LGI1 and ADAM22 regulate synaptic transmission.', *Science (New York, N.Y.)* **313**(5794), 1792–5.

Fukata, Y., Dimitrov, A., Boncompain, G., Vielemeyer, O., Perez, F. and Fukata, M. (2013), 'Local palmitoylation cycles define activity-regulated postsynaptic subdomains', *Journal of Cell Biology* **202**(1), 145–161.

Fukata, Y., Yokoi, N., Miyazaki, Y. and Fukata, M. (2017), 'The LGI1-ADAM22 protein complex in synaptic transmission and synaptic disorders.', *Neuroscience research* **116**, 39–45.

Fukaya, M., Ueda, H., Yamauchi, K., Inoue, Y. and Watanabe, M. (1999), 'Distinct spatiotemporal expression of mRNAs for the PSD-95/SAP90 protein family in the mouse brain.', *Neuroscience research* **33**(2), 111–8.

Fukaya, M. and Watanabe, M. (2000), 'Improved immunohistochemical detection of postsynaptically located PSD-95/SAP90 protein family by protease section pretreatment: a study in the adult mouse brain.', *The Journal of comparative neurology* **426**(4), 572–586.

Funke, L., Dakoji, S. and Bredt, D. S. (2005), 'Membrane-associated guanylate kinases regulate adhesion and plasticity at cell junctions.', *Annual review of biochemistry* **74**, 219–245.

Galili, T. (2015), 'dendextend: an R package for visualizing, adjusting and comparing trees of hierarchical clustering.', *Bioinformatics (Oxford, England)* **31**(22), 3718–20.

Garcia, R. A., Vasudevan, K. and Buonanno, A. (2000), 'The neuregulin receptor ErbB-4 interacts with PDZ-containing proteins at neuronal synapses.', *Proceedings of the National Academy of Sciences of the United States of America* **97**(7), 3596–601.

Gardoni, F., Picconi, B., Ghiglieri, V., Polli, F., Bagetta, V., Bernardi, G., Cattabeni, F., Di Luca, M. and Calabresi, P. (2006), 'A critical interaction between NR2B and MAGUK in L-DOPA induced dyskinesia.', *The Journal of neuroscience : the official journal of the Society for Neuroscience* **26**(11), 2914–2922.

Gatz, M., Reynolds, C. a., Fratiglioni, L., Johansson, B., Mortimer, J. a., Berg, S., Fiske, A. and Pedersen, N. L. (2006), 'Role of genes and environments for explaining Alzheimer disease.', *Archives of general psychiatry* **63**(2), 168–74.

Geinisman, Y., Ganeshina, O., Yoshida, R., Berry, R. W., Disterhoft, J. F. and Gallagher, M. (2004), 'Aging, spatial learning, and total synapse number in the rat CA1 stratum radiatum.', *Neurobiology of aging* **25**(3), 407–16.

Glantz, L. A., Gilmore, J. H., Hamer, R. M., Lieberman, J. A. and Jarskog, L. F. (2007), 'Synaptophysin and postsynaptic density protein 95 in the human prefrontal cortex from mid-gestation into early adulthood', *Neuroscience* **149**(3), 582–591.

Glasser, M. F., Coalson, T. S., Robinson, E. C., Hacker, C. D., Harwell, J., Yacoub, E., Ugurbil, K., Andersson, J., Beckmann, C. F., Jenkinson, M., Smith, S. M. and Van Essen, D. C. (2016), 'A multi-modal parcellation of human cerebral cortex', *Nature* **536**(7615), 171–178.

Gong, Y. and Lippa, C. F. (2010), 'Review: disruption of the postsynaptic density in Alzheimer's disease and other neurodegenerative dementias.', *American journal of Alzheimer's disease and other dementias* **25**(7), 547–55.

Gong, Y., Lippa, C. F., Zhu, J., Lin, Q. and Rosso, A. L. (2009), 'Disruption of glutamate receptors at Shank-postsynaptic platform in Alzheimer's disease.', *Brain research* **1292**, 191–8.

Gonzalez-Riano, C., Tapia-González, S., García, A., Muñoz, A., DeFelipe, J. and Barbas, C. (2017), 'Metabolomics and neuroanatomical evaluation of post-mortem changes in the hippocampus', *Brain Structure and Function* **222**(6), 2831–2853.

Gottschalk, M., Bach, A., Hansen, J. L., Krogsgaard-Larsen, P., Kristensen, A. S. and Strømgaard, K. (2009), 'Detecting protein-protein interactions in living cells: development of a bioluminescence resonance energy transfer assay to evaluate the PSD-95/NMDA receptor interaction.', *Neurochemical research* **34**(10), 1729–37.

Gräf, R., Rietdorf, J. and Zimmermann, T. (2005), 'Live cell spinning disk microscopy.', *Advances in biochemical engineering/biotechnology* **95**, 57–75.

Graham, T. L. and Whistler, R. L. (1975), 'Enzymatic synthesis and reactions of uridine 5'-(5-thio-alphaD-glucopyranosyl pyrophosphate).', *Archives of biochemistry and biophysics* **171**(2), 721–6.

Grant, S. G. (2012), 'Synaptopathies: diseases of the synaptome', *Current Opinion in Neurobiology* **22**(3), 522–529.

Gray, E. G. (1959), 'Axo-somatic and axo-dendritic synapses of the cerebral cortex: an electron microscope study', *Journal of anatomy* **93**, 420.

Graybiel, A. M. (1997), 'The Basal Ganglia and Cognitive Pattern Generators', *Schizophrenia Bulletin* **23**(3), 459–469.

Graziano, A., Liu, X.-B., Murray, K. D. and Jones, E. G. (2008), 'Vesicular glutamate transporters define two sets of glutamatergic afferents to the somatosensory thalamus and two thalamocortical projections in the mouse.', *The Journal of comparative neurology* **507**(2), 1258–76.

Hahn, C.-G., Wang, H.-Y., Cho, D.-S., Talbot, K., Gur, R. E., Berrettini, W. H., Bakshi, K., Kamins, J., Borgmann-Winter, K. E., Siegel, S. J., Gallop, R. J. and Arnold, S. E. (2006), 'Altered neuregulin 1-erbB4 signaling contributes to NMDA receptor hypofunction in schizophrenia.', *Nature medicine* **12**(7), 824–828.

Han, X., Shao, W., Liu, Z., Fan, S., Yu, J., Chen, J., Qiao, R., Zhou, J. and Xie, P. (2015), 'iTRAQ-based quantitative analysis of hippocampal postsynaptic density-associated proteins in a rat chronic mild stress model of depression.', *Neuroscience* **298**, 220–92.

Hanada, T., Lin, L., Tibaldi, E. V., Reinherz, E. L. and Chishti, A. H. (2000), 'GAKIN, a novel kinesin-like protein associates with the human homologue of the Drosophila discs large tumor suppressor in T lymphocytes.', *The Journal of biological chemistry* **275**(37), 28774–84.

Harigaya, Y., Shoji, M., Shirao, T. and Hirai, S. (1996), 'Disappearance of actin-binding protein, drebrin, from hippocampal synapses in Alzheimer's disease.', *Journal of neuroscience research* **43**(1), 87–92.

Harris, K. M., Perry, E., Bourne, J., Feinberg, M., Ostroff, L. and Hurlburt, J. (2006), 'Uniform Serial Sectioning for Transmission Electron Microscopy', *Journal of Neuroscience* **26**(47), 12101–12103.

Harris, K. M. and Weinberg, R. J. (2012), 'Ultrastructure of Synapses in the Mammalian Brain', *Cold Spring Harbor Perspectives in Biology* **4**(5), a005587–a005587.

Harrison, P. J., Heath, P. R., Eastwood, S. L., Burnet, P. W., McDonald, B. and Pearson, R. C. (1995), 'The relative importance of premortem acidosis and postmortem interval for human brain gene expression studies: selective mRNA vulnerability and comparison with their encoded proteins.', *Neuroscience letters* **200**(3), 151–4.

Hassabis, D., Kumaran, D., Vann, S. D. and Maguire, E. A. (2007), 'Patients with hippocampal amnesia cannot imagine new experiences.', *Proceedings of the National Academy of Sciences of the United States of America* **104**(5), 1726–31.

Hawrylycz, M. J., Lein, E. S., Guillozet-Bongaarts, A. L., Shen, E. H., Ng, L., Miller, J. A., van de Lagemaat, L. N., Smith, K. A., Ebbert, A., Riley, Z. L., Abajian, C., Beckmann, C. F., Bernard, A., Bertagnolli, D., Boe, A. F., Cartagena, P. M., Chakravarty, M. M., Chapin, M., Chong, J., Dalley, R. A., Daly, B. D., Dang, C., Datta, S., Dee, N., Dolbeare, T. A., Faber, V., Feng, D., Fowler, D. R., Goldy, J., Gregor, B. W., Haradon, Z., Haynor, D. R., Hohmann, J. G., Horvath, S., Howard, R. E., Jeromin, A., Jochim, J. M., Kinnunen, M., Lau, C., Lazarz, E. T., Lee, C., Lemon, T. A., Li, L., Li, Y., Morris, J. A., Overly, C. C., Parker, P. D., Parry, S. E., Reding, M., Royall, J. J., Schulkin, J., Sequeira, P. A., Slaughterbeck, C. R., Smith, S. C., Sodt, A. J., Sunkin, S. M., Swanson, B. E., Vawter, M. P., Williams, D., Wohnoutka, P., Zielke, H. R., Geschwind, D. H., Hof, P. R., Smith, S. M., Koch, C., Grant, S. G. N. and Jones, A. R. (2012), 'An anatomically comprehensive atlas of the adult human brain transcriptome', *Nature* **489**(7416), 391–399.

Haydon, P. G. (2001), 'GLIA: listening and talking to the synapse.', *Nature reviews. Neuroscience* **2**(3), 185–93.

He, Y., Chen, Z. J. and Evans, A. C. (2007), 'Small-world anatomical networks in the human brain revealed by cortical thickness from MRI.', *Cerebral cortex (New York, N.Y. : 1991)* **17**(10), 2407–19.

Henstridge, C. M., Jackson, R. J., Kim, J. M., Herrmann, A. G., Wright, A. K., Harris, S. E., Bastin, M. E., Starr, J. M., Wardlaw, J., Gillingwater, T. H., Smith, C., McKenzie, C.-A., Cox, S. R., Deary, I. J. and Spires-Jones, T. L. (2015), 'Post-mortem brain analyses of the Lothian Birth Cohort 1936: extending lifetime cognitive and brain phenotyping to the level of the synapse', *Acta Neuropathologica Communications* **3**(1), 53.

Henstridge, C. M., Pickett, E. and Spires-Jones, T. L. (2016), 'Synaptic pathology: A shared mechanism in neurological disease', *Ageing Research Reviews* **28**, 72–84.

Hill, M. D., Martin, R. H., Mikulis, D., Wong, J. H., Silver, F. L., TerBrugge, K. G., Milot, G., Clark, W. M., MacDonald, R. L., Kelly, M. E., Boulton, M., Fleetwood, I., McDougall, C., Gunnarsson, T., Chow, M., Lum, C., Dodd, R., Poublanc, J., Krings, T., Demchuk, A. M., Goyal, M., Anderson, R., Bishop, J., Garman, D. and Tymianski, M. (2012), 'Safety and efficacy of NA-1 in patients with iatrogenic stroke after endovascular aneurysm repair (ENACT): A phase 2, randomised, double-blind, placebo-controlled trial', *The Lancet Neurology* **11**(11), 942–950.

Hill, W. D., Davies, G., van de Lagemaat, L. N., Christoforou, A., Marioni, R. E., Fernandes, C. P. D., Liewald, D. C., Croning, M. D. R., Payton, A., Craig, L. C. A., Whalley, L. J., Horan, M., Ollier, W., Hansell, N. K., Wright, M. J., Martin, N. G., Montgomery, G. W., Steen, V. M., Le Hellard, S., Espeseth, T., Lundervold, A. J., Reinvang, I., Starr, J. M., Pendleton, N., Grant, S. G. N., Bates, T. C. and Deary, I. J. (2014), 'Human cognitive ability is influenced by genetic variation in components of postsynaptic signalling complexes assembled by NMDA receptors and MAGUK proteins.', *Translational psychiatry* **4**(1), e341.

Hillman, D. E. and Chen, S. (1984), 'Reciprocal relationship between size of postsynaptic densities and their number: constancy in contact area.', *Brain research* **295**(2), 325–43.

Hirao, K., Hata, Y., Deguchi, M., Yao, I., Ogura, M., Rokukawa, C., Kawabe, H., Mizoguchi, A. and Takai, Y. (2000), 'Association of synapse-associated protein 90/ postsynaptic density-95-associated protein (SAPAP) with neurofilaments.', *Genes to cells : devoted to molecular & cellular mechanisms* **5**(3), 203–10.

Hoenger, A. (2014), 'High-resolution cryo-electron microscopy on macromolecular complexes and cell organelles', *Protoplasma* **251**(2), 417–427.

Holtzman, D. M., Morris, J. C. and Goate, A. M. (2011), 'Alzheimer's Disease: The Challenge of the Second Century', *Science Translational Medicine* **3**(77), 1–77.

Honer, W. G. (2003), 'Pathology of presynaptic proteins in Alzheimer's disease: more than simple loss of terminals.', *Neurobiology of aging* **24**(8), 1047–62.

Honer, W. G., Dickson, D. W., Gleeson, J. and Davies, P. (1992), 'Regional synaptic pathology in Alzheimer's disease.', *Neurobiology of aging* **13**(3), 375–82.

Honer, W. G., Falkai, P., Chen, C., Arango, V., Mann, J. J. and Dwork, A. J. (1999), 'Synaptic and plasticity-associated proteins in anterior frontal cortex in severe mental illness.', *Neuroscience* **91**(4), 1247–55.

Hoover, B. R., Reed, M. N., Su, J., Penrod, R. D., Kotilinek, L. A., Grant, M. K., Pitstick, R., Carlson, G. A., Lanier, L. M., Yuan, L.-L., Ashe, K. H. and Liao, D. (2010), 'Tau mislocalization to dendritic spines mediates synaptic dysfunction independently of neurodegeneration.', *Neuron* **68**(6), 1067–81.

Huang, Y. Z., Wang, Q., Xiong, W. C. and Mei, L. (2001), 'Erbin is a protein concentrated at postsynaptic membranes that interacts with PSD-95.', *The Journal of biological chemistry* **276**(22), 19318–26.

Hung, A. Y. and Sheng, M. (2002), 'PDZ domains: structural modules for protein complex assembly.', *The Journal of biological chemistry* **277**(8), 5699–702.

Hunt, C. A., Schenker, L. J. and Kennedy, M. B. (1996), 'PSD-95 is associated with the postsynaptic density and not with the presynaptic membrane at forebrain synapses.', *The Journal of neuroscience : the official journal of the Society for Neuroscience* **16**(4), 1380–8.

Husi, H. and Grant, S. G. (2001*a*), 'Proteomics of the nervous system', *Trends in Neurosciences* **24**(5), 259–266.

Husi, H. and Grant, S. G. N. (2001*b*), 'Isolation of 2000-kDa complexes of N-methyl-D-aspartate receptor and postsynaptic density 95 from mouse brain', *Journal of Neurochemistry* **77**(1), 281–291.

Husi, H., Ward, M. a., Choudhary, J. S., Blackstock, W. P. and Grant, S. G. (2000), 'Proteomic analysis of NMDA receptor-adhesion protein signaling complexes.', *Nature neuroscience* **3**(7), 661–669.

Huttenlocher, P. R. and Dabholkar, A. S. (1997), 'Regional differences in synaptogenesis in human cerebral cortex.', *The Journal of comparative neurology* **387**(2), 167–78.

Hyman, B. T., Phelps, C. H., Beach, T. G., Bigio, E. H., Cairns, N. J., Carrillo, M. C., Dickson, D. W., Duyckaerts, C., Frosch, M. P., Masliah, E., Mirra, S. S., Nelson, P. T., Schneider, J. A., Thal, D. R., Thies, B., Trojanowski, J. Q., Vinters, H. V. and Montine, T. J. (2012), 'National Institute on Aging-Alzheimer's Association guidelines for the neuropathologic assessment of Alzheimer's disease.', *Alzheimer's & dementia : the journal of the Alzheimer's Association* **8**(1), 1–13.

Iasevoli, F., Tomasetti, C. and De Bartolomeis, A. (2013), 'Scaffolding proteins of the post-synaptic density contribute to synaptic plasticity by regulating receptor localization and distribution: Relevance for neuropsychiatric diseases'.

Ikonomovic, M. D., Klunk, W. E., Abrahamson, E. E., Mathis, C. A., Price, J. C., Tsopelas, N. D., Lopresti, B. J., Ziolko, S., Bi, W., Paljug, W. R., Debnath, M. L., Hope, C. E., Isanski, B. A., Hamilton, R. L. and DeKosky, S. T. (2008), 'Post-mortem correlates of in vivo PiB-PET amyloid imaging in a typical case of Alzheimer's disease.', *Brain : a journal of neurology* **131**(Pt 6), 1630–45.

Ingelsson, M., Fukumoto, H., Newell, K. L., Growdon, J. H., Hedley-Whyte, E. T., Frosch, M. P., Albert, M. S., Hyman, B. T. and Irizarry, M. C. (2004), 'Early Abeta accumulation and progressive synaptic loss, gliosis, and tangle formation in AD brain.', *Neurology* **62**(6), 925–31.

Ingelsson, M., Shin, Y., Irizarry, M. C., Hyman, B. T., Lilius, L., Forsell, C. and Graff, C. (2003), Genotyping of Apolipoprotein E: Comparative Evaluation of Different Protocols, *in* 'Current Protocols in Human Genetics', Vol. Chapter 9, John Wiley & Sons, Inc., Hoboken, NJ, USA, p. Unit9.14.

Irie, M., Hata, Y., Takeuchi, M., Ichtchenko, K., Toyoda, A., Hirao, K., Takai, Y., Rosahl, T. W. and Südhof, T. C. (1997), 'Binding of neuroligins to PSD-95.', *Science (New York, N.Y.)* **277**(5331), 1511–5.

Isokawa, M., Levesque, M. F., Babb, T. L. and Engel, J. (1993), 'Single mossy fiber axonal systems of human dentate granule cells studied in hippocampal slices from patients with temporal lobe epilepsy.', *The Journal of neuroscience : the official journal of the Society for Neuroscience* **13**(4), 1511–22.

Ito, H., Goto, S., Sakamoto, S. and Hirano, A. (1992), 'Calbindin-D28K in the basal ganglia of patients with parkinsonism', *Annals of Neurology* **32**(4), 543–550.

Ittner, L. M., Ke, Y. D., Delerue, F., Bi, M., Gladbach, A., van Eersel, J., Wölfing, H., Chieng, B. C., Christie, M. J., Napier, I. A., Eckert, A., Staufenbiel, M., Hardeman, E. and Götz, J. (2010), 'Dendritic function of tau mediates amyloid-beta toxicity in Alzheimer's disease mouse models.', *Cell* **142**(3), 387–97.

Jadhav, S., Cubinkova, V., Zimova, I., Brezovakova, V., Madari, A., Cigankova, V. and Zilka, N. (2015), 'Tau-mediated synaptic damage in Alzheimer's disease.', *Translational neuroscience* **6**(1), 214–226.

Jadhav, S., Katina, S., Kovac, A., Kazmerova, Z., Novak, M. and Zilka, N. (2015), 'Truncated tau deregulates synaptic markers in rat model for human tauopathy.', *Frontiers in cellular neuroscience* **9**, 24.

Jiang, Y.-h. and Ehlers, M. D. (2013), 'Modeling Autism by SHANK Gene Mutations in Mice', *Neuron* **78**(1), 8–27.

Johnson, J. W. and Ascher, P. (1987), 'Glycine potentiates the NMDA response in cultured mouse brain neurons', *Nature* **325**(6104), 529–531.

Jones, R. A., Harrison, C., Eaton, S. L., Llavero Hurtado, M., Graham, L. C., Alkhammash, L., Oladiran, O. A., Gale, A., Lamont, D. J., Simpson, H., Simmen, M. W., Soeller, C., Wishart, T. M. and Gillingwater, T. H. (2017), 'Cellular and Molecular Anatomy of the Human Neuromuscular Junction.', *Cell reports* **21**(9), 2348–2356.

Jourdren, L., Delaveau, T., Marquenet, E., Jacq, C. and Garcia, M. (2010), 'CORSEN, a new software dedicated to microscope-based 3D distance measurements: mRNA-mitochondria distance, from single-cell to population analyses.', *RNA (New York, N.Y.)* **16**(7), 1301–7.

Kallai, J., Csathó, A., Kövér, F., Makány, T., Nemes, J., Horváth, K., Kovács, N., Manning, J. T., Nadel, L. and Nagy, F. (2005), 'MRI-assessed volume of left and right hippocampi in females correlates with the relative length of the second and fourth fingers (the 2D:4D ratio).', *Psychiatry research* **140**(2), 199–210.

Kantarci, K., Yang, C., Schneider, J. A., Senjem, M. L., Reyes, D. A., Lowe, V. J., Barnes, L. L., Aggarwal, N. T., Bennett, D. A., Smith, G. E., Petersen, R. C., Jack, C. R. and Boeve, B. F. (2012), 'Antemortem amyloid imaging and $\beta$-amyloid pathology in a case with dementia with Lewy bodies.', *Neurobiology of aging* **33**(5), 878–85.

Karlebach, G. and Francks, C. (2015), 'Lateralization of gene expression in human language cortex.', *Cortex; a journal devoted to the study of the nervous system and behavior* **67**, 30–6.

Karson, C. N., Mrak, R. E., Schluterman, K. O., Sturner, W. Q., Sheng, J. G. and Griffin, W. S. (1999), 'Alterations in synaptic proteins and their encoding mRNAs in prefrontal cortex in schizophrenia: a possible neurochemical basis for 'hypofrontality'.', *Molecular psychiatry* **4**(1), 39–45.

Kay, K. R., Smith, C., Wright, A. K., Serrano-Pozo, A., Pooler, A. M., Koffie, R., Bastin, M. E., Bak, T. H., Abrahams, S., Kopeikina, K. J., McGuone, D., Frosch, M. P., Gillingwater, T. H., Hyman, B. T. and Spires-Jones, T. L. (2013), 'Studying synapses in human brain with array tomography and electron microscopy', *Nature Protocols* **8**(7), 1366–1380.

Kennedy, M. B. (1993), 'The postsynaptic density', *Curr Opin Neurobiol* **3**(5), 732–7.

Kennedy, M. B. (2000), 'Signal-Processing Machines at the Postsynaptic Density', *Science* **290**(5492), 750–754.

Key, M. (2012), 'A tutorial in displaying mass spectrometry-based proteomic data using heat maps', *BMC Bioinformatics* **13**(Suppl 16), S10.

Kim, E., Cho, K. O., Rothschild, A. and Sheng, M. (1996), 'Heteromultimerization and NMDA receptor-clustering activity of Chapsyn-110, a member of the PSD-95 family of proteins.', *Neuron* **17**(1), 103–13.

Kim, E., Naisbitt, S., Hsueh, Y.-P., Rao, A., Rothschild, A., Craig, A. M. and Sheng, M. (1997), 'GKAP, a Novel Synaptic Protein That Interacts with the Guanylate Kinase-like Domain of the PSD-95/SAP90 Family of Channel Clustering Molecules', *The Journal of Cell Biology* **136**(3), 669–678.

Kim, E., Niethammer, M., Rothschild, A., Jan, Y. N. and Sheng, M. (1995), 'Clustering of Shaker-type K+ channels by interaction with a family of membrane-associated guanylate kinases.', *Nature* **378**(6552), 85–8.

Kim, J., Basak, J. M. and Holtzman, D. M. (2009), 'The role of apolipoprotein E in Alzheimer's disease.', *Neuron* **63**(3), 287–303.

Kim, J. H., Liao, D., Lau, L.-F. and Huganir, R. L. (1998), 'SynGAP: a Synaptic RasGAP that Associates with the PSD-95/SAP90 Protein Family', *Neuron* **20**(4), 683–691.

Kim, Y., Ha, C. M. and Chang, S. (2013), 'SNX26, a GTPase-activating protein for Cdc42, interacts with PSD-95 protein and is involved in activity-dependent dendritic spine formation in mature neurons.', *The Journal of biological chemistry* **288**(41), 29453–66.

King, A., Maekawa, S., Bodi, I., Troakes, C., Curran, O., Ashkan, K. and Al-Sarraj, S. (2013), 'Simulated surgical-type cerebral biopsies from post-mortem brains allows accurate neuropathological diagnoses in the majority of neurodegenerative disease groups.', *Acta neuropathologica communications* **1**(1), 53.

Kistner, U., Wenzel, B. M., Veh, R. W., Cases-Langhoff, C., Garner, A. M., Appeltauer, U., Voss, B., Gundelfinger, E. D. and Garner, C. C. (1993), 'SAP90, a rat presynaptic protein related to the product of the Drosophila tumor suppressor gene dlg-A.', *The Journal of biological chemistry* **268**(7), 4580–3.

Klemann, C. J. H. M. and Roubos, E. W. (2011), 'The gray area between synapse structure and function-Gray's synapse types I and II revisited', *Synapse* **65**(11), 1222–1230.

Knott, G., Marchman, H., Wall, D. and Lich, B. (2008), 'Serial Section Scanning Electron Microscopy of Adult Brain Tissue Using Focused Ion Beam Milling', *Journal of Neuroscience* **28**(12), 2959–2964.

Knowlton, B. J., Mangels, J. A. and Squire, L. R. (1996), 'A Neostriatal Habit Learning System in Humans', *Science* **273**(5280), 1399–1402.

Ko, J., Kim, S., Chung, H. S., Kim, K., Han, K., Kim, H., Jun, H., Kaang, B.-K. and Kim, E. (2006), 'SALM synaptic cell adhesion-like molecules regulate the differentiation of excitatory synapses.', *Neuron* **50**(2), 233–45.

Koffie, R. M., Hashimoto, T., Tai, H.-C., Kay, K. R., Serrano-Pozo, A., Joyner, D., Hou, S., Kopeikina, K. J., Frosch, M. P., Lee, V. M., Holtzman, D. M., Hyman, B. T. and Spires-Jones, T. L. (2012), 'Apolipoprotein E4 effects in Alzheimer's disease are mediated by synaptotoxic oligomeric amyloid-$\beta$.', *Brain : a journal of neurology* **135**(Pt 7), 2155–68.

Koffie, R. M., Meyer-Luehmann, M., Hashimoto, T., Adams, K. W., Mielke, M. L., Garcia-Alloza, M., Micheva, K. D., Smith, S. J., Kim, M. L., Lee, V. M., Hyman, B. T. and Spires-Jones, T. L. (2009), 'Oligomeric amyloid beta associates with postsynaptic densities and correlates with excitatory synapse loss near senile plaques.', *Proceedings of the National Academy of Sciences of the United States of America* **106**(10), 4012–7.

Komiyama, N. H., Watabe, A. M., Carlisle, H. J., Porter, K., Charlesworth, P., Monti, J., Strathdee, D. J. C., O'Carroll, C. M., Martin, S. J., Morris, R. G. M., O'Dell, T. J. and Grant, S. G. N. (2002), 'SynGAP regulates ERK/MAPK signaling, synaptic plasticity, and learning in the complex with postsynaptic density 95 and NMDA receptor.', *The Journal of neuroscience : the official journal of the Society for Neuroscience* **22**(22), 9721–9732.

Kornau, H. C., Schenker, L. T., Kennedy, M. B. and Seeburg, P. H. (1995), 'Domain interaction between NMDA receptor subunits and the postsynaptic density protein PSD-95.', *Science (New York, N.Y.)* **269**(5231), 1737–40.

Krishnan, M. L., Van Steenwinckel, J., Schang, A.-L., Yan, J., Arnadottir, J., Le Charpentier, T., Csaba, Z., Dournaud, P., Cipriani, S., Auvynet, C., Titomanlio, L., Pansiot, J., Ball, G., Boardman, J. P., Walley, A. J., Saxena, A., Mirza, G., Fleiss, B., Edwards, A. D., Petretto, E. and Gressens, P. (2017), 'Integrative genomics of microglia implicates DLG4 (PSD95) in the white matter development of preterm infants.', *Nature communications* **8**(1), 428.

Kühlbrandt, W. (2014), 'The Resolution Revolution', *Science* **343**(March), 1443–1444.

Landsend, A. S., Amiry-Moghaddam, M., Matsubara, A., Bergersen, L., Usami, S., Wenthold, R. J. and Ottersen, O. P. (1997), 'Differential localization of delta glutamate receptors in the rat cerebellum: coexpression with AMPA receptors in parallel fiber-spine synapses and absence from climbing fiber-spine synapses.', *The Journal of neuroscience : the official journal of the Society for Neuroscience* **17**(2), 834–42.

Lau, C. G. and Zukin, R. S. (2007), 'NMDA receptor trafficking in synaptic plasticity and neuropsychiatric disorders.', *Nature reviews. Neuroscience* **8**(6), 413–26.

Laube, G., Röper, J., Pitt, J. C., Sewing, S., Kistner, U., Garner, C. C., Pongs, O. and Veh, R. W. (1996), 'Ultrastructural localization of Shaker-related potassium channel subunits and synapse-associated protein 90 to septate-like junctions in rat cerebellar Pinceaux.', *Brain research. Molecular brain research* **42**(1), 51–61.

Lee, H., Oh, W. C., Seong, J. and Kim, J. (2016), 'Advanced Fluorescence Protein-Based Synapse-Detectors', *Frontiers in Synaptic Neuroscience* **8**(JUN), 16.

Lee, H. W., Choi, J., Shin, H., Kim, K., Yang, J., Na, M., Choi, S. Y., Kang, G. B., Eom, S. H., Kim, H. and Kim, E. (2008), 'Preso, a novel PSD-95-interacting FERM and PDZ domain protein that regulates dendritic spine morphogenesis.', *The Journal of neuroscience : the official journal of the Society for Neuroscience* **28**(53), 14546–56.

Lein, E. S., Hawrylycz, M. J., Ao, N., Ayres, M., Bensinger, A., Bernard, A., Boe, A. F., Boguski, M. S., Brockway, K. S., Byrnes, E. J., Chen, L., Chen, L., Chen, T.-M., Chi Chin, M., Chong, J., Crook, B. E., Czaplinska, A., Dang, C. N., Datta, S., Dee, N. R., Desaki, A. L., Desta, T., Diep, E., Dolbeare, T. A., Donelan, M. J., Dong, H.-W., Dougherty, J. G., Duncan, B. J., Ebbert, A. J., Eichele, G., Estin, L. K., Faber, C., Facer, B. A., Fields, R., Fischer, S. R., Fliss, T. P., Frensley, C., Gates, S. N., Glattfelder, K. J., Halverson, K. R., Hart, M. R., Hohmann, J. G., Howell, M. P., Jeung, D. P., Johnson, R. A., Karr, P. T., Kawal, R., Kidney, J. M., Knapik, R. H., Kuan, C. L., Lake, J. H., Laramee, A. R., Larsen, K. D., Lau, C., Lemon, T. A., Liang, A. J., Liu, Y., Luong, L. T., Michaels, J., Morgan, J. J., Morgan, R. J., Mortrud, M. T., Mosqueda, N. F., Ng, L. L., Ng, R., Orta, G. J., Overly, C. C., Pak, T. H., Parry, S. E., Pathak, S. D., Pearson, O. C., Puchalski, R. B., Riley, Z. L., Rockett, H. R., Rowland, S. A., Royall, J. J., Ruiz, M. J., Sarno, N. R., Schaffnit, K., Shapovalova, N. V., Sivisay, T., Slaughterbeck, C. R., Smith, S. C., Smith, K. A., Smith, B. I., Sodt, A. J., Stewart, N. N., Stumpf, K.-R., Sunkin, S. M., Sutram, M., Tam, A., Teemer, C. D., Thaller, C., Thompson, C. L., Varnam, L. R., Visel, A., Whitlock, R. M., Wohnoutka, P. E., Wolkey, C. K., Wong, V. Y., Wood, M., Yaylaoglu, M. B., Young, R. C., Youngstrom, B. L., Feng Yuan, X., Zhang, B., Zwingman, T. A. and Jones, A. R. (2007), 'Genome-wide atlas of gene expression in the adult mouse brain', *Nature* **445**(7124), 168–176.

Lepeta, K., Lourenco, M. V., Schweitzer, B. C., Martino Adami, P. V., Banerjee, P., Catuara-Solarz, S., de La Fuente Revenga, M., Guillem, A. M., Haidar, M., Ijomone, O. M., Nadorp, B., Qi, L., Perera, N. D., Refsgaard, L. K., Reid, K. M., Sabbar, M., Sahoo, A., Schafer, N., Sheean, R. K., Suska, A., Verma, R., Vicidomini, C., Wright, D., Zhang, X.-D. and Seidenbecher, C. (2016), 'Synaptopathies: synaptic dysfunction in neurological disorders.', *Journal of neurochemistry* pp. 785–805.

Leuba, G., Savioz, A., Vernay, A., Carnal, B., Kraftsik, R., Tardif, E., Riederer, I. and Riederer, B. M. (2008), 'Differential changes in synaptic proteins in the Alzheimer frontal cortex with marked increase in PSD-95 postsynaptic protein.', *Journal of Alzheimer's disease : JAD* **15**(1), 139–51.

Leuba, G., Walzer, C., Vernay, A., Carnal, B., Kraftsik, R., Piotton, F., Marin, P., Bouras, C. and Savioz, A. (2008), 'Postsynaptic density protein PSD-95 expression in Alzheimer's disease and okadaic acid induced neuritic retraction', *Neurobiology of Disease* **30**(3), 408–419.

Lewis, D. A., Glantz, L. A., Pierri, J. N. and Sweet, R. A. (2003), 'Altered cortical glutamate neurotransmission in schizophrenia: evidence from morphological studies of pyramidal neurons.', *Annals of the New York Academy of Sciences* **1003**(1), 102–12.

Lewis, D. A. and Lieberman, J. A. (2000), 'Catching up on schizophrenia: natural history and neurobiology.', *Neuron* **28**(2), 325–34.

Li, D. (2010), 'Advancements on the zebrafish glioma model', *Chinese Journal of Cancer* **29**(6).

Li, X., Kumar, Y., Zempel, H., Mandelkow, E.-M., Biernat, J. and Mandelkow, E. (2011), 'Novel diffusion barrier for axonal retention of Tau in neurons and its failure in neurodegeneration.', *The EMBO journal* **30**(23), 4825–37.

Lim, C., Mufson, E. J., Kordower, J. H., Blume, H. W., Madsen, J. R. and Saper, C. B. (1997), 'Connections of the hippocampal formation in humans: II. The endfolial fiber pathway.', *The Journal of comparative neurology* **385**(3), 352–71.

Lipton, S. A. (2006), 'Paradigm shift in neuroprotection by NMDA receptor blockade: Memantine and beyond', *Nature Reviews Drug Discovery* **5**(2), 160–170.

Liu, X.-B., Murray, K. D. and Jones, E. G. (2004), 'Switching of NMDA receptor 2A and 2B subunits at thalamic and cortical synapses during early postnatal development.', *The Journal of neuroscience : the official journal of the Society for Neuroscience* **24**(40), 8885–95.

Lord, C. and Bishop, S. L. (2015), 'Recent Advances in Autism Research as Reflected in DSM-5 Criteria for Autism Spectrum Disorder', *Annual Review of Clinical Psychology* **11**(1), 53–70.

Love, S., Chalmers, K., Ince, P., Esiri, M., Attems, J., Jellinger, K., Yamada, M., McCarron, M., Minett, T., Matthews, F., Greenberg, S., Mann, D. and Kehoe, P. G. (2014), 'Development, appraisal, validation and implementation of a consensus protocol for the assessment of cerebral amyloid angiopathy in post-mortem brain tissue.', *American journal of neurodegenerative disease* **3**(1), 19–32.

Love, S., Siew, L. K., Dawbarn, D., Wilcock, G. K., Ben-Shlomo, Y. and Allen, S. J. (2006), 'Premorbid effects of APOE on synaptic proteins in human temporal neocortex.', *Neurobiology of aging* **27**(6), 797–803.

Lovero, K. L., Fukata, Y., Granger, A. J., Fukata, M. and Nicoll, R. A. (2015), 'The LGI1-ADAM22 protein complex directs synapse maturation through regulation of PSD-95 function.', *Proceedings of the National Academy of Sciences of the United States of America* **112**(30), 4129–37.

Lu, D., He, L., Xiang, W., Ai, W.-M., Cao, Y., Wang, X.-S., Pan, A., Luo, X.-G., Li, Z. and Yan, X.-X. (2013), 'Somal and dendritic development of human CA3 pyramidal neurons from midgestation to middle childhood: a quantitative Golgi study.', *Anatomical record (Hoboken, N.J. : 2007)* **296**(1), 123–32.

Luine, V. and Frankfurt, M. (2013), 'Interactions between estradiol, BDNF and dendritic spines in promoting memory.', *Neuroscience* **239**, 34–45.

Lynch, J. J., Rahwan, R. G., Witiak, D. T. and Cazer, F. D. (1983), 'Intracellular localization of the calcium antagonist propyl-methylenedioxyindene in cardiac tissue', *General Pharmacology* **14**(6), 571–578.

MacGillavry, H. D., Song, Y., Raghavachari, S. and Blanpied, T. A. (2013), 'Nanoscale scaffolding domains within the postsynaptic density concentrate synaptic AMPA receptors.', *Neuron* **78**(4), 615–22.

Mai, J. K. and Paxinos, G. (1997), *Atlas of the Human Brain*, 3rd edn, Elsevier, Amsterdam.

Makino, K., Kuwahara, H., Masuko, N., Nishiyama, Y., Morisaki, T., Sasaki, J., Nakao, M., Kuwano, a., Nakata, M., Ushio, Y. and Saya, H. (1997), 'Cloning and characterization of NE-dlg: a novel human homolog of the Drosophila discs large (dlg) tumor suppressor protein interacts with the APC protein.', *Oncogene* **14**(20), 2425–2433.

Makris, N., Preti, M. G., Asami, T., Pelavin, P., Campbell, B., Papadimitriou, G. M., Kaiser, J., Baselli, G., Westin, C. F., Shenton, M. E. and Kubicki, M. (2013), 'Human middle longitudinal fascicle: variations in patterns of anatomical connections', *Brain Structure and Function* **218**(4), 951–968.

Malenka, R. C., Kauer, J. A., Zucker, R. S. and Nicoll, R. A. (1988), 'Postsynaptic calcium is sufficient for potentiation of hippocampal synaptic transmission.', *Science (New York, N.Y.)* **242**(4875), 81–4.

Manning, C. F., Bundros, A. M. and Trimmer, J. S. (2012), 'Benefits and pitfalls of secondary antibodies: why choosing the right secondary is of primary importance.', *PloS one* **7**(6), e38313.

Masliah, E., Hansen, L., Albright, T., Mallory, M. and Terry, R. D. (1991), 'Immunoelectron microscopic study of synaptic pathology in Alzheimer's disease.', *Acta neuropathologica* **81**(4), 428–33.

Masliah, E., Mallory, M., Hansen, L., DeTeresa, R. and Terry, R. D. (1993), 'Quantitative synaptic alterations in the human neocortex during normal aging.', *Neurology* **43**(1), 192–7.

Masliah, E., Terry, R. D., Alford, M. and DeTeresa, R. (1990), 'Quantitative immunohistochemistry of synaptophysin in human neocortex: an alternative method to estimate density of presynaptic terminals in paraffin sections.', *The journal of histochemistry and cytochemistry : official journal of the Histochemistry Society* **38**(6), 837–44.

Masuko, N., Makino, K., Kuwahara, H., Fukunaga, K., Sudo, T., Araki, N., Yamamoto, H., Yamada, Y., Miyamoto, E. and Saya, H. (1999), 'Interaction of NE-dlg/SAP102, a neuronal and endocrine tissue-specific membrane-associated guanylate kinase protein, with calmodulin and PSD-95/SAP90. A possible regulatory role in molecular clustering at synaptic sites.', *The Journal of biological chemistry* **274**(9), 5782–90.

Matsuno, H., Ohi, K., Hashimoto, R., Yamamori, H., Yasuda, Y., Fujimoto, M., Yano-Umeda, S., Saneyoshi, T., Takeda, M. and Hayashi, Y. (2015), 'A naturally occurring null variant of the NMDA type glutamate receptor NR3B subunit is a risk factor of schizophrenia', *PLoS ONE* **10**(3), e0116319.

McGee, A. W., Dakoji, S. R., Olsen, O., Bredt, D. S., Lim, W. A. and Prehoda, K. E. (2001), 'Structure of the SH3-guanylate kinase module from PSD-95 suggests a mechanism for regulated assembly of MAGUK scaffolding proteins.', *Molecular cell* **8**(6), 1291–301.

McKhann, G. M., Knopman, D. S., Chertkow, H., Hyman, B. T., Jack, C. R., Kawas, C. H., Klunk, W. E., Koroshetz, W. J., Manly, J. J., Mayeux, R., Mohs, R. C., Morris, J. C., Rossor, M. N., Scheltens, P., Carrillo, M. C., Thies, B., Weintraub, S. and Phelps, C. H. (2011), 'The diagnosis of dementia due to Alzheimer's disease: Recommendations from the National Institute on Aging-Alzheimer's Association workgroups on diagnostic guidelines for Alzheimer's disease', *Alzheimer's & Dementia* **7**(3), 263–269.

Merchán-Pérez, A., Rodriguez, J.-R., Alonso-Nanclares, L., Schertel, A. and Defelipe, J. (2009), 'Counting Synapses Using FIB/SEM Microscopy: A True Revolution for Ultrastructural Volume Reconstruction.', *Frontiers in neuroanatomy* **3**, 18.

Meyer, D., Bonhoeffer, T. and Scheuss, V. (2014), 'Balance and Stability of Synaptic Structures during Synaptic Plasticity', *Neuron* **82**(2), 430–443.

Micheva, K. D., Busse, B., Weiler, N. C., O'Rourke, N. and Smith, S. J. (2010), 'Single-synapse analysis of a diverse synapse population: Proteomic imaging methods and markers', *Neuron* **68**(4), 639–653.

Micheva, K. D. and Smith, S. J. (2007), 'Array tomography: A new tool for imaging the molecular architecture and ultrastructure of neural circuits', **55**(1), 25–36.

Migaud, M., Charlesworth, P., Dempster, M., Webster, L. C., Watabe, A. M., Makhinson, M., He, Y., Ramsay, M. F., Morris, R. G., Morrison, J. H., O'Dell, T. J. and Grant, S. G. (1998), 'Enhanced long-term potentiation and impaired learning in mice with mutant postsynaptic density-95 protein.', *Nature* **396**(6710), 433–9.

Millar, T., Walker, R., Arango, J.-C., Ironside, J. W., Harrison, D. J., MacIntyre, D. J., Blackwood, D., Smith, C. and Bell, J. E. (2007), 'Tissue and organ donation for research in forensic pathology: the MRC Sudden Death Brain and Tissue Bank.', *The Journal of pathology* **213**(4), 369–75.

Miller, J. A., Ding, S.-L., Sunkin, S. M., Smith, K. A., Ng, L., Szafer, A., Ebbert, A., Riley, Z. L., Royall, J. J., Aiona, K., Arnold, J. M., Bennet, C., Bertagnolli, D., Brouner, K., Butler, S., Caldejon, S., Carey, A., Cuhaciyan, C., Dalley, R. A., Dee, N., Dolbeare, T. A., Facer, B. A. C., Feng, D., Fliss, T. P., Gee, G., Goldy, J., Gourley, L., Gregor, B. W., Gu, G., Howard, R. E., Jochim, J. M., Kuan, C. L., Lau, C., Lee, C.-K., Lee, F., Lemon, T. A., Lesnar, P., McMurray, B., Mastan, N., Mosqueda, N., Naluai-Cecchini, T., Ngo, N.-K., Nyhus, J., Oldre, A., Olson, E., Parente, J., Parker, P. D., Parry, S. E., Stevens, A., Pletikos, M., Reding, M., Roll, K., Sandman, D., Sarreal, M., Shapouri, S., Shapovalova, N. V., Shen, E. H., Sjoquist, N., Slaughterbeck, C. R., Smith, M., Sodt, A. J., Williams, D., Zöllei, L., Fischl, B., Gerstein, M. B., Geschwind, D. H., Glass, I. A., Hawrylycz, M. J., Hevner, R. F., Huang, H., Jones, A. R., Knowles, J. A., Levitt, P., Phillips, J. W., Šestan, N., Wohnoutka, P., Dang, C., Bernard, A., Hohmann, J. G. and Lein, E. S. (2014), 'Transcriptional landscape of the prenatal human brain', *Nature* **508**(7495), 199–206.

Mirra, S. S., Heyman, A., McKeel, D., Sumi, S. M., Crain, B. J., Brownlee, L. M., Vogel, F. S., Hughes, J. P., van Belle, G. and Berg, L. (1991), 'The Consortium to Establish a Registry for Alzheimer's Disease (CERAD). Part II. Standardization of the neuropathologic assessment of Alzheimer's disease.', *Neurology* **41**(4), 479–86.

Möller, C., Hafkemeijer, A., Pijnenburg, Y. A. L., Rombouts, S. A. R. B., van der Grond, J., Dopper, E., van Swieten, J., Versteeg, A., Steenwijk, M. D., Barkhof, F., Scheltens, P., Vrenken, H. and van der Flier, W. M. (2016), 'Different patterns of cortical gray matter loss over time in behavioral variant frontotemporal dementia and Alzheimer's disease.', *Neurobiology of aging* **38**, 21–31.

Mondragón-Rodríguez, S., Trillaud-Doppia, E., Dudilot, A., Bourgeois, C., Lauzon, M., Leclerc, N. and Boehm, J. (2012), 'Interaction of endogenous tau protein with synaptic proteins is regulated by N-methyl-D-aspartate receptor-dependent tau phosphorylation.', *The Journal of biological chemistry* **287**(38), 32040–53.

Monoranu, C. M., Apfelbacher, M., Grünblatt, E., Puppe, B., Alafuzoff, I., Ferrer, I., Al-Saraj, S., Keyvani, K., Schmitt, A., Falkai, P., Schittenhelm, J., Halliday, G., Kril, J., Harper, C., McLean, C., Riederer, P. and Roggendorf, W. (2009), 'pH measurement as quality control on human post mortem brain tissue: a study of the BrainNet Europe consortium.', *Neuropathology and applied neurobiology* **35**(3), 329–337.

Morigaki, R. and Goto, S. (2015), 'Postsynaptic Density Protein 95 in the Striosome and Matrix Compartments of the Human Neostriatum.', *Frontiers in neuroanatomy* **9**(November), 154.

Moriyoshi, K., Masu, M., Ishii, T., Shigemoto, R., Mizuno, N. and Nakanishi, S. (1991), 'Molecular cloning and characterization of the rat NMDA receptor.', *Nature* **354**(6348), 31–37.

Morrison, J. H. and Baxter, M. G. (2012), 'The ageing cortical synapse: hallmarks and implications for cognitive decline', *Nature Reviews Neuroscience* **13**(4), 240–250.

Morrison, P. D. and Pilowsky, L. S. (2007), 'Schizophrenia: more evidence for less glutamate.', *Expert review of neurotherapeutics* **7**(1), 29–31.

Mota, S. I., Ferreira, I. L. and Rego, A. C. (2014), 'Dysfunctional synapse in Alzheimer's disease – A focus on NMDA receptors', *Neuropharmacology* **76**(PART A), 16–26.

Mouritzen Dam, A. (1979), 'The density of neurons in the human hippocampus.', *Neuropathology and applied neurobiology* **5**(4), 249–64.

Mufson, E. J., Ikonomovic, M. D., Counts, S. E., Perez, S. E., Malek-Ahmadi, M., Scheff, S. W. and Ginsberg, S. D. (2016), 'Molecular and cellular pathophysiology of preclinical Alzheimer's disease.', *Behavioural brain research* **311**, 54–69.

Müller, B., Kistner, U., Veh, R., Cases-Langhoff, C., Becker, B., Gundelfinger, E. and Garner, C. (1995), 'Molecular characterization and spatial distribution of SAP97, a novel presynaptic protein homologous', *The Journal of neuroscience : the official journal of the Society for Neuroscience* **15**(3 pt. 2), 2354–2366.

Müller, B. M., Kistner, U., Kindler, S., Chung, W. J., Kuhlendahl, S., Fenster, S. D., Lau, L. F., Veh, R. W., Huganir, R. L., Gundelfinger, E. D. and Garner, C. C. (1996), 'SAP102, a novel postsynaptic protein that interacts with NMDA receptor complexes in vivo', *Neuron* **17**(2), 255–265.

Musiek, E. S. and Holtzman, D. M. (2015), 'Three dimensions of the amyloid hypothesis: time, space and 'wingmen'.', *Nature neuroscience* **18**(6), 800–6.

Nair, D., Hosy, E., Petersen, J. D., Constals, A., Giannone, G., Choquet, D. and Sibarita, J.-B. (2013), 'Super-resolution imaging reveals that AMPA receptors inside synapses are dynamically organized in nanodomains regulated by PSD95.', *The Journal of neuroscience : the official journal of the Society for Neuroscience* **33**(32), 13204–24.

Naisbitt, S., Valtschanoff, J., Allison, D. W., Sala, C., Kim, E., Craig, A. M., Weinberg, R. J. and Sheng, M. (2000), 'Interaction of the postsynaptic density-95/guanylate kinase domain-associated protein complex with a light chain of myosin-V and dynein.',

*The Journal of neuroscience : the official journal of the Society for Neuroscience* **20**(12), 4524–34.

Nelson, C. D., Kim, M. J., Hsin, H., Chen, Y. and Sheng, M. (2013), 'Phosphorylation of threonine-19 of PSD-95 by GSK-3beta is required for PSD-95 mobilization and long-term depression', *J Neurosci* **33**(29), 12122–12135.

Niethammer, M., Kim, E. and Sheng, M. (1996), 'Interaction between the C terminus of NMDA receptor subunits and multiple members of the PSD-95 family of membrane-associated guanylate kinases.', *The Journal of neuroscience : the official journal of the Society for Neuroscience* **16**(7), 2157–63.

Niethammer, M., Valtschanoff, J. G., Kapoor, T. M., Allison, D. W., Weinberg, R. J., Craig, A. M. and Sheng, M. (1998), 'CRIPT, a novel postsynaptic protein that binds to the third PDZ domain of PSD-95/SAP90.', *Neuron* **20**(4), 693–707.

Nithianantharajah, J., Komiyama, N. H., McKechanie, A., Johnstone, M., Blackwood, D. H., St Clair, D., Emes, R. D., van de Lagemaat, L. N., Saksida, L. M., Bussey, T. J. and Grant, S. G. N. (2013), 'Synaptic scaffold evolution generated components of vertebrate cognitive complexity.', *Nature neuroscience* **16**(1), 16–24.

Nourry, C., Grant, S. G. N. and Borg, J.-p. (2003), 'PDZ domain proteins: plug and play!', *Science's STKE : signal transduction knowledge environment* **2003**(179), RE7.

Nowak, L., Bregestovski, P., Ascher, P., Herbet, A. and Prochiantz, A. (1984), 'Magnesium gates glutamate-activated channels in mouse central neurones', *Nature* **307**(Feburary), 462–465.

Oh, S. W., Harris, J. A., Ng, L., Winslow, B., Cain, N., Mihalas, S., Wang, Q., Lau, C., Kuan, L., Henry, A. M., Mortrud, M. T., Ouellette, B., Nguyen, T. N., Sorensen, S. A., Slaughterbeck, C. R., Wakeman, W., Li, Y., Feng, D., Ho, A., Nicholas, E., Hirokawa, K. E., Bohn, P., Joines, K. M., Peng, H., Hawrylycz, M. J., Phillips, J. W., Hohmann, J. G., Wohnoutka, P., Gerfen, C. R., Koch, C., Bernard, A., Dang, C., Jones, A. R. and Zeng, H. (2014), 'A mesoscale connectome of the mouse brain', *Nature* **508**(7495), 207–214.

Ohnuma, T., Kato, H., Arai, H., Faull, R. L., McKenna, P. J. and Emson, P. C. (2000), 'Gene expression of PSD95 in prefrontal cortex and hippocampus in schizophrenia.', *Neuroreport* **11**(14), 3133–3137.

Ohtakara, K., Nishizawa, M., Izawa, I., Hata, Y., Matsushima, S., Taki, W., Inada, H., Takai, Y. and Inagaki, M. (2002), 'Densin-180, a synaptic protein, links to PSD-95 through its direct interaction with MAGUIN-1.', *Genes to cells : devoted to molecular & cellular mechanisms* **7**(11), 1149–60.

Okada, N., Fukunaga, M., Yamashita, F., Koshiyama, D., Yamamori, H., Ohi, K., Yasuda, Y., Fujimoto, M., Watanabe, Y., Yahata, N., Nemoto, K., Hibar, D. P., van Erp, T. G. M., Fujino, H., Isobe, M., Isomura, S., Natsubori, T., Narita, H., Hashimoto, N., Miyata, J., Koike, S., Takahashi, T., Yamasue, H., Matsuo, K., Onitsuka, T., Iidaka, T., Kawasaki, Y., Yoshimura, R., Watanabe, Y., Suzuki, M., Turner, J. A., Takeda, M., Thompson, P. M., Ozaki, N., Kasai, K. and Hashimoto, R. (2016), 'Abnormal asymmetries in subcortical brain volume in schizophrenia.', *Molecular psychiatry* **21**(10), 1460–6.

O'Kusky, J. and Colonnier, M. (1982), 'A laminar analysis of the number of neurons, glia, and synapses in the adult cortex (area 17) of adult macaque monkeys.', *The Journal of comparative neurology* **210**(3), 278–90.

Olichney, J. M., Hansen, L. A., Galasko, D., Saitoh, T., Hofstetter, C. R., Katzman, R. and Thal, L. J. (1996), 'The apolipoprotein E epsilon 4 allele is associated with increased neuritic plaques and cerebral amyloid angiopathy in Alzheimer's disease and Lewy body variant.', *Neurology* **47**(1), 190–6.

Olichney, J. M., Hansen, L. A., Hofstetter, C. R., Grundman, M., Katzman, R. and Thal, L. J. (1995), 'Cerebral Infarction in Alzheimer's Disease Is Associated With Severe Amyloid Angiopathy and Hypertension', *Archives of Neurology* **52**(7), 702–708.

Olichney, J. M., Hansen, L. A., Hofstetter, C. R., Lee, J. H., Katzman, R. and Thal, L. J. (2000), 'Association between severe cerebral amyloid angiopathy and cerebrovascular lesions in Alzheimer disease is not a spurious one attributable to apolipoprotein E4.', *Archives of neurology* **57**(6), 869–74.

Oliva, C., Escobedo, P., Astorga, C., Molina, C. and Sierralta, J. (2012), 'Role of the maguk protein family in synapse formation and function', *Developmental Neurobiology* **72**(1), 57–72.

O'Rourke, N. A., Weiler, N. C., Micheva, K. D. and Smith, S. J. (2012), 'Deep molecular diversity of mammalian synapses: why it matters and how to measure it.', *Nature reviews. Neuroscience* **13**(6), 365–79.

Ouimet, C. C., Langley-Gullion, K. C. and Greengard, P. (1998), 'Quantitative immunocytochemistry of DARPP-32-expressing neurons in the rat caudatoputamen', *Brain Research* **808**(1), 8–12.

Padurariu, M., Ciobica, A., Mavroudis, I., Fotiou, D. and Baloyannis, S. (2012), 'Hippocampal neuronal loss in the CA1 and CA3 areas of Alzheimer's disease patients.', *Psychiatria Danubina* **24**(2), 152–8.

Pak, D. T., Yang, S., Rudolph-Correia, S., Kim, E. and Sheng, M. (2001), 'Regulation of dendritic spine morphology by SPAR, a PSD-95-associated RapGAP.', *Neuron* **31**(2), 289–303.

Pascual, B., Masdeu, J. C., Hollenbeck, M., Makris, N., Insausti, R., Ding, S.-L. and Dickerson, B. C. (2015), 'Large-scale brain networks of the human left temporal pole: a functional connectivity MRI study.', *Cerebral cortex (New York, N.Y. : 1991)* **25**(3), 680–702.

Pedraza, O., Bowers, D. and Gilmore, R. (2004), 'Asymmetry of the hippocampus and amygdala in MRI volumetric measurements of normal adults.', *Journal of the International Neuropsychological Society : JINS* **10**(5), 664–78.

Peng, J., Kim, M. J., Cheng, D., Duong, D. M., Gygi, S. P. and Sheng, M. (2004), 'Semiquantitative proteomic analysis of rat forebrain postsynaptic density fractions by mass spectrometry.', *The Journal of biological chemistry* **279**(20), 21003–11.

Pereda, A. E. (2014), 'Electrical synapses and their functional interactions with chemical synapses', *Nature Reviews Neuroscience* **15**(4), 250–263.

Perry, E. K., Tomlinson, B. E., Blessed, G., Bergmann, K., Gibson, P. H. and Perry, R. H. (1978), 'Correlation of cholinergic abnormalities with senile plaques and mental test scores in senile dementia.', *British medical journal* **2**(6150), 1457–9.

Peters, A., Sethares, C. and Luebke, J. I. (2008), 'Synapses are lost during aging in the primate prefrontal cortex.', *Neuroscience* **152**(4), 970–81.

Pham, E., Crews, L., Ubhi, K., Hansen, L., Adame, A., Cartier, A., Salmon, D., Galasko, D., Michael, S., Savas, J. N., Yates, J. R., Glabe, C. and Masliah, E. (2010), 'Progressive accumulation of amyloid-beta oligomers in Alzheimer's disease and in amyloid precursor protein transgenic mice is accompanied by selective alterations in synaptic scaffold proteins.', *The FEBS journal* **277**(14), 3051–67.

Pletikos, M., Sousa, A. M. M., Sedmak, G., Meyer, K. A., Zhu, Y., Cheng, F., Li, M., Kawasawa, Y. I. and Sestan, N. (2014), 'Temporal specification and bilaterality of human neocortical topographic gene expression.', *Neuron* **81**(2), 321–32.

Price, J. L., Davis, P. B., Morris, J. C. and White, D. L. (1991), 'The distribution of tangles, plaques and related immunohistochemical markers in healthy aging and Alzheimer's disease.', *Neurobiology of aging* **12**(4), 295–312.

Proctor, D. T., Coulson, E. J. and Dodd, P. R. (2010), 'Reduction in post-synaptic scaffolding PSD-95 and SAP-102 protein levels in the Alzheimer inferior temporal cortex is correlated with disease pathology.', *Journal of Alzheimer's disease : JAD* **21**(3), 795–811.

Qiu, A., Wang, L., Younes, L., Harms, M. P., Ratnanather, J. T., Miller, M. I. and Csernansky, J. G. (2009), 'Neuroanatomical asymmetry patterns in individuals with schizophrenia and their non-psychotic siblings.', *NeuroImage* **47**(4), 1221–9.

Rabinowicz, T., Dean, D. E., Petetot, J. M. and de Courten-Myers, G. M. (1999), 'Gender differences in the human cerebral cortex: more neurons in males; more processes in females.', *Journal of child neurology* **14**(2), 98–107.

Rademacher, J., Caviness, V. S., Steinmetz, H. and Galaburda, A. M. (1993), 'Topographical variation of the human primary cortices: implications for neuroimaging, brain mapping, and neurobiology.', *Cerebral cortex (New York, N.Y. : 1991)* **3**(4), 313–29.

Rakic, P., Bourgeois, J. P., Eckenhoff, M. F., Zecevic, N. and Goldman-Rakic, P. S. (1986), 'Concurrent overproduction of synapses in diverse regions of the primate cerebral cortex.', *Science (New York, N.Y.)* **232**(4747), 232–5.

Rammes, G. (2009), 'Neramexane: a moderate-affinity NMDA receptor channel blocker: new prospects and indications.', *Expert review of clinical pharmacology* **2**(3), 231–238.

Rasband, M. N., Park, E. W., Zhen, D., Arbuckle, M. I., Poliak, S., Peles, E., Grant, S. G. N. and Trimmer, J. S. (2002), 'Clustering of neuronal potassium channels is independent of their interaction with PSD-95.', *The Journal of cell biology* **159**(4), 663–72.

Reig-Viader, R., Sindreu, C. and Bayés, (2017), 'Synaptic proteomics as a means to identify the molecular basis of mental illness: Are we getting there?', *Progress in Neuro-Psychopharmacology and Biological Psychiatry* .

Reiman, E. M., Caselli, R. J., Yun, L. S., Chen, K., Bandy, D., Minoshima, S., Thibodeau, S. N. and Osborne, D. (1996), 'Preclinical evidence of Alzheimer's disease in persons homozygous for the epsilon 4 allele for apolipoprotein E.', *The New England journal of medicine* **334**(12), 752–8.

Roche, K. W., Ly, C. D., Petralia, R. S., Wang, Y. X., McGee, A. W., Bredt, D. S. and Wenthold, R. J. (1999), 'Postsynaptic density-93 interacts with the delta2 glutamate receptor subunit at parallel fiber synapses.', *The Journal of neuroscience : the official journal of the Society for Neuroscience* **19**(10), 3926–34.

Rohrer, J. D., Warren, J. D., Omar, R., Mead, S., Beck, J., Revesz, T., Holton, J., Stevens, J. M., Al-Sarraj, S., Pickering-Brown, S. M., Hardy, J., Fox, N. C., Collinge, J., Warrington, E. K. and Rossor, M. N. (2008), 'Parietal Lobe Deficits in Frontotemporal Lobar Degeneration Caused by a Mutation in the Progranulin Gene', *Archives of Neurology* **65**(4), 506.

Rönicke, R., Mikhaylova, M., Rönicke, S., Meinhardt, J., Schröder, U. H., Fändrich, M., Reiser, G., Kreutz, M. R. and Reymann, K. G. (2011), 'Early neuronal dysfunction by amyloid $\beta$ oligomers depends on activation of NR2B-containing NMDA receptors', *Neurobiology of Aging* **32**(12), 2219–2228.

Roses, A. D. (1996), 'Apolipoprotein E alleles as risk factors in Alzheimer's disease.', *Annual review of medicine* **47**(1), 387–400.

Roth, M., Tomlinson, B. E. and Blessed, G. (1967), 'The relationship between quantitative measures of dementia and of degenerative changes in the cerebral grey matter of elderly subjects.', *Proceedings of the Royal Society of Medicine* **60**(3), 254–60.

Roy, M., Sorokina, O., Skene, N., Simonnet, C., Mazzo, F., Zwart, R., Sher, E., Smith, C., Armstrong, J. D. and Grant, S. G. N. (2018), 'Proteomic analysis of postsynaptic proteins in regions of the human neocortex.', *Nature neuroscience* **21**(1), 130–138.

Ruthirakuhan, M., Herrmann, N., Suridjan, I., Abraham, E. H., Farber, I. and Lanctôt, K. L. (2016), 'Beyond immunotherapy: new approaches for disease modifying treatments for early Alzheimer's disease', *Expert Opinion on Pharmacotherapy* **17**(18), 2417–2429.

Ryan, T. J. and Grant, S. G. N. (2009), 'The origin and evolution of synapses.', *Nature reviews. Neuroscience* **10**(10), 701–712.

Samarasekera, N., Al-Shahi Salman, R., Huitinga, I., Klioueva, N., McLean, C. A., Kretzschmar, H., Smith, C. and Ironside, J. W. (2013), 'Brain banking for neurological disorders.', *The Lancet. Neurology* **12**(11), 1096–105.

Samarasekera, N., Lerpiniere, C., Fonville, A. F., Farrall, A. J., Wardlaw, J. M., White, P. M., Torgersen, A., Ironside, J. W., Smith, C., Al-Shahi Salman, R. and Lothian Audit of the Treatment of Cerebral Haemorrhage (LATCH) collaborators (2015), 'Consent for Brain Tissue Donation after Intracerebral Haemorrhage: A Community-Based Study.', *PloS one* **10**(8), e0135043.

Sans, N., Petralia, R. S., Wang, Y. X., Blahos, J., Hell, J. W. and Wenthold, R. J. (2000), 'A developmental change in NMDA receptor-associated proteins at hippocampal synapses.', *The Journal of neuroscience : the official journal of the Society for Neuroscience* **20**(3), 1260–1271.

Sattler, R. and Tymianski, M. (2000), 'Molecular mechanisms of calcium-dependent excitotoxicity.', *Journal of molecular medicine (Berlin, Germany)* **78**(1), 3–13.

Saura, C. A., Choi, S.-Y., Beglopoulos, V., Malkani, S., Zhang, D., Shankaranarayana Rao, B. S., Chattarji, S., Kelleher, R. J., Kandel, E. R., Duff, K., Kirkwood, A. and Shen, J. (2004), 'Loss of presenilin function causes impairments of memory and synaptic plasticity followed by age-dependent neurodegeneration.', *Neuron* **42**(1), 23–36.

Schafer, D. P., Lehrman, E. K. and Stevens, B. (2013), 'The "quad-partite" synapse: Microglia-synapse interactions in the developing and mature CNS', *Glia* **61**(1), 24–36.

Scheff, S. (2003), 'Synaptic pathology in Alzheimer's disease: a review of ultrastructural studies', *Neurobiology of Aging* **24**(8), 1029–1046.

Scheff, S., Sparks, D. L. and Price, D. (1996), 'Quantitative Assessment of Synaptic Density in the Outer Molecular Layer of the Hippocampal Dentate Gyrus in Alzheimer's Disease', *Dementia and Geriatric Cognitive Disorders* **7**(4), 226–232.

Scheff, S. W., Ansari, M. A. and Mufson, E. J. (2016), 'Oxidative stress and hippocampal synaptic protein levels in elderly cognitively intact individuals with Alzheimer's disease pathology.', *Neurobiology of aging* **42**, 1–12.

Scheff, S. W., DeKosky, S. T. and Price, D. A. (1990), 'Quantitative assessment of cortical synaptic density in Alzheimer's disease', *Neurobiology of Aging* **11**(1), 29–37.

Scheff, S. W. and Price, D. A. (1998), 'Synaptic density in the inner molecular layer of the hippocampal dentate gyrus in Alzheimer disease.', *Journal of neuropathology and experimental neurology* **57**(12), 1146–53.

Scheff, S. W., Price, D. a., Ansari, M. a., Roberts, K. N., Schmitt, F. a., Ikonomovic, M. D. and Mufson, E. J. (2015), 'Synaptic change in the posterior cingulate gyrus in the progression of Alzheimer's disease.', *Journal of Alzheimer's disease : JAD* **43**(3), 1073–90.

Scheff, S. W., Price, D. A., Schmitt, F. A., DeKosky, S. T. and Mufson, E. J. (2007), 'Synaptic alterations in CA1 in mild Alzheimer disease and mild cognitive impairment.', *Neurology* **68**(18), 1501–8.

Scheff, S. W., Price, D. A., Schmitt, F. A. and Mufson, E. J. (2006), 'Hippocampal synaptic loss in early Alzheimer's disease and mild cognitive impairment.', *Neurobiology of aging* **27**(10), 1372–84.

Scheff, S. W., Price, D. A., Schmitt, F. A., Scheff, M. A. and Mufson, E. J. (2011), 'Synaptic loss in the inferior temporal gyrus in mild cognitive impairment and Alzheimer's disease.', *Journal of Alzheimer's disease : JAD* **24**(3), 547–57.

Scheff, S. W., Sparks, L. and Price, D. A. (1993), 'Quantitative assessment of synaptic density in the entorhinal cortex in Alzheimer's disease.', *Annals of neurology* **34**(3), 356–61.

Scheltens, P., Blennow, K., Breteler, M. M. B., de Strooper, B., Frisoni, G. B., Salloway, S. and Van der Flier, W. M. (2016), 'Alzheimer's disease.', *Lancet (London, England)* **388**(10043), 505–17.

Schermelleh, L., Heintzmann, R. and Leonhardt, H. (2010), 'A guide to super-resolution fluorescence microscopy', *The Journal of Cell Biology* **190**(2), 165–175.

Schnell, E., Sizemore, M., Karimzadegan, S., Chen, L., Bredt, D. S. and Nicoll, R. A. (2002), 'Direct interactions between PSD-95 and stargazin control synaptic AMPA receptor number', *Proceedings of the National Academy of Sciences* **99**(21), 13902–13907.

Schnell, S. A., Staines, W. A. and Wessendorf, M. W. (1999), 'Reduction of lipofuscin-like autofluorescence in fluorescently labeled tissue.', *The journal of histochemistry and cytochemistry : official journal of the Histochemistry Society* **47**(6), 719–30.

Schultz, W. (1998), 'Predictive reward signal of dopamine neurons.', *Journal of neurophysiology* **80**(1), 1–27.

Schüz, A. and Palm, G. (1989), 'Density of neurons and synapses in the cerebral cortex of the mouse.', *The Journal of comparative neurology* **286**(4), 442–55.

Schwenk, J., Harmel, N., Brechet, A., Zolles, G., Berkefeld, H., Müller, C. S., Bildl, W., Baehrens, D., Hüber, B., Kulik, A., Klöcker, N., Schulte, U. and Fakler, B. (2012), 'High-Resolution Proteomics Unravel Architecture and Molecular Diversity of Native AMPA Receptor Complexes', *Neuron* **74**(4), 621–633.

Seeley, W. W., Crawford, R. K., Zhou, J., Miller, B. L. and Greicius, M. D. (2009), 'Neurodegenerative diseases target large-scale human brain networks.', *Neuron* **62**(1), 42–52.

Selkoe, D. J. (2002), 'Alzheimer's disease is a synaptic failure.', *Science (New York, N.Y.)* **298**(5594), 789–91.

Selkoe, D., Mandelkow, E. and Holtzman, D. (2012), 'Deciphering Alzheimer disease.', *Cold Spring Harbor perspectives in medicine* **2**(1), a011460.

Serrano-Pozo, A., Frosch, M. P., Masliah, E. and Hyman, B. T. (2011), 'Neuropathological Alterations in Alzheimer Disease', *Cold Spring Harbor Perspectives in Medicine* **1**(1), a006189–a006189.

Shankar, G. M., Li, S., Mehta, T. H., Garcia-Munoz, A., Shepardson, N. E., Smith, I., Brett, F. M., Farrell, M. A., Rowan, M. J., Lemere, C. A., Regan, C. M., Walsh, D. M., Sabatini, B. L. and Selkoe, D. J. (2008), 'Amyloid-beta protein dimers isolated directly from Alzheimer's brains impair synaptic plasticity and memory.', *Nature medicine* **14**(8), 837–42.

Sheng, M., Sabatini, B. L. and Südhof, T. C. (2012), 'Synapses and Alzheimer's disease.', *Cold Spring Harbor perspectives in biology* **4**(5), a005777–a005777.

Shim, K. S. and Lubec, G. (2002), 'Drebrin, a dendritic spine protein, is manifold decreased in brains of patients with Alzheimer's disease and Down syndrome.', *Neuroscience letters* **324**(3), 209–12.

Shin, H., Hsueh, Y. P., Yang, F. C., Kim, E. and Sheng, M. (2000), 'An intramolecular interaction between Src homology 3 domain and guanylate kinase-like domain required for channel clustering by postsynaptic density-95/SAP90.', *The Journal of neuroscience : the official journal of the Society for Neuroscience* **20**(10), 3580–7.

Shinohara, Y., Hirase, H., Watanabe, M., Itakura, M., Takahashi, M. and Shigemoto, R. (2008), 'Left-right asymmetry of the hippocampal synapses with differential subunit allocation of glutamate receptors.', *Proceedings of the National Academy of Sciences of the United States of America* **105**(49), 19498–503.

Shors, T. J., Falduto, J. and Leuner, B. (2004), 'The opposite effects of stress on dendritic spines in male vs. female rats are NMDA receptor-dependent.', *The European journal of neuroscience* **19**(1), 145–50.

Siew, L. K., Love, S., Dawbarn, D., Wilcock, G. K. and Allen, S. J. (2004), 'Measurement of pre- and post-synaptic proteins in cerebral cortex: effects of post-mortem delay', *Journal of Neuroscience Methods* **139**(2), 153–159.

Sinclair, L. I., Tayler, H. M. and Love, S. (2015), 'Synaptic protein levels altered in vascular dementia', *Neuropathology and Applied Neurobiology* **41**(4), 533–543.

Soltau, M., Berhörster, K., Kindler, S., Buck, F., Richter, D. and Kreienkamp, H.-J. (2004), 'Insulin receptor substrate of 53 kDa links postsynaptic shank to PSD-95.', *Journal of neurochemistry* **90**(3), 659–65.

Song, M. S., Rauw, G., Baker, G. B. and Kar, S. (2008), 'Memantine protects rat cortical cultured neurons against $\beta$-amyloid-induced toxicity by attenuating tau phosphorylation', *European Journal of Neuroscience* **28**(10), 1989–2002.

Sporns, O. and Betzel, R. F. (2016), 'Modular Brain Networks.', *Annual review of psychology* **67**(1), 613–40.

Stan, A. D., Ghose, S., Gao, X.-M., Roberts, R. C., Lewis-Amezcua, K., Hatanpaa, K. J. and Tamminga, C. A. (2006), 'Human postmortem tissue: what quality markers matter?', *Brain research* **1123**(1), 1–11.

Stark, C., Breitkreutz, B.-J., Reguly, T., Boucher, L., Breitkreutz, A. and Tyers, M. (2006), 'BioGRID: a general repository for interaction datasets.', *Nucleic acids research* **34**(Database issue), 535–9.

Stathakis, D. G., Hoover, K. B., You, Z. and Bryant, P. J. (1997), 'Human Postsynaptic Density-95 (PSD95): Location of the Gene (DLG4) and Possible Function in Nonneural as Well as in Neural Tissues', *Genomics* **44**(1), 71–82.

Stathakis, D. G., Udar, N., Sandgren, O., Andreasson, S., Bryant, P. J., Small, K. and Forsman-Semb, K. (2002), 'Genomic Organization of Human DLG4, the Gene Encoding Postsynaptic Density 95', *Journal of Neurochemistry* **73**(6), 2250–2265.

Sultana, R., Banks, W. A. and Butterfield, D. A. (2010), 'Decreased levels of PSD95 and two associated proteins and increased levels of BCl2 and caspase 3 in hippocampus from subjects with amnestic mild cognitive impairment: Insights into their potential roles for loss of synapses and memory, accumulation of Abe', *Journal of neuroscience research* **88**(3), 469–77.

Sun, Y., Savanenin, A., Reddy, P. H. and Liu, Y. F. (2001), 'Polyglutamine-expanded Huntingtin Promotes Sensitization of N-Methyl-D-aspartate Receptors via Post-synaptic Density 95', *Journal of Biological Chemistry* **276**(27), 24713–24718.

Szirmai, I., Buzsáki, G. and Kamondi, A. (2012), '120 years of hippocampal Schaffer collaterals.', *Hippocampus* **22**(7), 1508–16.

Takahashi, R. H., Almeida, C. G., Kearney, P. F., Yu, F., Lin, M. T., Milner, T. A. and Gouras, G. K. (2004), 'Oligomerization of Alzheimer's beta-amyloid within processes and synapses of cultured neurons and brain.', *The Journal of neuroscience : the official journal of the Society for Neuroscience* **24**(14), 3592–9.

Takata, A., Iwayama, Y., Fukuo, Y., Ikeda, M., Okochi, T., Maekawa, M., Toyota, T., Yamada, K., Hattori, E., Ohnishi, T., Toyoshima, M., Ujike, H., Inada, T., Kunugi, H., Ozaki, N., Nanko, S., Nakamura, K., Mori, N., Kanba, S., Iwata, N., Kato, T. and Yoshikawa, T. (2013), 'A population-specific uncommon variant in GRIN3A associated with schizophrenia', *Biological Psychiatry* **73**(6), 532–539.

Takeuchi, M., Hata, Y., Hirao, K., Toyoda, A., Irie, M. and Takai, Y. (1997), 'SAPAPs. A family of PSD-95/SAP90-associated proteins localized at postsynaptic density.', *The Journal of biological chemistry* **272**(18), 11943–51.

Tamminga, C. a. and Holcomb, H. H. (2005), 'Phenotype of schizophrenia: a review and formulation', *Molecular Psychiatry* **10**(1), 27–39.

Tarpey, P., Parnau, J., Blow, M., Woffendin, H., Bignell, G., Cox, C., Cox, J., Davies, H., Edkins, S., Holden, S., Korny, A., Mallya, U., Moon, J., O'Meara, S., Parker, A., Stephens, P., Stevens, C., Teague, J., Donnelly, A., Mangelsdorf, M., Mulley, J., Partington, M., Turner, G., Stevenson, R., Schwartz, C., Young, I., Easton, D., Bobrow, M., Futreal, P. A., Stratton, M. R., Gecz, J., Wooster, R. and Raymond, F. L. (2004), 'Mutations in the DLG3 Gene Cause Nonsyndromic X-Linked Mental Retardation', *The American Journal of Human Genetics* **75**(2), 318–324.

Tavares, G. A., Panepucci, E. H. and Brunger, A. T. (2001), 'Structural characterization of the intramolecular interaction between the SH3 and guanylate kinase domains of PSD-95.', *Molecular cell* **8**(6), 1313–25.

Terry, R. D., Masliah, E., Salmon, D. P., Butters, N., DeTeresa, R., Hill, R., Hansen, L. A. and Katzman, R. (1991), 'Physical basis of cognitive alterations in alzheimer's disease: Synapse loss is the major correlate of cognitive impairment', *Annals of Neurology* **30**(4), 572–580.

Thal, D. R., Rub, U., Orantes, M. and Braak, H. (2002), 'Phases of A -deposition in the human brain and its relevance for the development of AD', *Neurology* **58**(12), 1791–1800.

The UniProt Consortium (2017), 'UniProt: the universal protein knowledgebase.', *Nucleic acids research* **45**(D1), D158–D169.

Thu, D. C. V., Oorschot, D. E., Tippett, L. J., Nana, A. L., Hogg, V. M., Synek, B. J., Luthi-Carter, R., Waldvogel, H. J. and Faull, R. L. M. (2010), 'Cell loss in the motor and cingulate cortex correlates with symptomatology in Huntington's disease', *Brain* **133**(4), 1094–1110.

Tippett, L. J., Waldvogel, H. J., Thomas, S. J., Hogg, V. M., Roon-Mom, W. v., Synek, B. J., Graybiel, A. M. and Faull, R. L. M. (2006), 'Striosomes and mood dysfunction in Huntington's disease', *Brain* **130**(1), 206–221.

Toga, A. W. and Thompson, P. M. (2003), 'Mapping brain asymmetry.', *Nature reviews. Neuroscience* **4**(1), 37–48.

Tomita, H., Vawter, M. P., Walsh, D. M., Evans, S. J., Choudary, P. V., Li, J., Overman, K. M., Atz, M. E., Myers, R. M., Jones, E. G., Watson, S. J., Akil, H. and Bunney, W. E. (2004), 'Effect of agonal and postmortem factors on gene expression profile: quality control in microarray analyses of postmortem human brain.', *Biological psychiatry* **55**(4), 346–52.

Tomita, S., Nicoll, R. A. and Bredt, D. S. (2001), 'PDZ protein interactions regulating glutamate receptor function and plasticity.', *The Journal of cell biology* **153**(5), 19–24.

Townsend, M., Shankar, G. M., Mehta, T., Walsh, D. M. and Selkoe, D. J. (2006), 'Effects of secreted oligomers of amyloid beta-protein on hippocampal synaptic plasticity: a potent role for trimers.', *The Journal of physiology* **572**(Pt 2), 477–92.

Trabzuni, D., Ryten, M., Walker, R., Smith, C., Imran, S., Ramasamy, A., Weale, M. E. and Hardy, J. (2011), 'Quality control parameters on a large dataset of regionally dissected human control brains for whole genome expression studies.', *Journal of neurochemistry* **119**(2), 275–82.

Trachtenberg, J. T., Chen, B. E., Knott, G. W., Feng, G., Sanes, J. R., Welker, E. and Svoboda, K. (2002), 'Long-term in vivo imaging of experience-dependent synaptic plasticity in adult cortex.', *Nature* **420**(6917), 788–794.

Tsiouris, J. A. and Brown, W. T. (2004), 'Neuropsychiatric Symptoms of Fragile X Syndrome', *CNS Drugs* **18**(11), 687–703.

Uylings, H. B. M., Rajkowska, G., Sanz-Arigita, E., Amunts, K. and Zilles, K. (2005), 'Consequences of large interindividual variability for human brain atlases: converging macroscopical imaging and microscopical neuroanatomy.', *Anatomy and embryology* **210**(5-6), 423–31.

Vos, S. J. B., van Rossum, I. A., Verhey, F., Knol, D. L., Soininen, H., Wahlund, L.-O., Hampel, H., Tsolaki, M., Minthon, L., Frisoni, G. B., Froelich, L., Nobili, F., van der Flier, W., Blennow, K., Wolz, R., Scheltens, P. and Visser, P. J. (2013), 'Prediction of Alzheimer disease in subjects with amnestic and nonamnestic MCI.', *Neurology* **80**(12), 1124–32.

Wang, E., Babbey, C. M. and Dunn, K. W. (2005), 'Performance comparison between the high-speed Yokogawa spinning disc confocal system and single-point scanning confocal systems', *Journal of Microscopy* **218**(2), 148–159.

Wang, J., Li, L., Shao, S.-S., He, Z., Chen, Y.-L., Kong, R., Zhang, X.-H., Gong, J.-H. and Song, R.-R. (2016), 'Association analysis of genetic variant of rs13331 in PSD95 gene with autism spectrum disorders: A case-control study in a Chinese population.', *Journal of Huazhong University of Science and Technology. Medical sciences = Hua zhong ke ji da xue xue bao. Yi xue Ying De wen ban = Huazhong keji daxue xuebao. Yixue Yingdewen ban* **36**(2), 285–8.

Wang, L., Joshi, S. C., Miller, M. I. and Csernansky, J. G. (2001), 'Statistical analysis of hippocampal asymmetry in schizophrenia.', *NeuroImage* **14**(3), 531–45.

Ward, J. H. (1963), 'Hierarchical Grouping to Oprimize an Objective Function', *Journal of the American Statistical Association* **58**(301), 236–244.

Weiler, N. C., Collman, F., Vogelstein, J. T., Burns, R. and Smith, S. J. (2014), 'Synaptic molecular imaging in spared and deprived columns of mouse barrel cortex with array tomography.', *Scientific data* **1**, 140046.

Weingarten, J., Laßek, M., Mueller, B. F., Rohmer, M., Lunger, I., Baeumlisberger, D., Dudek, S., Gogesch, P., Karas, M. and Volknandt, W. (2014), 'The proteome of the presynaptic active zone from mouse brain', *Molecular and Cellular Neuroscience* **59**, 106–118.

West, M. J., Slomianka, L. and Gundersen, H. J. G. (1991), 'Unbiased stereological estimation of the total number of neurons in the subdivisions of the rat hippocampus using the optical fractionator', *The Anatomical Record* **231**(4), 482–497.

Wiedenmann, B. and Franke, W. W. (1985), 'Identification and localization of synaptophysin, an integral membrane glycoprotein of Mr 38,000 characteristic of presynaptic vesicles.', *Cell* **41**(3), 1017–28.

Wilcock, G. K. and Esiri, M. M. (1982), 'Plaques, tangles and dementia. A quantitative study.', *Journal of the neurological sciences* **56**(2-3), 343–56.

Wilkinson, D. (2012), 'A review of the effects of memantine on clinical progression in Alzheimer's disease', *International Journal of Geriatric Psychiatry* **27**(8), 769–776.

Winblad, B., Amouyel, P., Andrieu, S., Ballard, C., Brayne, C., Brodaty, H., Cedazo-Minguez, A., Dubois, B., Edvardsson, D., Feldman, H., Fratiglioni, L., Frisoni, G. B., Gauthier, S., Georges, J., Graff, C., Iqbal, K., Jessen, F., Johansson, G., Jönsson, L., Kivipelto, M., Knapp,

M., Mangialasche, F., Melis, R., Nordberg, A., Rikkert, M. O., Qiu, C., Sakmar, T. P., Scheltens, P., Schneider, L. S., Sperling, R., Tjernberg, L. O., Waldemar, G., Wimo, A. and Zetterberg, H. (2016), 'Defeating Alzheimer's disease and other dementias: a priority for European science and society.', *The Lancet. Neurology* **15**(5), 455–532.

Witelson, S. F., Glezer, I. I. and Kigar, D. L. (1995), 'Women have greater density of neurons in posterior temporal cortex.', *The Journal of neuroscience : the official journal of the Society for Neuroscience* **15**(5 Pt 1), 3418–28.

Witter, M. P. (2007), 'The perforant path: projections from the entorhinal cortex to the dentate gyrus.', *Progress in brain research* **163**, 43–61.

Yao, I., Hata, Y., Ide, N., Hirao, K., Deguchi, M., Nishioka, H., Mizoguchi, A. and Takai, Y. (1999), 'MAGUIN, a novel neuronal membrane-associated guanylate kinase-interacting protein.', *The Journal of biological chemistry* **274**(17), 11889–96.

Yao, W. D., Gainetdinov, R. R., Arbuckle, M. I., Sotnikova, T. D., Cyr, M., Beaulieu, J. M., Torres, G. E., Grant, S. G. N. and Caron, M. G. (2004), 'Identification of PSD-95 as a Regulator of Dopamine-Mediated Synaptic and Behavioral Plasticity', *Neuron* **41**(4), 625–638.

Yates, A., Akanni, W., Amode, M. R., Barrell, D., Billis, K., Carvalho-Silva, D., Cummins, C., Clapham, P., Fitzgerald, S., Gil, L., Girón, C. G., Gordon, L., Hourlier, T., Hunt, S. E., Janacek, S. H., Johnson, N., Juettemann, T., Keenan, S., Lavidas, I., Martin, F. J., Maurel, T., McLaren, W., Murphy, D. N., Nag, R., Nuhn, M., Parker, A., Patricio, M., Pignatelli, M., Rahtz, M., Riat, H. S., Sheppard, D., Taylor, K., Thormann, A., Vullo, A., Wilder, S. P., Zadissa, A., Birney, E., Harrow, J., Muffato, M., Perry, E., Ruffier, M., Spudich, G., Trevanion, S. J., Cunningham, F., Aken, B. L., Zerbino, D. R. and Flicek, P. (2016), 'Ensembl 2016.', *Nucleic acids research* **44**(D1), 710–6.

Ying, Z., Bingaman, W. and Najm, I. M. (2004), 'Increased Numbers of Coassembled PSD-95 to NMDA-receptor Subunits NR2B and NR1 in Human Epileptic Cortical Dysplasia', *Epilepsia* **45**(4), 314–321.

Yu, J.-T., Tan, L. and Hardy, J. (2014), 'Apolipoprotein E in Alzheimer's disease: an update.', *Annual review of neuroscience* **37**(1), 79–100.

Zaidel, D. W., Esiri, M. M. and Harrison, P. J. (1997), 'The hippocampus in schizophrenia: lateralized increase in neuronal density and altered cytoarchitectural asymmetry.', *Psychological medicine* **27**(3), 703–13.

Zalfa, F., Eleuteri, B., Dickson, K. S., Mercaldo, V., De Rubeis, S., di Penta, A., Tabolacci, E., Chiurazzi, P., Neri, G., Grant, S. G. N. and Bagni, C. (2007), 'A new function for the fragile X mental retardation protein in regulation of PSD-95 mRNA stability', *Nature Neuroscience* **10**(5), 578–587.

Zecevic, N. and Rakic, P. (1991), 'Synaptogenesis in monkey somatosensory cortex.', *Cerebral cortex (New York, N.Y. : 1991)* **1**(6), 510–23.

Zempel, H., Thies, E., Mandelkow, E. and Mandelkow, E.-M. (2010), 'Abeta oligomers cause localized Ca(2+) elevation, missorting of endogenous Tau into dendrites, Tau phosphorylation, and destruction of microtubules and spines.', *The Journal of neuroscience : the official journal of the Society for Neuroscience* **30**(36), 11938–50.

Zhang, C., Wu, B., Beglopoulos, V., Wines-Samuelson, M., Zhang, D., Dragatsis, I., Südhof, T. C. and Shen, J. (2009), 'Presenilins are essential for regulating neurotransmitter release.', *Nature* **460**(7255), 632–6.

Zhang, J., Lewis, S. M., Kuhlman, B. and Lee, A. L. (2013), 'Supertertiary structure of the MAGUK core from PSD-95.', *Structure (London, England : 1993)* **21**(3), 402–13.

Zhang, J., Vinuela, A., Neely, M. H., Hallett, P. J., Grant, S. G. N., Miller, G. M., Isacson, O., Caron, M. G. and Yao, W. D. (2007), 'Inhibition of the dopamine D1 receptor signaling by PSD-95', *Journal of Biological Chemistry* **282**(21), 15778–15789.

Zhang, Y., Li, P., Feng, J. and Wu, M. (2016), 'Dysfunction of NMDA receptors in Alzheimer's disease', *Neurological Sciences* **37**(7), 1039–1047.

Zhou, D., Ren, J.-X., Ryan, T. M., Higgins, N. P. and Townes, T. M. (2004), 'Rapid tagging of endogenous mouse genes by recombineering and ES cell complementation of tetraploid blastocysts.', *Nucleic acids research* **32**(16), e128.

Zhu, J., Shang, Y., Chen, J. and Zhang, M. (2012), 'Structure and function of the guanylate kinase-like domain of the MAGUK family scaffold proteins', *Frontiers in Biology* **7**(5), 379–396.

Zhu, J., Shang, Y. and Zhang, M. (2016), 'Mechanistic basis of MAGUK-organized complexes in synaptic development and signalling', *Nature Reviews Neuroscience* **17**(4), 209–223.

Zoghbi, H. Y. and Bear, M. F. (2012), 'Synaptic Dysfunction in Neurodevelopmental Disorders Associated with Autism and Intellectual Disabilities', *Cold Spring Harbor Perspectives in Biology* **4**(3), a009886–a009886.

# A Supplemental Figures

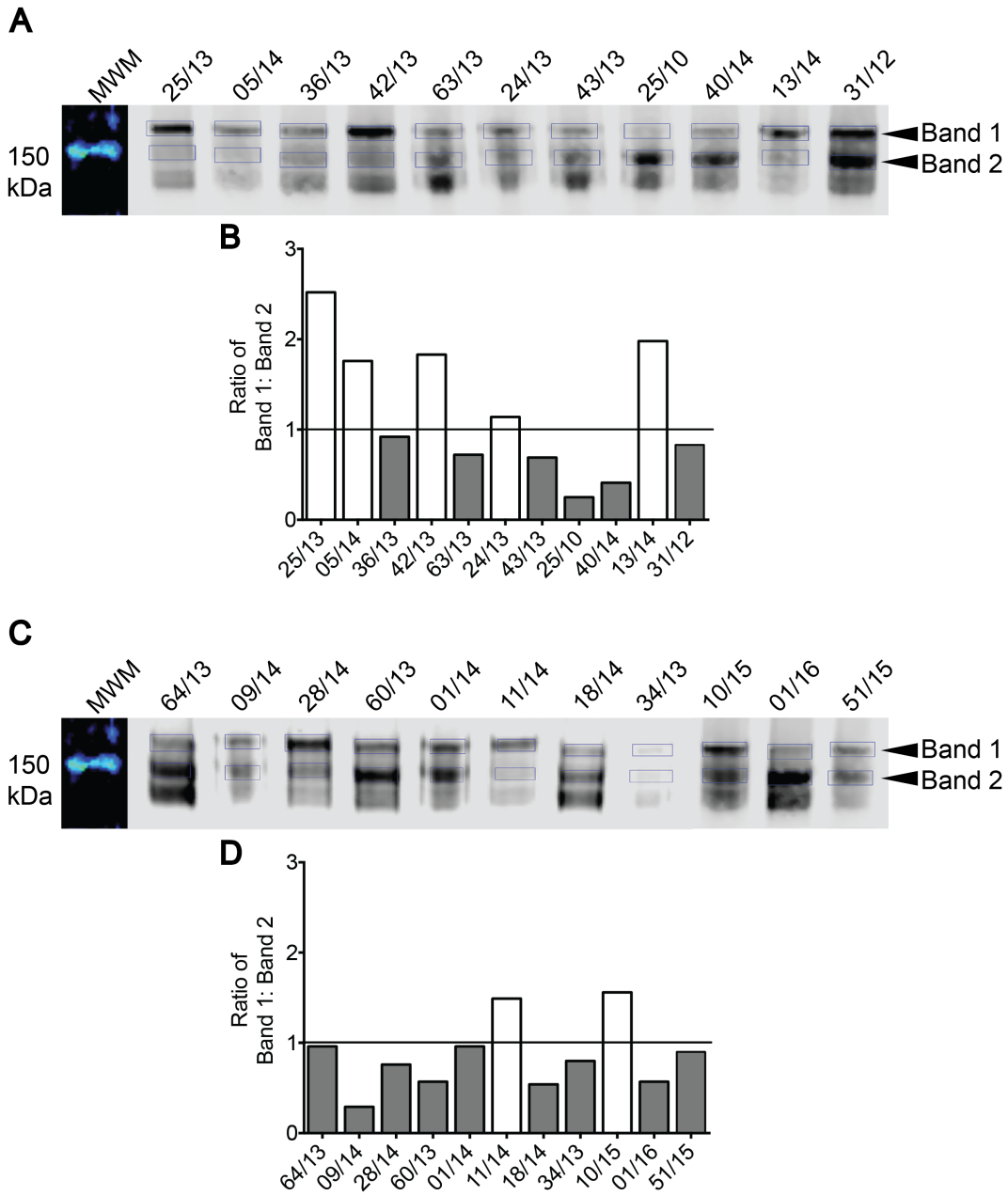


**Figure A.1 HUSPIR protein degradation blots.**

The post-mortem degradation of NMDAR2B was used as a marker of synaptic protein integrity. A ratio of degraded NMDAR2B of greater than 1 was considered of good quality. **A & C.** Examples of blots. Tissue tested was obtained from the cortical area BA41/42. **B & D.** Results of blot quantifications. Most cases did not show good preservation of synaptic proteins (darker bars). MWM - molecular weight marker.

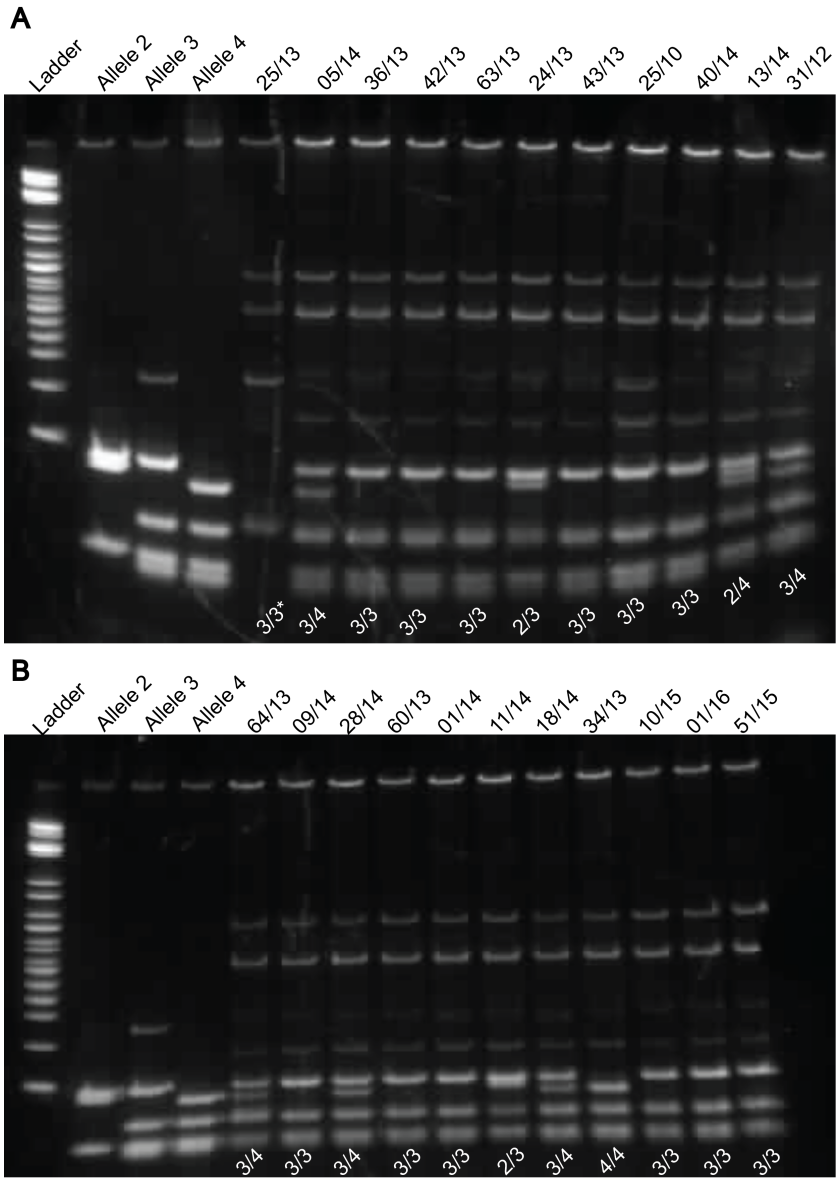


**Figure A.2 ApoE genotyping gels.**

**Panels A&B** ApoE genotypes: TBE acrylamide (20%) gels electrophoresis stained with ethidium bromide to demonstrate banding patterns used to genotype amplified DNA of selected study subjects digested with the *HhaI* restriction enzyme. Shown are amplified ApoE genes from the cortex (BA41/42) of 22 individuals. Results of genotyping of each individual are at the bottom of each gels. The first band shows the control ladder. The genotypes were determined by scoring a unique combination of DNA fragment sizes (Alleles 2-4). *Genotyping for case 25/13 in panel A was repeated and was found to be ApoE 3/3.

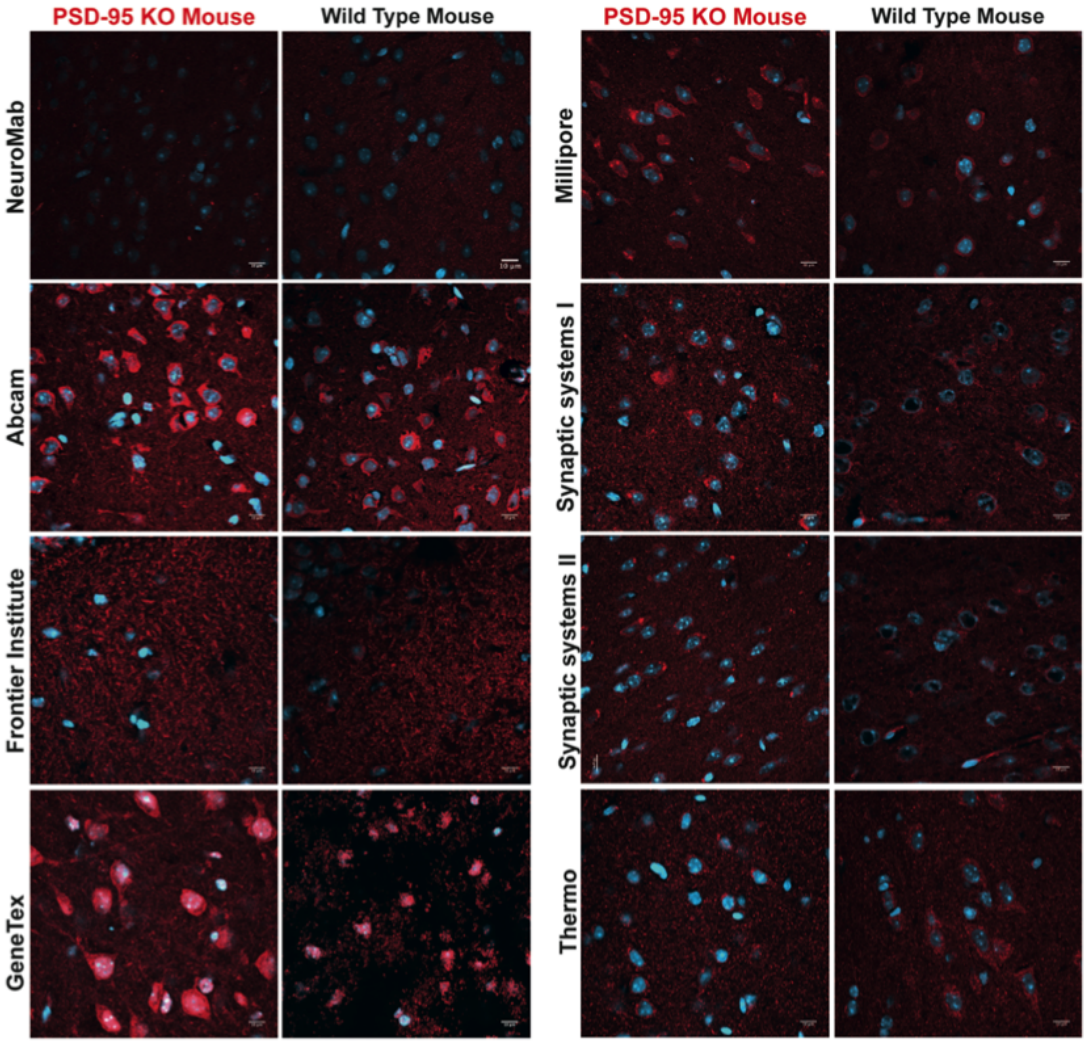


**Figure A.3 PSD-95 antibodies tested for specificity.**

Specificity of several PSD-95 antibodies was tested on KO tissue as shown in the figure. Only NeuroMab antibody showed a lack of staining with the PSD-95 KO mouse tissue under tested conditions.

# B Supplemental Tables

**Table B.1** Human subjects - additional data

| No | ID | Group | Brain Bank Cohort | Images (total no) | Slide index | Side patient |
|---|---|---|---|---|---|---|
| 1 | SD25/13 | Control | Control | 52836 | AG | L |
| 2 | SD36/13 | Control | Control | 42021 | V | R |
| 3 | SD23/13 | Control | Control | 64350 | AH | R |
| 4 | SD29/13 | Control | Control | 44895 | AH | R |
| 5 | SD38/13 | Control | Control | 37149 | AH | R |
| 6 | SD03/14 | Control | Control | 37440 | AL | R |
| 7 | SD32/13 | Control | Control | 57190 | AH | R |
| 8 | SD05/14 | Control | Control | 61060 | AK | L |
| 9 | SD24/15 | Control | Control/LBC | 48480 | AL | R |
| 10 | SD42/13 | Control | Control | 41382 | AK | L |
| 11 | SD10/15 | Control | Control | 30621 | AL | R |
| 12 | SD35/14 | Control | Control | 61104 | AK | L |
| 13 | SD14/13 | Control | Control | 37008 | AG | L |
| 14 | SD63/13 | Control | Control/LBC | 40548 | AK | L |
| | | | | | | |
| 1 | SD43/13 | Early AD | LINCHPIN | 45815 | AL | R |
| 2 | SD28/14 | Early AD | LINCHPIN | 60888 | AL | R |
| 3 | SD09/14 | Early AD | LINCHPIN | 52858 | AL | R |
| 4 | SD60/13 | Early AD | LINCHPIN | 46002 | AL | R |
| 5 | SD31/12 | Early AD | Control | 47096 | AL | R |
| 6 | SD13/14 | Early AD | LINCHPIN | 34104 | AL | R |
| 7 | SD11/14 | Early AD | LINCHPIN | 45492 | AL | R |
| 8 | SD40/14 | Early AD | LINCHPIN | 31790 | AL | R |
| 9 | SD01/14 | Early AD | LINCHPIN | 44793 | AL | R |
| 10 | SD18/14 | Early AD | LINCHPIN | 43197 | AL | R |
| | | | | | | |
| 1 | SD34/13 | Late AD | AD | 31133 | S | R |
| 2 | SD39/13 | Late AD | LINCHPIN | 37975 | AH | R |
| 3 | SD62/13 | Late AD | LINCHPIN | 52002 | AK | L |
| 4 | SD64/13 | Late AD | AD | 40180 | AK | L |
| 5 | SD11/13 | Late AD | AD | 31652 | S | R |
| 6 | SD18/13 | Late AD | AD | 38208 | AG | L |
| 7 | SD02/14 | Late AD | LINCHPIN | 46168 | AL | R |
| 8 | SD32/14 | Late AD | LINCHPIN | 46852 | AL | R |

Abbreviations: LINCHPIN - Lothian INtraCerebral Haemorrhage, Pathology, Imaging and Neurological Outcome study (Samarasekera et al., 2015); LBC - Lothian Birth Cohort (Henstridge et al., 2015); AD - Alzheimer's Disease.

**Table B.2** Brief description of neocortical areas

| No. | BA area | Name of cortex (cx) | Lobe | Gyrus | ABI Index* | Function |
|---|---|---|---|---|---|---|
| 1 | BA4 | Posterior frontal | Frontal | Precentral | 48/106 | Primary motor cx |
| 2 | BA6/8 | Posterior frontal | Frontal | Superior frontal & middle frontal | 16/106<br>19/106<br>48/106 | Premotor cx |
| 3 | BA9 | Rostral dorsolateral prefrontal | Frontal | Superior frontal | 13/106 | Associative frontal cx |
| 4 | BA11/12 | Rostral orbito-frontal | Frontal | Orbital and rectus | 13/106 | Associative frontal cx |
| 5 | BA17 | Striate | Occipital | Striate area | 87/106 | Primary visual cx |
| 6 | BA19 | Peristriate | Occipital | Occipital | 87/106 | Secondary visual cx |
| 7 | BA20/21 | Ventro-lateral temporal | Temporal | Mid-lateral temporal & inferolateral temporal cx | 48/106 | Associative temporal cx |
| 8 | BA37 | Lateral temporo -occipital | Occipito -temporal | Middle temporal, inferior temporal & inferior occipital | 87/106 | Associative occipito -temporal cx |
| 9 | BA38 | Temporal polar | Temporal | Planum polare | 19/106 | Associative temporal cx |
| 10 | BA39 | Inferior parietal | Parietal | Angular gyrus or supramarginal gyrus | 87/106 | Associative parietal cx |
| 11 | BA41/42 | Superior temporal | Temporal | Transverse temporal/ Superior temporal, (Heschl's gyrus) planum polare | 48/106 | Primary auditory cx/ secondary auditory cx |
| 12 | BA46 | Dorsolateral prefrontal | Frontal | Middle frontal | 13/106 | Associative frontal cx |
| 13 | BA44/45 | Ventrolateral prefrontal (Brocca's area) | Frontal | Pars opecularis & pars triangularis (of the inferior frontal gyrus) | 16/106 | Associative frontal cx |

**Table B.3** Overall PSD-95 puncta density values for 20 human brain areas

| | Case A | | | Case B | | | Case C | | | Case D | | |
|---|---|---|---|---|---|---|---|---|---|---|---|---|
| **Area** | **Median** | **Mean** | **SD** | **Median** | **Mean** | **SD** | **Median** | **Mean** | **SD** | **Median** | **Mean** | **SD** |
| BA4 | 29.47 | 30.88 | 4.55 | 31.22 | 32.6 | 9.71 | 26.78 | 26.92 | 3.95 | 25.79 | 27.01 | 5.61 |
| BA6 | 42.48 | 44.54 | 5.44 | 25.2 | 22.13 | 9.67 | 23.97 | 25.38 | 6.17 | 32.37 | 37.67 | 10.88 |
| BA9 | 45.89 | 45.69 | 4.47 | 14.22 | 16.73 | 8.21 | 32.59 | 33.92 | 7.01 | 29.27 | 28.84 | 4.22 |
| BA11 | 48.68 | 48.46 | 4.76 | 40.01 | 42.25 | 5.16 | 38.93 | 39.39 | 7.28 | 30.41 | 31.32 | 5.31 |
| BA17 | 33.92 | 32.64 | 6.47 | 20.58 | 22.94 | 8.10 | 33.24 | 30.57 | 6.62 | 39.85 | 40.28 | 8.40 |
| BA19 | 36.05 | 35.69 | 5.38 | 59.39 | 61.61 | 5.31 | 52.54 | 52.21 | 3.80 | 59.35 | 60.35 | 3.34 |
| BA20 | 38.39 | 36.20 | 5.26 | 14.02 | 17.68 | 7.77 | 54.70 | 54.32 | 4.71 | 47.60 | 47.27 | 2.94 |
| BA37 | 33.09 | 32.58 | 4.00 | 41.62 | 42.25 | 5.16 | 43.06 | 43.11 | 5.28 | 33.92 | 34.81 | 8.97 |
| BA38 | 39.17 | 39.23 | 5.00 | 56.63 | 53.62 | 6.65 | 28.46 | 30.24 | 6.91 | 53.71 | 52.78 | 4.03 |
| BA39 | 37.24 | 37.46 | 6.18 | 51.37 | 50.67 | 5.35 | 51.12 | 53.44 | 5.48 | 24.12 | 23.63 | 7.15 |
| BA41 | 39.49 | 39.33 | 5.97 | 30.23 | 31.86 | 6.71 | 49.04 | 44.93 | 11.95 | 44.66 | 44.38 | 5.50 |
| BA44 | 31.04 | 31.27 | 4.82 | 26.35 | 26.43 | 7.91 | 25.74 | 27.21 | 5.08 | 39.76 | 40.41 | 6.60 |
| BA46 | 29.38 | 29.94 | 5.56 | 27.58 | 27.47 | 4.78 | 37.87 | 38.25 | 3.29 | 34.61 | 35.26 | 4.23 |
| TH | 9.70 | 9.45 | 2.20 | 68.15 | 68.28 | 7.45 | 23.50 | 27.10 | 7.19 | 40.39 | 39.57 | 4.27 |
| CN | 11.32 | 11.03 | 1.90 | 5.84 | 8.49 | 5.31 | 39.31 | 39.77 | 3.18 | 33.38 | 33.88 | 3.09 |
| HC | 33.27 | 33.43 | 13.53 | 44.52 | 45.64 | 10.33 | 50.18 | 42.91 | 19.68 | 57.5 | 55.49 | 10.56 |
| CB | 17.70 | 17.52 | 4.74 | 36.68 | 37.62 | 8.51 | 32.28 | 33.99 | 5.98 | 36.39 | 34.05 | 9.88 |
| MB | 3.48 | 3.67 | 1.05 | 8.40 | 9.38 | 3.42 | 10.20 | 10.11 | 2.91 | 7.68 | 8.84 | 4.65 |
| PO | 4.13 | 4.97 | 1.85 | 6.60 | 6.36 | 2.39 | 6.92 | 7.26 | 2.67 | 6.47 | 6.62 | 2.16 |
| MD | 5.46 | 5.71 | 2.26 | 8.36 | 9.84 | 4.24 | 2.74 | 2.70 | 1.09 | 10.62 | 11.08 | 2.39 |

**Table B.4** Overall PSD-95 puncta intensity values for 20 human brain areas

| | Case A | | | Case B | | | Case C | | | Case D | | |
|---|---|---|---|---|---|---|---|---|---|---|---|---|
| **Area** | **Median** | **Mean** | **SD** | **Median** | **Mean** | **SD** | **Median** | **Mean** | **SD** | **Median** | **Mean** | **SD** |
| BA4 | 24.40 | 24.95 | 1.41 | 28.61 | 29.57 | 3.68 | 24.18 | 24.12 | 1.15 | 23.33 | 23.4 | 3.32 |
| BA6 | 33.18 | 35.02 | 4.87 | 25.78 | 26.27 | 2.53 | 23.93 | 23.74 | 1.32 | 29.01 | 30.22 | 5.99 |
| BA9 | 38.41 | 37.88 | 4.74 | 25.12 | 26.03 | 4.00 | 26.11 | 27.89 | 3.86 | 23.13 | 23.45 | 1.55 |
| BA11 | 32.37 | 33.27 | 4.56 | 27.67 | 28.99 | 2.53 | 27.69 | 28.31 | 2.77 | 24.54 | 25.28 | 1.94 |
| BA17 | 27.93 | 27.26 | 1.96 | 23.93 | 24.61 | 1.89 | 24.9 | 25.32 | 1.81 | 32.08 | 32.61 | 3.48 |
| BA19 | 26.86 | 27.23 | 1.46 | 42.4 | 44.03 | 5.91 | 43.83 | 44.66 | 4.47 | 48.44 | 50.1 | 6.63 |
| BA20 | 26.10 | 25.93 | 1.17 | 33.64 | 33.83 | 3.85 | 41.13 | 40.81 | 4.86 | 37.12 | 36.32 | 2.22 |
| BA37 | 24.75 | 24.69 | 1.16 | 27.36 | 27.45 | 2.51 | 30.53 | 30.74 | 4.13 | 27.46 | 27.34 | 3.68 |
| BA38 | 26.19 | 27.50 | 2.81 | 39.19 | 38.14 | 8.52 | 23.40 | 23.95 | 1.85 | 43.39 | 43.15 | 5.57 |
| BA39 | 25.96 | 25.35 | 2.52 | 37.75 | 38.46 | 3.95 | 37.47 | 39.68 | 6.63 | 23.99 | 24.21 | 1.98 |
| BA41 | 27.26 | 28.05 | 3.48 | 26.40 | 27.36 | 2.74 | 38.28 | 38.02 | 7.03 | 31.60 | 31.48 | 4.34 |
| BA44 | 25.18 | 25.19 | 0.94 | 28.59 | 28.95 | 3.31 | 27.01 | 28.04 | 2.39 | 29.44 | 29.9 | 2.68 |
| BA46 | 30.63 | 32.42 | 3.74 | 34.11 | 34.21 | 2.74 | 27.68 | 27.86 | 0.96 | 30.04 | 30.15 | 2.28 |
| TH | 20.24 | 20.41 | 1.23 | 59.67 | 61.17 | 6.14 | 31.96 | 32.93 | 2.18 | 36.61 | 38.09 | 3.63 |
| CN | 20.21 | 20.21 | 0.54 | 28.28 | 29.29 | 2.82 | 43.81 | 43.53 | 2.03 | 34.76 | 34.03 | 3.10 |
| HC | 27.85 | 28.81 | 3.04 | 28.24 | 27.84 | 3.30 | 28.13 | 29.15 | 5.85 | 35.53 | 36.74 | 5.39 |
| CB | 30.64 | 31.37 | 7.34 | 33.88 | 33.65 | 5.44 | 31.05 | 31.71 | 3.54 | 36.15 | 34.81 | 5.74 |
| MB | 20.68 | 20.79 | 1.24 | 22.43 | 21.97 | 1.42 | 24.65 | 23.86 | 2.68 | 20.80 | 20.52 | 1.55 |
| PO | 20.03 | 20.20 | 0.82 | 27.11 | 25.78 | 2.65 | 21.78 | 21.98 | 2.92 | 20.49 | 20.93 | 1.67 |
| MD | 21.78 | 22.22 | 1.67 | 24.14 | 24.42 | 2.21 | 18.14 | 18.09 | 0.73 | 20.87 | 21.09 | 0.84 |

**Table B.5** Overall PSD-95 puncta size values for 20 human brain areas

| | Case A | | | Case B | | | Case C | | | Case D | | |
|---|---|---|---|---|---|---|---|---|---|---|---|---|
| **Area** | **Median** | **Mean** | **SD** | **Median** | **Mean** | **SD** | **Median** | **Mean** | **SD** | **Median** | **Mean** | **SD** |
| BA4 | 0.30 | 0.29 | 0.02 | 0.31 | 0.31 | 0.03 | 0.26 | 0.27 | 0.03 | 0.26 | 0.26 | 0.04 |
| BA6 | 0.27 | 0.27 | 0.02 | 0.27 | 0.27 | 0.02 | 0.29 | 0.29 | 0.03 | 0.33 | 0.32 | 0.04 |
| BA9 | 0.29 | 0.29 | 0.02 | 0.21 | 0.21 | 0.05 | 0.32 | 0.32 | 0.03 | 0.26 | 0.26 | 0.02 |
| BA11 | 0.25 | 0.25 | 0.03 | 0.26 | 0.26 | 0.02 | 0.26 | 0.27 | 0.03 | 0.25 | 0.25 | 0.03 |
| BA17 | 0.29 | 0.29 | 0.03 | 0.19 | 0.20 | 0.04 | 0.27 | 0.26 | 0.03 | 0.28 | 0.28 | 0.02 |
| BA19 | 0.30 | 0.29 | 0.02 | 0.27 | 0.28 | 0.01 | 0.35 | 0.35 | 0.02 | 0.31 | 0.31 | 0.02 |
| BA20 | 0.28 | 0.28 | 0.02 | 0.15 | 0.18 | 0.05 | 0.30 | 0.30 | 0.02 | 0.35 | 0.34 | 0.02 |
| BA37 | 0.29 | 0.29 | 0.02 | 0.27 | 0.27 | 0.02 | 0.31 | 0.29 | 0.03 | 0.28 | 0.28 | 0.03 |
| BA38 | 0.27 | 0.27 | 0.02 | 0.30 | 0.30 | 0.03 | 0.28 | 0.28 | 0.04 | 0.36 | 0.36 | 0.02 |
| BA39 | 0.29 | 0.29 | 0.02 | 0.27 | 0.28 | 0.02 | 0.30 | 0.30 | 0.02 | 0.21 | 0.22 | 0.03 |
| BA41 | 0.27 | 0.28 | 0.02 | 0.26 | 0.25 | 0.03 | 0.33 | 0.33 | 0.02 | 0.34 | 0.33 | 0.04 |
| BA44 | 0.28 | 0.28 | 0.02 | 0.29 | 0.28 | 0.06 | 0.26 | 0.26 | 0.04 | 0.29 | 0.30 | 0.03 |
| BA46 | 0.31 | 0.31 | 0.04 | 0.24 | 0.23 | 0.02 | 0.27 | 0.27 | 0.02 | 0.27 | 0.28 | 0.03 |
| TH | 0.14 | 0.14 | 0.02 | 0.29 | 0.29 | 0.02 | 0.23 | 0.23 | 0.02 | 0.23 | 0.23 | 0.01 |
| CN | 0.30 | 0.30 | 0.02 | 0.26 | 0.25 | 0.04 | 0.35 | 0.36 | 0.01 | 0.27 | 0.27 | 0.02 |
| HC | 0.26 | 0.26 | 0.04 | 0.23 | 0.24 | 0.03 | 0.24 | 0.24 | 0.04 | 0.24 | 0.24 | 0.04 |
| CB | 0.20 | 0.21 | 0.03 | 0.22 | 0.22 | 0.02 | 0.21 | 0.22 | 0.04 | 0.23 | 0.22 | 0.03 |
| MB | 0.28 | 0.30 | 0.06 | 0.18 | 0.19 | 0.03 | 0.15 | 0.14 | 0.02 | 0.13 | 0.14 | 0.02 |
| PO | 0.35 | 0.35 | 0.03 | 0.21 | 0.20 | 0.04 | 0.20 | 0.23 | 0.08 | 0.19 | 0.20 | 0.06 |
| MD | 0.25 | 0.27 | 0.06 | 0.18 | 0.19 | 0.04 | 0.23 | 0.25 | 0.08 | 0.18 | 0.19 | 0.04 |

**Table B.6** Gender differences for PSD-95 synaptic parameters in 16 control human control hippocampal subregions

| | Women | | Men | | |
|---|---|---|---|---|---|
| **Region** | **Mean** | **SD** | **Mean** | **SD** | ***p* value** |
| **PSD95 Density** | | | | | |
| CA1-SML | 73.700 | 7.807 | 78.807 | 11.601 | 0.399 |
| CA1-SO | 73.313 | 3.002 | 72.504 | 9.018 | 0.851 |
| CA1-SP | 80.126 | 7.553 | 86.138 | 10.961 | 0.300 |
| CA1-SR | 77.729 | 7.687 | 83.873 | 12.428 | 0.340 |
| CA2-SML | 73.108 | 9.156 | 78.824 | 12.585 | 0.392 |
| CA2-SO | 76.357 | 5.923 | 79.816 | 9.191 | 0.467 |
| CA2-SP | 81.573 | 5.358 | 86.004 | 14.630 | 0.532 |
| CA2-SR | 75.865 | 7.037 | 82.006 | 11.060 | 0.288 |
| CA3-SL | 78.839 | 6.132 | 81.561 | 12.070 | 0.650 |
| CA3-SML | 60.732 | 8.755 | 71.279 | 18.285 | 0.253 |
| CA3-SO | 76.359 | 5.683 | 78.011 | 5.176 | 0.590 |
| CA3-SP | 81.751 | 6.113 | 85.397 | 10.817 | 0.505 |
| CA4 | 84.908 | 6.070 | 85.369 | 8.607 | 0.918 |
| DG-PL | 43.748 | 3.934 | 40.320 | 4.721 | 0.195 |
| DG-SG | 52.661 | 7.193 | 57.341 | 16.320 | 0.559 |
| DG-SM | 66.434 | 12.84 | 69.021 | 18.779 | 0.790 |
| **PSD95 Intensity** | | | | | |
| CA1-SML | 34345 | 2676 | 35883 | 4998 | 0.539 |
| CA1-SO | 25849 | 2818 | 26929 | 5590 | 0.700 |
| CA1-SP | 35910 | 2011 | 36639 | 5650 | 0.788 |
| CA1-SR | 32654 | 1952 | 34311 | 3662 | 0.371 |
| CA2-SML | 25469 | 3149 | 28834 | 4955 | 0.199 |
| CA2-SO | 20843 | 3614 | 25782 | 3595 | **0.030*** |
| CA2-SP | 30702 | 3096 | 31882 | 5190 | 0.654 |
| CA2-SR | 25026 | 3715 | 27848 | 4577 | 0.263 |
| CA3-SL | 24548 | 3580 | 29294 | 4588 | 0.070 |
| CA3-SML | 20549 | 1157 | 26085 | 7084 | 0.114 |
| CA3-SO | 22042 | 4067 | 25331 | 3485 | 0.136 |
| CA3-SP | 27161 | 3184 | 29705 | 4979 | 0.327 |
| CA4 | 25077 | 2892 | 29841 | 5952 | 0.122 |
| DG-PL | 25412 | 2949 | 26737 | 4556 | 0.577 |
| DG-SG | 28686 | 2685 | 29398 | 5573 | 0.795 |
| DG-SM | 30327 | 2853 | 33016 | 4774 | 0.277 |
| **PSD95 Size** | | | | | |
| CA1-SML | 0.1334 | 0.0034 | 0.1296 | 0.0075 | 0.309 |
| CA1-SO | 0.1274 | 0.0060 | 0.1263 | 0.0105 | 0.837 |
| CA1-SP | 0.1263 | 0.0048 | 0.1204 | 0.0081 | 0.165 |
| CA1-SR | 0.1239 | 0.0061 | 0.1226 | 0.0077 | 0.745 |
| CA2-SML | 0.1317 | 0.0052 | 0.1291 | 0.0071 | 0.483 |
| CA2-SO | 0.1271 | 0.0094 | 0.1245 | 0.0096 | 0.639 |
| CA2-SP | 0.1250 | 0.0041 | 0.1168 | 0.0079 | 0.054 |
| CA2-SR | 0.1264 | 0.0055 | 0.1227 | 0.0063 | 0.291 |
| CA3-SL | 0.1218 | 0.0015 | 0.1156 | 0.0103 | 0.206 |
| CA3-SML | 0.1104 | 0.0168 | 0.1126 | 0.0195 | 0.834 |
| CA3-SO | 0.1248 | 0.0038 | 0.1250 | 0.0128 | 0.974 |
| CA3-SP | 0.1158 | 0.0079 | 0.1167 | 0.0091 | 0.862 |
| CA4 | 0.1237 | 0.0066 | 0.1206 | 0.0081 | 0.469 |
| DG-PL | 0.1223 | 0.0054 | 0.1230 | 0.0071 | 0.846 |
| DG-SG | 0.1210 | 0.0063 | 0.1210 | 0.0082 | 0.915 |
| DG-SM | 0.1240 | 0.0063 | 0.1215 | 0.0062 | 0.416 |

Table of means, standard deviations and $p$ values for comparison of PSD-95 synaptic puncta densities, intensities and sizes between genders for 16 hippocampal subregions. Statistical comparisons between the two genders (women vs men) were performed using the unpaired Student t test. PSD-95 synaptic density is expressed in puncta per 100 $\mu m^2$, intensity in arbitrary units and size in $\mu m^2$.

**Table B.7** Gender differences for PSD-95 synaptic and neuronal densities in human control hippocampus

| **PSD-95** | **Density** | | | | |
|---|---|---|---|---|---|
| | Women | | Men | | |
| Region | Mean | SD | Mean | SD | *p* |
| CA1-SP | 82.73 | 5.12 | 80.07 | 11.96 | 0.74 |
| CA2-SP | 83.92 | 3.46 | 78.06 | 16.31 | 0.58 |
| CA3-SP | 84.12 | 0.79 | 80.04 | 13.18 | 0.62 |
| **Neuronal** | **Density** | | | | |
| | Women | | Men | | |
| Region | Mean | SD | Mean | SD | *p* |
| CA1-SP | 60.57 | 6.83 | 65.86 | 21.39 | 0.70 |
| CA2-SP | 90.92 | 7.28 | 93.96 | 17.71 | 0.79 |
| CA3-SP | 67.04 | 8.38 | 80.76 | 16.79 | 0.27 |

Table of means, standard deviations and p values for comparison of PSD-95 synaptic puncta densities and neuronal densities between genders. Data is based on a subgroup of cases also analysed using stereology for neuronal densities counts. Three cases for each gender were included as follows: women (SD10/15, SD63/13 and SD35/14) and men (SD23/13, SD24/15 and SD32/13). Statistical comparisons between the two genders (women vs. men) were performed using the unpaired Student t test. The hippocampal subregions analysed were the stratum pyramidale from CA1, CA2 and C3 (CA1-SP, CA2-SP and CA3-SP). PSD-95 synaptic density is expressed in puncta per 100 $\mu m^2$ and neuronal density in number of neurons x1000 per $mm^3$. Abbreviation: CA-SP, Cornu Ammonis - Stratum Pyramidale; SD, Standard Deviation.

**Table B.8** Left/right asymmetry differences for PSD-95 synaptic parameters in 16 control human control hippocampal subregions

| | Left | | Right | | |
|---|---|---|---|---|---|
| **Region** | **Mean** | **SD** | **Mean** | **SD** | ***p* value** |
| **PSD95 Density** | | | | | |
| CA1-SML | 70.610 | 5.902 | 81.762 | 10.715 | 0.410 |
| CA1-SO | 70.771 | 8.195 | 74.308 | 6.653 | 0.374 |
| CA1-SP | 78.924 | 7.140 | 87.790 | 10.563 | 0.603 |
| CA1-SR | 76.292 | 6.610 | 85.718 | 12.365 | 0.603 |
| CA2-SML | 68.765 | 8.06 | 82.795 | 10.055 | 0.759 |
| CA2-SO | 73.450 | 7.970 | 82.427 | 6.102 | 0.757 |
| CA2-SP | 78.259 | 7.180 | 89.043 | 13.276 | 0.480 |
| CA2-SR | 72.754 | 7.735 | 85.106 | 8.242 | 0.715 |
| CA3-SL | 75.712 | 7.001 | 84.245 | 10.988 | 0.343 |
| CA3-SML | 68.694 | 11.391 | 66.625 | 19.548 | 0.352 |
| CA3-SO | 74.528 | 4.735 | 79.590 | 4.663 | 0.758 |
| CA3-SP | 78.093 | 7.628 | 88.596 | 8.098 | 0.643 |
| CA4 | 81.954 | 8.118 | 87.641 | 6.550 | 0.350 |
| DG-PL | 43.853 | 4.820 | 39.811 | 3.887 | 0.182 |
| DG-SG | 49.767 | 6.660 | 60.095 | 16.126 | 0.574 |
| DG-SM | 58.642 | 11.093 | 75.188 | 16.684 | 0.928 |
| **PSD95 Intensity** | | | | | |
| CA1-SML | 33679 | 5707 | 36575 | 2522 | 0.791 |
| CA1-SO | 23713 | 4546 | 28666 | 3743 | 0.723 |
| CA1-SP | 35059 | 6647 | 37369 | 2206 | 0.658 |
| CA1-SR | 32854 | 4133 | 34368 | 2333 | 0.411 |
| CA2-SML | 24413 | 2839 | 30047 | 4198 | 0.555 |
| CA2-SO | 21834 | 4411 | 25656 | 3519 | 0.363 |
| CA2-SP | 30367 | 5780 | 32281 | 3354 | 0.407 |
| CA2-SR | 24619 | 4898 | 28506 | 3309 | 0.963 |
| CA3-SL | 26026 | 6163 | 28779 | 3299 | 0.540 |
| CA3-SML | 22947 | 5921 | 24978 | 6718 | 0.886 |
| CA3-SO | 22078 | 4338 | 25715 | 2894 | 0.326 |
| CA3-SP | 27474 | 5637 | 29788 | 3432 | 0.506 |
| CA4 | 26816 | 7193 | 29133 | 4012 | 0.925 |
| DG-PL | 24454 | 3968 | 27622 | 3652 | 0.822 |
| DG-SG | 29770 | 6632 | 28674 | 2800 | 0.231 |
| DG-SM | 30778 | 5839 | 33014 | 2687 | 0.997 |
| **PSD95 Size** | | | | | |
| CA1-SML | 0.1315 | 8.50E-3 | 0.1305 | 5.00E-3 | 0.215 |
| CA1-SO | 0.1277 | 8.69E-3 | 0.1260 | 9.59E-3 | 0.549 |
| CA1-SP | 0.1265 | 7.30E-3 | 0.1194 | 6.30E-3 | 0.294 |
| CA1-SR | 0.1283 | 7.10E-3 | 0.1189 | 3.30E-3 | 0.937 |
| CA2-SML | 0.1321 | 4.59E-3 | 0.1285 | 7.40E-3 | 0.733 |
| CA2-SO | 0.1290 | 3.80E-3 | 0.1226 | 1.12E-2 | 0.946 |
| CA2-SP | 0.1223 | 7.79E-3 | 0.1177 | 7.70E-3 | 0.188 |
| CA2-SR | 0.1254 | 3.50E-3 | 0.1229 | 7.49E-3 | 0.393 |
| CA3-SL | 0.1213 | 6.89E-3 | 0.1150 | 9.29E-3 | 0.659 |
| CA3-SML | 0.1233 | 1.78E-2 | 0.1033 | 1.32E-2 | 0.793 |
| CA3-SO | 0.1287 | 1.05E-2 | 0.1221 | 9.79E-3 | 0.596 |
| CA3-SP | 0.1218 | 8.00E-3 | 0.1124 | 6.49E-3 | 0.380 |
| CA4 | 0.1255 | 7.79E-3 | 0.1189 | 6.30E-3 | 0.963 |
| DG-PL | 0.1274 | 6.40E-3 | 0.1193 | 3.59E-3 | 0.645 |
| DG-SG | 0.1255 | 7.79E-3 | 0.1178 | 5.19E-3 | 0.764 |
| DG-SM | 0.1255 | 6.40E-3 | 0.1203 | 5.30E-3 | 0.639 |

Table of means, standard deviations and $p$ values for comparison of PSD-95 synaptic puncta densities, intensities and sizes between left/right side for 16 hippocampal subregions. Statistical comparisons between the two sides (left vs. right) were performed using the unpaired Student t test. PSD-95 synaptic density is expressed in puncta per 100 $\mu$m$^2$, intensity in arbitrary units and size in $\mu$m$^2$.

**Table B.9** Left/right asymmetry differences for PSD-95 synaptic and neuronal densities in human control hippocampus

| **PSD-95** | **Density** | | | | |
|---|---|---|---|---|---|
| | Left | | Right | | |
| Region | Mean | SD | Mean | SD | *p* |
| CA1-SP | 82.03 | 7.04 | 81.08 | 9.980 | 0.91 |
| CA2-SP | 82.38 | 3.13 | 80.30 | 14.05 | 0.85 |
| CA3-SP | 83.67 | 0.01 | 81.29 | 11.05 | 0.79 |
| **Neuronal** | **Density** | | | | |
| | Left | | Right | | |
| Region | Mean | SD | Mean | SD | *p* |
| CA1-SP | 58.88 | 8.72 | 65.39 | 17.49 | 0.66 |
| CA2-SP | 90.38 | 10.2 | 93.47 | 14.49 | 0.81 |
| CA3-SP | 62.20 | 0.42 | 79.75 | 13.86 | 0.17 |

Table of means, standard deviations and p values for comparison of PSD-95 synaptic puncta densities and neuronal densities between left/right side. Data is based on a subgroup of cases also analysed using stereology for neuronal densities counts. Two cases for left and four cases for right were included as follows: left (SD63/13 and SD35/14) and right (SD23/13, SD10/15, SD24/15 and SD32/13). Statistical comparisons between the two sides (left vs right) were performed using the unpaired Student t test. The hippocampal subregions analysed were the stratum pyramidale from CA1, CA2 and C3 (CA1-SP, CA2-SP and CA3-SP). PSD-95 synaptic density is expressed in puncta per 100 $\mu m^2$ and neuronal density in number of neurons x1000 per $mm^3$. Abbreviation: CA-SP, Cornu Ammonis - Stratum Pyramidale; SD, Standard Deviation.

**Table B.10** Summary of hippocampal PSD-95 puncta parameters data

| **Density** | | | | | | | | |
|---|---|---|---|---|---|---|---|---|
| **Group** | **n** | **mean** | **sd** | **min** | **Q1** | **median** | **Q3** | **max** |
| Control | 14 | 74.6984 | 8.3108 | 64.5289 | 69.5388 | 75.2706 | 75.8744 | 97.9048 |
| Early AD | 10 | 47.4157 | 2.7207 | 45.1569 | 46.1534 | 46.6021 | 46.8109 | 53.7148 |
| Late AD | 8 | 25.8597 | 3.0834 | 20.2957 | 24.9608 | 25.8980 | 27.7170 | 30.3009 |
| **Intensity** | | | | | | | | |
| **Group** | **n** | **mean** | **sd** | **min** | **Q1** | **median** | **Q3** | **max** |
| Control | 14 | 28886.8 | 3873.3 | 23711.7 | 26208.2 | 28831.5 | 29578.5 | 36796.8 |
| Early AD | 10 | 20608.0 | 1600.8 | 19257.7 | 19944.2 | 19996.9 | 20449.5 | 24901.8 |
| Late AD | 8 | 12726.4 | 3554.7 | 8436.9 | 10820.5 | 11642.9 | 14290.8 | 19147.3 |
| **Size** | | | | | | | | |
| **Group** | **n** | **mean** | **sd** | **min** | **Q1** | **median** | **Q3** | **max** |
| Control | 14 | 0.12259 | 0.00627 | 0.11009 | 0.11827 | 0.12272 | 0.12729 | 0.13286 |
| Early AD | 10 | 0.08948 | 0.00328 | 0.08560 | 0.08709 | 0.08885 | 0.09172 | 0.09540 |
| Late AD | 8 | 0.10072 | 0.00751 | 0.09056 | 0.09599 | 0.10053 | 0.10410 | 0.11347 |

**Table B.11** Dunn Kruskal-Wallis multiple comparison p-values adjusted with the Bonferroni method for hippocampal data

| **Density** | | | | | | |
|---|---|---|---|---|---|---|
| **Groups** | **Compared** | | | **Z** | **P.unadj** | **P.adj** |
| Control | vs. | Early | AD | 3.089572 | 2.004452e-03 | *6.013355e-03** |
| Control | vs. | Late | AD | 5.050980 | 4.395496e-07 | *1.318649e-06** |
| Early AD | vs. | Late | AD | 2.022600 | 4.311445e-02 | 1.293433e-01 |
| **Intensity** | | | | | | |
| **Groups** | **Compared** | | | **Z** | **P.unadj** | **P.adj** |
| Control | vs. | Early | AD | 2.957433 | 3.102124e-03 | *9.306373e-03** |
| Control | vs. | Late | AD | 4.999897 | 5.736083e-07 | *1.720825e-06** |
| Early AD | vs. | Late | AD | 2.090211 | 3.659884e-02 | 1.097965e-01 |
| **Size** | | | | | | |
| **Groups** | **Compared** | | | **Z** | **P.unadj** | **P.adj** |
| Control | vs. | Early | AD | 5.027910 | 4.958533e-07 | *1.487560e-06** |
| Control | vs. | Late | AD | 2.718767 | 6.552571e-03 | *1.965771e-02** |
| Early AD | vs. | Late | AD | -1.848431 | 6.453998e-02 | 1.936199e-01 |